

Physiological Non-Newtonian Blood Flow through Single Stenosed Artery

Khairuzzaman Mamun^{1, a)}, Mohammad Matiur Rahman^{1, b)}, Most. Nasrin Akhter^{1, c)}
and Mohammad Ali^{2, d)}

¹Department of Mathematics, Dhaka University of Engineering and Technology, Gazipur-1700, Bangladesh

²Department of Mechanical Engineering, Bangladesh University of Engineering and Technology, Dhaka-1000, Bangladesh

^{a)}Corresponding author: presidentmamun@gmail.com

^{b)} matiurrahman1975@gmail.com

^{c)} nasrin6092002@yahoo.com

^{d)} mali_buet@yahoo.com

Abstract. A numerical simulation to investigate the Non-Newtonian modelling effects on physiological flows in a three dimensional idealized artery with a single stenosis of 85% severity. The wall vessel is considered to be rigid. Oscillatory physiological and parabolic velocity profile has been imposed for inlet boundary condition. Where the physiological waveform is performed using a Fourier series with sixteen harmonics. The investigation has a Reynolds number range of 96 to 800. Low Reynolds number $k - \omega$ model is used as governing equation. The investigation has been carried out to characterize two Non-Newtonian constitutive equations of blood, namely, (i) Carreau and (ii) Cross models. The Newtonian model has also been investigated to study the physics of fluid. The results of Newtonian model are compared with the Non-Newtonian models. The numerical results are presented in terms of pressure, wall shear stress distributions and the streamlines contours. At early systole pressure differences between Newtonian and Non-Newtonian models are observed at pre-stenotic, throat and immediately after throat regions. In the case of wall shear stress, some differences between Newtonian and Non-Newtonian models are observed when the flows are minimum such as at early systole or diastole.

INTRODUCTION

The physiology of the cardiovascular system was studied step by step through many years. The role of the blood vessels has already been identified, when it was realized that the arteries and veins have different roles. Arteries carry blood with oxygen red blood cells, oxygen, white blood cells, nutrients, and other vital substances that the body requires from heart out to body, while veins carry blood with Carbon dioxide and various devoid of substance from body to heart. Arteries are strong, flexible blood vessels that are able to expand and contract. They expand as your heart beats, and contract between heartbeats. Veins are less flexible than arteries. Arteries contain endothelium, a thin layer of cells that keeps the artery smooth and allows blood to flow easily. Atherosclerosis starts when the endothelium becomes damaged, allowing Lower Density Lipoprotein (LDL cholesterol) to accumulate in the artery wall. The body sends macrophage white blood cells to clean up the cholesterol, but sometimes the cells get stuck there at the affected site. Over time this results in plaque being built up, consisting of bad cholesterol (LDL cholesterol) and macrophage white blood cells. This can cause severe diseases such as the development of atherosclerosis. As a result the arterial wall loses its elastic property which limits the area of blood flow. This narrowing of the artery is called arterial stenosis.

The comparison of stenosed flow behaviour with the normal one can provide the proper understanding of underlying mechanism behind the development of atherosclerosis. The flow turns to be abnormal in the reduced cross sectional area of the artery stated by Kader and Shenory [1]. The flow behaviour in the stenosed artery is quite different in comparison to the normal one. Stress and resistance to flow is much higher in stenosed artery. Chua and Shread [3] found that the flow through the constricted tube is characterized by high velocity jet generated at constricted region. Kader and Shenory [1] found the results from numerical simulation which demonstrated that velocity and stenotic jet length increases in increasing the severity of stenosis. Their results also demonstrate that the 3D stenotic CFD model is capable of predicting the changes in flow behaviour for increased severity of stenosis. Young et al. [4] studied the wall shear stress and pressure gradient in the stenosis and evaluated the cause of plaque rupture. The authors studied pulsatile blood flow through the stenosis with elastic wall to observe the lumen movement. According to their study the peak WSS occurred just before minimum lumen position. Pinto et al. [5] performed numerical simulation assuming a physiological pulsatile flow through different models of stenosis. In case of subject-specific anatomically realistic stenosed carotid bifurcation subjected to pulsatile inlet condition, the simulation results demonstrated the rapid fluctuation of velocity and pressure in post-stenotic region by S. Lee and S. Lee [7]. Ahmed and Giddens [6] studied both steady and pulsatile flow through 25%, 50% and 75% constriction of a rigid tube where Reynolds number ranged from 500 to 2000. In another study, the stenosis having different geometric profiles like trapezium, semi-ellipse and triangle were analyzed considering the Non-Newtonian behaviour by Lorenzini and Casalena [8]. The authors investigated that the length of flow disturbance is due to stenotic shape, downstream disturbance is due to stenotic walls and peak velocity depends on the shape of stenosis.

A number of studies were done to observe the effect of stenosis when blood flows through the stenosis of the artery, assuming blood as Newtonian. But the assumption of Newtonian behaviour of blood is acceptable for flow in large arteries, and of high Reynolds number and high shear rate stated by Rabby et al [2]. In case of pulsatile blood flow there are some moments (like diastole, early systole) when blood flow has low Reynolds number. Again in various arteries there are some constrictions called stenosis where blood flow has low Reynolds number or low shear rate. But when shear rate is low (less than 100 s^{-1}), the Non-Newtonian behaviour of blood flow is acceptable stated by Rabby et al [2]. It was also revealed that some diseased condition like severe myocardial infarction, cerebrovascular diseases and hypertension, blood exhibits remarkable Non-Newtonian properties by Chien[9]. According to Berger and Jou [10], if the shear rate is high, the blood behaves like a Newtonian fluid whose viscosity be $0.00345 \text{ Pa}\cdot\text{s}$. However, if the Reynolds number or shear rate of blood flow falls down due to various diseased conditions, its viscosity increases and blood exhibits Non-Newtonian property. In most cases, though, Non-Newtonian blood models would provide a more accurate representation of blood flow behavior within the arteries of interest, particularly for stenosed conditions. Studies had documented three types of Non-Newtonian blood properties: thixotropy, viscoelasticity and shear thinning. Thixotropy is a transient property of blood, which is exhibited at low shear rates and has a fairly long time scale. Mandal[11] suggested that this indicates a secondary importance in physiological blood flow. Mandal further explained, based on the research by Thurston [12, 13], that blood contains a number of particles and cells suspended within the flow that interact with each other significantly as to complicate two-phase modelling. Blood therefore exhibits significant viscoelastic properties, which is also a transient condition at the frequency range of common physiological condition. This has attracted significant research interest trying to determine useful mechanical properties to be employed in analytical calculations and simulations. Mandal [11], noted that the viscoelastic property of blood diminishes vary rapidly as shear rate rises. At physiological hematocrit values, which is the volume fraction of red blood cells in whole blood, this effect is not significant, suggesting that this Non-Newtonian behavior is of secondary importance for normal pulsatile blood flow. Mandal[11] therefore concluded that shear thinning is the dominant characteristic of blood. Studies had therefore attempted to fit experimentally measured blood flow behavior to shear thinning equations with modifications to take into account the hematocrit values in Cho and Kensey[14]; Walawender et al [15]; Cokelet et al [16]; Powell and Eyring[17]. A common property of these shear thinning equations was that the effective viscosity of the blood drops in regions of high shear rates and vice versa. From these studies several models were derived and validated against experimentally derived blood flow properties.

This study aims to incorporate the Newtonian & Non-Newtonian pulsatile flow through single stenosis to investigate the flow characteristics. Two Non-Newtonian models have been investigated, Carreau model and cross model, to determine their respective Non-Newtonian influences. Finally, an attempt has been made in this study to demonstrate the significant changes of flow behavior through the stenotic arteries.

MODEL DESCRIPTION

Geometry

Three dimensional stenotic arteries are used as geometry for this study shown in Fig. 1 (a). For this study, 85% stenotic artery (by area) is taken as geometry. The geometry of generated model in this study has a diameter (D) of 6 mm and a length (L) of 96 mm, where the length of pre stenotic, throat and post stenotic region are 4D, 2D and 10D respectively. The wall is considered to be rigid. The flow field mesh consists of 45496 nodes and 95592 elements for the geometry. Figure 1(b) shows the mesh in cross sectional inflow plane of the stenotic artery.

Blood Properties

Blood is taken as fluid where the blood is considered incompressible. The density of the blood is 1050kg/m^3 . In a Newtonian model for the blood viscosity, the value of μ is treated as a constant usually set to $\mu = 3.45 \times 10^{-3}\text{Pa}\cdot\text{s}$. But when blood is considered non-Newtonian fluid then the viscosity of the blood is calculated from two models such as Carreau model and cross model.

Cross Model for the Non-Newtonian Blood Viscosity

For non-Newtonian fluid Malcolm M. Cross [20] proposed a shear rate dependent viscosity model called Cross model. The Cross model is defined by-

$$\mu = \mu_{\infty} + (\mu_0 - \mu_{\infty}) \left[1 + \left(\frac{|\dot{\gamma}|}{\gamma_c} \right)^m \right]^{-1}$$

Where, $\mu_0 = 0.0364\text{Pa}\cdot\text{s}$ is the usual molecular blood viscosity when very zero shear rates, $\gamma_c = 2.63\text{ s}^{-1}$ is the reference shear rate, $\dot{\gamma}$ is the instantaneous shear rate, and $m=1.45$ is the constant.

Carreau Model

The Carreau model was proposed by Pierre Carreau [21] is defined by-

$$\mu = \mu_{\infty} + (\mu_0 - \mu_{\infty}) [1 + (\gamma_c \dot{\gamma})^2]^{n-1/2}$$

where $\mu_{\infty} = 0.00345\text{Pa}\cdot\text{s}$, $\mu_0 = 0.056\text{Pa}\cdot\text{s}$, $\gamma_c = 3.313\text{s}$, $\dot{\gamma}$ is the instantaneous shear rate, and $n=0.3568$.

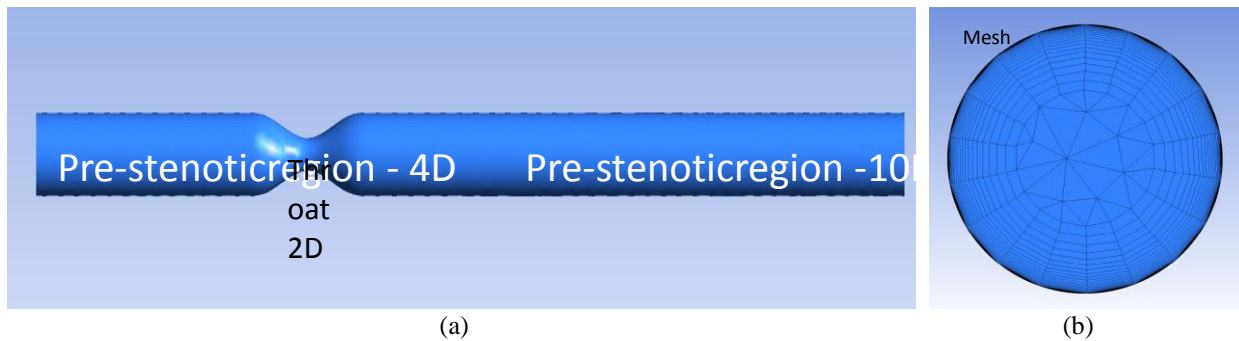


FIGURE 1. (a) Model of a stenotic artery; (b) mesh in cross sectional plane of a stenotic artery.

COMPUTATIONAL DETAILS

Governing Equation

Due to constriction, blood passes through the throat and post stenotic region with high velocity. Flow velocity at post stenotic region increases but pressure of that region decreases. So, moderate and severe arterial stenosis restricts the flow severely with creating turbulent flow characteristics. For this region, turbulent flow is expected at post stenotic region especially for 85% stenotic artery. Neither laminar flow modeling nor standard two-equation models are suitable for this kind of blood flow. So, Wilcox low-Re turbulence model is more acceptable for flow analysis found by Varghese and Frankel [19]. Therefore, low Re $k - \omega$ turbulent mode is taken for calculation.

Now, the Navier-Stokes equation can be given by-

$$\frac{\partial u_i}{\partial x_i} = 0 \quad (1)$$

$$\frac{\partial u_i}{\partial t} + u_j \frac{\partial u_i}{\partial x_j} = -\frac{1}{\rho} \frac{\partial p}{\partial x_i} + \frac{\partial^2 u_i}{\partial x_j \partial x_j} \quad (2)$$

Since each term of this equation is time averaged, the equation is referred to as a Reynolds averaged Navier-Stokes (RANS) equation. During this procedure, several additional unknown parameters appear which require additional equations to be introduced as turbulence models. The set of RANS equations are-

$$\frac{\partial p}{\partial t} + \frac{\partial(\rho u_i)}{\partial x_i} = 0 \quad (3)$$

$$\frac{\partial(\rho u_i)}{\partial t} + \frac{\partial(\rho u_i u_j)}{\partial x_j} = -\frac{\partial p}{\partial x_i} + \frac{\partial}{\partial x_j} \left[\mu \left(\frac{\partial u_i}{\partial x_j} + \frac{\partial u_j}{\partial x_i} - \frac{2}{3} \delta_{ij} \left(\frac{\partial u_k}{\partial x_k} \right) \right) \right] + \frac{\partial}{\partial t} (-\overline{\rho u_i' u_j'}) \quad (4)$$

In this equation $(-\overline{\rho u_i' u_j'})$ is an additional term known as the Reynolds's stress tensor, which can be approximated by using Boussinesq's hypothesis-

$$-\overline{\rho u_i' u_j'} = \mu_t \left(\frac{\partial u_i}{\partial x_j} + \frac{\partial u_j}{\partial x_i} \right) - \frac{2}{3} \left(\rho k + \mu_t \frac{\partial u_k}{\partial x_k} \right) \quad (5)$$

Eddy viscosity can be modelled as a function of the turbulence kinetic energy (k) and specific dissipation rate (ω); therefore it is referred to as the two-equation turbulent model.

The turbulence kinetic energy k and specific dissipation rate ω of standard $k - \omega$ model are determined by following two equations:

$$\text{The } k \text{ equation: } \quad \frac{\partial}{\partial t} (\rho k) + \frac{\partial}{\partial x_i} (\rho k u_i) = \frac{\partial}{\partial x_j} \left(\Gamma_k \frac{\partial k}{\partial x_j} \right) + G_k - Y_k + S_k \quad (6)$$

$$\text{The } \omega \text{ equation: } \quad \frac{\partial}{\partial t} (\rho \omega) + \frac{\partial}{\partial x_i} (\rho \omega u_i) = \frac{\partial}{\partial x_j} \left(\Gamma_\omega \frac{\partial \omega}{\partial x_j} \right) + G_\omega - Y_\omega + S_\omega \quad (7)$$

In these equations, G_k represents the generation of turbulence kinetic energy due to mean velocity gradients. G_ω represents the generation of ω . Γ_k and Γ_ω represent the effective diffusivity of k and ω , respectively. Y_k and Y_ω represent the dissipation of k and ω due to turbulence. S_k and S_ω are user-defined source terms.

A low Reynolds number correction factor controls the influence on the overall structure of the flow field, depending upon local conditions, and it is given as-

$$\alpha^* = \alpha_\infty^* \left(\frac{\alpha_\infty^* + Re_t/R_k}{1 + Re_t/R_k} \right) \quad (8)$$

Where, $Re_t = \frac{\rho k}{\mu \omega}$, $R_k = 6$, $\alpha_0^* = \frac{\beta_i}{3}$, $\beta_i = 0.072$, $\alpha_\infty^* = 1$. Closure Coefficient for the Transitional $k - \omega$ Model are- $\alpha_\infty^* = 1$, $\alpha_\infty = 0.52$, $\alpha_0 = 0.11111$, $\beta_\infty^* = 0.09$, $\beta_i = 0.072$, $R_k = 6$, and $R_\beta = 8$

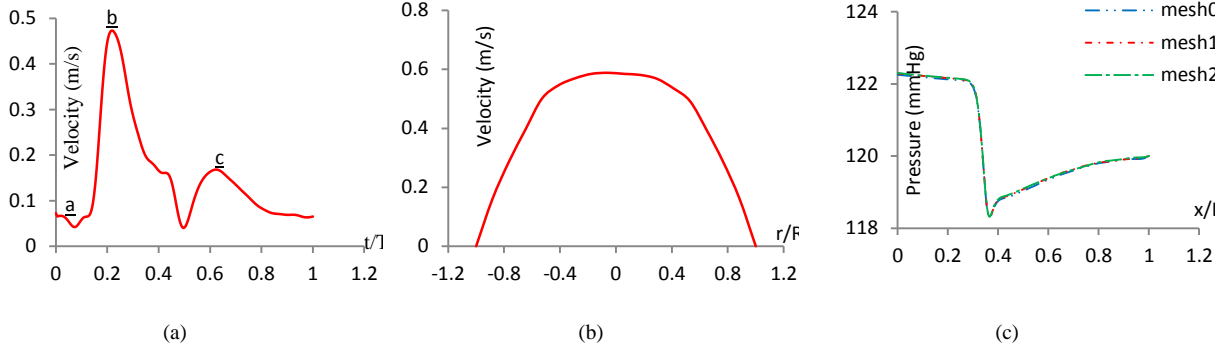


FIGURE 2. (a) Oscillatory physiological waveform, (b) parabolic inlet velocity profile, and (c) pressure distribution in 65% stenotic artery from different mesh sizes.

Boundary Condition

Since the blood flow through arterial stenosis is an unsteady phenomenon and the blood flow to be fully developed at inlet region, Oscillatory physiological parabolic velocity profile has been imposed for inlet boundary condition. For this purpose an user defined function has been written in C++ programming language to demonstrate the unsteady parabolic nature of velocity profile using the relation given by the following equations, $u_x = u \left(1 - \frac{y^2+z^2}{radius^2} \right)$, where $u = \sum_{n=0}^{n=16} (A_n \cos(\omega t) + B_n \sin(\omega t))$. A_n and B_n are the coefficients.

TABLE 1. Harmonic coefficients for pulsatile waveform shown in figure 2(a).

n	A_n	B_n	n	A_n	B_n	n	A_n	B_n
0	0.166667	0	6	-0.01735	0.01915	12	-0.00341	0.005463
1	-0.03773	0.0985	7	-0.00648	0.002095	13	-0.00194	0.000341
2	-0.10305	0.012057	8	-0.01023	-0.0078	14	-0.00312	-0.00017
3	0.007745	-0.06763	9	0.008628	-0.00663	15	0.000157	-0.00299
4	0.025917	-0.02732	10	0.002267	0.001817	16	0.001531	0.000226
5	0.037317	0.024517	11	0.005723	0.003352			

In this study Reynolds number varies from 96 to 800. Since cardiac pulse cycle is 0.82sec, ω is found from the calculation $\omega = \frac{2\pi}{0.82} = 7.66$ rad/sec. Fig. 2(a) and 2(b) show oscillatory physiological waveform and parabolic inlet velocity profile respectively. In figure 2(a), \underline{a} , \underline{b} , and \underline{c} represent the positions of early systole (0.041sec), peak systole (0.205 sec), and diastole (0.615 sec) respectively.

Numerical Scheme

The numerical simulations are performed by well-known software ANSYS Fluent 14.5. A pressure based algorithm is chosen as the solver type. This solver is generally selected for an incompressible fluid. As there is no heat transfer in the blood flow process, energy equation is not solved. Since turbulent is expected in 85% stenotic artery at post stenotic region, a low Reynolds number $k - \omega$ turbulent model is used throughout the work. In solution methods, the SIMPLE algorithm is selected for pressure-velocity coupling. First Order Upwind scheme is employed as a numerical scheme for discretization of the momentum equation. The time step is set to 0.00041 sec with 2000 number of total time steps. Maximum 10 iterations are performed per each time step.

Grid Independence Check

An extensive test is carried out with different sizes of mesh such as mesh0 (75511 element), mesh1 (82580 element) and mesh2 (90227 element) respectively. Fig 2(c) shows the pressure distributions for 65% stenosis artery

with mentioned mesh sizes. In all cases, the pressure distributions are same. It implies that the solution is grid independence.

RESULTS AND DISCUSSION

The computational results are conducted to study the influence of stenosis on the flow behaviour. The flow parameters like pressure and Wall Shear Stress (WSS) are observed at specific instants of pulse cycle for comparing the flow variation. The discussion is categorized with the observations of flow variation starting from early systole, peak systole and diastole, respectively.

It is known that blood is Bingham plastic fluid. So the viscosity of blood decreases with increase in share rate. When shear rate is greater than 100 then viscosity of blood is constant. The viscosity of Newtonian model is less than that of Non-Newtonian model when shear rate is less than 100, but viscosity of all models is equal when shear rate is equal to or greater than 100. When Reynolds number is very low then pressure and WSS of Newtonian model should be less than that of Non-Newtonian model but opposite scenario should be seen for velocity distribution. Since there are comparatively low Reynolds numbers at early systole and diastole, the results of Newtonian and Non-Newtonian condition should be different at early systole and diastole. On the other hand maximum Reynolds number is seen at peak systole. So the results of Newtonian and Non-Newtonian condition should follow each other at peak systole. Again the velocity of the throat region is high for any time instant. So the results of Newtonian and Non-Newtonian condition should be same at the throat region but different at the pre and post stenotic region. The results of pressure and Wall Shear Stress distribution are discussed with respective figures.

Figure 3, 4, and 5 reveal the centreline pressure distribution for Non-Newtonian (Carreau and Cross) and Newtonian models at early systole, peak systole and diastole respectively. At early systole significant pressure difference between Newtonian and Non-Newtonian models are observed at pre stenotic, throat and post stenotic region. Pressure of the Non-Newtonian (Carreau and cross) models are higher than that of Newtonian model which is natural and meets our expectation. Very small pressure fall at the throat region and very quick recovery of pressure after the throat region are observed. Due to high Reynolds number or high shear rate at peak systole, viscosity of Carreau, Cross and Newtonian model are same. Thus, pressure of the Non-Newtonian (Carreau and Cross) models follow the pressure of the Newtonian model. A very large pressure fall is noticed at the throat region, and it continues after the throat region. So peak systole is very dangerous time instant for 85% stenotic severity. At diastole pressure of the Cross model mostly follow the pressure of the Newtonian model but very little difference is observed in Carreau model. No significant pressure fall is occurred due to very low Reynolds number.

Wall Shear Stress (WSS) is another important parameter to apprehend the condition of severity of arterial stenosis. It is also responsible for the growth of arterial diseases. WSS is defined as $\tau = \mu \frac{du}{dr}$, where μ is the viscosity and $\frac{du}{dr}$ is the velocity gradient. So, WSS of Non-Newtonian fluid depends on the viscosity of the fluid and velocity gradient but WSS of Newtonian fluid does not depend on the viscosity because viscosity is a constant property of Newtonian fluid. Thus the results of WSS for Newtonian and Non-Newtonian model may be different.

Figure 6, 7, and 8 represent the distribution of wall shear stress for Non-Newtonian (Carreau & Cross) and Newtonian model at early systole, peak systole and diastole respectively. The wall shear stress distributions for all models are fairly similar. The difference in WSS magnitude is dependent on Reynolds number; therefore the largest difference occurs during the minimum flow such as early systole or diastole. More critically, at early systole and diastole the Carreau and cross model are found to have a slightly higher wall shear stress distribution than the Newtonian model at the pre and post stenotic regions due to low Reynolds number or high viscosity. This is more noticeable in the regions away from the stenosis. Again results of all models are same at the throat region because of high Reynolds number or low viscosity. At peak systole the results in WSS for all models follow each other because of high Reynolds number.

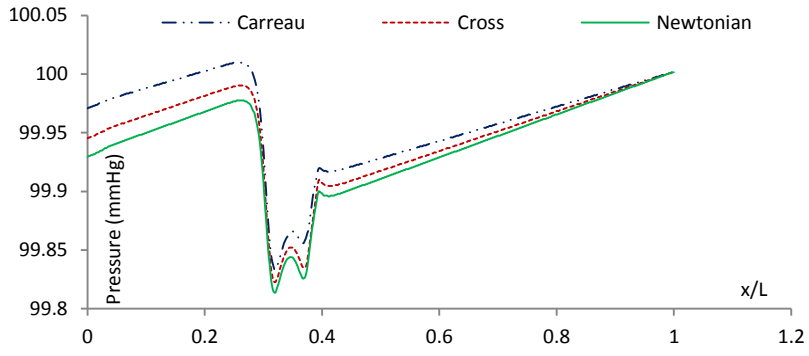


FIGURE 3. Distribution of pressure for Carreau, Cross, and Newtonian model at early systole.

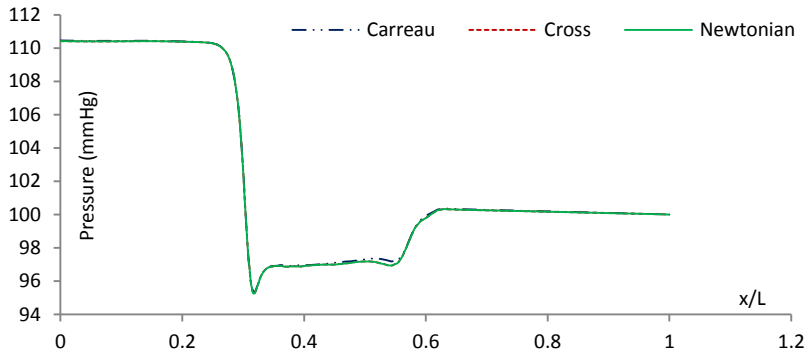


FIGURE 4. Distribution of pressure for Carreau, Cross, and Newtonian model at peak systole.

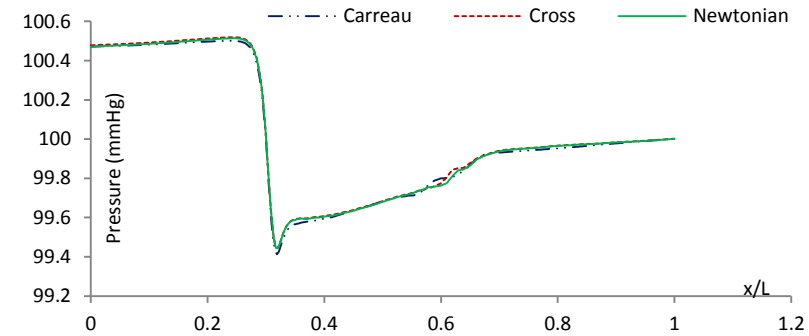


FIGURE 5. Distribution of pressure for Carreau, Cross, and Newtonian model at diastole.

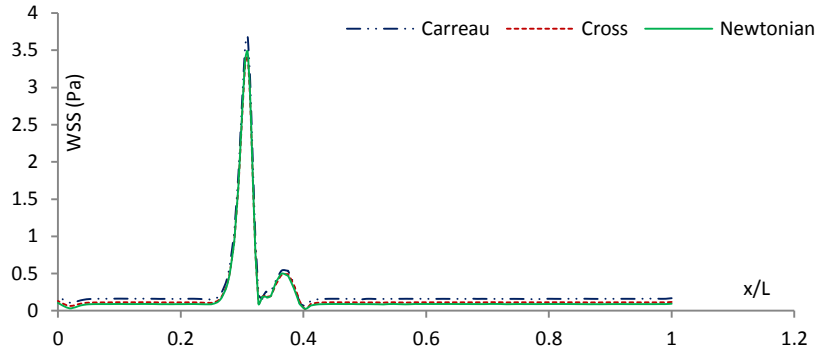


FIGURE 6. Distribution of Wall Shear Stress for Carreau, Cross, and Newtonian model at early systole.

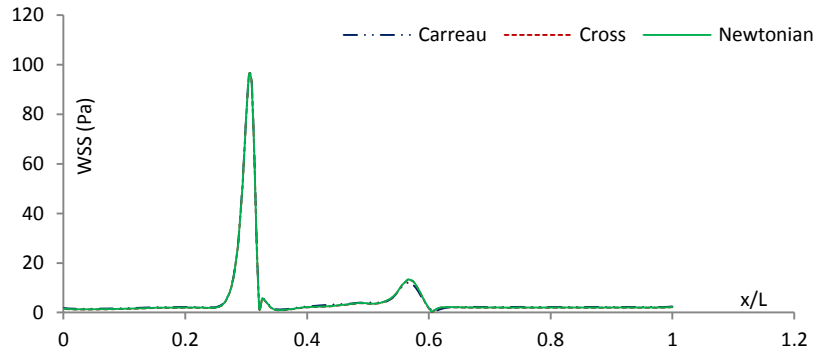


FIGURE 7. Distribution of Wall Shear Stress for Carreau, Cross, and Newtonian model at peak systole.

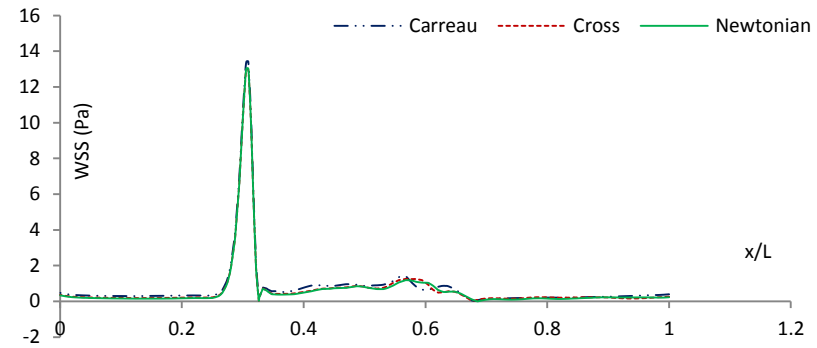


FIGURE 8. Distribution of Wall Shear Stress for Carreau, Cross, and Newtonian model at diastole.

CONCLUSION

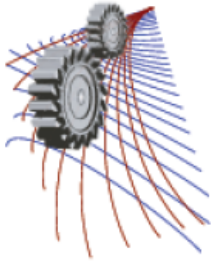
Many studies have been taken experimentally and theoretically treating blood as Newtonian fluid but in this paper blood is assumed as both Newtonian and Non-Newtonian for a comparative study among the model. It is noticed that difference in wall shear stress occurs during the minimum flow such as early systole or diastole due to low Reynolds number. The Non-Newtonian (Carreau & cross) models are found to have a slightly higher wall shear stress distribution than the Newtonian model at the pre and post stenotic regions. At peak systole a very large pressure fall is noticed at the throat region, and it continues after the throat region. So peak systole is very dangerous time instant for 85% stenotic severity. At early systole pressure of the Non-Newtonian (Carreau and cross) models are higher than that of Newtonian model throughout the geometry. At peak systole pressure of the Non-Newtonian (Carreau and Cross) models follow the pressure of the Newtonian model due to high Reynolds number.

Nomenclature

D	Diameter of the healthy artery	x	Axial location of the flow field
L	Length of the artery	g	Acceleration due to gravity
r	Radial location of the flow field	t	Time period of the inlet flow cycle
R	Radius of the healthy artery	u	Instantaneous velocity
U	Average velocity	WSS	Wall shear stress

REFERENCES

1. S. Khader and B. Shenoy, *World Journal of Modelling and Simulation* **7**, 113-122 (2011).
2. M. G. Rabby, A. Razzak, and Md. M. Molla, "Pulsatile non-Newtonian blood flow through a model of arterial stenosis," in *5th BSME International Conference on Thermal Engineering*, edited by A.K.M. Sadrul Islam, Ruhul Amin and Mohammad Ali, (Procedia Engineering, vol. 56, 2013), pp. 225-231.
3. C. Chua, and G. Shread, *The Anziam Journal*, 744–759 (2009).
4. V. Young, A. Patterson M. Graves, Z-Y LI, V. Tavani, T. Tang, and J. H. Gillard, *The British J. of Radiology*, S39-S45 (2009).
5. J. Pinto, K.L. Bessa, D.F. Legendre, and R.H. Mouth, *Physiological pulsatile waveform through axisymmetric stenosed arteries: Numerical Simulation* (ABCM Symposium in Bioengineering, vol. 01, 2006).
6. S.A. Ahmed, and D.P. Giddens, *J. Biomech.* **17**, 695-705 (1984).
7. S. Lee, and S. Lee, *Journal of Biomechanics* **41**, 2551–2561 (2008).
8. G. Lorenzini, and E. Casalena, *Journal of Biomechanics* **41**, 1862–1870 (2008).
9. S. Chien, "Hemorheology in clinical medicine," in *Recent advances in Cardiovascular Diseases 2* (1981), pp. 21.
10. S. A. Bereger and L. D. Jou, "Flows in stenotic vessels," in *Annual Review of Fluid Mechanics* (vol. 32, 2002) pp. 347-382.
11. P. K. Mandal, *International Journal of Non-Linear Mechanics* **40**, 151-164 (2005).
12. G. B. Thurston, *Journal of Biophysics* **12**, 1205-1212 (1972).
13. G. B. Thurston, *Biorheology* **10**, 375-381 (1973).
14. Y. I. Cho and K. R. Kensey, *Biorheology* **28**, 241-262 (1991).
15. W. P. Walawender, T. Y. Chen and D. F. Cala, *Biorheology* **12**, 111-119 (1975).
16. G. R. Cokelet, "Chapter 4 in Biomechanics: Its Functions and Objectives" in *The rheology of the human blood*, edited by Y. C. Fun, N. Perrone, and M. Anliker, (Prentice-Hall, Englewood Cliffs, 1972), pp. 63-103.
17. R. E. Powell and H. Eyring, *Nature* **154**, 427-428 (1944).
18. K. Mamun, M.N. Akhter, M.S.H. Mollah, M.A.N. Sheikh, and M. Ali, "Characteristics of pulsatile blood flow through 3-D geometry of arterial stenosis," in *The 6th BSME International Conference on Thermal Engineering*, edited by A.K.M. Sadrul Islam, M. Ruhul Amin, Mohammad Ali and Toshiaki Setoguchi (Procedia Engineering, vol. 150, 2015), pp. 877-884.
19. S.S. Varghese and S.H. Frankel, *J. Biomech* **125**, 445-460 (2003).
20. M. M. Cross, *Journal of Colloid Science* **20**, 417–437 (1965).
21. PJ Carreau, *Rheological equations from molecular network theories* (Transactions of The Society of Rheology, 1972), pp. 1957-1977.



CFD Analysis of Newly Designed Aerodynamic Shape for a Highway Passenger Bus to Reduce Drag Force

Md. Jahangir Alam^{1, a)} and Mohammad Mamun^{1, b)}

¹*Department of Mechanical Engineering, DUET, Gazipur-1700, Bangladesh*

²*Department of Mechanical Engineering, BUET, Dhaka-1000, Bangladesh*

^{a)}Corresponding author: jahangir@duet.ac.bd

^{b)}mdmamun@me.buet.ac.bd

Abstract. Making aerodynamic improvements of a large passenger vehicle (e.g. bus) is an important field for possible fuel consumption reduction. In this paper, we have focused on designing a new exterior body of a bus that would produce least amount of drag force while keeping its all commercial values unchanged. The CFD tools have been used to assess the quality of the design. Different coefficient values such as drag coefficient and pressure coefficient are obtained from CFD analysis. Key areas of interest for designing outer shape are modification of frontal shape (to reduce stagnation area) and rear end shape (to guide more air into wake region as well as to delay the separation to make the wake region narrower). Exterior shape of the bus (Length-12m, Width-2.6m and Height-4m) is designed by CAD tools. Then that three dimensional model of the bus is simulated for a zero degree yaw angle at a speed of 83 kmph for a Reynolds Number of 6.4 million.. The simulation showed a drag coefficient of 0.25 which is very low compare to any other passenger bus of equal size. Simulation is validated with Ahmad et al. This model is confirmed having 40% less air resistance than currently available bus of equal size when running at 83 kmph

INTRODUCTION

The interest in vehicle aerodynamics is driven by the rapid increase in the price of fossil fuels. Crude oil price per barrel has drastically increased in the last decade see Fig. 1. At highway speeds approximately 40% of the total fuel consumption of Bus and Truck is due to aerodynamic drag [1]. So making aerodynamics improvements is an important factor in the financial and environmental impact of the transport sector. Fuel economy obviously is improved by reducing the aerodynamic drag and the benefits can be calculated easily for constant-speed operation. However, the actual benefit for normal use will be less because drag reduction does not significantly reduce the energy required for acceleration at normal speeds [3]. R. H. Barnard [4] and W. H. Hucho [1] are two pioneers who have given a greater care and comprehensive treatment to Road vehicle aerodynamics. The main developments with vehicle aerodynamics probably occurred during the early 1980s, and the use of low-drag vehicles has now become common. Saltzman and Meyer [5] in their experimental studies on reduction of drag of trucks and busses showed that by tuning the exterior with rounded horizontal and vertical corners, smoothed under body and a boat tail, the coefficient of drag could be reduced to 0.242. Callen et al [6] in their experiments found out removal of rear view mirror alone would bring down the drag of the vehicle by 4.5%. Hucho and Emmelmann[7] found that detailed shape optimization of parts such as roof radii, rain channels, headlights also would result in considerable reduction of drag force. Carr [8] investigated the effects of streamlining the front end of the rectangular bodies in ground

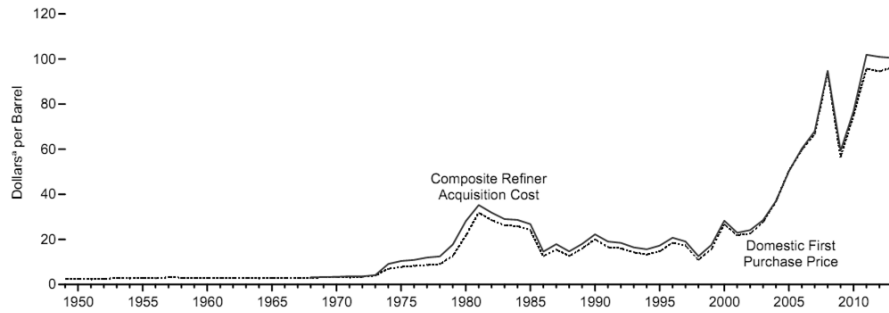


FIGURE 1. Crude oil prices 1949-2013 [2].

proximity. Experiments shown a stream lined front end with low leading edge resulted in a reduction of drag coefficient.

An experiment on the Volkswagen delivery van conducted by E. Moeller (1951) also reported by Schlichting (1968) that by making the front of this vehicle convex, with an inclined windshield and applying corner rounding (Figure 2) the drag coefficient is reduced to 0.42 from 0.76. [9] This reduction is achieved by having flow attached (no separation at the top and sides of the vehicle) with the body resulting lower form drag

Streamlined object produces low drag as there is no pressure drag, only viscous drag present. Unlike Busses commercial cars are now more streamlined than ever that’s why these cars have relatively low drag coefficient. Bluff bodies of busses are mainly responsible for generating huge drag force. So one way to reduce drag force of busses would be to make the body as streamlined as possible. In this research we have designed a new aerodynamic exterior shape of a bus to make it more streamlined with focusing to reduce drag force but keeping its commercial values intact.

GEOMETRY CREATION

A Three dimensional exterior body of the bus (Fig. 2) is created with having following dimensions shown in table 1

TABLE 1. Geometric Dimensions of the Bus.

Name	Value
Length	12 m
Width	2.6 m
height	4.0 m
Tire dimension	292/80R/22.5
Available floor space	29 m ²

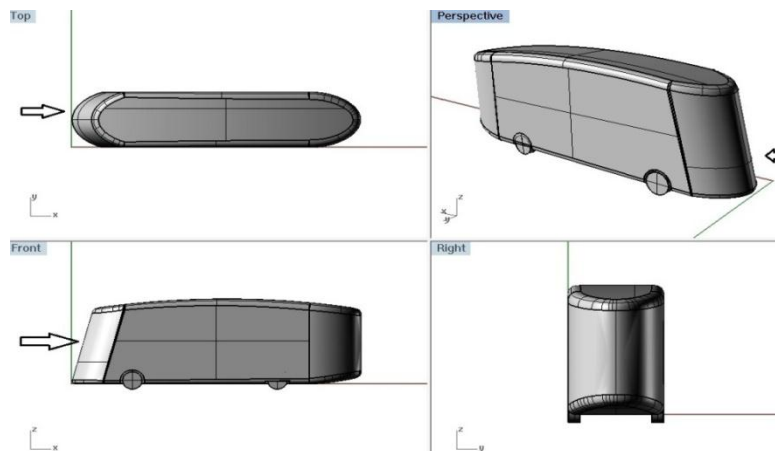


FIGURE 2. Different views of the Bus

Aerodynamic Features

Figure 2 shows different views of exterior shape of this bus. Followings are the unique features that this shape should provide.

- Elliptically curved front to reduce stagnation pressure area.
- Elliptically curved rear portion to guide fluid from both side into wake to reduce wake region.
- Inclined upper rear portion to guide fluid from top to fill wake region
- Inclined bottom rear to facilitate fluid flow from bottom of the body into vacuum region.
- Covered rear wheel to create less disturbance and recirculation in flow field.
- Fully covered under body even though it is difficult to achieve.

GRID GENERATION

Bus is a symmetric body that's why we can split it at symmetric plane. The computer memory needed is largely determined by the total number of cells. By considering half model with a symmetric boundary condition we can reduce number of cells. It is also worth mentioning that this is only valid for steady flows where there is no significant lateral energy transfer across the symmetry plane in the wake.

A rectangular box of 36 m x 4 m x 10 m is used as fluid domain. The bus was placed in that rectangular block that sectioned the bus in half, creating a plane of symmetry. The block simulated a wind tunnel and allowed for the outer surface of the bus to be studied. Because the bus was symmetrical, it was only necessary to study the forces on half the bus. The inlet of the wind tunnel was placed half bus-length in front of the bus and the outlet was 1.5 times bus-lengths behind the bus to capture the flow at wake at downstream of the bus (Fig. 3).

Finally a volume mesh of hexahedral cells type is generated with incorporating five boundary layers. These layers are necessary to accurately capture the flow field at the surface boundaries of the bus. There were 5 layers that were each 133mm in size. In external aerodynamic simulations it is usual to refine the cell region downstream of the immersed body in order to capture any unsteady or turbulent fluid phenomena caused by separation of the boundary layer. This separated region is normally known as the *wake*, and we used wake refinement method for refining the wake region (Fig. 4). Total no of cell produced is 1 million. Figure 4 shows the final meshed half bus body. Once the meshing is done, the model is ready for boundary conditions and simulations.

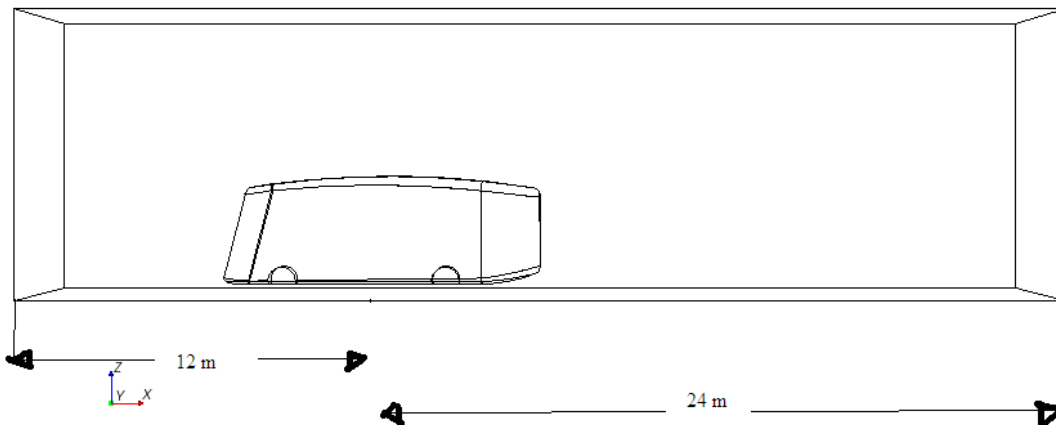


FIGURE 3. Bus model placed in the fluid domain

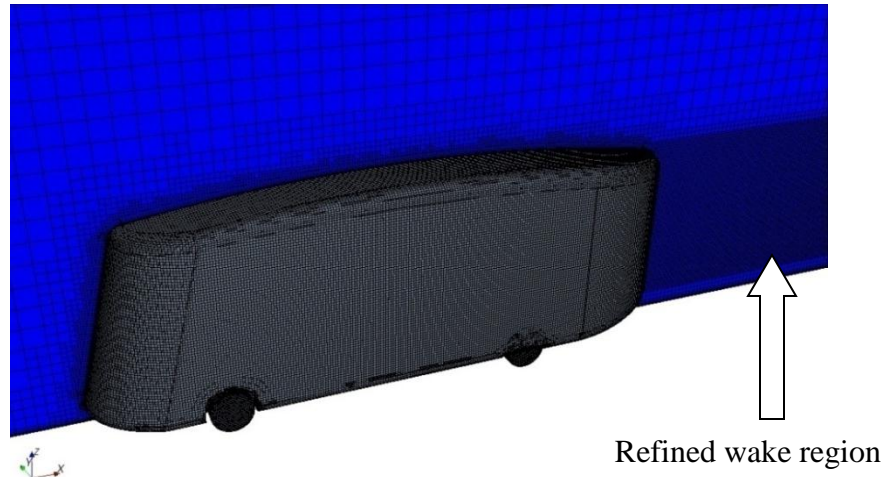


FIGURE 4. Completely meshed half bus body

Boundary Conditions

Boundary conditions Fig. 5 were applied on the meshed model prior to the simulation. The floor, walls (bus body with wheel) and ceiling of the test section are treated as a non-slip wall imitating the wind tunnel conditions. The inlet condition is specified as a velocity inlet and the outlet condition is specified as a pressure outlet at atmospheric pressure. The analysis was carried out with moving road and fixed road condition. In this work rotation of wheel was neglected. In the simulation only straight wind condition was considered at vehicle speed of 83 kmph.

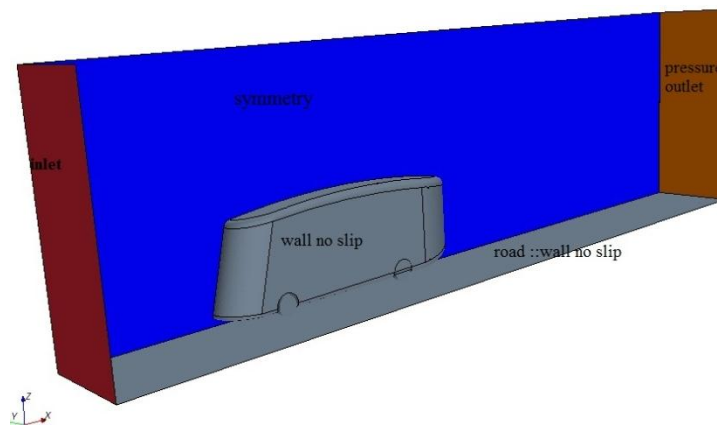


FIGURE 5. Boundary Condiions

Turbulence Modeling

Since the Mach number is below 0.3 the flow is considered to be incompressible and steady in nature. Reynolds-averaged Navier-Stokes RANS equations are solved. The energy equation is excluded as there is no heat transfer or temperature change. The segregated flow algorithm is sufficient in this case. The turbulence model selected was realizable K-Epsilon ($k-\epsilon$) as it is commonly used in external vehicle aerodynamics studies [10, 11, and 12]. Pressure velocity coupling was used to calculate the pressure field and the algorithm used was the Semi Implicit Method for Pressure Linked Equations (SIMPLE).

VALIDATION

In 2010 some people from Coventry University, UK and Jaguar Land Rover, Aerodynamics [13] have conducted a research on Mesh Optimization for Ground Vehicle Aerodynamics. For this purpose they carried out quite a few simulations over a car body. We picked one of them as a comparing medium and we simulated that car on our own. We ended up having a value almost similar to them. Authors of that research did not mention in details about the various dimension of that car except length over which they conducted their simulation. That's why we relied on our eye vision to identify different angle and dimension (Fig. 6). For this reason the value we got did not match exactly with the value what authors mentioned. So there is a reasonable percentage of error in results. Our simulated value of drag coefficient (C_d) is 0.42 and authors value of (C_d) is 0.34.

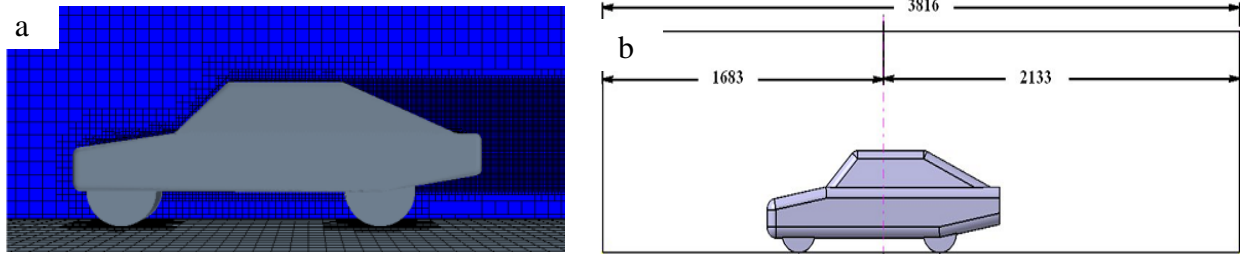


FIGURE 6. a) Drawn car model b) Authors used model [13]

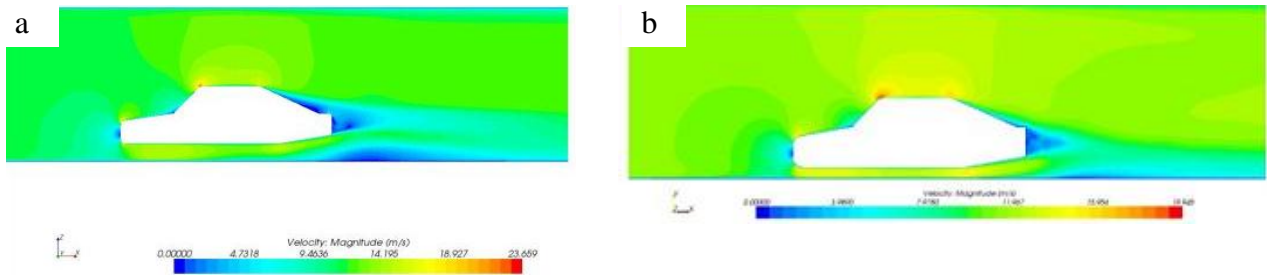


FIGURE 7. a) Simulated velocity contour. b) Authors given velocity contour [13]

It is apparent from above Fig. 7 that values of velocity are different but patterns are same. So from aforementioned validation process we can conclude that our CFD model is valid hence we can proceed to simulate our proposed bus model.

RESULT AND DISCUSSION

Simulations were run at 1 speed (83kmh) with zero yaw angle. Reynolds number is (6.4×10^6) based on the height of the bus. Generally, a solution is assumed converged when the residuals become constant and do not change with additional iterations. The residuals should decrease by multiple orders of magnitude before levelling off and typically settle at 0.001 or 0.0001 residual units. We achieved residuals between 0.001 and 0.0001 after 2000 iterations (Fig. 8) that were sufficiently low and it remains constant as iteration proceeds. So our simulation has converged completely

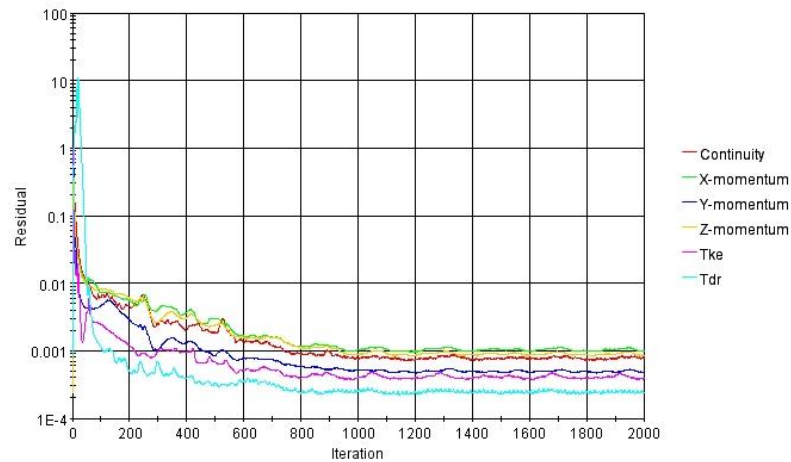


FIGURE 8. Residuals shows convergence of simulation

The value of C_d we obtain is **0.255** shown in Fig. 9 (a). Wheels are added to the frontal area of bus. This is the least value among currently running bus. As we did not consider wheel rotation that's why actual value of C_d of this bus will be slightly higher approximately 10-15% more. Still it remains as the least drag force generator highway bus

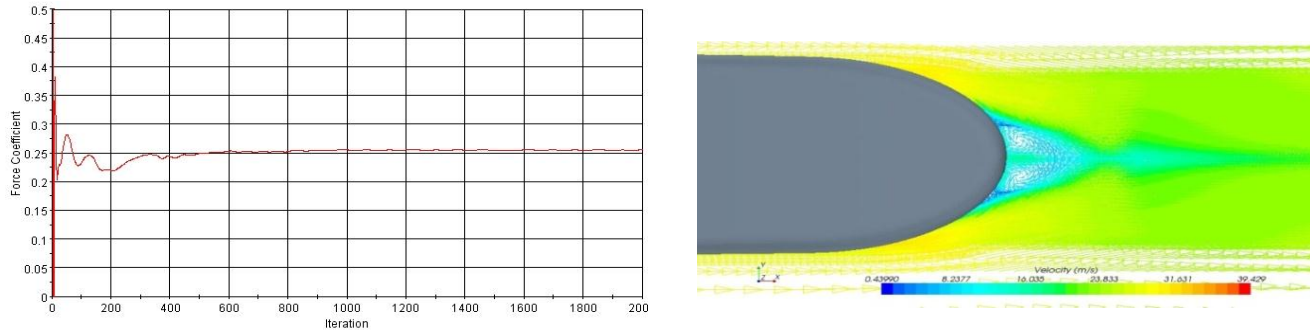


FIGURE 9. a) Drag monitor plot b) Velocity vector at the rear wake region

Figure 9 (b) justifies that making the rear portion elliptical, upper rear and bottom rear inclined are useful to reduce the wake region. This is one of the reasons of getting small drag coefficient value. As we have mentioned earlier that the narrower the wake the smaller the drag.

The reason behind making front and rear portion of this bus elliptical was to reduce stagnation area and to increase pressure respectively. Figure 10(a) & (b) shows very narrow stagnation area at front and a positive pressure at back side of the bus. Air gets stagnated at very thin line at the front, which results comparatively small total pressure at front that yields consequently lower drag force.

Figure 11 demonstrates how rear upper and rear bottom inclination facilitates fluid to enter into a region which otherwise could not be accessed by air and remain as a vacuum area. So this design modification has also proved useful to implement

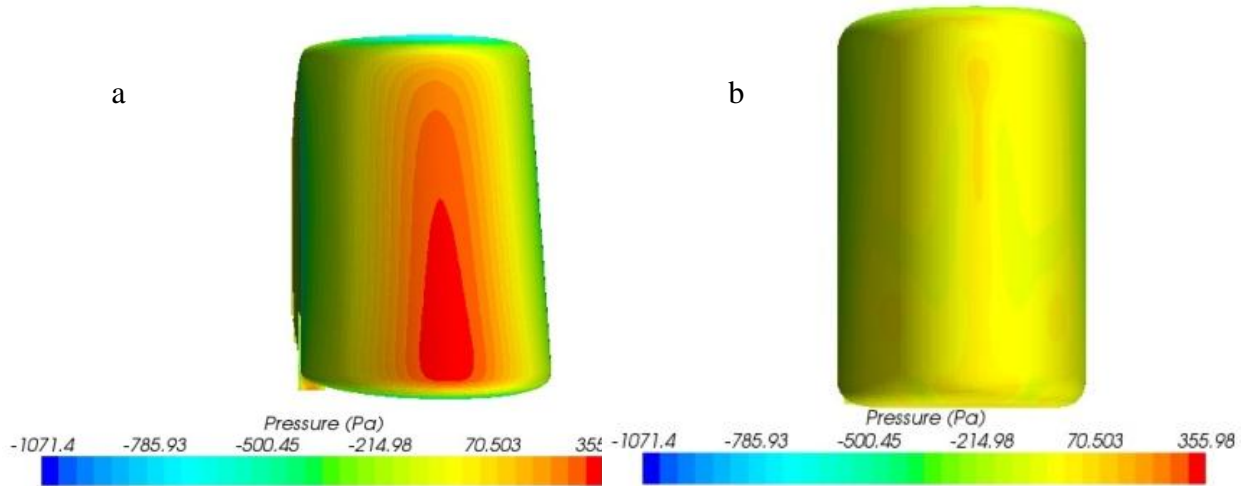


FIGURE 10. a) Pressure contour at front and (b) rear end of the bus.

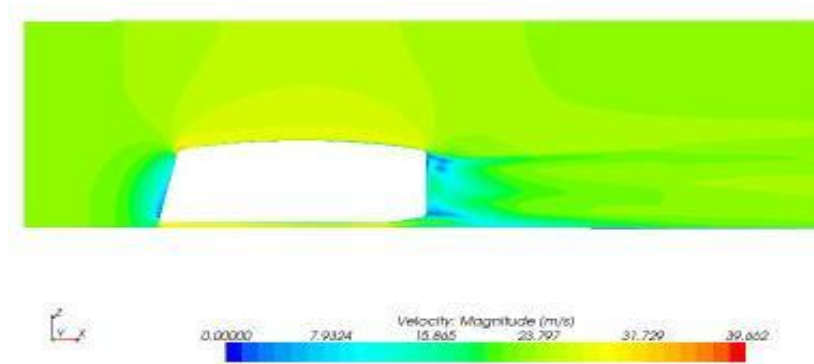


FIGURE 11. Velocity flow field at symmetry plane

Figure 12 shows the pressure coefficient on the front, top and back surface along the line shown. At the front surface stagnation air causes a positive pressure coefficient value. After this stagnation area air speed accelerates due to the windshield inclination angle which can be seen at the graph as decreasing pressure coefficient value. At the corner edge pressure coefficient value becomes minimum because air speed is maximum here. After corner edge as air travels along the top surface, air remains attached to the top surface (no separation occurred) till the rear elliptical portion that's why pressure coefficient curve shows a steady value. Separation occurs when air cannot follow the bus contour causes to drop pressure suddenly. The pressure coefficient at last becomes positive this is so significant because normally at back side no air could enter and leaves a vacuum region with a negative pressure coefficient. But here with our design modification there is no vacuum region at back side but a positive pressure region. So the difference between frontal and rear pressure is significantly low, which yields lower drag force

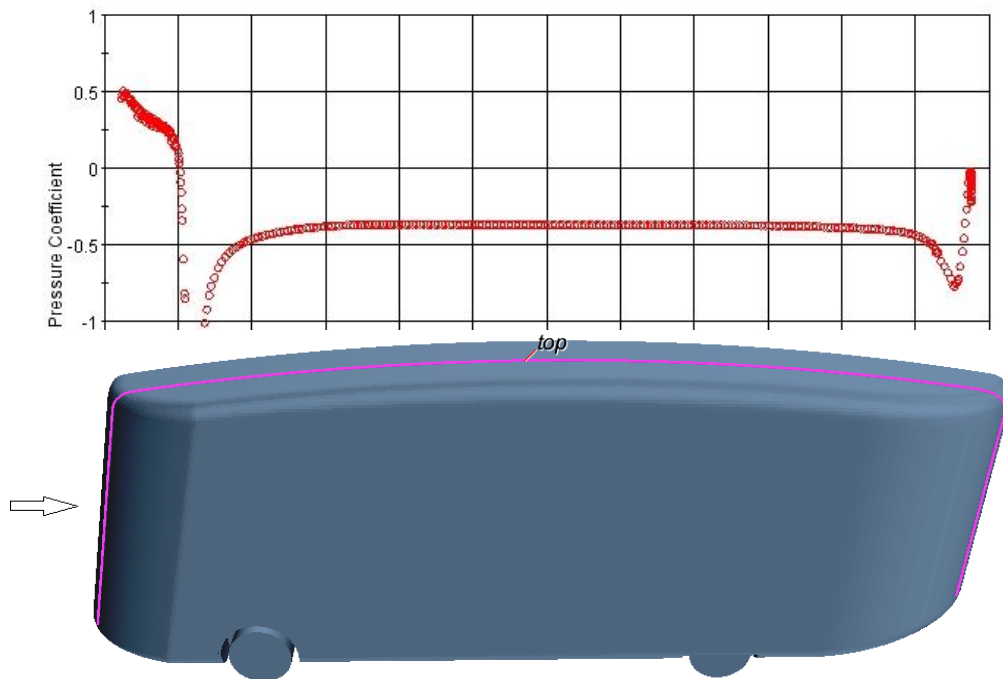


FIGURE 12. Pressure coefficient along the line shown.

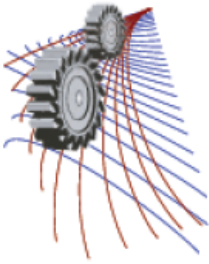
CONCLUSIONS

Drag coefficient of this redesigned exterior body is found to be much lower due to the combined effect of narrow wake region and less frontal stagnation area. Less drag force means less fuel burning at highway speed so environment friendly and economical. Curving the front and rear end of the bus may cost few passengers but it should not yield any profit loss in the long run.

REFERENCES

1. W. H. Hucho, *Aerodynamics of Road Vehicles*, (Society of Automotive Engineers, Warrendale, PA, 1998).
2. U.S. Energy Information Administration Monthly Energy Review June 2014, section 9 <http://www.eia.doe.gov/>
3. Richard Stone and K. Ball Jeffrey, *Automotive Engineering Fundamentals*. ISBN 0-7680-0987-1, P-435.
4. R. H Barnard, *Road Vehicle Aerodynamic Design*. ISBN 0-9540734-0-1
5. J. Asltzman Edwin. and R. Meyer Robert, "A reassessment of heavy duty truck aerodynamic design features and priorities," NASA/tp-1999-206574S
6. R. Mc. Callen, K. Salari, J. Ortega, F. Browand, M. Hammache, T. Hsu., (2004), "Effort to Reduce Truck Aerodynamic Drag - Joint Experiments and Computations Lead to Smart Design," AIAA Fluid Dynamics Conference.
7. W.H.Hucho and H.J. Emmelmann, "Aerodynamische Form optimierung, einweg zursteigerung der wirtschaftlichkeit von nutzfahrzeugen," Series.12, NO.31 1977.
8. G.W. Carr, "The aerodynamics of basic shapes of road vehicles, part 1, Simple rectangular bodies," MIRA report No.1982/2
9. Dr.Hermann Schlichting, *Boundary Layer Theory* .McGraw-Hill,1968ISBN 0-07-055334-3; P-35

10. Z. Yang and M.Schenkel, "*Assessment of Closed-Wall Wind Tunnel Blockage Using CFD*", SAE Technical Paper 2004-01-0672, 2004.
11. Z. Yang, A. Nastov, M. Schenkel, "*Further Assessment of Closed-Wall Wind Tunnel Blockage Using CFD*," SAE Technical Paper 2005-01-0868, 2005.
12. M. Moky, "*Wall Interference correction to drag measurements in Automotive Wind Tunnels*," JWEIA 1995.Vol. 56, Issues2-3.
13. Nor Elyana Ahmad, Essam Abo-Serie and Adrian Gaylard, "*Mesh Optimization for Ground Vehicle Aerodynamics*," CFD Letters Vol. 2(1) – March 2010. www.cfdl.issres.net.



Unsteady Laminar Flow with Convective Heat Transfer through a Rotating Curved Square Duct with Small Curvature

Rabindra Nath Mondal^{1, a)}, Titob Roy², Poly Rani Shaha³ and Shinichiro Yanase^{4, b)}

^{1,3}Department of Mathematics, Jagannath University, Dhaka-1100, Bangladesh

²Department of Mathematics, Vikarunnesa Nun School and College, Boshundhara, Dhaka, Bangladesh

⁴Department of Mechanical and Systems Engineering, Okayama University, Okayama 700-8530, Japan

^{a)}Corresponding author: rnmondal71@yahoo.com

^{b)}yanase@okayama-u.ac.jp

Abstract. Unsteady laminar flow with convective heat transfer through a curved square duct rotating at a constant angular velocity about the center of curvature is investigated numerically by using a spectral method, and covering a wide range of the Taylor number $-300 \leq Tr \leq 1000$ for the Dean number $Dn = 1000$. A temperature difference is applied across the vertical sidewalls for the Grashof number $Gr = 100$, where the outer wall is heated and the inner wall cooled, the top and bottom walls being adiabatic. Flow structures are examined for the effects of rotational parameter, Tr , and the pressure-driven parameter, Dn , for constant curvature 0.001. Time evolution calculations as well as their phase spaces show that the unsteady flow undergoes in the scenario ‘multi-periodic \rightarrow chaotic \rightarrow steady-state \rightarrow periodic \rightarrow multi-periodic \rightarrow chaotic’, if Tr is increased in the positive direction. For negative rotation, however, time evolution calculations show that the flow undergoes in the scenario ‘multi-periodic \rightarrow periodic \rightarrow steady-state’, if Tr is increased in the negative direction. Typical contours of secondary flow patterns and temperature profiles are obtained at several values of Tr , and it is found that the unsteady flow consists of two- to six-vortex solutions if the duct rotation is involved. External heating is shown to generate a significant temperature gradient at the outer wall of the duct. This study also shows that there is a strong interaction between the heating-induced buoyancy force and the centrifugal-Coriolis instability in the flow that stimulates fluid mixing and consequently enhance heat transfer in the fluid.

INTRODUCTION

The study of flows and heat transfer through a curved duct is of fundamental interest because of its importance in chemical, mechanical, civil and biological engineering. Due to engineering applications and their intricacy, flow in a rotating curved duct has become one of the most challenging research fields of fluid mechanics. Since rotating machines were introduced into engineering applications, such as in rotating systems, gas turbines, electric generators, heat exchangers, rocket engines, cooling systems and some separation processes, scientists have paid considerable attention to study flows through a rotating curved channel. The readers are referred to Nandakumar and Masliyah [1], Ito [2] and Yanase *et al.* [3] for some outstanding reviews on curved duct flows.

The fluid flowing in a rotating curved duct is subjected to two forces: the *Coriolis force* due to rotation and the *centrifugal force* due to curvature. For isothermal flows of a constant property fluid, the Coriolis force tends to produce vortices while centrifugal force is purely hydrostatic. When a temperature induced variation of fluid density occurs for non-isothermal flows, both Coriolis and centrifugal type buoyancy forces can contribute to the generation of vortices. These two effects of rotation either enhance or counteract each other in a non-linear manner depending on the direction of wall heat flux and the flow domain. Therefore, the effect of system rotation is more subtle and complicated and yields new; richer features of flow and heat transfer in general, bifurcation and stability in particular, for non-isothermal flows. Selmi *et al.* [4] examined combined effects of system rotation and curvature on the bifurcation structure of two-dimensional flows in a rotating curved square duct. Wang and Cheng [5], employing finite

volume method, examined the flow characteristics and heat transfer in curved square ducts for positive rotation and found reverse secondary flow for the co-rotation cases. Selmi and Nandakumer [6] and Yamamoto *et al.* [7] performed studies on the flow in a rotating curved rectangular duct. Mondal, Alam and Yanase [8] performed numerical prediction of non-isothermal flows through a rotating curved square channel with positive rotation. However, transient behavior of the unsteady solutions is not yet resolved, in detail, for the flow through a rotating curved square channel in consideration of buoyancy-Coriolis effect, which motivated the present study to fill up this gap. In the present paper, a comprehensive numerical study is presented for the unsteady solutions with convective heat transfer in a rotating curved square duct by using a spectral method. Studying the effects of rotation on the unsteady flow characteristics, caused by the combined action of centrifugal, Coriolis and buoyancy forces, is an important objective of the present study.

FLOW MODEL AND MATHEMATICAL FORMULATIONS

Consider fully developed two-dimensional flow of viscous incompressible fluid through a rotating curved square duct. The coordinate system with relevant notation is shown in Fig. 1, where x , y , and z axes are taken to be in the horizontal, vertical, and axial directions respectively. The outer wall of the duct is heated while the inner wall cooled, the top and bottom walls being adiabatic. The system rotates at a constant angular velocity Ω_T around the y' axis. The variables are made non-dimensional.

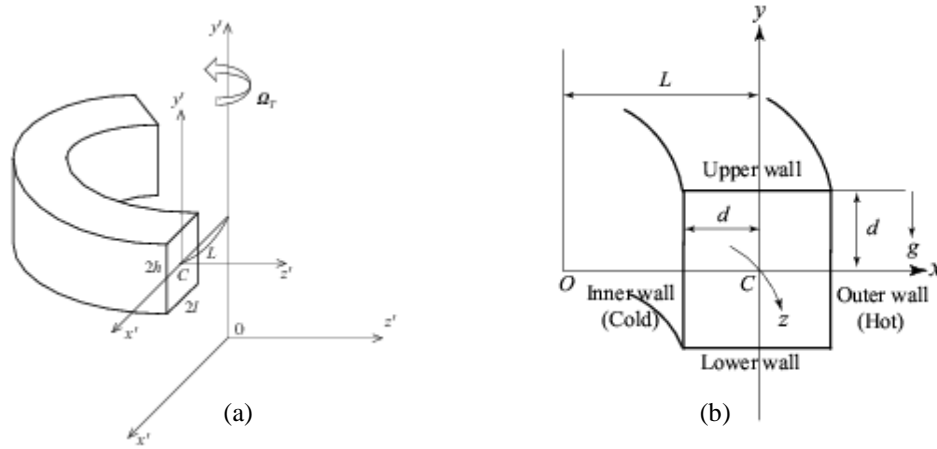


FIGURE 1. (a) Coordinate system of the rotating curved channel, (b) Cross section of the curved channel.

The flow field is assumed to be uniform in the z direction and so the sectional stream function ψ is introduced as

$$u = \frac{1}{1+\delta x} \frac{\partial \psi}{\partial y}, \quad v = -\frac{1}{1+\delta x} \frac{\partial \psi}{\partial x} \quad (1)$$

Then the basic equations for the axial velocity w , stream function ψ and temperature T are derived from the Navier-Stokes equations and the energy equation under the *Boussinesq approximation* as,

$$(1+\delta x) \frac{\partial w}{\partial t} = Dn - \frac{1}{2} \frac{\partial(w, \psi)}{\partial(x, y)} - \frac{\delta^2 w}{1+\delta x} + (1+\delta x) \Delta_2 w - \frac{1}{2} \frac{\delta}{(1+\delta x)} \frac{\partial \psi}{\partial y} w + \delta \frac{\partial w}{\partial x} - \delta Tr \frac{\partial \psi}{\partial y} \quad (2)$$

$$\left(\Delta_2 - \frac{\delta}{1+\delta x} \frac{\partial}{\partial x} \right) \frac{\partial \psi}{\partial t} = -\frac{1}{2} \frac{1}{(1+\delta x)} \frac{\partial(\Delta_2 \psi, \psi)}{\partial(x, y)} + \frac{1}{2} \frac{\delta}{(1+\delta x)^2} \left[\frac{\partial \psi}{\partial y} \left(2\Delta_2 \psi - \frac{3\delta}{1+\delta x} \frac{\partial \psi}{\partial x} + \frac{\partial^2 \psi}{\partial x^2} \right) - \frac{\partial \psi}{\partial x} \frac{\partial^2 \psi}{\partial x \partial y} \right] \quad (3)$$

$$+ \frac{\delta}{(1+\delta x)^2} \times \left[3\delta \frac{\partial^2 \psi}{\partial x^2} - \frac{3\delta^2}{1+\delta x} \frac{\partial \psi}{\partial x} \right] - \frac{2\delta}{1+\delta x} \frac{\partial}{\partial x} \Delta_2 \psi + w \frac{1}{2} \frac{\partial w}{\partial y} + \Delta_2^2 \psi - Gr(1+\delta x) \frac{\partial T}{\partial x} - \frac{1}{2} Tr \frac{\partial w}{\partial y},$$

$$\frac{\partial T}{\partial t} = \frac{1}{Pr} \left(\Delta_2 T + \frac{\delta}{1+\delta x} \frac{\partial T}{\partial x} \right) - \frac{1}{(1+\delta x)} \frac{\partial(T, \psi)}{\partial(x, y)} \quad (4)$$

The non-dimensional parameters Dn , Tr , Gr and Pr , which appear in equations (2) to (4) are defined as

$$Dn = \frac{Gd^3}{\mu\nu} \sqrt{\frac{2d}{L}}, \quad Gr = \frac{\beta g \Delta T d^3}{\nu^2}, \quad Tr = \frac{2\sqrt{2\delta} \Omega_T d^3}{\nu\delta}, \quad Pr = \frac{\nu}{\kappa} \quad (5)$$

The no slip boundary conditions for w and ψ are used as

$$w(\pm 1, y) = w(x, \pm 1) = \psi(\pm 1, y) = \psi(x, \pm 1) = \frac{\partial \psi}{\partial x}(\pm 1, y) = \frac{\partial \psi}{\partial y}(x, \pm 1) = 0 \quad (6)$$

and the temperature T is assumed to be constant on the walls as

$$T(1, y) = 1, \quad T(-1, y) = -1, \quad T(x, \pm 1) = x \quad (7)$$

NUMERICAL METHODS

Equations (2) to (4) are solved numerically by using the spectral method. By this method, the expansion functions $\phi_n(x)$ and $\psi_n(x)$ are expressed as

$$\left. \begin{aligned} \phi_n(x) &= (1-x^2) C_n(x), \\ \psi_n(x) &= (1-x^2)^2 C_n(x) \end{aligned} \right\} \quad (8)$$

where $C_n(x) = \cos(n \cos^{-1}(x))$ is the n -th order Chebyshev polynomial. $w(x, y, t)$, $\psi(x, y, t)$ and $T(x, y, t)$ are expanded in terms of $\phi_n(x)$ and $\psi_n(x)$ as

$$\left. \begin{aligned} w(x, y, t) &= \sum_{m=0}^M \sum_{n=0}^N w_{mn}(t) \phi_m(x) \phi_n(y) \\ \psi(x, y, t) &= \sum_{m=0}^M \sum_{n=0}^N \psi_{mn}(t) \psi_m(x) \psi_n(y) \\ T(x, y, t) &= \sum_{m=0}^M \sum_{n=0}^N T_{mn} \phi_m(x) \phi_n(y) + x, \end{aligned} \right\} \quad (9)$$

where M and N are the truncation numbers in the x and y directions respectively. The accuracy of the numerical calculations is investigated for M and N , and it is found that $M = 20$ and $N = 20$ gives sufficient accuracy of the numerical solutions. In order to calculate the unsteady solutions, the Crank-Nicolson and Adams-Bashforth methods together with the function expansion (9) and the collocation methods are applied to Eqs. (2) to (4).

resistance coefficient

We use the resistance coefficient λ as one of the representative quantities of the flow state. It is also called the hydraulic resistance coefficient, and is generally used in fluids engineering, defined as

$$\frac{P_1^* - P_2^*}{\Delta z^*} = \frac{\lambda}{dh^*} \frac{1}{2} \rho \langle w^* \rangle^2, \quad (10)$$

where quantities with an asterisk denote the dimensional ones, and d_h^* is the hydraulic diameter. Since $(P_1^* - P_2^*) / \Delta z^* = G$, λ is related to the mean non-dimensional axial velocity $\langle w \rangle$ as

$$\lambda = \frac{4\sqrt{2\delta} Dn}{\langle w \rangle^2}, \quad (11)$$

where $\langle w \rangle = \sqrt{2\delta} d / \nu \langle w^* \rangle$. In this paper, λ is used to calculate the unsteady solutions by numerical computations.

RESULTS AND DISCUSSION

We take a curved square duct of curvature 0.001 and rotate it around the centre of curvature with an angular velocity Ω_T . In this study, time evolution calculations are performed for the non-isothermal flows ($Gr = 100$) over a wide range of the Taylor Number for the Dean Number $Dn = 1000$. We performed unsteady flows for two cases of the duct rotation, Case I: Positive rotation and Case II: Negative rotation.

Case I: Positive Rotation

For positive rotation we performed time evolution calculations for $0 < Tr \leq 1000$ at $Dn = 1000$. Figure 2(a) shows time evolution of λ for $Tr = 150$. It is found that the unsteady flow is a multi-periodic oscillation, which is well justified by drawing the phase space of the time evolution result as shown in Fig. 2(b). Figure 2(c) shows typical contours of secondary flow patterns and temperature profiles for $Tr = 150$, where we find that the unsteady flow is a four-vortex solution. This is caused by the combined action of the centrifugal, Coriolis and buoyancy forces, which helped to increase the number of secondary vortices (Wang and Cheng [5]). To draw the contours of secondary flows (ψ) and temperature profiles (T), we use the increments $\Delta\psi = 0.6$ and $\Delta T = 0.2$ respectively. The right-hand side of each channel box of ψ and T indicates the outside direction of the duct curvature. In the figures of the secondary flows, solid lines ($\psi \geq 0$) show that the secondary flow is in the counter clockwise direction while the dotted lines ($\psi < 0$) in the clockwise direction. Similarly in the figures of temperature field, solid lines are those for $T \geq 0$ and dotted ones for $T < 0$. Then we performed time evolution of λ for $Tr = 750$ as shown in Fig. 3(a). It is found that the unsteady flow is a periodic solution. In order to observe the periodic oscillation more clearly, we draw the phase space of the time evolution result in Fig. 3(b) in the $\lambda - \gamma$ plane, where $\gamma = \iint \psi dx dy$, and it is found that the flow oscillates in a regular pattern, which confirms that the flow is periodic. Typical contours of secondary flow patterns and temperature profiles for $Tr = 750$ are shown in Fig. 3(c), and we see that the unsteady flow is a two-vortex solution. Then we performed time evolution of λ for $Tr = 1000$ as shown in Fig. 4(a). It is found that the unsteady flow at $Tr = 1000$ is a chaotic solution, which is well justified by drawing the phase space as shown in Fig. 4(b). As seen in Fig. 4(b), the flow creates multiple orbits, so that the unsteady flow at $Tr = 1000$ is purely chaotic solution. Typical contours of secondary flow patterns and temperature profiles for $Tr = 1000$ are shown in Fig. 4(c), where it is found that the chaotic oscillation at $Tr = 1000$ is a two-vortex solution.

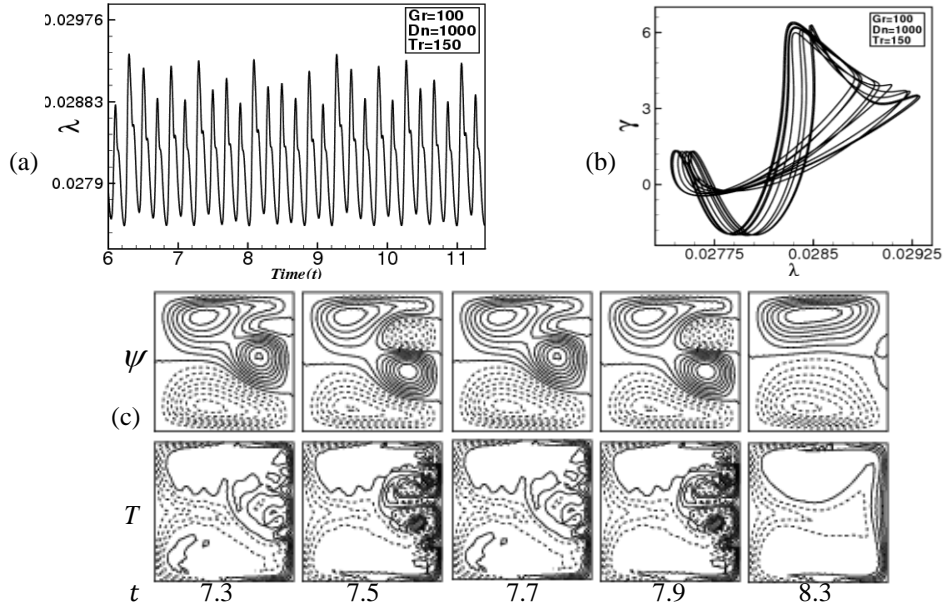


FIGURE 2. Time evolution results for $Dn = 1000$, $Gr = 100$ and $Tr = 150$. (a) Time evolution of λ , (b) Phase space, (c) Contours of secondary flow patterns (top) and temperature profiles (bottom) for $7.3 \leq t < 8.3$.

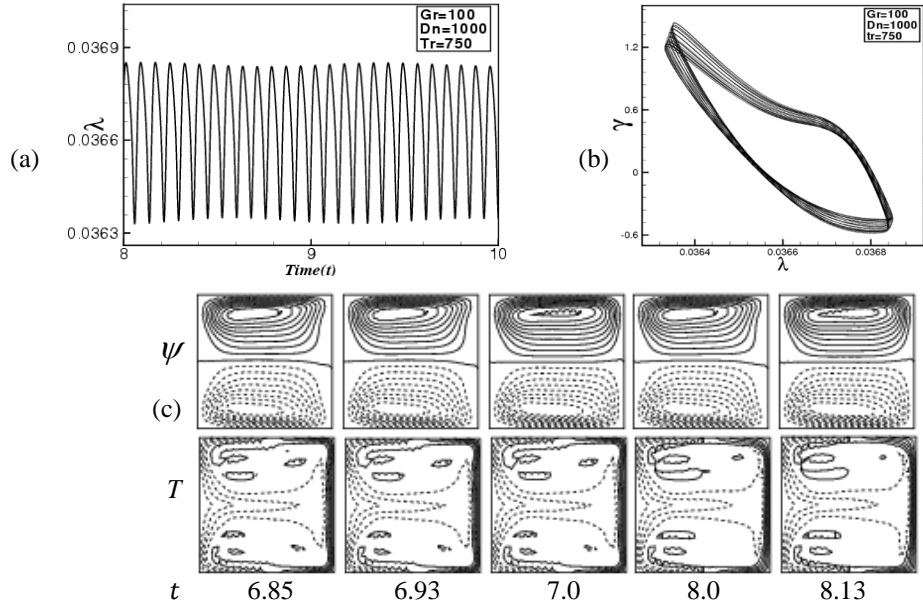


FIGURE 3. Time evolution results for $Dn = 1000$, $Gr = 100$ and $Tr = 750$. (a) Time evolution of λ , (b) Phase space, (c) Contours of secondary flow patterns (top) and temperature profiles (bottom) for $6.85 \leq t < 8.13$.

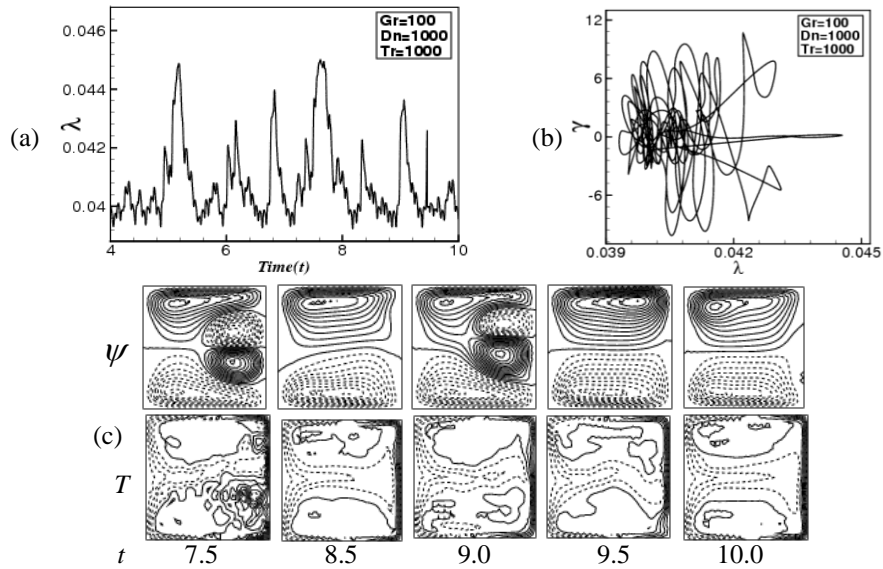


FIGURE 4. Time evolution results for $Dn = 1000$, $Gr = 100$ and $Tr = 1000$. (a) Time evolution of λ , (b) Phase space, (c) Contours of secondary flow patterns (top) and temperature profiles (bottom) for $7.5 \leq t < 10.0$.

Case II: Negative Rotation

For negative rotation, we performed time evolution calculations for $-300 \leq Tr < 0$ at $Dn = 1000$. Figure 5(a) shows time evolution of λ for $Tr = -150$. It is found that the unsteady flow at $Tr = -150$ is a multi-periodic oscillation, which is well justified by drawing the phase space as shown in Fig. 5(b). Figure 5(c) shows typical contours of secondary flow patterns and temperature profiles for $Tr = -150$, where it is found that the multi-periodic oscillation at $Tr = -150$ is a four-vortex solution. Then we performed time evolution of λ for $Tr = -151$ and it is interesting to notice that the flow suddenly turns into steady-state solution. The time evolution result for $Tr = -151$ is shown in Fig.

6(a). Since the flow is steady-state solution, a single contour of the secondary flow pattern and temperature profile for $Tr = -151$ is shown in Fig. 6(b), where it is found that the steady-state flow is also a four-vortex solution. If the rotational speed is increased more in the negative direction, the flow remains steady-state without changing its nature. Figure 7(a) shows unsteady result for $Tr = -300$, and it is found that the flow is a steady-state solution. Since the flow is steady-state, a single contour of secondary flow pattern and temperature profile is shown in Fig. 7(b) for $Tr = -300$, and it is found that the unsteady flow at $Tr = -300$ is a six-vortex solution. In this study, it is found that combined action of the centrifugal, Coriolis and buoyancy forces help to increase the number of secondary vortices, and as the secondary flow becomes stronger with multi-vortex solution, heat transfer is enhanced significantly from the heated wall to the fluid.

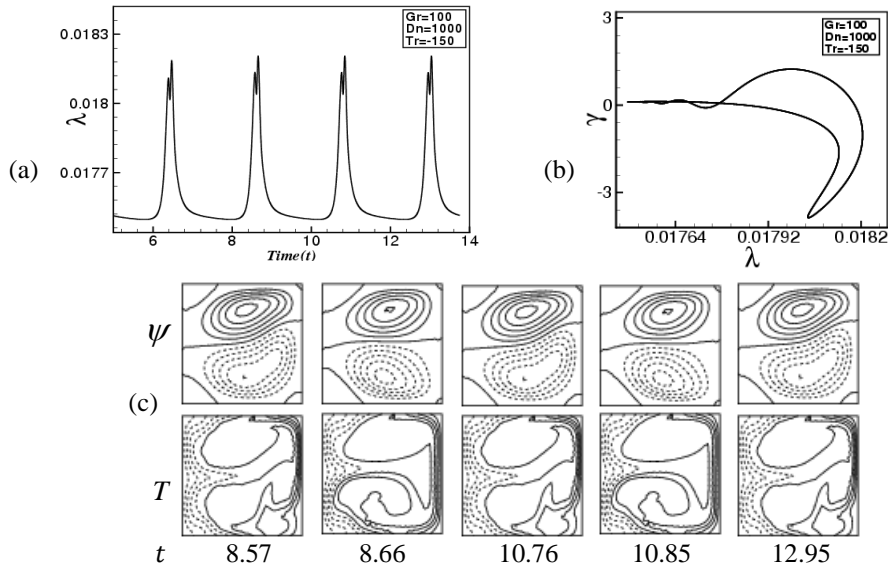


FIGURE 5. Time evolution results for $Dn = 1000$, $Gr = 100$ and $Tr = -150$. (a) Time evolution of λ , (b) Phase space, (c) Contours of secondary flow patterns (top) and temperature profiles (bottom) for $8.57 \leq t < 12.95$.

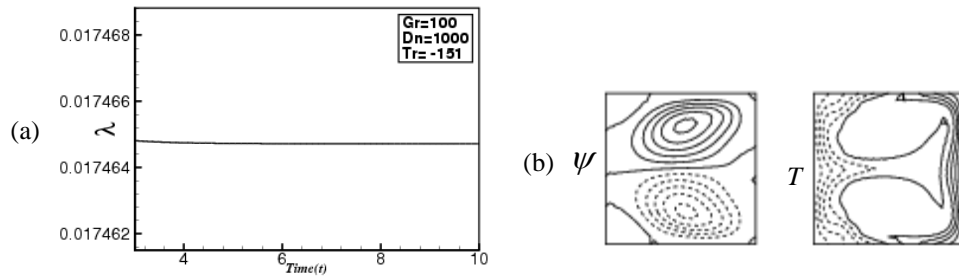


FIGURE 6. Time evolution results for $Dn = 1000$, $Gr = 100$ and $Tr = -151$. (a) Time evolution of λ , (b) Phase space, (c) Contours of secondary flow patterns (top) and temperature profiles (bottom) at $t = 8$.

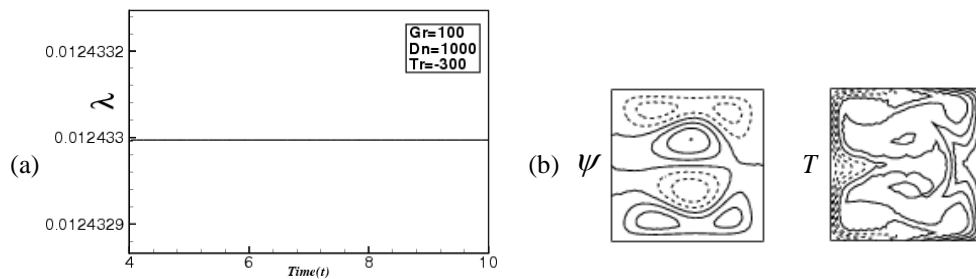


FIGURE 7. Time evolution results for $Dn = 1000$, $Gr = 100$ and $Tr = -300$. (a) Time evolution of λ , (b) Phase space, (c) Contours of secondary flow patterns (top) and temperature profiles (bottom) at $t = 8$.

CONCLUSIONS

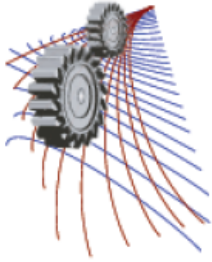
A numerical study is presented for the unsteady solutions through a rotating loosely coiled square duct of curvature 0.001. Numerical calculations are carried out by using a spectral method, and covering a wide range of the Taylor number $-300 \leq Tr \leq 1000$ for the Dean number $Dn = 1000$ and the Grashof number $Gr = 100$. We investigated unsteady flow characteristics for both the positive and negative rotation of the duct by time evolution calculations justified by their phase spaces, and it is found that the unsteady flow undergoes in the scenario '*multi-periodic* \rightarrow *chaotic* \rightarrow *steady-state* \rightarrow *periodic* \rightarrow *multi-periodic* \rightarrow *chaotic*', if Tr is increased in the positive direction. For negative rotation, however, it is found that time-dependent flow undergoes in the scenario '*multi-periodic* \rightarrow *periodic* \rightarrow *steady-state*', if Tr is increased in the negative direction. Phase spaces were found to be fruitful to clearly justify the transition as well as the unsteady flow characteristics. Typical contours of secondary flow patterns and temperature profiles are also obtained at several values of Tr , and it is found that there exist asymmetric two- to six- vortex solutions if the duct rotation is involved. It is found that the temperature distribution is consistent with the secondary vortices, and convective heat transfer is significantly enhanced as the secondary vortices become stronger. External heating is found to generate a significant temperature gradient at the outer wall of the duct. This study also shows that there is a strong interaction between the heating-induced buoyancy force and the centrifugal-Coriolis instability of the flow in the rotating curved channel that stimulates fluid mixing and consequently enhance heat transfer in the fluid.

ACKNOWLEDGMENTS

Rabindra Nath Mondal would gratefully acknowledge the financial support from the Japan Society for the Promotion of Science (JSPS), No. L15534, while Shinichiro Yanase expresses his cordial thanks to the Japan Ministry of Education, Culture, Sports, Science and Technology for the financial support through the Grant-in-Aid for Scientific Research, No. 24560196.

REFERENCES

1. K. Nandakumar and J. H. Masliyah, *Adv. Transport Process* **4**, 49–112 (1986).
2. H. Ito, *JSME International Journal* **30**, pp. 543–552 (1987).
3. S. Yanase, Y. Kaga and R. Daikai, *Fluid Dynamics Research* **31**, 151–183 (2002).
4. M. Selmi, K. Nandakumar and W. H. Finlay, *J. Fluid Mechanics* **262**, 353–375 (1994).
5. L. Q. Wang and K. C. Cheng, *Physics of Fluids* **8**, 1553–1573 (1996).
6. M. Selmi, and K. Nandakumar, *Physics of Fluids* **11**, 2030–2043 (1999).
7. K. Yamamoto, S. Yanase and M. M. Alam, *J. Phys. Soc. Japan* **68**, 1173–1184 (1999).
8. R. N. Mondal, M. M. Alam and S. Yanase, *Thammasat Int. J. Sci and Tech.* **12**(3), 24–43 (2007).



On the Onset of Secondary Flow and Unsteady Solutions through a Loosely Coiled Rectangular Duct for Large Aspect Ratio

Poly Rani Shaha¹, Sajal Kanti Rudro¹, Nayan Kumar Poddar¹ and Rabindra Nath Mondal^{1, a)}

¹*Department of Mathematics, Jagannath University, Dhaka-1100, Bangladesh*

^{a)}Corresponding author: rnmondal71@yahoo.com

Abstract. The study of flows through coiled ducts and channels has attracted considerable attention not only because of their ample applications in Chemical, Mechanical, Civil, Nuclear and Biomechanical engineering but also because of their ample applications in other areas, such as blood flow in the veins and arteries of human and other animals. In this paper, a numerical study is presented for the fully developed two-dimensional flow of viscous incompressible fluid through a loosely coiled rectangular duct of aspect ratio 4. Numerical calculations are carried out by using a spectral method, and covering a wide range of the Dean number, Dn , for two types of curvatures of the duct. The main concern of the present study is to find out effects of curvature as well as formation of secondary vortices on unsteady solutions whether the unsteady flow is steady-state, periodic, multi-periodic or chaotic, if Dn is increased. Time evolution calculations as well as their phase spaces are performed with a view to study the non-linear behavior of the unsteady solutions, and it is found that the steady-state flow turns into chaotic flow through various flow instabilities, if Dn is increased no matter what the curvature is. It is found that the unsteady flow is a steady-state solution for small Dn 's and oscillates periodically or non-periodically (chaotic) between two- and twelve-vortex solutions, if Dn is increased. It is also found that the chaotic solution is weak for small Dn 's but strong as Dn becomes large. Axial flow distribution is also investigated and shown in contour plots.

INTRODUCTION

Fluid flow through curved ducts and channels has been extensively used in many engineering applications, such as in turbo-machinery, refrigeration, air conditioning systems, heat exchangers, internal combustion engines and blade-to-blade passages in modern gas turbines. Dean [1] was the first who formulated the problem into mathematical terms for a curved channel flow. After that, many theoretical and experimental investigations have been made; the articles by Berger et al. [2] and Nandakumar and Masliyah [3] may be referenced for instance.

Flow through a curved rectangular duct has been investigated, both experimentally and numerically, with large aspect ratio by Akiyama et al. [4]. Ligrani and Niver [5] found secondary vortex patterns doing experiments in curved channels for Dean numbers from 40 to 220 and aspect ratio of 1 to 40. Yanase et al. [6] investigated flow in a curved duct and classified the flow range into three different regimes; steady-stable, periodic and chaotic. Very recently, an analytical solution for incompressible viscous flow through the curved rectangular ducts has been made by Norouzi and Biglari [7] by using perturbation method. The effect of duct curvature and aspect ratio on the flow field was investigated in that study. On the other hand, time dependent analysis of fully developed curved duct flows was first initiated by Yanase and Nishiyama [8] for a rectangular cross section. In that study, they investigated unsteady solutions for the case where dual solutions exist. Wang and Liu [9] performed numerical as well as experimental investigations of periodic oscillations for the fully developed flow in a curved square duct. Very recently, Mondal et al. [10] investigated spectral numerical study for non-isothermal flow through a curved rectangular duct of aspect ratios 1 to 3, and showed that the steady-state flow turns into chaotic flow through various flow instabilities if the

aspect ratio is increased. However, transient behavior of the unsteady solutions is not yet resolved for the flow through a curved rectangular duct of large aspect ratio with the effects of curvatures, which motivated us to do the present study. In the present paper, unsteady flow characteristics are investigated for fully developed two-dimensional flow of viscous incompressible fluid through a curved rectangular duct of aspect ratio 4 with curvatures 0.001 and 0.1 by using a spectral-based numerical scheme.

MATHEMATICAL MODEL AND GOVERNING EQUATIONS

Consider a fully developed two-dimensional (2D) flow of viscous incompressible fluid through a curved rectangular duct. The x , y and z axes are taken to be in the horizontal, vertical, and axial directions, respectively. It is assumed that the flow is uniform in the z direction, which is driven by a constant pressure gradient G along the center-line of the duct as shown in Fig. 1. The variables are made non-dimensional.

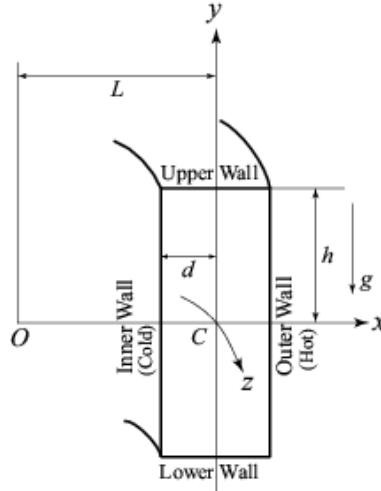


FIGURE 1. Coordinate system of the curved duct.

Since the flow field is uniform in the z -direction, the sectional stream function ψ is introduced as

$$u = \frac{1}{1+\delta x} \frac{\partial \psi}{\partial y}, \quad v = -\frac{1}{1+\delta x} \frac{\partial \psi}{\partial x} \quad (1)$$

Then the basic equations for the axial velocity w and stream function ψ are derived from the Navier-Stokes equations as,

$$(1+\delta x) \frac{\partial w}{\partial t} + \frac{1}{4} \frac{\partial(w, \psi)}{\partial(x, y)} - Dn + \frac{\delta^2 w}{1+\delta x} = (1+\delta x) \Delta_2 w - \frac{1}{4} \frac{\delta}{(1+\delta x)} \frac{\partial \psi}{\partial y} w + \delta \frac{\partial w}{\partial x} \quad (2)$$

$$\left(\Delta_2 - \frac{\delta}{1+\delta x} \frac{\partial}{\partial x} \right) \frac{\partial \psi}{\partial t} = -\frac{1}{4} \frac{1}{(1+\delta x)} \frac{\partial(\Delta_2 \psi, \psi)}{\partial(x, y)} + \frac{1}{4} \frac{\delta}{(1+\delta x)^2} \left[\frac{\partial \psi}{\partial y} \left(2\Delta_2 \psi - \frac{3\delta}{1+\delta x} \frac{\partial \psi}{\partial x} + \frac{\partial^2 \psi}{\partial x^2} \right) - \frac{\partial \psi}{\partial x} \frac{\partial^2 \psi}{\partial x \partial y} \right] + \frac{\delta}{(1+\delta x)^2} \times \left[3\delta \frac{\partial^2 \psi}{\partial x^2} - \frac{3\delta^2}{1+\delta x} \frac{\partial \psi}{\partial x} \right] - \frac{2\delta}{1+\delta x} \frac{\partial}{\partial x} \Delta_2 \psi + w \frac{1}{4} \frac{\partial w}{\partial y} + \Delta_2^2 \psi \quad (3)$$

where,

$$\Delta_2 \equiv \frac{\partial^2}{\partial x^2} + \frac{1}{16} \frac{\partial^2}{\partial y^2}, \quad \frac{\partial(f, g)}{\partial(x, y)} \equiv \frac{\partial f}{\partial x} \frac{\partial g}{\partial y} - \frac{\partial f}{\partial y} \frac{\partial g}{\partial x} \quad (4)$$

The Dean number, Dn , which appears in equation (2) is defined as $Dn = \frac{Gd^3}{\mu\nu} \sqrt{\frac{2d}{L}}$

The no slip boundary conditions for w and ψ are used as as

$$w(\pm 1, y) = w(x, \pm 1) = \psi(\pm 1, y) = \psi(x, \pm 1) = \frac{\partial \psi}{\partial x}(\pm 1, y) = \frac{\partial \psi}{\partial y}(x, \pm 1) = 0 \quad (5)$$

In this paper, unsteady solutions are obtained for curvatures $\delta = 0.001$ and $\delta = 0.1$ for the aspect ratio 4.

NUMERICAL CALCULATIONS

In order to solve Eqs. (2) and (3) numerically, the spectral method is used. By this method the expansion functions $\phi_n(x)$ and $\psi_n(x)$ are expressed as

$$\left. \begin{aligned} \phi_n(x) &= (1-x^2) C_n(x), \\ \psi_n(x) &= (1-x^2)^2 C_n(x) \end{aligned} \right\} \quad (6)$$

where $C_n(x) = \cos(n \cos^{-1}(x))$ is the n -th order Chebyshev polynomial. $w(x, y, t)$ and $\psi(x, y, t)$ are expanded in terms of $\phi_n(x)$ and $\psi_n(x)$ as

$$\left. \begin{aligned} w(x, y, t) &= \sum_{m=0}^M \sum_{n=0}^N w_{mn}(t) \phi_m(x) \phi_n(y) \\ \psi(x, y, t) &= \sum_{m=0}^M \sum_{n=0}^N \psi_{mn}(t) \psi_m(x) \psi_n(y), \end{aligned} \right\} \quad (7)$$

where M and N are the truncation numbers in the x - and y -directions respectively. For sufficient accuracy of the solutions, $M = 16$ and $N = 60$ have been considered. To calculate unsteady solutions, the Crank-Nicolson and Adams-Bashforth methods along with the function expansion (7) and the collocation methods are applied.

RESISTANCE COEFFICIENT

We use the resistance coefficient λ as one of the representative quantities of the flow state. It is also called the hydraulic resistance coefficient, and is generally used in fluids engineering, defined as

$$\frac{P_1^* - P_2^*}{\Delta z^*} = \frac{\lambda}{dh^*} \frac{1}{2} \rho \langle w^* \rangle^2, \quad (8)$$

where dh^* is the hydraulic diameter. The main axial velocity $\langle w^* \rangle$ is calculated by

$$\langle w^* \rangle = \frac{v}{16\sqrt{2\delta}} \frac{1}{-1} \int_{-1}^1 dx \int_{-1}^1 w(x, y, t) dy. \quad (9)$$

Since $(P_1^* - P_2^*) / \Delta z^* = G$, λ is related to the mean non-dimensional axial velocity $\langle w \rangle$ as

$$\lambda = \frac{32\sqrt{2\delta} Dn}{5 \langle w \rangle^2}. \quad (10)$$

RESULTS AND DISCUSSION

Case I: Unsteady Solutions for Curvature $\delta = 0.001$

We first perform time evolution calculations for $\delta = 0.001$. Time evolution of λ for $Dn = 100$ is shown in Fig. 2(a). It is found that the unsteady flow is a steady-state solution for $Dn = 100$. To observe the vortex structure and axial flow distribution, a single contour of the secondary flow pattern and axial flow distribution is shown in Fig. 2(b) for $Dn = 100$. As seen in Fig. 2(b), the steady-state flow is a symmetric two-vortex solution. Figure 3(a) shows time evolution result for $Dn = 210$, where we see that the unsteady flow is a multi-periodic solution, which is well justified by drawing the phase space as shown in Fig. 3(b) in the $\gamma - \lambda$ plane, where $\gamma = \iint \psi dx dy$. In Fig. 3(b), we observe that

the flow creates multiple orbits, which suggests that the flow is multi-periodic. Typical contours of secondary flow patterns and axial flow distribution is shown in Fig. 3(c) for one period of oscillation, where we observe that the flow oscillates between asymmetric two-vortex solutions. It is found that the transition from periodic to multi-periodic oscillation occurs between $Dn = 205$ and $Dn = 210$.

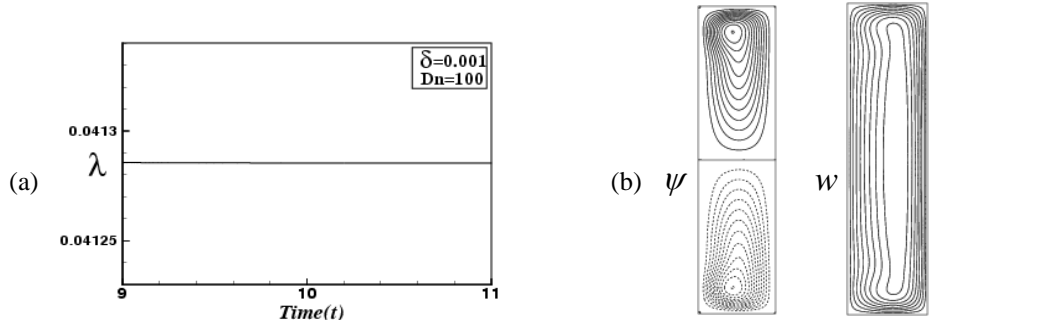


FIGURE 2. Unsteady results for $Dn = 100$ and $\delta = 0.001$. (a) Time evolution of λ , (b) Secondary flow patterns (left) and axial flow distribution (right) at $t = 10$.

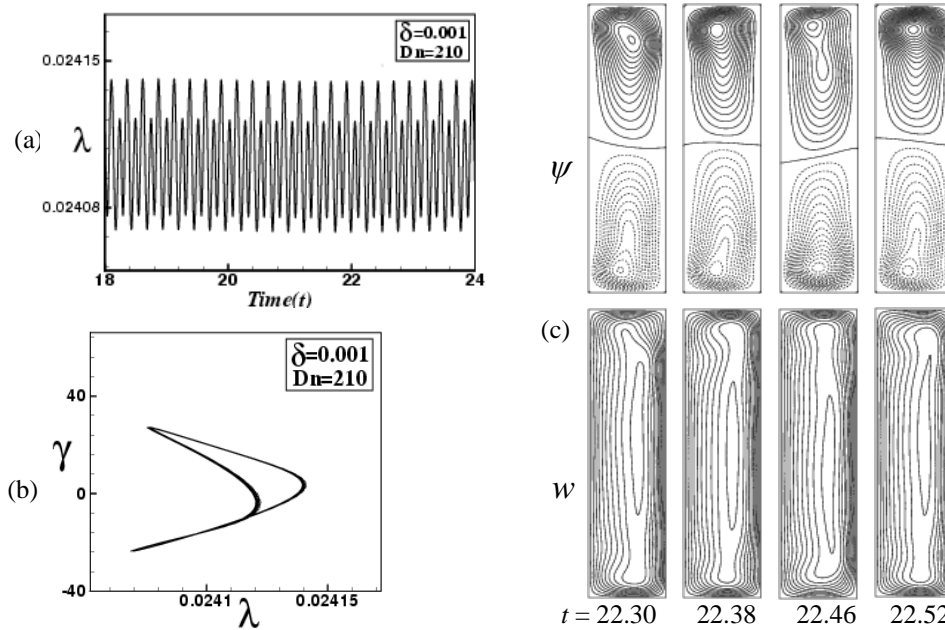


FIGURE 3. Unsteady results for $Dn = 210$ and $\delta = 0.001$. (a) Time evolution of λ , (b) Phase space in the $\gamma - \lambda$ plane, (c) Secondary flow patterns (top) and axial flow distribution (bottom) for $22.3 \leq t \leq 22.52$.

The result of time-dependent solution for $Dn = 220$ is also obtained and it is found that the flow oscillates irregularly (chaotic) between asymmetric four-vortex solutions. This chaotic oscillation is not shown here for brevity. It is found that the transition from multi-periodic to chaotic oscillation occurs between $Dn = 215$ and $Dn = 220$. The chaotic oscillation at $Dn = 220$ is termed as ‘transitional chaos’ (Yanase et al. [6]). Then we studied time evolution calculations for $Dn = 500$ and $Dn = 1000$. Figure 4(a) shows unsteady results for $Dn = 1000$. As seen in Fig. 4(a), the unsteady flow at $Dn = 1000$ oscillates in strongly irregular pattern, i.e. the flow is *strong chaotic*. To justify the chaotic oscillation more clearly, we draw the phase space of the time evolution result as shown in Fig. 4(b), where multiple orbits are seen to be distributed irregularly, which suggests that the flow is a strong chaotic for $Dn = 1000$. Then typical contours of secondary flow patterns and axial flow distribution are shown in Fig. 4(c), where it is seen that the chaotic oscillation at $Dn = 1000$ oscillates between asymmetric eight- to twelve-vortex solutions. This type of chaotic oscillation is called *strong chaos* (Yanase et al. [6]). We also found that the axial flow distribution is consistent with

the secondary vortices and the axial flow is shifted near the outer wall of the duct as Dn increases. In this study, we obtained large number of vortices because of strong centrifugal force.

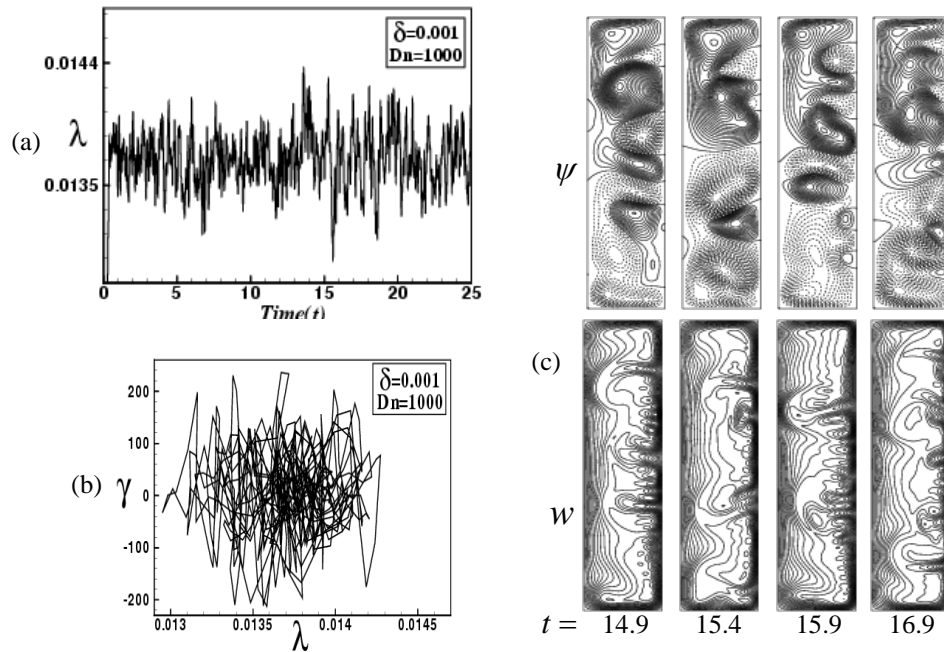


FIGURE 4. Unsteady results for $Dn = 1000$ and $\delta = 0.001$. (a) Time evolution of λ , (b) Phase space, (c) Secondary flow patterns (top) and axial flow distribution (bottom) for $14.9 \leq t \leq 16.9$.

Case II: Unsteady Solutions for Curvature $\delta = 0.1$

Now we investigated unsteady solutions for $\delta = 0.1$. Figure 5(a) shows unsteady solution for $Dn = 100$, which shows that flow is a steady-state solution. Since the flow is steady-state, a single contour of the secondary flow pattern and axial flow distribution is shown in Fig. 5(b), and it is found that the unsteady flow is a symmetric two-vortex solution for $Dn = 100$. Then we investigated time-dependent solutions for $Dn = 230$ and $Dn = 250$ and we found that the flow is a periodic oscillating flow for $Dn = 230$ but chaotic for $Dn = 250$. Therefore the transition from periodic to chaotic oscillation for $\delta = 0.1$ occurs between $Dn = 230$ and $Dn = 250$.

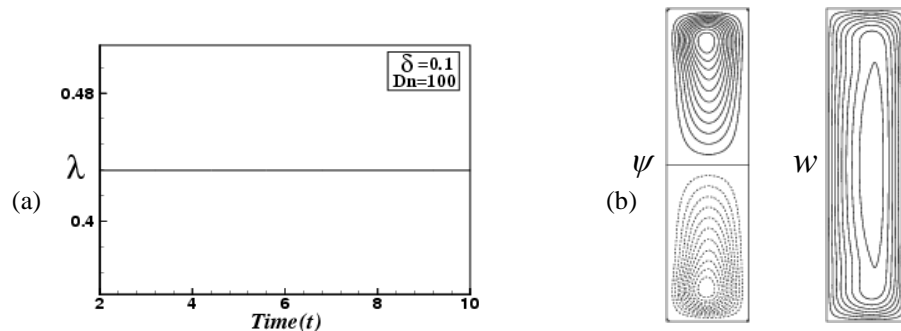


FIGURE 5. Unsteady results for $Dn = 100$ and $\delta = 0.1$. (a) Time evolution of λ for $Dn = 100$ and $\delta = 0.1$. (b) Secondary flow patterns (left) and axial flow distribution (right) at $t = 10$.

Figure 6(a) shows time-evaluation results for $Dn = 400$, which shows that the flow oscillates multi-periodically. This multi-periodic oscillation is well justified by drawing the phase space of the time evolution result as shown in Fig. 6(b). Typical contours of secondary flow patterns and axial flow distributions are shown in Fig. 6(c), and it is

found that the multi-periodic flow at $Dn = 400$ oscillates between asymmetric four- and six-vortex solutions. Then we studied time evolution calculation for $Dn = 1000$ as shown in Fig. 7(a). It is found that the flow oscillates in a strongly irregular pattern, i.e. the flow is strong chaotic. To well justify the chaotic oscillation, the orbits of the phase space is shown in Fig. 7(b). Then to observe the vortex structure of the chaotic flow characteristics at $Dn = 1000$, typical contours of secondary flow patterns and axial flow distribution are shown in Fig. 7(c), where it is seen that the chaotic solution at $Dn = 1000$ oscillates between asymmetric eight- to and ten-vortex solutions.

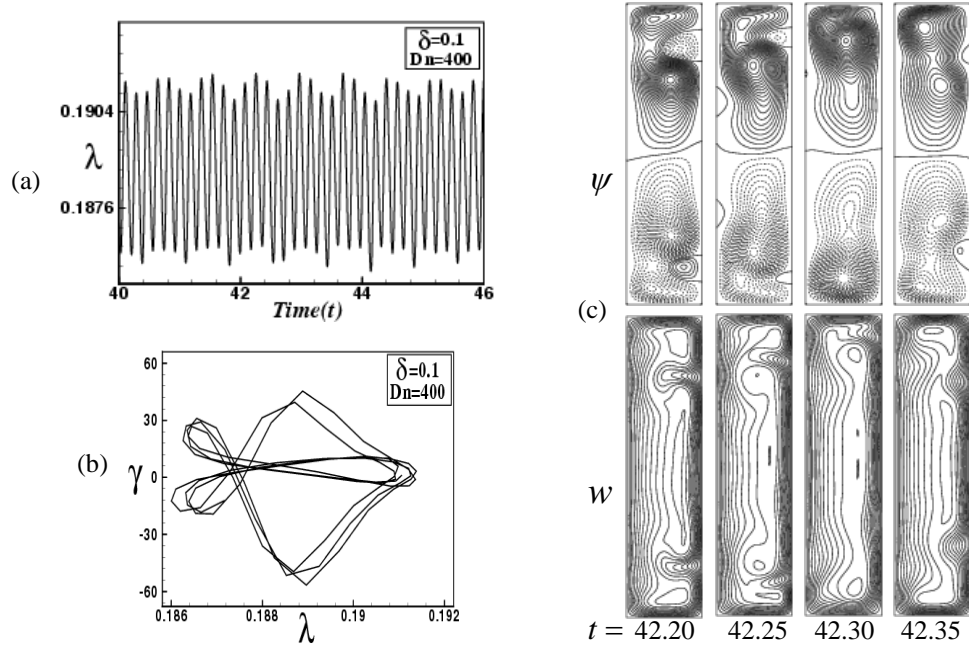


FIGURE 6. Unsteady results for $Dn = 400$ and $\delta = 0.1$. (a) Time evolution of λ , (b) Phase space, (c) Secondary flow patterns (top) and axial flow distribution (bottom) for $42.2 \leq t \leq 42.35$.

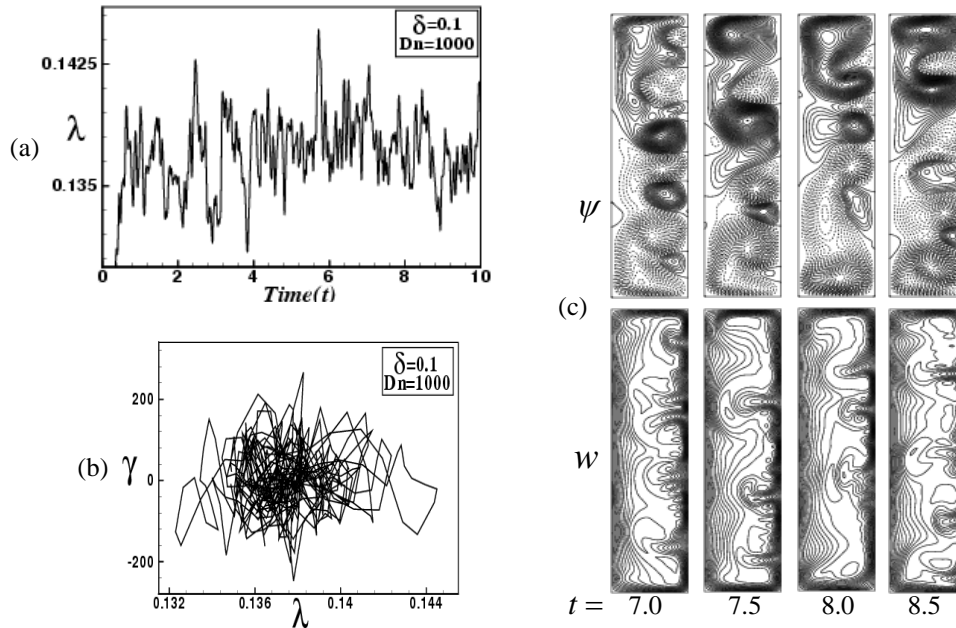


FIGURE 7. Unsteady results for $Dn = 1000$ and $\delta = 0.1$. (a) Time evolution of λ , (b) Phase space, (c) Secondary flow patterns (top) and axial flow distribution (bottom) for $7.0 \leq t \leq 8.5$.

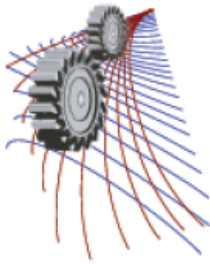
It is also found that the axial flow distribution is consistent with the secondary flows and the axial flow is shifted near the outer wall of the duct as Dn increases. In this study, it is found that the chaotic flow becomes weak as Dn is small but strong as Dn becomes large.

CONCLUSIONS

The present study covers a numerical study on unsteady fluid flow through a curved rectangular duct of aspect 4 by using a spectral method, and covering a wide range of the Dean number for curvatures 0.001 and 0.1. At first, we investigated unsteady solutions for $\delta = 0.001$, and it is found that the unsteady flow is a steady-state solution for $Dn = 100$ but periodic/multi-periodic for $Dn = 210$. The periodic flow oscillates between two-vortex solutions, while multi-periodic flows between two- and three-vortex solutions. The flow becomes chaotic at $Dn = 220$ and remains chaotic up to $Dn = 1000$. It is found that the multi-periodic flow oscillates between four- to eight-vortex solutions, while chaotic flows between eight- to twelve-vortex solutions, and the unsteady flow for $\delta = 0.001$ undergoes through various flow instabilities in the scenario '*steady-state* \rightarrow *periodic* \rightarrow *multi-periodic* \rightarrow *weak chaotic* \rightarrow *strong chaotic*', if Dn is increased. Then we studied unsteady solutions for $\delta = 0.1$ and it is found that the unsteady flow is a steady-state solution for $Dn = 100$ but periodic for $Dn = 230$. The steady-state or periodic flow consists of symmetric two-vortex solutions, while chaotic flow is comprised with asymmetric two- to six-vortex solutions. It is found that the unsteady flow at large Dn 's is always chaotic which oscillates between four- to ten-vortex solutions, and the flow undergoes in the scenario '*steady-state* \rightarrow *periodic* \rightarrow *chaotic* \rightarrow *periodic* \rightarrow *multi-periodic* \rightarrow *chaotic*', if Dn is increased. It is found that axial flow distribution is consistent with the secondary vortices and shifts near the outer wall of the duct as Dn increases.

REFERENCES

1. W. R. Dean, *Philos. Magazines* **4**, 208–223 (1927).
2. S. A. Berger, L. Talbot and L. S. Yao, *Rev. Fluid. Mechanics* **35**, 461–512 (1983).
3. K. Nandakumar and J. H. Masliyah, *Adv. Transport Processes* **4**, 49–112 (1986).
4. M. Akiyama, K. Kikuchi, J. Nakayama, I. Nishiwaki and K. C. Cheng, *Trans. JSME, Ser. B* **47**, 1705 (1981).
5. P. M. Ligrani and R. D. Niver, *Physics of Fluids* **31**, 3605 (1988).
6. S. Yanase, R. N. Mondal and Y. Kaga, *Int. J. Thermal Sciences* **44**, 1047–1060 (2005).
7. M. Norouzi and N. Biglari, *Physics of Fluids* **25**, 053602, 1–15 (20013).
8. S. Yanase and K. Nishiyama, *J. Phys. Soc. Japan* **57**(11), 3790–3795 (1988).
9. L. Wang and F. Liu, *Int. Journal of Non-Linear Mechanics* **42**, 1018 – 1034 (2007).
10. R. N. Mondal, S. Islam, K. Uddin and M. A. Hossain, *Applied Mathematics and Mechanics* **34**(9), 1107–1122 (2013).



Numerical Investigation on Flow and Pressure Characteristics for Plain and Modified Dump Combustor

Somnath Chakrabarti^{1, a)}, Smriti Ghosh^{1, b)} and Ashim Guha^{1, c)}

¹ *Department of Mechanical Engineering, Indian Institute of Engineering Science and Technology, Shibpur, (Formerly Bengal Engineering and Science University, Shibpur), Howrah – 711 103, West Bengal, India.*

a) Corresponding author: somnathbec@rediffmail.com

b) smritighosh47@gmail.com

c) aguhax@rediffmail.com

Abstract. In this paper, a numerical investigation has been carried out to study the flow and wall static pressure characteristics for a plain dump combustor and a modified dump combustor having different dimensional configuration under laminar and turbulent flow conditions. The Reynolds numbers (Re) for laminar and turbulent flow conditions are considered as 450 and 1.2×10^5 respectively. The turbulent parameters are solved by using the realizable $k-\epsilon$ model. Using CFD software GAMBIT 2.3.16 and FLUENT 6.3.26, flow characteristics, such as, streamline contour and wall static pressure have been investigated under the said laminar and turbulent flow conditions. From the study, it is observed that some primary recirculating bubbles are formed at the corner region near the throat for both considered flow conditions. Whereas, for modified dump combustor, some secondary recirculating bubbles are generated adjacent to the upper wall of restriction for both laminar and turbulent flow conditions. Under laminar flow condition, some tertiary recirculating bubbles are found near the exit of the modified dump combustor. In case of turbulent flow condition, tertiary recirculating bubbles are found at the exit of restriction. From the wall static pressure distribution, it is noted that the maximum value of wall static pressure rise at a particular location is always more in modified dump combustor as compared to plain dump combustor for both considered flow conditions.

INTRODUCTION

Dump combustors are sudden expansion configurations, in which air and fuel enter the combustion region through the inlet duct downstream the throat. The combustion occurs little downstream the throat and the flame is stabilized by the presence of recirculation region. The recirculation size is an important parameter for determining the efficiency of the dump combustor. In the present study, sudden expansion configuration having a central restriction ahead the throat is considered as modified dump combustor and plain dump combustor is considered as sudden expansion configuration having no restriction.

Several researches have been carried out on this field till now. Among them, Ghose et al. (2013) have numerically studied the effect of dome shape on static pressure recovery in a dump diffuser at different inlet swirl under turbulent flow condition at $Re = 1.2 \times 10^5$. Rahim and Khafaji (2012) have carried out both numerical and experimental investigations on the computation of turbulent swirling flows inside a can combustor model. Kumar and Dhiman (2012) have performed a numerical study on the laminar flow forced convection and heat transfer characteristics in a 2-d channel introducing an adiabatic circular cylinder. Das and Chakrabarti (2012) have numerically studied the wall static pressure characteristics of fluid passing through a sudden expansion with central restriction and fence. Das and Chakrabarti (2011) have carried out a numerical simulation on the modeling and analysis of a 2-d laminar sudden expansion combustor having central restriction at the inlet for a $Re = 50 - 200$. Ko and Sung (2001) have carried out a large eddy simulation for Reynolds numbers 5000 and 50000 under turbulent flow condition inside a sudden-expansion cylindrical chamber.

Nomenclature

Symbol	Quantity	Unit
L_i	Inlet length (i.e. length between the inlet and the throat section)	m
L_{ex}	Exit length (i.e. length between the throat and the inlet section)	m
W_1, W_2	Width of inlet and outlet duct respectively	m
W_R	Width of restriction	m
L_R	Length of restriction	m
D_R	Distance between the restriction location and throat	m
D_R^*	Non-dimensional distance between restriction location and throat	
Re	Reynolds number	
u_{in}	Magnitude of the inlet axial velocity	m/s
ρ	Density	kg/m ³
μ, μ_t	Dynamic and turbulent viscosity respectively	kg/m.s.
ν	Kinematic viscosity	m ² /s
P	Static pressure	pascal
P_{w-u}, P_{d-in}	Upper wall static pressure and inlet dynamic pressure respectively	pascal
K, ϵ	Turbulent kinetic energy and its dissipation rate respectively	
σ_t	Prandtl number of the turbulent kinetic energy	
σ_ϵ	Dissipation energy	

The objective of the present work is to carry out a numerical investigation on the streamline contour and upper wall static pressure characteristics of fluid flowing through a plain dump combustor and a modified dump combustor incorporating a central restriction at a certain distance ahead the throat under laminar and turbulent flow conditions.

MATHEMATICAL FORMULATION

Computational Domain

A schematic diagram of the computational domain for a plain dump combustor and a modified dump combustor under both laminar and turbulent flow conditions are shown in Fig. 1 (a) and (b) respectively.

Under laminar flow condition, the length of inlet duct (L_i) and width (W_1) are taken as 0.08m and 0.04m respectively. The length of outlet duct (L_{ex}) and width (W_2) have been chosen as 0.3m and 0.12m respectively. The length (L_R) and width (W_R) of central restriction have been taken as 0.06m and 0.02m respectively.

Under turbulent flow condition, the length of inlet duct (L_i) and width (W_1) are 0.1m and 0.054m respectively. The length of outlet duct (L_{ex}) and width (W_2) have been taken as 0.5572m and 0.1524m respectively. The length (L_R) and width (W_R) of central restriction have been chosen as 0.1524m. A non-dimensional distance between the throat and the inlet of restriction, $D_R^* = D_R / W_2 = 0.5$ has been used in the modified dump combustor. All the dimensions of the configurations have been taken from Ko and Sung (2001) and Ghose et al. (2013) under laminar and turbulent flow conditions respectively, except the exit length of the configuration and the length of the restriction.

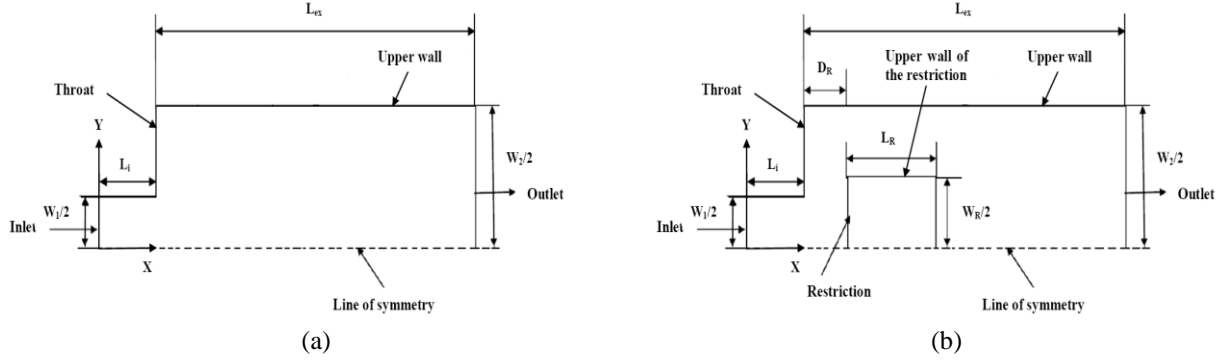


FIGURE 1. Schematic diagram of the computational domain (a) plain dump combustor (b) modified dump combustor.

Governing Equations

The flow is considered to be steady, two-dimensional and symmetric. The fluid is considered to be Newtonian and incompressible. Under these assumptions, the governing equations become,

Continuity equation:

$$\frac{\partial u}{\partial x} + \frac{\partial v}{\partial y} = 0 \quad (1)$$

Momentum equation in X-axis:

$$\rho \left(u \frac{\partial u}{\partial x} + v \frac{\partial v}{\partial y} \right) = -\frac{\partial p}{\partial x} + \mu \left[\frac{\partial}{\partial x} \left(\frac{\partial u}{\partial x} \right) + \frac{\partial}{\partial y} \left(\frac{\partial u}{\partial y} \right) \right] \quad (2)$$

Momentum equation in Y-axis:

$$\rho \left(u \frac{\partial v}{\partial x} + v \frac{\partial v}{\partial y} \right) = -\frac{\partial p}{\partial y} + \mu \left[\frac{\partial}{\partial x} \left(\frac{\partial v}{\partial x} \right) + \frac{\partial}{\partial y} \left(\frac{\partial v}{\partial y} \right) \right] \quad (3)$$

The governing realizable k- ϵ equations representing the turbulent properties are as follows,
k- equation

$$\rho \left(u \frac{\partial k}{\partial x} + v \frac{\partial k}{\partial y} \right) = \frac{\partial}{\partial x} \left[\left(\mu + \frac{\mu_t}{\sigma_k} \right) \frac{\partial k}{\partial x} + \left(\mu + \frac{\mu_t}{\sigma_k} \right) \frac{\partial k}{\partial y} \right] + \rho G - \rho \epsilon \quad (4)$$

ϵ - equation

$$\rho \left(u \frac{\partial \epsilon}{\partial x} + v \frac{\partial \epsilon}{\partial y} \right) = \frac{\partial}{\partial x} \left[\left(\mu + \frac{\mu_t}{\sigma_\epsilon} \right) \frac{\partial \epsilon}{\partial x} + \left(\mu + \frac{\mu_t}{\sigma_\epsilon} \right) \frac{\partial \epsilon}{\partial y} \right] + \rho C_{1\epsilon} S \epsilon + C_{1\epsilon} \frac{\epsilon}{k} C_{3\epsilon} G - \rho C_{2\epsilon} \frac{\epsilon^2}{k + \sqrt{\nu \epsilon}} \quad (5)$$

Where, G is the production term. Here, $C_{1\epsilon}$, $C_{2\epsilon}$, $C_{3\epsilon}$, C_{μ} , σ_k and σ_ϵ are the empirical turbulent constant. The values are considered according to the Launder and Spalding (1974) as, $C_{1\epsilon}$, $C_{2\epsilon}$, $C_{3\epsilon}$, C_{μ} and σ_ϵ are 1.44, 1.9, 0.09, 1.0 and 1.3 respectively. The turbulent viscosity, μ_t is given by $\mu_t = \rho C_{\mu} k^2 / \epsilon$.

Boundary Conditions

The boundary conditions considered for the problem are as follows:

No slip condition at the wall; uniform axial velocity at the inlet; constant pressure boundary at the exit; symmetry at the center line of the duct.

Numerical Procedure

Commercial software GAMBIT 2.3.16 is used to make the geometry and mesh of the computational domain. Commercial CFD software FLUENT 6.3.26 is used to solve the governing equations. The control volume technique on a non-uniform staggered grid arrangement following SIMPLE algorithm along with second order upwind scheme is employed to solve the governing discretised equations. The turbulent parameters are solved by using the realizable k- ϵ model. The convergence criteria of the iterative scheme have been considered as 10^{-3} .

In this numerical investigation, the working fluid is air. The density of air, is taken as 1.225 kg/m^3 . The viscosity of air, is taken as $1.7894 \times 10^{-5} \text{ kg/m.s}$. In case of laminar flow, the inlet velocity u is obtained from the considered value of the Reynolds number by using the relation, $Re = \rho u_{in} W_1 / \mu$. The Reynolds number for laminar flow is taken as 450. Whereas, in case of turbulent flow, the Reynolds number (Re) is considered as 1.2×10^5 , based on the inlet width (W_1) and the inlet axial velocity, $u_{in} = 32.37 \text{ m/s}$. In both cases, the dynamic pressure at inlet is obtained by using the relation, $P_{d-in} = \rho u_{in}^2 / 2$.

Validation of Results

The numerical predictions from the model are validated by comparing against both the experimental and numerical data of Ko and Sung (2002) for the same combustor geometry except the geometry of central restriction at $Re = 5000$ with corresponding inlet axial velocity, $u_{in} = 1.8259 \text{ m/s}$. In the present numerical analysis, the length of restriction is taken as $L_r^* = 3$ w.r.t the length of restriction $L_r = 0.15$ in Ko and Sung (2002). The validation result of the flow velocity along the centreline of modified dump combustor is shown in Fig. 2.

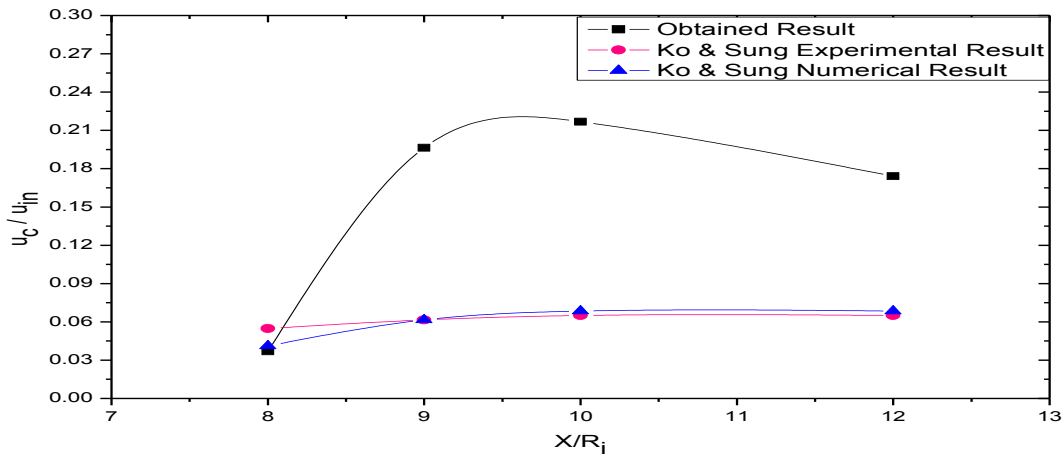


FIGURE 2. Variation of flow velocity along the centerline with those of Ko And Sung (2002) at $Re = 5000$ and $u_{in} = 1.8259 \text{ m/s}$.

From Fig. 2, it is noted that at $X/R_i = 8$, the obtained data (u_c/u_{in}) is quite close to both the experimental and numerical data of Ko and Sung (2002). Beyond that, some differences in the obtained data (u_c/u_{in}) values at $X/R_i = 9$, $X/R_i = 10$ and $X/R_i = 12$ are observed as compared to the data (u_c/u_{in}) values in Ko and Sung result at the same positions. Long length of central restriction and the difference in restriction geometry of the considered modified dump combustor model may be the prime cause on some disagreement in the flow velocity magnitude as compared to Ko and Sung result (2002). It is also noted that after $X/R_i = 10$, the error percentage between both results tends to reduce slightly.

RESULTS AND DISCUSSION

In this present investigation, the streamline contours and upper wall static pressure characteristics of fluid flowing through a plain dump combustor and a modified dump combustor under laminar and turbulent flow conditions for the considered Reynolds numbers have been examined.

Variation of Streamline Contour

Variation of Streamline Contour under Laminar Flow

Fig. 3 (a) shows the nature of streamline contour for a plain dump combustor and Fig. 3 (b) shows the nature of streamline contour for a modified dump combustor for $Re = 450$.

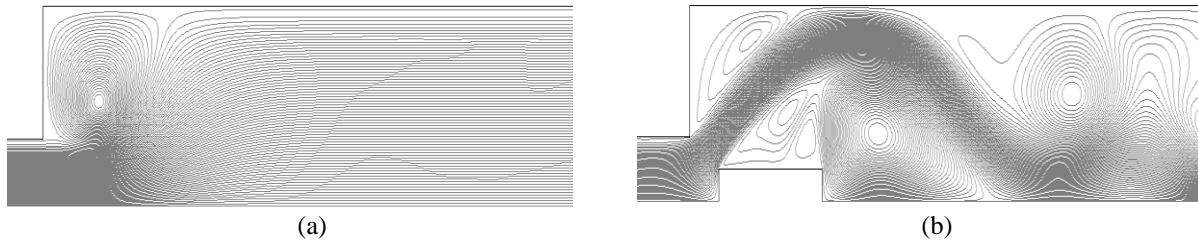


FIGURE 3. Stream line contour at $Re = 450$ for (a) plain dump combustor and (b) modified dump combustor configuration.

From Fig. 3 (a), it is observed that some recirculating bubbles exist at the corner regions ahead the throat of plain dump combustor. Whereas, from Fig. 3 (b), it is found that some primary recirculating bubbles form at the corner region ahead the throat as well as some secondary recirculating bubbles form at the central region above the upper wall region of the restriction of modified dump combustor. Some tertiary recirculating bubbles also start forming near the exit of modified dump combustor.

Variation of Streamline Contour under Turbulent Flow

Fig. 4 (a) shows the nature of streamline contour for a plain dump combustor configuration and Fig. 4 (b) shows the nature of streamline contour for a modified dump combustor configuration for Reynolds number 1.2×10^5 .

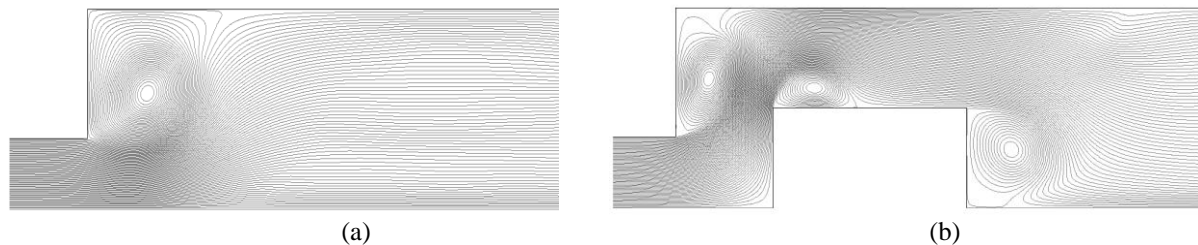


FIGURE 4. Stream line contour at $Re = 1.2 \times 10^5$ for (a) plain dump combustor and (b) modified dump combustor configuration.

From Fig. 4 (a), it can be revealed that for plain dump combustor, a corner recirculation zone occurs just ahead the throat. Whereas, from Fig. 4 (b), it is found that for modified dump combustor, a primary recirculation zone is observed ahead the throat. Some secondary recirculation zones are also formed adjacent to the upper wall of restriction and some tertiary recirculating bubbles also form at the exit of the restriction.

Under each flow condition, recirculating bubbles at the corner region form due to the flow separation that occurs downstream to the throat section. As the velocity of fluid particles reaches to a very small value near the wall region due to convective deceleration, the fluid particle cannot overcome the high downstream pressure that creates some flow recirculations near the wall.

In case of modified dump combustor, when fluid particle passes through a restricted passage, the flow gets accelerated. A flow separation occurs due to sudden detachment that forms some secondary recirculating bubbles at the central region above the upper restriction wall and some tertiary recirculating bubbles also form due to high rate of diffusion. These secondary and tertiary recirculating bubbles may provide another chance to the unburnt fluid particles to remix with air uniformly, which may increase the tendency of occurring complete combustion. These may also enhance the possibility of reducing No_x emission and may increase combustion efficiency.

Variation of Wall Static Pressure

Variation of Upper Wall Static Pressure under Laminar Flow

Fig. 5 depicts the variation of upper wall static pressure of a plain dump combustor and a modified dump combustor for $Re = 450$ under laminar flow condition.

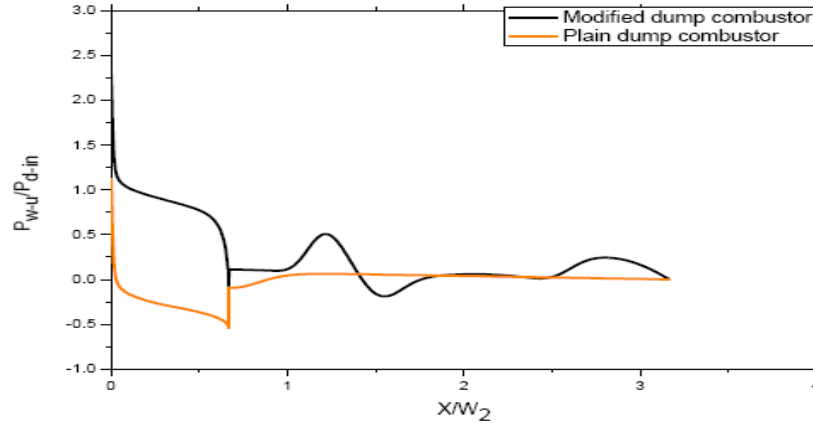


FIGURE 5. Upper wall static pressure variation for both for modified and plain dump combustor at $Re = 450$.

From Fig. 5, it is observed that for modified dump combustor, the static pressure along the upper wall gradually decreases from the inlet to the throat due to both convective acceleration and viscous effects. Beyond the throat, the magnitude of static pressure increases sharply. At the reattachment point, the magnitude of static pressure reaches to a peak value. Then, the static pressure droops down due to the internal fluid friction. The increasing trend of the pressure has been noted at another location near exit, where formation of tertiary recirculating bubble occurs due to higher diffusion. At the exit, it becomes equal to considered gauge pressure.

In case of plain dump combustor, it is found that the static pressure along the upper wall also decreases gradually from the inlet to the throat due to both convective acceleration and viscous effects. After the throat, as kinetic energy due to diffusion increases, the magnitude of static pressure also starts increasing up to a certain level. Near the exit, the flow reattaches with the wall and the static pressure remains almost constant up to the exit of the combustor.

Variation of Upper Wall Static Pressure under Turbulent Flow

Fig. 6 depicts the variation of static pressure along the upper wall of a plain dump combustor and a modified dump combustor for $Re = 1.2 \times 10^5$ under turbulent flow condition.

From Fig. 6, it is revealed that for the modified dump combustor, the static pressure along the upper wall gradually decreases from the inlet to the throat. Beyond the throat, as the flow passes through a suddenly expanded geometry, the magnitude of static pressure sharply increases. The magnitude of static pressure rises to a maximum at the reattachment point. In this region, a high downstream pressure is obtained. Then, again static pressure starts decreasing. Then, near from the exit of restriction, static pressure again gradually starts increasing. After the flow reattachment occurs, the static pressure remains uniform up to the exit of the combustor.

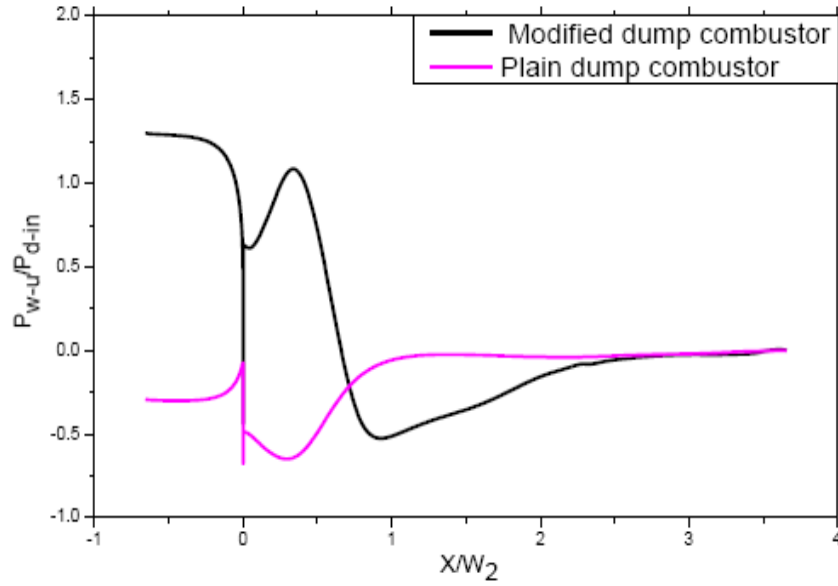


FIGURE 6. Upper wall static pressure variation for both for modified and plain dump combustor at $Re = 1.2 \times 10^5$.

It is noted that the maximum value of wall static pressure rise at a particular location is always more in modified dump combustor than that of plain dump combustor for both flow conditions. The maximum value of wall static pressure for modified dump combustor at the reattachment point adjacent to the upper restriction wall is significantly higher under turbulent flow condition as compared to under laminar flow condition. This high downstream pressure helps fluid particle to mix with air more uniformly in modified dump combustor. This may enhance the possibility of complete combustion and increase combustion efficiency. So, modified dump combustor may be more beneficial than plain dump combustor in industry.

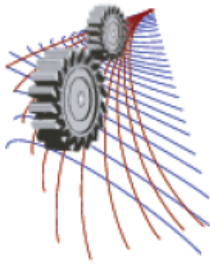
CONCLUSION

The following major conclusions can be made from the present study:

1. Secondary and tertiary recirculating bubbles in modified dump combustor help unburnt fluid particles to remix with air uniformly, which may enhance the possibility of occurring complete combustion.
2. Better combustion facility and high downstream pressure can be obtained using modified dump combustor under turbulent flow as compared to laminar flow condition.
3. In actual practice, it may be more effective to consider a modified dump combustor under turbulent flow condition to obtain better combustion efficiency as well as combustor performance.

REFERENCES

1. P. Ghose, A. Dutta and A. Mukhopadhyay, *Int. J. of Emerg. Tech. and Adv. Engg.* **3**, 465-471 (2013).
2. A. Rahim and D. A. Khafaji, *Int. J. of Mech. Engg. and Robot. Res.* **1**, 1-8, (2012).
3. A. Kumar and A. K. Dhiman, *Int. J. of Ther. Sci.* **52**, 176-185, (2012).
4. T. Das and S. Chakrabarti, *Int. J. of Emerg. Tech. and Adv. Engg.* **2**, 109-116, (2012).
5. T. Das and S. Chakrabarti, *Int. J. of Engg. Sci. Res-IJESR*, **2**, 371-380, (2011).
6. S. C. Ko and H. J. Sung, *J. of Flow, Turb. and Comb.* **68**, 269-287, (2002).
7. S. C. Ko and H. J. Sung, *J. of Turb.* **2**, 1-16, (2001).
8. B. E. Launder and D. B. Spalding, *Comp. meth. in Appl. Mech. and Engg.* **3**, 269-289, (1974).



Enhanced Heat Sink with Geometry Induced Wall-jet

Md. MahamudulHossain^{a)}, AmitavTikadar, Fazlulbari,AKM M. Morshed.

*Department of Mechanical Engineering
Bangladesh University of Engineering and Technology, Dhaka-1000.*

a)Corresponding author: sohel0991@gmail.com

Abstract. Mini-channels embedded in solid matrix have already proven to be a very efficient way of electronic cooling. Traditional mini-channel heat sinks consist of single layer of parallel channels. Although mini-channel heat sink can achieve very high heat flux, its pumping requirement for circulating liquid through the channel increase very sharply as the flow velocity increases. The pumping requirements of the heat sink can be reduced by increasing its performance. In this paper a novel approach to increase the thermal performance of the mini-channel heat sink is proposed through geometry induced wall jet which is a passive technique. Geometric irregularities along the channel length causes abrupt pressure change between the channels which causes cross flow through the interconnections thus one channel faces suction and other channel jet action. This suction and jet action disrupts boundary layer causing enhanced heat transfer performance. A CFD model has been developed using commercially available software package FLUENT to evaluate the technique. A parametric study of the velocities and the effect of the position of the wall-jets have been performed. Significant reduction in thermal resistance has been observed for wall-jets, it is also observed that this reduction in thermal resistance is dependent on the position and shape of the wall jet.

INTRODUCTION

The performance of most electronic components is adversely affected by the increase in its temperature. Whereas, the trend for making electronic circuits denser and more compact is growing rapidly, resulting in hotter and hotter electronic devices. This requires the thermal engineer to design more efficient, compact, and high heat flux electronic cooling devices. Mini-channel cooling has been already been proven to be an efficient and high performance cooling method. The mini-channel heat sink combines the attributes of high surface area per unit volume enabling large heat transfer. Mini-channel heat sink has been studied extensively both numerically and experimentally since its early introduction by Tuckerman and Pease [1] who performed experiments on silicon based mini-channel heat sink for electronic cooling. Toh et al. [2], Qu and Mudawra [3], Peterson and Cheng [4] carried out detailed numerical study of heat transfer in micro-channel heat sinks by solving three-dimensional Navier-Stokes and energy equation. Although mini-channel heat sinks are capable of dissipating high heat fluxes, the small flow rate produces a large temperature rise along the flow direction in both solid and liquid. Therefore, to minimize this temperature rise for large heat flux dissipation a higher mass flow rate of the coolant is required which leads to large pressure drop in the channels and increased pumping power.

The unfavorable temperature gradient and high pressure loss can be reduced by bonding several single layer mini-channels into a stack. Valafi and Zhu [5] first studied double layer cross flow heat sink for electronics cooling application and demonstrated that two layered mini-channel heat sink design is a substantial improvement over single layer conventional heat sink. For a fixed flow rate, the pressure drop is reduced by a factor almost equal to the number of layers, compared with single layered mini-channels. Wei [6-7] investigate two layered mini-channel for parallel and counter flow arrangement and reported thermal resistance as low as $0.09^{\circ}\text{C}/\text{W}/\text{cm}^2$ for both counter flow and parallel flow configurations and at a fixed pumping power the overall thermal resistance for a two-layered mini-channel is 30% less than that of a single-layered mini-channel. Lei and Ning [8] have studied multilayer mini-channel heat sink experimentally and numerically. Cheng [9] investigated multi layered mini-channel with passive micro structure and demonstrated better performance over smooth single layered mini-channel. Xuet. al.[11]

demonstrated that heat transfer in mini-channel can be enhanced by placing cross channel in the flow direction that will break and redevelop the thermal boundary layer. Lee and Garimella [12] investigated developing flow heat transfer in micro-channel and proposed analytical correlation between Nusselt number and non-dimensional flow length for developing flow in mini-channel. In the developing zone heat transfer rate is very high compare to developed zone. From the result of Al-Bakhit et al. [13], entrance region the developing velocity profiles lead to higher values of overall heat transfer coefficient. Morshedand khan[15] studied a multilayered micro-channel heat sink with interconnectors.

In this paper, the opportunities of hear transfer enhancement of two layered interconnected mini-channel heat sink by introducing wall-jet is investigated. This heat sink takes advantage of both the multi-layer and thermal boundary layer re-development due to cross flow of coolant between the interconnected channels. Conjugate heat and mass transfer equations are solved for this heat sink using commercially available CFD code FLUENT. The heat sink is compared based on thermal resistance and pressure drop penalty.

NOMENCLATURE

D_h hydraulic diameter (mm) u velocity (m/s) C_p specific heat (kj/kg-K) k thermal conductivity (w/m-K) R_t thermal resistance (K/w-cm ²) h_x local heat transfer coefficient(w/m ² -K) Re Reynolds number Nu_x local Nusselt number $T_{w,max}$ maximum temperature of the Heat sink(k) $T_{i,f}$ inlet temperature of coolant (k) $T_{x,w}$ local temperature of the heat sink (K)	L_h hydrodynamic entry length L_t thermal entry length x position along the channel Q volume flow rate (m ³ /s) q heat flux chip (w/cm ²) Pr Prandtl number Δp pressure difference (pa) Symbols in inlet out outlet f fluid pp pumping power Greek symbols ρ density (kg/m ³) μ liquid dynamic viscosity (kg/m-s)
---	---

SIMULATION METHODOLOGY

In this paper, the two-dimensional fluid flow and heat transfer characteristics were analyzed for the model numerically by using the commercial computational dynamics (CFD) package, FLUENT. The three dimensional configuration of the heat sink is presented in fig.1.

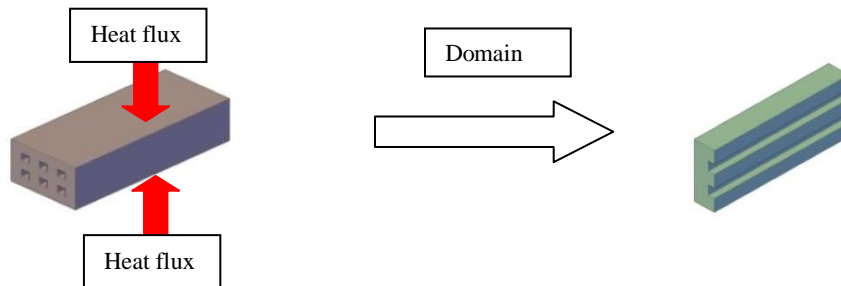


FIGURE 1. Configuration of the mini-channel heat sink

The two dimensional computational domain for the mini-channel is presented in Fig.2. The computational domain was mainly consists of two rectangular channels of 10mm×1mm (length ×height) separated by a wall of 10mm×3mm (length ×height) . Two interconnectors of 1mm×3mm (length ×height) were introduced within the wall as presented in fig.2(b) to fig.2(g). The wall jet effect was introduced by using both the interconnector and bump. Four Rectangular bump of 0.6mm×0.2mm (length×height) in different location were considered in the computational domain as presented in fig.2(c) to fig.2(f).To investigate the effect of size of wall jet four triangular bump of 0.6mm × 0.2mm (base × height) were placed as shown in Fig. 2 (g).

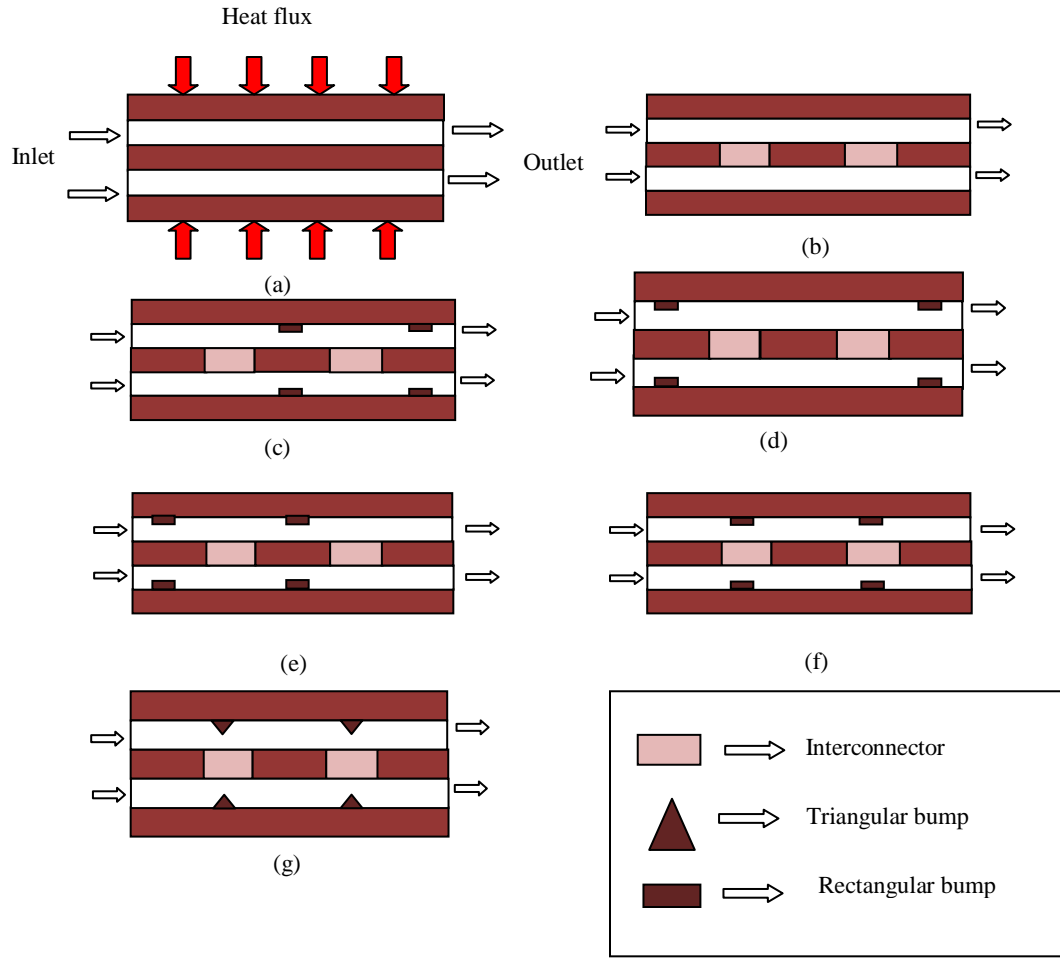


FIGURE 2.Computational domain of different configuration of the heat sink (2D)

MATHEMATICAL FORMULATION

Several assumptions were incorporated before establishing governing equations for the fluid flow and heat transfer in the mini-channel such as Incompressible fluid, Laminar flow in the mini-channel, Negligible radiation and natural convection heat loss, Negligible axial conduction, constant fluid properties. The incompressible governing equations used to describe the fluid flow and heat transfer in the system are expressed as follows:

Continuity

$$\nabla \vec{V} = 0 \quad (1)$$

Navier-Stokes equation:

$$\rho \frac{\partial \vec{V}}{\partial t} + \rho(\vec{V} \cdot \nabla \vec{V}) = -\nabla P + \nabla \cdot (\mu \nabla \vec{V}) \quad (2)$$

Energy equation:

$$\rho C_p \frac{\partial T}{\partial t} + \rho C_p (\vec{V} \cdot \nabla T) = k \nabla^2 T \quad (3)$$

The overall thermal resistance can be defined by-

$$R_t = \frac{T_{w,max} - T_{i,f}}{q} \quad (4)$$

The pumping power required to drive the coolant through the mini-channel is given by

$$PP = (P_{in} - P_{out}) \times Q \quad (5)$$

Local Nusselt number is calculated using the following equation

$$Nu_x = \frac{h_x D_h}{k} \quad (6)$$

A uniform velocity is applied at the channel inlet. Thus

$$u = u_{in}, v = 0, w = 0 \quad (7)$$

The inlet velocity was varied from 0.1m/s to 1.5m/s. The inlet temperature of the cooling water was set to a constant value at the channel inlet. A constant temperature of 300K was applied at the channel inlet and a uniform heat flux of 100W/cm² was applied at both the upper and lower surfaces of the heat sink model.

MODEL VALIDATION

Governing equations were solved using the laminar model. The computational model was verified using grid independence test. Two different sizes of uniform mesh were generated and compared based on center line temperature of the channel as presented in Fig. 3(a). For the two different sizes of mesh (total mesh 115000 and 242223) the difference in the temperature was found less than 0.06%. Therefore, 115000 meshes were considered adequate and this grid spacing was used for all the cases of this study.

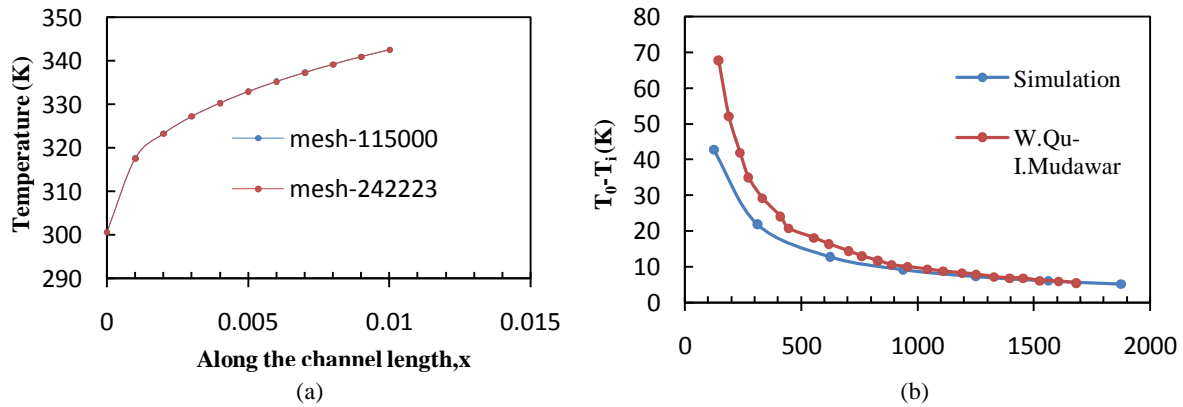


FIGURE 3 (a) Mesh independence test (b) Comparison of numerical simulation and experimental result from Qu and Mudawar[14]

Reynolds number and temperature difference between the inlet and outlet of heat sink were calculated for the model and compared with the experimental result of Qu and Mudawar [14] for thermally developing flow as presented in Fig.3(b). The numerical results and the experimental results are in well agreement, which validates the computational model used in this study, and gives us confidence for further investigation.

RESULTS AND DISCUSSION

The velocity and temperature map of the heat sink is presented in Fig. 4 for the velocity of 1.5m/s. As can be found in the figure, the velocity and thermal boundary layer was in the developing region throughout the channel. The finding is in consistent with the theoretical laminar velocity and thermal entry length ($L_h = 0.05 \times Re \times Dh$ and $L_t = L_h \times Pr$) 75mm considering water Prandtl number 1.

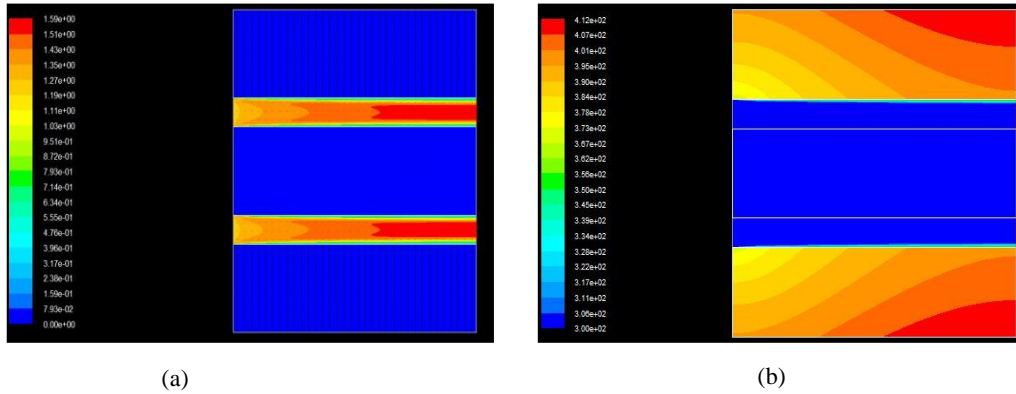


FIGURE 4.(a)Velocity and (b)Temperature map of the heat sink without interconnector and wall jet

Thermal resistance of the channel was observed to increase along the length of the channel. Due to the thermally developing flow within the channel, the thermal and velocity boundary layer thickness increases from inlet to outlet of the channel which decrease the local heat transfer coefficient, hence increase the local thermal resistance along the channel length as presented in Fig.5.

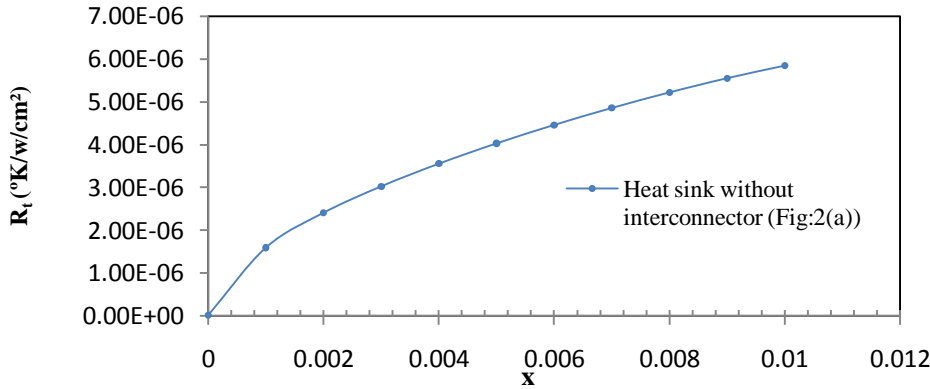
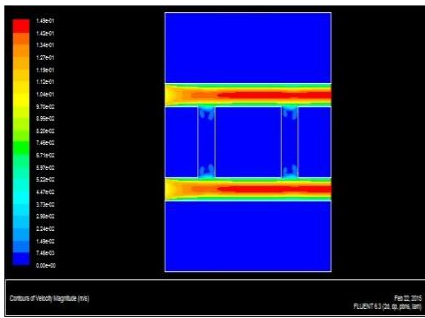
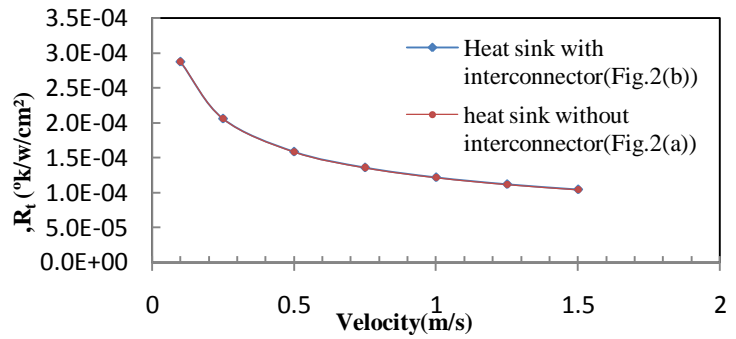


FIGURE 5. Local thermal resistance as a function of channel length

As part of the proposed concept for disruption of the boundary layer, the effect of interconnecting layered channels [Fig.2 (b)] was studied. The interconnectors allow the coolant to flow between the vertical channels. The effect of the interconnectors was observed to be very minimum and as observed from the velocity map, the cross flow was not very significant. If more flow can be drawn through the connectors more profound effect can be harnessed. The gravitational force does not play any significant role in creating the cross flow for the mini-channels. The cross flow occurs between the vertical channels due to pressure gradient between them. Pressure gradient can be created by using different inlet velocities of coolant through the channels, however introduction of different velocities create complexity in the design and application. In this proposed model same inlet velocity was used for all channels. As a result the cross flow was not significant to break the boundary layer to have a noticeable effect as presented in Fig. 7(a) and (b). The overall thermal resistance of the heat sink was observed to reduce by 0.1% for the interconnectors.



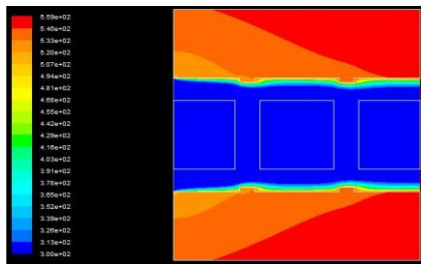
(a)



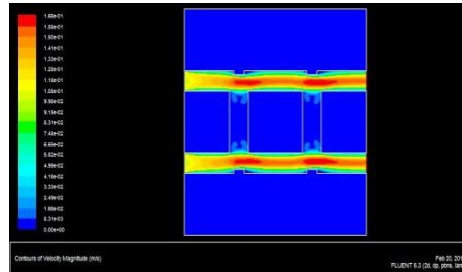
(b)

FIGURE 6.(a)Velocity contour of interconnected heat sink (b)Comparison of thermal resistance as a function of velocity

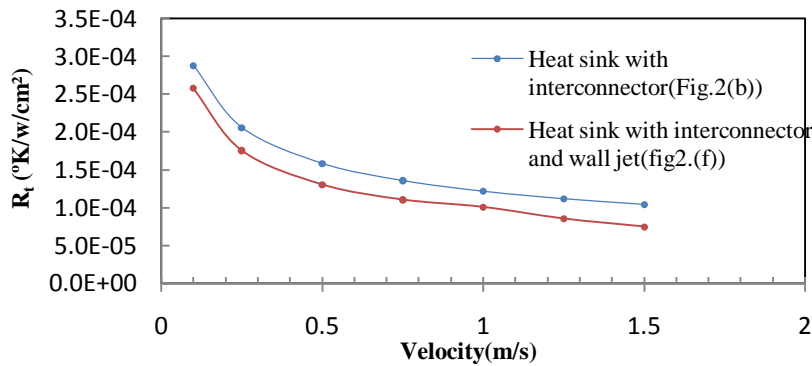
To introduce the cross flow, wall jet of different configurations are incorporated inside the channels as presented in Fig.2(c) to 2(g). In this study, four rectangular bumps were placed in each channel to introduce the wall jet. The proposed wall jet enhances the cross flow as can be observed from Fig.7(a) &(b). Due to high cross flow more disruption of velocity and thermal boundary layer was observed causing higher heat transfer rate.



(a)



(b)



(c)

FIGURE 7 .(a)Temperature (b)Velocity contour with wall jet (c)Comparison of thermal resistance for interconnecting channel with and without wall-jet

In the case of channels with wall jet, the maximum temperature is much less than the temperature rises in the interconnecting channels without wall jet. It is clearly noticed from the Fig.7© that the overall thermal performance of the interconnecting channels with wall jet is better than the interconnecting channels without wall jet. For velocity

0.75 m/s the thermal resistance of the interconnecting channels with wall jet was 19% less than the interconnecting channels without wall jet.

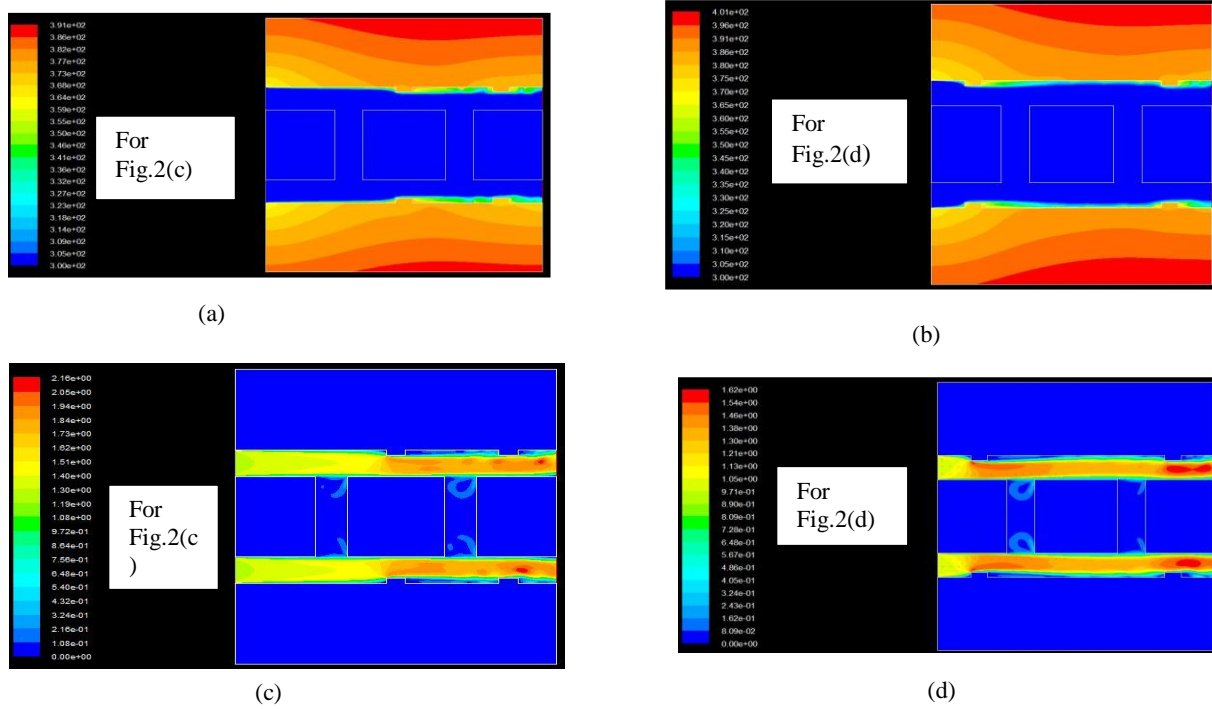


FIGURE 8.(a)& (b) Temperature and (b)&(d) velocity contour for different location of the wall jet.

The enhancement of heat transfer depends on the position and shape of the wall jet. In this study the effect of wall jet position was studied by placing the bump in three different positions of the interconnecting channels as shown in Fig.2 (c) to 2 (f). Wall jet position is important to avoid reverse flow within the channel; otherwise it adversely affects the thermal performance of the heat sink. The temperature and velocity contour for different positions of wall jet is shown in Fig.8. From the contour it is clear that the breaking of both the velocity and thermal boundary layer occurs around the wall jet as expected. Local heat transfer varies for different positions of wall jet.

To evaluate the dependency of thermal performance of the heat sink on the shape of the bump, four wall jet with triangular bump were placed. From Fig.9 it is observed that the interconnecting channel with triangular bump has higher overall thermal resistance (around 2.5 to 6% more) as compared to interconnecting channels with rectangular bump.

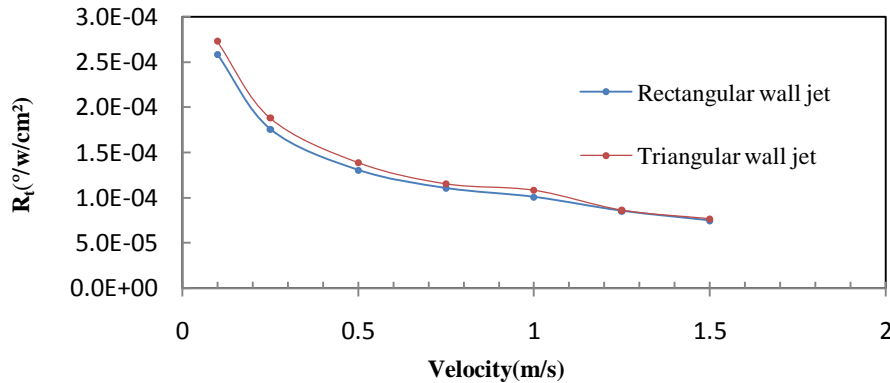


FIGURE 9.Comparison of overall thermal resistance of the heat sink with wall jet for different shape of bump

Pumping power requirement is also taken into consideration in this study. High pumping power requirements can offset the heat transfer enhancement. The variation of overall thermal resistance for different configurations of the heat sink for different pumping power is demonstrated in Fig.10. It was observed that the heat sink with and without interconnector has almost same performance. However, the heat sink with interconnector and wall jet has less overall thermal resistance as compared to the other two configurations for the same pumping power. So introducing interconnector without wall jet has little impact on the overall thermal performance of the heat sink and the heat sink will be most effective by introducing wall jet within the channel.

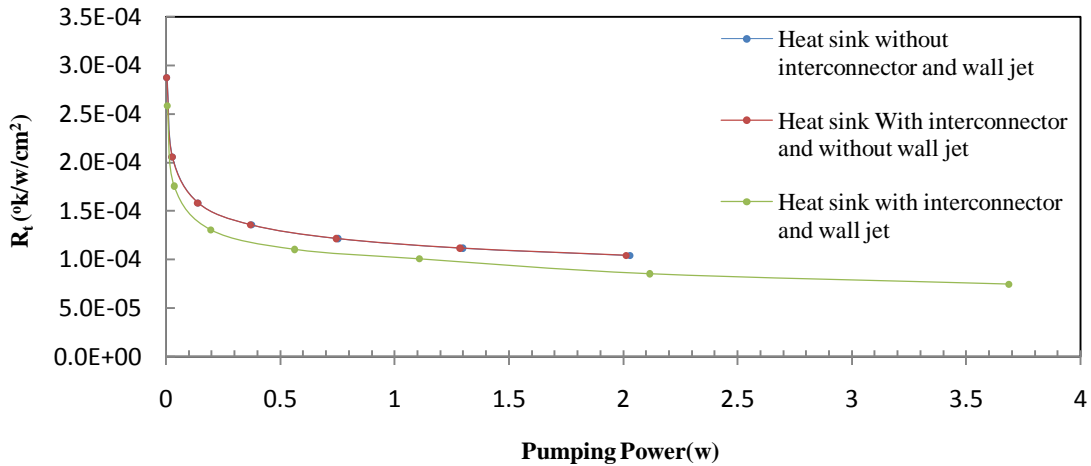


FIGURE 10. Thermal resistance as a function of pumping power for different configuration of layered heat sink

CONCLUSIONS

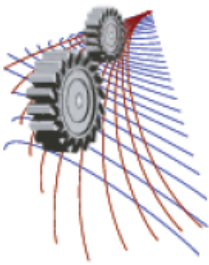
Heat removal from an electric chip is always challenging and very critical. The water cooled mini-channel heat sink is an attractive way to cool electronic chips. In this paper, two-dimensional simulations of the laminar heat transfer in a water cooled mini-channels heat sink were studied. Heat transfer rate from the heat sink decreases due to formation of thermal and velocity boundary layer. To enhance the heat transfer rate, wall jets of different shape and position were introduced. From the simulation results following conclusion can be drawn:

- Introducing interconnector has very little effect on the thermal performance of the heat sink as compared to channel without interconnector due to little disruption of the thermal boundary layer.
- Introducing wall jet has a very significant effect on the thermal performance due to local turbulence and disruption of the thermal and velocity boundary layer.
- Bump location to introduce the wall jet have significant effect. Wall jet introduced by the bump in front of the interconnector gives superior thermal performance as compared to other locations of the bump.
- Wall jet with rectangular bump provides better thermal performance compared to the wall jet with triangular bump

REFERENCES

1. Tuckerman, D.B. and R. Pease, Electron Device Letters, IEEE **2(5)**, 126-129 (1981).
2. Toh, K., X. Chen, and J. Chai, International Journal of Heat and Mass Transfer **45(26)**, 5133-5141 (2002).
3. Qu, W. and I. Mudawar, International Journal of heat and mass transfer **45(19)**, 3973-3985 (2002).
4. Li, J., G. Peterson, and P. Cheng, International Journal of Heat and Mass Transfer **47(19)**, 4215-4231 (2004).
5. Vafai, K. and L. Zhu, International Journal of Heat and Mass Transfer **42(12)**, 2287-2297 (1999).
6. Wei, X., Y. Joshi, and M.K. Patterson, Journal of Heat Transfer **129(10)**, 1432-1444 (2007).

7. Wei, X. and Y. Joshi, IEEE Transactions on **26(1)**, 55-61 (2003).
8. Cheng, Y., International communications in heat and mass transfer **34(3)**, 295-303 (2007).
9. Dixit, P., et al., A Physical **141(2)**, 685-694 (2008).
10. Xu, J., et al., International Journal of Heat and Mass Transfer **48(9)**, 1662-1674 (2005).
11. Lee, P.-S. and S.V. Garimella, International journal of heat and mass transfer **49(17)**, 3060-3067 (2006).
12. Al-Bakhit, H. and A. Fakhri. ASME 2005 Summer Heat Transfer Conference collocated with the ASME 2005 Pacific Rim Technical Conference and Exhibition on Integration and Packaging of MEMS, NEMS, and Electronic Systems. 2005. American Society of Mechanical Engineers.
13. Qu, W. and I. Mudawar, International Journal of Heat and Mass Transfer **45(12)**, 2549-2565 (2002).
14. A.K.M. M Morshed, and Jamil A. Khan. 14th International Heat Transfer Conference , American Society of Mechanical Engineers, 2010.



Possibilities of Tidal Power in Bangladesh

Pratik Roy^{1,a)}, Rupanker Das^{1,b)} and Shahriyar Hossain Topu^{1,c)}

¹*Department of Mechanical Engineering, Khulna University of Engineering & Technology, Khulna-9203, Bangladesh*

^{a)}Corresponding author: pratik.roy94@gmail.com

^{b)} rupankerdas@gmail.com

^{c)}topu.shahriyar@gmail.com

Abstract. From the beginning, fossil fuel (Gas, Coal, Oil etc.) is being mainly used to generate electricity. But it is not far off days that fossil fuel would be a story or museum article. So, in future, power crisis will be a common problem all over the world. Bangladesh is not out of it. To solve this problem government is trying to find alternative way and other different policies. These policies meet up power crisis temporarily, but not permanently. So our government is looking up to the alternative source like renewable energy. Renewable energies are solar, wind, tidal, geothermal etc. Among these tidal wave is more predictable. The tide closely follows the moon during its rotation around the earth, creating diurnal tide and ebb cycles. During high tide, water can be trapped in the coastal basin and this water head can be used to drive a turbine and produce large amount of power which is very reliable and continuous. Bangladesh has good potential for harnessing wave power from the Bay of Bengal. In our research tidal power would be economical and very low compared to most other power plants for Bangladesh. So our main objective is to introduce tidal power as an alternative source to meet up power crisis of Bangladesh.

INTRODUCTION

Nowadays power crisis is the main concern for Bangladesh Government. The generated electricity is far less than the actual demand in our country. In 2012-13, the year-wise electricity generation capacity of our country was about 8525MW and highest electricity generation was 6350MW. But our electricity demand is above 10000MW. A major portion of total population in our country still does not have the access to electricity. Only 59.6% of its 161 million people have access to electricity. In rural areas, where more than 70% of the population lives, only 42% have access to electricity. To develop our economy it is very necessary to solve our power crisis. Bangladesh largely depends on natural gas and hydropower stations to generate major portion of power. About 6817MW electricity is produced from natural gas and hydropower. [1] But it is not enough to meet up our power demand. In order to come out from this problem a quick solution was made up by our government. Our government was starting to use rental power plants. This was temporary and quick and also thought out to be advantageous for the government. But after starting these plants it was evident that this has been a harmful step for the whole power generation system. It is very costly and has very bad effects on our environment. So, our government should look up for renewable energy sources for meeting up our power demand as well as minimizing environmental pollution. Among all renewable energy sources tidal power is common and old source and also efficient. Tidal power or tidal energy is a form of hydropower that converts the energy of tides into electrical power. Energy derived from the motion of ocean tides or waves has several potential advantages over other renewable energy resources including greater power density, greater predictability and closer proximity to major load centers. Bangladesh has a long coastal area with 2~8 m tidal head/height rise and fall [2], most of which is protected against flooding by embankment and sluice gates. Therefore, the potential for tidal power in the country is significant because the barrages necessary for creating controlled flow through turbines (to tap tidal power) are also needed for flood control. However, there is no research that has been conducted yet where the coastal engineering infrastructure is already present (like Bangladesh Coastal Island). So, our government should give their attention into the field of tidal power as soon as possible.

HISTORICAL BACKGROUND

The history of capturing ocean energy has begun from the late 18th century. Monsieur Girard received the first recorded patent for wave energy conversion in 1799. The patented device consisted of a ship attached to shore with waves driving pumps and other machinery. [3] Only occasional attempts to harness the ocean's energy were made between 1800 and the late 1960's. However, in 1966, the world's first and second large-scale tidal power plant was situated at the estuary of the Rance River in St. Malo, France. This ocean tidal power station still operates today, producing 240MWh of power each year. [4] The world's biggest tidal power station with an output capacity of 254MW is located on Lake Sihwa in South Korea. [5] The other tidal power stations are Swansea bay tidal lagoon in United Kingdom (240MW), MeyGen tidal energy project in Scotland (86MW), Annapolis Royal Generating Station in Canada (20MW) etc. [6]

CONCEPT

Tidal power has great potential for future power generation because of the massive size of the oceans and if there is one thing we can safely predict and be sure of on this planet, it is coming and going of the tide. This is the distinct advantage over other sources that are not as predictable and reliable, such as wind and solar. Tides come and go for the gravitational force of the moon and sun and also the rotation of the earth. The gravitational forces of the sun and the moon on the rotating earth cause the ocean's water to bulge upwards, resulting in tides with two high tides occurring every 24 hours and 50 minutes; every rise and fall stores a large amount of potential energy. This energy of the tides comes from the rotational energy of the earth. This energy can be utilized to generate electricity through the use of tidal generators. The large underwater turbines are placed in areas with high tidal movements and designed to capture the kinetic motion of the ebbing and surging of ocean tides in order to produce electricity. The tidal energy (potential energy) available in a volume of water is [7],

$$E = \frac{1}{2} A \rho g h^2 \quad (1)$$

This tidal energy is enough to turn the turbine which, in turn, creates electricity. The generation of electricity from tides is very similar to hydroelectricity generation, except that water is able to flow in both directions during tide and ebb and electricity is created utilizing two-way turbines. It is known as two-way tidal power generation system. There also exists another system known as one way tidal power generation system in which one way turbine is occupied. Whole process of tidal power generation is shown below:

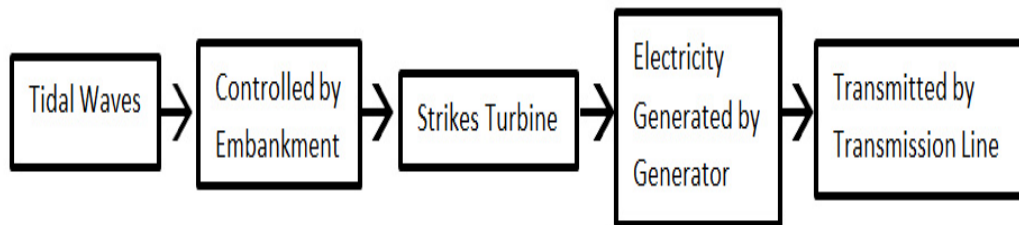


FIGURE 1. Flow diagram of tidal power generation.

POSSIBILITIES

There are two main reasons for which Bangladesh has a great possibility in tidal power generation. They are:

Ocean victory

Now Bangladesh has great possibilities in the field of tidal power generation. Because recently, Bangladesh has gained large ocean area from two neighbor countries- India and Myanmar. It is a great victory for Bangladesh. From this ocean victory Bangladesh has been assured rights over 118,813 square kilometers or territorial sea. Now, Bangladesh has a 200 nautical miles exclusive economic zone and access to open sea, thus preventing it from turning into a 'sea-locked country'. [8] This exclusive economic zone is a sea-zone over which Bangladesh has sovereign rights for the use and exploration of marine resources, including oil and gas. Huge potential energy is available in this large sea-zone which can be utilized by generating electricity.

Spot availability

Spot selection is the first step to construct a tidal power generation plant. Without perfect spot, electricity generation from tidal wave will not be feasible. So, spot selection is the most important factor for constructing a tidal power generation plant. Coastal area where always high tide waves are available (>5m) and which is suitable for embankment should be chosen for tidal power generation. Considerable stability of selected spot such as stable tidal wave, minimum possibility of natural disaster etc. for constructing a tidal power generation plant should also be considered. The spot should also be away from locality and have easy transformation system. Bangladesh has so many available spot for constructing tidal power generation plant. After ocean victory, there are so many spot for constructing a plant, but it is the main concern to select a perfect spot for a power plant so that it will satisfy all possible criteria and advantages like availability of high tide waves, suitable for embankment, considerable stability, away from locality, easy transformation systems, large enough to construct a power plant. Bangladesh has such coastal areas in Hiron Points, Sundarikota, Mongla, Char Changa, Cox's Bazar, Golachipa, Patuakhali, Sandwip, Barishal etc. Those spots are suitable for constructing a large tidal power plant as well as producing enough electricity from tidal waves.

TABLE 1. Probability of Power generation from tide in Bangladesh. [9]

Name of the Station	Tidal Range (m)	Output Power (MW)
Sandwip	5.53	28.83
Cox's Bazar	3.54	11.82
Hiron Points	2.90	7.93
Golachipa	3.55	11.88
Patuakhali	3.54	11.82
Barishal	3.9	14.34
Sundarikota	4.78	21.54
Mongla	4.8	21.72
Char Changa	5.6	29.57
Total		176.64

But among all of them Sandwip is the best spot for tidal power generation. There is a geographical reason behind this:

Sandwip is an island along the south eastern coast of Bangladesh. Sandwip is a sub-division of Chittagong district located at 22.490513°N 91.421185°E. It is situated at the estuary of the Meghna river on the Bay of Bengal and separated from the Chittagong coast by the Sandwip channel. The entire island is 50 kilometres long and 5-15 kilometres wide with an area of 762.42 square kilometres.



FIGURE 2. Sky Scenario of Sandwip from Google map.

Sandwip has a very large potential for tidal power generation with a tidal variation of 5-6m. A flood control barrage exists around the entire island and this contains 28 sluice gates. Considering each sluice gate is capable for one turbine and one generator, a very large amount of power approximately 16.49MW can be generated from Sandwip. [10]

TABLE 2. Summarized of Sandwip project. [10]

Parameter	Value
Tidal range	4.86m
No. of sluice gates	28
No. of turbine uses	05
Basin area	4*10 ⁶ m ²
Construction time	4 years
Cost	US \$10.37 millions
Output power	16.49 MW

ADVANTAGES

For its many advantages, nowadays it becomes popular in many countries of the world. Tidal power plant is economic and it needs fewer instruments. Fuel is not necessary for this type of power station. The main advantage of this type of power plant is renewability. Sea water is always available and predictable, so, a significant amount of energy can be produced all the time. It is also highly efficient. Since no fuel is used, tidal power plant is very environment friendly. It does not produce any greenhouse gas and it is not harmful for land and its ecosystem.

DISADVANTAGES

With many advantages, tidal power plant has some disadvantages which cannot be neglected. It is not harmful for land but it creates hazard in sea life and the ecosystem of the ocean. Equipment for transporting electricity from beach

to land is very expensive. Moreover, the beauty of the beach and the houses and hotels attached in the beach will be lost for construction of tidal plant. For that reason, country will not be afforded to earn foreign exchanges from tourists and many business farms will be closed.

CONCLUSION

Tidal energy is a kind of renewable energy with large potential. It has many advantages over solar and wind energy. The availability of tidal energy is highly predictable and not subject to the impact of weather condition. The energy density is also higher than solar and wind. However, the high demand in technology and capital investment has hindered the development of tidal energy in our country. So, the tidal energy project has not started yet. But with the development of innovative tidal turbine system and coastal infrastructure, the popularization of tidal energy can be expected in our country which will be so much helpful for solving our present power crisis and meeting our increasing power demand in future.

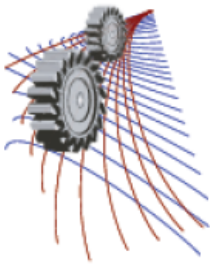
ACKNOWLEDGEMENTS

We are indebted to The Almighty God, Who is the most gracious, most merciful, the cherisher and sustainer of the worlds for giving us the strength and speed to do the topics.

We would like to express our sincere thanks and heartfelt gratitude to our academic supervisor: Engr. Md. Rasedul Islam, Lecturer at Department of Mechanical Engineering, Khulna University of Engineering and Technology (KUET) whose vision and passion have inspired large part of this work.

REFERENCES

1. "A Report on Four Years Achievement of Present Government in Power Sector", Bangladesh Power Development Board, 21 July, 2015.
2. Md. Mahbubuzzaman, M. Shahidul Islam, Md. Mahfuzar Rahman, "Harnessing tidal power", The Daily Star, July 13, 2010.
3. Kari Burman, Dr. Andry Walker, "Ocean Energy Technology: Overview, Federal Management Program (FEMP)", The U.S. Department of Energy, July 2009.
4. Ltd., (Nova Scotia) IEEE Standard, "519-1992-Recommended practices and requirements for harmonic control in electrical power systems", The Institute of Electrical and Electronics Engineers, 1993, pp. 1-112.
5. Moataz Abdelmegid, "The Shiwa Lake Tidal Power Plant: The World's Largest Tidal Power Station", Planetarium Science Center, June 2012.
6. Alice Kenning, "Tidal giants- the world's five biggest power plants", Power technology, Kable Intelligence Limited, April 2014.
7. Bryans A.G., Fox B., Crossley P.A., O'Malley M., "Impact of tidal generation on power system operation in Ireland", IEEE Transactions on Power Systems, 2005, 2034-2040.
8. Md. Anisul Islam, "Second victory at sea", The Prothom Alo, July 10, 2014.
9. Shohana Rahman Deeba, Nahid-Al-Masood, *Impact of Integrating Tidal Power Generation on the Reliability of Bangladesh Power System*, International Journal of Energy and Power (IJEP), Vol.2 Issue 2, May 2013.
10. Md. Alamgir Hossain, Md. Zakir Hossain, Md. Atiqur Rahman, *Prospective and Challenge of Tidal Power in Bangladesh*, International Journal of Electrical, Computer, Energetic, Electronic and Communication Engineering, Vol.8, No.7, 2014.



Analysis of Pressure Distributions on Combinations of Cylinders Due to the Effect of Wind Loading

Kapil Ghosh ^{a)}, Anup Saha ^{b)}, Md. Quamrul Islam ^{c)} and Mohammad Ali ^{d)}

Department of Mechanical Engineering, Bangladesh University of Engineering and Technology, Dhaka-1000, Bangladesh.

^{b)} Corresponding author: anup106@me.buet.ac.bd

^{a)} kapil05me@gmail.com

^{c)} qaumrul@me.buet.ac.bd

^{d)} mali@me.buet.ac.bd

Abstract. With the rapid growth of population, design and construction of taller buildings are being emphasized now-a-days. Especially the design of the group of tall buildings is economic to take care of the housing problem of the huge population. As buildings become taller, effect of wind on them also increases. In this research work, experiments have been conducted to investigate the wind effect on a combination of pentagonal and hexagonal cylinders. The test was conducted in an open circuit wind tunnel at a Reynolds number of $Re = 4.22 \times 10^4$ based on the face width of the cylinder across the flow direction in a uniform flow velocity of 13.5 m/s. A pentagonal cylinder was placed in the upstream and another two hexagonal cylinders were in the downstream. The transverse and longitudinal spacing between the cylinders were varied and the surface static pressures at the different locations of the cylinders were measured with the help of inclined multi-manometers. From the measured values of surface static pressures, pressure coefficients were calculated. Due to the non-dimensional analysis, the results may be applied directly for engineering problems regarding wind loads around a group of skyscrapers, chimneys, towers, oil rigs or marine structures.

INTRODUCTION

During the last half century much emphasis has been given to the study of wind loading on buildings and structures. In the past, there were some occurrences of disastrous collapse of suspension bridges and damages to buildings and structures, which stimulated the relevant researchers to pay attention for performing researches in this field. Many researchers started their work mainly on isolated bluff bodies. Later, they started conducting work on a group of buildings and structures.

Lee [1] conducted the study of the effect of turbulence on the surface pressure field of a square prism. He presented measurements of the mean and fluctuating pressures on a square cylinder placed in a two-dimensional uniform and turbulent flow. It was observed that the addition of turbulence to the flow raised the base pressure and reduced the drag of the cylinder. Hussain and Islam [2] measured coefficient of pressure and coefficient of lift on circular, parabolic and elliptic shell roof in a uniform velocity. The investigation was performed in a small wind tunnel. As the experiment was carried out in a uniform velocity, the estimated results would be higher than that in reality. Mandal and Faruk [3] measured the static pressure distributions on the single cylinder with square and rectangular cross-section having rounded corners in uniform cross flow at zero angle of attack. Koenig and Roshiko [4] described in their paper an experimental investigation of the shielding effects of various disks placed co-axially in the upstream of an axisymmetric flat faced cylinder. For certain combinations of the diameter and gap ratios they observed a considerable decrease in the drag of such a system. By flow visualization technique they showed that for such optimum shielding the upstream surface, which separated from the disk reattached smoothly onto the front edge on the downstream cylinder. Hossain [5] investigated the wind load on octagonal cylinders arranged in both single and staggered form. It was observed that the drag coefficients become remarkably smaller compared to

those for a sharp-edged square cylinder. Miran and Sohn [6] investigated the influence of corner radius on flow past a square cylinder at a Reynolds number 500. Combination of pentagonal and hexagonal cylinders for study is a newer avenue in this kind of analysis, although it has considerable practical significance. This analysis is analogous to that of flow around a combination of tall pentagonal and hexagonal-shaped buildings.

EXPERIMENTAL SET-UP

Wind Tunnel

Figure 1 shows the schematic diagram of open circuit subsonic wind tunnel, at the exit end of which the test was conducted. The wind tunnel was 5.93 m long with a test section of 460 mm x 460 mm cross section. The cylinder was fixed to the side walls of the extended portion at the exit end. The axis of the cylinder was at the same level to that of the wind tunnel. To generate the wind velocity, two axial flow fans are used. Each of the fans is connected with the motor of 2.25 kilowatt and 2900 rpm.

Construction Details and Positioning of the cylinders

For the study, two hexagonal cylinders and one pentagonal cylinder of identical size were constructed. Each of the cylinders was made of seasoned teak wood in order to avoid the bucking and expansion due to the change of temperature and humidity and each of them was of 50mm width. The tapping positions on the cross-section of the cylinder are shown in Fig. 2. Pressure coefficients are measured at each of the tapping points. Each face of the cylinder contained five tappings. Each tapping was identified by a numerical number from 1 to 30 for hexagonal cylinders and from 1 to 25 for pentagonal cylinders. The distance between the consecutive tapping points was equal (Δd). However, the location of the corner tapping was at a distance of $1/2(\Delta d)$. Pentagonal cylinder was positioned in the upstream side and another two hexagonal cylinders were positioned in the downstream side designed as the rear cylinders.

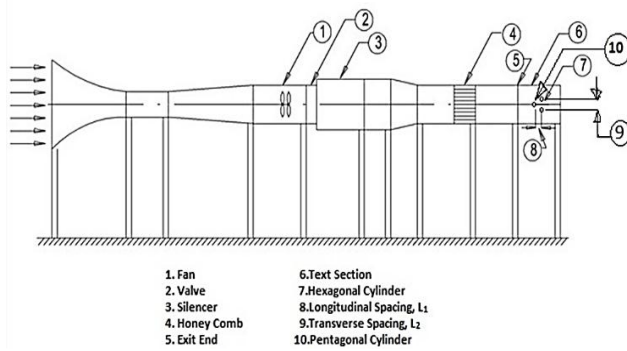


FIGURE 1. Schematic diagram of wind tunnel.

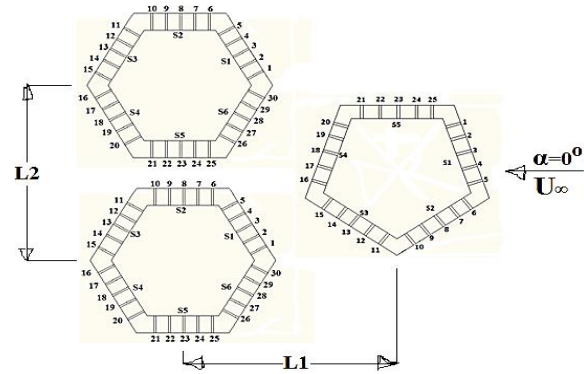


FIGURE 2. Positioning of the cylinders.

MATHEMATICAL MODEL

Pressure Coefficient has been calculated using the following equation,

$$C_p = \frac{\Delta P}{\frac{1}{2} \rho U_\infty^2} \quad (1)$$

Now making the pressure balance one can find,

$$P_0 = P + \Delta h_w \times \gamma_w \quad (2)$$

Where, γ_w is the specific weight of manometric liquid and Δh_w is the suction head in the manometer limb. The manometric liquid is water. From equation (2), ΔP can be obtained as,

$$\Delta P = P - P_0 = -\Delta h_w \times \gamma_w \quad (3)$$

Therefore inserting the value of ΔP , pressure coefficient may be written as,

$$C_p = -\frac{\Delta h_w \times \gamma_w}{\frac{1}{2} \rho U_\infty^2} \quad (4)$$

RESULT AND DISCUSSION

Graphs

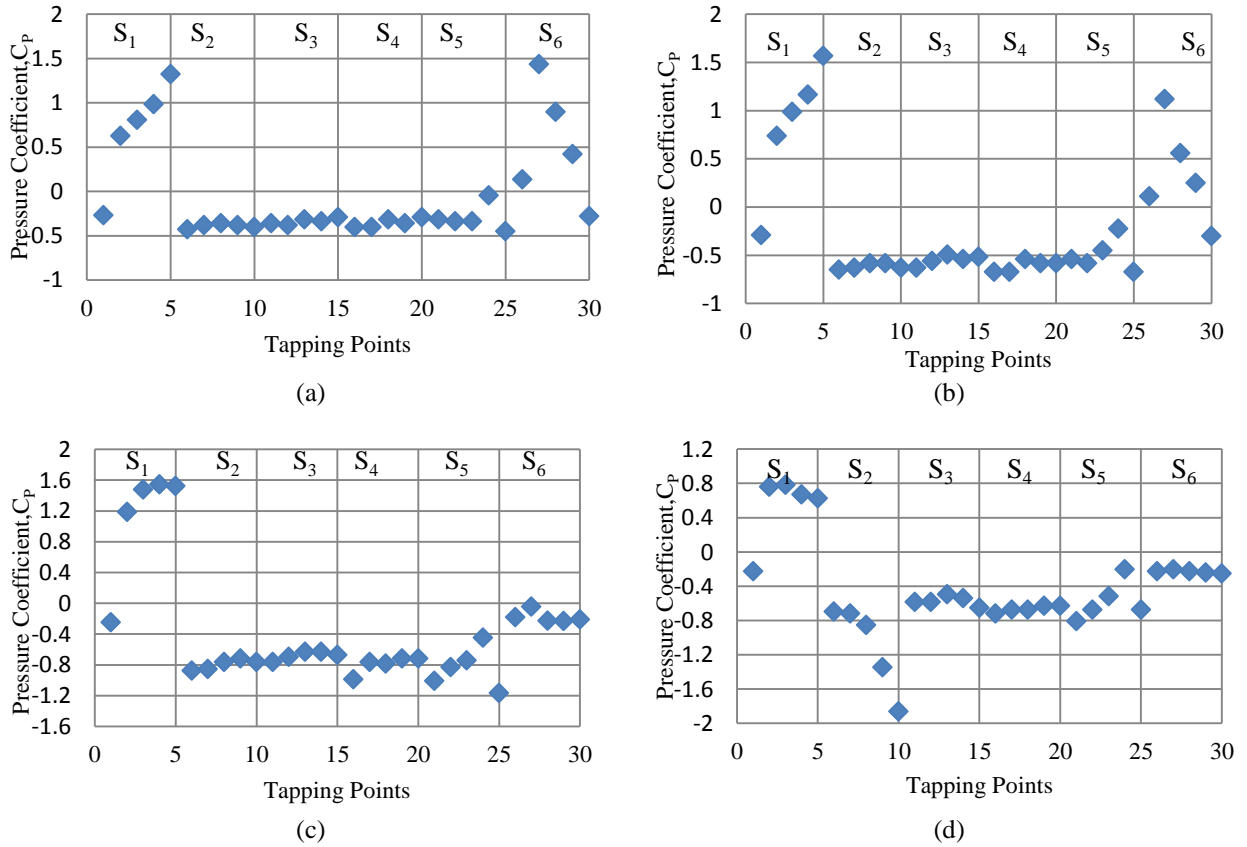
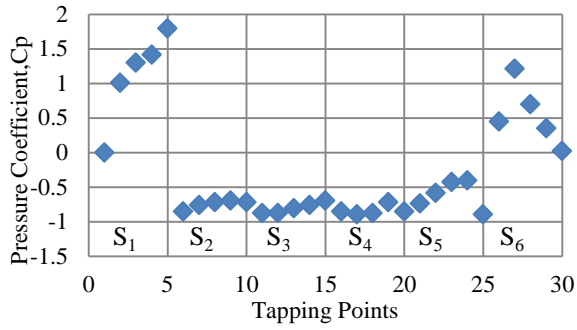
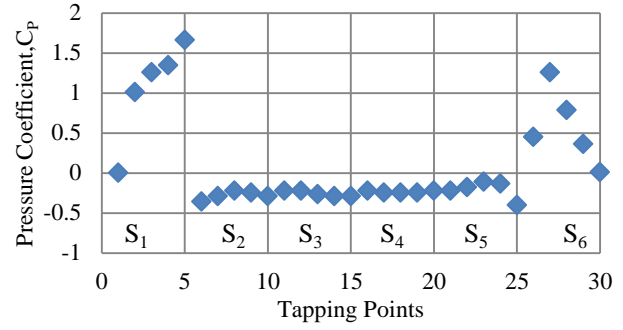


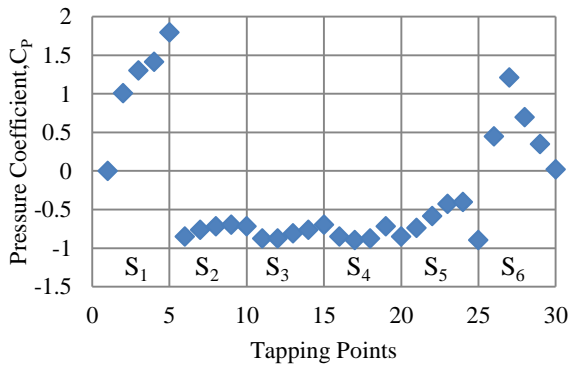
FIGURE 3. C_p distribution on hexagonal cylinders (a) at $L_1=1D, L_2=3D$ (b) at $L_1=2D, L_2=3D$ (c) at $L_1=4D, L_2=3D$ (d) at $L_1=6D, L_2=3D$.



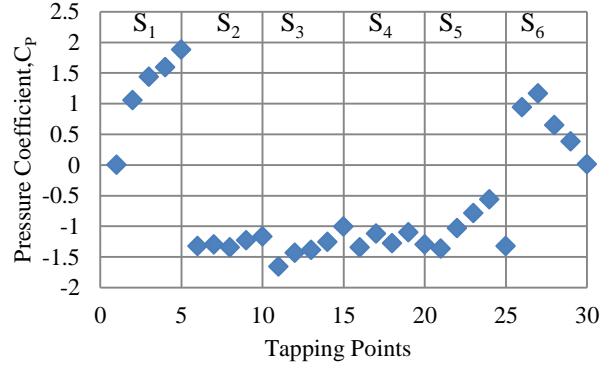
(a)



(b)

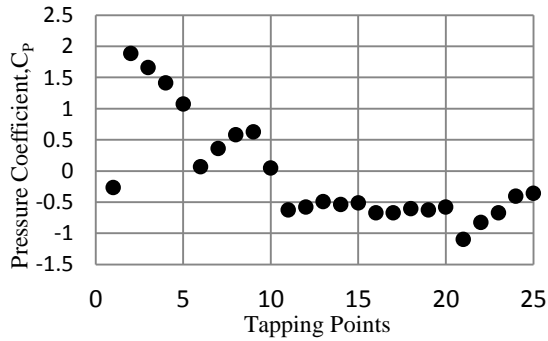


(c)

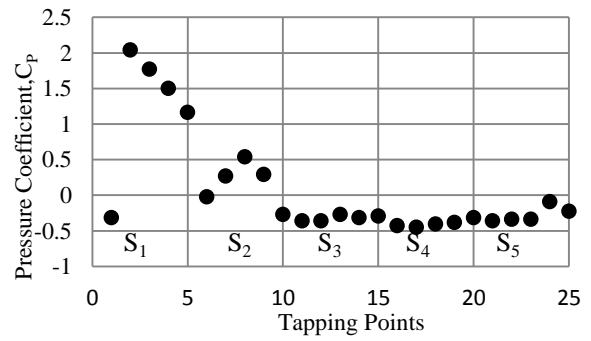


(d)

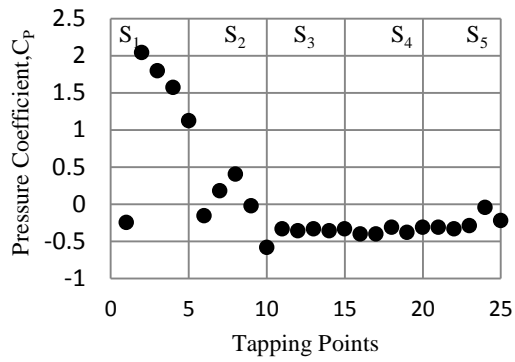
FIGURE 4. C_p distribution on hexagonal cylinders (a) at $L_1=1D$, $L_2=5D$ (b) at $L_1=2D$, $L_2=5D$ (c) at $L_1=4D$, $L_2=5D$ (d) at $L_1=6D$, $L_2=5D$.



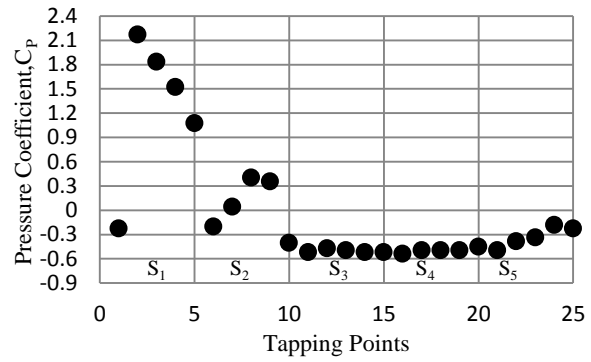
(a)



(b)

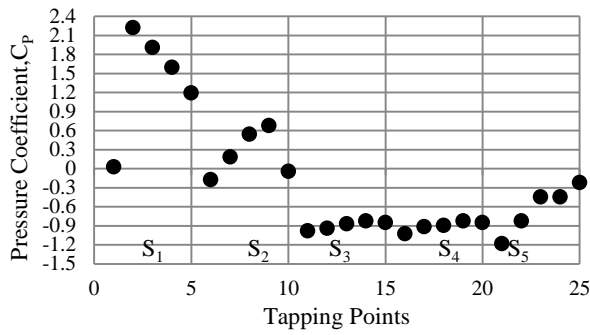


(c)

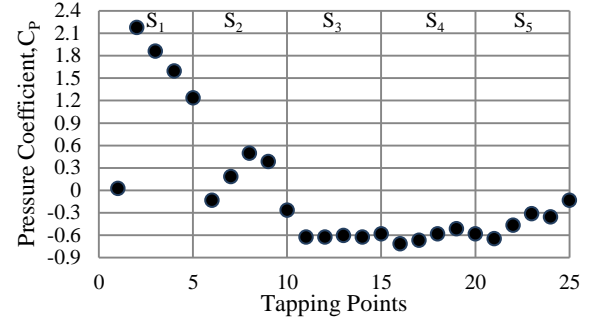


(d)

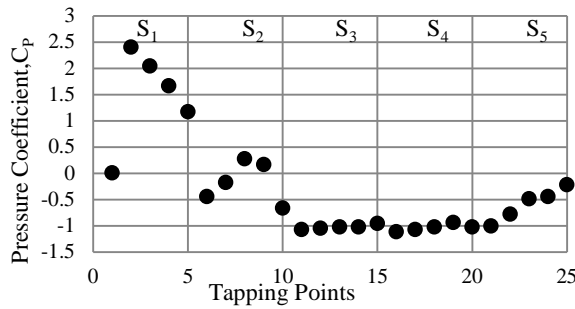
FIGURE 5. C_p distribution on pentagonal cylinders (a) at $L_1=1D$, $L_2=3D$ (b) at $L_1=2D$, $L_2=3D$ (c) at $L_1=4D$, $L_2=3D$ (d) at $L_1=6D$, $L_2=3D$.



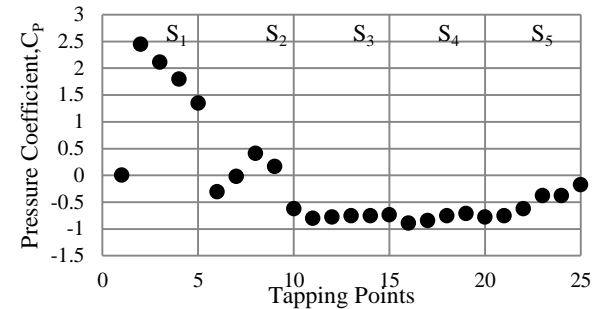
(a)



(b)



(c)



(d)

FIGURE 6. C_p distribution on pentagonal cylinders (a) at $L_1=1D$, $L_2=5D$ (b) at $L_1=2D$, $L_2=5D$ (c) at $L_1=4D$, $L_2=5D$ (d) at $L_1=6D$, $L_2=5D$.

Distribution of Pressure Coefficients on Hexagonal Cylinders

The C_p -distribution on the hexagonal cylinder of the group at $L_1=6D$, $L_2=3D$ is shown in Fig. 3(d). It can be seen from this figure that the C_p -distribution is not symmetric. There is little effect on the C_p -distribution of the hexagonal cylinder due the presence of the pentagonal cylinder. While on surface S_2 there is high suction near the tapping point 10. Probably, the shear layer deviates much in the outward direction near this point.

In Fig. 3(c), the C_p -distribution on the hexagonal cylinder at $L_1=4D$, $L_2=3D$ has been presented. It can be observed from this figure that there has been appreciable change in the back pressure due to presence of the pentagonal cylinder. However, C_p -distribution on the surfaces S_2 to S_5 is of uniform nature approximately.

As shown in Fig. 3(b), the C_p -distribution on the hexagonal cylinder at $L_1=2D$, $L_2=3D$ is symmetric. The surfaces from S_2 to S_5 show uniform C_p -distribution approximately. There is a stagnation point at tapping point 3 on surface S_1 . The C_p -distribution at $L_1=1D$, $L_2=3D$ is almost close to that at $L_1=2D$, $L_2=3D$, as shown in Fig. 3(a). The C_p -distribution is more uniform between surface S_2 and S_5 . There is also a stagnation point on surface S_1 at tapping point 4. The C_p -distribution on the hexagonal cylinder of the group at inter-spacing L_2 of 5D with each case of inter-spacing L_1 of 1D, 2D, 4D and 6D is shown in Fig. 4(a), 4(b), 4(c), 4(d) respectively and these are more or less similar to the inter-spacing L_2 of 3D.

Distribution of Pressure Coefficients on Pentagonal Cylinders

The C_p -distribution on the pentagonal cylinder of the group at $L_1=6D$, $L_2=3D$ is shown in Fig. 5(d). It can be observed from this figure that there is remarkable effect on C_p -distribution due the presence of the hexagonal cylinder. From S_3 to S_5 , the C_p -distribution is more uniform. It is observed from Fig. 5(c) that on the pentagonal Cylinder of the group at $L_1=4D$, $L_2=3D$, the pattern of the C_p -distribution is similar as that of the $L_1=6D$, $L_2=3D$ but the values increases. The C_p -distribution is more uniform on the surfaces S_3 to S_5 .

However, a picture is seen in Fig. 5(b) for the C_p -distribution on the pentagonal cylinder of the group at $L_1=2D$, $L_2=3D$, the pattern of the C_p -distribution is similar as that of the $L_1=4D$, $L_2=3D$ but the value increases for the surfaces S_3 to S_5 and C_p -distribution is more uniform.

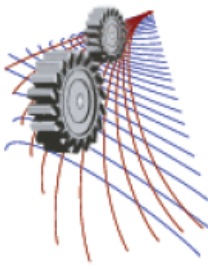
At $L_1=1D$, $L_2=3D$ on the pentagonal Cylinder of the group, there is a drop of the pressure on the surfaces S_2 to S_5 compared to that for the pentagonal cylinder at $L_1=2D$, $L_2=3D$, which is shown in Fig. 5(a). The C_p -distribution on the pentagonal cylinder of the group at inter-spacing L_2 of 5D with each case of inter-spacing L_1 of 1D, 2D, 4D and 6D is shown in Figs. 6(a), 6(b), 6(c), 6(d) respectively and these are more or less similar to the inter-spacing L_2 of 3D.

CONCLUSIONS

Analyzing the value of the pressure coefficients at various tapping points on the cylinders, several important conclusions can be drawn. There is significant effect on C_p -distribution on the pentagonal cylinder due the presence of the hexagonal cylinders behind it. A symmetric C_p distribution was found around the hexagonal cylinder when $L_1=2D$, $L_2=3D$. For the same interspacing between the cylinders, a stagnation point was also observed on the front face of the hexagonal cylinder. The findings of this experimental endeavor can be served as an aid while analyzing the wind effects on the group of tall buildings having similar cross-section of this study. Since the study has been conducted at zero angle of attack only, the authors recommend further investigation by varying the angle of attack.

REFERENCES

1. B.E. Lee, Journal of Fluid Mechanics, **6(9)** 263-282 (1975).
2. M.K.M. Hossain, M.Q. Islam, A.C. Mandal, S. Saha, Journal of Mechanical Engineering, **38** 52-57 (2007).
3. A.C. Mandal, G.M.G. Faruk, Journal of Mechanical Engineering, **41(1)** 42-49 (2010).
4. K. Koenig, A. Roshiko, Journal of Fluid Mechanics, **156** 167-204 (1985).
5. M.J. Hossain, M.Q. Islam, M. Ali, International Journal of Renewable Energy Research, **3(1)** 77-89 (2013).
6. S. Miran, C.H. Sohn, International Journal of Numerical Methods for Heat & Fluid Flow, **25(4)** 686-702 (2015).



MHD Couette Flow Of Viscous Incompressible Fluid With Hall Current And Suction

Afroja Parvin¹ Tanni Alam Dola² and Md. Mahmud Alam^{3,a)}

^{1,3} *Mathematics Discipline, Science, Engineering and Technology School, Khulna University, Khulna-9208, Bangladesh*

² *Department of Civil Engineering, Bangladesh University of Engineering and Technology, Dhaka- 1000, Bangladesh*

^{a)}Corresponding author: alam_mahmud2000@yahoo.com

Abstract. An electrically conducting viscous incompressible fluid bounded by two parallel non-conducting plates has been investigated in the presence of Hall current. The fluid motion is uniform at the upper plate and the uniform magnetic field is applied perpendicular to the plate. The lower plate is stationary while upper plate moves with a constant velocity. The governing equations have been non-dimensionalized by using usual transformations. The obtained governing non-linear coupled partial differential equations have been solved by using implicit finite difference technique. The numerical solutions are obtained for momentum and energy equations. The influence of various interesting parameters on the flow has been analyzed and discussed through graph in details. The values of Nusselt number and Skin- Friction for different physical parameters are also elucidated in the form of graph.

INTRODUCTION

The last few decades, a great deal of research work have been done about the magneto hydrodynamic (MHD) effects on Couette flow and channel flows of a Newtonian fluid with heat transfer with or without Hall currents. In the space between two infinite parallel planes at a constant distance in time is filled with a viscous, incompressible fluid and if one plate is rest while another plate is moving with a constant velocity, then the simplest flow compatible with the Navier-Stokes equations and these boundary conditions is the stationary parallel motion with linear velocity profile. This is called Couette flow. The Couette flow in a rectangular channel of an electrically conducting viscous fluid under the action of a transversely applied magnetic field has immediate applications in many devices such as, MHD pumps, accelerators, aerodynamics heating, polymer technology, petroleum industry; purification of crude oil and fluid droplets sprays [1]. The steady flow of an electrically conducting fluid between two infinite parallel plates in the presence of a transverse uniform magnetic field was first studied by Hartmann [2]. Attia [3] studied the Unsteady MHD couette flow with heat transfer in the presence of uniform suction and injection. Tao [4] discussed the magneto hydrodynamic effects on the formation of Couette flow. Soundalgekar and Uplekar [5] broadly discussed the Hall effects in MHD Couette flow with heat transfer. Sayed-Ahmed and Attia [6] examined the effect of the Hall term and the variable viscosity on velocities and temperature fields of the MHD flows. The unsteady MHD Couette flow between two infinite parallel porous plates with uniform suction and injection in the cases of impulsive and uniformly accelerated movement of the lower plate was studied by Seth et al. [7]. Attia [8] studied the unsteady couette flow and heat transfer of a dusty conducting fluid between two parallel plates with variable viscosity and electrical conductivity. Das [9] studied the effect of suction and injection on MHD three dimensional Couette flow and Heat transfer through a porous medium. Hence our aim is to study Unsteady MHD Couette flow of viscous incompressible fluid with Hall current and suction. The system is considered as such that the upper plate is moving with a uniform velocity while the lower plate is fixed. Constant pressure gradient acts on the flow, a uniform suction from above and a uniform injection from below and a uniform magnetic field is applied perpendicular to the plates. Very small value of Magnetic Reynolds Number [10] is assumed to neglect the strong effect of induced magnetic field. The two plates are kept at

two different but constant temperatures. The governing momentum and energy equations are solved numerically using the implicit finite difference method. Eventually the effect of various interesting parameters on shear stress and Nusselt number at moving plate have been elucidated in the form of graph in details.

Mathematical Formulation:

The physical configuration and the boundary condition of the problem is shown in Figure 1. The fluid is assumed to be laminar, incompressible and flows between two infinite horizontal plates. These plates are located at the $y = \pm h$ planes and extend from $x = 0$ to ∞ and from $z = 0$ to ∞ . The upper plate moves with a uniform velocity U_0 while the lower plate is stationary. Both the upper and lower plates are kept at two constant temperatures are T_2 and T_1 respectively, with $T_2 > T_1$. A constant pressure gradient applied in the x -direction, and a uniform magnetic field B_0 is applied in the positive y -direction and is assumed undisturbed as the induced magnetic field is neglected by assuming a very small magnetic Reynolds number. Due to consideration of Hall Effect a

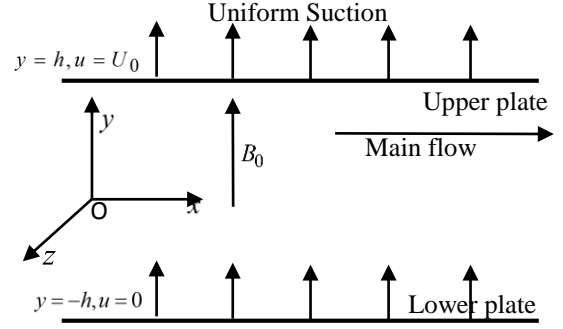


Figure 1. The geometrical configuration

z component for the velocity is expected to arise. Thus the fluid velocity vector is $\mathbf{q} = u\hat{i} + v\hat{j} + w\hat{k}$

By using generalized Ohm's Law, the unsteady MHD viscous incompressible fluid flows are governed by the following equations is given by; $\frac{\partial v}{\partial y} = 0$

which gives $v = -v_o$ (constant).

$$\text{Momentum equation in } x \text{ axis: } \frac{\partial u}{\partial t} - v_o \frac{\partial u}{\partial y} = -\frac{1}{\rho} \frac{dp}{dx} + \frac{\mu}{\rho} \frac{\partial^2 u}{\partial y^2} - \frac{1}{\rho} \left[\frac{\sigma B_o^2}{1+m^2} (u + mw) \right] \quad (2)$$

$$\text{Momentum equation in } z \text{ axis: } \frac{\partial w}{\partial t} - v_o \frac{\partial w}{\partial y} = \frac{\mu}{\rho} \frac{\partial^2 w}{\partial y^2} - \frac{1}{\rho} \left[\frac{\sigma B_o^2}{1+m^2} (w - mu) \right] \quad (3)$$

$$\text{Energy equation: } \frac{\partial T}{\partial t} - v_o \frac{\partial T}{\partial y} = \frac{k}{\rho c_p} \frac{\partial^2 T}{\partial y^2} + \frac{\mu}{\rho c_p} \left[\left(\frac{\partial u}{\partial y} \right)^2 + \left(\frac{\partial w}{\partial y} \right)^2 \right] + \frac{1}{\rho c_p} \left[\frac{\sigma B_o^2}{1+m^2} (u^2 + w^2) \right] \quad (4)$$

with the corresponding boundary conditions are $t > 0$

$$\begin{aligned} u = 0, w = 0, T = T_1 & \text{ at } y = -h \\ u = U_o, w = 0, T = T_2 & \text{ at } y = h \end{aligned}$$

To obtain the governing equations and the boundary condition in dimensionless form the following non-dimensional quantities are used as;

$$X = \frac{x}{h}, Y = \frac{y}{h}, U = \frac{u}{U_o}, W = \frac{w}{U_o}, P = \frac{p}{\rho U_o^2}, \tau = \frac{t U_o}{h}, \theta = \frac{T - T_1}{T_2 - T_1}$$

Using the above non-dimensional variables in equations (2- 4) and boundary conditions it can be written as;

$$\frac{\partial U}{\partial \tau} - \frac{S}{R_E} \frac{\partial U}{\partial Y} = -\frac{dP}{dX} + \frac{1}{R_E} \left[\frac{\partial^2 U}{\partial Y^2} - \frac{H_a^2}{(1+m^2)} (U + mW) \right] \quad (5)$$

$$\frac{\partial W}{\partial \tau} - \frac{S}{R_E} \frac{\partial W}{\partial Y} = \frac{1}{R_E} \left[\frac{\partial^2 W}{\partial Y^2} - \frac{H_a^2}{(1+m^2)} (W - mU) \right] \quad (6)$$

$$\frac{\partial \theta}{\partial \tau} - \frac{S}{R_E} \frac{\partial \theta}{\partial Y} = \frac{1}{P_r} \frac{\partial^2 \theta}{\partial Y^2} + E_c \left[\left(\frac{\partial U}{\partial Y} \right)^2 + \left(\frac{\partial W}{\partial Y} \right)^2 \right] + \frac{H_a^2 E_c}{(1+m^2)} (U^2 + W^2) \quad (7)$$

Where non-dimensional parameters are as follows;

$$H_a^2 = \frac{\sigma B_o^2 h^2}{\mu}, R_E = \frac{\rho U_o h}{\mu}, P_r = \frac{\rho c_p U_o h}{k}, E_c = \frac{U_o \mu}{\rho c_p h (T_2 - T_1)} \text{ and } S = \frac{\rho v_o h}{\mu}$$

And the dimensionless boundary conditions are;

$$\tau > 0 \quad \begin{array}{l} U = 0, W = 0, \theta = 0 \quad \text{at } Y = -1 \\ U = 1, W = 0, \theta = 1 \quad \text{at } Y = 1 \end{array}$$

Shear Stress and Nusselt Number

From velocity field, the influence of various parameters on Shear stress for both plates has been examined. Shear stress in x -

direction for stationary and moving plate is $\tau_{x1} = \mu_o \left(\frac{\partial U}{\partial Y} \right)_{Y=-1}$ and $\tau_{x2} = \mu_o \left(\frac{\partial U}{\partial Y} \right)_{Y=1}$ respectively. Shear stress in z - direction

for stationary and moving plate is $\tau_{z1} = \mu_o \left(\frac{\partial W}{\partial Y} \right)_{Y=-1}$ and $\tau_{z2} = \mu_o \left(\frac{\partial W}{\partial Y} \right)_{Y=1}$ respectively. From temperature field, the influence

of various parameters on Nusselt number for both plates has been studied. Nusselt number for stationary and moving plate is

$N_{u1} = -\mu_o \left(\frac{\partial T}{\partial Y} \right)_{Y=-1}$ and $N_{u2} = -\mu_o \left(\frac{\partial T}{\partial Y} \right)_{Y=1}$ respectively.

Numerical Technique

To solve the non-dimensional system by implicit finite difference method, a set of finite difference equations is required. For this reason the area within the boundary layer is divided by some perpendicular lines of y axis as shown in Figure 2. It is assumed that the maximum length of boundary layer is $Y_{max} = 2$. i.e. Y varies from -1 to 1 and the number of grid spacing in Y directions is $n = (100)$. Hence the constant mesh size along Y -axis becomes $\Delta Y = 0.02 (-1 \leq Y \leq 1)$ with a smaller time step $\Delta t = 0.0001$.

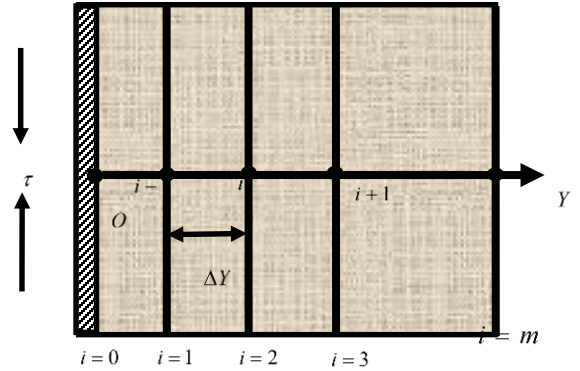


Figure 2. Implicit Finite Difference

Let U', W' and θ' denotes the value of U, W and θ at the end of the

time-step respectively. Using implicit finite difference, the following appropriate set of finite difference equation is obtained as;

$$\frac{U'_i - U_i}{\Delta \tau} - \frac{S}{R_E} \frac{U_{i+1} - U_i}{\Delta Y} = -\frac{dP}{dX} + \frac{1}{R_E} \left[\left(\frac{U_{i+1} - 2U_i + U_{i-1}}{\Delta Y^2} \right) - \frac{H_a^2}{1+m^2} (U_i + mW_i) \right] \quad (8)$$

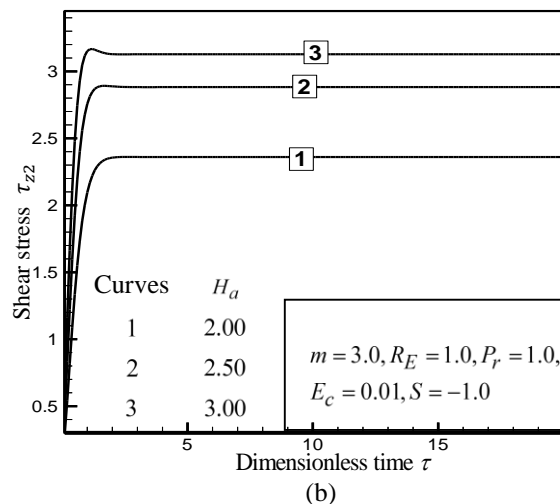
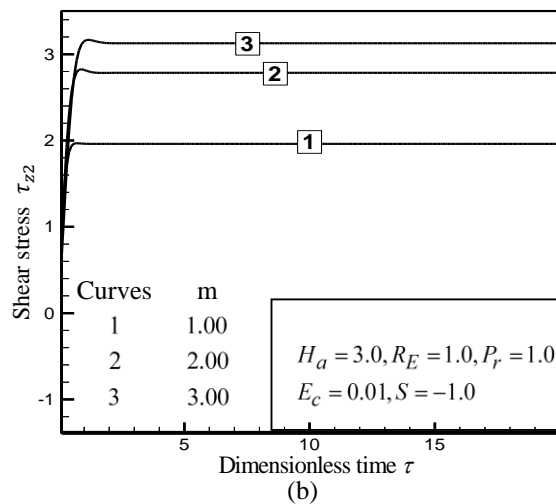
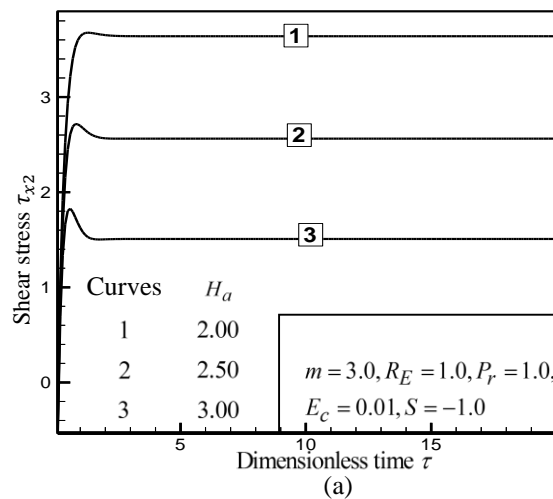
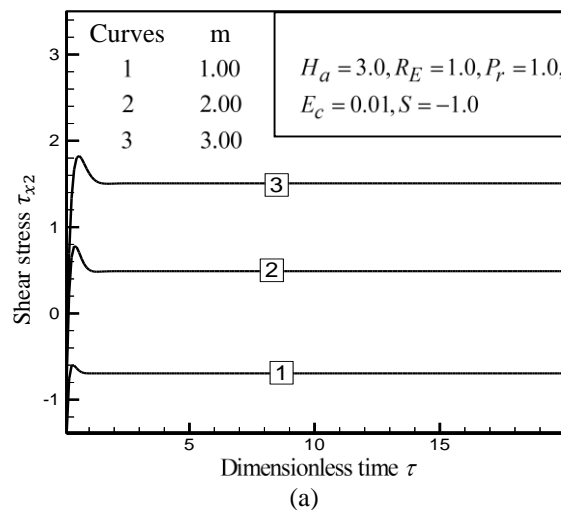
$$\frac{W'_i - W_i}{\Delta \tau} - \frac{S}{R_E} \frac{W_{i+1} - W_i}{\Delta Y} = \frac{1}{R_E} \left[\left(\frac{W_{i+1} - 2W_i + W_{i-1}}{\Delta Y^2} \right) - \frac{H_a^2}{1+m^2} (W_i - mU_i) \right] \quad (9)$$

$$\frac{\theta'_i - \theta_i}{\Delta\tau} - \frac{S}{R_E} \frac{\theta_{i+1} - \theta_i}{\Delta Y} = \frac{1}{P_r} \left[\frac{\theta_{i+1} - 2\theta_i + \theta_{i-1}}{\Delta Y^2} \right] + E_c \left[\left(\frac{U_{i+1} - U_i}{\Delta Y} \right)^2 + \left(\frac{W_{i+1} - W_i}{\Delta Y} \right)^2 \right] + \frac{H_a^2 E_c}{1+m^2} [(U_i)^2 + (W_i)^2] \quad (10)$$

with the finite difference boundary conditions

$$U_L = 0, W_L = 0, \theta_L = 0 \text{ at } L = -1$$

$$U_L = 1, W_L = 0, \theta_L = 1 \text{ at } L = 1$$



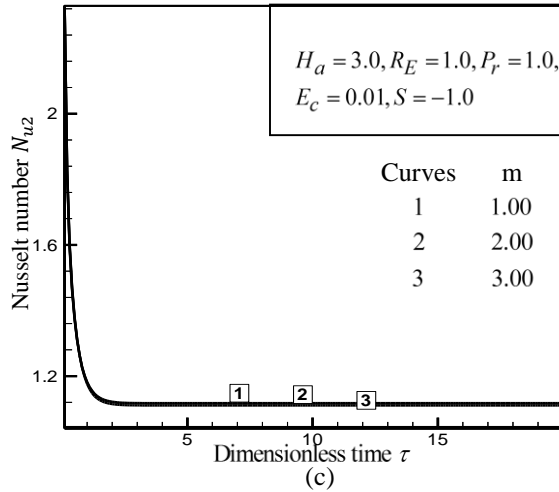


Figure 3: Illustration of Shear stress of (a) Primary velocity (b) Secondary velocity and (c) Nusselt number at moving wall for different values of Hall

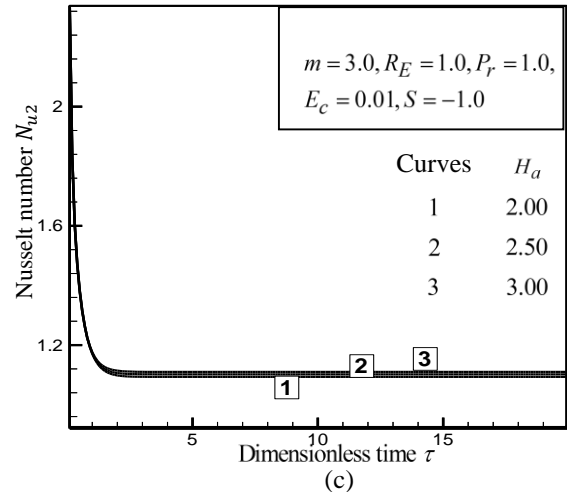
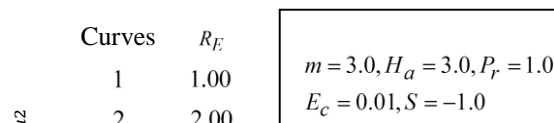
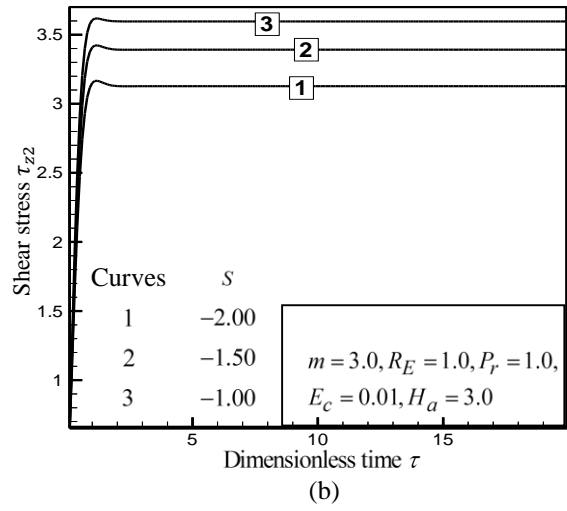
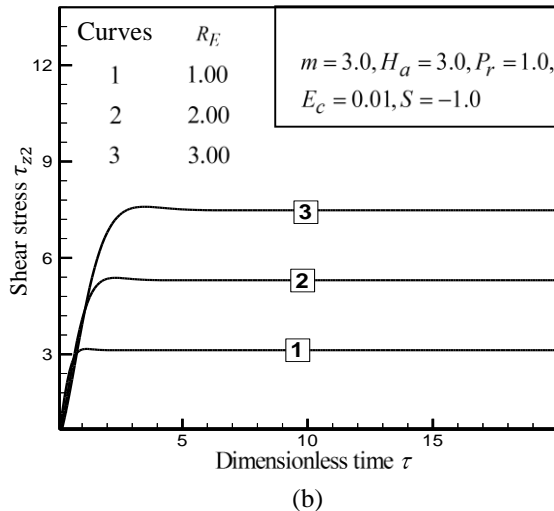
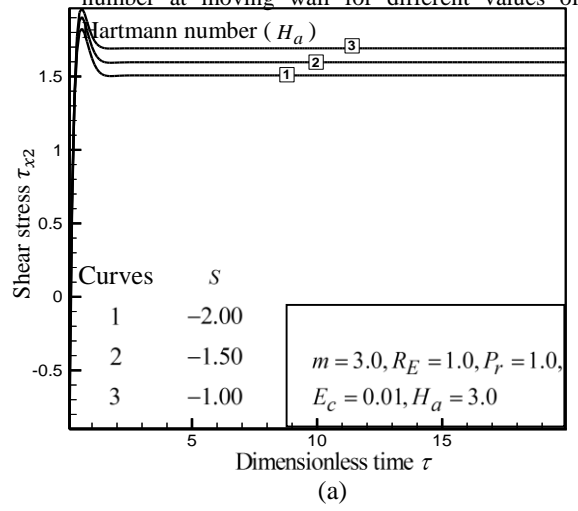
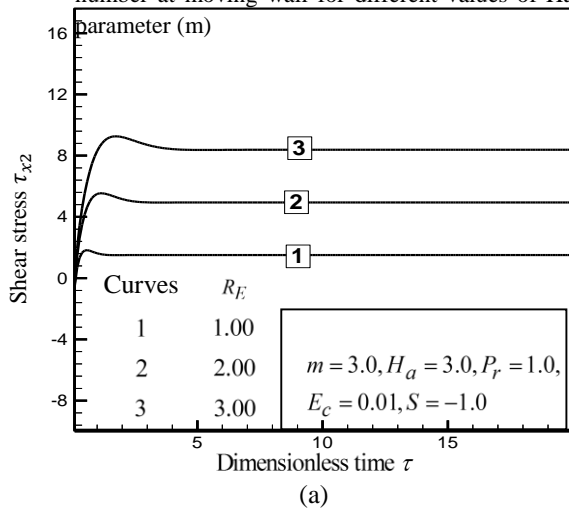


Figure 4: Illustration of Shear stress of (a) Primary velocity (b) Secondary velocity and (c) Nusselt number at moving wall for different values of



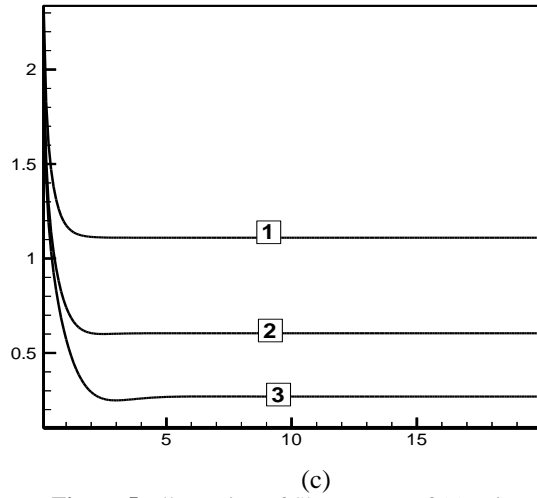


Figure 5: Illustration of Shear stress of (a) Primary velocity and (c) Nusselt number at moving wall for different values of

Results and discussions

To examine the physical situation

of the problem, the effects of various Suction Parameter (Shear stress and nusselt number at moving plate has been elucidated in Figures 3-8. To obtain the solutions the computations have been carried upto $\tau = 20.00$. The results of computation shows little changes for $\tau = 0.1$ to $\tau = 7.0$ but after that $\tau = 7.0$ until $\tau = 20.00$ the results remain approximately same. The effects of Hall parameter (m) on shear stress both for primary and secondary velocity and Nusselt number at moving plate is illustrated in Figure 3(a-c). It is observed that with the increase of m , shear stress for primary velocity increases as the effective conductivity $\left(= \frac{\sigma}{1+m^2} \right)$ decreases with that of m which reduces the magnetic

dumping force on U . In the same way, Shear stress for secondary velocity increases as W is a result of hall effect. On the other hand, the reverse effect is observed for Nusselt number. The effects of Hartmann number (H_a) on shear stress both for primary and secondary velocity and Nusselt number at moving plate is illustrated in Figure 4(a-c). It is seen that with the increase of H_a shear stress for primary velocity decreases, showing the effect of dragging the magnetic field as Hartmann number gives a measure of the relative importance of drag forces resulting from magnetic induction and viscous forces while shear stress for secondary velocity increases. Furthermore with the increase of H_a Nusselt number at moving plate increases.

The effects of Reynolds number R_E on shear stress both for primary and secondary velocity and Nusselt number at moving plate is illustrated in Figure 5(a-c). It is clear from the figure that with the increase of R_E shear stress for both primary and secondary velocity increases as large values of R_E indicates that viscosity effect is very small. On the other hand Nusselt number decreases. The Effects of Suction parameter S on shear stress both for primary and secondary velocity and Nusselt Number at moving plate is illustrated in Figure 6(a-c). It is observed that with the increase of suction parameter, shear stress for both primary and secondary velocity decreases. In contrast, with the increase of suction parameter Nusselt number increases.

Conclusion

The major findings of this project are mentioned here;

1. With the increase of Hall parameter m , shear stress for both velocity at moving wall increases while opposite scenerio is observed for Nusselt number.

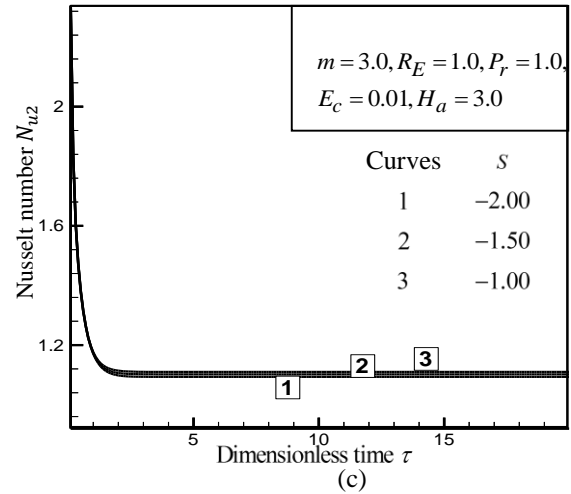


Figure 6: Illustration of Shear stress of (a) Primary velocity (b) Secondary velocity and (c) Nusselt number at moving wall for different values of

Suction Parameter (Shear stress and nusselt number at moving plate has been elucidated in Figures 3-8.

To obtain the solutions the computations have been carried upto $\tau = 20.00$. The results of computation shows little changes for $\tau = 0.1$ to $\tau = 7.0$ but after that $\tau = 7.0$ until $\tau = 20.00$ the results remain approximately same. The effects of Hall parameter (m) on shear stress both for primary and secondary velocity and Nusselt number at moving plate is illustrated in Figure 3(a-c). It is observed that with the increase of m , shear stress for primary velocity increases as the effective conductivity $\left(= \frac{\sigma}{1+m^2} \right)$ decreases with that of m which reduces the magnetic

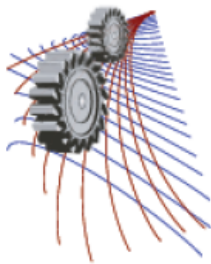
dumping force on U . In the same way, Shear stress for secondary velocity increases as W is a result of hall effect. On the other hand, the reverse effect is observed for Nusselt number. The effects of Hartmann number (H_a) on shear stress both for primary and secondary velocity and Nusselt number at moving plate is illustrated in Figure 4(a-c). It is seen that with the increase of H_a shear stress for primary velocity decreases, showing the effect of dragging the magnetic field as Hartmann number gives a measure of the relative importance of drag forces resulting from magnetic induction and viscous forces while shear stress for secondary velocity increases. Furthermore with the increase of H_a Nusselt number at moving plate increases.

The effects of Reynolds number R_E on shear stress both for primary and secondary velocity and Nusselt number at moving plate is illustrated in Figure 5(a-c). It is clear from the figure that with the increase of R_E shear stress for both primary and secondary velocity increases as large values of R_E indicates that viscosity effect is very small. On the other hand Nusselt number decreases. The Effects of Suction parameter S on shear stress both for primary and secondary velocity and Nusselt Number at moving plate is illustrated in Figure 6(a-c). It is observed that with the increase of suction parameter, shear stress for both primary and secondary velocity decreases. In contrast, with the increase of suction parameter Nusselt number increases.

2. Shear stress at x direction for moving plate decreases with the increase of Hartmann number H_a while at z direction it increases. Furthermore, increasing effect is found for Nusselt number.
3. Shear stress for both velocity increases but Nuselt number at moving plate decreases with the increase of Reynolds number R_E .
4. With the increase of Suction parameter S at moving wall, Shear stress decreases but Nusselt number increases.

References

1. B.K. and Jha, *Heat and Mass Transfer* (2001).
2. H.A. Attia, *Research Journal of Physics* **1(1)**, (2007).
3. H.A. Attia, *Engineering Modeling* **22**, (2009).
4. I.N. Tao, *Journal of Aerospace Science* **27**, pp. 334 (1960).
5. V.M. Soundalgekar and A.G.Uplekar, *IEEE Transactionson Plasma Science* PS-**14** pp. 579–583 (1986).
6. M. E. Sayed-Ahmed and H. A. Attia, *International Communications in Heat and Mass Transfer* **27(8)**, pp. 1177–1187 (2000).
7. G.S. Seth, Ansari, Md.S. and R. Nandkeolyar , *Tamkang Journal of Science and Engineering* **14(1)** (2011).
8. H. A. Attia, *Applied Mathematics and Computation* **177**, 308–318 (2006).
9. S.S. Das, *Journal of Naval Architecture and Marine Engineering* **6**, pp. 41-51 (2009).
10. G.W. Sutton, A. Sherma, *Engineering Magneto hydrodynamics*, McGraw-Hill, New York, (1965).



Soret and Dufour Effects on MHD Viscoelastic Fluid Flow Through a Vertical Flat Plate with Constant Suction

Sheikh Imamul Hossain^{a)} and Md. Mahmud Alam^{b)}

Mathematics Discipline, Khulna University, Khulna-9208

^{b)} Corresponding author: alam_mahmud2000@yahoo.com

^{a)} s.imamul.ku@gmail.com

Abstract. An attempt is made to represent the numerical solution of magnetohydrodynamics (MHD) viscoelastic fluid flow through an infinite vertical flat plate with constant suction in the presence of Soret and Dufour effects. The expressions of non-dimensional, coupled partial momentum, energy and concentration differential equations are obtained with the help of the usual non-dimensional variables. Implicit finite difference method is imposed to obtain the non-dimensional equations. Also the stability conditions and convergence criteria are analyzed. The effects of the various parameters entering into the problem on shear stress, Nusselt number, and Sherwood number are demonstrated graphically with physical interpretation.

INTRODUCTION

The most common non-Newtonian fluid is viscoelastic fluid. It has two properties, one is viscous property and another one is elastic property at the time of undergoing deformation and so it is named as viscoelastic fluids. Its importance is increasing day by day due to its many engineering, biological, industrial and chemical aspects. Some common viscoelastic fluids are engine oils, paints, honey, shampoo, ointments, gels, molten plastics, blood and so on. These appear in many industrial process, chemical reaction and pharmaceutical industries.

From the above point of applications, the analysis of viscoelastic fluids started about 1964 by Beard and Walters [1]. Rajagopal et al. [2] studied the boundary layer flow of a viscoelastic fluid over a stretching sheet. The study of boundary layer flow of a viscoelastic fluid through a vertical plate has wide range of applications in the field of chemical engineering and production of synthetic sheets. This is also consequential to the production of heavy crude oils by means of thermal process. Heat and mass transfer analysis are the fundamental scopes in fluid dynamics analysis. Flow and heat transfer of a viscoelastic fluid over a flat plate with a magnetic field and a pressure gradient has been analyzed by kumar et al. [3]. Dufour and Soret Effects on unsteady MHD Free Convection and mass transfer fluid flow through a porous medium in a rotating system have been investigated by Islam and Alam [4]. Heat and mass transfer for Soret and Dufour's effect on mixed convection boundary layer flow over a stretching vertical surface in a porous medium filled with a viscoelastic fluid in the presence of magnetic field has been examined by Gbadeyan et al. [5]. Hossain and Alam [6] have extended the work of Gbadeyan et al. [5] by implicit finite difference method.

Hence our aim of this work is to extend the work of Hossain and Alam [6] when a magnetic field is imposed in a direction which is perpendicular to the free stream. The problem has been solved by implicit finite difference method. The governing equations involved in this problem have been transformed into non-similar coupled partial differential equations by usual transformations. Stability and convergence criteria are analyzed for finding the restriction of the parameters. Finally, the comparison of the present results with the results of Gbadeyan et al. [5] has been discussed.

MATHEMATICAL MODEL

Consider the unsteady one-dimensional laminar flow of an incompressible viscoelastic fluid (obeying second grade model) through a vertical plate $y=0$ with Soret and Dufour effects. The positive x coordinate is measured along the plate in the direction of fluid motion and the positive y coordinate is measured normal to the plate. Since the plate is infinite and the motion is unsteady so all the flow variables depend only upon y and time t . A uniform magnetic field \mathbf{B} is imposed to the plate ($y=0$) to be acting along the y -axis which is assumed to be electrically non-conducting. Assumed that $\mathbf{B}=(B_x, B_y, B_z)=(0, B_0, 0)$ is the magnetic field vector. The magnetic Reynolds number of the flow is taken to be small so that the induced magnetic field is negligible in comparison with the applied magnetic field. The variable temperature T_w and variable concentration C_w at wall of the plate occupied with viscoelastic fluid of uniform ambient temperature T_∞ and uniform ambient concentration C_∞ . The physical configuration of the above problem is shown in Figure 1.

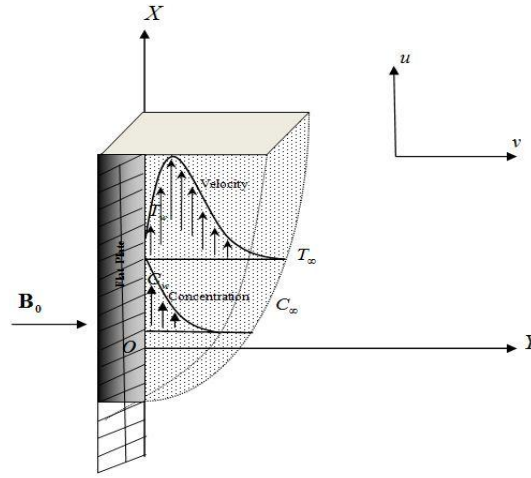


FIGURE 1. Physical configuration of the flow

Within the framework of the above state assumptions and using the dimensionless quantities $\bar{U} = \frac{u}{U_0}$, $Y = \frac{yU_0}{\nu}$, $\tau = \frac{tU_0^2}{\nu}$, $\bar{\theta} = \frac{T - T_\infty}{T_w - T_\infty}$ and $\bar{\phi} = \frac{C - C_\infty}{C_w - C_\infty}$ in the equations relevant to the problem is governed by the following coupled non-linear non-dimensional partial differential equations under the electromagnetic Boussinesq approximations as;

$$\frac{\partial \bar{U}}{\partial \tau} - S \frac{\partial \bar{U}}{\partial Y} = G_r \bar{\theta} + G_m \bar{\phi} + \frac{\partial^2 \bar{U}}{\partial Y^2} - M \bar{U} + K \left[\frac{\partial^3 \bar{U}}{\partial \tau \partial Y^2} - S \frac{\partial^3 \bar{U}}{\partial Y^3} \right] \quad (1)$$

$$\frac{\partial \bar{\theta}}{\partial \tau} - S \frac{\partial \bar{\theta}}{\partial Y} = \frac{1}{Pr} \frac{\partial^2 \bar{\theta}}{\partial Y^2} + ME_c \bar{U}^2 + Du \frac{\partial^2 \bar{\phi}}{\partial Y^2} \quad (2)$$

$$\frac{\partial \bar{\phi}}{\partial \tau} - S \frac{\partial \bar{\phi}}{\partial Y} = \frac{1}{Sc} \frac{\partial^2 \bar{\phi}}{\partial Y^2} + Sr \frac{\partial^2 \bar{\theta}}{\partial Y^2} \quad (3)$$

The corresponding boundary conditions are;

$$\begin{aligned}\bar{U} = 1, \bar{\theta} = 1, \bar{\phi} = 1 \text{ at } Y = 0 \\ \bar{U} \rightarrow 0, \bar{\theta} \rightarrow 0, \bar{\phi} \rightarrow 0 \text{ as } Y \rightarrow \infty\end{aligned}\quad (4)$$

where, Grashof number of heat transfer, $G_r = \frac{\nu g \beta (T_w - T_\infty)}{U_0^3}$; Grashof number of mass transfer,

$$G_m = \frac{\nu g^* \beta (C_w - C_\infty)}{U_0^3}; \text{ Dimensionless Viscoelastic Parameter, } K = k_0 \frac{U_0^2}{\nu^2}; \text{ Magnetic Parameter, } M = \frac{1}{\rho} \frac{\sigma B_0^2 \nu}{U_0^2};$$

Suction parameter, $S = \frac{v_0}{U_0}$; Prandtl number, $P_r = \frac{\nu \rho c_p}{k}$; Eckert Number, $E_c = \frac{U_0^2}{c_p (T_w - T_\infty)}$; Dufour number,

$$D_u = \frac{D_m (C_w - C_\infty)}{\nu (T_w - T_\infty)}; \text{ Schmidt number, } S_c = \frac{\nu}{D_m}; \text{ Soret number, } S_r = \frac{D_T (T_w - T_\infty)}{\nu (C_w - C_\infty)}.$$

SHEAR STRESS, NUSSELT NUMBER AND SHERWOOD NUMBER

From the velocity, the effects of various parameters on the local and average shear stress have been calculated.

The following equation represents the local shear stress at the plate. Local shear stress $\tau_L = \mu \left(\frac{\partial u}{\partial y} \right)_{y=0}$ which is

proportional to $\left(\frac{\partial \bar{U}}{\partial Y} \right)_{Y=0}$. From the temperature field, the effects of various parameters on the local heat transfer

coefficients have been investigated. The following equation represents the local heat transfer rate that is well known

Nusselt number. Local Nusselt number, $N_{uL} = \mu \left(-\frac{\partial T}{\partial y} \right)_{y=0}$ which is proportional to $\left(-\frac{\partial \bar{\theta}}{\partial Y} \right)_{Y=0}$. From the

concentration field, the effects of various parameters on the local mass transfer coefficients have been analyzed. The

following equation represents the local mass transfer rate that is well known Sherwood number. Local Sherwood

number, $S_{hL} = \mu \left(-\frac{\partial C}{\partial y} \right)_{y=0}$ which is proportional to $\left(-\frac{\partial \bar{\phi}}{\partial Y} \right)_{Y=0}$.

NUMERICAL ANALYSIS

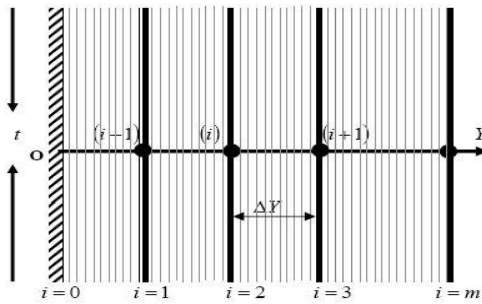


FIGURE 2. Implicit finite difference space

To solve the non-dimensional system by implicit finite difference technique, it is required to set finite difference equations. Here, the region within the boundary layer is divided by some perpendicular lines of Y – axis, where Y – axis is normal to the medium as shown in Figure 2. It is assumed that the maximum length of boundary layer is Y_{\max} ($= 35$) as corresponding to $Y \rightarrow \infty$ i. e., Y varies from 0 to 35 and the number of grid spacing in Y direction is 200. The constant mesh along Y axis becomes $\Delta Y = 0.175(0 \leq Y \leq 35)$ with the smaller time step $\Delta \tau = 0.001$.

Let \bar{U}_i^{n+1} , $\bar{\theta}_i^{n+1}$ and $\bar{\phi}_i^{n+1}$ denote the and values of \bar{U}_i^n , $\bar{\theta}_i^n$ $\bar{\phi}_i^n$ at the end of a time-step respectively. Using the implicit finite difference approximation and the system of partial differential equations (5)-(8) an appropriate set of finite difference equations have been obtained as;

$$\begin{aligned} \frac{\bar{U}_i^{n+1} - \bar{U}_i^n}{\Delta \tau} - S \frac{\bar{U}_{i+1}^n - \bar{U}_i^n}{\Delta Y} &= G_r \bar{\theta}_i^n + G_m \bar{\phi}_i^n + \frac{\bar{U}_{i+1}^n - 2\bar{U}_i^n + \bar{U}_{i-1}^n}{(\Delta Y)^2} - M \bar{U}_i^n \\ + K \left[\frac{\bar{U}_{i+1}^{n+1} - 2\bar{U}_i^{n+1} + \bar{U}_{i-1}^{n+1} - \bar{U}_{i+1}^n + 2\bar{U}_i^n - \bar{U}_{i-1}^n}{\Delta \tau (\Delta Y)^2} - S \frac{\bar{U}_{i+3}^n - 3\bar{U}_{i+2}^n + 3\bar{U}_{i+1}^n - \bar{U}_i^n}{(\Delta Y)^3} \right] \end{aligned} \quad (5)$$

$$\frac{\bar{\theta}_i^{n+1} - \bar{\theta}_i^n}{\Delta \tau} - S \frac{\bar{\theta}_{i+1}^n - \bar{\theta}_i^n}{\Delta Y} = \frac{1}{P_r} \frac{\bar{\theta}_{i+1}^n - 2\bar{\theta}_i^n + \bar{\theta}_{i-1}^n}{(\Delta Y)^2} + ME_c \bar{U}_i^{2n} + D_u \frac{\bar{\phi}_{i+1}^n - 2\bar{\phi}_i^n + \bar{\phi}_{i-1}^n}{(\Delta Y)^2} \quad (6)$$

$$\frac{\bar{\phi}_i^{n+1} - \bar{\phi}_i^n}{\Delta \tau} - \frac{\bar{\phi}_{i+1}^n - \bar{\phi}_i^n}{\Delta Y} = \frac{1}{S_c} \frac{\bar{\phi}_{i+1}^n - 2\bar{\phi}_i^n + \bar{\phi}_{i-1}^n}{(\Delta Y)^2} + S_r \frac{\bar{\theta}_{i+1}^n - 2\bar{\theta}_i^n + \bar{\theta}_{i-1}^n}{(\Delta Y)^2} \quad (7)$$

The boundary conditions with the finite difference scheme are as;

$$\begin{aligned} \bar{U}_i^n &= 1, \bar{\theta}_i^n = 1, \bar{\phi}_i^n = 1 \\ \bar{U}_L^n &= 0, \bar{\theta}_L^n = 0, \bar{\phi}_L^n = 0 \text{ where } L \rightarrow \infty \end{aligned} \quad (8)$$

Here the subscript i degenerate the grid points with Y coordinates and superscript n represents the value of time, $\tau = n\Delta \tau$, where, $n = 0, 1, 2, \dots$. The velocity (\bar{U}), temperature ($\bar{\theta}$) and concentration ($\bar{\phi}$) distributions at all interior nodal points may be computed by successive applications of the above finite difference equations. The numerical values of the local Shear Stress, Nusselt number and Sherwood number are evaluated by five-point approximate formula for the derivatives. The stability condition and convergence criteria of the problem are as furnished as $P_r \geq 0.07$ and $S_c \geq 0.07$ which are not shown in details for brevity.

RESULTS AND DISCUSSION

In order to reveal the steady-state solutions, the computations have been carried out up to dimensionless time $\tau = 120$. It is observed that the numerical values of \bar{U} , $\bar{\theta}$ and $\bar{\phi}$ however, show a little changes after dimensionless time $\tau = 60$. Thus the solutions for dimensionless time $\tau = 60$ are essentially steady-state solutions. It has been seen that the graphical representation of various dimensionless parameters have been reached its highest convergence when mesh size is taken as $n = 200$ (figure 3(a) and 3(b)). Therefore the flow parameters have been illustrated graphically in figures (4-5) with dimensionless time $\tau = 60$ and mesh size $n = 200$. For brevity, effects of two parameters have been illustrated.

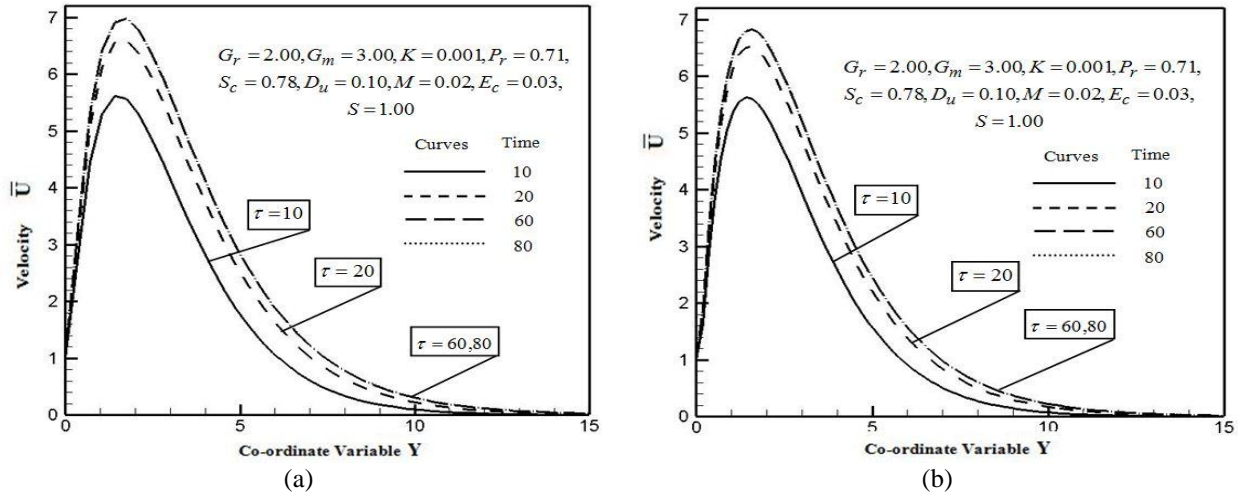


FIGURE 3. Steady state solution for $S_r = 2.00$ at different time intervals with (a) mesh size $n = 100$ (b) mesh size $n = 200$

The graphical results are plotted from numerical solutions by using the computational software Tecplot 9.0. figures 4(a-b) are plotted to present the influence of Dufour number D_u on both fluid velocity and shear stress. It is noted that in figure 4(a) the velocity of the fluid has been increased as Dufour number D_u increased. A similar behavior is also expected in figure 4(b) due to the fact that increasing the velocity means increasing the shear stress for a certain parameter. In figure 4(b), the shear stress increases with the increase of Dufour number D_u .

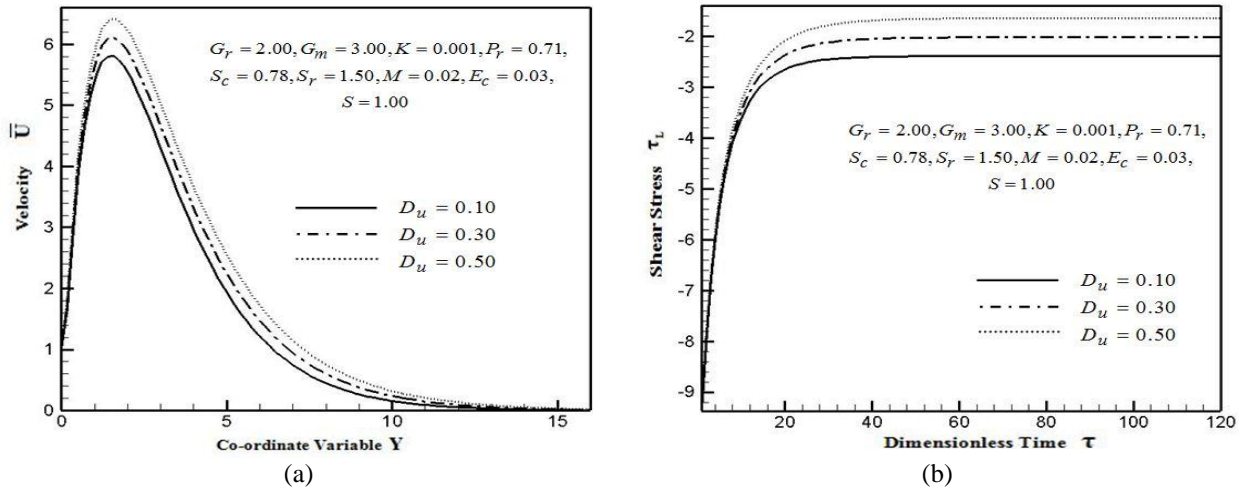


FIGURE 4. (a) Velocity profiles (b) Shear stress for different values of Dufour number D_u

figures 5(a-b) are plotted to show the effect of Soret number S_r on fluid velocity and shear stress. figure 5 (a) depicts that the fluid velocity has been seen increasing effect due to increase of Soret number S_r . figure 5 (b) is illustrated to display the effect of Soret number S_r on fluid shear stress. It is clearly seen that, fluid shear stress has been increased with the increase of Soret number S_r .

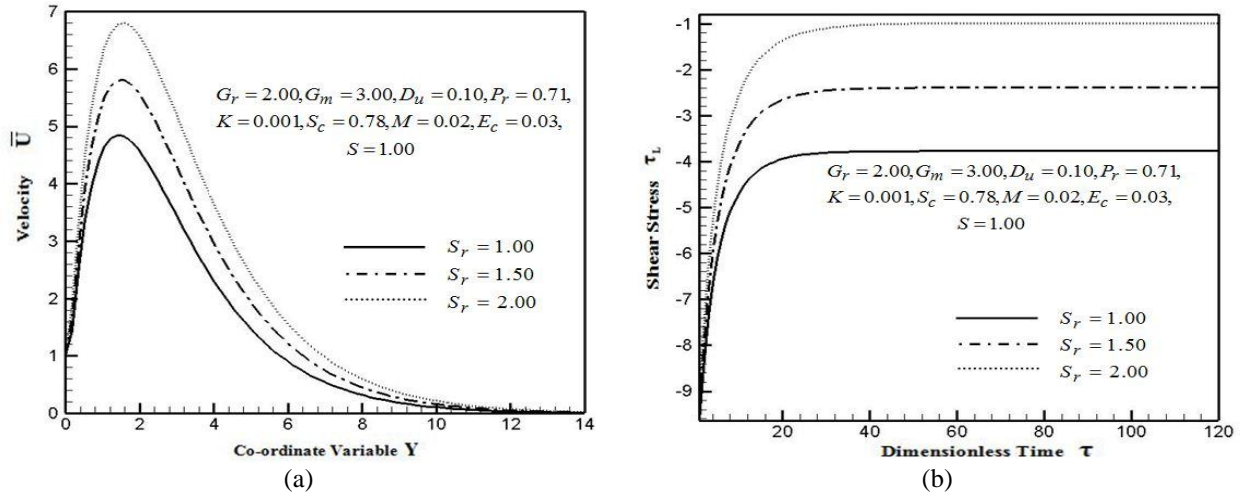


FIGURE 5. (a) Velocity profiles (b) Shear stress for different values of Soret number S_r

COMPARISON

Qualitative comparison of the present results with previous results is presented in a tabular form.

TABLE 1. Qualitative comparison of the present results with the previous results

Increased Parameter	Previous Results Given By Gbadeyan et al.[5]	Present Results
D_u	Increase	Increase
S_r	Increase	Increase

Finally, a qualitative comparison of the present steady-state results with the published results (Gbadeyan et al. [5]) is presented graphically in figures 6(a-b).

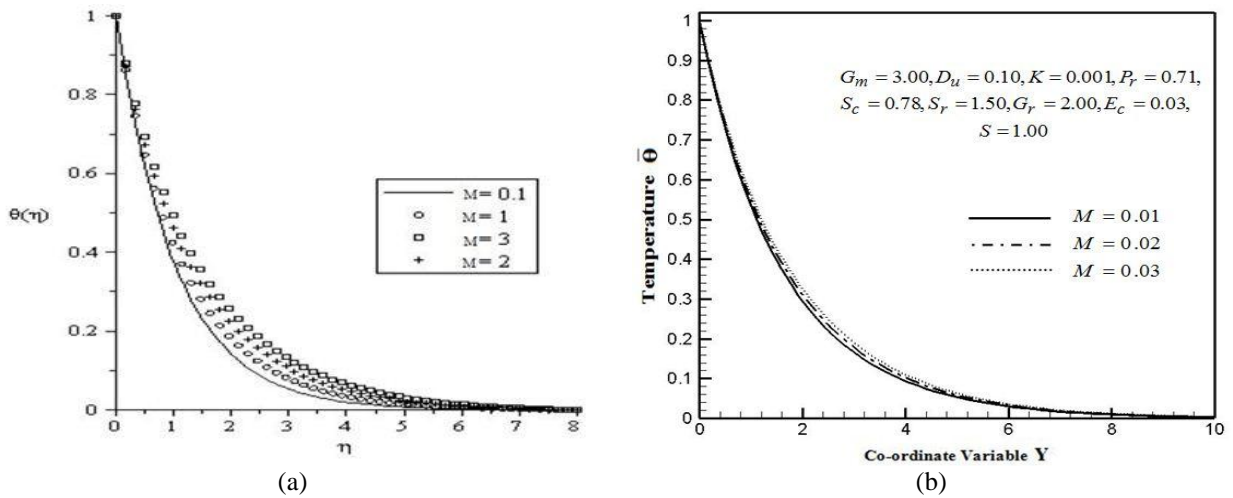


FIGURE 6. Temperature profiles (a) Published result (Gbadeyan et al. [5]) (b) Present result for different values of Magnetic parameter M

The results are seen qualitatively same behavior but quantitatively different. In this work, the implicit finite difference method has been used as a solution technique but Gbadeyan et al. [5] has used similarity technique with shooting method as a solution technique.

CONCLUSIONS

Implicit finite difference method has been applied to solve the model and also shown the effects of Soret and Dufour number on MHD viscoelastic fluid flow through a vertical flat with constant suction. The accuracy of the obtained results is checked through the imposed conditions and graphs. The obtained results are qualitatively good in case of all the flow parameters but not shown for brevity. The following main results are concluded from this study;

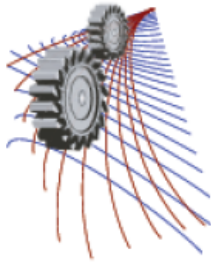
1. For the increase of Dufour number D_u , the velocity and the shear stress have been increased.
2. Velocity and shear stress of the fluid have been increased with the increase of Soret number S_r .

ACKNOWLEDGMENTS

This work is financed and supported by National Science and Technology (NST) under **Ministry of Science and Technology, Government of the People's Republic Bangladesh.**

REFERENCES

1. D.W. Beard and K. Walters, Mathematical Proceedings of the Cambridge Philosophical Society **60(3)**, 667-674 (1964).
2. K. R. Rajagopal, T. Y. Na, A. S. Gupta, Rheologica Acta **23**, 213-215 (1984).
3. M. Kumar, H.S. Takhar, G. Nath, Indian Journal of pure and applied Mathematics **28(1)**, 109-121 (1997).
4. N. Islam and M.M. Alam, Bangladesh Journal of Science and Industrial Research **43(2)**, 159-172 (2008).
5. J.A. Gbadeyan, A.S. Idowu, A.W. Ogunsola, O.O. Agboola, P.O. Olanrewaju, Global Journal of science Frontier Research **11(8)**, 96-114 (2011).
6. S.I. Hossain and M.M. Alam, Procedia Engineering **105**, 309-316 (2015).



Effect of Angle of Attack on an Optimized Vortex Induced Vibrated Energy Harvester: A Numerical Approach

Md. Rejaul Haque^{1, a)}, M Arshad Zahangir Chowdhury^{1, b)} and Anjan Goswami^{1, c)}

¹*Department of Mechanical Engineering, Bangladesh University of Engineering and Technology (BUET), Dhaka-1000, Bangladesh*

^{a)} Corresponding author: md.rejaulh@yahoo.com

^{b)} arshad.zahangir.bd@gmail.com

Abstract. A two-dimensional numerical study of flow induced vibration is reported in this paper to investigate flow over a semi-circular D-shaped bluff body oriented at different angles-of-attack to determine an optimized design for energy harvesting. Bluff body structure governs fluid streamlines; therefore obtaining a suitable range of “lock in frequency” for energy harvesting purpose is dependent on refining and optimizing bluff body’s shape and structure. A cantilever based novel energy harvester design incorporates the suitable angle-of-attack for optimized performance. This optimization was done by performing computations for 30°, 60° and 90° angles-of-attack. The frequency of vibration of the body was calculated at different Reynolds Number. A Fast Fourier Transformation yielded frequency of vortex shedding. From the wake velocity profile, lift oscillation and frequency of vortex shedding is estimated. Strouhal numbers of the body were analyzed at different angles-of-attack. A higher synchronized bandwidth of shedding frequencies is an indication of an optimized harvester design at different Reynolds number. The ‘D’ shaped bluff bodies (with angle of attack of 300,600 and 900) are more suitable than that of cylindrical shaped bluff bodies. The research clearly stated that, bluff bodies shape has a prominent influence on vortex induced vibration and semicircular bluff body gives the highest vibration or energy under stated conditions.

INTRODUCTION

Now-a-days great efforts are made to invent energy storage devices that have longer life span and require less maintenance. Conventional energy storage devices such as batteries, springs etc. have comparatively shorter life span and require regular expensive maintenance. Reduction of operating cost is therefore greatly depended on minimization of maintenance and proliferation of operating life. Extracting the energy of a flowing fluid from ambient environment and harvesting it provides a low cost alternative to these problems. Fluid motion is converted to steady fluid oscillation through a cantilever attached body that vibrates if fluid motion is induced [1]. This phenomenon merely employs Helmholtz resonators for conversion of fluid motion to steady fluid oscillation. Strained piezoelectric materials are most suitable for energy harvester design [2] since this conversion mechanism generates very high potential difference. Moreover, employing strained piezoelectric materials results in downsizing of the overall energy harvester design that have wide ranging applications. Lift and drag force induced vibration component directly convert kinetic energy of fluid to electrical power irrespective of the component being piezoelectric, electromagnetic or electrostatic [3]. An asymmetric vortex street is the reason for unequal pressure distribution among upper and lower surface of the body. Therefore a periodic variation of lift and drag force occurs, that has period equal to that of vortex shedding frequency. If the body is allowed unrestricted movement in the vertical direction, vibration is induced to the body. This is termed vortex induced vibration (VIV) [4]. When the vortex shedding frequency and the natural frequency of the body are in tandem, the phenomenon is termed “Lock-in”. Once the vortex shedding frequency is very close to the natural frequency of the body a shift in frequency of

vortex shedding occurs, resulting in very high vibration amplitude. These are suitable for a cantilever attached energy harvester. “Lock-in” frequency is closely analyzed for harvester design.

Nomenclature

ρ	density	F_L	lift forces
μ	Dynamic viscosity	U_{mean}	mean velocity of fluid
u	velocity component along the X-axis	f_s	frequency of vortex shedding
v	velocity component along the Y-axis	D	characteristic length of the bluff-body
P	pressure	Re	Reynolds number
F_D	drag force	St	Strouhal number
α	angle of attack		

Our investigation is concerned with vortex induced vibration of a semi-circular D-shaped bluff body oriented at an angle-of-attack of 30°, 60° and 90° respectively. Moreover, a circular bluff-body is also analyzed to validate our computation. The study is conducted without a cantilever beam attached. The range of Reynolds number studied is up to 270. The flow regime at different fluid velocities is realized by utilizing the laminar flow module of the Finite Element Solver in order to calculate the frequency of vortex shedding. Furthermore, Strouhal number is analyzed for all the angles-of-attack to predict the suitable orientation of the D-shaped body for the purpose of determining the optimized design of a cantilever-based fluid flow energy harvester.

NUMERICAL APPROACH

Fluid Flow

In order to explore the capability of different bluff bodies and effects of angle-of-attack to provide suitable range of synchronized region of frequency for optimization purpose, the physics of fluid flow is utilized. The fluid flow is assumed to be incompressible. The governing equations are:

Continuity equation:

$$\frac{\partial u}{\partial x} + \frac{\partial v}{\partial y} = 0 \quad (1)$$

Momentum equations:

$$\rho \left[u \frac{\partial u}{\partial x} + v \frac{\partial u}{\partial y} \right] = -\frac{\partial P}{\partial x} + \mu \left[\frac{\partial^2 u}{\partial x^2} + \frac{\partial^2 u}{\partial y^2} \right] \quad (2)$$

$$\rho \left[u \frac{\partial v}{\partial x} + v \frac{\partial v}{\partial y} \right] = -\frac{\partial P}{\partial y} + \mu \left[\frac{\partial^2 v}{\partial x^2} + \frac{\partial^2 v}{\partial y^2} \right] \quad (3)$$

In order to evaluate the dimensionless drag and lift coefficient it is imperative to know the distribution of viscous force and shear stress over the bluff body. The coefficients are defined as follows:

$$C_D = \frac{2F_D}{\rho U_{mean}^2 D} \quad (4)$$

$$C_L = \frac{2F_L}{\rho U_{mean}^2 D} \quad (5)$$

Reynolds Number

The drag and lift coefficients are independent of the shape of the body. However, they depend on the dimensionless Reynolds number. The Reynolds Number (Re) is defined as the ratio of inertia force to viscous force. The Reynolds number is defined as follows:

$$\text{Re} = \frac{\rho U_{mean} D}{\mu} \quad (6)$$

Strouhal Number

The Strouhal Number (St) is a dimensionless number that relates frequency of vortex shedding for a particular size of the bluff body for different flow regimes characterized by different flow velocities. Hence it is very useful for the analysis. It is defined as follows:

$$\text{St} = \frac{f_s D}{U} \quad (7)$$

COMPUTATIONAL METHODS

Computational Flow Regime

The solver performs a finite element analysis for laminar flow, 2D unsteady, incompressible fluid flow through a channel. The height and length of the channel is 0.4m and 2.2m respectively. As shown in Figure.1, the bluff-body is placed perpendicularly to the direction of the velocity field of the fluid flow and at a distance of 0.2m from the channel inlet. The characteristic lengths of the bodies are kept constant at 0.1m. The left wall is considered fluid inlet through which fluid enters with normal inflow velocity profile and the right wall of the channel is considered as outlet through which the fluid leaves the domain. Fluid velocity ranges from 0.3-2.7 ms^{-1} , dynamic viscosity is 0.0000179 Pa.s and the density of fluid is 1.23 kg/m^3 .

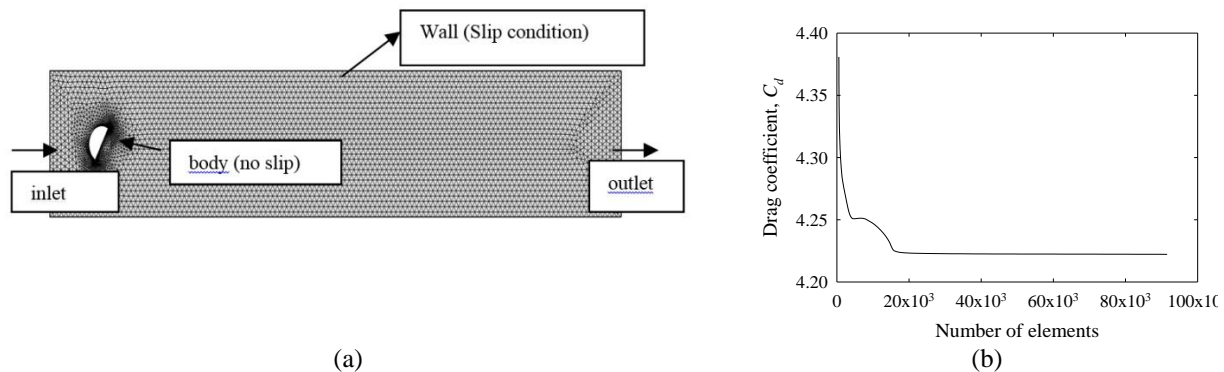


FIGURE 1. (a) Computational domain (b) Grid independency test

Boundary conditions

Since fluid velocity plays a key role in the research, normal inflow velocity with values ranging from 0.3 m/s to 2.7 m/s is considered for inlet boundary condition. Pressure with no viscous stress is applied for outlet boundary condition. To negate viscous effects, on the longer sides of the rectangular flow regime, the slip boundary condition is applied. This also takes into account the fact that boundaries are considerably far apart in practical applications. Due to the slip condition, there is no viscous effect at the walls. However, the viscous effects on the bluff-body surface are of interest to the study, therefore no-slip condition is applied there.

Grid generation

The computational domain is divided into small units of simple shapes or cells or mesh for solving the governing equations numerically by finite element method (FEM). The two dimensional computational domain is divided into triangular cells as shown in Figure 1(a). Moreover, a grid independency test is performed by increasing global number of cells and running the computation progressively on finer grids or cells. This minimizes discretization error in mesh generation. Beyond 20000 or higher number of mesh elements, the value of the estimated drag coefficient varies negligibly as shown in Figure 1(b). Therefore, the 40000 mesh elements are sufficient for our computation.

RESULTS

Velocity contours

The velocity contours at different angles-of-attack clearly demonstrate the developing vortex at the upper end and shed vortex at the lower end in the wake of the bluff-body in Figure 2.

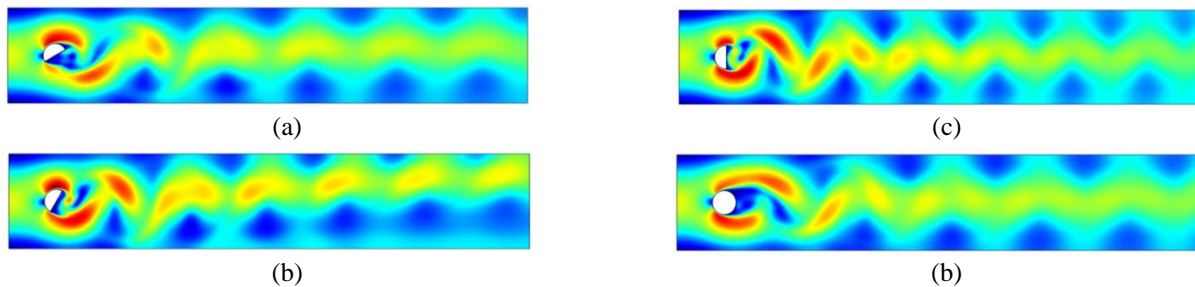
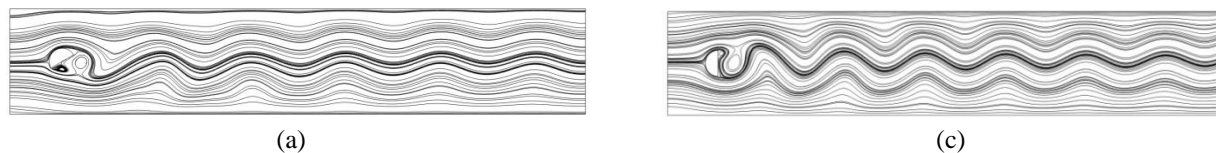


FIGURE 2. Velocity contour at $Re = 270$ and $t=7s$ for (a) D-shape body at 30° (b) D-shape body at 60° (c) D-shape body at 90° (d) Circular bluff body

Streamline distribution

The streamline distribution is presented in the following figure for $t=7s$.



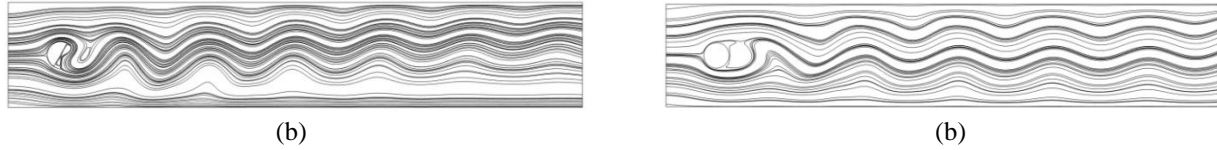


FIGURE 3. Streamline distribution at $Re = 270$ and $t=7s$ for (a) D-shape body at 300 (b) D-shape body at 600 (c) D-shape body at 900 (d) Circular bluff body.

The peak velocity ($6.78ms^{-1}$) is obtained with the D-shape body (60° angle of attack) as a very higher red color region is observed near the body. As the shape of the body changes from semicircular to cylindrical, the velocity decreases.

In case of Figure 3(a), two wakes are seen immediately after the body and the recirculation zone is tiny. From Figure 3(b), the formation of vortices is observed close to cylinder. These vortices are along the centreline of the flow. Figure 3(c) illustrates the recirculation zone near the region of the bluff body. The vortices formed by circular bluff body is however is larger than D-shaped bluff body thus confirming that bluff bodies' shape plays a vital role. It appears that angles of attack develops huge amount of flow disturbances which leads to a modest amount of oscillation. This driving oscillating forces generated from the bluff-body induced by the von Kármán vortex streets will mechanically strain an attached piezoelectric cantilever at the trailing edge, and hence power could be generated.

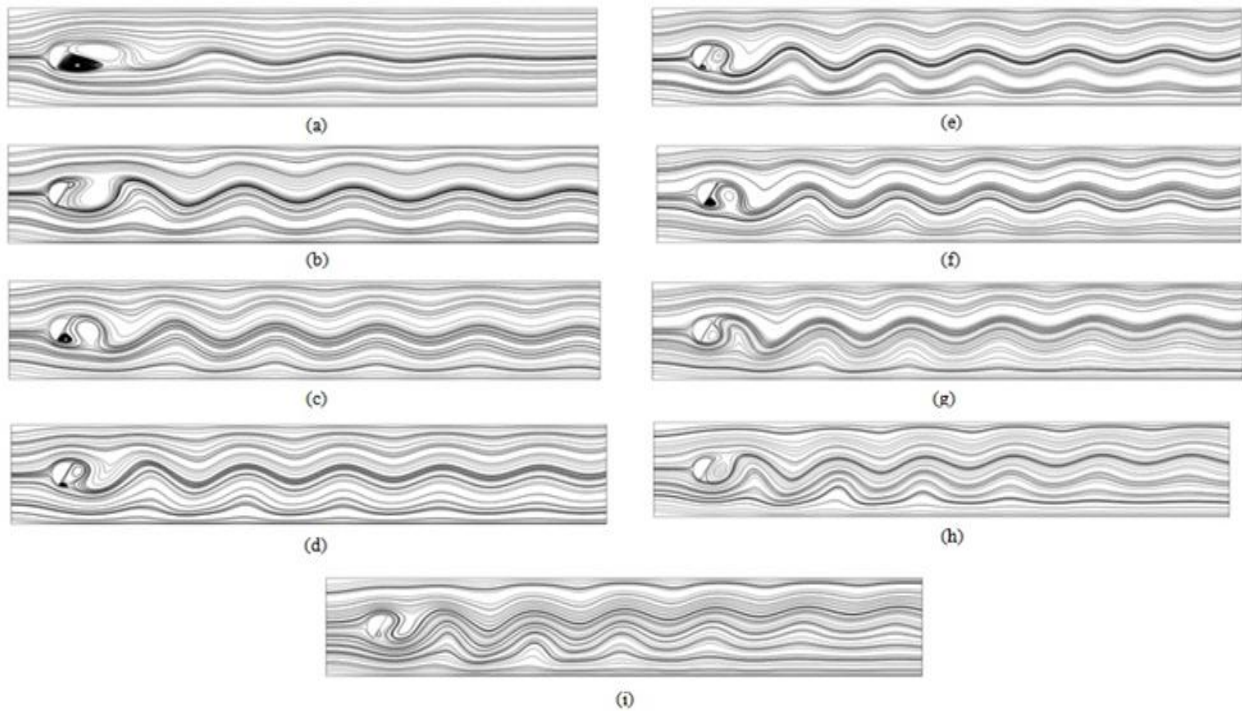


FIGURE 4. Streamline distribution at $t=7s$ for D-shaped bluff body at a) $Re=30$ b) $Re=60$ c) $Re=90$ d) $Re=120$ e) $Re=150$ f) $Re=180$ g) $Re=210$ h) $Re=240$ i) $Re=270$

Figure 4 illustrates that at comparatively higher $Re \leq 90$, downstream of the bluff-body, the von Karman path is evident and a fixed pair of vortices emerge. Until $Re = 270$, the laminar vortex street is present in the flow regime.

However, as shown in Figure 5(a), for an angle-of-attack of 60° the lift coefficient increases gradually with increasing Reynolds number for $Re \leq 90$ and approaches a constant value. This progression is also noticed for angle-of-attack of 30° for $Re \leq 180$. For cylindrical bluff body the lift coefficient variation decreases throughout the Reynolds number range.

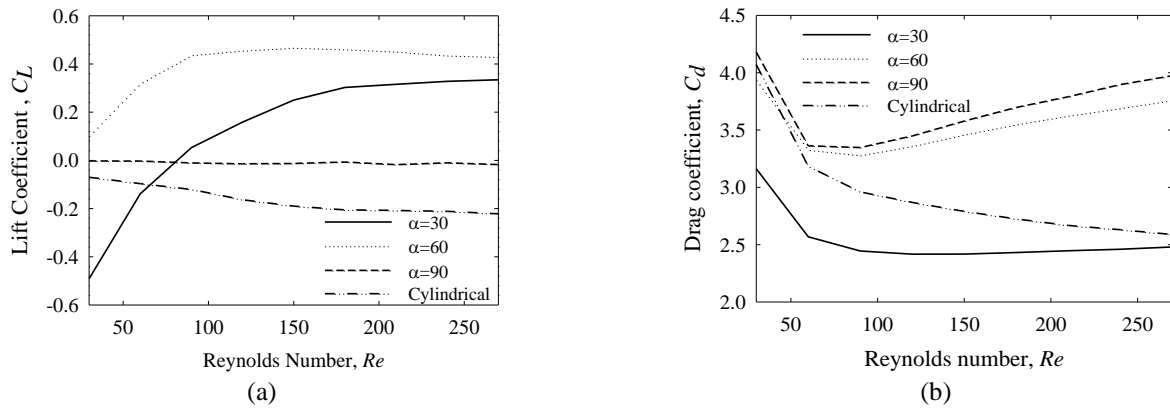


FIGURE 5. Variation of a) Lift coefficient b) Drag coefficient with Reynolds number.

The drag coefficient (CD) variation for angles-of-attack of 60° and 90° is analogous as shown in Figure 5(a). However; CD is comparatively higher at every Reynolds number for angles-of-attack of 60° than 90° . The drag coefficient of cylindrical shaped bluff-body decreases sharply up to $Re = 60$. The decrease is much more pronounced for D-shaped bluff body at angle-of-attack of 30° . Figure 6(a) demonstrates the Fourier coefficient variation with frequency. The most pronounced spikes occur at 3 ± 0.5 Hz, 5.5 ± 0.5 Hz, 9 ± 0.5 Hz for increasing mean velocity. The frequency spikes shift to the right with increasing mean inflow velocity.

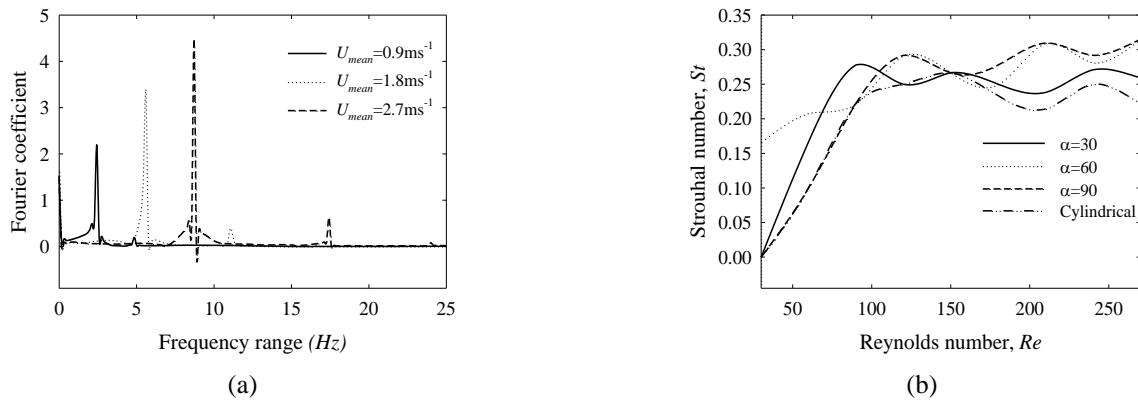


FIGURE 6. Variation of a) Fourier coefficient with frequency b) Strouhal number with Reynolds number for different angles-of-attack at $Re=270$.

The Strouhal number for different bluff body is found to be between 0.2 and 0.3 for a wide range of Reynolds number. This is in agreement with the experimental values as reported by [5]. Their experimental investigation concluded that most bluff bodies have Strouhal number of approximately 0.2.

The Strouhal number variation with Reynolds number for all the bluff-bodies are presented in Figure 6(b). Below Reynolds number of 100, the Strouhal number was found to be significantly higher for D-shaped bluff body at 60° angle-of-attack. So, at a low Reynolds number, it is the best optimized option. However, a gradual decrease of Strouhal number was observed for cylindrical bluff-body. Beyond $Re \geq 100$, the Strouhal number shows a sinusoidal behavior for all the bluff-bodies and angles-of-attack. Moreover, the increase is higher for 90° angle-of-attack D-shaped bluff-body compared to that of others. This is indicative of the fact that shedding frequency is not constant but it fluctuates inside a frequency range which is dependent on the bluff body shape and Reynolds number. At comparatively higher Reynolds number where the increase is progressively nonlinear for Strouhal number, is the operable range for an optimized energy harvester. Moreover, since the D-shaped bluff-body at 90° angle-of-attack has comparatively lower drag coefficient at every Reynolds number than that of the other orientation, it results in

reduced shear surface force. These two effects yield a better optimized design for the cantilever attached energy harvester design.

CONCLUSION

The research predicts that vortex shedding frequency is not constant value and it fluctuates within a frequency range which is a function of bluff-body shape, its orientation (angle-of-attack) and flow velocity (Reynolds number). The von Karman vortex street due to the vortex induced vibration of the bluff-bodies generates an oscillating force. This force has capability to mechanically strain an attached piezoelectric cantilever at the trailing edge. This strain will then generate power.

Although wake from both 90° angle-of-attack and 60° angle-of-attack D-shaped bluff-body present near equal fluctuant shedding frequency range as evident from Strouhal number distribution, the 90° angle-of-attack flow configuration has comparatively lower drag coefficient throughout the operating range than that of others.

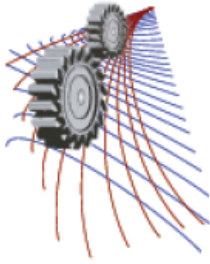
Hence, a D-shaped bluff-body at 90° angle-of-attack is suitable for an optimized piezoelectric cantilever attached energy harvester design under present consideration.

ACKNOWLEDGMENT

The authors are grateful for the resources and support provided by the Department of Mechanical Engineering at Bangladesh University of Engineering and Technology (BUET).

REFERENCES

1. S. Kim, C. Ji, P. Galle, F. Herrault, X. Wu, J.H. Lee, C. Choi and M.G. Allen, *J. Micromech. Microeng.* **19**, 940-950 (2009).
2. S.P. Beebly, M.J. Tudor and N.M. White, *Measurement Science and Technology*, **17**, article R175 (2006).
3. H.D. Akaydin, E. Niell and A. Yiannis, *J. Intel. Mat. Sys. Struct.*, **21**, 1263-78 (2010).
4. M. Zhao and L. Chengb, *Journal of Fluids and Structures*, **31**, 125-140 (2012).
5. C.H.K. Williamson and G.L. Brown, *Journal of Fluids and Structures*, **12**, 1073-1085 (1998).



Study the Effect of Chemical Reaction and Variable Viscosity on Free Convection MHD Radiating Flow Over an Inclined Plate Bounded by Porous Medium

M. Ali^{1, 3, a)}, M.A. Alim¹, R. Nasrin¹ and M.S. Alam²

¹Department of Mathematics, Bangladesh University of Engineering and Technology, Dhaka-1000

²Department of Mathematics, Chittagong University of Engineering and Technology, Chittagong-4349

³Department of Mathematics, Chittagong University of Engineering and Technology, Chittagong-4349

^{a)}Corresponding author: ali.mehidi93@gmail.com

Abstract. An analysis is performed to study the free convection heat and mass transfer flow of an electrically conducting incompressible viscous fluid about a semi-infinite inclined porous plate under the action of radiation, chemical reaction in presence of magnetic field with variable viscosity. The dimensionless governing equations are steady, two-dimensional coupled and non-linear ordinary differential equation. Nachtsgeim-Swigert shooting iteration technique along with Runge-Kutta integration scheme is used to solve the non-dimensional governing equations. The effects of magnetic parameter, viscosity parameter and chemical reaction parameter on velocity, temperature and concentration profiles are discussed numerically and shown graphically. Therefore, the results of velocity profile decreases for increasing values of magnetic parameter and viscosity parameter but there is no effect for reaction parameter. The temperature profile decreases in presence of magnetic parameter, viscosity parameter and Prandtl number but increases for radiation parameter. Also, concentration profile decreases for the increasing values of magnetic parameter, viscosity parameter and reaction parameter. All numerical calculation are done with respect to salt water and fixed angle of inclination of the plate.

INTRODUCTION

The magnetohydrodynamic (MHD) boundary layer flow of heat and mass transfer problems have become in view of its significant applications in industrial manufacturing processes such as plasma studies, petroleum industries, magneto-hydrodynamics power generator, cooling of nuclear reactors, boundary layer control in aerodynamics, glass fiber production and paper production. Besides, the fluid flow through a porous medium have also numerous engineering and geophysical applications, such as, filtration process in chemical engineering and purification, in agriculture to study the underground water resources, in petroleum technology to study the movement of natural gas, oil and water through the oil reservoirs. In view of these important applications, many researchers have studied MHD free convective heat and mass transfer flow in a porous medium, some of them are Sahin and Kalita (2013) investigated the effects of porosity and MHD on a horizontal channel flow of a viscous incompressible electrically conducting and radiating fluid through a porous medium in the presence of thermal radiation, Alharbi *et al.* (2010) studied heat and mass transfer in MHD visco-elastic fluid flow through a porous medium over a stretching sheet with chemical reaction, Seddeek and Abdel Meguid (2006) analyzed the effects of radiation and thermal diffusivity on heat transfer over a stretching surface with variable heat flux, Ali *et al.* (2014) studied the radiation and thermal diffusion effects on a steady MHD free convection heat and mass transfer flow past an inclined stretching sheet with hall current and heat generation, Rajput and Kumar (2012) considering the radiation effects on MHD flow past an impulsively started vertical plate with variable heat and mass transfer by Laplace transform technique. If the surrounding temperature of the fluid is higher then radiation effects play an important role but this situation does not exist in space technology. In this situation the researchers have to take into

account the effect of thermal radiation and mass diffusion. So the present work is focused on steady MHD boundary layer flow of an incompressible, electrically conducting and viscous fluid about an inclined porous plate with variable viscosity in porous medium by quasi-linearization technique.

Nomenclature	
<i>MHD</i>	magnetohydrodynamic
c_p	specific heat at constant pressure, $\text{Jkg}^{-1}\text{K}^{-1}$
κ	thermal conductivity, $\text{w m}^{-1}\text{K}^{-1}$
α	angle of inclination, degree
g	acceleration due to gravity, ms^{-2}
γ	viscosity parameter
σ	electrical conductivity, sm^{-1}
K	permeability of the porous medium
D_m	coefficient of mass diffusion, m^2s^{-1}
μ_*	coefficient of viscosity, $\text{kg m}^{-1}\text{s}^{-1}$
μ	variable viscosity
ν	kinematics viscosity, m^2s^{-1}
ρ	fluid density, kg m^{-3}
B_0	magnetic field intensity, Am^{-1}
β	thermal expansion coefficient, k^{-1}
β^*	concentration expansion coefficient, $\mu \text{mm}^{-1}\text{k}^{-1}$
u	velocity component along X axis, ms^{-1}
U_0	stream velocity constant
V_0	suction velocity
v	velocity component along Y axis, ms^{-1}
C	concentration, kg m^{-3}
C_w	plate concentration, kg m^{-3}
C_∞	free stream concentration
T	fluid temperature, k^{-1}
T_w	plate temperature, k^{-1}
T_∞	free stream temperature
ψ	stream function

MATHEMATICAL FORMULATION OF THE PROBLEM AND SIMILARITY ANALYSIS

Let us consider a steady two dimensional laminar MHD viscous incompressible electrically conducting fluid along an inclined stretching sheet with an acute angle (α), X- direction is taken along the leading edge of the inclined stretching sheet and Y is normal to it and extends parallel to X-axis. A magnetic field of strength B_0 is introduced to the normal to the direction of the flow. Let u and v be the velocity components along the X and Y axis respectively in the boundary layer region. Under the above assumptions and usual boundary layer approximation, the dimensional governing equations of continuity, momentum, concentration and energy are:

Equation of continuity:

$$\frac{\partial u}{\partial x} + \frac{\partial v}{\partial y} = 0 \quad (1)$$

Momentum equation:

$$u \frac{\partial u}{\partial x} + v \frac{\partial u}{\partial y} = \frac{1}{\rho} \frac{\partial}{\partial y} \left(\mu^* \frac{\partial u}{\partial y} \right) + g\beta(T - T_\infty) \cos \alpha + g\beta^*(C - C_\infty) \cos \alpha - \frac{\sigma B_0^2 u}{\rho} - \frac{v}{K} u \quad (2)$$

According to Carey and Mollendorf (1978), the variable viscosity is taken of the form $\mu^* = \mu[1 + \gamma(\theta - 1/2)]$, where γ is the viscosity parameter.
Energy Equation:

$$u \frac{\partial T}{\partial x} + v \frac{\partial T}{\partial y} = \frac{\kappa}{\rho c_p} \frac{\partial^2 T}{\partial y^2} - \frac{\partial q_r}{\partial y} \quad (3)$$

Concentration Equation:

$$u \frac{\partial C}{\partial x} + v \frac{\partial C}{\partial y} = D_m \frac{\partial^2 C}{\partial y^2} - C_r(C - C_\infty) \quad (4)$$

By using the Rosseland approximation, we have the radiative heat flux $q_r = -\frac{4\sigma^*}{3K_0} \frac{\partial T^4}{\partial y}$, where σ^* the Stefan-Boltzman is constant, K_0 is the Rosseland mean absorption coefficient. Assuming that, the difference in temperature within the flow are such that T^4 can be expressed as a linear combination of the temperatures. We expand T^4 in Taylors series about T_∞ as follows:

$$T^4 = T_\infty^4 + 4T_\infty^3(T - T_\infty) + 6T_\infty^2(T - T_\infty)^2 + \dots \dots \dots \text{and neglecting the higher order terms beyond the first degree in } (T - T_\infty); \text{ we have } T^4 \approx -3T_\infty^4 + 4T_\infty^3 T. \text{ Therefore } q_r = -\frac{16\sigma^*}{3K_0} T_\infty^3 \frac{\partial T}{\partial y}. \text{ So the equation (3)}$$

$$\text{becomes} \quad u \frac{\partial T}{\partial x} + v \frac{\partial T}{\partial y} = \frac{\kappa}{\rho c_p} \frac{\partial^2 T}{\partial y^2} + \frac{16\sigma^*}{3K_0} T_\infty^3 \frac{\partial^2 T}{\partial y^2} \quad (5)$$

The above equations are subject to the following boundary conditions:

$$u = U_0 x, v = V_0, T = T_w, C = C_w \text{ at } y = 0 \text{ and } u = 0, T = T_\infty, C = C_\infty \text{ as } y \rightarrow \infty$$

Introducing the stream function $\psi(x, y)$ as defined by $u = \frac{\partial \psi}{\partial y}$ and $v = -\frac{\partial \psi}{\partial x}$

To convert the governing equations into a set of similarity equations, we introduce the following similarity transformation:

$$\psi = x\sqrt{v} U_0 f(\eta), \eta = y\sqrt{\frac{U_0}{v}}, \theta(\eta) = \frac{(T - T_\infty)}{(T_w - T_\infty)}, \phi(\eta) = \frac{C - C_\infty}{C_w - C_\infty}$$

From the above transformations, the non-dimensional, nonlinear and coupled ordinary differential equations are obtained as follows:

$$[1 + \gamma(\theta - 1/2)]f''' + f'' - f'^2 + \gamma\theta f'' - (M + N)f' + Gr\theta \cos \alpha + Gm\phi \cos \alpha = 0 \quad (6)$$

$$(1 + RPr)\theta'' + Pr f \theta' = 0 \quad (7)$$

$$\phi'' + Scf\phi' - C_r^* \phi' = 0 \quad (8)$$

The transform boundary conditions:

$$f = -S f' = 1, \theta = 1, \phi = 1 \text{ at } \eta = 0, \text{ and } f' = 0, \theta = \phi = 0 \text{ as } \eta \rightarrow \infty$$

Where f' , θ and φ are the dimensionless velocity, temperature and concentration respectively, η is the similarity variable, η_∞ is the value of η at which boundary conditions is achieved, the prime denotes differentiation with respect to η . Also

$$M = \frac{\sigma B_0^2}{\rho U_0}, N = \frac{\nu}{K U_0}, Gr = \frac{g\beta(T_w - T_\infty)}{U_0^2 x}, Gm = \frac{g\beta^*(C_w - C_\infty)}{U_0^2 x}, Pr = \frac{\mu c_p}{\kappa^*}, Sc = \frac{\nu}{D_m},$$

$$R = \frac{16\sigma^* T_\infty^3}{3K_0}, C_r^* = \frac{C_r \nu}{D_m U_0} \text{ and } S = -\frac{V_0}{\sqrt{\nu U_0}}$$

are the magnetic parameter, porosity parameter, Grashof number, modified Grashof number, Prandtl number, Schmidt number, radiation parameter, reaction parameter, and suction parameter respectively.

RESULTS AND DISCUSSION

Numerical calculation for the distribution of velocity, temperature and concentration profiles across the boundary layer for different values of the parameters are carried out. For the purpose of our simulation we have chosen $Pr = 1.0$, $Gr = 5.0$, $Gm = 2.0$, $Sc = 0.22$, and $\alpha = 60^\circ$ while the parameters are varied over range as shown in the figures. Fig.1 (a) clearly demonstrates that the velocity profile starts from maximum value at the surface and then decreasing until it reaches to the minimum value at the end of the boundary layer for all the values M . It is interesting to note that the effect of magnetic field is more prominent at the point of peak value, because the presence of M in an electrically conducting fluid introduces a force like Lorentz force which acts against the flow if the magnetic field is applied in the normal direction as in the present problem. As a result velocity profile is decreased but there is no effect for reaction parameter on velocity profile which are shown in Fig.1 (c). Again, noticeable decreasing effect are observed for the increasing values of viscosity parameter are shown in Fig.1 (b).

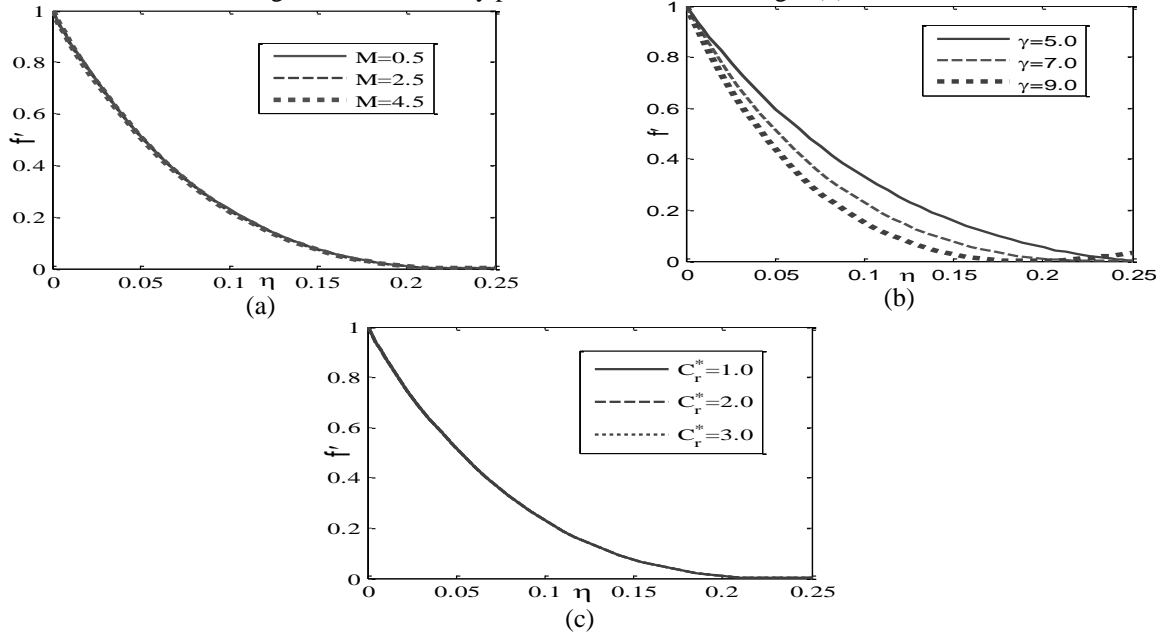


FIGURE 1. Variation of velocity with time (a) M , (b) γ and (c) C_r^* .

Again, Fig. 2(a) – Fig. 2(d) show the temperature profiles obtained by the numerical simulation for various values of entering parameters. From these figures we see that, the temperature profile is starting at the highest point of the plate surface and asymptotically decreases to zero far away from the plate satisfying the boundary condition which assist the accuracy of the numerical results obtained. From Fig. 2(b) it is observed that in the certain interval of η , the temperature profile is decreased and then increased for increasing values of viscosity parameter γ . Again,

the decreasing effect are observed for magnetic parameter and Prandtl number but reverse trend arises for radiation parameter. That is, the thermal boundary layer thickness decreases as the Pr increases implying higher heat transfer. It is due to the fact that smaller values of Pr means increasing thermal conductivity and therefore it is able to diffuse away from the plate more quickly than higher values of Pr , hence the rate of heat transfer is reduced as a result the heat of the fluid in the boundary layer increases.

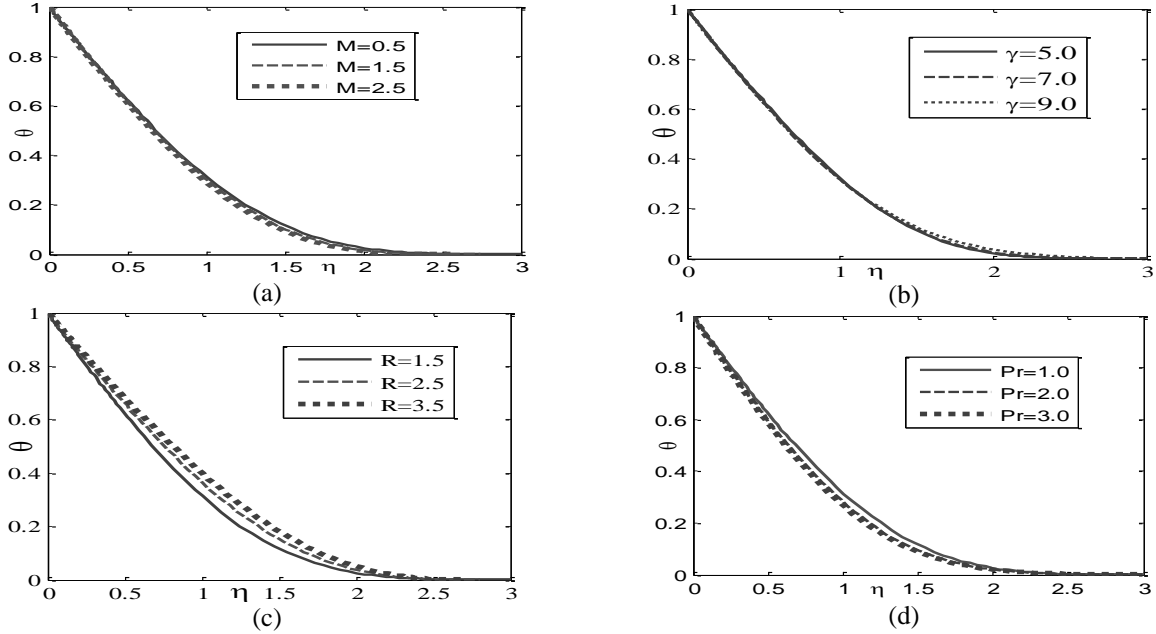


FIGURE 2. Variation of temperature with Time (a) M , (b) γ , (c) R and (d) Pr .

Again Fig.3 (a) - Fig. 3 (c) shows the concentration profiles obtained by the numerical simulation for various values of entering non-dimensional parameters. From these figures it is observed that the concentration profiles are decreased for increasing values of mentioned parameters.

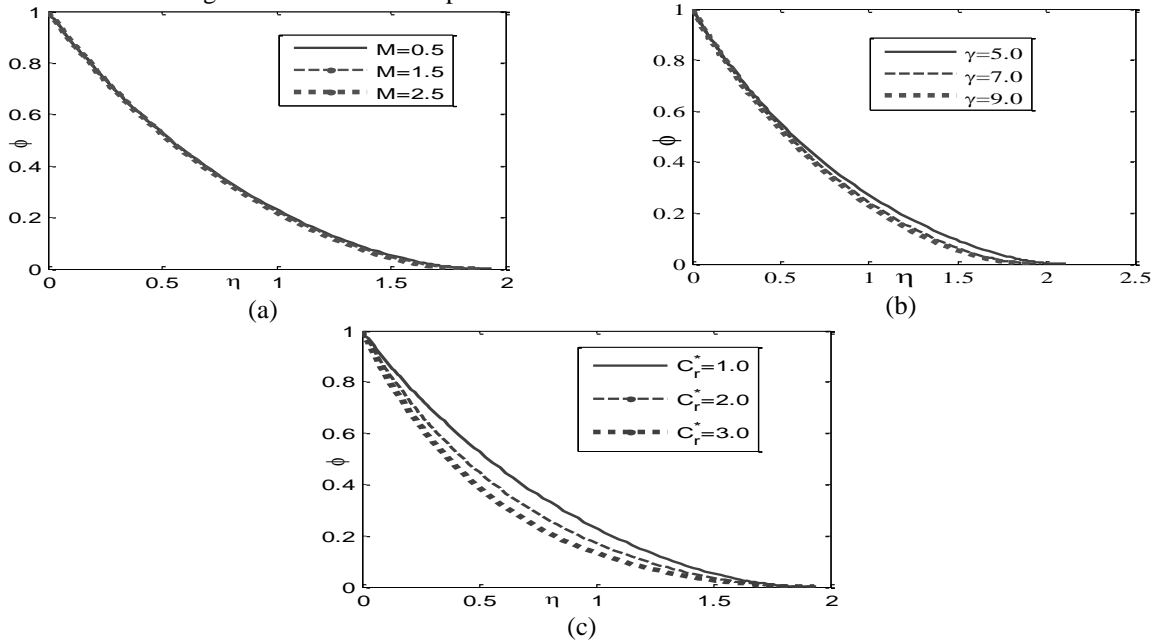


FIGURE 3. Variation of concentration with Time (a) M , (b) γ and (c) C_r^* .

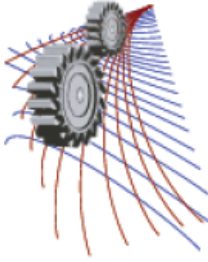
CONCLUSIONS

Following are the conclusions made from above analysis:

- The magnitude of velocity decreases with increasing magnetic parameter causing of Lorentz force but there is no effect for the increasing values of reaction parameter. Again, noticeable decreasing effect are observed for the increasing values of viscosity parameter.
- It is interesting to note that, in the certain interval of η , the temperature profile is decreased and then increased for increasing values of viscosity parameter but decreasing effect are observed for magnetic parameter and Prandtl number whereas the thermal boundary layer is increased for radiation parameter.
- The decreasing effects are observed for increasing values of magnetic parameter, viscosity parameter and reaction parameter on concentration profile.

REFERENCES

1. S. Ahmed and K. Kalita, J. Engg. Phys. **86**, (2013).
2. S. M. Alharbi, M. A. A. Bazid and S. M. El Gendy, Appl. Math. **1**, (2010).
3. M. A. Seddeek and M. S. A. Meguid, Phys. Lett. A, **348**, (2006).
4. M. Ali, M. S. Alam, M. M. Alam and M. A. Alim, J. Math. **9**, (2014).
5. U. S. Rajput and S. Kumar, Int. J. Appl. Math. Mech. **8**, (2012).
6. V. P. Carey and J.C. Mollendorf, J. H. Tran. **2**, (1978).



Study of Pressure Response during Kick Situation in a Wellbore

Al Amin^{1, a)}, Munzarin Morshed^{1, b)}, Syed Imtiaz² and Mohammad Azizur Rahman²

¹Memorial University of Newfoundland, Canada

²Memorial University of Newfoundland, Canada

^{a)}Corresponding Author: al.amin@mun.ca

^{b)}mm3112@mun.ca

Abstract. Drilling operations are vulnerable to catastrophic accidents. One of the common reasons for these incidents is the development of abnormal pressure, which may occur due to a sudden influx of reservoir fluids. When this imbalance in pressure occurs, the reservoir pressure has the ability to push the reservoir fluid into the wellbore. This may lead to severe accident, such as blowout of the drilling rig. Prior detection of the kick situation can help us to identify and mitigate the abnormal situations. Thus, it is necessary to understand the computational flow assurance phenomena in the wellbore system. The main target of this work is to investigate the abnormal pressure response occurring in a two phase flow involving air and water. This paper focuses on CFD analysis of two phase fluid flow through a wellbore. This study provides a platform for future research in the field of Managed pressure drilling.

INTRODUCTION

Drilling operations are susceptible to catastrophic accidents. Due to increasing demand of hydrocarbon resources, petroleum industries are paying more attention in developing efficient techniques for extraction of oil and gas reserves. The conventional drilling process has a very limited option to prevent accidents. However, techniques such as Managed Pressure Drilling (MPD) is used to precisely manage the wellbore pressure when drilling with a narrow window between 1.38×10^6 and 2.068×10^6 Pa of the pore pressure and fracture pressure [1]. It is believed that about 40% of the drilling problems happen as a result of pressure issues, lost return or kicks and stuck pipes [2]. The undesired influx of reservoir fluid or gas into the wellbore is termed as kick. When barriers such as cement or mud fails to overcome the reservoir pressure the influx of fluid occurs. A wrong action in preventing this abnormal situation may lead to uncontrolled flow from the well leading to a blowout situation.

This study is focused on developing a CFD model of the influx situation in a wellbore which provides platform to Managed Pressure Drilling (MPD) techniques in early detection of kick situations. It is challenging to estimate the actual frictional losses in a drilling system. Generally, the frictional loss models such as Herschel-Bulkley model, Bingham plastic model or Power law model are used across the industry to estimate the frictional pressure drop. For simplicity, we have only considered a vertical two phase flow situation involving air and water. For theoretical calculations we considered the Begg's and Brill correlations[3]. According to Hamid (2003)[4], Begg's and Brill correlation has 8.42% of average error from the experimental data. Comparing the same correlation with a revised version of Begg's and Brill correlation developed in 1977[5], the absolute error with experimental values were quite higher than the initial version. So, in our study we only considered the initial correlations for comparison with CFD

results. This study is limited to a fixed water inlet velocity. In further studies, the transient behaviour of the influx situations will be presented.

THE KICK DETECTION AND CONTROL MODEL

The main goal of understanding the pressure response is to integrate the multiphase flow phenomena with the traditional pressure management equations available in the literature. A proper evaluation of the pressure can also help to estimate the influx quantity and take corrective actions to avoid accidents. Thus our kick prevention model is shown in Figure 1.

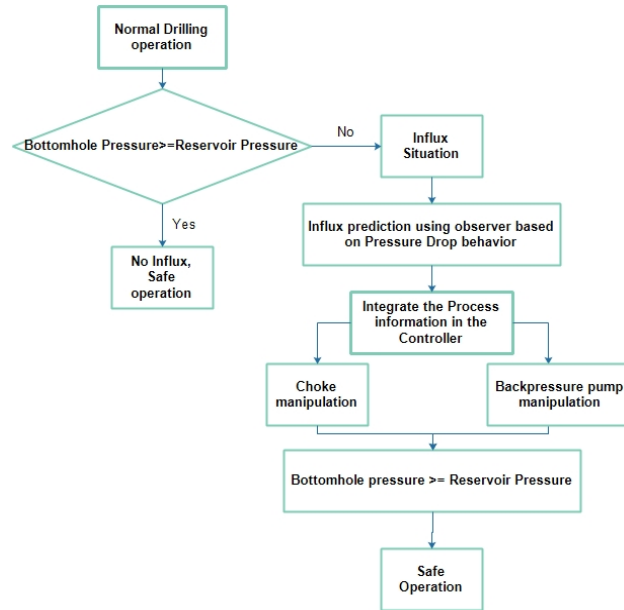


FIGURE 1. Influx Attenuation model in the perspective of Multiphase flow.

Several attempts were made previously to include the multiphase flow phenomena with the control algorithm. Even though, Managed Pressure Drilling system is being developed from last couple of decades, an exact multiphase flow model is not yet integrated with the controller system properly. Table 1 represents the different method's comparison in terms of error in estimating two phase pressure drop obtained from Hamid et al[6].

Table 1. Comparison of Measured and Predicted Pressure Losses for the Gas-Water Wells[6].

Method	Average Error %	Absolute Error %
Aziz, Govier and Fogarasi	136.49	143.11
Hagedorn and Brown	-28.53	28.94
Begg's and Brill	8.42	21.46
Begg's and Brill (revised)	0.59	30.38

NUMERICAL MODELS

For numerical study of the flow behavior commercial CFD package named Ansys Fluent was used. For multiphase flow analysis in the software the Volume of Fluid (VOF) model[7] was used along with the k-ε viscous model. This VOF model could analyze two or more non-miscible fluid by tracking the volume fraction of each of the fluids throughout the domain and solving one set of momentum equations. Therefore, VOF model in ANSYS Fluent has some limitation. It's a pressure base solver not density based solver. Moreover, all control volume should be filled with single phase or a combination of phases, it cannot calculate void region without any fluid. The continuity equation for volume fraction of one or more phases can track the interfaces between the phases. The nth phase has the following equation 1 [7].

$$\frac{1}{\rho_b} \left[\frac{\partial}{\partial t} (\alpha_b \rho_b) + \nabla \cdot (\alpha_b \rho_b \vec{v}_b) \right] = S_{\alpha_b} + \sum_{a=1}^n (m_{ab} - m_{ba}) \quad (1)$$

Here, mass transfer from phase b to phase a is m_{ba} and the mass transfer from phase a to phase b is m_{ab} . Moreover, the source term on the right-hand side of the above equation S_{α_b} is zero but a constant or user define mass source can be specified for individual phases.

For the preliminary phase volume fraction calculation the above volume fraction equation would not be used, instead the following equation 2 will be used.

$$\sum_{b=1}^n \alpha_b = 1 \quad (2)$$

The momentum equation is also solved throughout the model domain and the phases which share the resulting velocity. In case if there is a large velocity difference existing among the phases, the precision of the calculated velocity near the interface can be negatively affected. Therefore, the momentum equation is shown below.

$$\frac{\partial}{\partial t} (\rho \vec{v}) + \nabla \cdot (\rho \vec{v} \vec{v}) = -\nabla p + \nabla \cdot [\mu (\nabla \vec{v} + \nabla \vec{v}^T)] + \rho \vec{g} + \vec{F} \quad (3)$$

Here, equation 3 is dependent on the volume fraction of all phases through ρ and μ properties. The k- ϵ standard wall function model was used as viscous model. The principle assumption in this model is that, the flow is fully turbulent and the effect of molecular viscosity is negligible.

The volume of fluid model has been used to analyze this multiphase flow simulation. The convergence of the residual has been ensured when the summation of the absolute normalized residual of the transport equation reached below 10^{-4} . The inlet flow conditions for the simulation were similar to the experimental setup.

Geometry and Mesh Settings of the Model

For CFD simulation a 1 inch 2D vertical pipe geometry was considered with an overall depth of 4.8 meters. The diameter of the vertical pipe represents the hydraulic diameter of the annulus section. At a depth of 4.7 meters an air inlet is considered which is placed horizontally having an inner diameter of 0.5 inches. The overall domain was discretized using finer mesh maximum size 7×10^{-4} m. The maximum mesh size was 7×10^{-5} m.

CFD Settings in Fluent

As discussed before, in order to simulate the multiphase flow phenomena, Volume of Fluid (VOF) model was used in fluent setup. Two distinct phases i.e. air and water is used in the simulation. The reason for using water is because it is readily available in any drilling facility. For reducing the computational effort air was used as a reservoir gas. However, in future simulations different mud water properties and gas properties will be used. Velocity inlet boundary condition was used for water inlet and air inlet. Pressure outlet conditions were used in the outlet boundary condition. The water inlet velocity was kept constant at 2.9237 m/s and the air inlet velocity was varied from 10.52 m/s to 63.15 m/s.

THEORETICAL COMPARISON

For theoretical comparison, Begg's and Brill correlation[3] was used. Begg's and Brill correlation is one of the most popular multipurpose correlations which can handle all types of flow. This correlation is based on experimental data of horizontal, vertical and inclined pipe for air-water flow in 25.4 mm and 38.1 mm diameter pipe. While calculating the volume fraction the flow pattern needs to be determined either by flow pattern map or using condition and then the gas- liquid mixture density and velocity determined according to the appropriate flow regime. The transition for the correlation at no slip condition is defined as follows.

$$L_1^* = 316 \alpha_L^{0.302} \quad (4)$$

$$L_2^* = 0.0009252 \alpha_L^{i-2.4684} \quad (5)$$

$$L_3^* = 0.1 \alpha_L^{i-1.4516} \quad (6)$$

$$L_4^* = 0.5 \alpha_L^{i-6.738} \quad (7)$$

The Froude mixture number is the ratio of inertia force to stratified force. It can be represented by the following equation.

$$Fr_m = \frac{(V_m)^2}{gD} \quad (8)$$

After determining the in situ volume fraction in horizontal pipe Beggs and Brill [3] developed an equation to predict liquid volume fraction in two-phase flow in all condition. When the value of liquid volume fraction $\alpha_L(0)$ for horizontal flow and coefficient C are calculated, the liquid volume fraction at any angle can be determined. Therefore the liquid volume fraction at any angle can be calculated from the following equation.

$$\alpha_L(\theta) = \alpha_L(0) \left[1 + C \left\{ \sin(1.8\theta) - \frac{1}{3} \sin^3(1.8\theta) \right\} \right] \quad (9)$$

In the statistical analysis Beggs and Brill showed that from inclination angle of 0° to 90° for both uphill and downhill test the average error for is -0.28%. After obtaining the liquid holdup the mixture density can be calculated. Thus the hydrostatic pressure drop can be obtained from the following formula.

$$\Delta P_{HH} = \rho_m g L \sin \theta \quad (10)$$

The two phase friction factor can be obtained from the following equation.

$$f_{tp} = f_{NS} e^S \quad (11)$$

Here, f_{NS} is no slip friction factor and S is a constant calculated based on liquid holdup. Thus, if L is the length in meter, D is the diameter in meter, v_m is the mixture velocity and ρ_{NS} is no slip density, the frictional pressure drop equation takes the following form.

$$\Delta P_f = \frac{2f_{tp} v_m^2 \rho_{NS} L}{D} \quad (12)$$

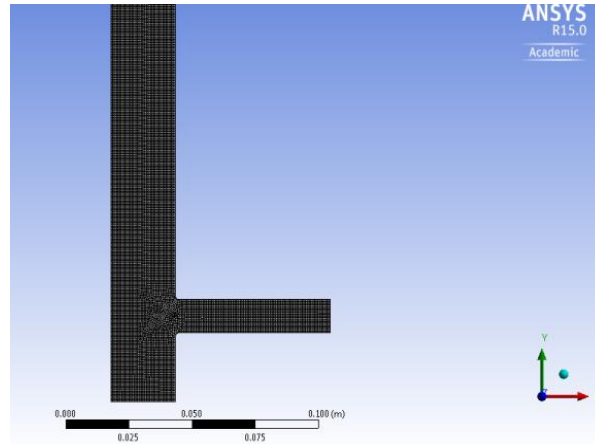


FIGURE 2. Mesh Settings for CFD simulation.

RESULTS

This study is mainly focused on the pressure loss analysis in a vertical pipe. The pressure profile of the CFD simulation at different water fraction is show in the Figure 3 below.

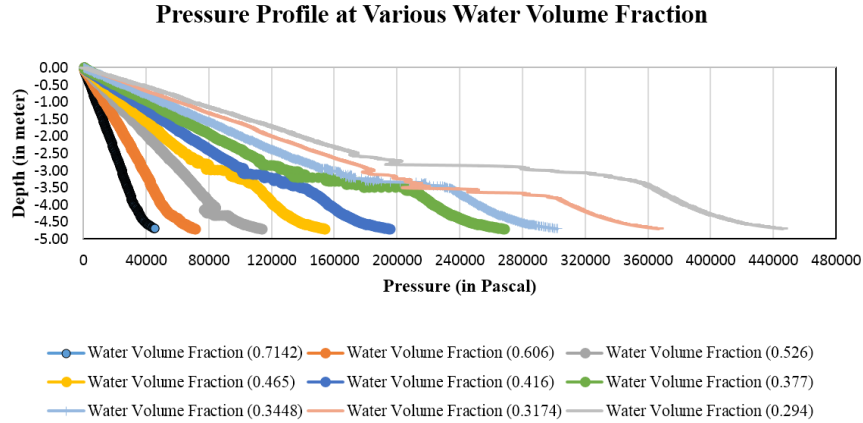


FIGURE 3. Pressure Drop at various water volume fraction.

It can be seen that at higher air volume fraction, the fluctuation in the pressure profile increase resulting in greater pressure drop. The pressure drop using CFD simulation was compared with the Begg’s and Brill correlation. The maximum deviation between two studies was found to be approximately 25%. Figure 4. represents a typical air volume fraction profile obtained in our CFD simulation. Besides this, the influx situation as significant role in changing the behavior of pressure drop at various water fractions. This situation might arise due to increase in turbulence when the reservoir fluid gets into the system at a depth of around 4.7 m.

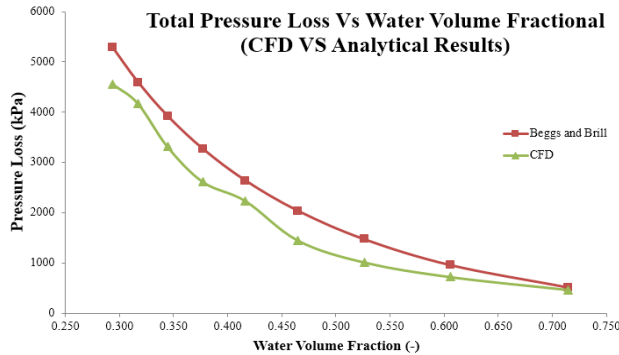


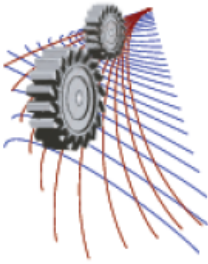
FIGURE 4. Comparison of CFD results with results from Begg’s and Brill Correlation.

CONCLUSION

From this study we observed that, CFD simulation can act as a vital tool for estimating the pressure drop in the annulus section of the wellbore. Even though, the Begg’s and Brill correlations were based on the 24.5 mm pipe diameter experimental results, the comparison of the results with the current study lacks the experimental validation. The study is still underway to obtain some experimental results which can be used to eliminate the errors obtained while comparing with the correlation.

REFERENCES

1. P. McDonald, "A probabilistic approach to risk assessment of managed pressure drilling in offshore applications," *Contract*, **106**, (2008).
2. M. Rohani, "Managed-Pressure Drilling; Techniques and Options for Improving Operational Safety and Efficiency," *Pet. Coal*, **54** (2012), pp. 24–33.
3. D. H. Beggs, J. P. Brill, and others, "A study of two-phase flow in inclined pipes," *J. Pet. Technol.*, **25** (1973), pp. 607–617.
4. L. W. Lake, "Petroleum Engineering Handbook," (Society of Petroleum Engineers, 2006).
5. K. E. Brown, "Technology of artificial lift methods, Volume 1, Inflow performance, multiphase flow in pipes, the flowing well," (PennWell Publishing Company, 1977).
6. K. Hamid and others, "Comparison of Correlations For Predicting Wellbore Pressure Losses in Gas-Condensate and Gas-Water Wells," in *Canadian International Petroleum Conference* (2003).
7. "ANSYS FLUENT 12.0 User's Guide." (Ansys Inc., 2009).



Experimental and Computational Analysis of Pressure Response in a Multiphase Flow Loop

Munzarin Morshed,^{1, a)} Al Amin,^{1, b)} Mohammad Azizur Rahman,² and Syed Imtiaz²

¹Graduate Student, Memorial University of Newfoundland, Canada

²Assistant Professor, Memorial University of Newfoundland, Canada

^{a)}Corresponding Author: mm3112@mun.ca

^{b)}al.amin@mun.ca

Abstract. The characteristics of multiphase fluid flow in pipes are useful to understand fluid mechanics encountered in the oil and gas industries. In the present day oil and gas exploration is successively inducing subsea operation in the deep sea and arctic condition. During the transport of petroleum products, understanding the fluid dynamics inside the pipe network is important for flow assurance. In this case the information regarding static and dynamic pressure response, pressure loss, optimum flow rate, pipe diameter etc. are the important parameter for flow assurance. The principal aim of this research is to represent computational analysis and experimental analysis of multi-phase (L/G) in a pipe network. This computational study considers a two-phase fluid flow through a horizontal flow loop with at different Reynolds number in order to determine the pressure distribution, frictional pressure loss profiles by volume of fluid (VOF) method. However, numerical simulations are validated with the experimental data. The experiment is conducted in 76.20 mm ID transparent circular pipe using water and air in the flow loop. Static pressure transducers are used to measure local pressure response in multiphase pipeline.

INTRODUCTION

Multiphase flow phenomenon is a common type of flow widely used in almost all chemical and petroleum industries. Different forms of flow pattern may be observed when two or more than two phases flow simultaneously. In the industries multiphase mixture subsists and it requires the prediction of phase distribution in the system for collecting, pumping, transporting and accumulating such mixture for certain operating condition. These flow patterns can be termed as Multiphase flow pattern. It is a very important phenomenon especially for the oil and gas industries where there is pipeline transportation of gas and oil mixtures, steam flow in water type boiler tubes, steam generators and in Boiling Water Reactors. The type of flow occurring from various combination of the flow parameters may be desirable or avoided based on the requirement of the users. There are several parameters on which the multiphase flow depends on such as mass exchange rate, energy, momentum, interfacial area per unit volume, momentum difference between vapor and liquid. A proper estimation of the flow regime corresponding to its flow parameter would help the industries to operate based on its desired operational limits.

The initial research on multiphase flow started back in 1949 by Lockhart- Martinelli [1]. The method provided good result for two phase flow in a horizontal pipe. Later in 1954, Baker [2] performed some experiments which brought some distinctive change in the Lockhart- Martinelli [1] equations which could flow patterns in horizontal pipelines. Baker [2], suggested different correlations for each flow regimes for two phase flow. However, Dukler et al. (1964) [4] performed experiment with Lockhart-Martinelli [1] pressure drop correlations with large number of

data points and concluded that Lockhart-Martinelli [1] correlation provides better approximation of flow regimes except in wavy flow. Till now there is very little research work which addressed the pressure drop characteristics which is associated with flow pattern. A better understanding of multiphase flow regime development will help save huge amount of money in the industrial sector.

LITERATURE REVIEW

A multiphase flow can be defined as the fusion of two or more distinct phases (such as solid, water, and gas) flowing through a pipeline. The activities of multiphase flow are much more diverse compared to that of single phase flow. The differentiating aspect of multiphase flow is the variance in the physical distribution of the phases in the pipe flow, an attribute known as flow pattern or flow regime. The flow regime depends on the relative magnitudes of the forces acting on the fluids. These forces such as buoyancy, turbulence, inertia and surface-tension forces, which vary significantly with flow rates, pipe diameter, pipe inclination and fluid properties.

Liquid Gas Flow Regime

The basic theory of two-phase and its flow regime concepts are explained in this part. Usually, two phase flow implies gas and liquid flow through a pipeline system, simultaneously. Moreover the gas and liquid interface is deformable, so it's hard to predict the region occupied by gas or liquid phase. When two phases flows through a pipeline different type of interfacial distribution can form. Some of the common distribution are: bubbly flow, where there are dispersion of small sized bubbles with liquid; Slug flow in which each gas bubbles form a large slug shape that is often a bullet shape; Stratified flow, where the liquid and gas phase are separated and the gas flows on the top as its lighter than liquid; and Annular flow where liquid flow as a film on the wall of the pipe. The multiphase flow rate often described in terms of liquid superficial velocity and gas superficial flow velocity. The superficial velocity mainly used in the flow regime maps and also an important term in gas-liquid multiphase flow. The superficial velocity is such that the fluid is flowing without the presence of other fluid and no slip between the two phases is considered. In other words from Crowe [5] superficial velocity (V_{sg} , V_{sl}) is the total amount of fluid (Q_{gas} , Q_{liquid}) throughout divided by the cross section area (A) of the pipe ($V_{sg} = Q_{gas}/A$, $V_{sl} = Q_{liquid}/A$).

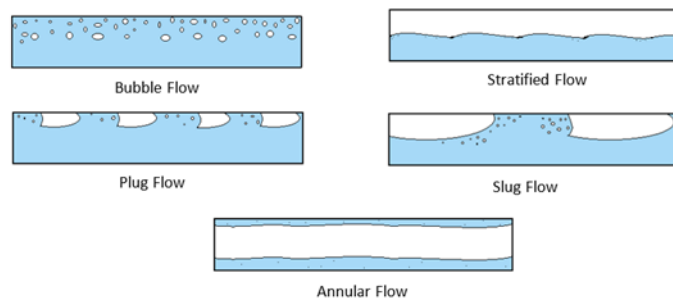


FIGURE 1. Liquid-gas flow regimes in horizontal pipelines.

The volume fraction, which is the ratio of the liquid or gas flowrate and the total fluid flowrate. The input volume fraction of each phase may vary from in-situ volume fraction. The gravity and buoyancy force also has major impact on the flow regime, pressure drop, volume fraction or heat transfer in the pipeline system [6]. The flow regimes for horizontal pipe are Disperse bubbly flow, Plug flow, Stratified flow, Stratified wave flow, Slug flow and Annular dispersed flow.

Numerical Analysis

Volume of fluid (VOF) model has been used for the numerical analysis. This VOF model could analyze two or more non-miscible fluid by tracking the volume fraction of each of the fluids throughout the domain and solving one set of momentum equations. Therefore, VOF model in ANSYS Fluent has some limitation like it's a pressure base

solver not density based solver. Moreover, all control volume should be filled with single phase or a combination of phases, it cannot calculate void region without any fluid.

The continuity equation for volume fraction of one or more phases can track the interfaces between the phases. The n^{th} phase has the following equation.

$$\frac{1}{\rho_b} \left[\frac{\partial}{\partial t} (\alpha_b \rho_b) + \nabla \cdot (\alpha_b \rho_b \vec{v}_b) \right] = S_{\alpha_b} + \sum_{a=1}^n (m'_{ab} - m'_{ba}) \quad (1)$$

Here mass transfer from phase b to phase a is m'_{ba} and the mass transfer from phase a to phase b is m'_{ab} . Moreover, the source term on the right-hand side of the above equation S_{α_b} is zero but a constant or user define mass source can be specified for individual phases. For the preliminary phase volume fraction calculation the above volume fraction equation would not be used, instead the following equation will be used,

$$\sum_{b=1}^n \alpha_b = 1 \quad (2)$$

The momentum equation is also solved throughout the model domain and the phases share the resulting velocity. In case where there is large velocity difference exist among the phases, the precision of the calculated velocity near the interface can be negatively affected. Therefore, the momentum equation is,

$$\frac{\partial}{\partial t} (\rho \vec{v}) + \nabla \cdot (\rho \vec{v} \vec{v}) = -\nabla p + \nabla \cdot [\mu (\nabla \vec{v} + \nabla \vec{v}^T)] + \rho \vec{g} + \vec{F} \quad (3)$$

Here, this equation is dependent on the volume fraction of all phases through ρ and μ properties.

Numerical setup

The simulation was performed to compliment and validate the experimental investigation. It duplicates the experimental geometry and condition in the pipeline. The pipeline geometry was simulated from the long test section. Furthermore, the test section is also reduced few feet to reduce the simulation run time. The pipeline geometry was simulated first only for the horizontal test section then to the whole loop starting from the horizontal section to vertical and inclined test section. Two dimensional geometry of the experimental setup has been used in the simulation. To reduce the time and size of the simulation the horizontal section is kept 4 meter, vertical section is kept 1.2 meter and the inclined section is kept 1 meter, which the size of the test section of the setup and the air inlet has been considered 1 inch and the water inlet was considered 2.9 inch inner diameter. Moreover, the geometry was drawn in SolidWorks 2014 and then imported in ANSYS Fluent 15 solver to compute the numerical simulation. The mesh in the simulation has a fine mesh with minimum size of 3×10^{-4} , max face size of 3×10^{-3} and 1.2 growth rates. Therefore the mesh has 129849 nodes and 124814 elements. The inlet flow conditions for the simulation were similar to the experimental setup.

EXPERIMENTAL SETUP

The experiments were performed in a flow loop system shown in the Figure 2 schematic. The experimental setup has horizontal, vertical and inclined section. However, in this paper we are only considering the horizontal section as 4 meter test section. The experimental setup is 60 meter long closed cycle system for water and open cycle system for air. The liquid is pumped by 5HP pump that creates the required large volume water flow through DN 80 or 2.9 i.d. PVC clear pipes. The airline of the flow loop had DN 15 and DN 25 mild steel pipe which supply air form lab air supply at 670 kPa (100 psi) shut in pressure. It also include a DN 25 ball check valve just prior to the air and the liquid mixing zone to prevent any liquid from entering the air pipeline. There are two Omega PX603-100G5V pressure transducer with a range of 0 to 100 psi in 2 meter distance horizontal test section. There are some specific experimental conditions used for this setup. The air flow range is about 85 L/min to 3300 L/min (Approx.), the water flow range is almost 250 L/min to 850 L/min. At this range the experimental setup mostly give slug flow for two phase flow, it also give bubble flow and wavy flow at some range.

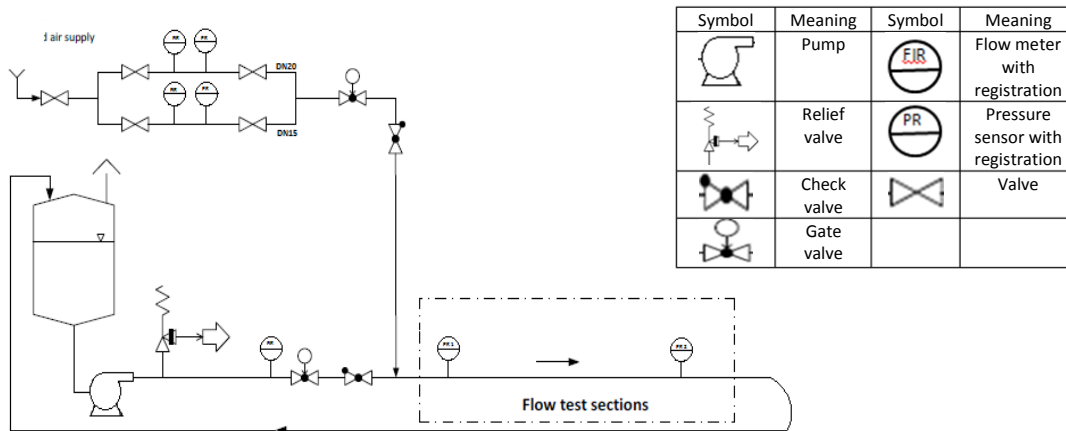


FIGURE 2. Schematic of Experimental Setup (Horizontal Test Section).

DISCUSSION AND RESULTS

Flow Regime in the horizontal section

The experimental values have been used to make a flow regime for the horizontal pipe. This flow regime map has been compared with Taitel and Duckler [7] and Mandhane [8] where water and air superficial velocity has been used. In the Taitel and Duckler Flow map for horizontal pipe in the Figure 3 almost all the experimental data points fall in the respected flow regime area. However in the Mandhane [8] flow map in Figure 4 the data for the slug and dispersed bubble flow data fitted in the graph accordingly. Therefore, Taitel and Duckler [9] map predicted most of the point in the respected flow regime. Moreover the experimental setup can mostly predict the slug and bubble flow regime. Due to certain water flow rate range this setup can't give proper stratified, wavy or annular flow regime.

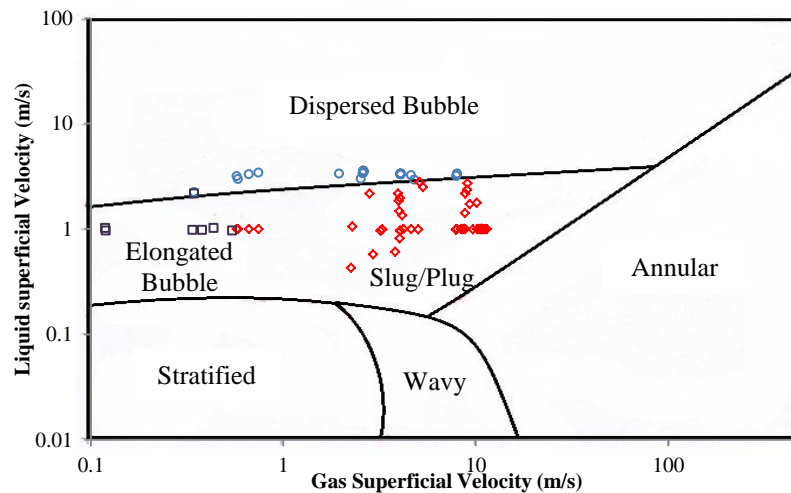


FIGURE 3. Comparison of the Taitel and Duckler [9] (adapted) flow map with experimental data in horizontal pipe.

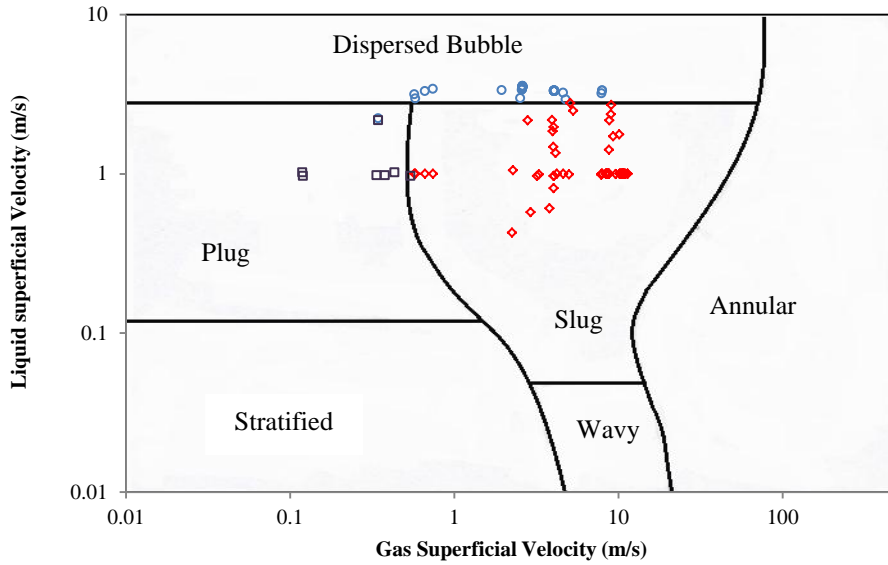


FIGURE 4. Comparison of the Mandhane [8] (adapted) flow regime map with experimental data obtained in horizontal pipe.

The experimental values and CFD values are compared with the two common gas-liquid pressure drop correlation, i.e. Lockhart and Martinelli correlation and Darcy-Weisbach correlation. In 2-phase flow the major pressure loss occur due to liquid flow than gas flow. The Figure 5 shows that when the gas to liquid ratio (GLR) increases until the value is 3.5 and start decreasing after that, because the water flowrate start decreasing and frictional loss is also decreasing.

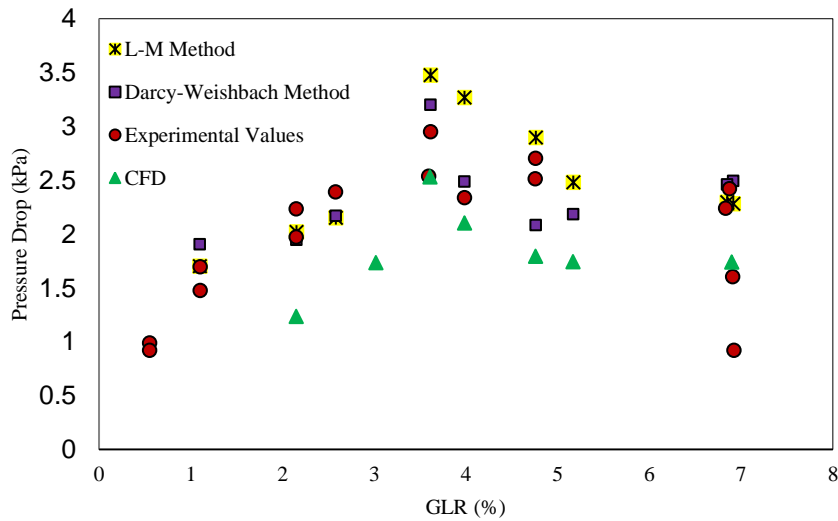


FIGURE 5. Comparison of the theoretical and experimental and computational pressure drop profile with the change of gas to liquid ratio.

CONCLUSIONS

Finally, after performing experiments and computational simulations with various combinations of air flow and water flow rate, the flow regime maps, pressure drop relations were verified with the available theoretical

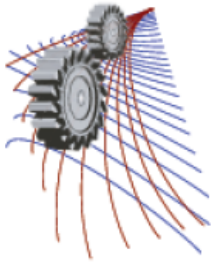
correlations. In the future work, utilizing this experimental setup we have plan to analyze pressure response, volume fraction and other flow characteristics for 3-phase flow and Non-Newtonian two and three phase flow. Moreover, doing the computational analysis for the whole loop horizontal, vertical and inclined section.

ACKNOWLEDGEMENTS

Authors acknowledge the financial support from RDC and NSERC. Moreover we also acknowledge the lab support and technical support from Matt Curtis.

REFERENCES

1. R. W. Lockhart and R. C. Martinelli, *Chem. Eng. Prog* **45**, 39–48 (1949).
2. O. Baker, *Oil gas J.*, **53**, 185–190 (1954).
3. A. E. Dukler, M. Wicks, and R. G. Cleveland, *AIChE J.*, **10**, 38–43 (1964).
4. C. T. Crowe, *Multiphase flow handbook* (CRC press, 2005).
5. R. Balasubramaniam, E. Rame, J. Kizito, and M. Kassemi, “*Two phase flow modeling: Summary of flow regimes and pressure drop correlations in reduced and partial gravity*,” National Aeronautics and Space Administration, Glenn Research Center (2006).
6. N. I. Heywood and M. E. Charles, *Int. J. Multiph. Flow*, **5**, 341–352 (1979).
7. J. M. Mandhane, G. A. Gregory, and K. Aziz, *Int. J. Multiph. Flow*, **1**, 537–553 (1974).
8. L. E. Gomez, O. Shoham, and Y. Taitel, *Int. J. Multiph. Flow*, **26**, 517–521 (2000).
9. S. K. Chandrakar, M. N. Biswas, and A. K. Mitra, “Two-phase gas non-Newtonian liquid flow in vertical pipe with improved gas dispersion,” in *Second International Conference on Multiphase Flow* (London, 1985), pp. 197–213.



Study of NACA 0010 Symmetric Airfoil with Leading Edge Rotating Cylinder in a Subsonic Wind Tunnel

Md. Nurul Huda^{1, a)}, Tabassum Ahmed^{1, b)}, SM Shakil Ahmed^{1, c)}, Md. Abdus Salam^{1, d)}, Md. Rayhan Afsar^{1, e)}, Kh. Md. Faisal^{1, f)} and M. A. Taher Ali^{1, g)}

¹Department of Aeronautical Engineering, Military Institute of Science and Technology, Mirpur Cantonment, Dhaka-1216, Bangladesh

^{a)}Corresponding author: toyon153@gmail.com

^{b)}tabyae4@gmail.com

^{c)}smsshakilahmed1@gmail.com

^{d)}head@ae.mist.ac.bd

^{e)}rayhan@ae.mist.ac.bd

^{f)}faisal@ae.mist.ac.bd

^{g)}matali@ae.mist.ac.bd

Abstract. In the ever growing aviation industry, the need of high-performance aircraft is increasing day by day. Moreover, high performance aircraft demands improved aerodynamic characteristics such as high lift to drag ratio (L/D). Ever since the concept of boundary layer introduced by Prandtl, scientists all over the world are trying to solve the problem of boundary layer flow separation, thus try to increase the aerodynamic characteristics (L/D) and reduce aerodynamic drag (D). In this research paper, it is attempted to reduce the effect of flow separation over an airfoil using a rotating cylinder in front of a modified NACA 0010 symmetrical airfoil. This airfoil was modified with a leading edge rotating cylinder. The experiment was conducted in a subsonic wind tunnel. First the aerodynamic parameters of the setup were taken at different angles of attack while the rotation of the cylinder was kept zero. After that the aerodynamic parameters of the setup were measured at different angles of attack while changing the rpm of the cylinder. Then coefficient of lift (C_L) and coefficient of drag (C_D) were plotted with respect to angle of attack and results were compared with and without the rotation of the leading edge cylinder. Although it is believed that NACA 0010, a symmetrical airfoil, does not provide any lift at zero angle of attack but at zero angle of attack with a rotating cylinder in the leading edge of the same airfoil produces sufficient amount of lift. Moreover, at different angles of attack a rotating cylinder improves the flow separation at the trailing edge, thus improves the lift to drag ratio (L/D) and decreases the induced drag.

NOMENCLATURE

C_L – Coefficient of lift

C_D – Coefficient of drag

L - Lift

D - Drag

- U_c – Tangential velocity of the rotating cylinder
- U - Velocity of the wind tunnel flow
- F_m - The Magnus force vector
- w - Angular velocity vector of the object
- v - Velocity of the fluid (or velocity of object, depends on perspective)
- S - Air resistance coefficient across the surface of the object

INTRODUCTION

The experiment has been conducted with the intent to apply “MAGNUS EFFECT” on aircraft wing to increase the lift by limiting the flow separation on the upper and lower surface of the wing. The Magnus effect uses principle of Bernoulli's equation. Bernoulli's equation states that if the velocity of a moving fluid increased, the pressure must decrease. In case of this study the rotating cylinder increases the velocity in the upper surface thus decreases the pressure, therefore the pressure difference causes lift. The force of the Magnus effect can be calculated with the following equation:

$$F_m = S(w * v) \text{----- (1)}$$

According to Newton’s third law of motion, the equal and opposite reaction of the Magnus force vector (F_m) is lift (L) in this study

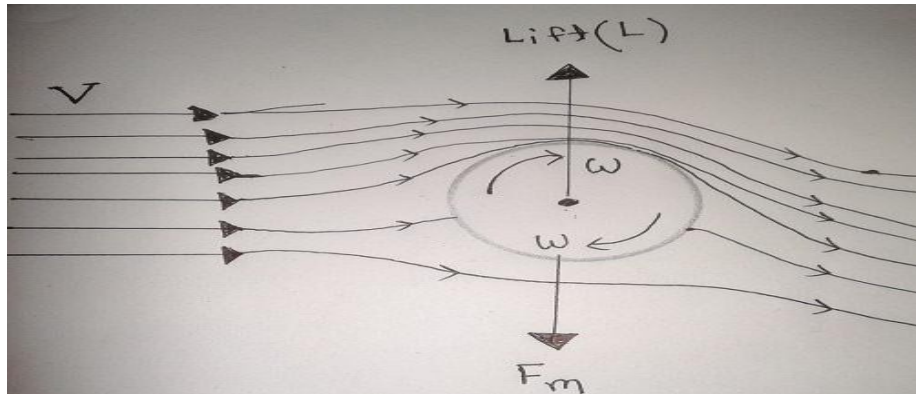


FIGURE 1.Magnus Effect in a rotating cylinder

The main purpose of this experiment is to delay the flow separation of the boundary layer in the wall of the wing by limiting the relative velocity between the surface and the free stream. This separation delay, interferes with the production of the wake. Additional circulation provides the differential velocity which injects momentum into the boundary layer in the upper surface with respect to the lower surface. Another major factor that considerably contributes to the generation of high lift is vorticity.

EXPERIMENTAL SETUP

The experiment was conducted in AF100 (subsonic wind tunnel). AF-100 subsonic wind tunnel is an open circuit suction type wind tunnel and offers variety of experiments.



FIGURE 2.AF-100 subsonic wind tunnel

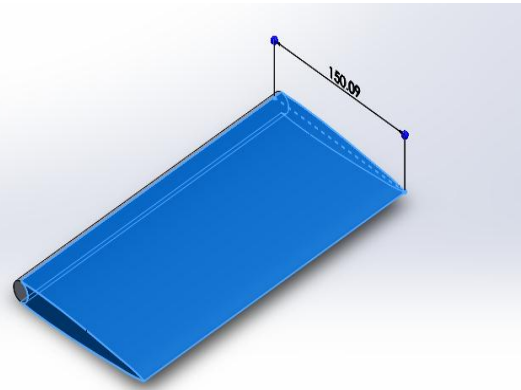


FIGURE 3.Chord of modified airfoil with cylinder

The tested specimen is the combination of a rotating cylinder and a modified NACA 0010 zero camber airfoil. The original airfoil coordinate is modified to accommodate the rotating cylinder properly in the leading edge of the wing. The final dimensions used for the experiment are tabulated below.

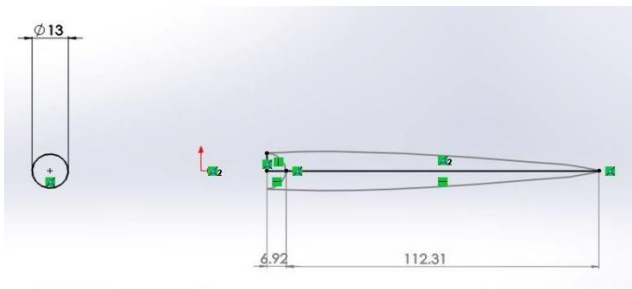


FIGURE 4.Dimension of modified airfoil with cylinder

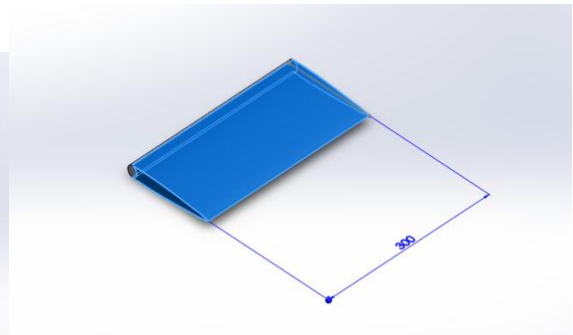


FIGURE 5.Span of modified airfoil with cylinder

TABLE 1. Airfoil and cylinder data

Specimens	Dimension (mm)
Chord of modified NACA 0010 airfoil	150
Diameter of rotating cylinder	13
Span of the wing	300
Distance between cylinder and airfoil	1.5
Maximum thickness	14 (at 25% chord)

A holder (included with the AF100 wind tunnel) supports the model in the tunnel. The model has the characteristics of a three dimensional airfoil. The results from the full-width airfoil (the modified NACA 0010 airfoil with rotating cylinder) with the tapped (NACA 0010 airfoil) airfoil model can be compared.



FIGURE 6.Modified NACA 0010 airfoil with cylinder



FIGURE 7.Model with setup to rotate cylinder

To control the rotating cylinder an "Arduino" was used to run a DC geared motor. The shaft of DC geared motor was inserted into one end of the cylinder. A potentiometer was used to control the motor rpm which goes as 30, 60, 90,120 rpm corresponding the wind tunnel velocity.

RESULTS

According to the formula stated earlier it is clear that, to increase the Magnus force vector (F_m), the angular velocity vector of the object (w) must be increased.

$F_m \propto w$ [As velocity of the fluid (v), air resistance coefficient across the surface of the object (S) is kept constant]

The rotation of the cylinder (i.e. w) was increased to see the resulting lift increment. The experiment results were compared with the available NACA 0010 airfoil to justify its effect on wing performance. Coefficient of lift (C_L) and coefficient of drag (C_D) NACA 0010 at different angle of attack was plotted in a graph keeping the wind tunnel air flow velocity 30 ms^{-1} .

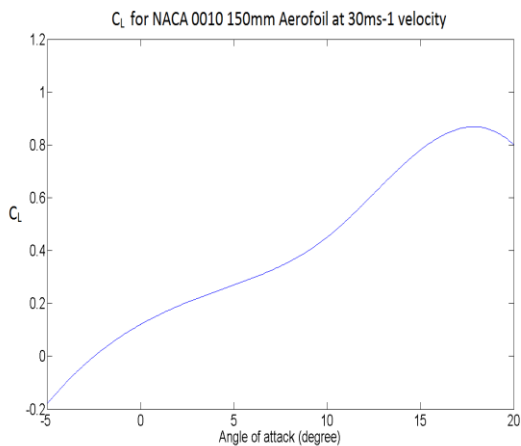


FIGURE 8. C_L for NACA 0010 150mm airfoil at 30 ms^{-1}

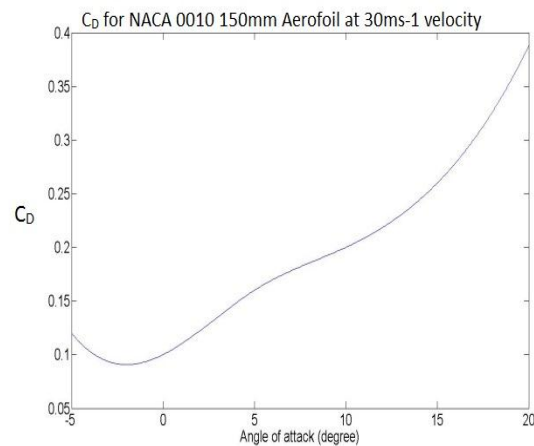


FIGURE 9. C_D for NACA 0010 150mm airfoil at 30 ms^{-1}

To calculate the coefficient of lift and coefficient of drag variation, modified NACA 0010 airfoil was first inserted in the wind tunnel with keeping the rotation of the cylinder zero ($U_c/U=0$) and then rotating the cylinder twice the velocity of wind tunnel air flow ($U_c/U=2$).

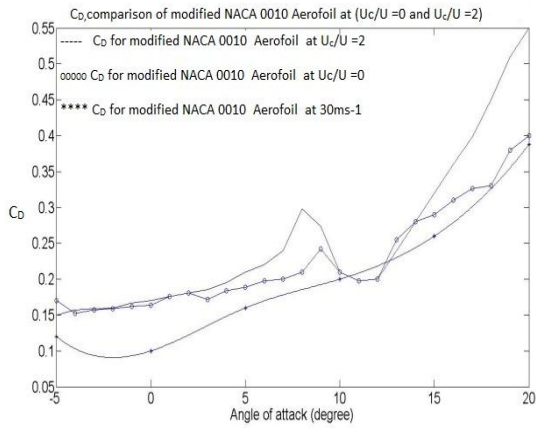


FIGURE 10. Comparison of C_D at 30 ms⁻¹

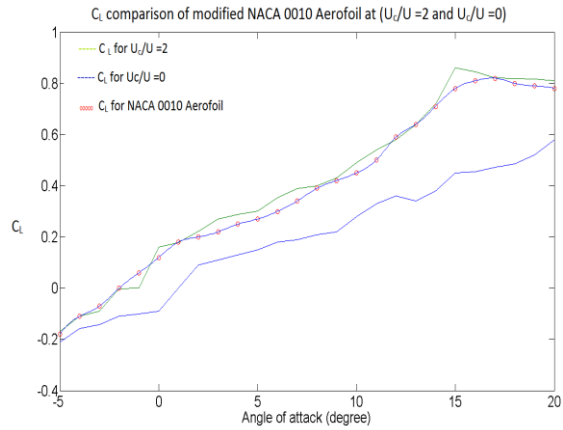


FIGURE 11. Comparison of C_L at 30 ms⁻¹

To compare the C_L , C_D for $U_c/U=0$ and $U_c/U=2$, data obtained in the experiment were plotted in the graphs.

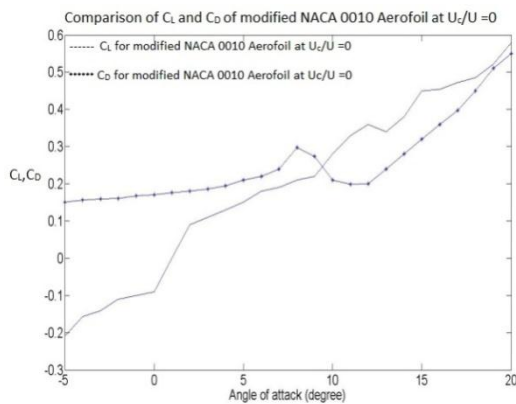


FIGURE 12. Comparison of C_L, C_D (when $U_c/U=0$) at 30 ms⁻¹

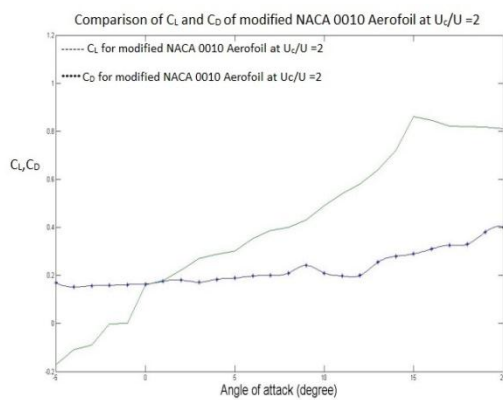


FIGURE 13. Comparison of C_L, C_D (when $U_c/U=2$) at 30 ms⁻¹

DISCUSSION

Study of NACA 0010 Symmetric Airfoil with Leading Edge Rotating Cylinder in a Subsonic Wind Tunnel highlights the following findings.

When the leading edge rotating cylinder was kept at zero RPM ($U_c/U=0$)

The coefficient of lift (C_L) decreased (around 60% of NACA 0010 airfoil) substantially because of vorticity created by the gap between the cylinder and airfoil. The coefficient of drag (C_D) increased (around 135% of NACA 0010

airfoil) substantially because of the motor mount and the supporting stick. The surface roughness of the model certainly contributed to the generation of drag. There was no such significant improvement of C_L/C_D for $U_c/U=0$ because of the high coefficient of drag (C_D) and low coefficient of lift (C_L). There was a sharp downfall of drag due to minimum flow separation at the upper and lower surface.

When the leading edge rotating cylinder was kept at twice tangential velocity that of airflow velocity ($U_c/U=2$)

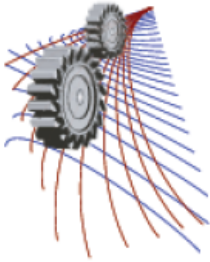
Rotating cylinder at the leading edge evidently improved suction over the nose. The efficiency mainly depends on the surface smoothness, as the tested specimen had surface roughness it affected the experimental result. Increased rotation of leading edge cylinder delayed the flow separation from the upper surface. This resulted in a higher C_{Lmax} (145% at 16 degree angle of attack) compared to theoretical delay in flow separation. It occurred practically in a slower way, because the motor mounted to rotate the cylinder in the model created much disturbance in the upstream flow. The onset flow separation was delayed up to higher angle of attack (10-20 degree) resulting in a flatter stall peak.

CONCLUSION

Limitations of tested model include the motor mount to rotate the cylinder which creates a substantial amount of drag, unavailability of any other effective mechanism. Another limitation was the limited size of the model. As wind tunnel can accommodate a (300*300mm) model, but the model size was reduced (300*150mm) to accommodate the motor. This affected the co-efficient of lift (C_L) tremendously. NACA 0010 model that came with the wind tunnel had a nice coating which made the surface smooth but the tested model had surface roughness which contributed to the generation of drag. To get better result from this experiment, a better model with smooth surface coating and minimum gap between the rotating cylinder and modified NACA 0010 150 mm airfoil is required. Further research can be done obtaining data at $U_c/U=3$, $U_c/U=4$ and making comparison for drawing logical conclusions.

REFERENCES

1. F. Mokhtarian and V. J. Modi "Fluid Dynamics of Airfoils with Moving Surface Boundary-Layer Control", University of British Columbia, Vancouver, Canada, (February 1988) VOL. 25, NO. 2.
2. V. J. Modi and F. Mokhtarian "Effect of Moving Surfaces on the Airfoil Boundary-Layer Control", University of British Columbia, Vancouver, B.C., Canada and T. Yokomizo Kanto Gakuin University, Yokohama, Japan (Aug. 15-17, 1988) VOL. 27, NO. 1.
3. Roskam, J. "Methods of estimating drag polars of subsonic airplanes", published by author, 1971.
4. Torenbeek, EG "Synthesis of subsonic airplane design", Klumer academic publishers, 1982.
5. T.H.G. Megson, "Aircraft structures for engineering students (4th edition)".
6. UIUC airfoil co-ordinate database.
7. Aerofoil investigate database.
8. Hoerner, S. "Fluid dynamic drag", published by author, 1958.



Prediction of Ship Resistance in Head Waves Using RANS Based Solver

Hafizul Islam^{1, a)} and Hiromichi Akimoto^{1, b)}

¹*Division of Ocean Systems Engineering, Korea Advanced Institute of Science and Technology (KAIST), Daejeon, South Korea.*

^{a)}Corresponding author: hafiz26@kaist.ac.kr

^{b)}akimoto@kaist.ac.kr

Abstract. Maneuverability prediction of ships using CFD has gained high popularity over the years because of its improving accuracy and economics. This paper discusses the estimation of calm water and added resistance properties of a KVLCC2 model using a light and economical RaNS based solver, called SHIP_Motion. The solver solves overset structured mesh using finite volume method. In the calm water test, total drag coefficient, sinkage and trim values were predicted together with mesh dependency analysis and compared with experimental data. For added resistance in head sea, short wave cases were simulated and compared with experimental and other simulation data. Overall the results were well predicted and showed good agreement with comparative data. The paper concludes that it is well possible to predict ship maneuverability characteristics using the present solver, with reasonable accuracy utilizing minimum computational resources and within acceptable time.

INTRODUCTION

Computational fluid dynamics or CFD has been a revolution in the world of engineering. Starting from the motion of ships and jet planes to the dynamics of a tennis ball, it can solve any problem, as long as the right set of equations is applied. CFD is very efficient because it allows exploration of new engineering frontiers in the most economical way. As a result, CFD analysis has become crucial in the design phase of big structures, like ships. Due to their enormous size and expense, it is very difficult to revise the design of a ship after it is built. Thus, more and more research is being done on how to predict the stability and maneuvering capabilities of a ship in the design phase using CFD.

Maneuverability prediction in the design phase is nothing new for the shipping industries. According to reports of 20th– 24th IITC, the first symposium on Naval Maneuverability was held in Washington DC in 1960. However, back then work was mostly experiment based. Numerical prediction for maneuverability using the boundary layer method was first introduced in 1980. However, it failed to predict pressure in the stern part properly. This had led to the development of various RaNS models throughout the 1980s. In 1990, it was found that RaNS models showed high promise but failed to predict detail shape of velocity contours in central parts of wake. Later in 1993, Deng et al. revealed that the problem was in inadequate turbulence modeling. The 1994 Tokyo workshop brought a breakthrough in free surface calculation using RaNS. For The Gothenburg 2000 workshop [1], three new ship models- KCS, KVLCC and DTMB 5415 were introduced with experimental results for validation. The self-propulsion system included CFD models were also introduced in this workshop. In The SIMMAN 2008 workshop [2], benchmarking was conducted for both EFD based and CFD based methods. The Gothenburg 2010 workshop [3] discussed global and local flow variables, grid dependency, and turbulence modeling.

Over the years, CFD in maneuverability prediction has gone through and is still going through continuous improvement. However, with increase in prediction accuracy, computational time has increased as well, despite the fact that, computing capacity has increased significantly over the years. The requirement of high computational

resources has driven us to high performance computers and reduced the economy of CFD. The target of this research is to establish a solver named 'SHIP Motion' that can solve ship maneuverability problems using minimum computational resources and produce reasonably accurate results. This paper contains validation data for calm water test and added resistance prediction in head waves for a KVLCC2 to demonstrate the solver's capability in predicting such cases.

SOLUTION PROCESS

Mathematical Model and Computational Mesh

The mathematical model of the solver has been elaborately discussed by Islam [4], Kim [5] and Orihara [6] in their theses respectively. Thus, only a brief overview of the solver has been included in this paper.

The governing equation for the mathematical model is the Reynolds averaged Navier-Stokes (RaNS) equation and continuity equation. Two sets of coordinate system, body fixed and earth fixed, have been used. The spatial discretization is by Finite Volume Method (FVM). 3rd order upwind differencing has been used for advection, whereas, discretization in space is by 2nd order central difference scheme. Definition of physical values are in staggered manner. Free surface capturing is by Marker density method, where, 3rd order upwind scheme performs space differencing and 2nd order Adams-Bashforth solves time differencing. Two type of turbulence models have been incorporated, Baldwin-Lomax and Dynamic sub-grid scale model. Wall function has been used to reduce dependency on mesh for capturing boundary layer properties. Parallel processing is by the shared memory model of OpenMP.

A Marker and Cell (MAC) type pressure solution algorithm has been employed. The pressure is obtained by solving the Poisson equations using the SOR method and velocity components are gained by correcting the velocity predictor with the implicitly evaluated pressure. In the overlapping grid system, inner domain moves according to floating body's equation of motion and outer domain represents free surface. Grid points located at the overlapping region exchange information through interpolation to update both the domains at every time step.

In this research, an overset structured single block mesh system has been used. The coarse rectangular outer mesh with high resolution around the free surface has been used to capture the free surface deformation. The fine O-H type inner mesh around the hull surface has been used for capturing the flow properties around the hull surface. For both the domains, the orientation of x-axis is from bow to stern ward direction, y-axis is positive towards starboard and z-axis is upward positive. Figure 1 shows the fine inner mesh (a), coarse outer mesh (b) and their combined arrangement (c) respectively.

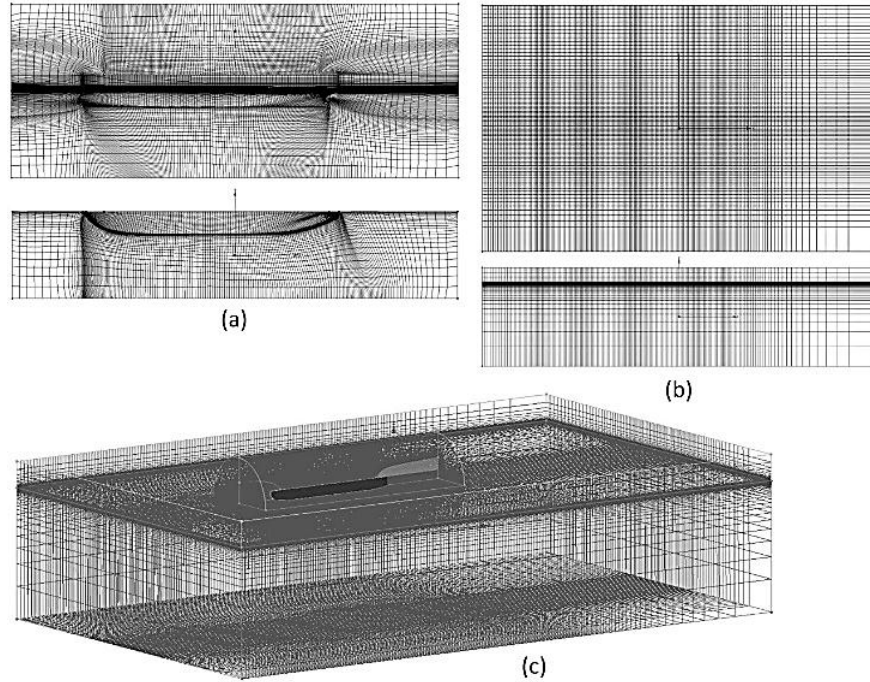


FIGURE 1. Mesh arrangement used for simulation, (a) inner mesh domain (front and bottom view), (b) outer mesh domain (top and front view) and (c) combined mesh domains (isometric view).

Ship Model

The model ship used in this research for validation and simulation of new cases, is the KRISO Very Large Crude Carrier 2 (KVLCC2). Table 1 provides the specifications of the KVLCC2 model and Fig. 2 shows its side view and body planes. All the simulations have been performed in non-dimensional scale.

TABLE 1. Specifications of the oil tanker ship model KVLCC2

Specification	Unit	KVLCC2 ship (full scale)
Length between perpendicular	L_{pp} (m)	320.0
Breadth	B (m)	58.0
Depth	D (m)	30.0
Draft	T (m)	20.8
Wetted surface area	S (m ²)	27194.0
Displacement volume	V (m ³)	312622
LCB from mid-ship	LCB (m)	11.136
K_{yy}	K_{yy} (m)	0.25 L_{pp}

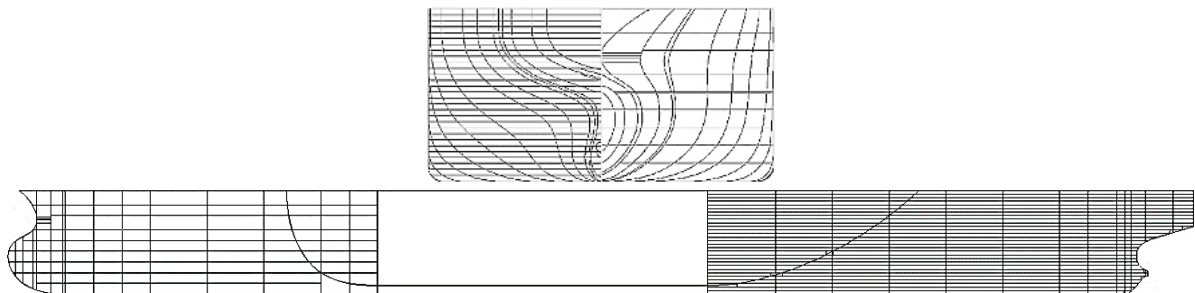


FIGURE 2. Body planes and side view of the KVLCC2 ship model

Computational Resource

The OpenMP memory sharing model used in the solver limits its use to multi cores of only one node, not cluster of nodes. Each simulations in this paper was performed in a single node of Intel(R) Xeon(R) CPU with 8 cores, clock speed 2.27 GHz and 8 GB of physical memory. The standard non-dimensional time step used was 1.5×10^{-4} and for simulating each non-dimensional time for added resistance, the required physical time was about 75 minutes per case. All the simulations were run up to 8 non-dimensional times for attaining stable results.

RESULTS

The development of the present solver, SHIP_Motion comes with a long history and several researchers have verified and validated the code for different type of ship models at different stages of development. This paper mainly presents validation study of the solver for tanker ship model, KVLCC2, for calm water and added resistance prediction in short waves.

Calm Water Resistance

Calm water resistance prediction is the estimation of drag force for a ship while moving forward in calm water. Ship's drag resistance is summation of frictional resistance and pressure resistance. Frictional resistance arises from the hull surface friction and pressure resistance is mainly the wave making resistance encountered by ship during its forward motion.

For grid dependency analysis in resistance prediction, three different mesh resolutions for inner mesh were tested. Dependency on the outer resolution was not tested for present case. The mesh resolutions applied are shown in Table 2 and results for calm water simulation for KVLCC2 model has been shown in Figs. 3, 4 and 5. For comparison, experimental data has been taken from Chalmers University, presented in Gothenburg 2010 workshop [7].

TABLE 2. Mesh configuration used in calm water simulation

	Dimension of inner domain			Dimension of outer domain			Total mesh
	I	J	K	I	J	K	
Mesh 1	167	25	88	147	32	42	565,000
Mesh 2	130	20	74	147	32	42	390,000
Mesh 3	107	18	52	147	32	42	298,000

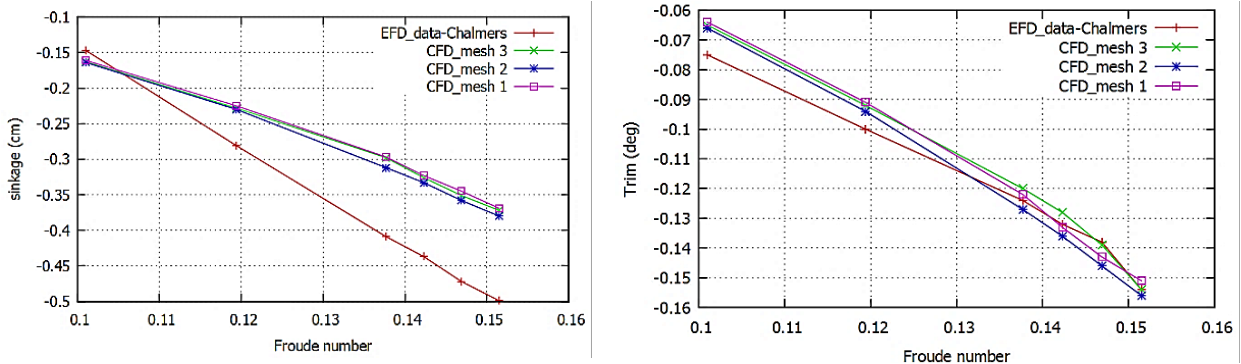


FIGURE 3. Sinkage (left) and trim (right) prediction for KVLCC2 by three different meshes

The simulation results shown by Figs. 3 and 4. Figure 3 show the sinkage and trim prediction at different Froude and Reynolds number. Sinkage is slightly miss predicted at higher R_n numbers. However, the difference in full scale is around 1.5 mm. Thus, the results is considered to be in acceptable level. Figure 3 also shows trim prediction. Trim results are well predicted by the solver. Figure 4 shows the calm water resistance prediction. It shows that, application of higher resolution and better mesh distribution improves the prediction by the RaNS solver. However,

the difference in resistance prediction slightly increases in higher Froude number. At higher speed, RaNS solvers slightly miss-predicts the hollow and hump produced at bow front.

A grid uncertainty analysis has also been performed following a procedure proposed by Celik et al. [8] for resistance prediction. Figure 5 shows the analysis result for Fr number 0.101. For uncertainty analysis, grid resolution in the o-xy plane, i.e., the free surface has been considered. According to analysis, the grid convergence index for mesh 3 to 2 is 0.07 and for mesh 2 to 1 is 0.008. The grid convergence is monotonous for the drag predictions. So, the prediction result should improve with higher resolution mesh. Further detail on grid analysis has been reported by Islam [4].

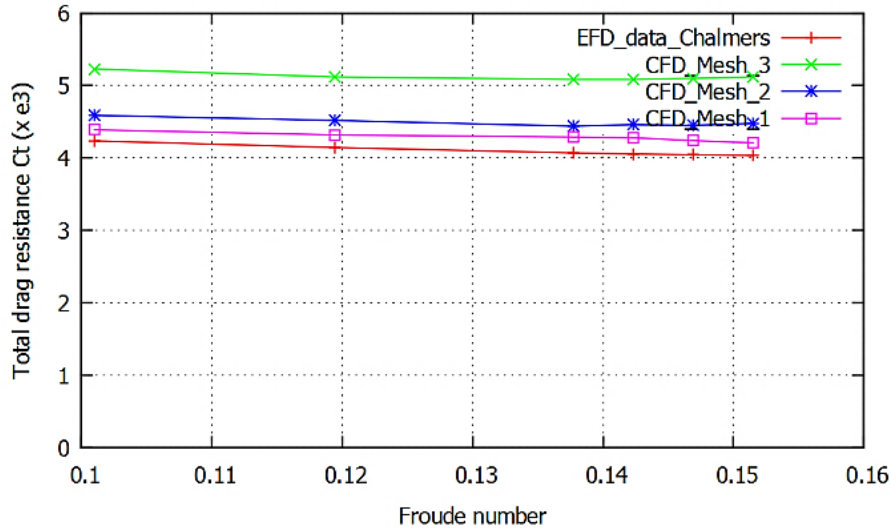


FIGURE 4. Calm water resistance prediction for KVLCC2 by three different meshes

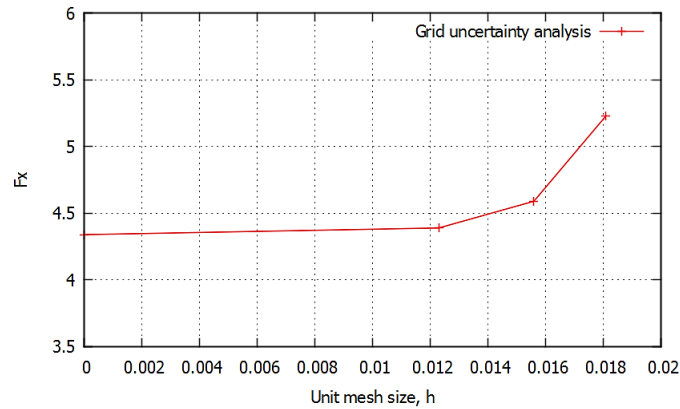


FIGURE 5. Grid uncertainty analysis on calm water resistance prediction

Added Resistance in Head Wave Condition

Added resistance is mainly the additional resistance a ship faces while making its way through the waves. This resistance part is created by the loss of energy to both, radiated waves caused by ship motion, and diffraction of

incident waves on ship hull. However, energy distribution among these two components are dependent on the ratio of incident wave length to ship length (λ/L).

In case of added resistance calculation, sufficient mesh resolution is required at the bow and stern part to properly capture the radiated waves, and at the entire hull form near the water line to capture the incident waves. Resolution and dimension of the outer mesh is also important to capture the free surface deformation with reasonable accuracy.

In order to validate the added resistance prediction by SHIP_Motion, head wave simulations were performed and the results were compared with experimental data from different research groups, which were reported by Kim et al. [9]. All simulations were performed in symmetry condition, i.e., half hull (port side hull) was simulated and only heave and pitch motion were set free and the inner mesh contained extended deck to avoid green water problem. For conversion of simulation results to that of comparable state, following conversions were used.

$$\text{Added resistance coefficient, } C_{aw} = Fr^2 \times \frac{1}{(A/L)^2} \times \left(\frac{L}{B}\right)^2 \times \Delta f \quad (1)$$

Where, Fr is the Froude number, B is ship's width and Δf is the difference between wave drag force and calm water drag force.

$$\text{Heave Response Amplitude Operator (RAO), } \frac{z}{A} = \frac{z/L}{A/L} \quad (2)$$

Here, z is the heave amplitude, L is ship length and A is incoming wave amplitude.

$$\text{Pitch Response Amplitude Operator (RAO), } \frac{\theta}{Ak} = \frac{\theta \times \lambda/L}{(A/L) \times 360} \quad (3)$$

Here, θ is pitch amplitude, L is ship length, A is incoming wave amplitude and λ is the wave length.

The calm water resistance predicted for the present case is 4.14×10^{-3} , while the experimental result is 4.096×10^{-3} . The simulation conditions for head wave cases are described in Table 3. Added resistance prediction results have been shown in Fig. 6. The experimental data shown here came from experimental facilities of MOERI and Tokyo University, and simulation results were produced by WAVIS, in-house code of MOERI. Figure 7 shows response amplitude operators (RAOs) for heave and pitch motions. The simulations have been kept limited to short wave lengths as ships are rarely exposed to wave lengths beyond $0.8L$ [9].

TABLE 3. Head wave simulation conditions for the non-dimensional KVLCC2 model

Ship model	KVLCC2
Froude number	0.142
Ship speed (in knots)	7.95
Reynolds number	4.6×10^8
Wave amplitude, A/L	0.005, 0.0094
Degrees of freedom	2DOF (Heave and pitch)
Mesh resolution (inner)	197 x 25 x 109
Mesh dimension (inner)	1.8L x 0.35L
Mesh resolution (outer)	190 x 43 x 61
Mesh dimension (outer)	3.8L x 1L x 1L

*A = wave amplitude and L = Ship length.

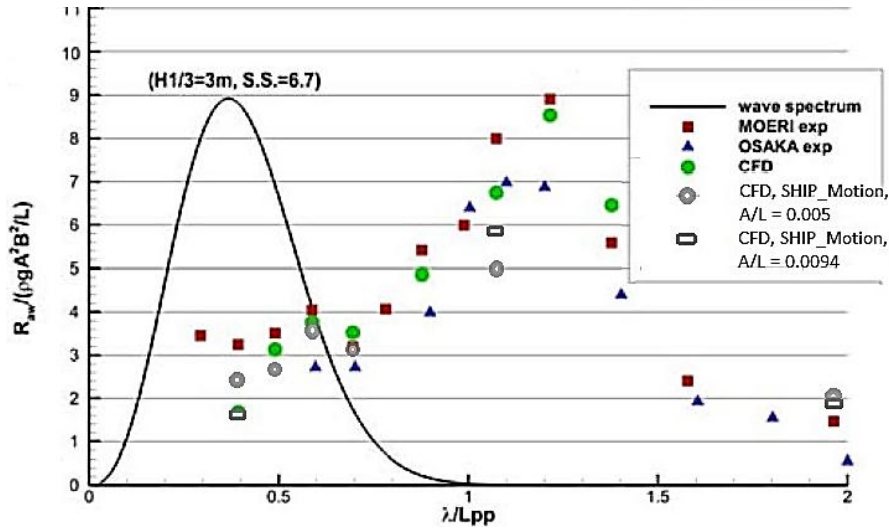


FIGURE 6. Added resistance coefficient in head waves for KVLCC2 at $A/L = 0.005, 0.0094$ [9]

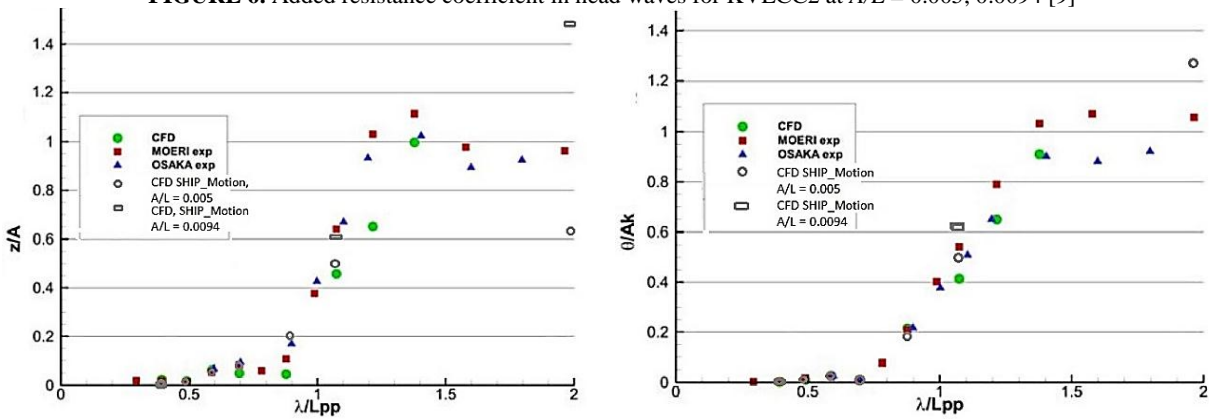


FIGURE 7. Heave and Pitch RAO in head waves for KVLCC2 at $A/L = 0.005, 0.0094$

CONCLUSION

In this paper, calm water and added resistance simulation have been performed for a tanker model. In calm water simulation, three different mesh resolution have been used to show the solver's monotonous convergence with increasing mesh resolution. The added resistance simulation has been performed with a high mesh resolution and results have been compared with other experimental and simulation data.

The calm water results show that, the deviation observed for highest mesh resolution is around 7%. However, the solver improves resistance prediction with improved mesh resolution. As for sinkage result, the deviation found from experimental data is in millimeter scale. The trim results have been well predicted.

In case of ship simulation in head waves, the high deviation observed for low wavelength cases is mainly because of numerical diffusion for low wave lengths. Overall, the results agree well with both experimental data. However, as two experimental data show deviation among themselves, it may not be justified to quantify the deviation for simulation results. The heave and pitch RAOs also show good agreement with comparison data.

Thus, it may be concluded that the solver is well capable of simulating and predicting ship maneuverability characteristics both in calm water and in head wave condition with reasonable accuracy, using minimum computational resource and within acceptable time.

REFERENCES

1. L. Larsson, F. Stern and V. Bertram, *Journal of Ship Research* **47**, 63-81 (2003).
2. "Summary of proceedings of SIMMAN 2008 Workshop," 2008.
3. L. Larsson, F. Stern and M. Visonneau, "CFD in Ship Hydrodynamics- Results of the Gothenburg 2010 Workshop," in *L. Eça et al. (eds.), MARINE 2011, IV International Conference on Computational Methods in Marine Engineering, Computational Methods in Applied Sciences.*, 2011.
4. H. Islam, "Prediction of ship resistance in oblique waves using RaNS based solver," MS Thesis, Division of Ocean Systems Engineering, KAIST, 2015.
5. K. Hyunchul, "Hydrodynamic force derivative estimation of a ship by computational fluid dynamics," 2014.
6. H. Orihara, "Development and Application of CFD simulation technology for the performance estimation of ship in waves," 2005.
7. L. Larsson, F. Stern and M. Visonneau, "CFD in Ship Hydrodynamics- Results of the Gothenburg 2010 Workshop," in *MARINE 2011, IV International Conference on Computational Methods in Marine Engineering, Computational Methods in Applied Sciences*, 2011.
8. I. B. Celik, U. Ghia, P. J. Roache, C. J. Freitas, H. Coleman and P. E. Raad., *Journal of Fluids Engineering, Transactions of the ASME*, 2008.
9. J. Kim, I.-R. park, K.-S. Kim, Y.-C. Kim, Y. sik Kim and S.-H. Van, "Numerical Towing Tank Application to the Prediction of Added Resistance Performance of KVLCC2 in Regular Waves," in *Proceedings of the Twenty-third (2013) International Offshore and Polar Engineering (ISOPE) Anchorage, Alaska, USA, June 30-July 5, 2013.*, 2013.
10. ITTC-Report, "Seakeeping Committee: Final Report and Recommendations to the 27th ITTC," 2014.

APPENDIX

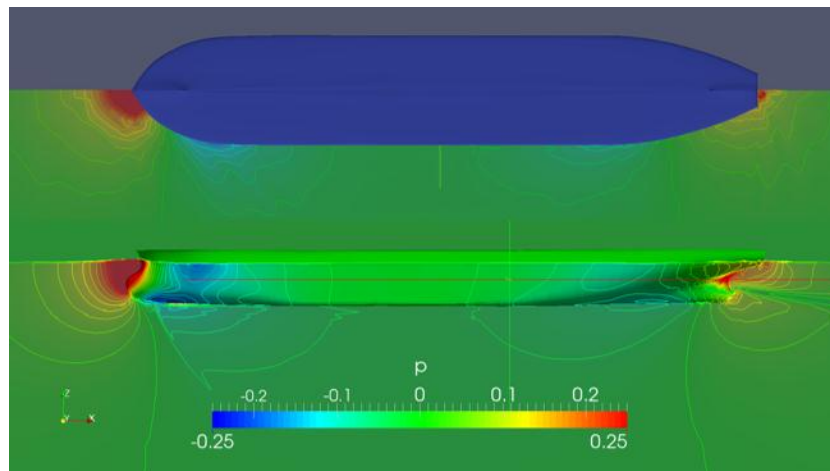


FIGURE. Pressure distribution at free surface and ship hull surface in calm water

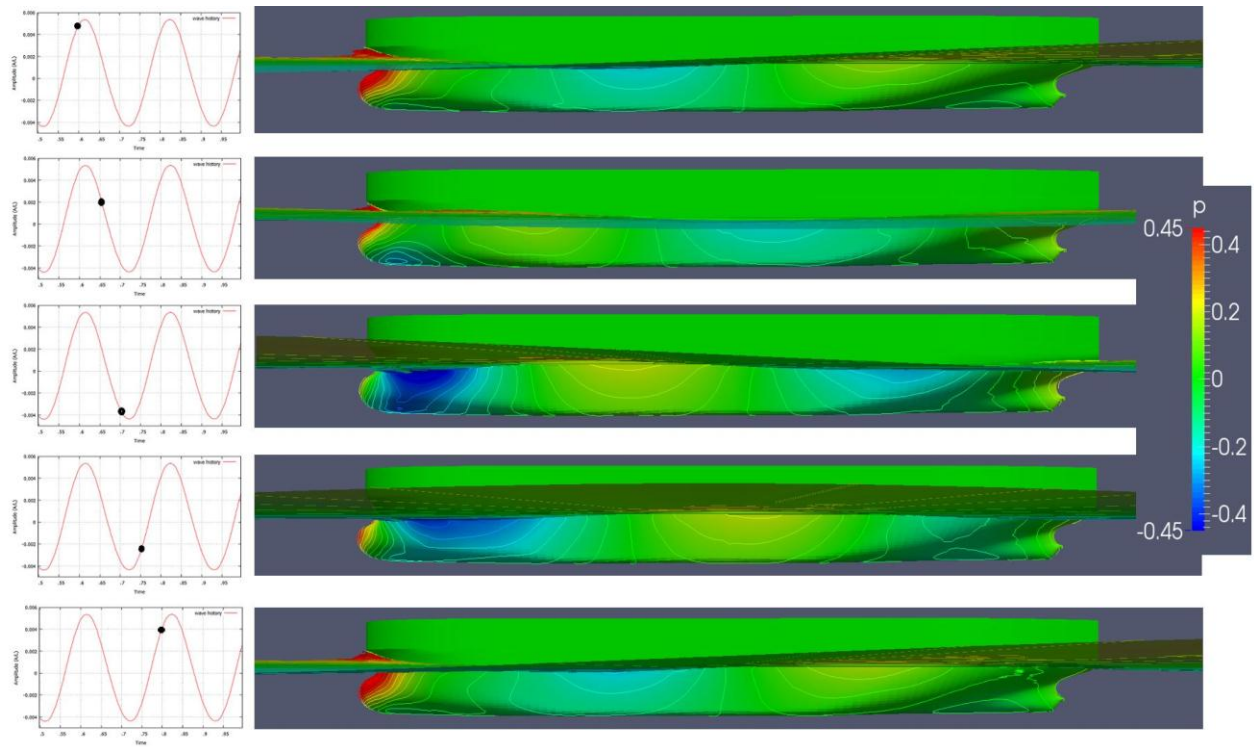
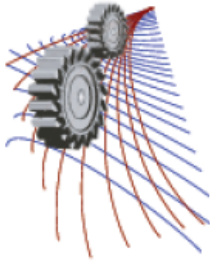


FIGURE. Pressure distribution at hull surface of KVLCC2 in head waves ($\lambda/L = 0.7$, $A/L = 0.005$)



Design and Analysis of Flow through Centrifugal Compressor Based on Closed Loop Brayton Cycle with CO₂ as Working Fluid

Kaveeshwar Ganesh Vikas^{1, a)} and M. Govardhan^{1, b)}

¹*Department of Mechanical Engineering, I.I.T. Madras, Chennai 600 036, India*

^{b)}Corresponding author: gova@iitm.ac.in

^{a)}ganeshkaveeshwar@gmail.com

Abstract. A closed loop Brayton cycle using carbon dioxide (CO₂) as working fluid results in a significant reduction in the size of its components. As new forms of such cycles are being developed, a suitable compression system needs to be evolved. The main objective is to analyze and simulate the flow of CO₂ inside a centrifugal compressor impeller. The flow is simulated at sub critical conditions, with inlet pressure varying from 1 ata. to 15 ata. and speeds ranging from 21789 rpm to 17431 rpm. The CO₂ compressor is found to accommodate higher mass flow rates at high inlet pressures effectively resulting in the reduction of the component size for a greater power output. There is however very little change on the total pressure ratio and efficiency of the compressor.

INTRODUCTION

Last few decades have witnessed a phenomenal growth in the demand for power which has driven the suppliers to find new sources of energy and increase the efficiency of power generation process. An upcoming technology in this regard is the CO₂ based Brayton cycle which has applications in vast areas. Power generation of CO₂ based Brayton cycle can vary from few kilowatts for waste heat recovery to hundreds of megawatts in sodium cooled fast reactors.

The advantages of using supercritical CO₂ as the working fluid of a closed cycle Brayton cycle gas turbine is widely recognised. Development of this technology is an attractive proposition for solar, geothermal and nuclear energy conversion. The concept of exploiting the small compression work which takes place in Brayton cycle operated with super critical CO₂ to obtain high conversion efficiency at a moderate cycle temperature was studied by Angelino [1], Feher [2] and Dostalet al.[3]. A proof concept in detail was presented by Wright et al. [4]. Though there are numerous studies on turbomachinery components like compressors or turbines operating with steam, gas and air, there are only few studies covering unconventional behaviour of the fluids whose thermodynamic properties are in the range of vapour-liquid critical point, (Colona et al. [5], Harnick et al. [6]). Fluid properties close to critical point strongly deviate from the ideal gas laws. CO₂ is sufficiently stable below 923K though it is unstable over 923K, Takagi et al. [7]. A CO₂ based Brayton cycle is being studied for power generation due to significant increase in the efficiency of power generation and a reduction in the size of the plant, [4, 7-10]. One of the main components of such a setting is its compressor. For preliminary experimental study of the system, the compressor is generally not coupled to the turbine. Simulating the flow conditions inside the compressor becomes very crucial in order to accurately predict the performance of the system. The main objective of this project is to analyze and simulate the flow of CO₂ inside a centrifugal compressor suitable for closed loop Brayton cycle.

OVERVIEW OF THE SOLUTION METHODOLOGY

Discretisation of the governing equations was achieved by discretising the domain into finite control volumes using a mesh. The governing equations are integrated over each control volume in such a way that mass, momentum, energy etc. are conserved in a discrete sense for each control volume.

Continuity equation for steady state

$$\frac{\partial \rho}{\partial t} + \nabla \cdot (\rho C) = 0 \quad (1)$$

Where $C = u\hat{i} + v\hat{j} + w\hat{k}$

If the flow is assumed steady, $\frac{\partial \rho}{\partial t} = 0$ and continuity equation then reduces to:

$$\nabla \cdot (\rho C) = 0 \quad (2)$$

Momentum equation for steady state

$$\nabla \cdot (\rho C \otimes C) = \nabla \cdot (-\rho \delta + \mu(\nabla C + (\nabla C)^T)) + S_M \quad (3)$$

\otimes denotes the tensor product defined by:

$$U \otimes V = \begin{bmatrix} U_x V_x & U_x V_y & U_x V_z \\ U_y V_x & U_y V_y & U_y V_z \\ U_z V_x & U_z V_y & U_z V_z \end{bmatrix}$$

S_M refers to momentum sources.
Energy equation for steady state

$$\nabla \cdot (\rho C h_o) = \nabla \cdot (\lambda \nabla T) + S_E \quad (4)$$

$$h_o = h + \frac{1}{2} U^2 \quad (5)$$

Where $h = h(p, T)$ and h = specific total enthalpy

If viscous work is significant, an additional term is used in the RHS of the energy equation to account for the effect of viscous shear and the energy equation then becomes:

$$\nabla \cdot (\rho C h_o) = \nabla \cdot (\lambda \nabla T) + \left[\nabla \cdot \left\{ \mu \left[\nabla C + (\nabla C)^T - \frac{2}{3} \nabla \cdot C \delta \right] C \right\} + S_E \right] \quad (6)$$

A total of seven unknowns are involved, (C, v, w, p, T, h, ρ) in the above equations but the set can be closed by adding two algebraic thermodynamic equations: equation of state relating ρ to T and p and constitutive equation relating h to T and p .

Equation of state for ρ :
For ideal gases:

$$\rho = \frac{w(p + p_{ref})}{R_o} \quad (7)$$

Equation of state for enthalpy (Constitutive equation):
The algebraic thermodynamic relation for enthalpy is:

$$h_2 - h_1 = \int_{T_1}^{T_2} C_p dT + \int_{p_1}^{p_2} \left[v - T_2 \left(\frac{\partial v}{\partial T} \right) \right] dp \quad (8)$$

In the above equation, the first part is equivalent to the change in enthalpy for an ideal gas and the second step is a correction required for the real fluid. If both density and specific heat are constants, the above equation reduces to:

$$dh = C_p dT + \frac{dp}{\rho} \quad (9)$$

COMPUTATIONAL MODEL

The geometric details of this compressor are reported by McKain et al. [10] prepared for Lewis Research Center, NASA, USA, (Fig.1). A structured mesh is created using ANSYS 14.5 Turbogrid with 231 755 nodes, 208642 elements and 3 passages between the hub and shroud profiles. Figure 2 show the mesh topology (left) and mesh structure at 50% span of the blade (right). The mesh size is chosen after a grid convergence test, to be optimally accurate and computationally cheaper.

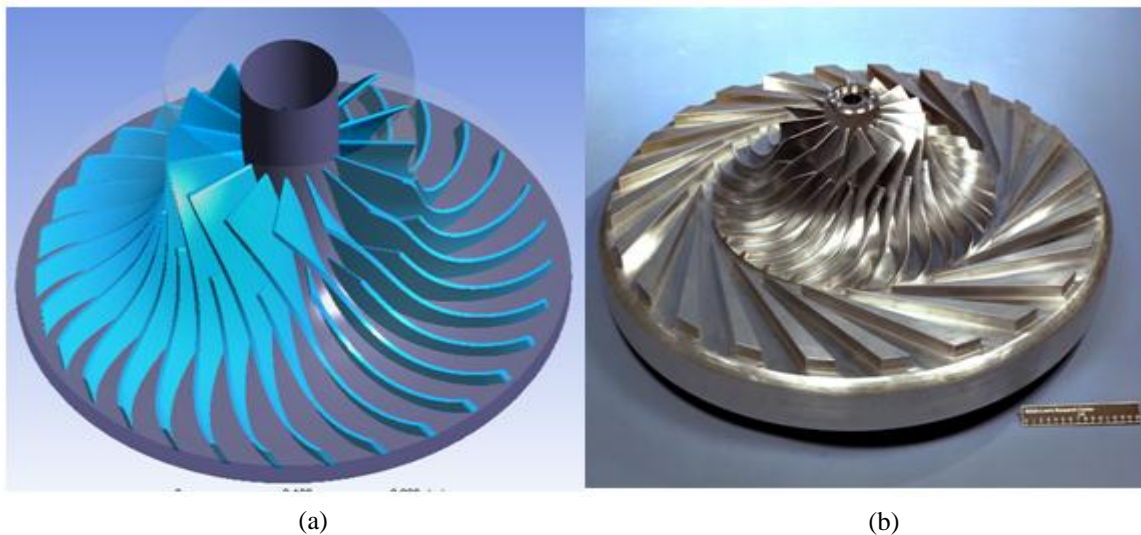


FIGURE 1. (a) NASA CC3 compressor model using ANSYS Bladegen, (b) NASA CC3 impeller model with vaned diffuser

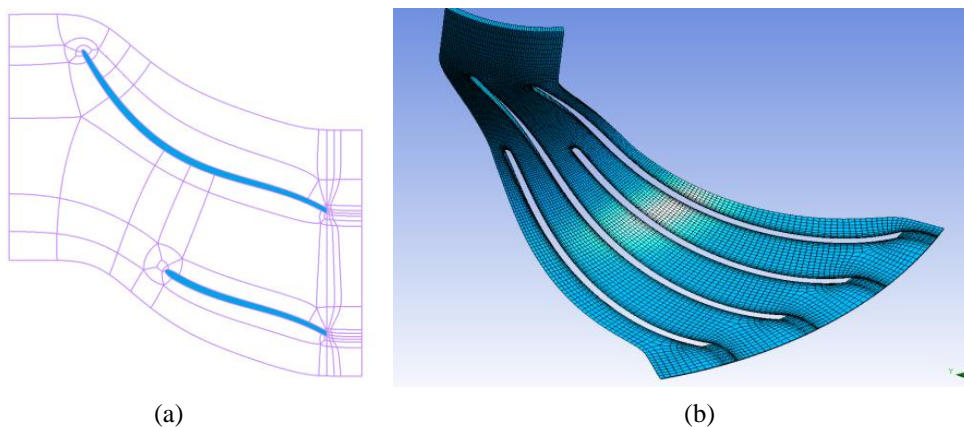


FIGURE 2. (a) Mesh topology and (b) mesh at 50% span

The mesh is then exported to Ansys14.5 CFX for computing numerical solution. A RANS based $k-\epsilon$ turbulence model is used due to better convergence rate, computationally faster and of comparable accuracy with SST model in this case. The boundary conditions are; inlet total pressure and outlet mass flow. The side walls are periodic; the flow

is perpendicular to inlet domain. Main blade, splitter blade, hub and shroud are no slip walls, while shroud is the only counter rotating wall. The analysis is steady state type with fluid properties as defined in the Ansys14.5 library – Air Ideal Gas. The shroud tip clearance is given to be 0.081mm. The NASA model was computed and the results are validated with the results of Kulkarni et al. [9]. The variation of static pressure matched very well.

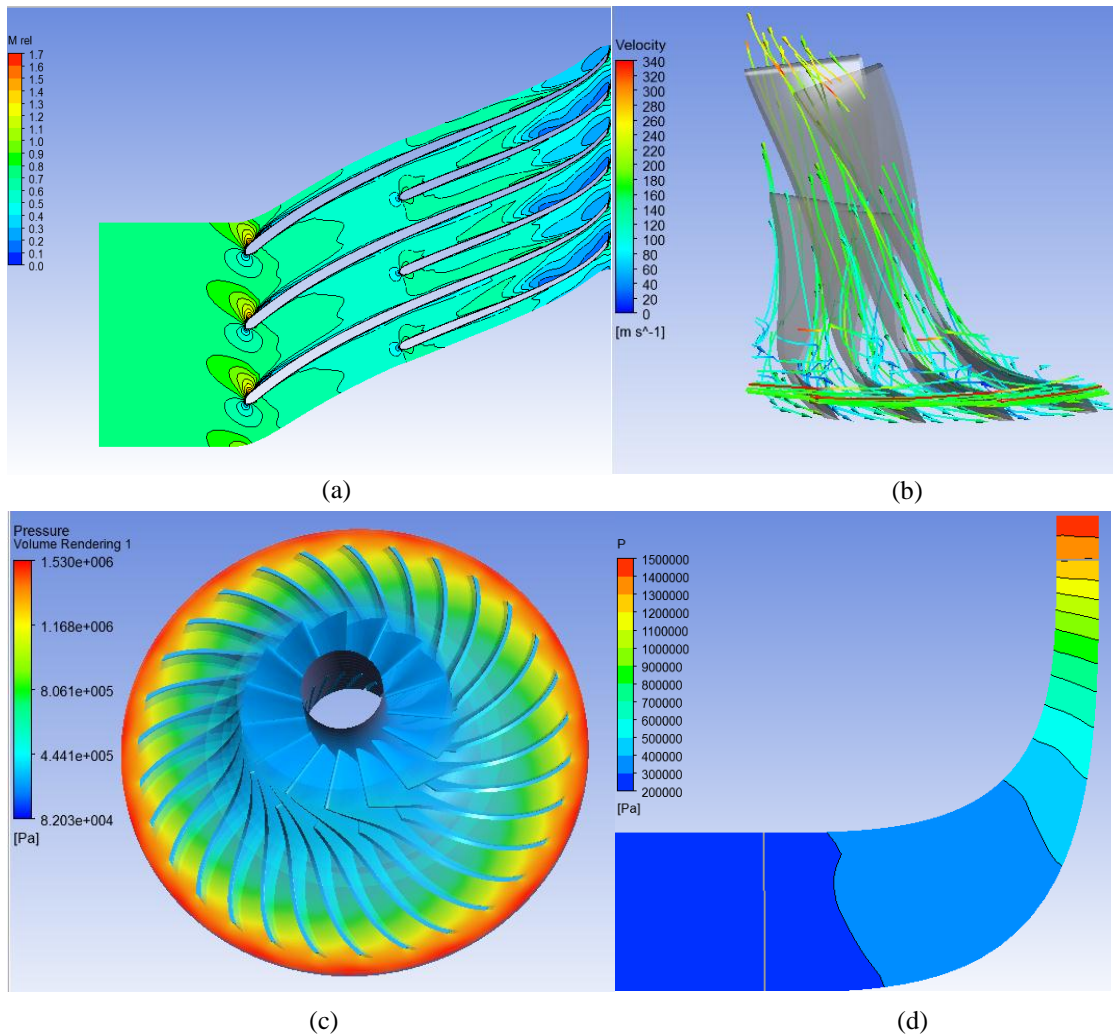


FIGURE 3.(a) Relative Mach number at 50% span, (b) Velocity streamlines at trailing edge, (c)Meridional Pressure contour, (d) Pressure map throughout impeller region ($m = 34$ kg/s, inlet pressure 6 ata. and speed 21789 rpm)

RESULTS AND DISCUSSION

Results were obtained and post processed for thirty four cases. Inlet pressure was varied from 1 ata. to 15 ata., speed of the compressor was varied from 17431 rpm to 21789 rpm. The mass flow rates were also varied depending on the operating conditions. The results thus obtained are presented in the following section.

The compressor operating range is found out by iterating tentative mass flow rate at that inlet pressure. Simulation is done for each mass flow rate and depending upon the convergence characteristics, operating range is determined. At pressure ratio higher than operating range, the compressor is likely to go into surge while at higher mass flow rates choking takes place. Both these conditions are highly undesirable since it is detrimental to the whole Brayton loop.

Figure 3 (Top-Left) indicates that the flow is largely subsonic inside the passage except for a very small part at the leading tip of the main blade, where CO₂ comes in contact with the rotating blade for the first time. Figure 3 (Top – Right) shows the velocity streamlines along the passage. Due to the unavoidable clearance given to the blade and shroud, some amount of gas escapes the original passage. A large clearance has an undesirable influence on the efficiency of the impeller. Figure 3 (Bottom – Right) is the meridional static pressure contour depicting the gradual increase in the pressure along the meridional plane. Figure 3 (Bottom – Left) shows the symmetric static pressure contours along the whole of impeller.

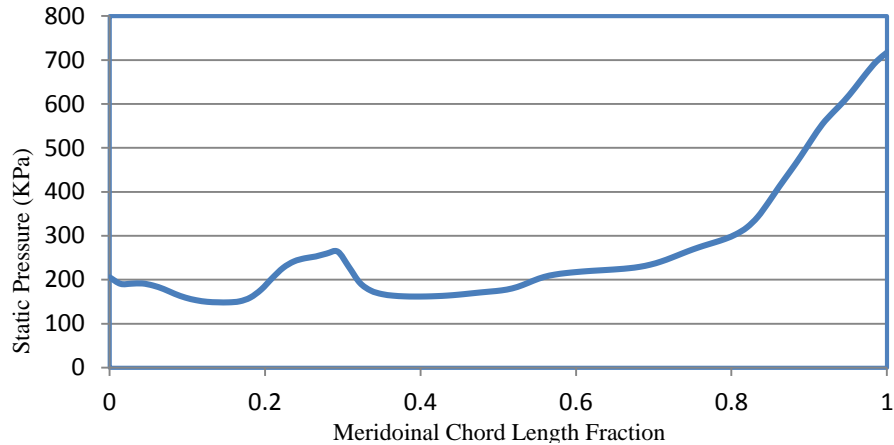


FIGURE 4. Static pressure vs meridional chord fraction at 50% span (volume flow rate 3.71 m³/s, near choke flow), N = 21789 rpm.

When the compressor was run nearer to the choking conditions, the flow becomes unstable. Figure 4 shows static pressure distribution along meridional flow direction at a speed of 21789 rpm and mass flow rate of 20 kg/s. The pressure rise is irregular. The condition persists because of the excessive mass flow rate inside the compressor, resulting in large regions where the relative Mach number was greater than 1.0 causing shock interaction and instabilities in the flow. The static pressure at the trailing edge is close to 700 kPa which is close to critical pressure of CO₂. Remarkable change of fluid properties like density, viscosity, heat transfer rates etc. occur at critical point which affects the flow inside the compressor significantly. The non-uniform static pressure rise in the impeller at this operating point indicates non-ideal flow conditions in the impeller blade passage, (Fig.4).

Figure 5 shows the rise in static pressure for different inlet pressures and equivalent mass flow rate defined as $m \frac{T_{01}^{0.5}}{P_{01}}$. It is observed that the result is in line with the performance trend expected from a centrifugal compressor. The operating range is quite large at lower inlet pressures. As the inlet pressure and consequently inlet relative Mach number increases, the range at which compressor works without surge and choke becomes narrower. At an input pressure of 1200 kPa, the range of the compressor is extremely small. The static pressure ratio by the compressor using CO₂ as working fluid exceeds 4.0 with subsonic conditions.

Table 1 shows typical results for various inlet pressures and near equal volume flow rates. For a given volume flow rate, due to tremendous increase in density, mass flow rates increase substantially. Interestingly, total pressure ratio, isentropic and polytropic efficiencies do not change except near choke mass flow rates. As the inlet pressure increases, the density of the CO₂ increases so as input power reaching around 15 MW. The compressor was simulated for a moderate inlet pressure of 300 kPa and wide range of mass flow rates. Column 3 shows the results under near choking condition. There is a significant decrease in efficiency and total pressure ratio of the compressor. The isentropic efficiency for this case is 69% while for 17kg/s mass flow rate it is 90% while the total pressure ratio drops to 4.9 from a value of 9.9 for 17kg/s mass flow rate. As Table 1 shows, the isentropic and polytropic efficiencies do not vary with inlet pressure.

CONCLUSIONS

The performance of NASA CC3 compressor impeller is reported with CO₂ as working fluid. It is observed that the operating range of mass flow rate for each inlet pressure is quite small. As the inlet pressure is gradually increased, the power consumed by the compressor also increases without any significant loss to the efficiency and overall pressure ratio. If such a compressor is a part of a high pressure closed loop Brayton cycle coupled with a suitable turbine, very high amount of power can be produced at remarkably reduced plant sizes. Upward value of inlet pressure is constrained by supercritical state of CO₂.

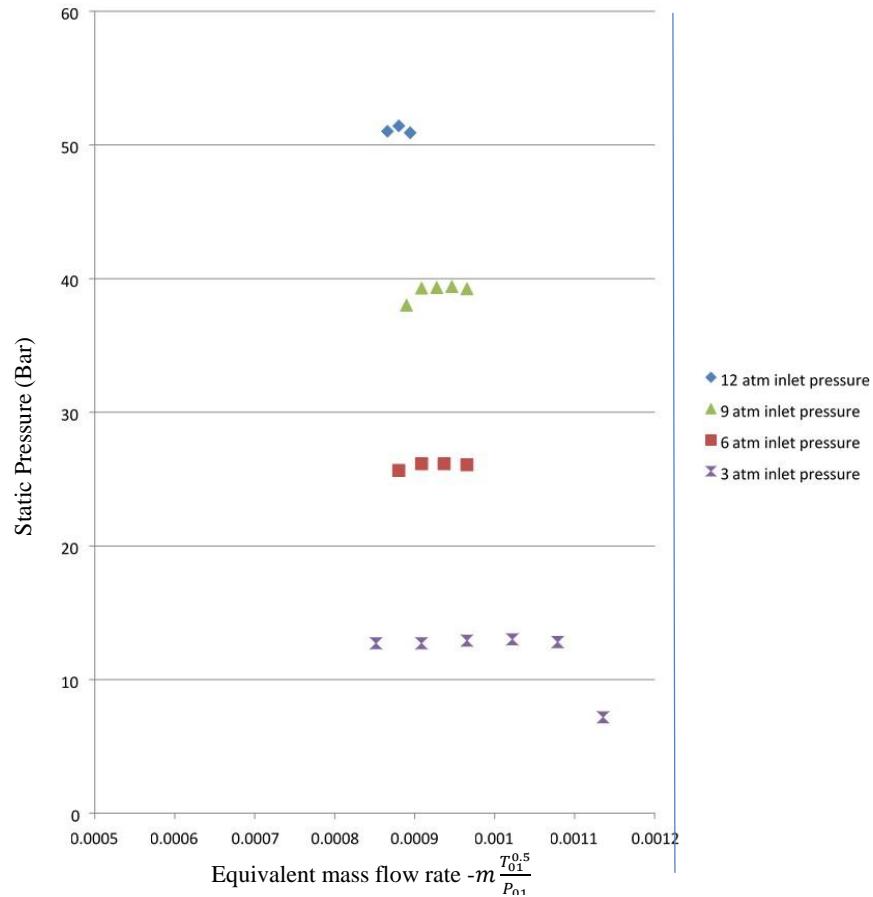


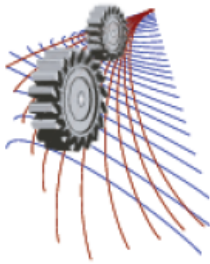
FIGURE 5. Impeller trailing edge static pressure vs. corrected mass flow rate

Table 1. Performance of CO₂ Compressor at various inlet pressures at 21789 rpm

1	2	3	4	5	6	7
	300 kPa	300 kPa	600 kPa	900 kPa	1200 kPa	1500 kPa
Inlet volume flow rate (m³/s)	2.91	3.71	2.94	2.91	2.94	3.05
Mass flow rate (kg/s)	16.0	20.0	31.0	48.0	63.0	82.0
Input power (MW)	2.95	3.021	5.95	8.83	11.9	15.43
Total pressure ratio	9.85	4.9159	9.92	9.78	9.96	10.19
Total temperature ratio	1.73	1.59	1.73	1.73	1.73	1.73
Isentropic efficiency	89.48	69.82	89.93	89.29	90.09	91.20
Polytropic efficiency	91.74	74.28	92.09	91.58	92.23	93.11

REFERENCES

1. G. Angelino, *ASME, J. Engg. Power***10**, 272-287(1969).
2. E.G., Feher, *Energy converters*, 85-90(1968).
3. V. Dostal, M.J. Driscoll, and P. Hejzlar, "A supercritical carbon dioxide cycle for next generation nuclear reactors", MIT-ANP series, MIT Boston, MA, MIT-ANP-TR-100, (2004).
4. S.A. Wright, R.F. Radel, M.E. Vernon, G.E. Rochau, and P.S. Pickard, "Operation and analysis of a supercritical CO₂ Brayton cycle", Sandia Lab Report SAND2010-0171, (2010).
5. P. Colonna, J. Harinck, S. Rebay, and A. Guardone, *J. Propulsion Power*, 282-294 (2008).
6. J. Harinck, P. Colonna, A. Guardone, and S. Rebay, *ASME, J. Turbomachinery*, 011001 (2010).
7. K. Takagi, Y. Mutto, T. Ishizuka, H. Kikura, and M. Aritomi, *Journal of Power and Energy Systems***4**, 138-149(2010).
8. Benjamín Monge Brenes, "Design of supercritical carbon dioxide centrifugal compressors", Ph.D. thesis, GMTS, Seville, 2014.
9. S. Kulkarni, A.B. Timothy, J.S. Gary, "Computational study of the CC3 impeller and vaneless diffuser experiment", NASA/TM - 2013-216566, 49th Joint Propulsion Conference and Exhibit, (2013).
10. T.F. Mckain, and G.H. Holbrook, "Coordinates for a high performance 4:1 pressure ratio centrifugal compressor", NASA Contractor Report 204134, (1997).



The Effect of Solidity on the Performance of H-Rotor Darrieus Turbine

S. M. Rakibul Hassan^{1, a)}, Mohammad Ali^{2, b)} and Md. Quamrul Islam^{2, c)}

¹*Department of Mechanical Engineering, Bangladesh University of Engineering and Technology, Dhaka-1000, Bangladesh*

^{a)}Corresponding author: rakibulhassan21@gmail.com

^{b)}mali@me.buet.ac.bd

^{c)}quamrul@me.buet.ac.bd

Abstract. Utilization of wind energy has been investigated for a long period of time by different researchers in different ways. Out of which, the Horizontal Axis Wind Turbine and the Vertical Axis Wind Turbine have now advanced design, but still there is scope to improve their efficiency. The Vertical Axis Wind Turbine (VAWT) has the advantage over Horizontal Axis Wind Turbine (HAWT) for working on omnidirectional air flow without any extra control system. A modified H-rotor Darrieus type VAWT is analysed in this paper, which is a lift based wind turbine. The effect of solidity (i.e. chord length, no. of blades) on power coefficient (C_p) of H-rotor for different tip speed ratios is numerically investigated. The study is conducted using time dependent RANS equations using SST $k-\omega$ model. SIMPLE scheme is used as pressure-velocity coupling and in all cases, the second order upwind discretization scheme is chosen for getting more accurate solution. In results, different parameters are compared, which depict the performance of the modified H-rotor Darrieus type VAWT. Double layered H-rotor having inner layer blades with longer chord gives higher power coefficient than those have inner layer blades with smaller chord.

INTRODUCTION

Though the maximum extractable power from wind is limited by the Betz limit, Engineers still have scopes to improve the wind turbine. Due to successful researches on Horizontal Axis Wind Turbine (HAWT) take it to a very advanced level and now it is possible to produce megawatts of electricity in a wind farm. On the other hand Vertical Axis Wind Turbine (VAWT) has the advantages of producing power at low speed wind irrespective to wind direction. The Savonius type VAWT is a low speed, high torque, drag basis wind turbine, which has a very simple design and hence a lower production costs. The Darrieus type VAWT is a high speed, low torque, lift basis wind turbine. As Darrieus wind turbine has high starting torque, sometime Savonius rotor is combined with Darrieus wind turbine to produce that starting torque. Electricity generation is also possible from both Savonius and Darrieus type VAWT and analyses on designs have been being done by researchers to produce maximum electricity.

In 1982 Paul G. Migliore and John R Fritschen [1] experimented Darrieus VAWT with a variety of airfoil shapes and found that higher C_p can be achieved with symmetric NACA airfoil of lower thickness. Later this effect of thickness was investigated by researchers and the same results have been found [8, 12]. Mohamed et al. found LS(1)-0413 more efficient than NACA 0018 in their numerical study of H-rotor wind turbine [2]. Danao et al. [8] studied the blade thickness and camber effects and found that cambered airfoil produces higher torque in both upwind and downwind, while inverted cambered airfoil generate torque mostly in upwind region. Cambered airfoils of NACA 63 series provide wider operating range than symmetric NACA airfoils [1, 2].

The performance of H-rotor VAWT was discussed mathematically with both single streamtube model [13] and double-multiple streamtube model [10], which is effective to predict the behavior of wind turbine before numerical and experimental study. An unsteady 2D CFD model of H-rotor has been developed and investigated by R. Lanzafame et al. [7] in order to evaluate its performance. In case of numerical analysis, solution of URANS (Unsteady Reynolds Average Navier-Stokes) equations estimate better efficiency for VAWT than estimated by solving steady RANS (Reynolds Average Navier-Stokes) equations [5]. In case of 3D modeling

aspect ratio is an important factor and it should be lower for achieving higher power coefficient [9]. Dominy et al. [11] shows that three bladed H-rotor has better self-starting capability than two bladed H-rotor, because three bladed VAWT is orientation independent. In past days effect of solidity is studied by different researchers. With the increase in solidity, Power Coefficient drops and moved to lower tip speed ratio [16, 17]. Increase in chord length and decrease in no. of blades improve power coefficient but at the same time radial force increases, which is undesirable from the structural perspective [3, 16].

In this paper, 2D H-rotor vertical axis wind turbine with NACA 0012 airfoil has been studied for different solidity. The effect of number of blades is studied. A novel design of multilayer bladed wind turbine is introduced and its performance is compared with the established designs.

GEOMETRIC MODEL

As mentioned earlier, thinner airfoils are efficient. So NACA 0012 airfoil model is used in this study. Four different models are analyzed and two of them are of the novel design introduced in this paper.

General Data:

Blade profile: NACA 0012

Wind Turbine Diameter (D): 1.03m

Chord Length (c): 85.8 mm

Rotor Height: 1m (2D)

H-Rotor VAWT consists of 3 blades as shown in Fig. 1(a) and 6 blades as shown in Fig. 1.(b) are studied. Then the new models of multilayer VAWT are analyzed. In the third model as shown in Fig. 1.(c), blades in different layers have different chord length and in the fourth one as shown in Fig. 1. (d), all blades have same chord length. As a result, the third and fourth models have solidity of 0.75 and 1.0 respectively. The distances for inner layer from the center of the turbine are half of the turbine radius for both cases.

TABLE 1. Details of all Geometric Models

Model	No. of Airfoil (N)	No. of Layers	Solidity (σ)	Radius (R)	Chord Length (c)
(a)	3	1	0.5	0.515 m	0.0858 m
(b)	6	1	1.0	0.515 m	0.0858 m
(c)	6	2	0.75	Inner: 0.2575 m	Inner: 0.0429 m
				Outer: 0.515 m	Outer: 0.0858 m
(d)	6	2	1.0	Inner: 0.2575 m	Inner: 0.0858 m
				Outer: 0.515 m	Outer: 0.0858 m

NUMERICAL MODEL

Computational Domain

For solving the rotational vertical axis wind turbine, the entire zone is divided into two different parts; Stationary zone and Rotating zone. These two zones are connected at interface. The size of the computational domain should be larger enough to allow the vortices to shed off and at the same time it should be smaller enough to save computational time and expense. Here, the computational domain is 10 times wider and 15 time longer then the turbine diameter. The downstream of the domain is 10D away from the center of the turbine. The diameter of rotational zone is 1.25 times of the turbine diameter as shown in figure.

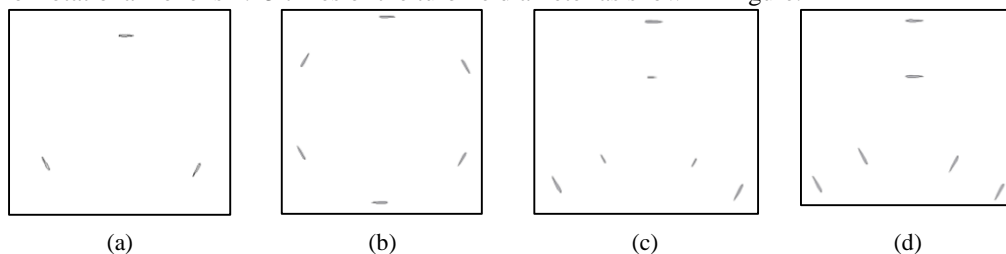


FIGURE 1. Geometric Model of Vertical Axis Wind Turbine (a) 3 Bladed, Single Layered, $\sigma=0.5$ (b) 6 Bladed, Single Layered, $\sigma=1.0$ (c) 6 Bladed, Double Layered, $\sigma=0.75$ (d) 6 Bladed, Double Layered, $\sigma=1.0$

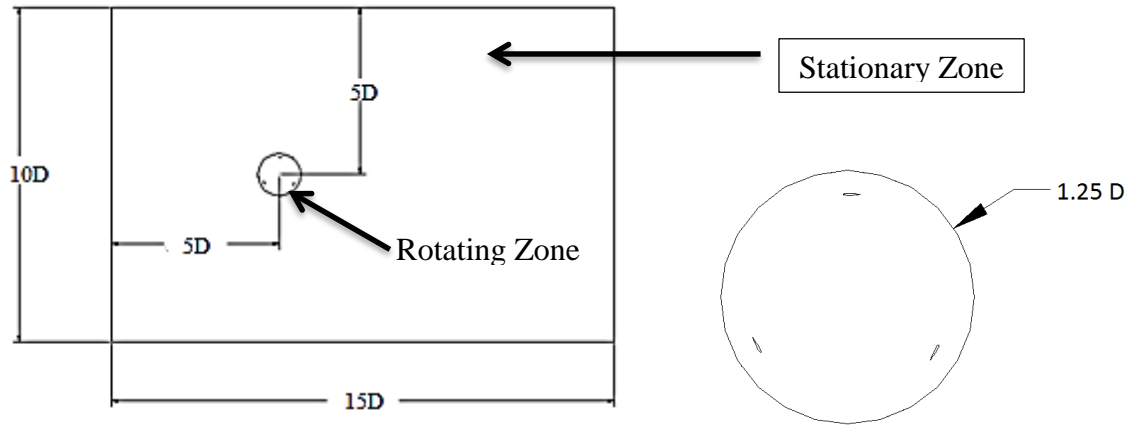


FIGURE 2.Computational Domain of Vertical Axis Wind Turbine

Mesh Generation

Whole computational domain is divided into control volumes using tri-mesh technique. Density of mesh is higher near the airfoil region. No. of mesh on a blade surface is about 1720 with mesh size 0.1 mm. Total no. of cells for different models are given in table 2. Mesh size increases from the airfoil surface to outer direction as shown in table 3.

TABLE 2. Total No. of cells:

	Model 1	Model 2	Model 3	Model 4
Total no. of cells	493016	599628	559900	609280

TABLE 3. Mesh Sizing

	For Rotating Zone:	For Stationary Zone
Start size	0.0001 m (at airfoil)	0.003 m (at interface)
Growth Rate	1.1	1.1
Size Limit	0.003 m	0.250m

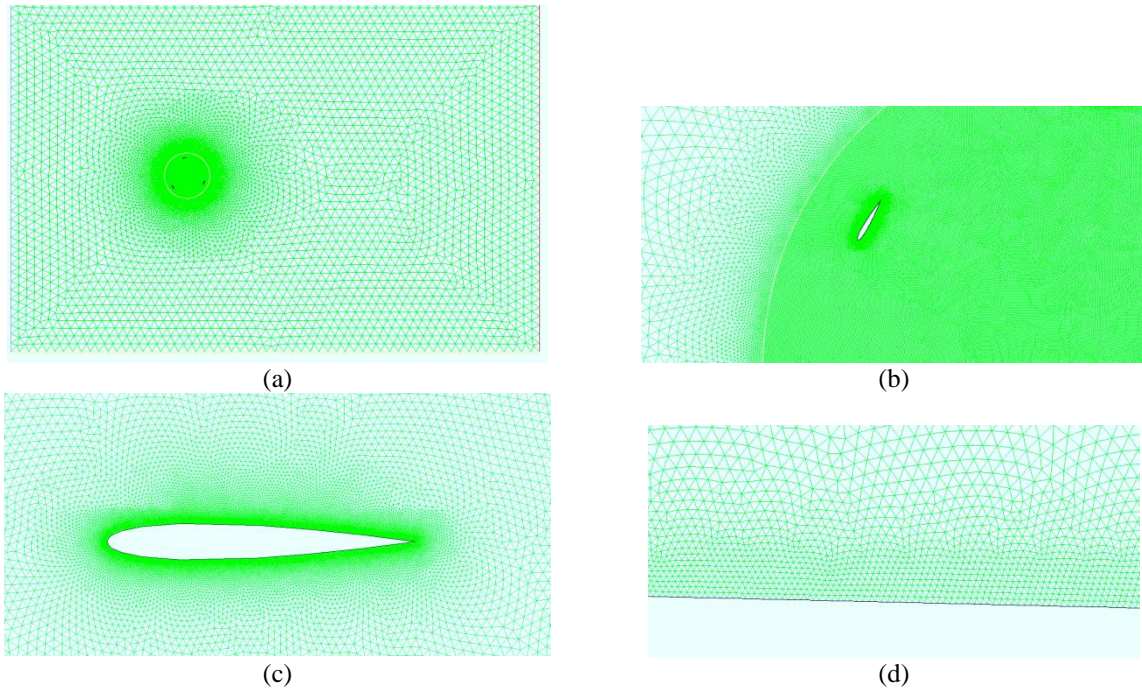


FIGURE 3.Generated Mesh (a) full domain (b) mesh near interface zone (c) around airfoil (d) very close to airfoil

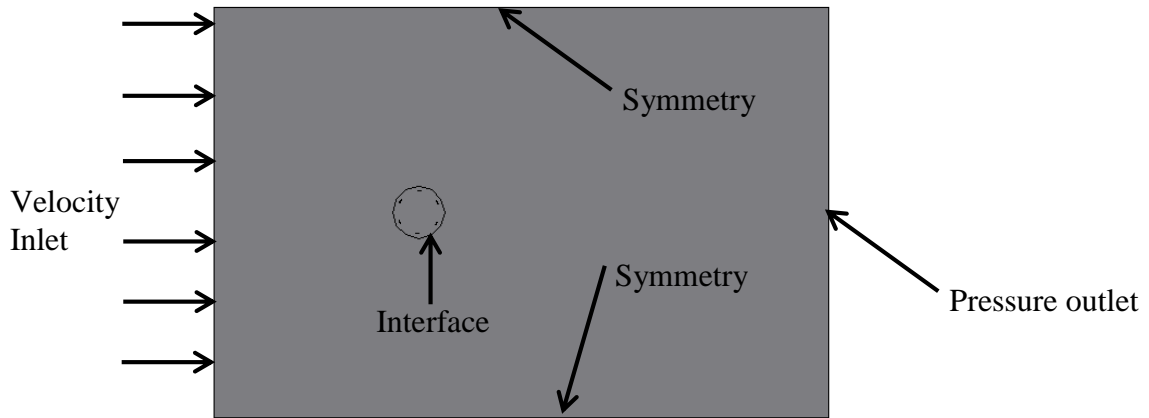


FIGURE 4. Boundary Types

Boundary Conditions

Velocity Inlet and Pressure outlet are used as boundary types respectively for upstream and downstream boundaries of computational domain. Both top and bottom boundaries are defined as Symmetry. The interface of the Rotating and Stationary zones is assigned as Interface type boundary. All blades are defined as wall type boundary. For $k-\omega$ method, value of kinetic energy (k) and specific dissipation rate (ω) at inlet boundary are required for simulation. Following equations are used to find these values at inlet, Kinetic Energy at Inlet,

$$k = \frac{1}{2} (u_x^2 + u_y^2 + u_z^2)$$

Dissipation Rate at Inlet,

$$\omega = \frac{\varepsilon}{k\beta^*}$$

Where, $\varepsilon = c_\mu^{3/4} k^{3/2} l^{-1}$

Here, $c_\mu = \beta^* = 0.009$ and $l = 0.07 \times \text{Characteristic length}$ (i.e. chord length)

Inlet Velocity, $u_x = 4 \text{ m/s}$; Outlet Pressure: 1 atm; Inlet Kinetic energy, $k = 8 \text{ m}^2/\text{s}^2$

Inlet Specific Dissipation Rate, $\omega = 1528.97 \text{ s}^{-1}$

NUMERICAL METHOD

For Numerical Analysis of the H-rotor VAWT, unsteady Reynolds Average Navier-Stokes equations are solved. Considering the turbulence present in the system, $k-\omega$ SST (Shear Stress Transport) turbulence model is numerically calculated for solution. $k-\omega$ SST turbulence model is preferred over other turbulence model as recommended by different researchers [2,5]. This is more reliable and effective to gain precise result. This model has the combined advantages of achieving good result of $k-\omega$ model and maintaining the far-field stability of the $k-\varepsilon$ model. Second order upwind discretization scheme is chosen for all cases because of its lower numerical diffusivity and reliability. SIMPLE pressure-velocity coupling is considered for the simulation.

In order to solve the rotating body of VAWT, moving mesh technique is used. The time steps was chosen such that, each rotation of rotating zone is about one degree. This ensures better convergence and continuous result over a complete cycle.

TABLE 4. Values of Ω for different λ

λ	1	1.5	2	2.5	2.75	3	3.25	3.5	3.75	4	4.25	5
$\Omega = u\lambda/R$	7.77	11.65	15.55	19.42	21.36	23.3	25.2427	27.78	29.13	31	33.01	38.84

All convergence criteria are set to 10^{-4} . Moment created by the turbine is also monitored to ensure the convergence of solution. The moment created by the turbine gives a periodic curve. The solution was considered as converged, when difference in amplitude is less than 5% which takes 8-10 cycles approximately.

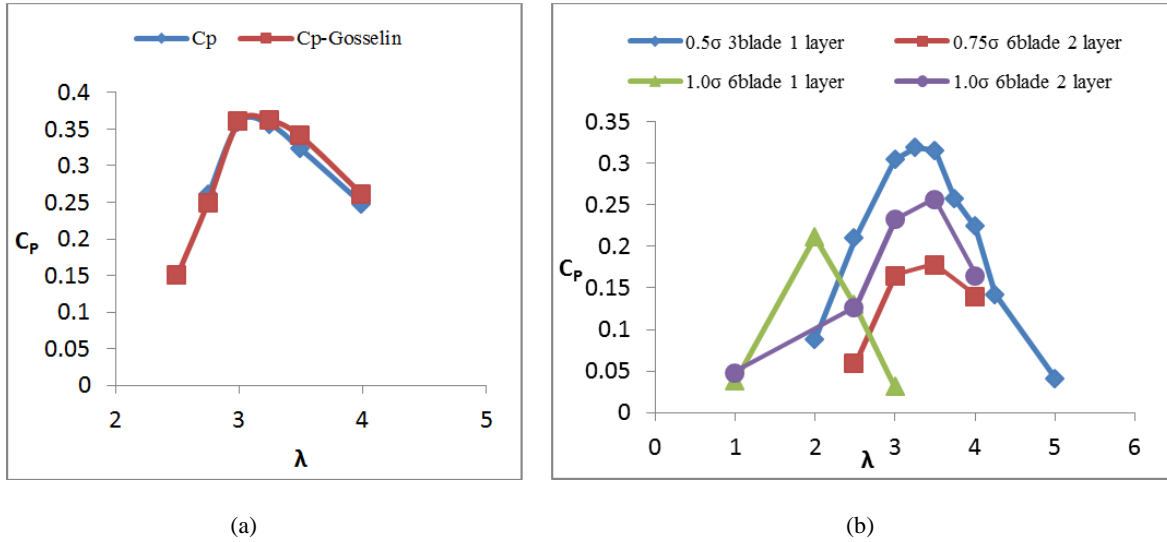


FIGURE 5.(a) Comparison of C_p vs. λ curve for validation (b) C_p vs. λ curve for different models

RESULT AND DISCUSSION

H-rotor VAWT with NACA 0015 airfoils has been simulated considering same boundary condition as Gosselin et al. [4]. The result with convergence criteria 10^{-4} shows almost same C_p vs. λ curve with a very little difference, which can be observed in table 5 and Fig. 5(a). Thus the code is validated for this current work.

TABLE 5. Comparative result for wind turbine with NACA 0015

λ	C_t	C_p	C_p -Gosselin
2.75	0.094196	0.259038	0.25
3	0.119667	0.359	0.36
3.25	0.109591	0.35617	0.362
3.5	0.092186	0.322652	0.34
4	0.061882	0.247528	0.26

As seen in the Fig. 5(b), for single layered H-rotor, increase in solidity of wind turbine always decreases the maximum power coefficient. For 6 bladed single layered VAWT with solidity 1, maximum C_p is 0.2113 and occurs at tip speed ratio (λ) 2 which is 33.6 % less than the maximum C_p of 3 bladed single layered VAWT with solidity 0.5 at $\lambda=3.25$.

But in case of double layered VAWT we can see some significant difference. 6 bladed double layered VAWT with $\sigma=1.0$ gives $(C_p)_{\max} = 0.255$ at $\lambda=3.5$, while 6 bladed double layered VAWT with $\sigma=0.75$ gives $(C_p)_{\max} = 0.176$ at $\lambda=3.5$. Model (d) gives higher maximum C_p than maximum C_p for single layer VAWT with solidity 1.0. At the same time, the inner layer blades' chord length play important role. Here, model (d) gives higher C_p than model (c), though the solidity of model (d) is higher. So it can be said that for double layer H-rotor VAWT, blade chord length ratio is more important than solidity.

The inner layer blades are actually facing a lower tip speed ratio than the tip speed ratio experienced by outer layer. The ratio of speed ratio ($\Omega R_{\text{layer}}/u_x$) of outer layer to inner layer is equal to the ratio of their distance from center of the wind turbine. In this analysis the speed ratio experienced by the inner layer is half of the speed ratio experienced by outer layer. At the same time the inner layer blades experienced an angle of attack larger than the stall angle. So for some tip speed ratio the inner layer produce negative torque. This is the reason for lower maximum power coefficient achieved by double layered VAWT.

CONCLUSION

In this paper, the effect of solidity on H-rotor VAWT has been numerically investigated and it can be concluded by the following statements,

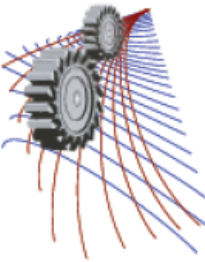
1. With the increase in solidity, $(C_p)_{\max}$ decreases and shifted to the lower tip speed ratio.

2. A novel design of double layered VAWT is introduced. The double layered Darrieus H-rotor shows better performance for the inner layer airfoils with longer chord. C_p of these wind turbines depend on the individual power coefficients of outer layer blades and inner layer blades.
3. For double layered H-rotor VAWT, blade chord length ratio is more important than solidity.
4. For equal solidity maximum power coefficient for a double layered H-rotor VAWT is higher than the single layered H-rotor VAWT.

Further researches on this new double layered design (e.g. ratio of inner layer blades to outer layer blades, ratio of their distances, angular position of blades etc.) may improve its performance and hence it will be able to generate power with higher power coefficient.

REFERENCES

1. Paul G. Migliore and John R. Fritschen, No. SERI/TR-11045-1. Solar Energy Research Institute, Golden, Colorado (USA), 1982.
2. M. H. Mohamed, A. M. Ali and A. A. Hafiz, Engineering Science and Technology, an International Journal, **18** (1), 1-13 (2015).
3. Marco Raciti Castelli, Stefano De Betta and Ernesto Benini, Castelli, M. Raciti, Stefano De Betta, and Ernesto Benini, World Academy of Science, Engineering and Technology **61**, 305-311 (2012).
4. Rémi Gosselin, Guy Dumas and Matthieu Boudreau, *21st Annual Conference of the CFD Society of Canada*, (Sherbrooke, Quebec, 2013) pp. 1-16.
5. Ion Mălăel and Horia Dumitrescu, U.P.B. Sci. Bull., Series D, **76**(1), 2014
6. Ion Mălăel, Horia Dumitrescu and Vladimir Cardoso, Global Journal of Researches in Engineering: I Numerical Methods, **14**(1), 2014
7. Rosario Lanzafame, Stefano Mauro and Michele Messina, *ATI 2013 - 68th Conference of the Italian Thermal Machines Engineering Association*, Energy Procedia 45, Bologna, 2013, Edited by Gian Luca Morini, Michele Bianchi, Cesare Saccani and Alessandro Cocchi, (Elsevier, 2014), pp. 131 – 140.
8. Louis Angelo Danao, Ning Qin and Robert Howell, Journal of Power and Energy, **226**(7), 867-881 (2012)
9. S. Brusca, R. Lanzafame and M. Messina, International Journal Energy Environmental Engineering **5**, 333–340 (2014).
10. Conaill E. Soraghan, William E. Leithead, Hong Yue and Julian Feuchtwang, *31st AIAA Applied Aerodynamics Conference*, San Diego, CA, 2013, (American Institute of Aeronautics and Astronautics, Reston, VA, 2013), pp. 1-12.
11. R. Dominy, P. Lunt, A. Bickerdyke and J. Dominy, *Proceedings of the I MECH E*, part A : journal of power and energy, 221 (1), edited by Chris Lawn, (Sage Journal, 2007), pp. 111-120.
12. Yan Chen and Yongsheng Lian, Engineering Application of Computational Fluid Mechanics, 1-12 (2015).
13. Bhavesh Patel and Vishal Kevat, International Journal of Advanced Engineering Technology, **4**(2), 86-89 (2013).
14. M. H. Mohamed, *Asia-Pacific Forum on Renewable Energy 2011*, Energy, 47, edited by Hyungkee Yoon and Jong Min Choi, (Elsevier, 2012) pp. 522-530
15. Mohammad Rashedul Hasan, Md. Rasedul Islam, G.M. Hasan Shahariar and Mohammad Mashud, *9th International Forum on Strategic Technology (IFOST), Cox's Bazar*, 2014, (IEEE, 2014), pp. 318-321.
16. Taher G. Abu-El-Yazied, Ahmad M. Ali, Mahdi S. Al-Ajmi, Islam M. Hassan, American Journal of Mechanical Engineering and Automation **2**(1), 16-25 (2015).
17. Shengmao Li and Yan Li, *Power and Energy Engineering Conference (APPEEC)*, 2010 Asia-Pacific. (IEEE, 2010), pp. 1-4.



Effects of Non Newtonian Spiral Blood Flow through Arterial Stenosis

Md. Mahmudul Hasan^{1, a)}; Mahbub Alam Maruf¹ and Mohammad Ali¹

¹ *Department of Mechanical Engineering, Bangladesh University of Engineering and Technology (BUET), Dhaka-1000, Bangladesh.*

^{a)} *Corresponding author: mhasan.buet09@gmail.com*

Abstract. The spiral component of blood flow has both beneficial and detrimental effects in human circulatory system. A numerical investigation is carried out to analyze the effect of spiral blood flow through an axisymmetric three dimensional artery having 75% stenosis at the center. Blood is assumed as a Non-Newtonian fluid. Standard $k-\omega$ model is used for the simulation with the Reynolds number of 1000. A parabolic velocity profile with spiral flow is used as inlet boundary condition. The peak values of all velocity components are found just after stenosis. But total pressure gradually decreases at downstream. Spiral flow of blood has significant effects on tangential component of velocity. However, the effect is mild for radial and axial velocity components. The peak value of wall shear stress is at the stenosis zone and decreases rapidly in downstream. The effect of spiral flow is significant for turbulent kinetic energy. Detailed investigation and relevant pathological issues are delineated throughout the paper.

INTRODUCTION

At present, congenital and acquired cardiovascular diseases have become one of the most important causes of morbidity and mortality in the world. Among the acquired cardiovascular diseases, atherosclerosis is the most common. These diseases are often characterized by arterial stenosis. Arterial stenosis refers to the localized narrowing of arterial passages. This stenosed artery is responsible to reduce the maximum flow of blood by contributing more resistance to flow. It happens as a result of coagulation of calcium and fatty materials such as cholesterol and triglyceride. This deposition is named as plaque. Pressure, wall shear stress (WSS) and blood velocity, which are known as hemodynamic parameter, play a very important role in the localization of disease. In the worst cases plaque may rupture, causing the formation of thrombus cause of death of the tissues. This is the main reason for brain strokes or heart attack and sometimes causes inadequate blood flow in the lower part of the body. That's why, for both congenital and acquired cardiovascular diseases, a deep understanding of the altered blood flow conditions can enable the optimization of interventions employed to treat these conditions. In recent years, researchers are interested to simulate the blood flow by computational techniques in a model of three dimensional arteries. The hemodynamical characteristics of flow through stenosis have been continually investigated numerically and experimentally for single as well as multiple restrictions. An experimental investigation of pulsating flow through a smooth constriction was conducted by Ahmed¹. These experiments were conducted over physiologically relevant mean Reynolds number of 600 based on the tube diameter and the time-averaged value of upstream centerline velocity. A numerical investigation was carried out for laminar sinusoidal pulsating flow through a modeled arterial stenosis with a trapezoidal profile by Hasan and Das². Finite element based numerical technique was used to solve the fluid flow governing equations. The effects of pulsation, stenosis severity, Reynolds number and Womersley number on the flow behavior were studied. Investigation of physiological pulsatile flow in a model arterial stenosis using large-eddy and direct numerical simulations was done by Molla³. Physiological pulsatile flow in a 3D model of arterial stenosis was investigated by using large eddy simulation (LES) technique. The effect of spiral flow of blood was studied by Paul⁴. They investigated for 75% reduction in cross sectional area

by standard $k-\omega$ model for Reynolds number 500 and 1000 considering blood as a Newtonian fluid. A numerical simulation of unsteady blood flow through multi-irregular arterial stenosis was conducted by Mustapha ⁵. In current paper, effects of spiral flow in blood are numerically investigated by CFD analysis. Standard $k-\omega$ model is used to simulate the model. Blood is considered as a Non-Newtonian fluid and Reynolds number of 1000. Artery wall is assumed as rigid.

Nomenclature

- D : Artery diameter (m)
- ρ : Density (kg/m^3)
- μ : Dynamic viscosity (Ns/m^2)
- V : Stream wise bulk velocity (m/s)
- v : Instantaneous velocity (m/s)
- Ω : Spiral velocity (rad/sec)
- Re : Reynolds number
- R : Radius of blood vessel (m)
- r : Radial location from axis of artery (m)

PROBLEM FORMULATIONS

A 75%, axisymmetric three dimensional artery is considered here. A parabolic velocity profile with swirling flow is used as inlet boundary condition. The stenosis in the blood vessel is created by using cosine formulae. The total length of the model is taken as 540mm (27D) where diameter $D=20$ mm. The model is shown in Figure.1. Four different spiral velocities are used for investigation. The inlet boundary condition for the stream wise velocity and spiral speed are written in C-language using the interface of User Defined Function (UDF) of Fluent and linked with the solver.

Figures

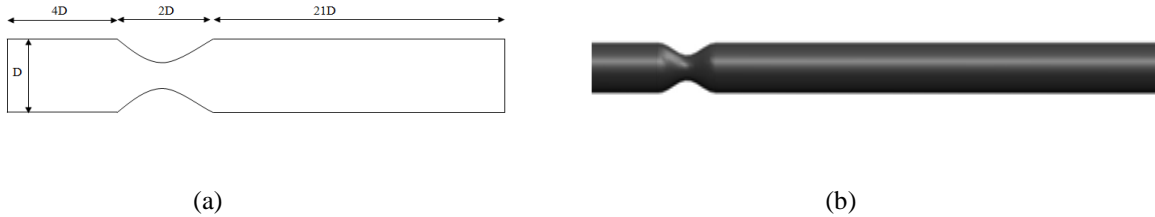


FIGURE 1. (a) 2D model of stenosed artery (b) 3D model of stenosed artery.

NUMERICAL METHOD

Governing equations

The most complete model, we have of the flow of fluid, is the Navier Stokes equations. These equations are nevertheless a model: they are not the physical truth. They represent the conservation laws. They are as follows.

1. Conservation of mass

$$\frac{\partial \rho}{\partial t} + \frac{\partial(\rho u)}{\partial x} + \frac{\partial(\rho v)}{\partial y} = 0 \quad (1)$$

2. Conservation of momentum

$$\frac{\partial(\rho u)}{\partial t} + \frac{\partial(\rho u^2)}{\partial x} + \frac{\partial(\rho uv)}{\partial y} = \frac{\partial \tau_{xx}}{\partial x} + \frac{\partial \tau_{xy}}{\partial y} \quad (2)$$

$$\frac{\partial(\rho v)}{\partial t} + \frac{\partial(\rho v^2)}{\partial x} + \frac{\partial(\rho uv)}{\partial y} = \frac{\partial \tau_{xy}}{\partial x} + \frac{\partial \tau_{yy}}{\partial y} \quad (3)$$

Discretization of the Domain

ANSYS FLUENT is used for the present computation. This CFD tool will solve the governing integral equations for the conservation of mass and momentum. The domain consists of 921416 cells, 2793268 faces and 951246 nodes. The geometry is created in solid works and imported in Ansys fluent. Quadrilateral cells were used for this simple geometry because they can be stretched easily to account for different flow gradients in different directions. The cells near the surface have high aspect ratios. For viscous flow through the stenosis, finely spaced grid was constructed to calculate the details of the flow near the wall. Three different mesh numbers are used for grid independent test.

Figure

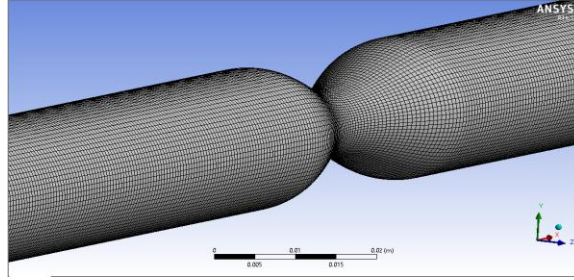


FIGURE 2. Discretization of the Domain using Fluent meshing tool.

Boundary Conditions

Inlet-flow: for the geometry, fully developed inlet-flow condition has been assumed as parabolic. The axial velocity distribution is given by,

$$v(x, y) = 2V \left[1 - \left(\frac{r}{R} \right)^2 \right] \quad (4)$$

Outlet-flow: In case of outlet boundary condition, the gauge pressure is assumed to be zero Pascal.

Wall: At all solid boundaries in the flow geometry, the no-slip condition has been used. It can be mathematically expressed as,

$$u_{wall} = 0, \text{ and } v_{wall} = 0 \quad (5)$$

Fluid Property

Fluid Material is blood, which is the working fluid in this problem. For this analysis blood is assumed as Non Newtonian fluid. Density and Viscosity have been taken as constant. Here, typical values of density, $\rho = 1060 \text{ kg/m}^3$

and viscosity, $\mu=0.00371$ N.s/m² are used to calculate velocity from the equation $Re = \rho V D/\mu$. There are several models used to solve Non Newtonian fluid problem in CFD. Carreau fluid model is used here to solve the problem.

Grid-Independence Test

Since numerical results are greatly depend on the mesh generation, a grid-independence test is performed to find out the optimum number of elements to discretize the computational domain. Wall static pressure and axial velocity at different position are used as comparing variables for grid independence test. Grid 1 consists of 921416 cells, Grid 2 consists of 578835 cells and Grid 3 consists of 1435082 cells.

Figures

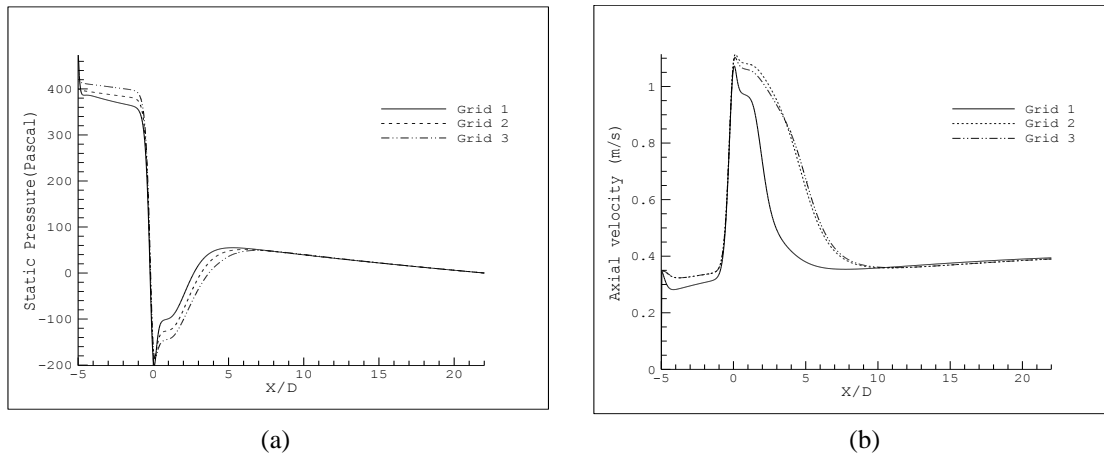


FIGURE 3. (a) Static pressure for different grids (b) Axial velocity for different grids.

Validation of results

Before going to the detailed discussion, the computational results have been validated to verify the results. The validation has been done by comparing computational results with the experimental results obtained by Ahmed and Giddens¹. Single stenosis with 75% severity model is considered for validation. Validation was done for steady inlet velocity condition. Velocity profiles in the post stenotic regions are compared for $Z= D, 2.5D$. Where Z is the normalized distance from the centre of the stenosis. From the comparison it can be shown that, axial velocity pattern are very much similar to the experimental pattern.

Figures

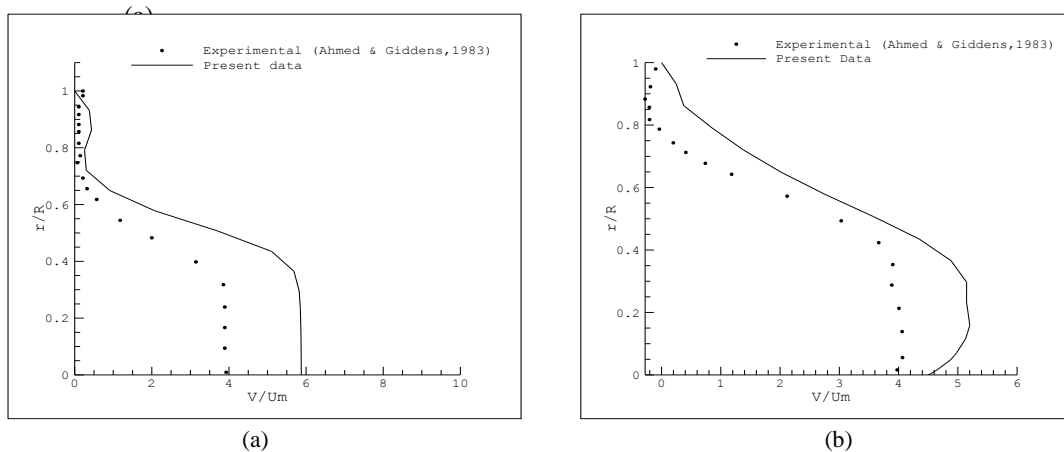


FIGURE 4. (a) Velocity profile comparison of the computational results with experimental Results at $Z=D$ (b) at $Z=2.5D$.

RESULTS AND DISCUSSION

CFD simulation is carried out to observe the effects of spiral flow of blood on different hemodynamic parameter. Figure. 5 show that Spiral flow has a great influence on tangential velocity only, but for axial and radial velocity, its effects are negligible. All velocity components get their maximum value just after stenosis, then gradually decreases to their initial value at downstream.

Figures

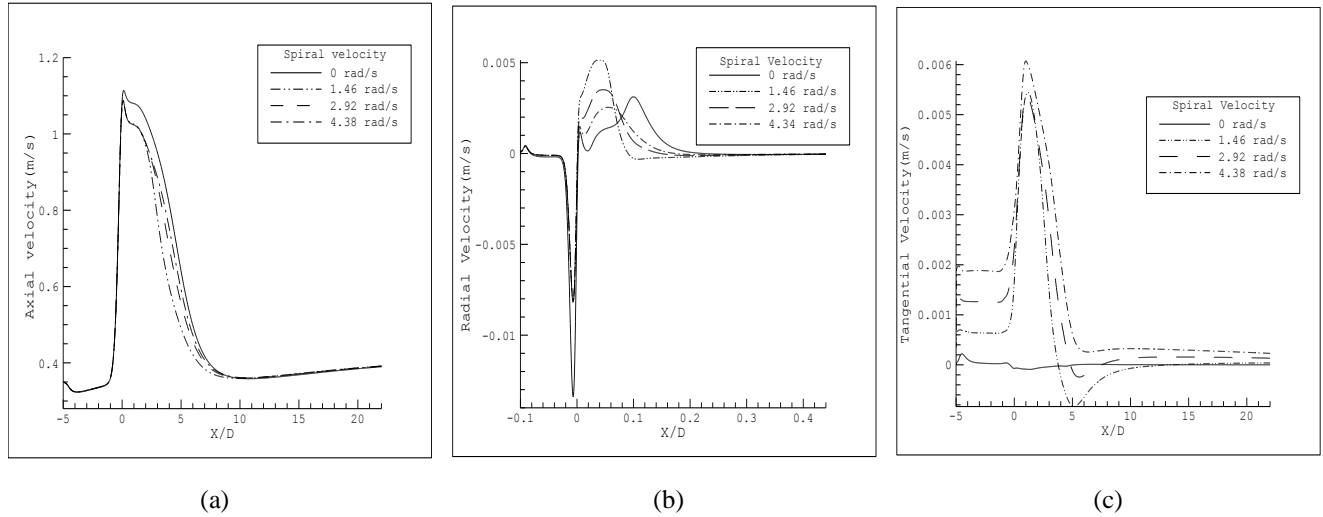
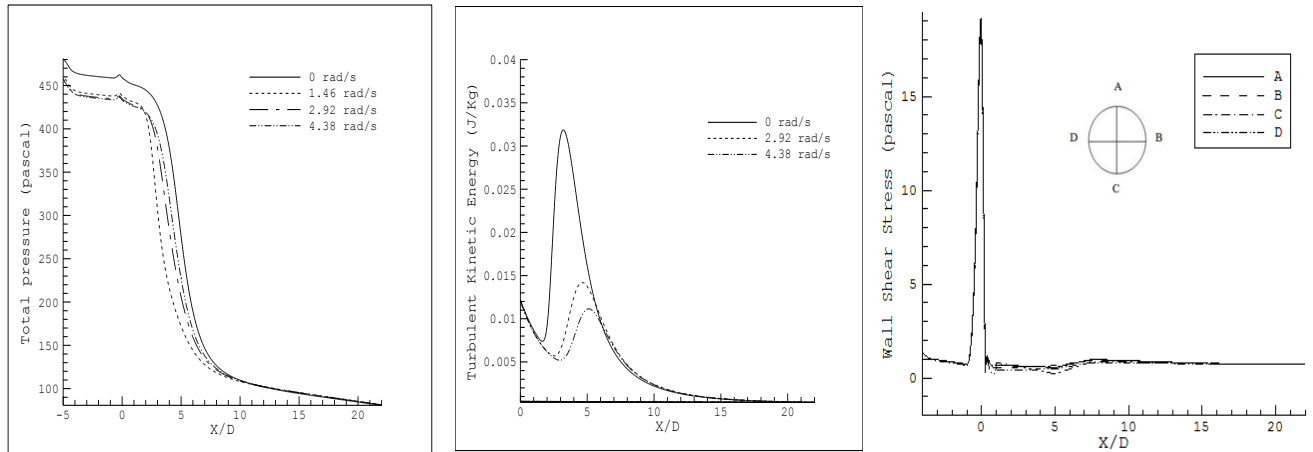


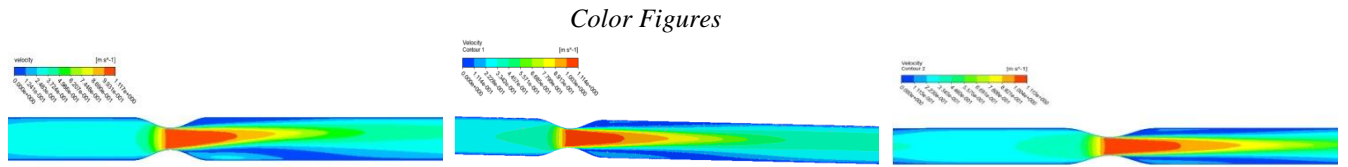
FIGURE 5. (a) Axial (b) Radial (c) Tangential velocity along the stenosed artery for different spiral speeds.

The centreline total pressure decreases drastically along the centreline of the stenosed artery. The spiral velocity has little effects on centreline total pressure. Turbulence kinetic energy (TKE) decreases with the increase of spiral speed. Wall shear stress (WSS) tends to rise at the centre of the stenosis. The reason for this rise of shear stress at the centre of the stenosis is the interaction of vortex with artery wall.

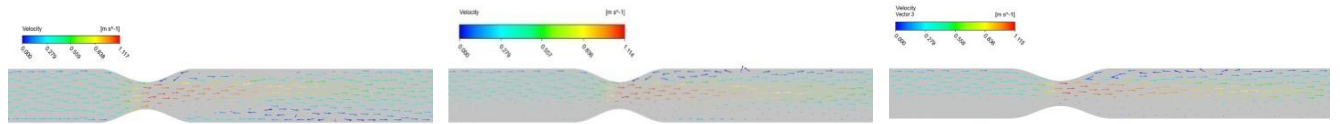
Figures



(a) (b) (c)
FIGURE 6. (a) Centreline total pressure (b) TKE (c) WSS along the length of stenosed artery for different spiral speeds.

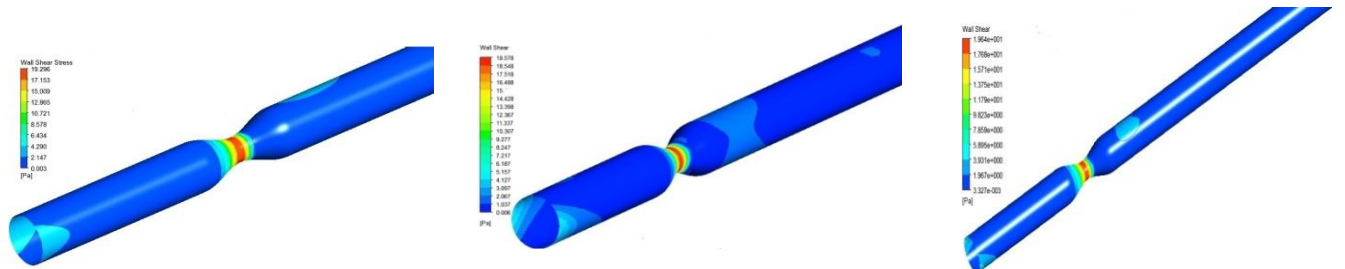


(a) (b) (c)
FIGURE 7. Contour plot for spiral speed (a) 0 rad/s (b) 2.92 rad/s (c) 4.38 rad/s.



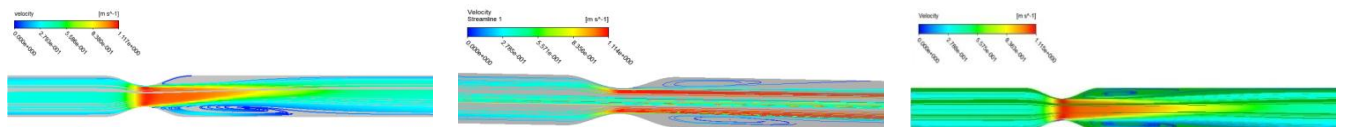
(a) (b) (c)

FIGURE 8. Velocity Vector for spiral speed (a) 0 rad/s (b) 2.92 rad/s (c) 4.38 rad/s.



(a) (b) (c)

FIGURE 9. Wall Shear Stress for spiral speed (a) 0 rad/s (b) 2.92 rad/s (c) 4.38 rad/s.



(a) (b) (c)

FIGURE 10. Stream Lines for spiral speed (a) 0 rad/s (b) 2.92 rad/s (c) 4.38 rad/s.

CONCLUSION

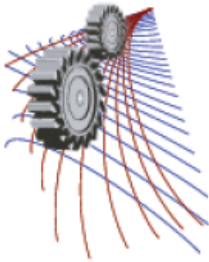
The spiral component of blood flow has both beneficial and detrimental effects in human circulatory system. The rise of the turbulent kinetic energy in the post-stenotic region is responsible to cause damage to the blood-cell materials and to activate platelets in the blood, and subsequently, they create many pathological diseases. However, the results show that the spiral effect reduces the turbulent kinetic energy, which is a beneficial effect. At the same time spiral flow produces oscillating wall shear stress in the post stenosis, which is a detrimental effect, as the oscillating shear stress usually influences to cause potential damage to the inner side of a post-stenotic blood vessel, known as endothelium. In addition, the strong circulation in the post-stenosis due to the spiral effect is harmful as it may cause the blood to be clotted in the post-stenosis, which is a potential source of stroke. As the spiral flow has potential clinical significance, therefore, the results have some significant impacts on the understanding of blood flow dynamics and its relevance in arterial diseases.

ACKNOWLEDGEMENTS

This work has been done using different facilities of the Department of Mechanical Engineering, Bangladesh University of Engineering and Technology (BUET).

REFERENCES

1. S. A. Ahmed and D. P. Giddens, *Journal of Biomechanical Engineering* **16**, 505-516 (1983).
2. A. B. M. T. Hasan and D. K. Das, *Journal of Applied Fluid Mechanics* **1**(2), 25-35 (2008).
3. M. C. Paul, M. M. Molla, and G. Roditi, *Medical Engineering & Physics* **31**, 153-159 (2009).
4. M. C. Paul and A. Larman, *Medical Engineering and Physics*, **31** (9). pp. 1195-1203. ISSN 1350-4533, 2009.
5. N. Mustapha, P. K. Mandal, P. R. Johnston, and N. Amin, *Applied Mathematical Modelling* **34**(6), 1559-1573 (2010).



CFD Study of Detailed Flow Field and Performance of Swirling Savonius Wind Turbine

Abdullah Al-Faruk^{1, 2, a)}, Ahmad Sharifian^{2, b)} and Andrew P. Wandel^{2, c)}

¹*Department of Mechanical Engineering, Khulna University of Engineering & Technology
Khulna 9203, Bangladesh*

²*Computational Engineering and Science Research Centre, University of Southern Queensland
Toowoomba 4350, Australia*

a)Corresponding author: alfaruk.bd@gmail.com, U1031944@usq.edu.au

b)sharifia@usq.edu.au

c)andrew.wandel@usq.edu.au

Abstract. A novel hybrid wind turbine (Swirling Savonius, SST) that combines the conventional Savonius turbine and the split channel capable of inducing swirling flow has been suggested. Previous works indicate a performance improvement in the SST compared to the conventional Savonius turbine. However, the lack of detailed descriptions of the flow field around the SST inhibits complete understanding of performance of the hybrid turbine. The aim of this study is to numerically explore the 3D unsteady flow field around the rotor, and develop a dynamic simulation method for predicting the aerodynamic coefficients using ANSYS-CFX. Simulations results were compared with the experimental results with a good accuracy. A discussion on the detailed flow field characteristics, including velocity vector, velocity streamlines, pressure distribution, vorticity analysis, and examination of power and torque coefficients behavior are presented.

INTRODUCTION

Wind power has now firmly established itself as the mainstream electrical generation option with the least cost when adding new capacity to the grid, and the price continues to fall [1]. Greenpeace predicted that wind power could reach nearly 2000 GW by 2030 supplying 16.7% to 18.8% of global electricity, helping save over 3 billion tons of CO₂ emissions annually [1]. Solar energy, on the other hand, covers a minor portion of global energy demands and generates less than 1% of the total electricity supply [2]. This is due to solar power being considered the most expensive type of renewable energy, although renewable sources may serve the best solution for decentralized energy supply for remote communities [3, 4]. However, the main challenge for stand-alone applications in remote regions is that the renewable energy sources are dependent on unpredictable factors such as weather and climatic conditions and may not match the load demand. The complementary nature of solar and wind energy can overcome the weaknesses of one through the strengths of the other. The hybrid renewable power generation with energy storage device may render the renewable energy sources more reliable and affordable means of generating electricity.

Among the wind turbines, Savonius wind turbine has many advantages over others such as simplicity in construction, self-starting and operating capability at low wind speed, and better visibility to animals, and free from harmful low frequency noise [5]. The Savonius turbines are popular for ventilation and pumping applications, but not employed for large scale power production projects because of low power coefficient (17% maximum) and slow running behavior [6]. Improving the power coefficient of the Savonius turbine can pave the way for using it for the local generation of electricity in rural environments where power is crucial for human development.

An innovative technique of performance improvement was proposed by combining the split channel mechanism with the primary Savonius wind turbine mechanism to a new hybrid design of Swirling Savonius turbine (SST) [7]. They proposed the hot air sourced from either solar thermal system or industrial waste heat as the heat source for the split channel. Split channels are capable of inducing swirling flow using hot air plume at the bottom of the channel

[8]. An increase in rotational speed and power coefficient of the SST compared to conventional Savonius turbine was reported [7]. Experimentally investigation on the geometrical parameters of the SST rotor confirmed a 25.5% increase in power coefficient compared to the optimum conventional Savonius turbine [5]. The SST rotor consists of two identical blades which are moved sideways and overlap like the conventional Savonius turbine as shown in Fig. 1. Unlike the conventional rotor of 180° blade arc angle, the inner tips of the blades extend further to construct the split channel which accommodate inside the turbine geometry [5]. A bottom hole acts as the hot air inlet of the swirling chamber, whereas, the top end plate provides an opening to the chamber.

(a) (b)

FIGURE 1. Schematic diagrams of (a) conventional and (b) Swirling Savonius turbines

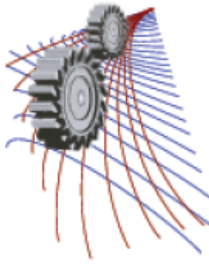
The lack of detailed descriptions of the flow field around the SST prevents complete understanding of working behavior of the turbine. To understand the combined mechanism of the hybrid rotor, a discussion on the detailed flow field characteristics, including the velocity vectors, velocity streamlines, pressure and temperature distributions, and vorticity analysis in the swirling chamber are required. In the present study, a computational fluid dynamics (CFD) model is developed using the finite volume based package of ANSYS-CFX 14.5 to explore the 3D unsteady flow pattern around the rotor, to understand the torque generation mechanism, and to analyze the performance of the hybrid turbine.

MODEL DEVELOPMENT

The geometry of SST rotor and the computational domains of the numerical modelling were developed using DesignModeler, a program of ANSYS Workbench. The rotor dimensions were chosen as the same as one of the experimental rotors which were 33.70 cm height and 31.05 cm diameter. The cylindrical domain had a diameter equivalent to 1.4 times of rotor diameter, so the diameter of the cylindrical rotating domain was 43.47 cm. The blades were 3 mm thick and the end plates were modelled as a circular disk of 4 mm thickness and diameter of 34.16 cm; 10% larger than the rotor diameter. The rotor aspect ratio, blade arc angle, and blade overlap ratio were 1.08, 195° and 0.25, respectively. The diameter of swirling chamber inlet and outlet were 25 mm and 100 mm, respectively.

To determine the domain size necessary to ensure that the boundary conditions had a minimal effect on the performance parameters, a series of domain size independence tests were performed. The dimensions of the computational domain were determined in multiples of the rotor diameter. Five different sized domains from five to fifteen times of rotor diameter ($5\times D$ to $15\times D$, see Fig. 2(a) for illustration) were simulated with the same numerical settings. The results showed that for the smallest domain ($5\times D$; 155 cm cross-stream width by 233 cm stream wise length), a considerable increase in torque coefficient was observed. However, the change in the maximum torque coefficient between the $7.5\times D$ domain and the $15\times D$ domain is less than 5%. The height of the calculation domain was determined by the rotor height as illustrated by Fig. 2(b). The convergence study demonstrates that the distance of top boundary from rotor top has negligible effects. The maximum values of the torque coefficient vary around 2% ranging from the domain height of $1.5\times H$ to $3\times H$ with the $10\times D$ domain.

ANSYS Meshing was used to discretize the computational domains which consist two parts: fixed and rotating. The sliding meshes were located in the circular region circumscribed by the interface as shown in Fig. 2. The rotating domain was constructed with an unstructured mesh to ensure a better adaption to the curved geometry of the blade



Finite Element Analysis of MHD Natural Convection in a Rectangular Cavity and Partially Heated Walls

Shahidul Alam^{1, b)}, M. A. Alim^{2, a)}, A. H. Bhuiyan²

¹*Department of Mathematics, Dhaka University of Engineering and Technology (DUET), Gazipur-1700, Bangladesh*

²*Department of Mathematics, Bangladesh University of Engineering and Technology (BUET), Dhaka- 1000, Bangladesh*

^bCorresponding author: a0alim@gmail.com

^ashdlalam@gmail.com

^bahalim.du@gmail.com

Abstract. In this paper a numerical study is presented of two-dimensional laminar steady-state on magneto-hydrodynamics (MHD) free convection for heat flow patterns within rectangular enclosures. A finite element analysis is performed to investigate the effects of uniform heating and is also used for solving the Navier-Stokes and Energy balance equations. The horizontal bottom wall is divided into three sections. The middle section of the horizontal bottom wall was kept temperature at T_h and the other two parts of the horizontal bottom wall were kept thermal insulation while the left and right vertical walls and the top wall of the cavity were maintained constant temperature T_c with $T_h > T_c$. Parametric studies of the fluid flow and heat transfer in the enclosure are performed for magnetic parameter Hartmann number ($Ha = 0, 50, 100$), Rayleigh number ($Ra = 10^3 - 10^6$) and Prandtl number $Pr=0.71$. The streamlines, isotherms, average Nusselt number at the hot wall and velocity profiles and temperature distribution of the fluid in the enclosure are presented for the parameters. The numerical results indicated that the Hartmann number and Rayleigh number have strong influence on the streamlines and isotherms. Also the mentioned parameters have significant effect on average Nusselt number at the hot wall and average temperature of the fluid in the enclosure.

INTRODUCTION

The basic problem of free convection in cavity has received considerable attention from researchers. Most of the cavities commonly used in industries are cylindrical, rectangular, square and triangular etc. Rectangular cavities have received a more considerable attention for its application in various fields. Tanmoy et al. [1] studied mixed convection flow within a square cavity with uniform and non-uniform heating of bottom wall. Lyican and Bayazitoglu [2] performed an analytical study of natural convective heat transfer within trapezoidal enclosure. Roy and Basak [3] studied natural convection flows in a square cavity with non-uniformly heated wall(s). Kuyper and Hoogendoorn [4] investigated Laminar natural convection flow in trapezoidal enclosures to study the influence of the inclination angle on the flow and the dependence of the average Nusselt numbers on the Rayleigh number. Varol et al. [5,6] recently studied magnetohydrodynamics (MHD) for various inclinations of trapezoidal enclosures filled with either fluid or porous medium on natural convection. Oztop et al. [7] investigated natural convection in wavy enclosures with volumetric heat sources. Kahveci and Öztuna [8] studied MHD natural convection flow and heat transfer in a laterally heated partitioned enclosure. Basak et al. [9] investigated energy flows due to natural convection within trapezoidal enclosures with hot bottom wall and cold side walls in the presence of insulated top walls. Luo and Yang [10] analyzed multiple fluid flow and heat transfer solutions in a two sided lid-driven cavity. Molla et al. [11] have studied problem

of magnetohydrodynamic natural convection flow on a sphere in presence of heat generation or absorption. Nithyadevi et al [12] using a numerical simulation on magnetohydrodynamic natural convection in a square cavity with partially heated cooled side walls. They found that the flow and the heat transfer rate in the cavity affected by the sinusoidal temperature profile and by the magnetic field at lower values of Grashof number. Moreover they found that the maximum rate of heat transfer occurs for the active portions located at the middle of the side walls. Mahmoodi and Talea'pour [13] investigated numerically magnetohydrodynamic free convection in a square cavity with hot left wall, cold top wall and insulated right and bottom wall. They found that a clockwise primary eddy inside the cavity regardless the Rayleigh number and Hartman number. Also they found that the magnetic field decrease the intensity of free convection and flow velocity. Recently Hasanuzzaman et al. [14] investigated Magnetohydrodynamic natural convection in trapezoidal cavities.

In the light of the above literature review and to the best of authors' knowledge there is no published articles which have addressed natural convection in a rectangular cavity in presence of magnetic field with partially heated walls. So, the purpose of the present study is to investigate the effects of MHD on natural convection in a rectangular cavity and partially heated walls numerically. The results are presented in terms of streamlines and isotherms inside the cavity, vertical component of the velocity along the horizontal centerline of the cavity, local Nusselt number along the hot wall, and average Nusselt number of the hot wall.

PHYSICAL MODEL

Geometry of the rectangular cavity with boundary conditions considered in the present paper is shown in Fig. 1. The height and length of the cavity are denoted H and L respectively. The middle section of the horizontal bottom wall was kept temperature at T_H and the other two parts of the horizontal bottom wall were kept thermal insulation while the left and right side and the top walls of the cavity were maintained constant temperature T_C with $T_H > T_C$.

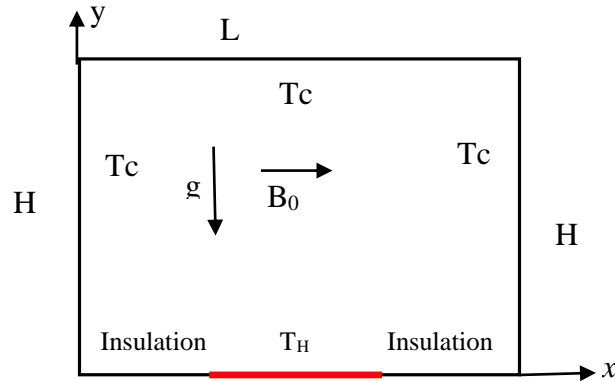


FIGURE 1. Schematic view of the cavity with boundary conditions considered in the present paper

MATHEMATICAL FORMULATION

The continuity, momentum and energy equations for laminar, steady state, two-dimensional free convection with a magnetic field in x-direction, in non-dimension are as follows:

$$\frac{\partial U}{\partial X} + \frac{\partial V}{\partial Y} = 0 \quad (1)$$

$$U \frac{\partial U}{\partial X} + V \frac{\partial U}{\partial Y} = -\frac{\partial P}{\partial X} + \text{Pr} \left(\frac{\partial^2 U}{\partial X^2} + \frac{\partial^2 U}{\partial Y^2} \right) \quad (2)$$

$$\rho \left(\frac{\partial V}{\partial X} + \frac{\partial V}{\partial Y} \right) = -\frac{\partial P}{\partial Y} + \mu \left(\frac{\partial^2 V}{\partial X^2} + \frac{\partial^2 V}{\partial Y^2} \right) + Ra Pr \theta - Ha^2 Pr V \quad (3)$$

$$U \frac{\partial \theta}{\partial X} + V \frac{\partial \theta}{\partial Y} = \left(\frac{\partial^2 \theta}{\partial X^2} + \frac{\partial^2 \theta}{\partial Y^2} \right) \quad (4)$$

Where Ra , Pr and Ha are the Rayleigh, Prandtl and Hartman numbers and are defined as:

$$Ra = \frac{g\beta(T_h - T_c)L^3}{\alpha\nu}, Pr = \frac{\nu}{\alpha}, Ha = B_0L\sqrt{\frac{\sigma}{\rho\nu}} \quad (5)$$

The effect of magnetic field into the momentum equation is introduced through the Lorentz force term $\vec{j} \times \vec{B}$ that is reduced to $-\sigma B_0 v^2$.

To computation of the rate of heat transfer, Nusselt number along the hot wall of the enclosure is used that is as follows:

$$Nu_y = \frac{\frac{\partial \theta}{\partial x}|_{x=0}}{(\theta_h - \theta_c)} Nu = \int_0^1 Nu_y dY \quad (6)$$

The boundary conditions are:

On the left wall of the square cavity: $U = 0, V = 0, \theta = 1$ and right wall of the cavity: $U = 0, V = 0, \theta = 0$

On the heated elliptic block: $U = 0, V = 0, \theta = 1$

NUMERICAL ADVANCE

Partial differential equations governing the flow and temperature field are solved by using finite element method. The quadratic triangular element is used to develop the finite element equations. For the velocities and temperature all the six nodes are used and for the pressure only the corner nodes are used. Different types of grid densities have been selected to assess the accuracy of the numerical simulation procedure. The nonlinear algebraic equations arising from the finite element formulation are solved by applying the Newton-Raphson iteration technique. Validation of the code was done by comparing streamlines and isotherms with results shown in Fig. 2 by Hasanuzzaman et al. [14]. As can be observed from the figure, very good agreement exists between the two results

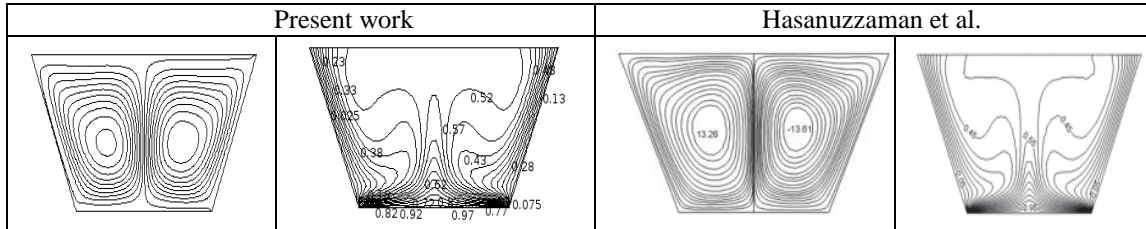


FIGURE 2. Comparison of streamlines and isotherms for $Ha=10$ and $Ra=10^6$

RESULT AND DISCUSSION

In this section, results of the numerical study on magnetohydrodynamic free convection fluid flow and heat transfer in a rectangle cavity field with an electric conductive fluid with $Pr = 0.71$ are presented. The results have been obtained for the Rayleigh number ranging from 10^3 to 10^6 and the Hartman number varying from 0 to 100. The results are presented in terms of streamlines and isotherms inside the cavity, the vertical velocity component along the horizontal midline of the cavity, the local Nusselt number along the hot wall. Variation of streamlines and isotherms inside the cavity with Rayleigh number and Hartman number are shown in Fig. 3 and 4 respectively. As can be observed from the figures with existence of symmetrical boundary conditions about the vertical centerline of the cavity, the flow and temperature fields are symmetrical about this line. As can be seen from the streamlines in the Fig. 3, a pair of counter-rotating eddies are formed in the left and right half of the cavity for all Rayleigh number and Hartman numbers considered. Each cell ascends through the symmetry axis, then faces the upper wall and moves horizontally and finally descends along the corresponding cold side wall. Condition dominant heat transfer is observed from the isotherms in

Fig. 4 at $Ra = 10^3$ and $Ha = 0$. With increase in Rayleigh number, the isotherms are condensed next to the side walls which mean increasing heat transfer through convection. Formation of thermal boundary layers can be found from the isotherms at $Ra = 10^5$ and 10^6 and at $Ha = 0$. At $Ha = 100$ the shape of the core of eddies converts to isosceles triangle and locates close to the hot bottom wall.

Variation of the vertical velocity component along the horizontal centerline of the cavity with the Rayleigh number and for $Ha = 0$ are shown in Fig. 5(a). It can be seen from the figure that the absolute value of maximum and minimum value of velocity increases with increasing the Rayleigh number (increasing the buoyant force). Effect of Hartman number on vertical component of the velocity along the horizontal midline of the cavity at $Ra = 10^6$ is shown in Fig. 5(b). As can be seen from the figure with increase in Hartman number motivates the flow velocity to decreases. A very slow fluid velocity occurs at $Ha = 100$. It is found that free convection heat transfer decreases with increase in fluid velocity via increasing the Hartman number.

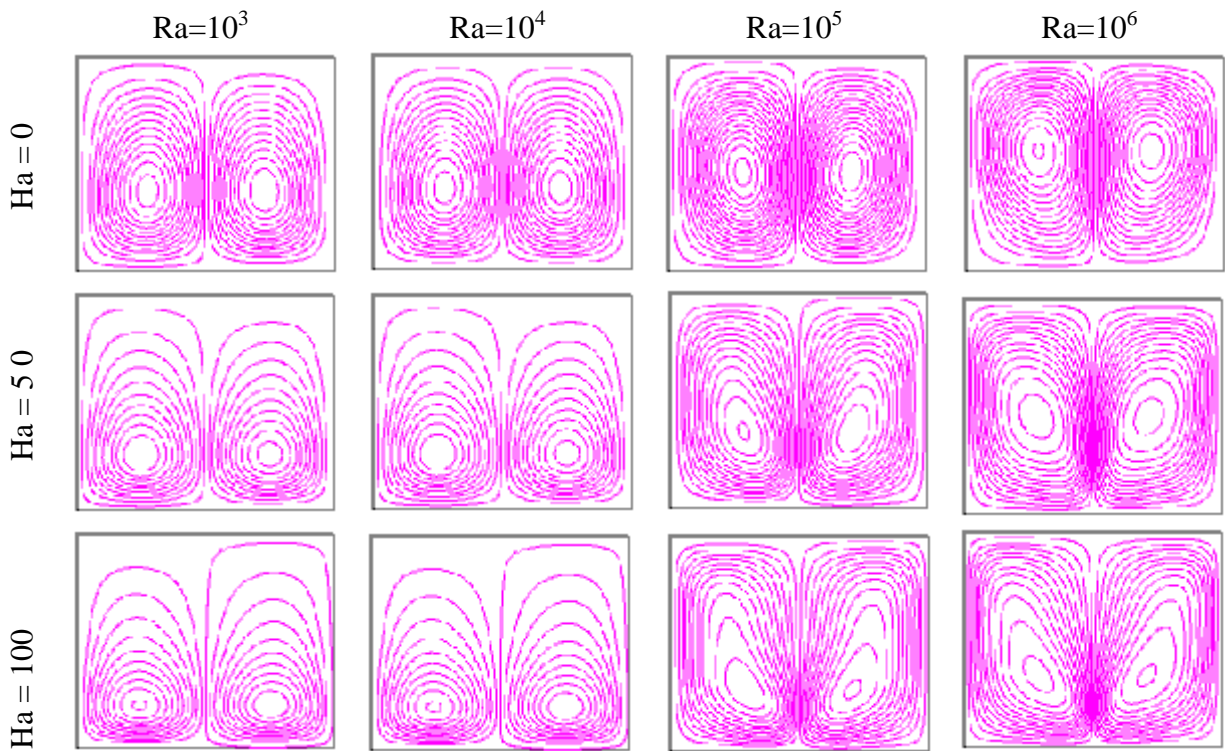


FIGURE 3. Streamlines at different Rayleigh numbers and Hartman numbers.

At $Ha = 100$ the shape of the core of eddies converts to isosceles triangle and locates close to the hot bottom wall. Variation of the vertical velocity component along the horizontal centerline of the cavity with the Rayleigh number and for $Ha = 0$ are shown in Fig. 5a. It can be seen from the figure that the absolute value of maximum and minimum value of velocity increases with increasing the Rayleigh number (increasing the buoyant force). Effect of Hartman number on vertical component of the velocity along the horizontal midline of the cavity at $Ra = 10^6$ is shown in Fig. 5b. As can be seen from the figure with increase in Hartman number motivates the flow velocity to decreases. A very slow fluid velocity occurs at $Ha = 100$. It is found that free convection heat transfer decreases with increase in fluid velocity via increasing the Hartman numbers.

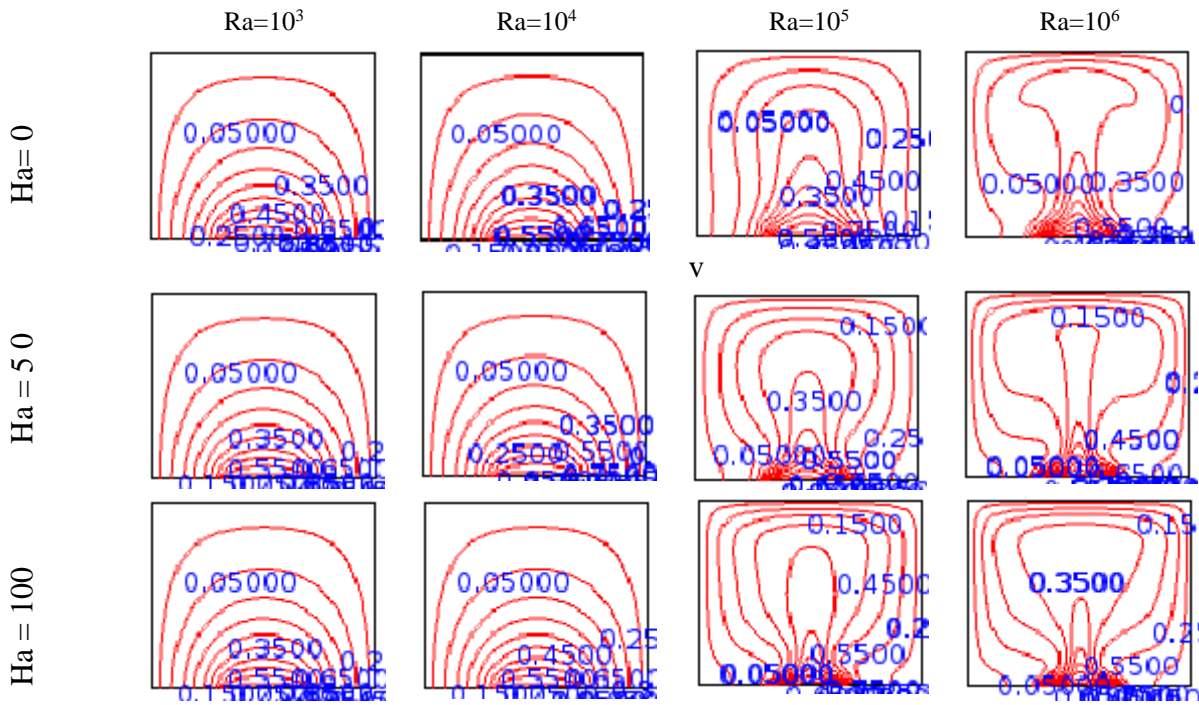


FIGURE 4. Isotherms at different Rayleigh numbers and Hartman numbers.

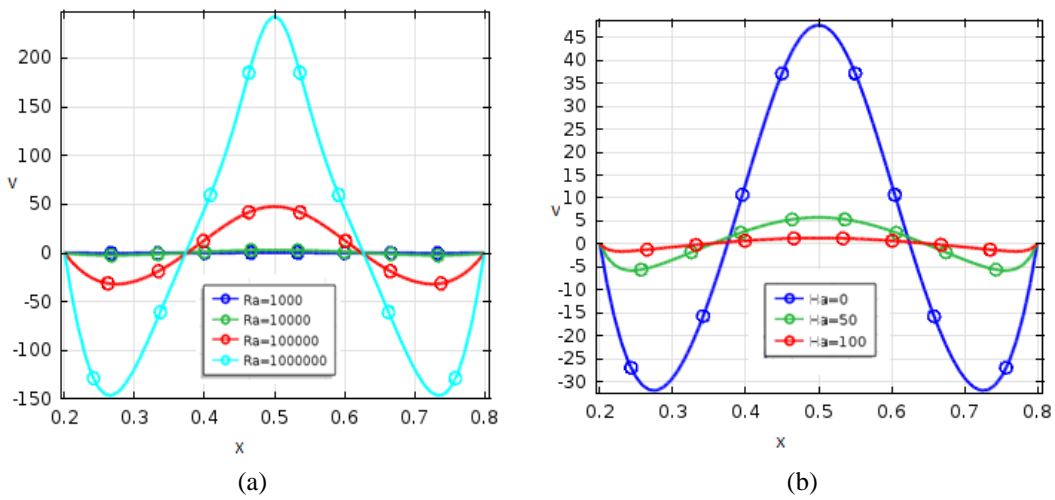


FIGURE 5. Variation of vertical velocity component along the horizontal central line of the cavity (a) with Rayleigh number at $Ha = 0$. (b) with Hartman number at $Ra = 10^6$.

CONCLUSIONS

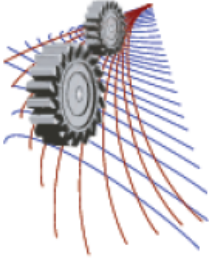
Using a numerical simulation based on the finite element method, the Magnetohydrodynamic free convection fluid flow and heat transfer in a rectangle cavity heated from below and cooled from vertical walls filled with an electric

conductive fluid with Prandtl number of 0.71 was studied numerically. The numerical procedure was validated by comparing the average Nusselt number for a differentially-heated rectangle enclosure obtained by the code with the existing results in the literature. Very good agreements were observed between them. Subsequently, a parametric study was performed and the effects of Rayleigh number and the Hartman number on the fluid flow and heat transfer were investigated.

For all cases considered, two counter rotating eddies were formed inside the cavity regardless the Rayleigh and the Hartman number. The obtained result showed that the heat transfer mechanism, temperature distribution and the flow characteristics inside the cavity depended strongly upon both the strength of the magnetic field and the Rayleigh number. Also it was found that using the longitudinal magnetic field results in a force (Lorentz force) opposite to the flow direction that tends to decrease the flow velocity. Moreover, it was observed that, for low Rayleigh number, by increase in the Hartman number, free convection is suppressed and heat transfer occurs through conduction mainly.

REFERENCES

1. T. Basak, S. Roy, P. K. Sharma and I. Pop, *International Journal of Thermal Science* **48**, 891-912 (2009).
2. L. Lyican and Y. Bayazitoglu, *ASME Trans. J. Heat transfer* **102**, 640-647 (1980).
3. S. Roy and T. Basak, *Int. J. Engrg. Science* **45**, 668-680(2005).
4. R. A. Kuyper and C.J. Hoogendoorn, *Num. Heat transfer,A* **28**, 55 – 67 (1995).
5. Y. Varol, H. F. Oztop and I. Pop, *Int. J. Thermal Science* **47(10)**, 1316-1331 (2008).
6. Y. Varol, H.F. Oztop and I. Pop, *International Communications in Heat and Mass Transfer* **36**, 6-15 (2009).
7. Hakan F. Oztop, Eiyad Abu-Nada, Y. Varol and Ali Chamkha, *Int. J. Thermal Science* **50**, 502-514 (2011).
8. K. Kahveci and S. Öztuna, *European Journal of Mechanics - B/Fluids* **28(6)**, 744-752 (2009).
9. T. Basak, S. Roy and I. Pop, *Int.J. Heat Mass Transfer* **52**, 2471-2483, (2009).
10. W. J. Luo and R. -J. Yang, *Int. J. of Heat and Mass Transfer* **50**, 2394-2405 (2007).
11. M. M. Molla, M. A. Taher, Md. M. K.Chowdhury and M. A. Hossain, *Nonlinear Analysis: Modelling and Control* **10(4)**, 349-363 (2005).
12. Nithyadevi, P. Kandaswamy, S. Malliga Sundari, *Int. J. Heat Mass Tran.* **52**, 1945– 195 (2009).
13. M. Mahmoodi, Z. Talea'pour, *Computational Thermal Sciences* **3**, 219-226 (2011).
14. M. Hasanuzzaman, Hakan F. Özttop, M.M. Rahman, N.A. Rahim, R. Saidur, Y. Varol, *International Communications in Heat and Mass Transfer* **39**, 1384–1394 (2012).



Symmetric To Asymmetric Transition of Transitional Plane Fountains in Linearly Stratified Fluids

Mohammad Ilias Inam^{1, a)}, Wenxian Lin^{1, 2}, S.W. Armfield³ and Yinghe He¹

¹ College of Science, Technology & Engineering, James Cook University, Townsville QLD 4811, Australia

²Solar Energy Research Institute, Yunnan Normal University, Kunming, Yunnan 650092, China

³School of Aerospace, Mechanical & Mechatronic Engineering, The University of Sydney, NSW 2006, Australia

^{a)}Corresponding author: mohammadilias.inam@my.jcu.edu.au

Abstract. The onset of asymmetry and entrainment in transitional fountains is a key for the understanding of turbulence generation and entrainment mechanisms in fountains. The symmetric to asymmetric transition is governed by the Reynolds number (Re) and the Froude number (Fr), plus the dimensionless temperature stratification parameter (s), if the ambient fluid is stratified. In this study, a series of three-dimensional direct numerical simulations (DNS) were carried out using ANSYS Fluent 13 for transitional plane fountains in linearly-stratified fluids with Re , Fr and s varying over the ranges $9 \leq Re \leq 100$, $2 \leq Fr \leq 10$, and $0.1 \leq s \leq 0.7$ to demonstrate the onset of asymmetry in plane fountains and the critical conditions for the asymmetric transition. The results show that a larger Fr or Re value will lead to an earlier asymmetric transition and a stronger asymmetric behaviour at the fully developed stage, whereas on the contrary the stratification (s) stabilizes the flow and delays the asymmetric transition, resulting in higher critical Fr and Re values for the asymmetric transition when s increases. It is further found that when s is constant, the critical Re value for the asymmetric transition decreases up to $Fr = 7$ and beyond that it becomes independent of Fr .

INTRODUCTION

Fountains are common in numerous industrial and environmental settings, such as natural ventilation, volcanic eruptions, cumulus clouds, reverse cycle air-conditioning, to name just a few. A fountain forms when a dense fluid is injected vertically upward into a less dense fluid. The injected fluid will experience a negative buoyancy force due to the density difference between the injected fluid and the ambient fluid. The momentum of the injected fluid will gradually reduce until the fountain attains the maximum penetration height. Subsequently, it will reverse the flow direction and flow back around the core of the upward flow and an intrusion will form on the bottom surface which moves outward.

When ejected into a homogeneous ambient fluid, the behavior of a fountain is governed by the Reynolds number, Re , and the Froude number, Fr , defined as follows,

$$Re = \frac{W_0 X_0}{\nu}, \quad Fr = \frac{W_0}{\sqrt{g X_0 (\rho_0 - \rho_a) / \rho_0}} = \frac{W_0}{\sqrt{g X_0 \beta (T_a - T_0)}} \quad (1)$$

where X_0 is the radius of the orifice for a round fountain or the half-width of the slot for a plane fountain at the fountain source, W_0 is the average inlet velocity of the injected fluid at the source, g is the gravitational acceleration, ρ_0 , T_0 and ρ_a , T_a are the densities and temperatures of the injected fluid at the fountain source and the ambient fluid, and ν and β are the kinematic viscosity and the coefficient of volumetric expansion of the fluid, respectively. The second expression for Fr is valid when the Oberbeck-Boussinesq approximation is valid.

Fountains injected into a linearly stratified ambient fluid are also governed by the stratification of the ambient fluid, which is quantified by a dimensionless temperature stratification parameter, s , which is defined as follows if the Oberbeck-Boussinesq approximation is valid,

$$s = \frac{d\theta_{a,z}}{dz} \quad (2)$$

where $\theta_{a,z} = (T_{a,z} - T_{a,0}) / (T_{a,0} - T_0)$ and $z = Z/X_0$ are the dimensionless temperature of the ambient fluid at height Z (Z is the coordinate in the vertical direction as sketched in Fig. 1) and the dimensionless height, $T_{a,z}$ and $T_{a,0}$ are the temperatures of the ambient fluid at height Z and at the bottom. The gravity is acting in the negative Z direction.

Numerous studies have been done on both round and plane fountains in homogeneous or stratified ambient fluids, although the majority of them have focused on the maximum fountain penetration height. The readers are referred to a recent review by Hunt & Burridge [1] for some details of the progress. Nevertheless, it is strongly believed that the understating of the onset of asymmetry, unsteadiness and entrainment in fountains, which is currently lacking, is the key to elucidate the mechanisms for the transition to turbulence and entrainment in fountains. Lin & Armfield [2] studied the behaviour of transitional round fountains in homogeneous fluids over the ranges $1 \leq Fr \leq 8$ and $200 \leq Re \leq 800$ with direct numerical simulations (DNS) and their results show that Re has a stronger influence on entrainment than Fr does. The DNS results by Williamson *et al.* [3] for weak turbulent round fountains in homogeneous ambient fluids over the ranges $20 \leq Re \leq 3494$ and $0.1 \leq Fr \leq 2.1$ demonstrate that there is a continuum of behaviour over this transitional Fr range, from hydraulically driven buoyancy controlled flow to momentum ruled flow. Gao *et al.* [4] studied the onset of asymmetry and three-dimensionality of transitional round fountains in linearly stratified fluids over the ranges $1 \leq Fr \leq 8$ and $100 \leq Re \leq 500$ at $s = 0.03$ using three-dimensional DNS results, and showed that a critical Re exists between 100 and 200 for round fountains at $Fr = 2$ for the symmetric to asymmetric transition and similarly a critical Fr exists between 1 and 2 for round fountains at $Re = 200$ for the symmetric to asymmetric transition. Nevertheless, both [3] and [4] revised only round transitional fountains at relatively small Fr values. Recently, Inam *et al.* [5] reported the asymmetric behaviour of plane fountains over the ranges $25 \leq Re \leq 300$ and $0.1 \leq s \leq 0.5$ at fixed $Fr = 10$ using three dimensional DNS results. Their results show that those plane fountains maintain symmetry during the early developing stage and Re plays a positive role to destabilize the flow whereas on the contrary s plays a positive role to stabilize the flow. They also found that asymmetric transition occurs earlier at a higher Re , whereas on the opposite the increase of s delays the onset of the asymmetry. In this study, the work by Inam *et al.* [5] is extended to transitional plane fountains over the range at $9 \leq Re \leq 100$, $2 \leq Fr \leq 6$, and $0.2 \leq s \leq 0.7$, with the focus on the critical conditions for the symmetric to asymmetric transition in transitional plane fountains in linearly stratified fluids.

NUMERICAL METHODS

The physical model and the computational domain under consideration is a rectangular container with dimensions $H \times B \times L$ (Height \times Width \times Length), as sketched in Fig. 1. Initially the domain is filled by a stationary linearly stratified Newtonian fluid (water) with a constant temperature gradient $dT_{a,z}/dZ$. At the bottom floor centre, along the Y direction, a narrow slot with width $2X_0$ serves as the source for plane fountains. The remainder of the bottom floor is assumed to be rigid, non-slip and adiabatic. The two vertical surfaces at $Y = \pm B/2$ in the X - Z plane are assumed to be periodic whereas the two vertical surfaces at $X = \pm L/2$ in the Y - Z plan are assumed to be outflows. The top surface is also assumed to be a wall. At time $t = 0$, a fluid with temperature of T_0 ($T_0 < T_{a,0}$) is injected upward from the fountain source with uniform velocity W_0 into the domain to initiate the plane fountain flow, which is maintained during the whole course of the DNS run.

The governing equations for the flows are the Navier-Stokes and temperature equations. With the assumptions of incompressible flow and the Oberbeck-Boussinesq approximation, these three-dimensional equations were discretized on a non-uniform rectangular mesh using the finite volume method. The viscous and diffusion terms were discretized with the 2nd-order central difference scheme and the QUICK scheme was used for the advection terms. The time integration of the advective and diffusive terms was implemented by the 2nd-order Adams-Bashforth and Crank-Nicolson schemes, respectively. A PRESTO (PREssure STaggering Option) scheme was used for the pressure gradient. For all DNS runs, X_0 was fixed at 0.002 m and $T_{a,0}$ was fixed at 300 K, whereas T_0 and W_0 varied based on the targeted Re and Fr values, respectively, for all simulations. ANSYS Fluent 13 was used to for all these three-dimensional DNS runs. The domain has the dimensions $H \times B \times L = 0.2 \text{ m} \times 0.05 \text{ m} \times 1.5 \text{ m}$, which was found to be sufficiently large to minimize the effect of the outflow and periodic boundary conditions on the region of the main interest of this study. In the regions of $-25 \leq X/X_0 \leq 25$, $0 \leq Z/X_0 \leq 50$ and $-25 \leq Y/X_0 \leq 25$, a finer rectangular mesh was used as velocity and temperature have larger gradients in these regions, whereas in the

remaining regions where temperature and velocity gradients are very small, a coarser non-uniform rectangular mesh with varied expansion ratios was used. After a thorough mesh and time step independence test, it was found that the mesh with 2.12 million grids and the time step of 0.025 s were appropriate and thus chosen for all DNS runs.

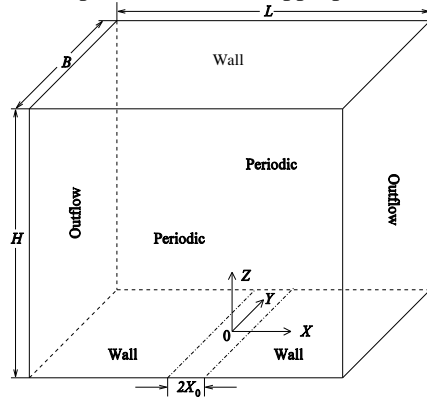


FIGURE 1. Sketch of the computational domain under consideration and the boundary conditions.

RESULTS AND DISCUSSION

Typical evaluation of fountain flow

A plane fountain can be asymmetric in both the X and Y directions. Theoretically if a plane fountain maintains the symmetry with respect to $X = 0$ in the Y - Z plane (also referred to being symmetric in the X direction), U must be zero or negligible (due to inevitable numerical errors in DNS) over the whole plane at $X = 0$ in the Y - Z plane. Any non-zero value of U at $X=0$ in the Y - Z plane will indicate that the flow is asymmetric in the X direction. Similarly, V must be zero or negligible everywhere at $X = 0$ in the Y - Z plane if the fountain maintains symmetry along the Y direction, and any non-zero value of V on that plane will indicate that the asymmetric behaviour occurs along the Y direction.

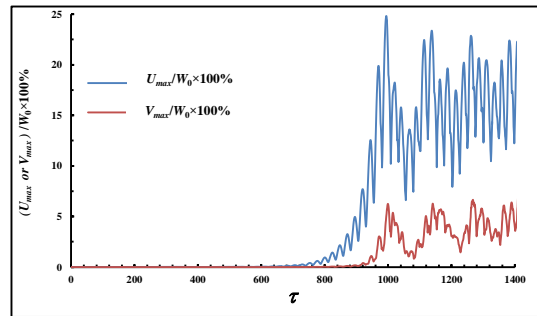


FIGURE 2. Time series of U_{max}/W_0 (%) and V_{max}/W_0 (%) at $X = 0$ in the Y - Z plane of the plane fountain with $Fr = 3$, $Re = 100$ and $s = 0.1$.

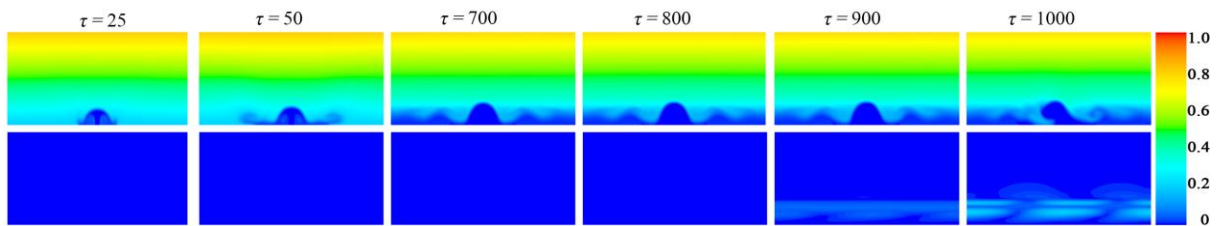


FIGURE 3. Snapshots of transient contours of temperature (first row) and U (second row) of the plane fountain with $Fr = 3$, $Re = 100$ and $s = 0.1$ at $Y=0$ in the X - Z plane. The temperature and velocity were normalized by $[T(Z)-T_0]/(T_{a,Z=100X_0}-T_0)$ and U_{max}/W_0 , respectively, and the time was made dimensionless by $\tau=t/(X_0/W_0)$.

The onset of asymmetry in the X and Y directions is demonstrated quantitatively, as an example, in Fig. 2 for a plane fountain with $Fr = 3$, $Re = 100$ and $s = 0.1$ with the time series of U_{max}/W_0 and V_{max}/W_0 , both in percentage, where U_{max} and V_{max} are the maximum velocities of U and V at $X = 0$ in the Y - Z plane, respectively. From this figure, it is observed both U_{max}/W_0 and V_{max}/W_0 are essentially zero at the early developing stage, until τ equals to about 800 and 935, respectively. This indicates that the fountain is initially symmetric in both the X and Y directions, but subsequently becomes asymmetric in both directions. It is also observed that the onset of asymmetry in the X direction occurs earlier than that in the Y direction. These behaviour features can also be shown by the transient contours of temperature and U at $Y=0$ in the X - Z plane, as presented in Fig. 3. The figure shows that a significant asymmetric feature is observed from the normalize temperature contour at $\tau \sim 1000$, while the contours of U show that until τ equals 800 the value of U/W_0 is almost zero, confirming the symmetric flow during the initial stage of the flow and the subsequent asymmetric behavior. This behaviour is also observed for other plane fountains considered in this study. To distinguish the symmetric behaviour from the asymmetric behaviour, it is assumed in this paper that a flow is symmetric whenever the value of U_{max}/W_0 on $X=0$ in the Y - Z plane is less than 0.5% during the whole DNS run and is asymmetric when U_{max}/W_0 is 0.5% or higher.

Effect of Fr on asymmetric behavior

Figure 4 presents the normalized contours of temperature and U at fully developed stage for different Fr in the range of $2.875 \leq Fr \leq 6$, all at $Re = 100$ and $s = 0.1$. It is clear from the first column that the plane fountain at $Fr = 2.875$ maintains symmetry throughout the whole DNS run but the fountains with $Fr \geq 03$ become asymmetric. This implies that there is a critical Fr between 2.875 and 3 for the transition from the symmetric behaviour to the asymmetric behaviour, at $Re = 100$ and $s = 0.1$. Another noticeable observation is that the extent of asymmetry increases with Fr . A more evident demonstration of the asymmetric behaviour at different Fr is clearly exhibited in Fig. 5, where the time series of U_{max}/W_0 at $X=0$ in the Y - Z plane for the plane fountains corresponding to those in Fig. 4 are presented. The figure clearly shows that the flows are symmetric at the early stages for all Fr values, but significant values of U_{max}/W_0 are observed at the lateral stages when $Fr \geq 3$. The results also show that in general the onset of asymmetry occurs earlier when Fr is increased.

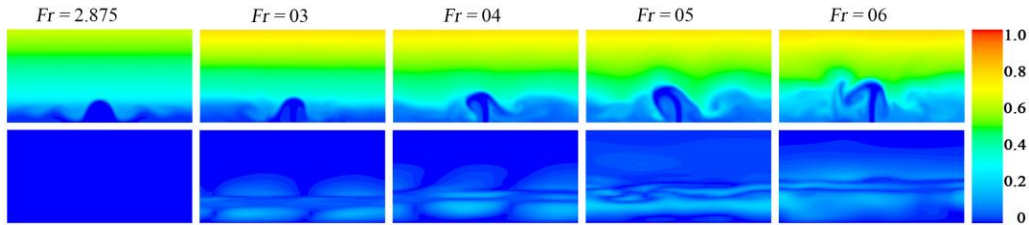


FIGURE 4. Contours of normalized temperature (first row) and U (second row) of plane fountains at the fully developed stage for different Fr in the range of $2.875 \leq Fr \leq 6$, all at $Re = 100$ and $s = 0.1$.

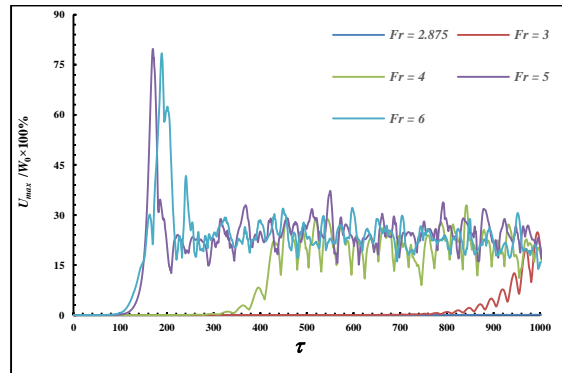


FIGURE 5. Time series of U_{max}/W_0 at $X=0$ in the Y - Z plane for plane fountains at different Fr in the range of $2.875 \leq Fr \leq 6$, all at $Re = 100$ and $s = 0.1$.

Effect of Re on asymmetric behavior

Figure 6 presents the normalized contours of temperature and U at fully developed stage for different Re in the range of $28 \leq Re \leq 100$, all at $Fr = 5$ and $s = 0.1$. The plane fountain at $Re = 28$ is found to maintain symmetry during the whole DNS run, as can be seen from the corresponding temperature and velocity contours. The plane fountains at $Re \geq 30$ become asymmetry at the fully developed stage, clearly indicating that a critical Re exists between 28 and 30 for the transition from the symmetric behaviour to the asymmetric behaviour when Fr and s are fixed at $Fr = 5$ and $s = 0.1$. It is also observed that the extent of asymmetric behaviour is higher at a higher Re . The effect of Re on the symmetric-to-asymmetric transition and the asymmetric behaviour is also clearly demonstrated by the time series of U_{max}/W_0 at $X=0$ in the Y - Z plane for these fountains, as shown in Fig. 7, where it is observed that all plane fountains remain symmetric during the early stage, but subsequently become asymmetric when Re is beyond 28. It is also observed that whereas asymmetry delays at lower Re conditions and becomes symmetry at Re equal to 28. The results also show that the onset of asymmetry occurs earlier when Re is increased.

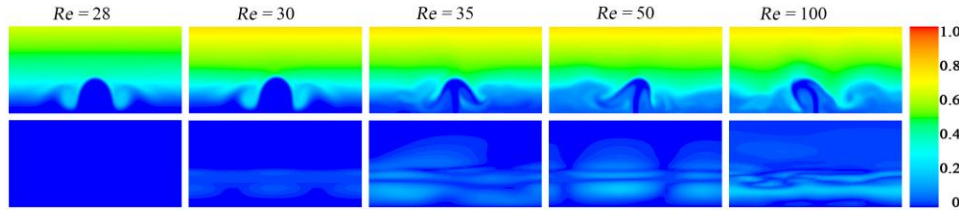


FIGURE 6. Contours of normalized temperature (first row) and U (second row) of plane fountains at the fully developed stage for different Re in the range of $28 \leq Re \leq 100$, all at $Fr = 5$ and $s = 0.1$.

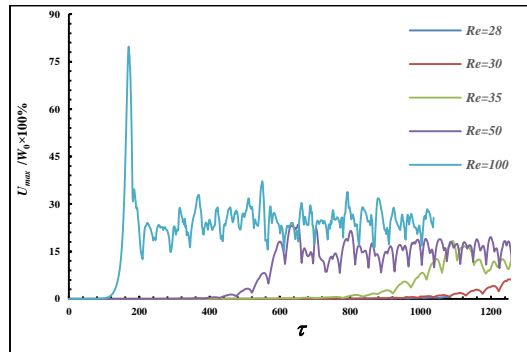


FIGURE 7. Time series of U_{max}/W_0 at $X=0$ in the Y - Z plane for plane fountains at different Re in the range of $28 \leq Re \leq 100$, all at $Fr = 5$ and $s = 0.1$.

Effect of s on asymmetric behavior

The effect of s on asymmetric behaviour is demonstrated by the results presented in Fig. 8 where the normalized temperature and U contours at the fully developed stage are presented for plane fountains with different s in the range $0.2 \leq s \leq 0.7$, all at $Fr = 5$ and $Re = 100$. It is observed from this figure that the extent of asymmetry decreases when s increases, and there is no asymmetric behaviour at all when s is equal to 0.7. This indicates that at $Fr = 5$ and $Re = 100$ a critical s for the symmetric-to-asymmetric transition exists between 0.5 and 0.7. These observations are further confirmed by the time series of U_{max}/W_0 at $X=0$ in the Y - Z plane at different s in the range $0.2 \leq s \leq 0.7$ at $Fr = 5$ and $Re = 100$, as depicted in Fig. 9. Again the plane fountains are symmetric at the early stage at different s , similar to those as different Fr and Re . However, the onset of asymmetry occurs at a later time when s increases, and when $s = 0.7$, there is no asymmetric behaviour observed over the whole course of the DNS run.

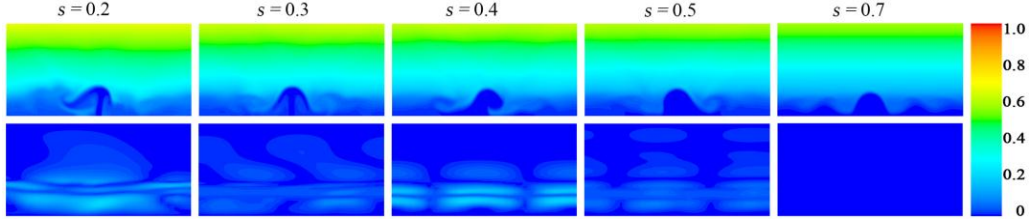


FIGURE 8. Contours of normalized temperature (first row) and U (second row) of plane fountains at the fully developed stage for different s in the range of $0.2 \leq s \leq 0.7$, all at $Fr = 5$ and $Re = 100$.

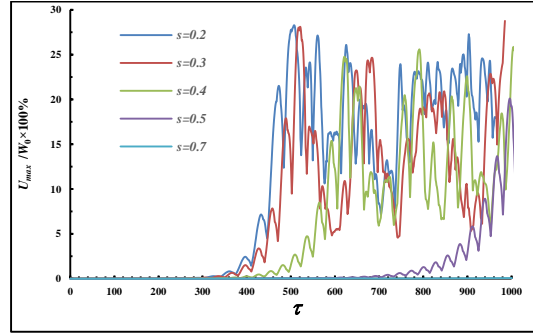


FIGURE 9. Time series of U_{max}/W_0 at $X=0$ in the $Y-Z$ plane for plane fountains at different s in the range of $0.2 \leq s \leq 0.7$, all at $Fr = 5$ and $Re = 100$.

Critical conditions for the symmetric-to-asymmetric transition

From the above results, it was observed that the onset of asymmetry in plane fountains occurs earlier at a higher Fr or Re , but is delayed when s is increased. It also demonstrated that there is a critical Fr , Re and s for the symmetric-to-asymmetric transition whenever the other two dimensionless parameters are fixed. To further quantify the critical conditions for the symmetric-to-asymmetric transition in plane fountains, more DNS runs were carried out, with the obtained critical conditions for the symmetric-to-asymmetric transition summarized in Fig. 10, where the regime map for plane fountains in linearly stratified ambient fluids at different values of Fr , Re and s is presented. The results presented in Fig. 10(a) show that at $Re = 100$, the critical conditions for the symmetric-to-asymmetric transition can be quantified by the empirical linear relation $Fr = 4.8s + 2.445$, which divides the $Fr-s$ plane into two distinctive regimes. In the bottom regime, the plane fountain will maintain symmetry all the time, whereas in the above regime, the fountain will be symmetric only at the early developing stage and will become asymmetric at the later stage. At $Fr = 5$, as shown in Fig. 10(b), the critical conditions for the symmetric-to-asymmetric transition can be quantified by the empirical relation $Re = 19.375e^{3.035s}$, which divides the $Re-s$ plane into two distinctive regimes, and similarly in the bottom regime, the plane fountain will maintain symmetry all the time, whereas in the above regime, the fountain will be symmetric only at the early developing stage and will become asymmetric at the later stage. Figure 10(c) presents the results for the critical conditions for the symmetric-to-asymmetric transition in the $Re-Fr$ plane at $s = 0.1$. It is seen that the critical conditions for the symmetric-to-asymmetric transition also divide the $Re-Fr$ plane into two distinctive regimes, although no empirical relation is found to quantify the critical conditions in this case. The results show that the critical Re value is significantly reduces when Fr increases, dropped by 78.8% at $Fr = 7$ when compared to that at $Fr = 3$. It is further observed that when Fr is beyond 7, the symmetric-to-asymmetric transition is essentially independent of Fr and at around 22.

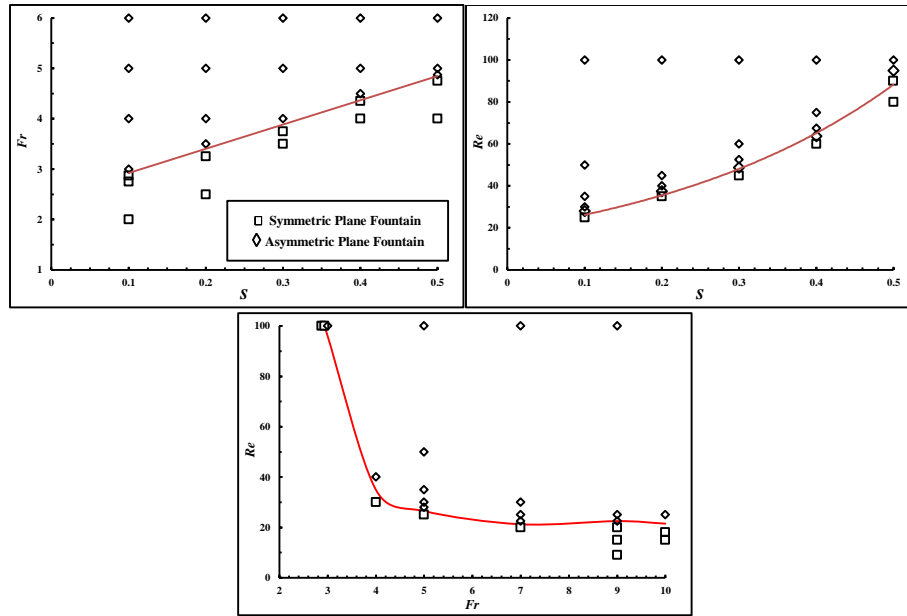


FIGURE 10. Regime map for the symmetric-to-asymmetric transition for plane fountains in linearly stratified ambient fluids at different values of Fr , Re and s : (a) in the Fr - s plane at $Re=100$; (b) in the Re - s plane at $Fr=5$; and (c) in the Re - Fr plane at $s=0.1$. The solid red lines are the demarcation line to distinguish the symmetric behavior regime from the asymmetric behavior regime.

CONCLUSION

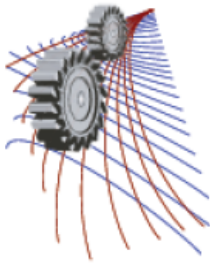
The DNS results on plane fountains in linearly stratified fluids over the ranges $9 \leq Re \leq 100$, $2 \leq Fr \leq 10$, and $0.1 \leq s \leq 0.7$ show that the fountains remain symmetry at the early developing stage. However, asymmetric behaviour occurs subsequently at the later stage when Fr or Re is sufficiently high or s is sufficiently small. It is also shown that in general the onset of asymmetry occurs earlier when Fr or Re is increased, but occurs later when s is increased. Empirical relations to quantify the critical conditions for the symmetric-to-asymmetric transition for plane fountains in linearly stratified fluids are also developed with the DNS results.

ACKNOWLEDGEMENTS

The support from the National Natural Science Foundation of China (51469035, 51266016) and the Australian Research Council (ARC) is gratefully acknowledged. M. I. Inam also thanks James Cook University for the JCUPRS scholarship.

REFERENCE

1. G. Hunt, H. Burridge, *Annu. Rev. Fluid Mech.* **47**, 195-220 (2015).
2. W. Lin, S. Armfield, *Int. J. Heat Mass Transfer.* **51**, 5226-5237 (2008).
3. N. Williamson, S. Armfield, W. Lin, *J. Fluid Mech.* **655**, 306-326 (2010).
4. W. Gao, W. Lin, T. Liu, S.W. Armfield, "Onset of asymmetry and three-dimensionality in transitional round fountains in a linearly stratified fluid," in *Proc. 18th Australasian Fluid Mech. Conf.*, Launceston, Australia, Paper-213, 2012.
5. M.I. Inam, W. Lin, S. Armfield, Y. He, *Int. J. Heat Mass Transfer.* **90**, 1125-1142 (2015).



Investigation of Drag Reduction Through a Flapping Mechanism on Circular Cylinder

Md.Asafuddoula Asif¹, Avijit Das Gupta¹, MD. Juwel Rana¹,
Dewan Hasan Ahmed^{2,a)}

¹Mechanical Engineering, Department of Mechanical and Production Engineering, Ahsanullah University of Science and Technology, Dhaka, Bangladesh

² Department of Mechanical and Production Engineering, Ahsanullah University of Science and Technology, Dhaka, Bangladesh

^{a)}Corresponding author: dhahmed.mpe@aust.edu

Abstract During flapping wing, a bird develops sufficient lift force as well as counteracts drag and increases its speed through different orientations of feathers on the flapping wings. Differently oriented feathers play a significant role in drag reduction during flying of a bird. With an objective to investigate the effect of installation of such flapping mechanism as a mean of drag reduction in case of flow over circular cylinder, this concept has been implemented through installation of continuous and mini flaps, made of MS sheet metal, where flaps are oriented at different angles as like feathers of flapping wings. The experiments are carried out in a subsonic wind tunnel. After validation and comparison with conventional result of drag analysis of a single cylinder, effects of flapping with Reynolds number variation, implementation of different orientations of mini flaps and variation of different interspacing distance between mini flaps are studied to find the most effective angle of attack of drag reduction on the body of circular cylinder. This research show that, installation of continuous flap reduces value of drag co-efficient, C_D up to 66% , where as mini flaps are found more effective by reducing it up to 73%. Mini flaps of $L/s=6.25$, all angled at 30° , at the 30° angular position on the body of circular cylinder has been found the most effective angle of attack for drag reduction in case of flow over circular cylinder.

INTRODUCTION

Cylindrical surface have manifold aerodynamic applications. Shell (body) of the rockets, main body of aero planes, surrounding body of aero plane propellers, different automobile parts, different athletic equipments etc are some of the different use of cylindrical bodies which posses aerodynamic applications. As a result, since the beginning of aerodynamic research, to increase the aerodynamic efficiency by reducing the drag of cylindrical body is considered the topic of keen interest of many researchers. Numerous experimental and computational researches have been implemented regarding this aspect of research.

NOMENCLATURE

C_D	co-efficient of drag
Re	Reynolds number
W/R	ratio of width of the flaps to radius of the tested object (Circular cylinder)
L/s	ratio of length of the tested object (circular cylinder) to interspacing distance between mini flaps
P_U	upstream pressure
P_D	downstream pressure

C_P co-efficient of pressure

Scruton and Rogers [1] established the common co-efficient of drag, C_D profile for circular cylinders for Reynolds number, Re ranging from 1×10^4 to 1×10^7 while investigating Reynolds number variation effect. The C_D for circular cylinder at low Reynolds number ranging from 1×10^4 to 1×10^5 remains almost constant as 1.2, but at high Reynolds number C_D varies from 0.4 to 0.8. Among numerous efforts of drag reduction of circular cylindrical body, use of splitter or flapping plate detached or attached in either downstream or upstream with the transversely placed circular cylinder in the direction of flow has emerged as an expandable research field in this arena.

Considering researches based on using detached splitter plate as an effective medium of drag reduction for circular cylinders, Miyata and Oshsima [2] using detached splitter plate observed that pressure drag decreased up to 30% during their experimental investigation of flow around a circular cylinder at a Reynolds number of 10^4 . Rajkumar et al. [3] studied the effect of upstream splitter plate on drag reduction of a circular cylinder both experimentally and numerically and found an optimum aspect ratio at which the drag experienced by the cylinder was minimum. Wu et al. [4-5] conducted a series of investigations on attached splitter or flapping plate over a stationary circular cylinder. Through their numerical simulations, they have observed that there are some typical flow pattern and drag reduction due to the motion of the flapping plate [4]. Wu et al. [5] also numerically investigated efficient suppression of cylinder vibration and significant drag force reduction using a hinged flat plate. Ozkan and Akilli [6] used attached permeable plates at downstream of a circular cylinder and found that permeable plate elongates the vortex formation length and reduces the fluctuations in the wake region. Assi et al. [7] used pivoting the parallel plates behind the circular cylinder and found with effective vibration suppression and significant drag reductions. Bao and Tao [8], found increased drag reduction at relatively shorter plate lengths and experienced maximum drag reduction at critical attachment angle between 40° and 50° when the dual plates are attached at the rear surface. Kunze and Brucker [9] experimentally investigated the influence of flexible self-adaptive hairy flaps on the dynamics of a cylinder wake and vortex shedding

One of the most important and influential motion in bird's flying technique is flapping. Although, flapping flight of birds follow the main flying principle of bird's, but the movement of the wings is more complicated. When bird flaps its wings down together with forward motion of the body, it tilts to lift its wings forward for propulsion. Generally, flapping involves two stages; the down-stroke and the up-stroke. Down-stroke provides majority of the thrust force and counteracts drag through reducing it. During the up-stroke, the wing is slightly folded inwards to reduce the energetic cost of flapping-wing flight providing also increased thrust and reduced drag. Such adoption of different orientations of feather at a time during flapping has direct significant impact on aerodynamic properties like thrust, lift and drag. Using this flapping phenomenon of birds, this research has been conducted by using different sized flaps of sheet metal at different angular positions on the body of a circular cylinder. The main objective of the research has been focused on finding the maximum drag reduction on circular cylinder using such flapping mechanism for both large and mini flaps.

EXPERIMENTAL METHOD

The research work has been conducted on a 450mm x 450mm low speed subsonic wind tunnel. Wind speed is created with the help of a 76 cm (30 inch) diameter suction blower of around 9000 cfm with 3HP motor with speed control facility through a 3 phase dimmer. The object used in the experiment is a 5.08 cm (2 inch) diameter and 43.18 cm (17 inch) long circular cylinder accurately marked with angular positions on the body. Continuous flaps of equal length of object of different width i.e. $W/R=0.25$, $W/R=0.5$, $W/R=0.75$ and $W/R=1$ have been used. On the other hand, five mini flaps of $W/R=0.25$ and $L=6.35$ cm (2.5 inch) is used at a time with varying interspacing distance, s . All data of pressure and velocity are collected using a digital pressure gauge connected along a pitot static tube, called Digital Pressure and Flow Meter. Fig. 1 shows the experimental object for (a) large flap, (b) mini flap and (c) angular position on cylinder. After selecting upstream velocity U_∞ , upstream and downstream pressures are measured through pre-calibrated position of test section at definite flapping angle and orientations of flaps for certain angular position on the body of circular cylinder. Then drag co-efficient is measured using following equation-

$$C_D = \frac{F_D}{\frac{1}{2} \times \rho \times U_\infty^2} = \frac{P_U - P_D}{\frac{1}{2} \times \rho \times U_\infty^2} \dots \dots \dots (1)$$

Here, drag force $F_D = P_U - P_D$.

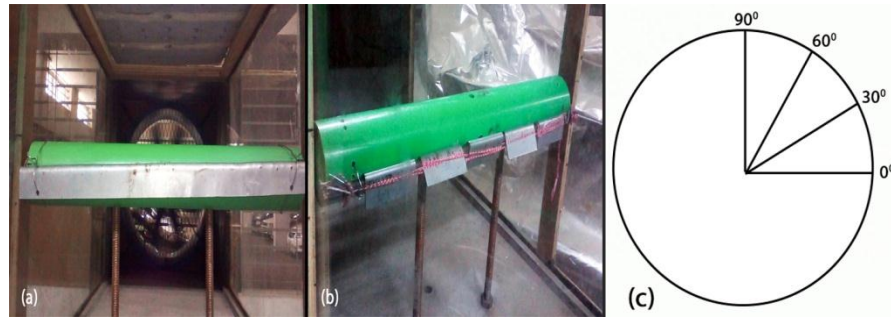
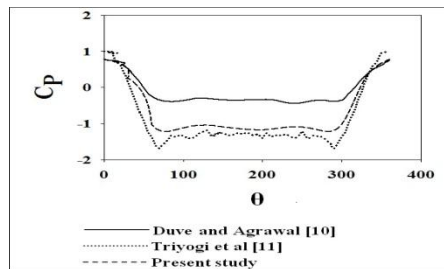


FIGURE 1. Experimental set up with (a) continuous flap and (b) differently oriented mini flaps (c) angular positions on cylinder

EXPERIMENTAL VALIDATION

FIGURE 2. Experimental validation of C_P profile

Present experiments are based on the measurement of drag force through pressure differences. Thus, the results of pressure and drag coefficient present experimental set up have been validated with the conventional results found in literature. Pressure data are validated through C_P profile observation with Duve and Agrawal [10] and Triyogi et al [11] shown in Fig. 2. Due to the set up (wind tunnel) C_D profile of drag co-efficient, C_D in the are found approximately 1.2 and constant within low Reynolds Scruton and Rogers [1] showing Results of pressure and drag show the reasonable agreement



speed limitation of the experimental cannot be obtained. Although all data experimental set up of present study, C_D profile is observed almost number zone which matches with both value and range similarity. coefficient from the experiments with the literature.

RESULTS AND DISCUSSION

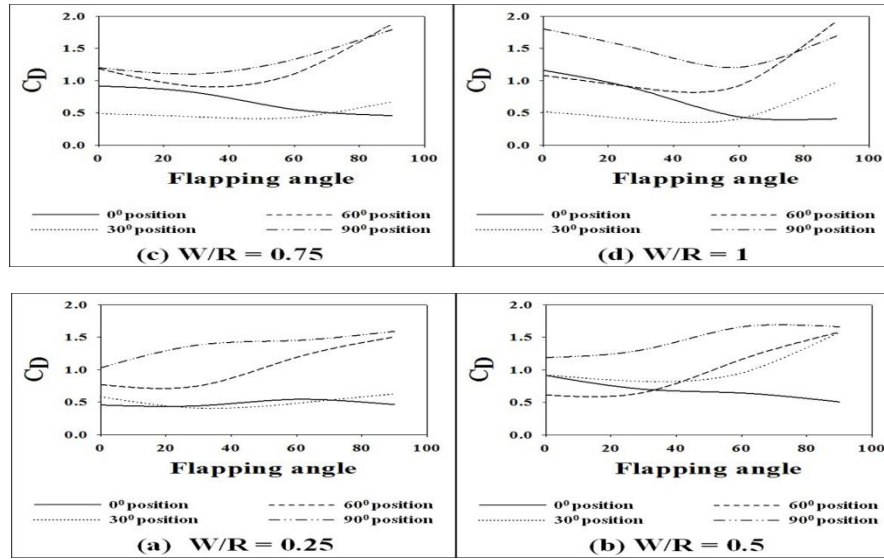


FIGURE 3. Co-drag for flap (a) $W/R=0.5$, and (d) $W/R=1$

efficient of continuous $W/R=0.25$, $W/R=0.75$

Results of flapping of four continuous flaps ($W/R=0.25$, $W/R=0.5$, $W/R=0.75$ and $W/R=1$) are presented in Fig. 3 for four different angular positions 0° , 30° , 60° and 90° on the body of the circular cylinder at a fixed upstream velocity $U_\infty=16.3$ m/s. Each continuous flap has also been flapped at four different angles of attacks 0° , 30° , 60° and 90° at particular angular position of the cylinder. From Fig. 3(a), for $W/R=0.25$ flap, the lowest drag co-efficient, C_D has appeared in the profile for 0° angular position ranging near about 0.4 to 0.6 for different flapping angle and gives the reduction of nearly 66% from cylinder's regular C_D value of 1.2. However, for other W/R ratios, C_D decreases from 0.8 to 0.4 for different flapping angles. In other cases the values of C_D increases for different flapping angles due to the pressure fluctuation and vortex generation behind the cylinder. For all four flaps except $W/R=0.5$ flap, 30° angular position profile shows greater drag reduction ranging between 0.5 to 0.6. But for $W/R=0.5$ flap shows completely different increasing profile for the particular position. It may be caused due to the presence of greater drag force due the formation of vortex at that particular angle of attack. However, both 60° and 90° angular position profile all four continuous flap show increment of C_D thus indicating drag increment instead of drag reduction. Hence, flapping at only 0° and 30° angular positions have been considered for further investigation. Moreover, all these results for four continuous flaps, it is found that gradual decrement in drag maintaining angular sequence has been only observed for $W/R=0.25$ flap. Other three flaps show dissimilarity in accordance with cylinder's angular positions as well as angles of attack during flapping. Thus $W/R=0.25$ flap has been for further investigations.

Effect of Reynolds number variation on flapping of $W/R=0.25$ flap

Effect of Reynolds number variation ranging from 3.27×10^4 to 5.34×10^4 for flapping $W/R=0.25$ flap at 0° and 30° angular position of the object has been presented here in Fig. 4(a) and (b). It is observed that all four profiles for four different Reynolds number follow conventional concept of low drag co-efficient, C_D at higher values of Re . Although

due to effect of flapping here significant drag reduction have been observed ranging between 0.4 to 0.8 for both 0° and 30° angular position on body of the object.

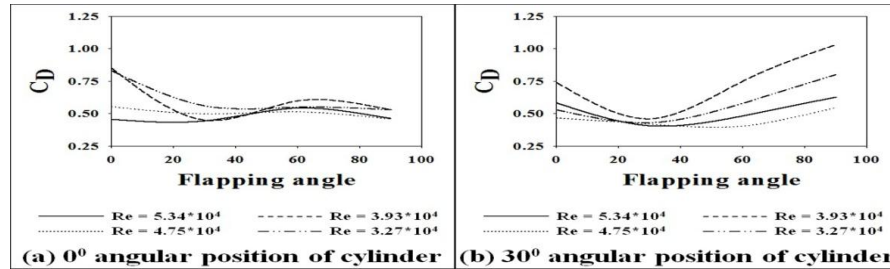


FIGURE 4. Effects of Reynolds number variation (a) 0° angular position and (b) 30° angular position

Effect of Interspacing Distances On Flapping Mini Flaps

Firstly, with mini flaps, effect of four different interspacing distances, s at fixed upstream velocity $U_\infty=16.3$ m/s have been studied and presented in Fig. 5. The minimum drag co-efficient, C_D that is 0.32 is found for $L/s=6.25$ at 30° angular position of the object. Comparing with the continuous flap, mini flap with inter space helps to recover the pressure at the downstream of the cylinder, however, increasing the inter space further increase the fluctuation of the pressure and generates the vortex. Analyzing all four profiles for both cases, more uniform results have occurred for $L/s=6.25$ due to the air quantity passing uniformly through this particular interspacing distance between flaps caused less vortex and hence generated minimum drag and thus for further investigation $L/s=6.25$ has been considered

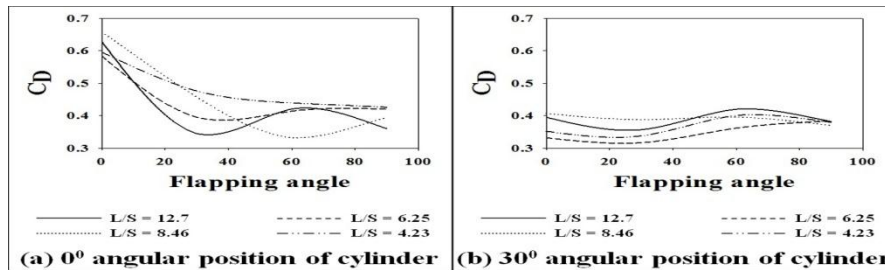


FIGURE 5. Effect of various interspacing distances between mini flaps at (a) 0° angular position and (b) 30° angular position

Effect of different orientations of mini flaps on drag reduction

Experimental study has been continued to reduce drag using several different orientations through angular arrangement of five mini flaps at the time of observation. Five different cases are observed listed below in Table 1. Results presented in Fig. 6(a) and (b) show that combination of different angle of attack have slightly increased drag while minimum drag up to 0.32 has been observed during study for particular flapping of mini flap before

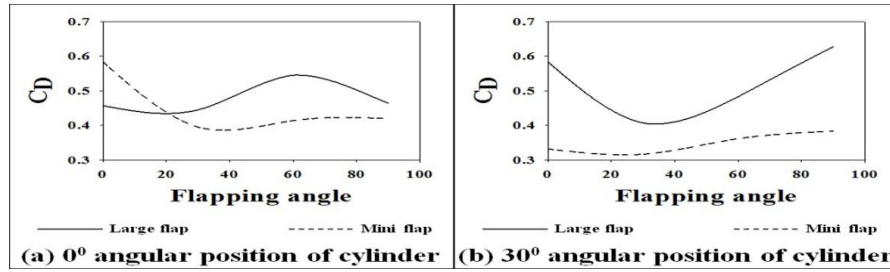


FIGURE 6. Result of effect at different orientations of mini flaps (a) 0° angular position of the object and (b) 30° angular position of the object

TABLE 1. Different orientation sequence of mini flap

	Case 1	Case 2	Case 3	Case 4	Case 5
Flap's angle orientation according to flap number	$0^\circ-30^\circ-0^\circ-30^\circ-0^\circ$	$30^\circ-0^\circ-30^\circ-0^\circ-30^\circ$	$0^\circ-60^\circ-0^\circ-60^\circ-0^\circ$	$60^\circ-0^\circ-60^\circ-0^\circ-60^\circ$	$0^\circ-60^\circ-0^\circ-30^\circ-0^\circ$

Comparison of drag reduction between continuous flap and mini flaps

For comparison, flaps with best result among continuous flap $W/R=0.25$ flap and mini flaps with $L/s=6.25$ at same Reynolds number 5.34×10^4 have been selected. Results of flapping at 0° and 30° angular positions on the surface of the object have been presented in Fig. 7 showing significant drag reduction with the use of mini flaps than continuous flap.

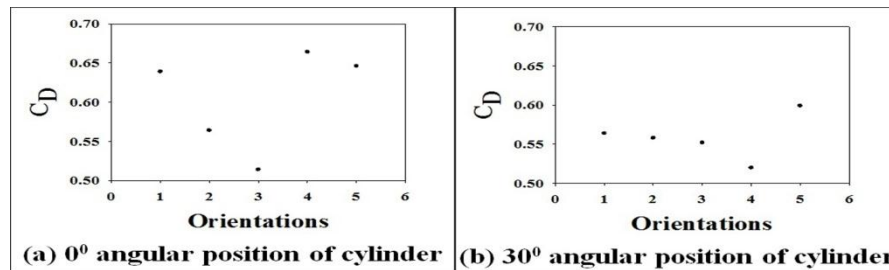


FIGURE 7. Comparison between continuous flap and mini flap (a) 0° angular position and (b) 30° angular position

CONCLUSIONS

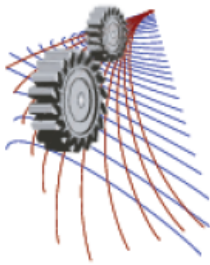
It is visualized from the results of the present study that, flapping mechanism on circular cylinder plays an influential role on drag reduction. Major drag reductions have been found for flapping at 0° and 30° angular positions on the surface of the object. Mini flaps have appeared more effective in drag reduction than continuous flaps. Increment in Reynolds number and installation of mini flaps with suitable interspacing distance at effective angle of attack also reduces drag co-efficient, C_D significantly. The lowest drag co-efficient, C_D is found through present study is 0.32 showing almost 73.3% drag reduction for mini flaps. Such kind of installation can bring effective results and major effects through practical implementation on cylindrical surfaces having aerodynamic applications in real life.

ACKNOWLEDGEMENT

This work was supported by the Department of Mechanical and Production Engineering (MPE), Ahsanullah University of Science and Technology (AUST).

REFERENCES

1. Scruton, C., and E.W.E. Rogers, Steady and unsteady wind loading of buildings and structures [and discussion], *Philosophical Transactions of the Royal Society of London*, **269**, 1199, 353-383, 1971.
2. M. Miyata, T. Ohshima, Control of flow around a circular cylinder by a small strip of thin plate in the near wake, 11th Australasian Fluid Mechanics Conference, University of Tasmania, Hobart, Australia, 14-18 December, 1992.
3. M.R. Rajkumar, A.S. Rijas G. Venugopal, Flow past a cylinder with upstream splitter plate, 10th International Conference on Heat Transfer, Fluid Mechanics and Thermodynamics, Orlando, Florida, 14-26 July, 2014.
4. J. Wu, C. Shu, Numerical study of flow characteristics behind a stationary circular cylinder with a flapping plate, *Phys. Fluids* 23, 073601 (2011).
5. J. Wu, C. Shu, N. Zhao, Numerical investigation of vortex-induced vibration of a circular cylinder with a hinged flat plate, *Phys. Fluids* 26, 063601 (2014).
6. G.M. Ozkan H. Akilli, Flow control around bluff bodies with attached permeable plates, *International Journal of Mechanical, Aerospace, Industrial and Mechatronics Engineering* Vol:8, No:5, 2014.
7. G.R.S. Assi, P.W. Bearman, N. Kitneyb, M.A. Tognarelli, Suppression of wake-induced vibration of tandem cylinders with free-to-rotate control plates, *Journal of Fluids and Structures* 26 (2010) 1045–1057.
8. Y. Bao, J. Tao, The passive control of wake flow behind a circular cylinder by parallel dual plates, *Journal of Fluids and Structures* 37 (2013) 201–219.
9. S. Kunze, C. Brucker, Control of vortex shedding on circular cylinder using self-adaptive hairy-flaps, *Comptes Rendus Mecanique* September 18, 2011.
10. S.C. Duve, M.K. Agrawal, An experimental study of pressure co-efficient and flow using sub sonic wind tunnel: the case of a circular cylinder, *International Journal of Emerging Technology and Advanced Engineering* (ISSN 2250-2459, Volume 4, Issue 2, February 2014).
11. Y. Triyogi, D. Suprayogi, E. Spirda, Reducing the drag on a circular cylinder by upstream installation of an I-type bluff body as passive control, *Proc. IMechE J. Mechanical Engineering Science* 223, 2291-2296 (2009).



Mixed Convection Analysis in Lid-driven Cavity with Sinusoidally Curved Bottom Wall Using CNT-Water Nanofluid

Mohieminul Islam Khan^{a)}, Khan Md. Rabbi^{b)}, Saadbin Khan^{c)}, M.A.H. Mamun^{d)}

Department of Mechanical Engineering, Bangladesh University of Engineering & Technology, Dhaka-1000, Bangladesh

^{a)}Corresponding author: ovlash_eg@yahoo.com

^{b)}khanrabbi92@gmail.com

^{c)}khansaadbin@gmail.com

^{d)}arifhasan@me.buet.ac.bd

Abstract. Mixed convection in a lid-driven enclosure with a curved bottom wall has been investigated using CNT (Carbon Nanotube)-water nanofluid in this paper. The curvature of the bottom wall follows the sine function. Studies have been made with different amplitudes ($\lambda = 0.05, 0.1, 0.15$) of the sine function hence wall curvature. The curved wall at the bottom is heated and the top wall is kept at a relatively low temperature. Left vertical and right vertical surface are assumed to be adiabatic. Top wall has been moving at a constant lid velocity U_0 at right direction. Galerkin method of FEA (Finite Element Analysis) has been used to solve the governing equations. Different parameters like Richardson number ($Ri = 0.1 \sim 10$) at a fixed Reynolds number ($Re = 100$), solid volume fraction of CNT particle ($\phi = 0 \sim 0.09$) are used to observe better heat transfer rate. Streamlines, isothermal lines and average Nusselt number plots are included to discuss the result of the investigation. A 2D plot between average Nusselt number and solid volume fraction of CNT-water nanofluid is also given to analyse heat transfer rate. It is observed that higher value of Richardson number shows better heat transfer rate. Finally, the paper concludes that better heat transfer is achieved at higher amplitude ($\lambda = 0.15$) of curved surface at higher solid volume fraction ($\phi = 0.09$).

INTRODUCTION

The importance of mixed convection flow in a lid-driven cavity has been enhanced substantially due to their ever increasing engineering applications such as in lubrication technologies, electronic cooling, food processing, nuclear reactors [1-3], home ventilation, electronic cooling devices and solar collectors [4]. To overcome low thermal conductivity of traditional working fluids various measures have been taken over the recent few years. Using combination of fluid and metallic particles with high thermal conductivity is one of them which is called nanofluid [5]. Many subsequent studies have shown that nanofluids yield significant improvement in the heat transfer performance in a diverse range of engineering fields [6-8]. Choi et al. [9] suggested that introducing nanoparticles into the base fluid resulted in higher thermal performance for the resultant nanofluid. From the experimental work of Eastman et al. [10] it was seen that an increase in thermal conductivity of approximately 60% was obtained for a nanofluid consisting of water and 5 vol. % CuO nanoparticles. Das et al. [11] also found out that 2–4-fold increase in thermal conductivity was obtained for water-based nanofluids containing Al_2O_3 or CuO. The convective heat transfer characteristics of nanofluids depends mainly on the thermal properties of both the base fluid and the ultra-fine (<100nm) particles as well as physical properties of the base fluid, the flow pattern, flow structure and the volume fraction, dimensions and the shape of the suspended particles. Thermal performance of lid-driven enclosures using solid nanoparticles in base fluid has been investigated numerically very frequently in the past few years. Tiwari et al. [12] studied the mixed convection heat transfer performance of Cu-water nanofluid confined within a

two-sided lid-driven square cavity with moving vertical walls kept at different constant temperatures. The results showed that the Richardson number and the direction of the moving walls had significant effects on both the fluid flow and the heat transfer within the cavity. A similar investigation was conducted by Muthamilselvan et al. [13] on rectangular enclosure with different boundary conditions. Nikfar et al. [14] worked using the same nanofluid with wavy sidewalls. Both study showed that the addition of nanoparticles resulted in a significant improvement in the mean Nusselt number and thus enhanced the rate of convection heat transfer. Moreover, the results showed that the amplitude, wavelength and waveform of the wavy wall had critical effect on the flow and temperature fields thereby they directly affected the heat transfer performance.

The present study is driven by the aforementioned motivation. Heat transfer of nanofluid in a lid-driven cavity with a sinusoidally wavy wall at bottom is studied here. The amplitudes of the sine function are changed in order to find out which amplitude is more effective. Also Richardson number is varied in each case for better characteristics.

PROBLEM SPECIFICATION

The geometry considered in this paper is a cavity according to Fig. 1. Width and height of the cavity is denoted by L . The 2-D Cartesian co-ordinate system is defined and the effect of the gravity is shown on the negative y -axis. Top surface of the cavity is moving from left to right horizontally at a constant velocity U_0 . Bottom wall is considered to follow sine function with three different amplitudes 0.05, 0.1 and 0.15 which is denoted by parameter $\lambda = a/L$.

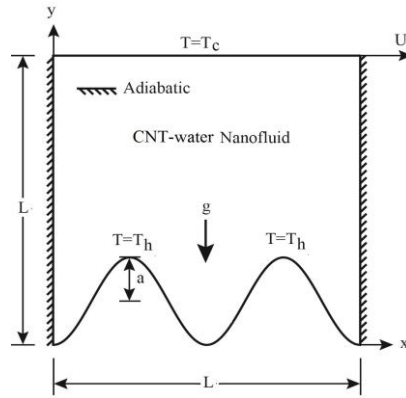


FIGURE 1. Schematic diagram for the cavity with wavy bottom wall

Top surface is kept at relatively low temperature T_c where the wavy bottom wall is uniformly heated and maintained at T_h . Left and right vertical surfaces are assumed to be adiabatic. The cavity is filled with CNT-water nanofluid. Nanoparticles and water are assumed to be in thermal equilibrium with no slip between them. The nanofluid is considered Newtonian and incompressible and the flow is assumed to be laminar. The density variation is considered according to the Boussinesq approximation. Other thermo-physical properties of the nanofluid are assumed to be constant. The thermo-physical properties of nanoparticles and water are presented in Table 1.

TABLE 1. Thermophysical properties of CNT particles and water

Property	Water	CNT
Specific heat, C_p (J/kg K)	4179	702
Thermal conductivity, k (W/mK)	0.613	3500
Thermal expansion coefficient, β (K ⁻¹)	21×10^{-5}	0.85×10^{-5}
Density, ρ (kg/m ³)	997.1	1300

MATHEMATICAL FORMULATION

Assumptions have been made that the nanofluid is a Newtonian fluid and the flow is steady laminar flow. Incompressible Navier–Stokes equation has been applied for the two dimensional flow. Governing equations in non-dimensional form can be written as,

$$\frac{\partial(U\gamma)}{\partial X} + \frac{\partial(V\gamma)}{\partial Y} = \frac{\partial}{\partial X} \left(\Gamma_\gamma \frac{\partial \gamma}{\partial X} \right) + \frac{\partial}{\partial Y} \left(\Gamma_\gamma \frac{\partial \gamma}{\partial Y} \right) + S_\gamma \quad (1)$$

Here, γ , Γ_γ and S_γ signify dependent variable, diffusion term and source term respectively (see Table 2)

Table 2. A summary of the governing non-dimensional equations

Equations	γ	Γ_γ	S_γ
Continuity	1	0	0
U-momentum	U	$\mu_{nf} / \rho_{nf} \alpha_{nf}$	$-\partial P / \partial X$
V-momentum	V	$\mu_{nf} / \rho_{nf} \alpha_{nf}$	$-\partial P / \partial Y + (\rho\beta)_{nf} / \rho_{nf} \beta_f Ra Pr \Theta$
Energy	Θ	α_{nf} / α_f	0

The density of nanofluid,

$$\rho_{nf} = (1-\phi) \rho_f + \phi \rho_s \quad (2)$$

ρ_{nf} is assumed to be constant. Here, ϕ is the solid volume fraction has significant effect on heat transfer. The thermal diffusivity of nanofluid is quite different from the conventional fluid and can be expressed by,

$$\alpha_{nf} = k_{nf} / (\rho c_p)_{nf} \quad (3)$$

$$(\rho c_p)_{nf} = (1-\phi) (\rho c_p)_f + \phi (\rho c_p)_s \quad (4)$$

Again the thermal expansion coefficient $(\rho\beta)_{nf}$ of the nanofluid can be found by,

$$(\rho\beta)_{nf} = (1-\phi) (\rho\beta)_f + \phi (\rho\beta)_s \quad (5)$$

Dynamic viscosity (μ_{nf}) of the nanofluid can be expressed by the following equation,

$$\mu_{nf} = \mu_f / (1-\phi)^{2.5} \quad (6)$$

Effective thermal conductivity of the nanofluid can be expressed as

$$k_{nf} / k_f = \left[k_s + 2k_f - 2\phi(k_f - k_s) \right] / \left[k_s + 2k_f + \phi(k_f - k_s) \right] \quad (7)$$

Here, k_s = thermal conductivity of the nanoparticles, k_f = thermal conductivity of the base fluid

Following scales are used to get the non-dimensional governing equation.

$$X = \frac{x}{L}, Y = \frac{y}{L}, U = \frac{uL}{\alpha_f}, V = \frac{vL}{\alpha_f}, P = \frac{(p + \rho_f g y)L^2}{\rho_{nf} \alpha_f^2}, \Theta = \frac{T - T_c}{T_h - T_c}, Ra = g \beta_f L^3 \frac{T_h - T_c}{\alpha_f \nu_f}, Pr = \frac{\nu_f}{\alpha_f} \quad (8)$$

Here, Θ = non-dimensional temperature, Ra = Rayleigh number, Pr = Prandtl number

$$\text{On the top horizontal wall: } U = 1, V = 0, \Theta = 0. \quad (9)$$

$$\text{On the bottom wavy walls: } U = V = 0, \Theta = 1. \quad (10)$$

$$\text{On the vertical side walls: } U = V = 0, \frac{\partial \Theta}{\partial X} = 0 \quad (11)$$

For the bottom wavy heated surface average Nusselt number is evaluated by,

$$Nu = -\frac{k_{nf}}{k_f} \int_0^1 \frac{\partial \Theta}{\partial Y} dX \quad (12)$$

Stream function from the velocity components of a two dimensional flow can be expressed as,

$$U = \frac{\partial \Psi}{\partial Y}, V = -\frac{\partial \Psi}{\partial X} \quad (13)$$

NUMERICAL METHOD

In order to discretize the governing equations and corresponding boundary conditions mentioned in the mathematical modeling section, Galerkin method of Finite Element Analysis (FEA) has been used. The converging criterion was defined as a relative residual value of less than 10^{-6} .

Code Validation

In order to validate the numerical code presented in the present investigation, a previously studied test case is employed using the presented code. Mixed convection of Cu-water nanofluid in a lid driven cavity with sinusoidal heating on sidewalls is considered which is studied earlier by Abbasian et al. [4]. Simulation is performed using the presented code at $Ri = 1$, $Gr = 100$ for two cases of volume fraction of nanoparticles $\phi = 0.1$ and $\phi = 0$. From the figure it is clearly seen that the comparison of isotherm is found out to be clearly favorable.

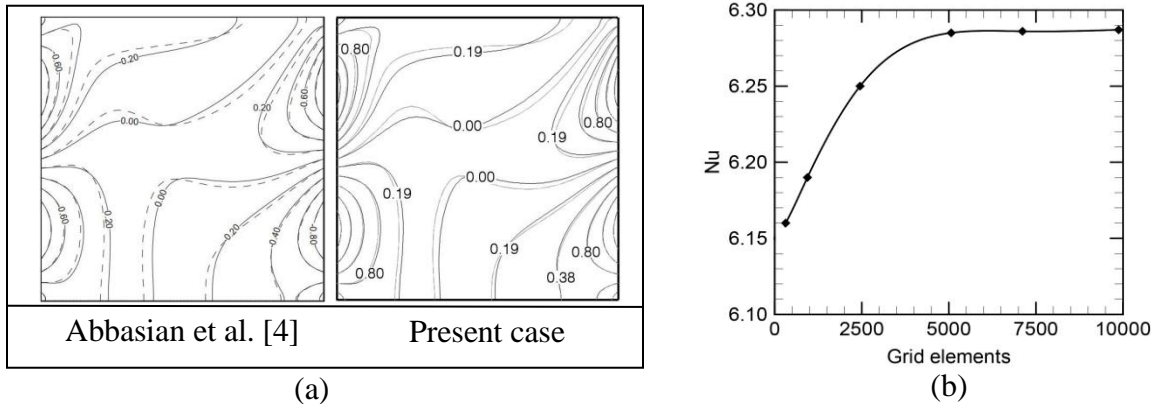


FIGURE 2. (a) Comparison of isotherm between Abbasian et al. [4] and current study at $Ri = 1$, $Gr = 100$ for $\phi = 0.1$ (black line) and $\phi = 0$ (gray line) and (b) Variation of Nusselt number with different grid elements at $Ri = 1$, $Re = 100$, $\phi = 0.1$ for $\lambda = 0.15$.

Grid Independency Test

A grid independency test is performed to guarantee the optimal comprise between numerical accuracy and computational time limit. From fig. 2 (b) variation of average Nusselt number is investigated considering mixed convection for six different number (314, 940, 2452, 5067, 7114 and 9875) of grid elements at $Ri = 1$, $Re = 100$, $\phi = 0.1$ and $\lambda = 0.15$. From number of elements 5067 no mentionable variation of Nu is observed. Further improvement of mesh size does not result in any significant change in Nusselt number. Therefore, a number of 5067 elements is selected as the ideal mesh size.

RESULT AND DISCUSSION

Effect of Amplitude on Streamline and Isotherms

From Fig. 3, by observing the streamlines for $Ri = 1$ and various sinusoidal wavy surface wall amplitude (λ) it can be seen that single large fully developed clockwise eddy is formed inside the cavity due to nanofluid. Based on the amplitude of the wavy wall the core position varies. As $Gr = 1000$, buoyancy force cannot overcome the effect of viscous force. Hence the flow inside the cavity is basically established by the moving top surface. That is the reason why the location of the core of the eddy is more near to the moving top wall than the bottom wall. From fig. 4 by observing the isotherms for a constant Ri and various λ , it can be observed that the isotherms are bundled at a greater extent near the bottom surface where the gathering rather quiet light in the interior of the cavity. Thus it indicates that a steep temperature gradients in the vertical direction in this part of the cavity, while the inner part has a very weak temperature gradients. When $\lambda = 0.05$ the isotherms cluster more into the peak region of the curve of

the bottom surface. It is due to the cavity area reduction. For the two other cases ($\lambda = 0.1$ and 0.15) the heavy cluster areas are akin at the peak areas.

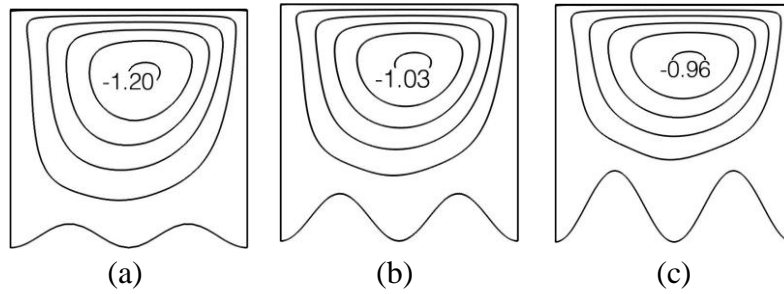


FIGURE 3. Comparison of streamline contours for (a) $\lambda = 0.05$; (b) $\lambda = 0.1$; (c) $\lambda = 0.15$ for $Ri = 1$, $\varphi = 0.09$ and $Gr = 1000$.

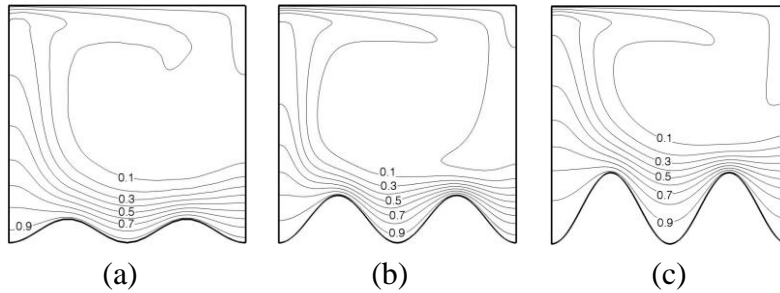


FIGURE 4. Comparison of isotherm contours for (a) d) $\lambda = 0.15$; (b), (e) $\lambda = 0.1$; (c), (f) $\lambda = 0.05$ for $Ri = 1$, $\varphi = 0.09$ and $Gr = 1000$.

Analysis of Mid-plane Vertical Velocity

Fig. 5 represents mid-plane vertical velocity, V along the x -location of the cavity. It was taken for different Richardson Number and different amplitude of wavy wall (λ). The figure indicates that the velocity increases close to the cold surface at left. It is expected due to thermal buoyancy effect as the wall creates the most temperature difference. Figure shows that when Ri is lowest, amplitude of velocity is higher at high λ . At $Ri = 0.1$ velocity is higher for $\lambda = 0.15$ than $\lambda = 0.05$, though the difference is not much mentionable. But as Richardson number goes up, buoyancy force becomes more dominant and amplitude of vertical velocity gradient is decreased. At $Ri = 10$ velocity amplitude is notably high for $\lambda = 0.05$ than $\lambda = 0.15$.

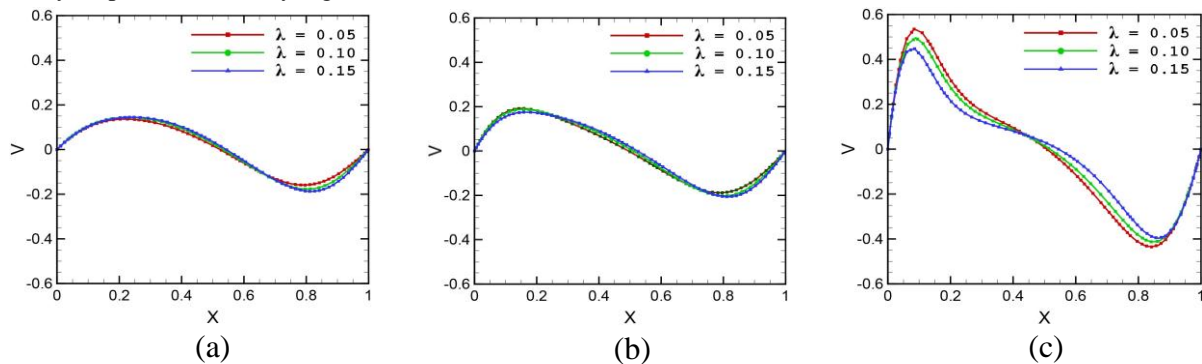


FIGURE 5. Comparison of mid-plane velocity at different λ for (a) $Ri = 0.1$; (b) $Ri = 1$; (c) $Ri = 10$.

Effect of Different Parameters on Average Nusselt Number

Fig. 6(a) presents the change of average Nusselt number, Nu for volume fraction $\varphi = 0.09$ with Richardson number, Ri for different λ . From the figure it can be clearly seen that Nu increases exponentially with the increment

of Ri . At a same Ri , average Nusselt number is different for different λ . Nu is higher for higher λ ($= 0.15$) whereas Nu is lowest for the minimum λ ($= 0.05$). It is also seen that with the increment of Ri , increment rate of Nu increases as the value of λ goes down. As a result the amplitude of Nu difference decreases with Ri increase. Fig. 6(b) shows the variation of Nu for a constant Ri ($=1$) at ϕ . It is evident that, Nu increases linearly with the increment of volume fraction at any λ . As the volume fraction, ϕ is the measurement of nanoparticles quantity in nanofluid it can be said that with the increment of nanoparticle volume Nusselt number increases. Apparently at a certain ϕ , average Nusselt number is maximum for stronger wave amplitude ($\lambda = 0.15$) and lower as the amplitude gets lower. It is minimum at $\lambda = 0.05$. Also the difference between the amplitudes of Nu decreases with λ value reduction.

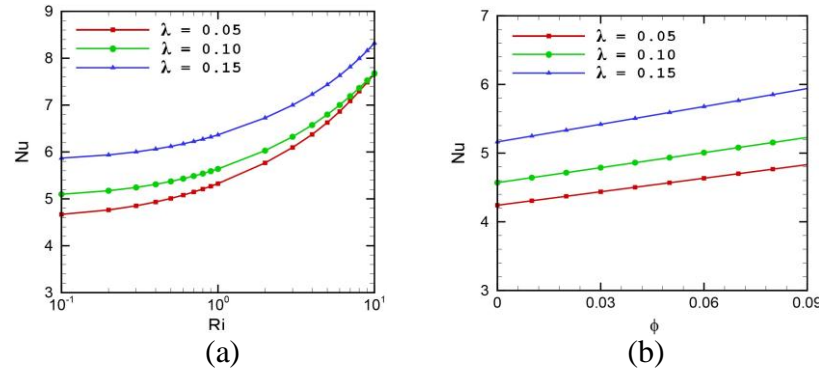


FIGURE 6. Variation of average Nusselt number for different λ with (a) Richardson number Ri and (b) solid volume fraction ϕ .

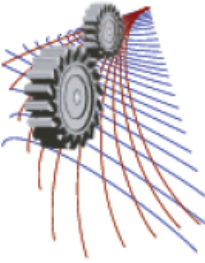
CONCLUSION

In the present study, a numerical investigation of mixed convection in a lid-driven cavity with a sinusoidally curved bottom wall has been performed using CNT-water nanofluid. Following results have been obtained from the investigation:-

- Inclusion of nanoparticles (CNT) in base fluid signifies augmentation in heat transfer performance.
- As Richardson number increases, heat transfer rate increases significantly.
- Velocity profile changes drastically for higher Richardson number and maximum amplitude of the wavy bottom wall.
- Better heat transfer is observed for maximum amplitude of wavy bottom wall.

REFERENCES

1. J. R. Koseff, A. K. Prasad, The lid-driven Fluids Eng. **106**, 390–398 (1984).
2. M. Morzinski, C.O. Popiel. Heat Trans. **12** (1988) 265–273.
3. R. Iwatsu, J. M. Hyun, Int. J. Heat Mass Trans. **38**, 3319-3328 (1995).
4. A. A. Abbasian Arani, S. Mazrouei Sebdani, M. Mahmoodi, A. Ardeshiri, M. Aliakbari, Superlatt. Microstruct. **51**, 893–911 (2012).
5. C. C. Cho, C. L. Chen, C. K. Chen, Int. J. Therm. Sci. **68**, 181-190 (2013).
6. S. K. Das, S. U. S. Choi, H. E. Patel, Heat Trans. Engg. **27**, 3-19 (2006).
7. X. Q. Wang, A. S. Mujumdar, Int. J. Therm. Sci. **46**, 1-19 (2007).
8. Z. Haddad, H. F. Oztop, E. Abu-Nada, A. Mataoui, Ren. Sust. Ener. Rev. **16**, 5363-5378 (2012).
9. S. U. S. Choi, ASME, Fluids Engineering Division **231**, 99–105 (1995).
10. J. A. Eastman, S. U. S. Choi, S. Li, W. Yu, L.J. Thompson, Appl. Phys. Lett. **78**, 718–720 (2001).
11. S. K. Das, N. Putra, P. Thiesen, W. Roetzel, ASME J. Heat Trans. **125**, 567–574 (2003).
12. R. K. Tiwari, M. K. Das, Int. J. Heat Mass Trans. **50**, 2002-2018 (2007).
13. M. Muthamilselvan, P. Kandaswamy, J. Lee, Commun. Nonlin. Sci. Numer. Simul. **15**, 1501–1510 (2010).
14. M. Nikfar, M. Mahmoodi, Engineering Analysis with Boundary Elements **36**, 433-455 (2012).



Numerical Analysis of Mixed Convection in Lid-driven Cavity Using Non-Newtonian Ferrofluid with Rotating Cylinder Inside

Khan Md. Rabbi^{a)}, Moinuddin Shuvo^{b)}, Rabiul Hasan Kabir^{c)}, Satyajit Mojumder^{d)},
 Sourav Saha^{e)}

Department of Mechanical Engineering, Bangladesh University of Engineering and Technology, Dhaka-1000, Bangladesh

^{a)}Corresponding author: khanrabbi92@gmail.com

^{b)}moinuddinshuvo@gmail.com

^{c)}rabiulhasankabir@gmail.com

^{d)}sjit018@gmail.com

^{e)}souravsahame17@gmail.com

Abstract. Mixed convection in a lid-driven square enclosure with a rotating cylinder inside has been analyzed using non-Newtonian ferrofluid (Fe_3O_4 -water). Left vertical wall is heated while the right vertical wall is kept cold. Bottom wall and cylinder surface are assumed to be adiabatic. Top wall has a moving lid with a constant velocity U_0 . Galerkin method of finite element analysis has been used to solve the governing equations. Numerical accuracy of solution is ensured by the grid independency test. A variety of Richardson number ($Ri = 0.1 - 10$) at a governing Reynolds number ($Re = 100$), power law index ($n = 0.5 - 1.5$), rotational speed ($\Omega = 0 - 15$) and solid volume fraction of ferrous particles ($\phi = 0 - 0.05$) are employed for this present problem. To illustrate flow and thermal field, streamline and isotherms are included. Average Nusselt number plots are shown to show overall heat transfer rate. It is observed that better heat transfer is achieved at higher rotational speed (Ω), Richardson number (Ri) and power law index (n). This paper also concludes significant variation in streamline and isotherm patterns for higher solid volume fraction (ϕ) of non-Newtonian ferrofluid.

INTRODUCTION

Mixed convection is interpreted by combination of natural and forced convection which occurs due to the interpretation of pressure and buoyant force. A wide number of engineering and environmental applications are related to the analysis of mixed convection in a lid driven cavity. Recent studies [1-3] show that mixed convection in a lid driven cavity is a benchmark problem for the study of interaction of the shear driven flow and free convection.

Selimefendigil et al. [4] showed that for a mixed convection of ferrofluid filled lid driven cavity in presence of two rotating cylinders. Variations are observed in flow patterns and thermal transport within the cavity with the change of Reynolds number, magnetic dipole strength and angular velocity.

The viscosity of non-Newtonian fluids is dependent on shear rate or shear rate history. Hojjat et al. [5] showed that for a convective heat transfer co-efficient Nusselt number of non-Newtonian nanofluids through a uniformly heated circular tube are remarkably higher than those of base fluid. They also proposed an empirical co-relation to predict the heat transfer co-efficient of non-Newtonian nanofluids. Atta Sojoudi et al. [6] studied the steady natural convection of non-Newtonian power law fluid in their study. Ching Yang Cheng [7] showed that under mixed thermal boundary conditions, both the surface heat flux and surface temperature were found to decrease when the power law viscosity index of the non-Newtonian power law fluid in porous media increased.

An overview from recent year's numerical investigation reveals that mixed convection in a lid driven cavity has received a great interest from scientists and engineers. Applications such as solidification, coating, float glass production, cooling of electronic devices, we may come across mixed convection in a nanofluid filled lid driven square cavity with a rotating cylinder. The importance of the position of the rotating cylinder and the angular speed of the cylinder were given importance in related investigation [8-9].

Nomenclature		β	thermal expansion coefficient (1/K)
g	gravitational acceleration (m/s ²)	σ	electrical conductivity
k	fluid thermal conductivity (W/m K)	μ	dynamic viscosity (Pa s)
Nu	average Nusselt number	ν	kinematic viscosity (m ² /s)
P	non-dimensional pressure	\bar{T}	non-dimensional temperature
Pr	Prandtl number	ρ	density (kg/m ³)
n	power law index	ψ	stream function
Re	Reynolds number	ϕ	solid volume fraction
T	temperature (K)		
τ	shear tensor stress		
x, y	dimensionless coordinates (-)	Subscripts	
u, v	dimensionless velocity components (-)	h, c	hot, cold
Greek symbols		p	ferrous particles
α	thermal diffusivity (m ² /s)	f	base fluid (water)
		ff	ferrofluid

PROBLEM SPECIFICATION

Fig. 1 represents the physical model of the present study along with the boundary conditions. The length of the cavity walls is assumed to be L . The Left vertical wall is being heated at a temperature ($T = T_h$) and right vertical wall and top walls are kept at a lower temperature ($T = T_c$) respectively. The top wall is moving right with a constant velocity of U_0 . There is a cylinder of diameter $D = 0.3L$ at the center of the cavity which is rotating counter-clockwise with rotational speed Ω . The gravity is working along the negative Y -axis. The cavity is filled with non-Newtonian ferrofluid (Fe_3O_4 - water). Heat transfer by radiation and viscous dissipation effects are neglected.

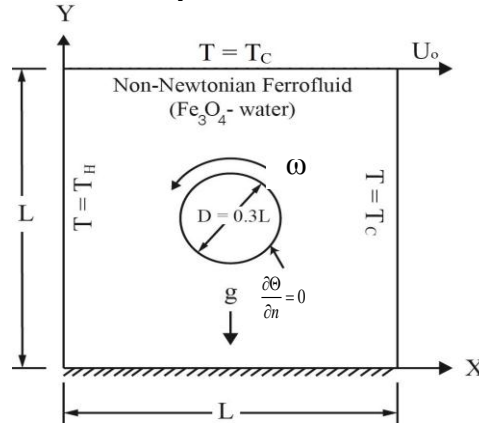


FIGURE 1. Schematic diagram of the square cavity having rotating circular at the center.

MATHEMATICAL FORMULATION

Conservation equation of mass, momentum and energy in a two dimensional Cartesian coordinate system can be written in non-dimensional form as follows:

$$\frac{\partial u}{\partial x} + \frac{\partial v}{\partial y} = 0, \quad (1)$$

$$\left(u \frac{\partial u}{\partial x} + v \frac{\partial u}{\partial y} \right) = -\frac{\partial P}{\partial x} + \frac{1}{\text{Re}} \frac{\rho_f}{\rho_{ff}} \frac{1}{(1-\varphi)^{2.5}} \left[2 \frac{\partial}{\partial x} \left(\frac{\mu_f}{N} \frac{\partial u}{\partial x} \right) + \frac{\partial}{\partial y} \left(\frac{\mu_f}{N} \left(\frac{\partial u}{\partial y} + \frac{\partial v}{\partial x} \right) \right) \right], \quad (2)$$

$$\left(u \frac{\partial v}{\partial x} + v \frac{\partial v}{\partial y} \right) = -\frac{\partial P}{\partial y} + \frac{1}{\text{Re}} \frac{\rho_f}{\rho_{ff}} \frac{1}{(1-\varphi)^{2.5}} \left[2 \frac{\partial}{\partial x} \left(\frac{\mu_f}{N} \frac{\partial v}{\partial y} \right) + \frac{\partial}{\partial x} \left(\frac{\mu_f}{N} \left(\frac{\partial u}{\partial y} + \frac{\partial v}{\partial x} \right) \right) \right] + \frac{(\varphi\beta)_{ff}}{\varphi_{ff}\beta_f} \text{Ri}\bar{T}, \quad (3)$$

$$u \frac{\partial \bar{T}}{\partial x} + v \frac{\partial \bar{T}}{\partial y} = \frac{\alpha_{ff}}{\alpha_f} \frac{1}{\text{Re Pr}} \left[\frac{\partial^2 \bar{T}}{\partial x^2} + \frac{\partial^2 \bar{T}}{\partial y^2} \right], \quad (4)$$

Following scales are implemented to get the non-dimensional governing equations,

$$x = \frac{\bar{x}}{L}, y = \frac{\bar{y}}{L}, u = \frac{\bar{u}}{u_0}, v = \frac{\bar{v}}{u_0}, \Omega = \frac{\omega L}{2u_p}, P = \frac{\bar{P}}{\rho_{ff}u_0^2}, \bar{T} = \frac{T - T_c}{T_h - T_c}. \quad (5)$$

$$\rho_{ff} = (1-\varphi)\rho_f + \varphi\rho_p. \quad (6)$$

$$(\rho C_p)_{ff} = (1-\varphi)(\rho C_p)_f + \varphi(\rho C_p)_p. \quad (7)$$

$$\sigma_{ff} = (1-\varphi)\sigma_f + \varphi\sigma_p. \quad (8)$$

The thermal conductivity of the ferrofluid is obtained by Maxwell-Garnett model [10] and stated as-

$$k_{ff} = \left[k_f (k_p + 2k_f) - 2\varphi(k_f - k_p) \right] / \left[(k_p + 2k_f) + \varphi(k_f - k_p) \right] \quad (9)$$

Purely-viscous non-Newtonian fluid which follows the Ostwald–DeWaele model [11] the shear stress tensor is:

$$\tau_{ij} = 2\mu_{ff}D_{ij} = \mu_{ff} \left(\frac{\partial \bar{u}_i}{\partial x_j} + \frac{\partial \bar{u}_j}{\partial x_i} \right) \quad (10)$$

The dynamic viscosity of ferrofluid is expressed by Brinkman model [12],

$$\mu_{ff} = \mu_f (1-\varphi)^{-0.25}, \bar{\mu}_f = N \left\{ 2 \left[\left(\frac{\partial \bar{\mu}}{\partial x} \right)^2 + \left(\frac{\partial \bar{v}}{\partial y} \right)^2 \right] + \left(\frac{\partial \bar{v}}{\partial x} + \frac{\partial \bar{u}}{\partial y} \right)^2 \right\}^{\frac{(n-1)}{2}} \quad (11)$$

Boundary conditions used to solve the present problem are mentioned in Table 1.

TABLE 1. Boundary conditions in non- dimensional form.

Boundary Wall	Bottom	Top	Vertical Left	Vertical Right	Cylinder Wall
Flow Field	$u = 0, v = 0$	$u = 1, v = 0$	$u = 0, v = 0$	$u = 0, v = 0$	$u = -2\Omega (y - y_c), v = 2\Omega (x - x_c)$
Thermal Field	$\partial \bar{T} / \partial n = 0$	$\bar{T} = 0$	$\bar{T} = 1$	$\bar{T} = 0$	$\partial \bar{T} / \partial n = 0$

The non-dimensional governing parameters are defined below,

$$Pr = \frac{\nu_f}{\alpha_f}, Gr = \frac{g\beta_f(T_h - T_c)L^3}{\mu_f\alpha_f}, Re = \frac{\rho_f u_0 L}{\mu_f}, Ri = \frac{Gr}{Re^2} \quad (12)$$

Average Nusselt number is evaluated at the heated left vertical wall and can be expressed as-

$$Nu = - \int_0^1 \frac{\partial \bar{T}}{\partial X} dY \quad (13)$$

NUMERICAL PROCEDURE, CODE VALIDATION AND GRID INDEPENDENCY TEST

Galerkin weighted residuals method of finite element scheme is adopted to find numerical solution for the present problem. Here, resulting set of algebraic equations are solved using iteration technique. A convergence criterion is set as $|z^{c+1} - z^c| \leq 10^{-6}$, where z is the general dependent variable and c is the iteration number. Fig. 2(a)

represents the comparison of streamline and isotherm between Kefayati et al. [13] and present case at $Ri = 1$, $n = 0.6$, $Gr = 100$, $Pr = 10$ for $\phi = 0.09$. Again grid independency test is performed for examining the accuracy of the numerical results of this study. For the grid independency test, the Y -velocity is observed at $Ri = 1$, $Re = 100$, $n = 0.5$, $\Omega = 15$ and $\phi = 0.05$ at the mid plane. Fig. 2(b) shows that 1264, 2898, 7346 and 10762 elements have been inspected for the observation. From the figure, it can be observed that mid plane Y -velocity for 7346 and 10762 mesh elements almost overlaps thus 7346 mesh elements can be regarded as the optimum grid for the present study.

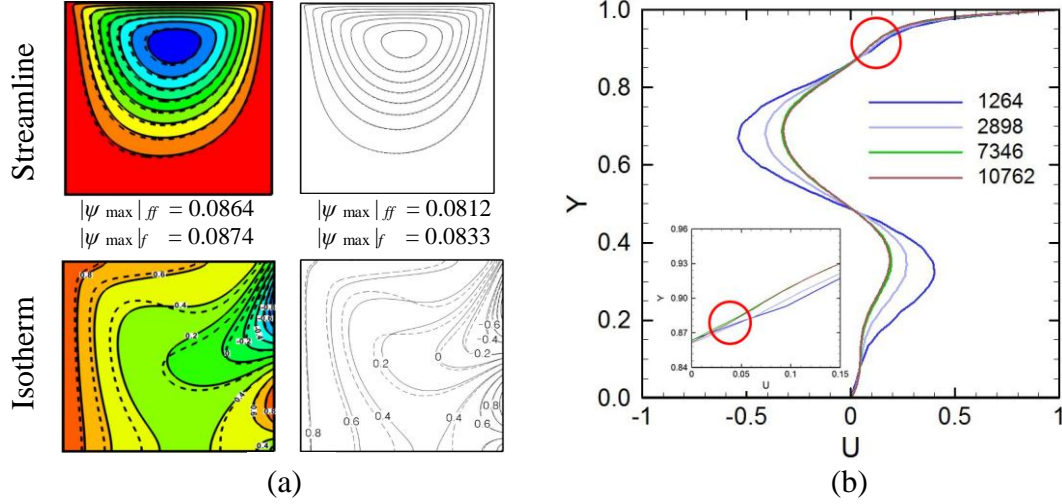


FIGURE 2. Comparison of streamline and isotherms between Kefayati et al. [13] and present case at $Ri = 1$, $n = 0.6$, $Gr = 100$, $Pr = 10$ for $\phi = 0.09$ and b) Variation of mid-plane x -velocity with y -location for different mesh elements at $Ri = 1$, $Re = 100$, $n = 0.5$, $\Omega = 15$ and $\phi = 0.05$, $Pr = 10$

RESULT AND DISCUSSION

In the present investigation, effect of non-Newtonian ferrofluid on mixed convection heat transfer has been analysed. Effect of different pertinent parameters (n , Ω and Ri) has been analyzed.

Effect of Power Law Index (n) and Rotational Speed (Ω) on Streamline (ψ) and Isotherm (θ) Contours

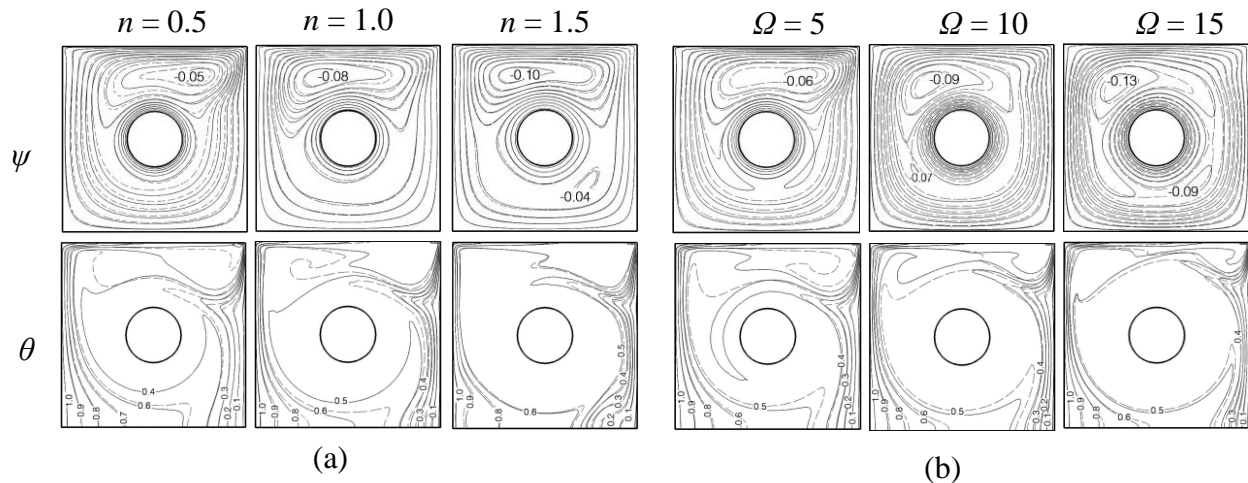


FIGURE 3. Effect of (a) power law index (n) and (b) rotational speed (Ω) on streamline (ψ) and isotherm (θ) contours at $Ri = 1.0$ for $\phi = 0$ (dashed line) and $\phi = 0.05$ (solid line).

From the Fig. 3(a) we see the strength of the flow field enhances with the increment of power law index (n). The working fluid inside the cavity absorbs energy from the heated wall and moves up improving the buoyancy force. Near the moving wall, fluid particles fall in a downward direction following a traced path-way. Thus recirculation zones are formed. For dilatant fluid ($n > 1$), the vortices are stronger. Streamline around the rotating cylinder also gets elongated for more dilatant fluids ($n = 1.5$). More distorted isothermal lines are found which ensures more convection dominated regime. For pseudo-plastic fluids ($n < 1$), isothermal lines are more parallel which dictates conduction dominated regime. Fig. 3(b) illustrates that higher rotational speed of cylinder ensures stronger recirculation zone near the lid-driven top wall. For lower rotational speed, lid-speed dominates over the vortex, thus creating lid-biased recirculation zone. When the cylinder rotates in counter clock-wise direction, it accelerates the fluid flow adjacent to the moving lid. Isothermal lines are also effected by the higher rotational speed significantly. At $\Omega = 15$, more distorted isothermal contours are found. Higher rotational speed is expected to ensure higher heat transfer rate. More importantly, it is also observed that ferrofluid has more distinguishing effect on streamline and isotherm patterns when working fluid possess shear-thinning behaviour ($n < 1$).

Effect of Different Parameters on Velocity Profile and Average Nusselt Number (Nu)

Fig. 4 demonstrates the y -velocity (v) along with x -location at a plane ($y = 0.2x$) just under the rotating cylinder. It is significant from Fig. 4(a) that at $Ri = 1$, $\Omega = 15$ and $\phi = 0.05$, velocity profile changes drastically as power law index increases. For dilatant fluid ($n > 1$), velocity gradient is higher, indicating of increment in overall heat transfer. Fig. 4(b) shows that increment of rotational speed of the cylinder effects the velocity field for surrounding fluid particles at $Ri = 1$, $n = 0.5$ and $\phi = 0.05$. Again, Fig. 4(c) illustrates that higher solid volume fraction of ferrous particles also exhibits higher velocity of magnitude.

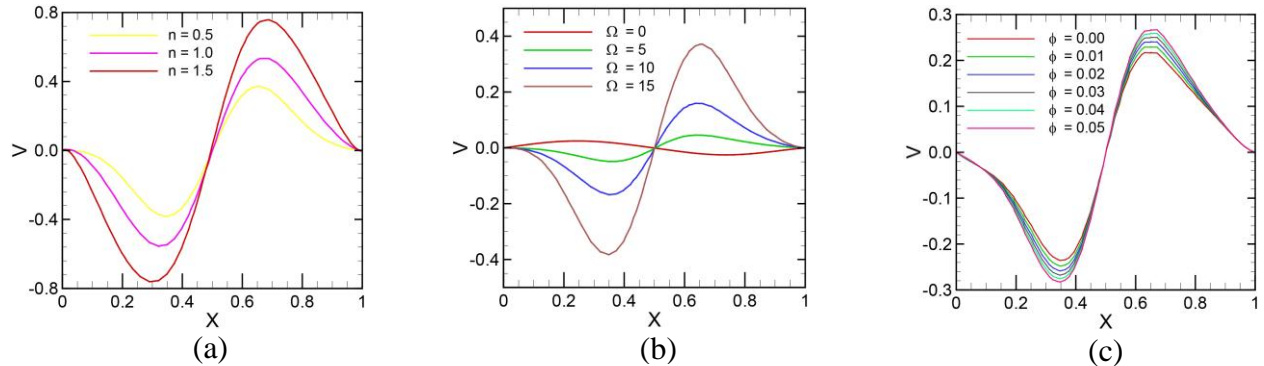


FIGURE 4. Variation of y -velocity (V) with x -location (X) at different (a) power law index, (b) rotational speed, (c) solid volume fraction.

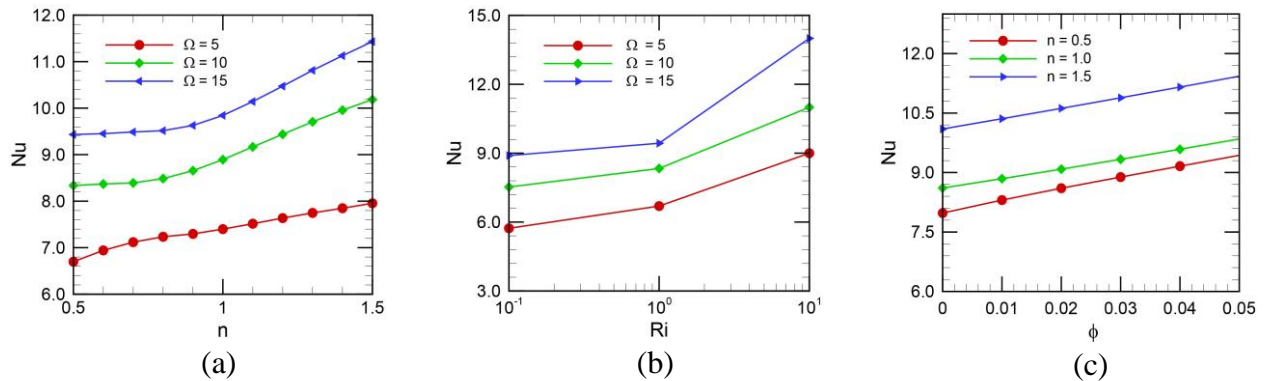


FIGURE 5. Effect of (a) power law index, (b) Richardson number, (c) solid volume fraction on average Nusselt number.

Fig. 5 demonstrates the effect of power law index (n), Richardson number (Ri) and solid volume fraction (φ) on overall heat transfer. It is observed from Fig. 5(a) that at $Ri = 1$, for any rotational speed of the cylinder, average Nusselt number increases with the increment of power law index. This is due to the higher thermal gradient near the heated wall.

It is noted that, up to $n = 1$ (Newtonian fluid), there is no mentionable variation in Nusselt number. But as the working fluid acts dilatant, higher heat transfer rate is found. This is due to dominance of convection discussed previously while analyzing thermal field. From Fig. 5(b), it is observed that at $n = 0.5$, Nu increases with the increment of Ri because of higher buoyancy dominance. As the Ω increases, fluid mixing near the rotating cylinder becomes stronger hence advances convection current. Eventually, higher Nu is achieved for higher rotational speed ($\Omega = 15$). Fig. 5(c) describes the effect of solid volume fraction of ferrous particles in base fluid (water) on average Nusselt number at $\Omega = 15$. The addition of solid ferrous particles (Fe_3O_4) in base fluid (water) results in the increment of the diffusion term which enhances buoyancy effect. Thus higher temperature gradient is observed at the heated wall while improvising ferrofluid as cooling medium. Better heat transfer rate has been achieved for non-Newtonian dilatant ferrofluid ($n = 1.5$, $\varphi = 0.05$) at $Ri = 1$ and $\Omega = 15$.

CONCLUSION

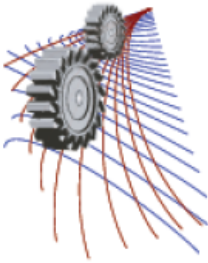
Mixed convection analysis using non-Newtonian ferrofluid in lid-driven cavity with rotating cylinder at the center has been analyzed. Dilatant fluid ($n > 1$) shows more strong flow and thermal field at higher rotational speed of cylinder. Power law index, rotational speed, Richardson number and solid volume fraction has a significant impact on velocity profile. More than 46% better heat transfer has been recorded at higher rotational speed ($\Omega = 15$) in case of dilatant ferrofluid. Non-Newtonian ferrofluid exhibits better heat transfer (more than 15%) than non-Newtonian fluid. Further investigation can be made to develop a critical range of different pertinent parameters in this regard.

ACKNOWLEDGMENTS

The authors would like to express their gratitude to Multiscale Mechanical Modeling and Research Network (MMMRN) for their continuous support and thoughtful insight and advice.

REFERENCES

1. K. Khanafer and S. M. Aithal, *Int. J. Heat Mass Trans.* **66**, 200-209 (2013).
2. A. W. Islam and M. A. R. Sharif and E.S. Carlson, *Int. J. Heat Mass Trans.* **55**, 5244-5255 (2012).
3. B. Ghasemi and S. M. Aminossadati, *Int. Commun. Heat Mass Trans.* **37**, 1142-1148 (2010).
4. F. Selimefendigil and H. F. Oztop, *Int. J. Eng. Sci. Technol.* **18**, 439-451 (2015).
5. M. Hojjat and S. G. Etemad and R. Bagheri, J. Thibault, *Int. J. Therm. Sci.* **50**, 525-531 (2011).
6. A. Sojoudi and S. C. Saha, Y. T. Gu, M. A. Hossain, *Adv. Mech. Engg.* **5** (2013).
7. C. Y. Cheng, *Int. Commun. Heat Mass Trans.* **36**, 693-697 (2009).
8. D. Chatterjee and S. K. Gupta and B. Mondal, *Int. Commun. Heat Mass Trans.* **56**, 71-78 (2014).
9. V. A. F. Costa and A. M. Raimundo, *Int. J. Heat Mass Trans.* **53**, 1208-1219 (2010).
10. J. Maxwell, *A Treatise on Electricity and Magnetism* (Oxford University Press, Oxford, 1873).
11. H. Ozoe, *S. W. AIChE. J.* **18**, 1196 - 1207 (1972).
12. H. Brinkman, *J. Chem. Phys.* **20** 571-581 (1952).
13. G. H. R. Kefayati, *Pow. Tech.* **266**, 268-281 (2014).



Comparison of Aerodynamic Characteristics of Pentagonal and Hexagonal Shaped Bridge Decks

Md. Naimul Haque^{1, a)}, Hiroshi Katsuchi^{2, b)}, Hitoshi Yamada^{2, c)} and Mayuko Nishio^{2, d)}

¹Department of Civil Engineering, Chittagong University of Engineering and Technology, Chittagong-4349, Bangladesh.

²Department of Civil Engineering, Yokohama National University, Yokohama, 240-8501, Japan.

^{a)}Corresponding author: naimulce@gmail.com

^{b)}katsuchi@ynu.ac.jp

^{c)}y-yamada@ynu.ac.jp

^{d)}nishio@ynu.ac.jp

Abstract. Aerodynamics of the long-span bridge deck should be well understood for an efficient design of the bridge system. For practical bridges various deck shapes are being recommended and adopted, yet not all of their aerodynamic behaviors are well interpreted. In the present study, a numerical investigation was carried out to explore the aerodynamic characteristics of pentagonal and hexagonal shaped bridge decks. A relative comparison of steady state aerodynamic responses was made and the flow field was critically analyzed for better understanding the aerodynamic responses. It was found that the hexagonal shaped bridge deck has better aerodynamic characteristics as compared to the pentagonal shaped bridge deck.

INTRODUCTION

Aerodynamic stability is one of the most important design aspects for the long-span bridge decks and depends greatly on the shape of the bridge deck. An aerodynamically stable pentagonal shaped bridge deck was proposed by a group of researchers [1,2] from Japan as shown in Fig.1(a). Based on their detailed wind tunnel study a bottom plate slope (θ) of 12° was recommended for shaping the pentagonal shaped bridge deck to obtain optimum aerodynamic responses. Depending on their recommendation a number of long-span bridges have already been shaped and placed the bottom plate slope (θ) at around 12° to optimize the aerodynamic responses. However, those practical bridge decks were shaped as hexagon (Fig.1(b)) instead of pentagon to fulfill the structural and maintenance requirements. The aerodynamics and response of a hexagonal shaped bridge deck may vary from that of a pentagonal shaped bridge deck and depending on that the optimum value of bottom plate slope (θ) may also differ. Therefore, it is important to know that how the aerodynamics and response of a hexagonal shaped bridge deck varies from a pentagonal one due to its practical importance.

In the present study, a numerical investigation was carried out to explore the aerodynamic characteristics of pentagonal and hexagonal shaped bridge decks. A relative comparison of aerodynamic responses was made and the flow field was critically analyzed for better understanding the aerodynamic responses. First, the mean and rms (root mean square) value of steady-state force coefficients of the bridge decks were compared. Then, pressure, velocity and vorticity distributions were plotted to explain the static responses and to apprehend the flow characteristic due to variation of the deck shape from pentagon to hexagon. Simulations were carried out at a Reynolds number (Re_B) of 6.0×10^4 .

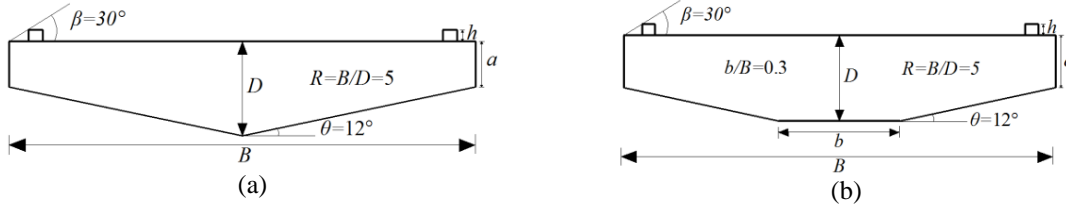


FIGURE 1. Geometric configuration of the considered bridge decks: a) Pentagonal shaped bridge deck and b) Hexagonal shaped bridge deck

NUMERICAL FORMULATIONS

The ensemble averaged Navier-Stokes equations called unsteady Reynolds-Averaged Navier-Stokes (URANS) equation was used to model the flow. The flow was assumed to be two-dimensional and incompressible in nature. The governing equations were as follows;

$$\frac{\partial \bar{U}_i}{\partial x_i} = 0 \quad (1)$$

$$\frac{\partial \bar{U}_i}{\partial t} + \bar{U}_j \frac{\partial \bar{U}_i}{\partial x_j} = -\frac{1}{\rho} \frac{\partial \bar{P}}{\partial x_i} + \frac{\partial}{\partial x_j} \left[\nu \left(\frac{\partial \bar{U}_i}{\partial x_j} + \frac{\partial \bar{U}_j}{\partial x_i} \right) - (\overline{u'_i u'_j}) \right] \quad (2)$$

where, \bar{U}_i and x_i were the averaged velocity and position vectors respectively, t was the time, \bar{P} was the averaged pressure, ρ was the air density, ν was the fluid viscosity. The turbulence modeling was attained by utilizing the $k-\omega$ SST turbulence model [3,4]. Convective and diffusive terms in the governing equations were discretized with second order accurate central differencing schemes. For time integration second order accurate backward differentiation formulae method was utilized. PISO (Pressure implicit with splitting of operator) algorithm was utilized to solve these discretized equations. An open source code OpenFOAM was used as a solver.

Simulations were performed in a two dimensional domain with $48D$ in length and $25D$ in height, where D was the height of the bridge deck section. The object was placed at $18D$ downstream of the inlet. The outlet boundary was placed at $25D$ downstream of the object and height of the domain was $25D$. The domain was sufficiently large to avoid unnecessary disturbance of the boundary conditions. At the outlet, pressure boundary condition, at the top and bottom of the domain, slip boundary condition and at the body, non-slip boundary condition was implemented. The domain was discretized spatially by a non-uniform structured grid and the cell size was varied gradually with a geometric progression of 1.05 in all directions. Around 108,000 numbers of elements were used to discretize the flow around the target bridge deck sections. Further details of the model, grid system and validation can be found in [5,6].

RESULTS AND DISCUSSIONS

Figure 1 shows the geometric configuration of the considered bridge decks. The side (R) and width ratios (W) were selected based on our survey on practical bridges where we found that for this kind of bridges the side (R) and the width ratios (b/B) vary from 5 to 8 and from 0.2 to 0.45 respectively. The curb angle (β) was set to 30° depending on previous recommendations [5,7]. Table 1 summarizes the mean and rms value of the selected force coefficients. The hexagonal shaped bridge deck owned much better stationary aerodynamic responses as compared to the pentagonal shaped bridge deck. In case of hexagonal shaped bridge deck, the drag decreased 11.34%, the negative lift increased 78.25% and the moment decreased around 98%. However, the rms value of the lift force (C_L') and moment coefficient (C_M') increased when the deck shape was altered from pentagon to hexagon. Similar to the rms value, the strouhal number (S_{tB}) also increased in case of hexagonal shaped bridge deck.

All the steady state force coefficients presented in Table1 were calculated by the surface pressure distribution. The mean and rms value of surface pressure coefficients are plotted in Fig.2 for further detailed comparison of these two deck shapes. The variation of the deck shape from pentagon to hexagon mainly affected the bottom surface mean pressure (in Fig.2(a)). As the deck became hexagonal in shape the side depth (a) increased, as a result the leading edge

TABLE 1. Steady state force coefficient comparison of the pentagonal and hexagonal shaped bridge decks

Force coefficients	Pentagonal bridge deck	Hexagonal bridge deck	Percentage variation (%)
Mean value of drag force coefficient (C_D)	0.538	0.477	11.34
Mean value of lift force coefficient (C_L)	-0.308	-0.549	78.25
Mean value of moment coefficient (C_M)	-0.0634	-0.00089	98.60
rms value of lift force coefficient (C_L')	0.036	0.0419	16.39
rms value of moment coefficient (C_M')	0.00686	0.00845	23.18
Strouhal number (S_{IB})	0.871	1.016	16.65

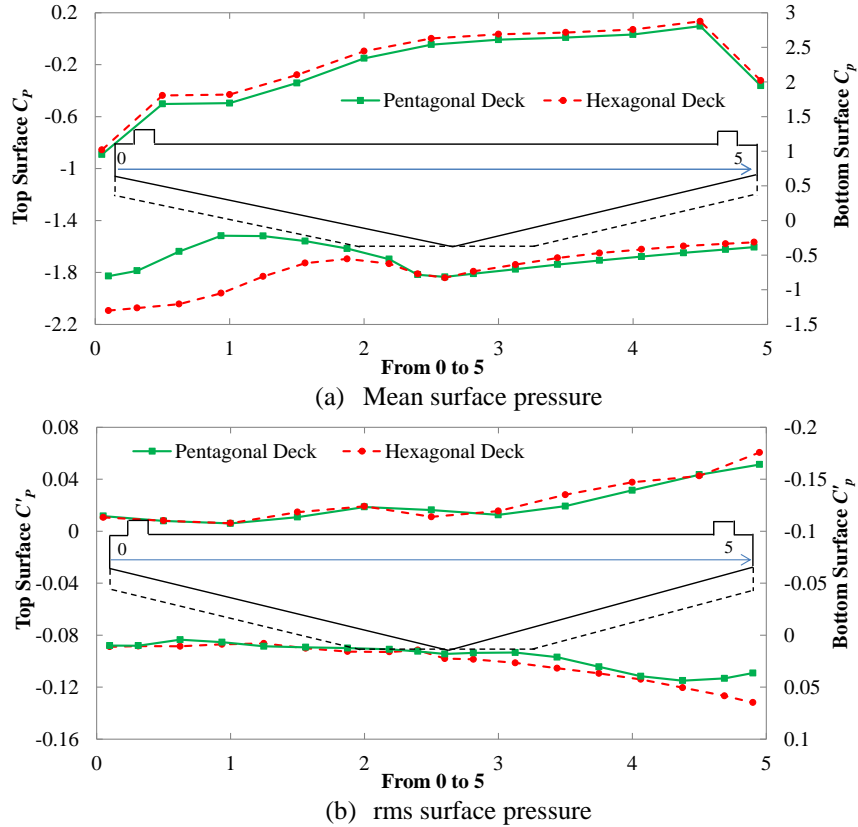


FIGURE 2. Surface pressure distribution around the bridge decks

suction increased, yet the bottom surface trailing edge side larger pressure recovery occurred. Along with the bottom surface the top surface pressure was also affected. The hexagonal deck experienced a bit larger suction throughout the top surface of the deck. However, the amount of suction increased at the bottom surface leading edge side was much larger as compared to the any other places. Therefore, the bottom surface leading edge suction increased the downward force and thereafter the negative lift value in case of hexagonal shaped bridge deck. For the same reason the counter-clockwise moment tendency increased and decreased the negative moment tendency of the bridge deck.

The rms pressure fluctuation are plotted in Fig.2(b). In both of the cases the trailing edge side had a much larger value of rms fluctuation as compared to the leading edge side. However, unlike mean surface pressure, the rms surface pressure didn't show noticeable sensitivity towards the variation of the deck shape. A slight increase of rms fluctuation could be noticed at the bottom surface trailing edge side for the hexagonal shaped bridge deck. The vorticity field around the bridge decks are plotted in Fig.3. Clear after-body vortex shedding was found for both of the bridge decks. It was presumed that this after-body vortex shedding increased the trailing edge rms pressure fluctuation. No massive difference in vortex structures was noticed, yet in case of hexagonal shaped bridge deck the vortices were found more regular as compared to the pentagonal shaped bridge deck.

The instantaneous velocity fields along one lift cycle are compared in Fig.4. Very high correlation between the lift magnitude and the position of the vortex was observed. In case of pentagonal shaped bridge deck the bottom vortex (VB) formed at the lower corner with much smaller in size. However, as the deck became hexagonal in shape, the side depth (a) increased and the nose location went down. As a result, the bottom vortex (VB) formed at the side of the deck became larger in size and more synchronized in nature with the top vortex (VT), those increased the rms fluctuation of the hexagonal shaped bridge deck. Further, similar to the mean pressure distribution (Fig.2(a)), the velocity distribution also depicted that the hexagonal shaped deck experiences larger bottom surface leading edge separation as compared to the pentagonal shaped bridge deck.

Another important trend was the pentagonal deck had a larger bottom surface trailing edge separation. In case of hexagonal shaped bridge deck, due to appearance of the bottom horizontal plate (b) the deck became more streamlined, increased the flow velocity that increases the flow reattachment tendency at the trailing edge side. The velocity distributions at the vertical plane at various locations around the bridge decks are plotted in Fig.5. As can be seen the general observation we made earlier has clearly reflected in Fig.5. Specially, at the trailing edge in Fig.5(c) of

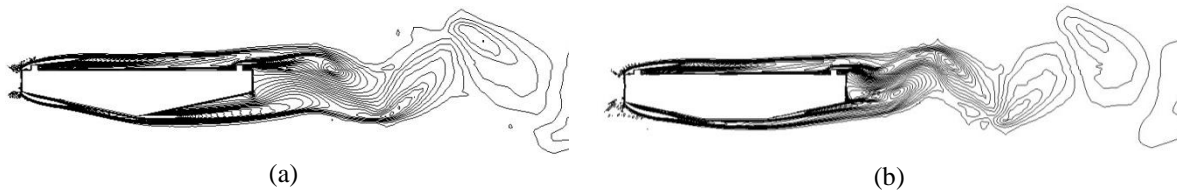


FIGURE 3. Vorticity field around the bridge decks: a) Pentagonal shaped bridge deck and b) Hexagonal shaped bridge deck

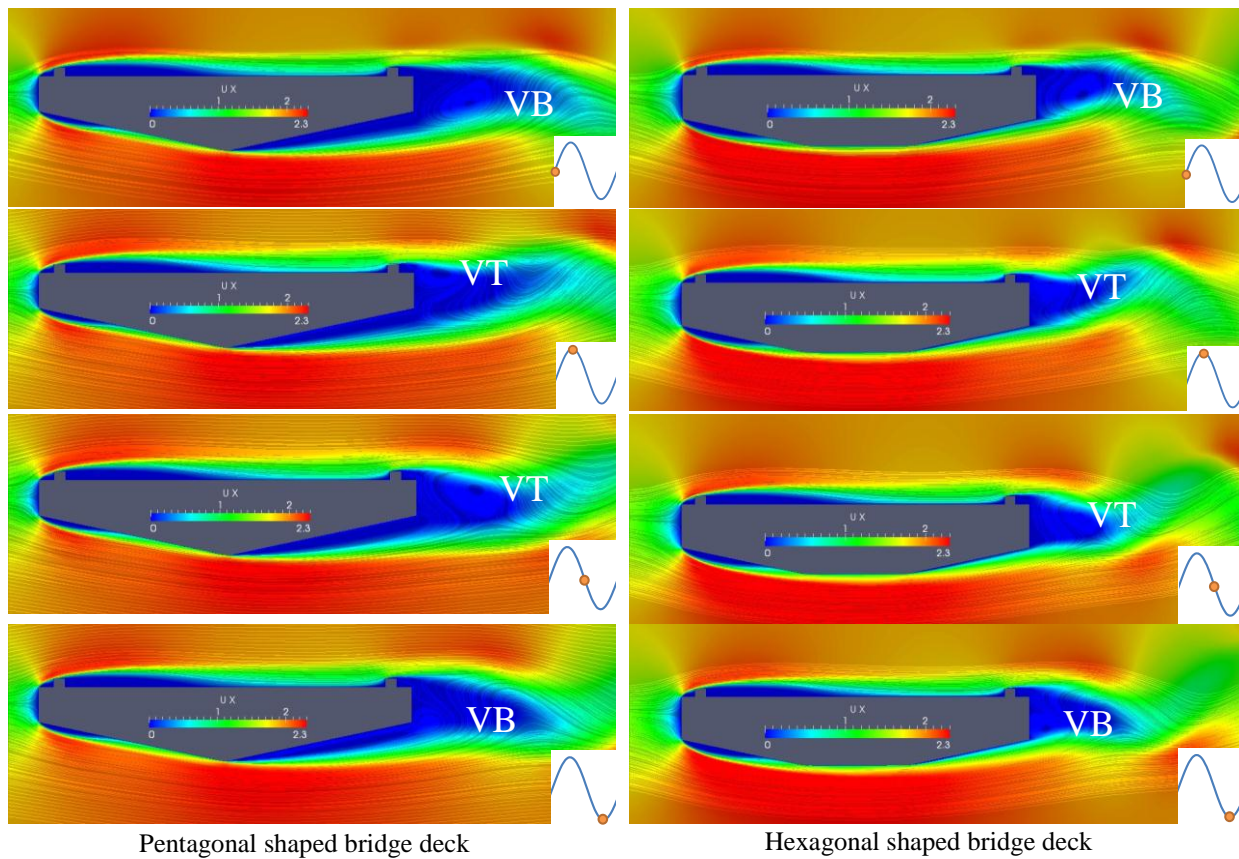


FIGURE 4. Comparison of the instantaneous velocity distribution around the bride deck along one cycle of the periodic lift force coefficients

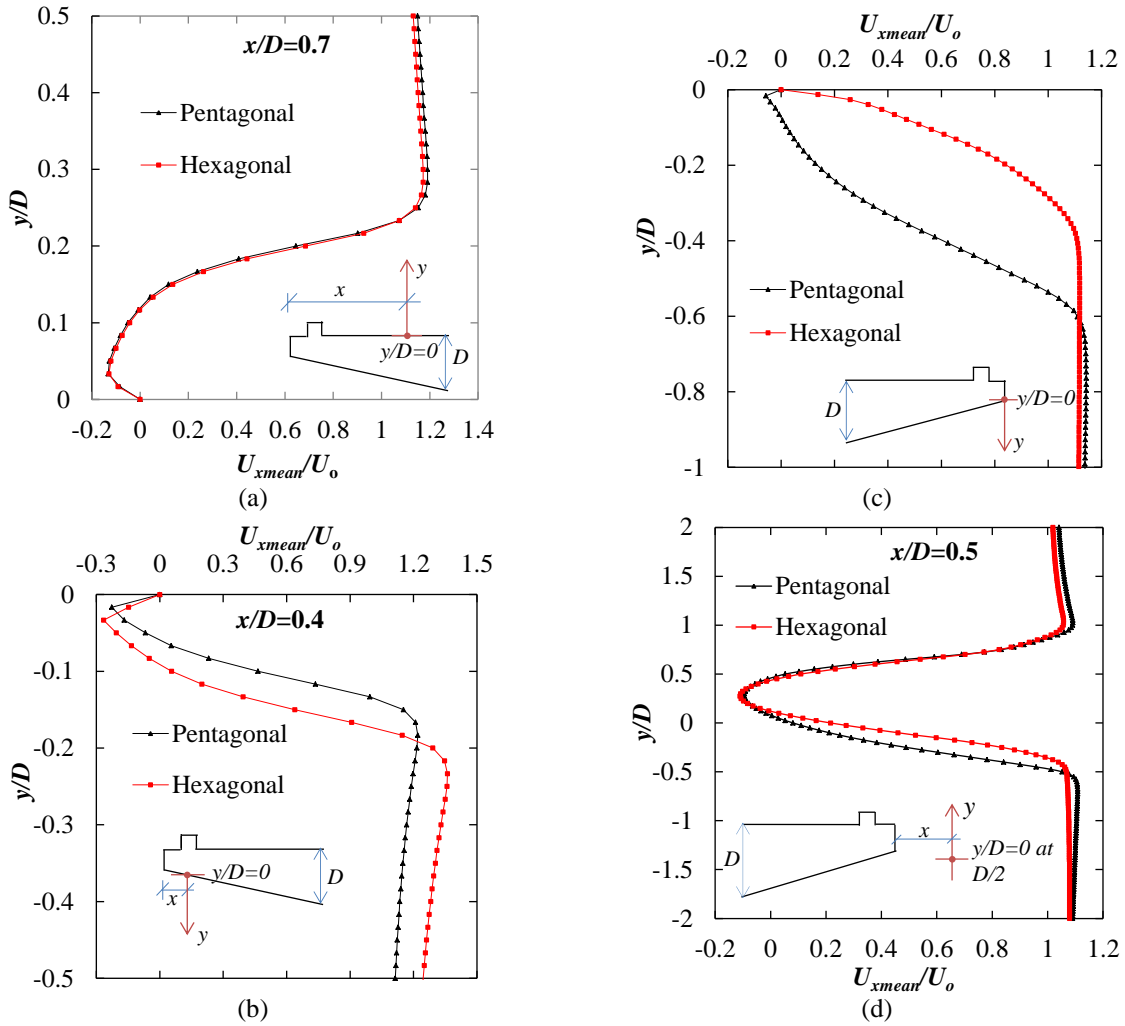


FIGURE 5. Comparison of velocity distribution at various locations around the bridge decks: a) top surface leading edge, b) bottom surface leading edge, c) bottom surface trailing edge and d) wake of the bridge deck

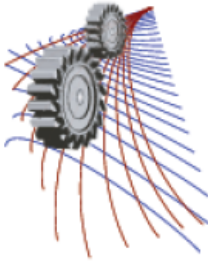
hexagonal shaped bridge deck, boundary layer forms clearly indicating no separation, yet the pentagonal shaped bridge deck experiences clear boundary layer separation. As a result, the wake of the bridge deck became smaller (Fig.5(d)) in case of hexagonal shaped bridge deck resulted smaller drag force coefficients.

CONCLUSIONS

A relative comparison of steady-state aerodynamic characteristics of pentagonal and hexagonal shaped bridge deck was made. It was discovered that the aerodynamics of a hexagonal shaped bridge deck differs noticeably from a pentagonal shaped bridge deck. At the current Reynolds number (R_{eB} of 6.0×10^4) and considered geometry ($R=5$), we found that a hexagonal shaped bridge deck has better steady-state aerodynamic performance over a pentagonal shaped bridge deck. When the deck shape was altered from pentagonal to hexagonal shape, the side depth (a) and the bottom horizontal plate (b) of the bridge deck became the most influential parameters from aerodynamic point of view as they affected the leading edge and trailing edge flow separation significantly. However, the observation was made only for a specific value of the important shaping parameters ($\theta=12^\circ$ and $R=5$), depending on the variation of shaping parameters the mechanism may alter. Further, detailed investigation by taking into consideration the influence of various shaping parameters is required for further understanding the aerodynamics of a hexagonal shaped bride.

REFERENCES

1. Y. Kubo, K. Yoshida, E. Tuji, K. Kimura, and K. Kato, "Development of aerodynamically stable bridge girder cross section for long span bridges," In proceedings of 12th Int. Conf. on Wind Engineering, (1-6 July, Cairns, Australia, 2007), pp.239-246.
2. T. Noda, Y. Kubo, K. Kimura, K. Kato, K. Okubo, and K. Yoshida, *Journal of Civil Engineering (JSCE)* **65**, 797-807 (2009).
3. F.R. Menter, *AIAA Journal* **32**, 1589-1605 (1994).
4. F.R. Menter, M. Kuntz, and R. Langtry, *Turbulence, Heat and Mass Transfer* **4**, 625-632 (2003).
5. M. N. Haque, H. Katsuchi, H. Yamada and M. Nishio, *Journal of Structural Engineering (JSCE)* **61A**, 375-387 (2015).
6. M. N. Haque, H. Katsuchi, H. Yamada and M. Nishio, *KSCE Journal of Civil Engineering*. DOI: 10.1007/s12205-015-0696-2
7. Y. Kubo, K. Hayashida, T. Noda and K. Kimura, "Mechanism on reduction of aerodynamic forces and suppression of aerodynamic response of a square prism due to separation interface method," In Proceedings of 6th Int. Colloq. On Bluff Body Aerodynamics and Applications, (20-24 July, Milano, Italy 2008), pp.1-4.



An Experimental Investigation of Wind Flow Over Tall Towers in Staggered Form

Proma Anwar^{1, a)}, Md. Quamrul Islam^{2, b)} and Mohammad Ali^{3, c)}

¹*Department of Physical Sciences, Independent University Bangladesh*

²*Department of Mechanical Engineering, Bangladesh University of Engineering and Technology, Dhaka*

^{a)}Corresponding author: proma_a@yahoo.com

^{b)}quamrul@me.buet.ac.bd

^{c)}mali@me.buet.ac.bd

Abstract. In this research work an experiment is conducted to see the effect of wind loading on square, pentagonal and Hexagonal shape cylinders in staggered form. The experiment is done in an open circuit wind tunnel at a Reynolds number of 4.23×10^4 based on the face width of the cylinder across the flow direction. The flow velocity has been kept uniform throughout the experiment at 14.3 m/s. The test has been conducted for single cylinders first and then in staggered form. Angle of attack is chosen at a definite interval. The static pressure at different locations of the cylinder is measured by inclined multi-manometer. From the surface static pressure readings pressure coefficients are calculated first, then drag and lift coefficients are calculated using numerical Integration Method. These results will surely help engineers to design buildings with such shapes more efficiently. All the results are expressed in non-dimensional form, so they can be applied for prototype buildings and determine the wind loading at any wind speed on structures of similar external shapes.

INTRODUCTION

The effect of wind loading on buildings and structures has been considered for design purposes since late in the 19th century; but starting from that time up to about 1950, the studies in this field have not been considered seriously. Building and their components are to be designed to withstand the code specified wind loads. In recent years, much emphasis has been given on “The study of wind effect on buildings and structures” in the different corners of the world. Even researchers in Bangladesh have taken much interest in this field. Till now, little attention has been paid to the flow over the bluff bodies like square cylinders, rectangular cylinders, hexagonal cylinders, octagonal cylinders etc. and some information is available concerning the flow over them in staggered condition.

Now-a-days, both the studies with models and full-scale buildings are being performed to compare the result for varying the validity of the former. Barriga, A.R.[1] studied the effects of angle of attack, turbulence intensity and scale on the pressure distribution of a single square cylinder placed in a turbulent cross flow. Biswas, N. [2] performed an experimental investigation of wind load on tall buildings with square cross section having rounded facet in a uniform flow. Five different facet dimensions were considered in the study. The study included both the single cylinder and the group consisting of two cylinders. Islam, A.T.M. and Mandal, A.C. [3] conducted an experimental investigation of static pressure distributions on a group of rectangular cylinders in a uniform cross flow. They determined the effects of longitudinal spacing and side dimension of the rectangular cylinders. Finally, they calculated the lift and drag coefficients from the measured data of surface static pressure. Farok, G.M.G.

[4]carried out an experimental investigation of wind effect on rectangular cylinders with rounded corners. They considered both the single cylinder and group of cylinders in their study. Hussain, H. S. and Islam, O. [5] measured coefficient of pressure and coefficient of lift on circular, parabolic and elliptic shell roof in a uniform velocity.

NOMENCLATURE

U_α	Free stream Velocity
A	Area of the Cylinder
F_D	Drag Force
F_L	Lift force
C_L	Coefficient of lift
C_D	Coefficient of drag
C_P	Coefficient of pressure
α	angle of attack
γ_a	specific weight of air
dp/dn	pressure gradient
ΔP	Pressure difference
Δh_w	manometer reading
γ_w	Specific weight of Manometric Liquid

EXPERIMENTAL SETUP

Wind Tunnel

The test was done in an open circuit subsonic wind tunnel. The tunnel consists of various components such as, fan, valve, silencer, honey comb etc. It is 5.93 meter long with a test section of 460-mm x 460 mm cross-section. In order to make the flow uniform a honeycomb is fixed near the end of the wind tunnel. There is a converging bell mouth shaped entry. To generate the wind velocity, two axial flow fans are used. Each of the fans is connected with the motor of 2.25 kilowatt and 2900 rpm. There is a butterfly valve to control the wind speed. There is a silencer just after the butterfly valve. The axis of the model coincides with that of the wind tunnel. The converging mouth entry is incorporated in the wind tunnel for smooth entry of air into the tunnel and to maintain uniform flow into the duct free from outside disturbances.

The induced flow through the wind tunnel is produced by two-stage rotating axial flow fan of capacity 18.16 m³/s at the head of 152.4 mm of water and 1475 rpm. In each case of the tests, wind velocity is measured directly with the help of a pitot tube. The flow velocity in the test section was maintained at 13.5m/s approximately. The sidewalls were made of plywood. In one side, the model cylinder was fastened with the side wall using nut and bolt. The bolt was fixed with one end of the cylinder. Through the other end of the cylinder, the plastic tubes were taken out in order to connect them with the inclined multi-manometer. There was a provision for rotation of the test cylinder at various angles to obtain the wind load at different angles of attack. The Reynolds number was 4.22×10^4 based on the projected width of the cylinder across the flow direction.

Construction of the Cylinders

In this case one square, one pentagonal and one hexagonal cylinder of identical size were constructed. Each of the cylinders was made of seasoned teak wood in order to avoid the bucking and expansion due to the change of temperature and humidity. The tapping positions on the cross-section of the cylinder are shown in Figure 1 & Figure 2. The width of the cylinders was 50mm as shown in the figure. Each face of the cylinder contained five tapplings. In Figure 3.4 the tapping positions on the longitudinal section of the cylinder is shown. The distance between the consecutive tapping points was equal (Δd) as shown in the figure.

Each tapping was identified by a numerical number from 1 to 20 for square cylinder and from 1 to 25 for pentagonal cylinder and from 1 to 30 for hexagonal cylinder as can be seen from the figure. It can be seen from the longitudinal section that the tapplings were not made along the cross-section of the cylinder. On one side of the cylinder a steel plate was attached through which there was a bolt for fixing the cylinder with the side wall of the extended tunnel as shown in figure 3.

The other side of the cylinder was hollow through which the plastic tubes were allowed to pass. The plastic tubes were connected with the copper capillary tubes at one side and at the other side with the inclined multi-manometer. The manometer liquid was water. The tapplings were made of copper tubes of 1.71 mm outside diameter. Each tapping was of 10mm length approximately. From the end of the copper tube flexible plastic tube of 1.70 mm inner diameter was press fitted.

Schematic Diagrams of the cylinders

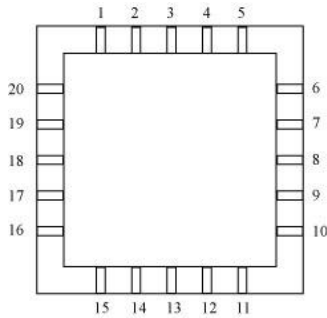


FIGURE 1. Cross section of a square cylinder showing tapping point

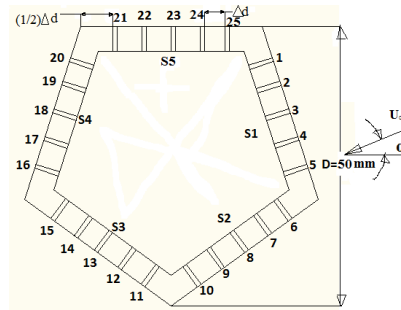


FIGURE 2. Tapping points shown on cross-section of a pentagonal cylinder

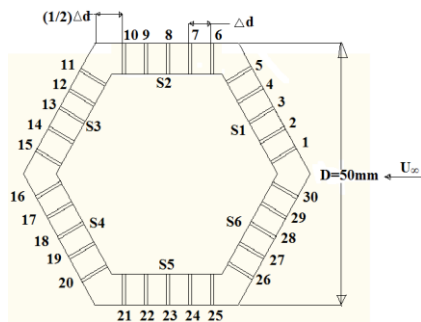


FIGURE 3. Tapping points shown on cross-section of a Hexagonal Cylinder

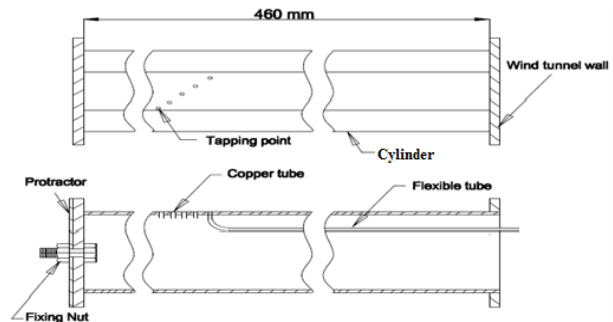


FIGURE 4. Tapping positions on the longitudinal section of the cylinder

MATHEMATICAL MODEL

By definition Pressure coefficient,

$$C_p = \frac{\Delta P}{\frac{1}{2}\rho U_\infty^2} \quad (1)$$

Drag coefficient,

$$C_D = \frac{F_d}{\frac{1}{2}\rho A U_\infty^2} \quad (2)$$

Lift coefficient,

$$C_L = \frac{F_L}{\frac{1}{2}\rho A U_\infty^2} \quad (3)$$

RESULTS AND DISCUSSION

In this part pressure coefficients, lift coefficients and drag coefficients are discussed for a square, pentagonal and hexagonal cylinder at various angle of attack. The pressure coefficients are calculated from the measured values of surface static pressure, then the drag and lift coefficients are calculated by numerical integration method. The flow velocity was kept constant at 14.3 m/s.

Distribution of pressure coefficients (Staggered Cylinders)

From the surface of the staggered square, pentagonal and hexagonal cylinders 25 tapping points were chosen. A cross-section of square, pentagonal and hexagonal cylinder is shown in Fig. 1, Fig.2 and Fig.3. Each five tappings are considered one surface, identified by S_1, S_2, S_3, S_4, S_5 . Static pressure readings are taken for angle of attack 0° to 70° at a step of 10° . On Fig. 4, one can see a stagnation point at surface S_2 on tapping point 7 at an angle of attack zero degree for the pentagonal cylinder. Pressure coefficients are positive on all the surfaces. It is also seen that the pressure coefficients are decreasing but at tappings 10 to 24 are almost uniform. When angle of attack is 10° , the pressure coefficients are slightly increased on tappings 1 to 5 and slightly dropped on Tapping 5 to 9 and 21 to 24. No stagnation point is found. At angle of attack 20° , C_p values are increased in S_1 and S_5 and dropped on S_2 . No stagnation point is found. At 30° , there is no stagnation point and C_p values are uniform on surfaces S_2 to S_4 . At 40° , pressure coefficients are positive on all surfaces. S_2 and S_4 have almost uniform C_p and there is no stagnation point. At 50° , C_p values are uniform on surface S_2 to S_4 . All C_p values are positive. No stagnation point is found. At angle 60° , pressure coefficients are almost same as 40° . Slight decrease of C_p on surface S_1 and increase on S_5 is seen. On other surfaces C_p values are found almost uniform.

Variation of Lift and Drag Coefficients

Variation of drag coefficient at various angles of attack on staggered square, pentagonal and hexagonal cylinder is shown in Figure 13. It can be noticed from Figure. 13 that there is significant drop in the drag coefficient values for the staggered cylinders in comparison to that of the square cylinder (according to reference [6]) and the values are higher than the hexagonal cylinder. It is seen from this figure that at zero angle of attack, the drag coefficient is

about 1.47 and at all other angles of attack, the values are close to 1.5 except at angle of attack of 10° and 20° , where the value is around 1.30 and 1.40 respectively. The values of the drag coefficient at various angles of attack for the staggered square, pentagonal and hexagonal cylinders can be explained from the C_p -distribution curves. In Figure. 14 the variation of lift coefficient at various angles of attack on staggered square, pentagonal and hexagonal cylinder is shown. It can be noticed from this figure that the variation of the lift coefficient on the staggered square, pentagonal and hexagonal cylinder is more or less similar with the variation of lift coefficient for the single square cylinder except at angle of attack of 0° . The values of the lift coefficients for the staggered cylinders can be explained from the C_p -distribution curves

Graphs

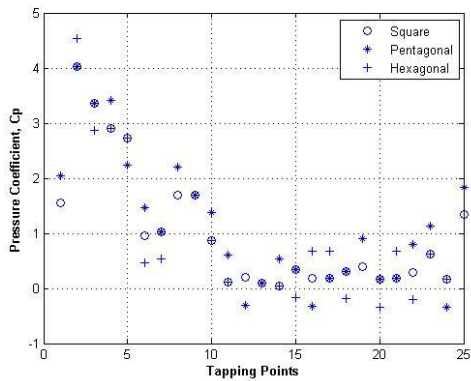


FIGURE 5. Distribution of pressure coefficients for angle of attack $\alpha=0^\circ$

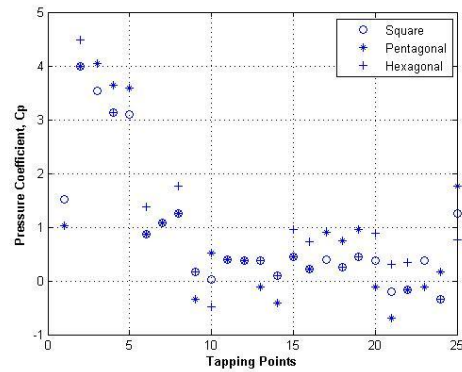


FIGURE 6. Distribution of pressure coefficients for angle of attack $\alpha=10^\circ$

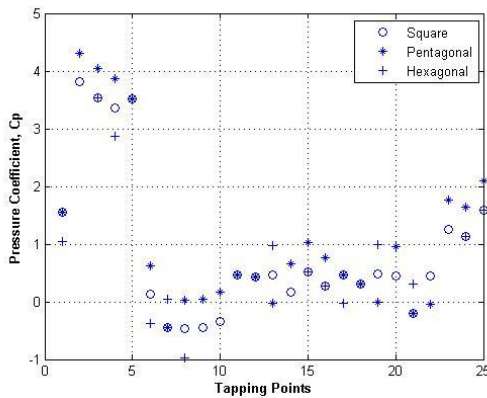


FIGURE 7. Distribution of pressure coefficients for angle of attack $\alpha=20^\circ$

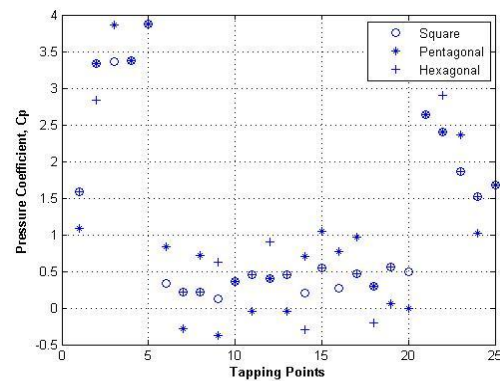


FIGURE 8. Distribution of pressure coefficients for angle of attack $\alpha=30^\circ$

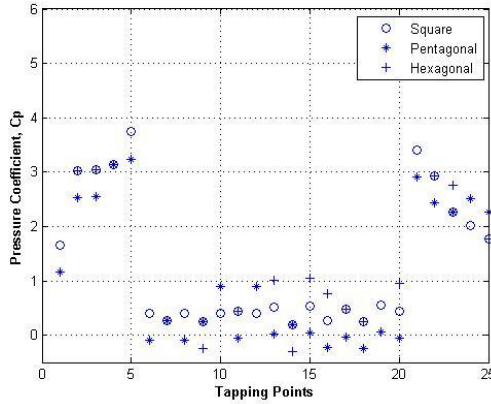


FIGURE 9. Distribution of pressure coefficients for angle of attack $\alpha=40^\circ$

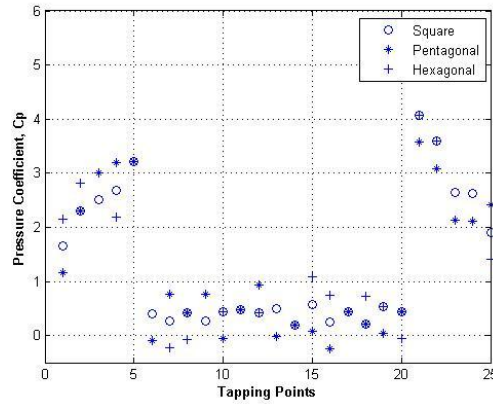


FIGURE 10. Distribution of pressure coefficients for angle of attack $\alpha=50^\circ$

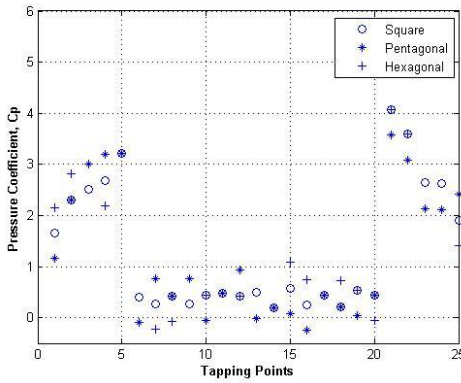


FIGURE 11. Distribution of pressure coefficients for angle of attack $\alpha=60^\circ$

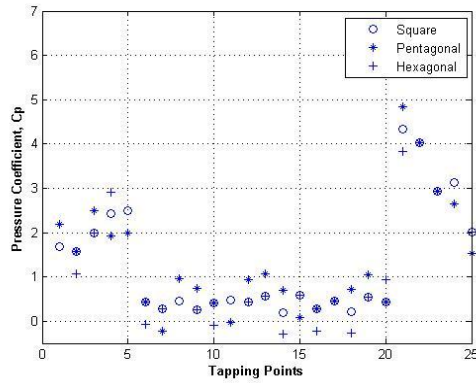


FIGURE 12. Distribution of pressure coefficients for angle of attack $\alpha=70^\circ$

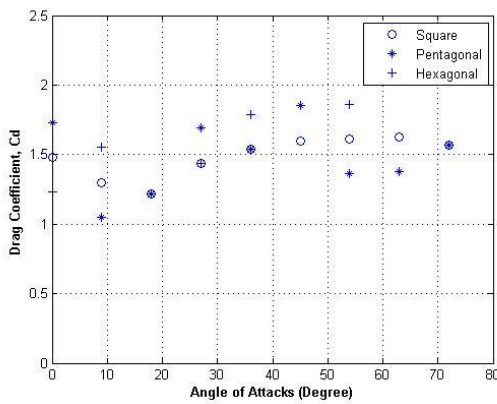


FIGURE 13. Variation of drag coefficients at different tapping points

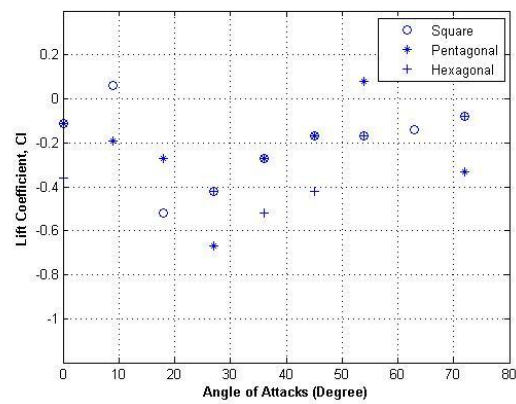


FIGURE 14. Variation of lift coefficients at different tapping points

CONCLUSION

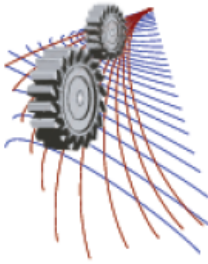
The following conclusions are drawn in regard to the wind effect on staggered square, pentagonal and hexagonal cylinder. There is significant drop in the drag coefficients in comparison to the single square cylinder. The variation of lift coefficient is slightly shifted and the pattern is more or less similar with the variation of lift coefficient for the single square cylinder except for angle of attack 0^0 . The stagnation point is found on front surface. This result is applicable when wind load is to be considered for a staggered square, pentagonal and hexagonal cylinder.

ACKNOWLEDGMENTS

This work was supported and supervised by Dr. Md. Quamrul Islam and Dr. Mohammad Ali, Department of Mechanical Engineering. Sincerest thanks to the staffs and instructor of Fluid Mechanics Laboratory of Mechanical Engineering Department of BUET, Dhaka for their kind cooperation in constructing, fabricating and assembling different parts and components of the experimental set-up

REFERENCES

1. A.R. Barriga, C.T. Crowe, and J.A. Roberson, "Pressure Distribution on a Square Cylinder at a Small Angle of attack in a Turbulent Cross Flow", Proceedings of the 4th International Conference on Wind Effects on Buildings, London, UK 1975, pp.89-93.
2. N. Biswas, "An Experimental Investigation of Wind load on tall Buildings with Square Cross-section having Rounded Facet," M. Sc. thesis, BUET, 2008.
3. A.T.M. Islam, and A.C. Mandal, "Experimental Analysis of Aerodynamic Forces for Cross- flow on single Rectangular Cylinder," Mechanical Engineering Research Bulletin **13**, 36-51 (1990).
4. G.M. G. Farok, "An Experimental Investigation of Wind Effect on Rectangular Cylinders with Rounded Corners", M.Sc. thesis, BUET, 2004.
5. H.S. Hussain and O. Islam, Journal of the Institution of Engineers **1**, (1973).



Molecular Dynamics Study on the Effect of Boundary Heating Rate on the Phase Change Characteristics of Thin Film Liquid

Mohammad Nasim Hasan^{1, a)}, A. K. M. Monjur Morshed^{1, b)}, Kazi Fazle Rabbi^{1, c)}
and Mominul Haque^{1, d)}

¹*Department of Mechanical Engineering, Bangladesh University of Engineering and Technology (BUET)
Dhaka-1000, Bangladesh*

^{a)}Corresponding author: nasim@me.buet.ac.bd.com

^{b)} shavik@me.buet.ac.bd.com

^{c)} rabbi35.me10@gmail.com

^{d)} mominulmarup@gmail.com

Abstract. In this study, theoretical investigation of thin film liquid phase change phenomena under different boundary heating rates has been conducted with the help of molecular dynamics simulation. To do this, the case of argon boiling over a platinum surface has been considered. The study has been conducted to get a better understanding of the nano-scale physics of evaporation/boiling for a three phase system with particular emphasis on the effect of boundary heating rate. The simulation domain consisted of liquid and vapor argon atoms placed over a platinum wall. Initially the whole system was brought to an equilibrium state at 90K with the help of equilibrium molecular dynamics and then the temperature of the bottom wall was increased to a higher temperature (250K/130K) over a finite heating period. Depending on the heating period, the boundary heating rate has been varied in the range of 1600×10^9 K/s to 8×10^9 K/s. The variations of argon region temperature, pressure, net evaporation number with respect to time under different boundary heating rates have been determined and discussed. The heat fluxes normal to platinum wall for different cases were also calculated and compared with theoretical upper limit of maximum possible heat transfer to elucidate the effect of boundary heating rate.

INTRODUCTION

Diverse science and engineering applications have drawn the keen interest of many researchers into phase transition and molecular dynamics. So, they have been employing and taking new topics in their studies to understand the science and engineering applications' physics on a sub-microscopic level. By simulating atomic and molecular motions, it is possible to gain atomistic insight into molecular structure and kinetics. Powerful experimental techniques (X-ray diffraction, NMR) can resolve atomic structure, but not dynamics. Many studies have been conducted to understand nanoscale heat transfer mechanisms to develop practical heat transfer solutions problems and questions related to evaporation/explosive boiling at nanoscale surfaces. Previously various studies have been reported on such matters. Yi et al. [1] simulated the vaporization phenomenon of an ultra-thin layer of liquid argon on a platinum surface for two different superheat temperatures. Yu and Wang [2] performed NEMD simulation to study the evaporation of the thin film, equilibrium vapor pressure as well as non-evaporating liquid layer in a nanoscale triple-phase system. Morshed et al. [3] performed molecular dynamics simulation to study the effect of nanostructures on evaporation and explosive boiling of thin liquid films. Seyf and Zhang [4] performed non

equilibrium molecular dynamics to study effect of nano textured array of conical features on explosive boiling over flat substrate. Shavik et al. [5] performed molecular dynamics study to investigate the effect of nanostructured surface under different wetting conditions on explosive boiling of thin liquid argon film. Weidong et al. [6] monitored the space and time dependences of temperature, pressure, density number, and net evaporation to investigate the phase transition process on a flat surface with and without nanostructures. Hens et al. [7] investigated bubbleformation on a platinum substrate with particular emphasis on the surface texture. Maroo and Chung [8] performed molecular dynamics simulation of platinum heater and associated nano-scale liquid argon film evaporation and colloidal adsorption characteristics.

Nomenclature		
r	Distance between molecules (Å)	<i>Greek Symbols</i>
t	Time	ϵ Energy parameter of LJ potential (eV)
T_w	Wall temperature (K)	σ Length parameter of LJ potential (Å)
T	Temperature (K)	ϕ Energy (eV)
T_E	Initial Temperature at stage three (K)	<i>Subscripts</i>
P	Pressure	Ar Argon
b	Heating Rate (K/s)	Pt Platinum

Although aforementioned studies modelled the evaporation or boiling of thin liquid films on flat or nanostructured surfaces, studies related to evaporation or explosive boiling of thin liquid films under different boundary heating rates are rare. In the present work, a comprehensive molecular dynamics investigation has been conducted to improve the understanding on this effect of boundary heating rates on the thin film liquid phase change phenomena.

SIMULATION METHOD

Figure 1(a) illustrates the three phase system domain which consisted of a platinum plate at the bottom. The argon region comprised of liquid argon film over the bottom plate and vapor argon in between liquid argon and upper end of the domain. The simulation domain has a dimension of 7.35nm(x) × 70nm(y) × 7.35nm (z). The bottom plate comprised of eight monolayers of platinum atoms with different purposes. The bottom layer was fixed to prevent deformation of the plate atoms; thermostat was applied to the next two layers which functioned as the heat source; the remaining five layers conducted the heat to the liquid argon. For each plate, approximately 5476 platinum atoms were arranged in FCC (1 0 0) lattice structure corresponding to its density of $21.45 \times 10^3 \text{ kg/m}^3$. Liquid argon layers of 3 nm height were placed at top of the bottom plate corresponding to its density of $1.367 \times 10^3 \text{ kg/m}^3$. The rest of the space of the domain was filled with approximately 475 argon vapor atoms. To avoid the escape of gaseous atoms non periodic fixed boundary condition was applied at the other end in the y direction of the simulation domain. Periodic boundary conditions were applied to the x and z directions. For the molecular dynamics simulation, the well-known Lenard–Jones (Lj) potential [10] was employed to calculate the intermolecular forces:

$$\phi(r) = 4\epsilon \left[\left(\frac{\sigma}{r} \right)^{12} - \left(\frac{\sigma}{r} \right)^6 \right] \quad (1)$$

ϵ and σ in Eq. (1) represents the energy parameter and the length parameter respectively. For hydrophilic substrate, Hens et al. [7] suggested $\epsilon_{Ar-Ar} < \epsilon_{Ar-Pt}$. The L-J potential parameters for argon-argon and argon-platinum used in this study are: $\sigma_{Ar-Ar} = 3.405 \text{ nm}$, $\epsilon_{Ar-Ar} = 1.67 \times 10^{-21} \text{ J}$, $\sigma_{Pt-Pt} = 2.475 \text{ nm}$, $\epsilon_{Pt-Pt} = 8.32 \times 10^{-20} \text{ J}$, $\sigma_{Ar-Pt} = 2.94 \text{ nm}$, $\epsilon_{Ar-Pt} = 3.27 \times 10^{-21} \text{ J}$. In this study the cutoff distance for L-J potential used was $4\sigma_{Ar-Ar}$. Time step of 5 fs was chosen for whole simulation. These parameters were chosen in a way to describe the mutual or reciprocal actions between atoms. The whole simulation consisted of four stages. In 1st stage the entire system was maintained at $T_E = 90 \text{ K}$ under equilibrium molecular dynamics using langevin thermostat and the system was run for 0.5 ns. Once the whole system was in equilibrium, the thermostat was removed only for the fluid domain and the system was run for another 0.5 ns (2nd stage) for equilibration. At the end of 2nd stage, the wall temperature was raised from equilibration temperature (90K) to a higher target temperature (250K) within a finite heating period (t_h) ranging from 0.1 ns to 5 ns that resulted in different boundary heating rates ranging from $1600 \times 10^9 \text{ K/s}$ to $32 \times 10^9 \text{ K/s}$. A special case has been considered in which the wall temperature was raised from 90K to 130K within 5 ns in which the boundary heating rate assumes a much lower value ($8 \times 10^9 \text{ K/s}$). In the final stage of the simulation, the wall temperature (T_w) is

maintained at the target temperature (250K or 130K) for some time such that total simulation period becomes 6 ns. To check whether the argon is in equilibrium state the temperature, pressure was monitored during the equilibration period. The simulations were performed using LAMMPS [11] and visualization was done by VMD (Visual Molecular Dynamics) [12] and OVITO(Open Visualization Tool) [13].

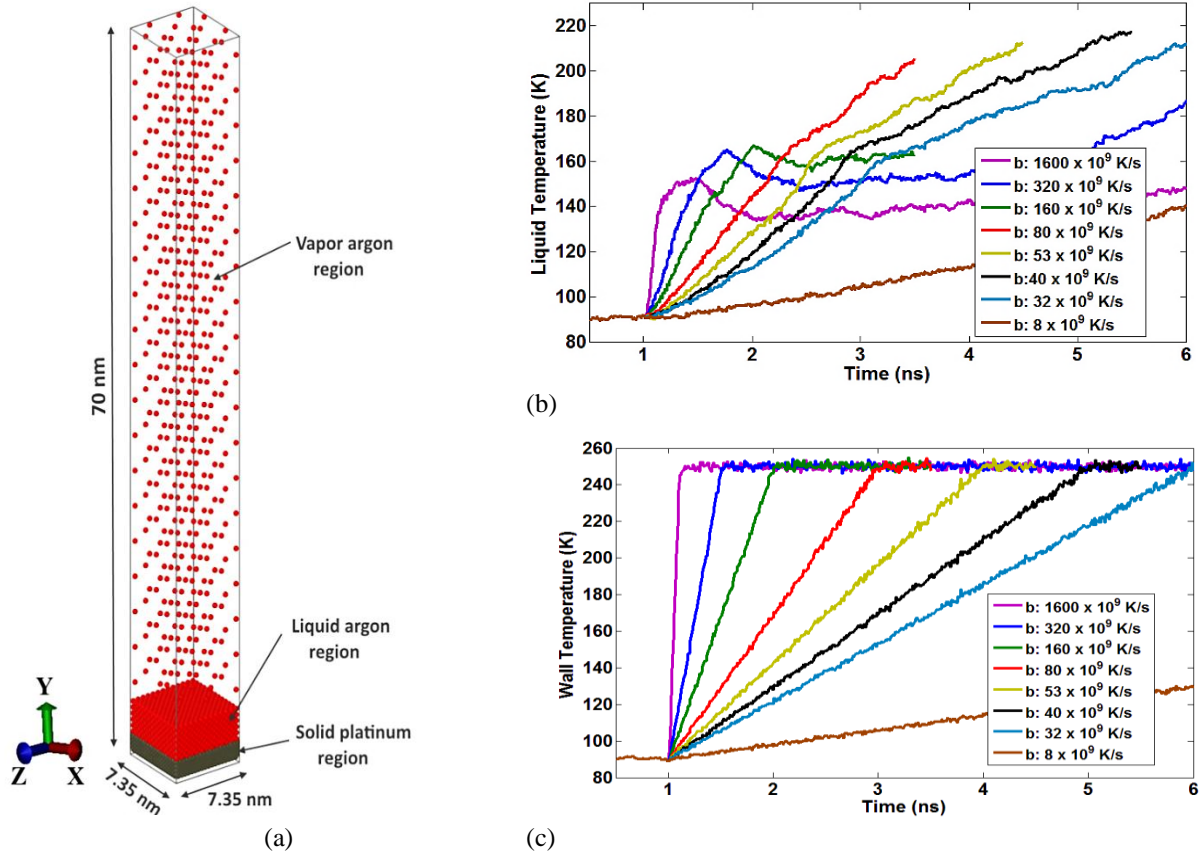


FIGURE 1.(a) Initial Configuration of the simulation, (b) Temperature History of argon region, (c) Temperature History of hydrophilic surface.

TABLE 1.Boundary heating rates considered in the present study

$T_E = 90\text{K}$								
	$T_w = 250\text{K}$				$T_w = 130\text{K}$			
t_h (ns)	0.1	0.5	1.0	2.0	3.0	4.0	5.0	5.0
$b \times 10^{-9}$ (K/s)	1600	320	160	80	53	40	32	8

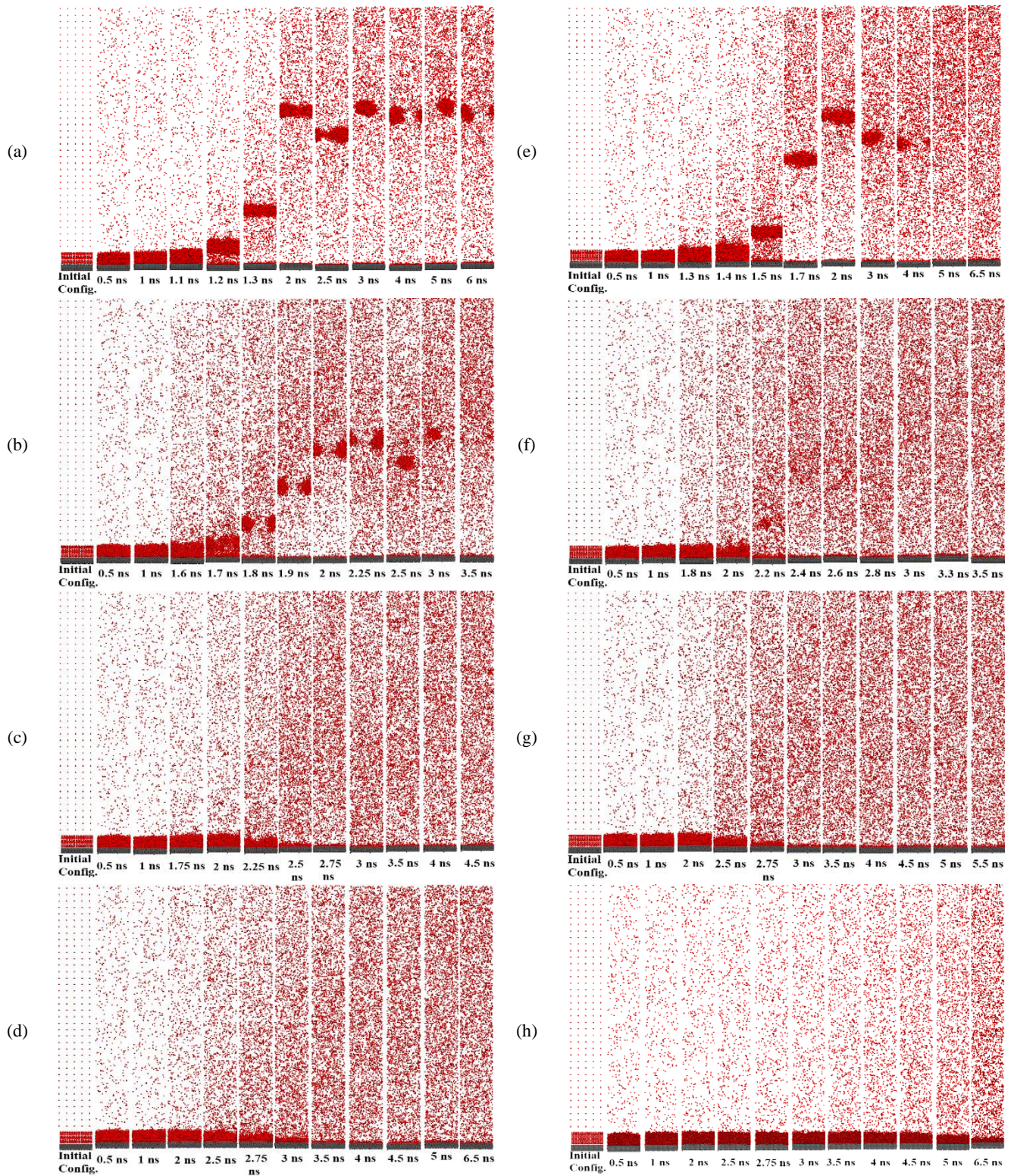


FIGURE 2. Snapshots from the simulation domain. (a) 1600×10⁹ K/s, (b) 320×10⁹ K/s, (c) 160×10⁹ K/s, (d) 80×10⁹ K/s, (e) 53×10⁹ K/s, (f) 40×10⁹ K/s, (g) 32×10⁹ K/s, (h) 8×10⁹ K/s

RESULTS AND DISCUSSION

In this study, total eight different wall heating rates at the bottom plate have been considered as tabulated in Table 1. Here, t_h is the time within which bottom wall temperature increases from the equilibrium temperature, T_E (90K) to the target temperature, T_w (250K/130K). The boundary heating rate (b) thus can be obtained as per Eq. (2):

$$T_w = T_E + bt_h \quad (2)$$

Figure 1(b) depicts the temperature history of argon region for all boundary heating rates under consideration. As shown in Fig. 1(b), the temporal variation of argon temperature follows two distinct patterns depending on the boundary heating rate (b). For first three cases as mentioned in Table 1, when the boundary heating rate is extremely high, the temperature of argon initially increases abruptly and then starts decreasing. Later, argon temperature again starts increasing. This is due to the fact that in case of very high heating rates, the liquid argon layer nearby the solid wall surpasses the critical temperature and it vaporizes while other layers above are still in the liquid phase. This low density vapor because of its low heat transfer coefficient slowed down energy flow from solid wall and temperature falls at different times approximately around 1.2ns, 1.5ns, 1.7ns for heating rate 1600×10^9 K/s, 320×10^9 K/s and 160×10^9 K/s respectively. Similar pattern of temporal variation of argon temperature has also been reported by Shavik et al. [5] and Weidong et al. [6]. For comparatively lower heating rates (80×10^9 - 32×10^9 K/s) as shown in Fig. 1(b) argon temperature continues to increase with time. However, the rate of increasing argon temperature with time is not uniform rather two distinctive regions is quite evident in all curves as shown in Fig. 1(b). This variation in the slope of time-temperature curve indicates complete phase change of liquid argon to vapor in the domain. Figure 1(c) shows the time variation of wall temperature. Heating rates can be easily realized from the curve and gives clear picture of how temperature changed with time.

Figure 2 illustrates the snapshots of the simulation domain at some specific instant of time for all cases of boundary heating rate. These Figs. give molecular insight into the phase transition for various cases. From the snapshots as shown in Figs. 2(a)-(c) the temporal variation of argon temperature observed in Fig. 1(b) can easily be interpreted. The fast vaporization of liquid layer that leads to the formation of liquid cluster in the domain is very much evident for the cases of high boundary heating rates. From snapshots of Figs. 2(a)-(c) it has been found that the cluster formation occurred at approximately 1.2 ns, 1.5 ns, 1.7 ns for heating rates 1600×10^9 K/s, 320×10^9 K/s, 160×10^9 K/s respectively. Later on the liquid argon cluster disintegrates into vapor due to energy transfer from the bottom plate as well as by collision of atoms. Thus the number of vapor atoms and heat transfer to the vapor region increases. From the snapshots in Figs. 2(d), (e), (f) and (g) it is obvious that there isn't any noticeable liquid argon cluster formation. Therefore, the phase change process resembles a molecular diffusion process rather an explosive boiling. As a result, no sharp drop in argon temperature with time has been noted in Fig. 1(b) for these cases (80×10^9 - 32×10^9 K/s). The snapshots also show during cluster formation that the higher the heating rate, the faster the rate of vaporization and the faster the simulation domain reaches the equilibrium vapor argon state.

From Fig. 3(a) it is very clear that due to volume constraint of the system, increase in temperature results in the increase in system pressure and interestingly, pressure variation exactly follows the temperature variation of the simulation domain. For the first three higher heating rates faster cluster formation causes lower temperature and lower pressure. Fig. 3(b) shows the spatial argon number density along the y axis at 2ns of the simulation. As shown in Fig. 3(b), the presence of higher argon density has been located at 43 nm, 41 nm, and 31 nm along y axis for boundary heating rate 1600×10^9 K/s, 320×10^9 K/s and 160×10^9 K/s respectively. This confirms the presence of liquid argon cluster at these distances which is also evident in the snapshots of Figs. 2(a)-(c). The maxima of these curves as depicted in Fig. 3(b) gives clear picture of faster vaporization. This occurs because the slower the cluster formation the more the energy taken from solid wall resulting in reduction of vaporization time. For other heating rates there isn't such noticeable rise in number density which agrees with the snapshots presented in Figs. 2(d)-(g).

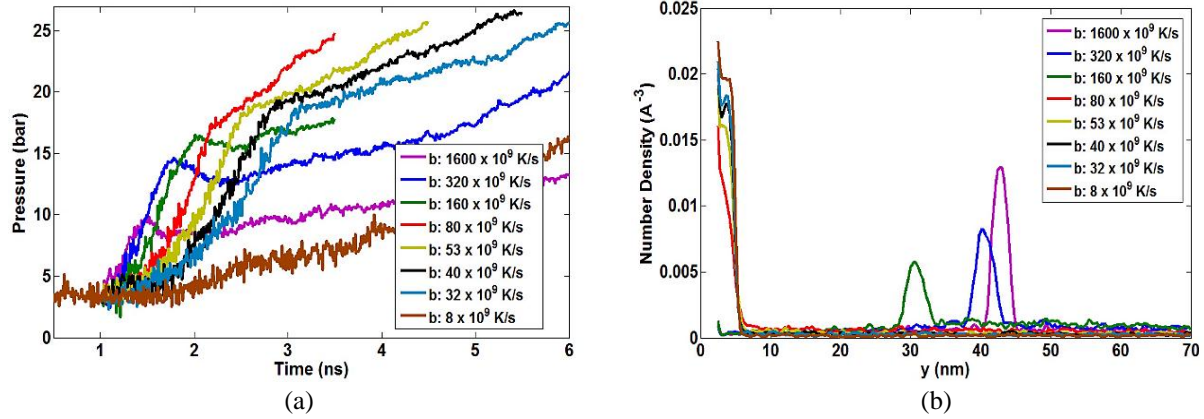


FIGURE 3. Pressure history of argon region (a). Spatial Density distribution of argon region (b)

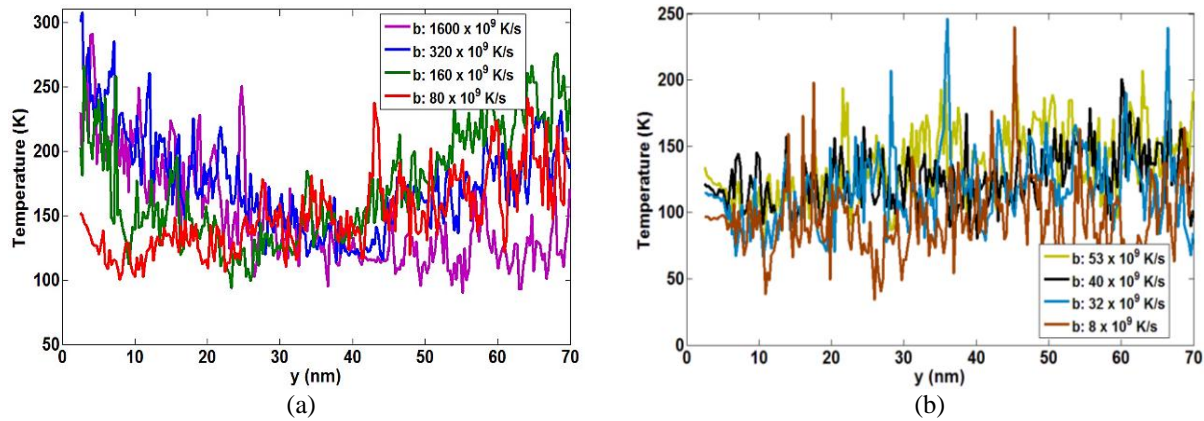


FIGURE 4. Spatial temperature distribution for argon region along y axis (a) and (b)

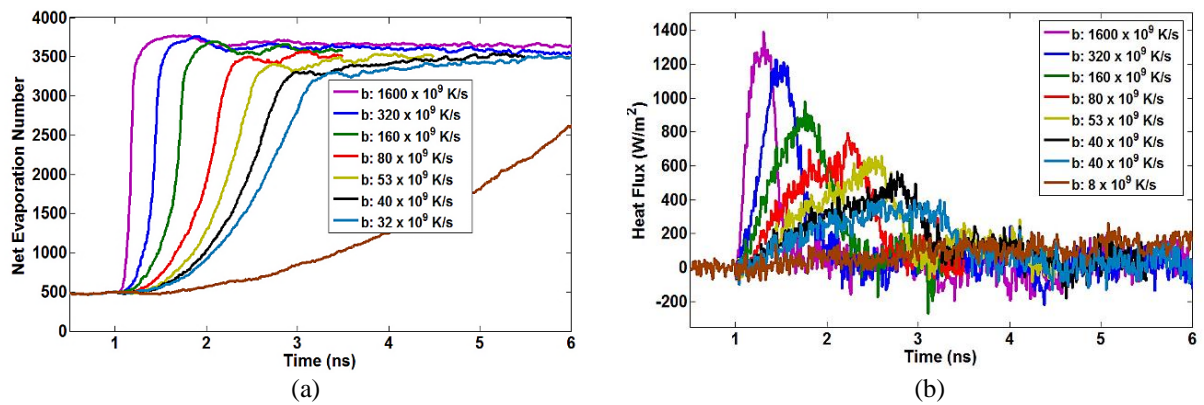


FIGURE 5. Net evaporation number (a). Heat flux normal to the bottom plate (b)

TABLE 2.Heat flux at different heating rate, b

Heating rate, b ×10⁻⁹ (K/s)	1600	320	160	80	53	40	32	8
Heat flux (MW/m²)	1400	1200	980	800	650	520	400	277

The formation and presence of cluster argon during heating process is also visible from the Fig. 4 which shows the spatial temperature distribution along the y axis at 2ns. From the snapshots of Figs. 2(a)-(c), it has been shown that the presence of the liquid argon cluster is at a distance of 43, 41, 31nm along the y axis for boundary heating rate 1600×10^9 K/s, 320×10^9 K/s and 160×10^9 K/s respectively. As shown in Fig. 4(a) a corresponding temperature drop might be identified in these positions. The minima of spatial temperature curve in Fig. 4(a) corresponds a value of about 150K which is very close to the critical temperature of argon. For other cases with slower boundary heating, as depicted in Fig. 4(b), instantaneous spatial temperature distribution does not descend along y axis indicating the absence of any liquid cluster. Figure 5(a) shows the time variation of argon atoms in the vapor region at various boundary heating rates. As shown in Fig. 5(a), higher magnitude of boundary heating rates results in higher evaporation rate. So, higher heating rates enhance explosive boiling and evaporation.

For comparing the effectiveness of heat transfer process, heat fluxes normal to the bottom plate were evaluated. The temporal variation of wall heat flux is shown in Fig. 5(b). The profiles of the heat flux as well as the order of magnitude are in good agreement with previous study conducted by Shavik et al. [5], Maroo and Chung [8], and Yamamoto and Matsumoto [9]. Maximum heat fluxes have been evaluated for all cases of boundary heating rates under consideration as tabulated in Table 2. From Table 2 it can be found that higher heating rate offers higher maximum wall heat flux. So for the first seven cases the higher the heating rate the higher the heat flux and the faster the argon region reaches 250K. For the last case where the heating rate is very low (8×10^9 K/s) heat flux addition at a very small rate continues for whole simulation time and by the end of the simulation run argon region temperature rises to only 130K.

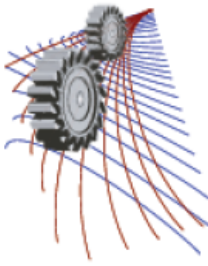
CONCLUSION

The characteristics of liquid to vapor phase change phenomena for a thin liquid film depends much on boundary heating rate. Depending on the boundary heating rate, the process may be governed either by molecular diffusion or explosive boiling. The formation of liquid cluster at very high boundary heating rate greatly affects the temperature as well as pressure profile of the system. As obtained in the present study, for a liquid argon layer of 3 nm, a boundary heating rate more than 80×10^9 K/s results in noticeable rise of liquid layer to the vapor region i.e. formation of liquid cluster. For heating rate lower than 80×10^9 K/s cluster formation does not take place and the temperature of the argon region steadily increases with gradual vaporization of liquid argon. Pressure change follows the trend of temperature change. Higher heat flux requires higher heating rate as faster change in temperature of the surface is required. In case of higher boundary heating rates, the evaporation rate in the simulation domain reaches equilibrium state faster than the lower boundary heating rates.

REFERENCES

1. P. Yi, D. Poulidakos, J. Walther, G. Yadigaroglu, *Int. J. Heat Mass Transfer* **45**, 2087–2100 (2002).
2. J. Yu and H. Wang, *Int. J. Heat Mass Transfer* **55**, 1218-1225 (2012).
3. A.K.M.M. Morshed, Taitan C. Paul, Jamil A. Khan, *Applied Physics A* **105**, 445-451 (2011).
4. H.R. Seyf and Y. Zhang, *Int. J. Heat Mass Transfer* **66**, 613-624 (2013).
5. Sheikh Mohammad Shavik, Mohammad Nasim Hasan, A.K.M. Monjur Morshed, "Molecular dynamics study on explosive boiling of thin liquid argon film on nanostructured surface under different wetting conditions," *InterPACKICNMM2015-48352*.
6. Weidong Wang, Haiyan Zhang, Conghui Tian and Xiaojie Meng, "Numerical experiments on evaporation and explosive boiling of ultra-thin liquid argon film on aluminum nanostructure substrate."

7. A. Hens, R. Agarwal, G. Biswas, *Int. J. Heat Mass Transfer* **71**, 303-312 (2014).
8. S.C. Maroo and J.N. Chung, *J. Colloid Interface Sci.* **328**, 134–146 (2008).
9. T. Yamamoto and M. Matsumoto, *J. Therm. Sci. Technol. Jpn.* **7**, 334–349 (2012).
10. J.E. Lennard-Jones, A.F. Devonshire, *Philos. Trans. R. Soc. Lond. Ser. A, Math. Phys. Sci.* **163**, 53-70 (1937).
11. LAMMPS User's Manual (<http://lammps.sandia.gov> – Sandia National Laboratories, USA).
12. Humphrey W, Dalke A, Schulten K. VMD: Visual Molecular Dynamics. *J Mol Graph.* 1996; 1433: 1996
13. Stukowski A. Visualisation and analysis of atomistic simulation data with OVITO-the open visualisation tool, *Model Simul Mater Sci Eng.* 2010; 18: 015012



Turbulent Flow Analysis on Bend and Downstream of the Bend for Different Curvature Ratio

Rana Roy Chowdhury^{1, 2, a)}, Suranjan Biswas^{2, b)}, Md. Mahbubul Alam^{3, c)} and A.K.M.Sadrul Islam^{4, d)}

¹Post Graduate Student, Department of Mechanical Engineering, CUET, Chittagong- 4349, Bangladesh

²Karnaphuli Gas Distribution Company Ltd., Chittagong-4203, Bangladesh

³Department of Mechanical Engineering, CUET, Chittagong- 4349, Bangladesh

⁴Department of Mechanical and Chemical Engineering, IUT, Gazipur- 1704, Bangladesh

^{a)}Corresponding author: engr.rrc@gmail.com

^{b)}suranjan.me@gmail.com

^{c)}mahbub87@yahoo.com

^{d)}sadrul05@gmail.com

Abstract. A CFD analysis on the bend and downstream of the bend has been carried out for turbulent flow through 90 degree bend pipe with different curvature ratios using standard k-epsilon turbulence model. Numerical results are compared with the existing experimental results, and then a detailed study has been performed to investigate the flow characteristics. For different curvature ratios, the static pressure distributions along inner, outer wall and pressure loss factor with different Reynolds number is analyzed. The obtained results show that pressure distribution and pressure loss factor are dependent for different Reynolds number and curvature ratio throughout the bend. Again, It is observed that the disturbance of the flow due to bend exists for a downstream distance of 50D from the central plane of the bend.

INTRODUCTION

Fluid flows through pipe bends are found in many engineering applications. Such as, High Temperature Gas Cooled Reactor (HTGR), Pressurized Water Reactor (PWR), CANDU type reactor, torus reactor, oil and gas production field with their distribution networks, heat exchangers, internal combustion engines, solar collectors, the cooling system of processing industries, electronic components and nuclear power plants. Moreover, due to its simplicity, low cost, reliability and repeatability; it is used for flow measurement and flow accelerated corrosion (FAC) rate analysis under high pressure and temperature owing to the wicked measuring environment and restriction of reactor structure [3]. On contrary to that, installing a bend in the fluid flow field produces high disturbances which is good for intentional chemical mixing but can affect the heat transfer rates which is very dangerous for nuclear power plant, also reduce the accuracy of flow measuring devices and not too much expected for other engineering purposes. Thus, the flow through a bend and its disturbance at the downstream tangent has drawn attention by the researchers. Most of the experimental and numerical analyzes are investigated the flow phenomena through a bend. But, very limited papers have focused the flow in the downstream tangent of the bend (Al-Rafai et Al., 1990, Sudo et Al., 1998, Kim et Al., 2014). Hence, the present analysis is carried out in a view to understanding the flow characteristics at the bend and how far downstream of the bend the flow becomes to be fully developed.

SOLUTION METHODOLOGY

For turbulent flow through bend pipes, the mass and momentum equation along with the standard k-ε model has been adopted for the present computation. The SIMPLE algorithm which is based on a finite volume discretization of the governing equations as suggested by Patankar (1980) is used for numerical modeling [6].

Governing Equations

Conservation equation in dimensionless form for the axis-symmetric flow of a liquid through the bend pipes are written in a cylindrical co-ordinate system as:

Continuity Equation:

$$\frac{\partial V_r}{\partial r} + \frac{V_r}{r} + \frac{\partial V_z}{\partial z} = 0 \quad (1)$$

Momentum Equations:

r-momentum:

$$\begin{aligned} \frac{\partial V_r}{\partial t} + \frac{\partial}{\partial r}(V_r V_r) + \frac{\partial}{\partial z}(V_z V_r) + \frac{V_r^2 - V_\theta^2}{r} = -\frac{\partial p_1}{\partial r} + \frac{2}{\text{Re}} \frac{\partial}{\partial r} (v_{\text{eff}} \frac{\partial V_r}{\partial r}) + \frac{2}{\text{Re}} \frac{v_{\text{eff}}}{r} (\frac{\partial V_r}{\partial r} - \frac{V_r}{r}) \\ + \frac{1}{\text{Re}} \frac{\partial}{\partial z} \left\{ v_{\text{eff}} \left(\frac{\partial V_r}{\partial z} + \frac{\partial V_z}{\partial r} \right) \right\} \end{aligned} \quad (2)$$

z-momentum:

$$\frac{\partial V_z}{\partial t} + \frac{\partial}{\partial r}(V_r V_z) + \frac{\partial}{\partial z}(V_z^2) + \frac{V_r V_z}{r} = -\frac{\partial p_1}{\partial z} + \frac{1}{\text{Re}} \frac{1}{r} \frac{\partial}{\partial r} \left\{ r v_{\text{eff}} \left(\frac{\partial V_z}{\partial r} + \frac{\partial V_r}{\partial z} \right) \right\} + \frac{2}{\text{Re}} \frac{\partial}{\partial z} (v_{\text{eff}} \frac{\partial V_z}{\partial z}) \quad (3)$$

θ-momentum:

$$\frac{\partial V_\theta}{\partial t} + \frac{\partial}{\partial r}(V_r V_\theta) + \frac{\partial}{\partial z}(V_z V_\theta) + \frac{2V_r V_\theta}{r} = \frac{1}{\text{Re}} \frac{1}{r^2} \frac{\partial}{\partial r} \left\{ r^2 v_{\text{eff}} \left(\frac{\partial V_\theta}{\partial r} - \frac{V_\theta}{r} \right) \right\} + \frac{1}{\text{Re}} \frac{\partial}{\partial z} (v_{\text{eff}} \frac{\partial V_\theta}{\partial z}) \quad (4)$$

Where, $p_1 = p + \frac{2}{3}(\rho k)$, $v_{\text{eff}} = \mu_{\text{eff}} / \rho$, $\mu_{\text{eff}} = \mu + \mu_t$, $\mu_t = \frac{c_\mu \rho k^2}{\varepsilon}$

Turbulent Kinetic Energy (k) Equation:

$$\begin{aligned} \frac{\partial k}{\partial t} + \frac{\partial}{\partial r}(V_r k) + \frac{\partial}{\partial z}(V_z k) + \frac{V_r k}{r} = \frac{1}{\text{Re}} \frac{1}{r} \frac{\partial}{\partial r} \left(r \frac{v_t}{\sigma_k} \frac{\partial k}{\partial r} \right) + \frac{1}{\text{Re}} \frac{\partial}{\partial z} \left(\frac{v_t}{\sigma_k} \frac{\partial k}{\partial z} \right) + \\ \frac{1}{\text{Re}} v_t \left[2 \left\{ \left(\frac{\partial V_r}{\partial r} \right)^2 + \left(\frac{V_r}{r} \right)^2 + \left(\frac{\partial V_z}{\partial z} \right)^2 \right\} + \left(\frac{\partial V_\theta}{\partial r} - \frac{V_\theta}{r} \right)^2 + \left(\frac{\partial V_r}{\partial z} + \frac{\partial V_z}{\partial r} \right)^2 + \left(\frac{\partial V_\theta}{\partial z} \right)^2 \right] - \varepsilon \end{aligned} \quad (5)$$

Turbulent kinetic Energy Dissipation rate (ε) Equation:

$$\begin{aligned} \frac{\partial \varepsilon}{\partial t} + \frac{\partial}{\partial r}(V_r \varepsilon) + \frac{\partial}{\partial z}(V_z \varepsilon) + \frac{V_r \varepsilon}{r} = \frac{1}{\text{Re}} \frac{1}{r} \frac{\partial}{\partial r} \left(r \frac{v_t}{\sigma_\varepsilon} \frac{\partial \varepsilon}{\partial r} \right) + \frac{1}{\text{Re}} \frac{\partial}{\partial z} \left(\frac{v_t}{\sigma_\varepsilon} \frac{\partial \varepsilon}{\partial z} \right) + \frac{1}{\text{Re}} c_{1\varepsilon} \frac{\varepsilon}{k} v_t \\ \left[2 \left\{ \left(\frac{\partial V_r}{\partial r} \right)^2 + \left(\frac{V_r}{r} \right)^2 + \left(\frac{\partial V_z}{\partial z} \right)^2 \right\} + \left(\frac{\partial V_\theta}{\partial r} - \frac{V_\theta}{r} \right)^2 + \left(\frac{\partial V_r}{\partial z} + \frac{\partial V_z}{\partial r} \right)^2 + \left(\frac{\partial V_\theta}{\partial z} \right)^2 \right] - c_{2\varepsilon} \frac{\varepsilon^2}{k} \end{aligned} \quad (6)$$

The empirical constants for equation (5) & (6) are taken as follows:

$$\sigma_k = 1.0, \sigma_\varepsilon = 1.3, c_{1\varepsilon} = 1.44, c_{2\varepsilon} = 1.92$$

Problem Specification

The steady state turbulent flow through 90° bend pipe with 100 mm diameter (D) along with the upstream and downstream length of 60D are analyzed considering the incompressible fluid is water: density $\rho=1000\text{Kg/m}^3$, dynamic viscosity $\mu=0.008\text{ Pa.s}$. Again, by varying the radius of curvature (R) thus with different R/D ratios the flow characteristics are analyzed at the bend and downstream of the bend. Further, for validation purpose the geometry has been adopted as specified in the reference [2] by Sudo et Al.

RESULTS AND DISCUSSION

The numerical results are compared with the existing experimental results of Sudo et al. [2] in Fig. 1 and found the present analysis agree well with the reference data. Then, the wall static pressure distributions, wall shear stress and pressure loss factor with different Reynolds number for different curvature ratio (R/D) are analyzed. Again, flow characteristics such as flow profile and turbulence intensity are analyzed to achieve a fully developed profile at the downstream tangent of the bend.

Flow Analysis of the Bend

The inner and outer wall static pressure distribution at the different location of the bend with different Re numbers for R/D=1 are presented in Fig. 2(a) and Fig. 2(b). At the inner wall, the positive pressure gradient is appeared up to $\Theta=30^\circ$ locations and then an adverse pressure gradient is seen at further downstream. The reverse is occurred for the outer wall side due to the strong action of centrifugal force. It is also clear that the higher pressure region is in the outer wall as the flow decelerates and lower pressure in the inner wall due to flow accelerates throughout the bend.

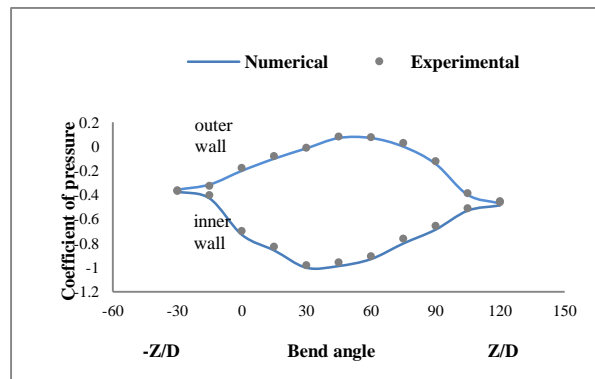


FIGURE 1. Comparison of numerical and experimental results

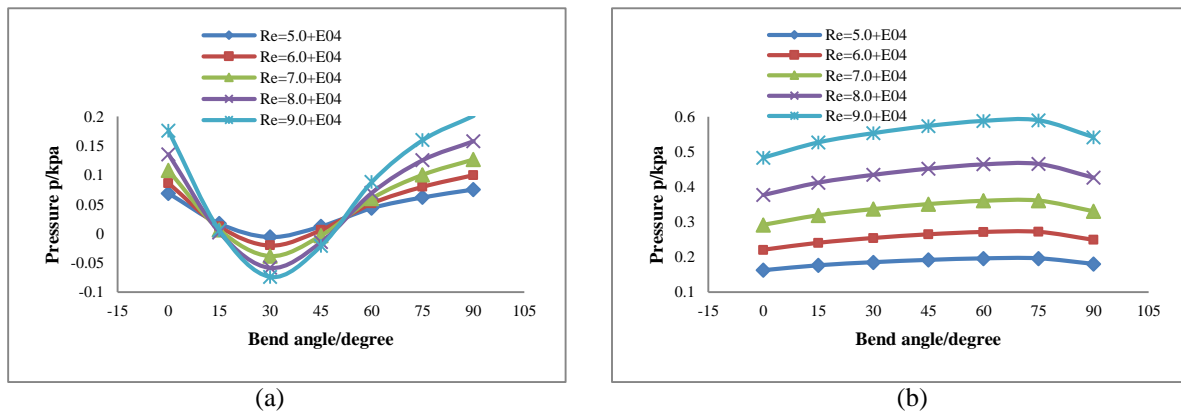


FIGURE 2. static pressure distribution (a) Inner wall, (b) Outer wall

It is believed that flow accelerated corrosion (FAC) mostly appeared in the high wall shear stress side of the flow field. The inner and outer wall shear stress for different Re with different bend location for R/D=1 are shown in Fig. 3 which yields that, the maximum wall shear stress is appeared at the inner side just near the entrance of the bend. Thus, it can be predicted that the maximum FAC should be expected at the the inner side of the bend, if the reverse is true then other phenomena beyond the fluid mechanics and the pipe surface are responsible. In Fig. 4 the wall static pressure for R/D ratios (1 to 5) with different Re numbers at several locations (0°, 30°, 45° and 90°) of the bend are presented. It is seen that the wall static pressure varied with Re for different R/D ratios. Again, the inner and outer wall pressure difference is increased for small R/D ratio as Re increased. Another important parameter, the pressure drop characteristic for different bend with different Re numbers are represented in Fig. 5, where the pressure loss factor is defined as $k_l = \Delta p / 0.5 \rho u_b^2$, where u_b is the bulk velocity and Δp is the total pressure loss across a bend. It is observed that as R/D increases the factor k_l decreases because the separation zone is large for small R/D and for large R/D the influence of friction is dominant. Again, due to higher velocity heads the pressure loss factor k_l decreases as Re increases for same R/D ratio.

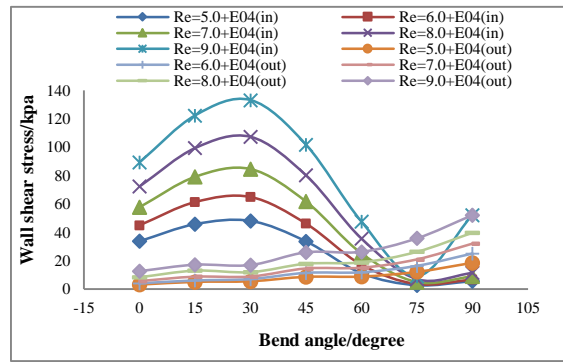


FIGURE 3. Inner and outer wall shear stress distribution

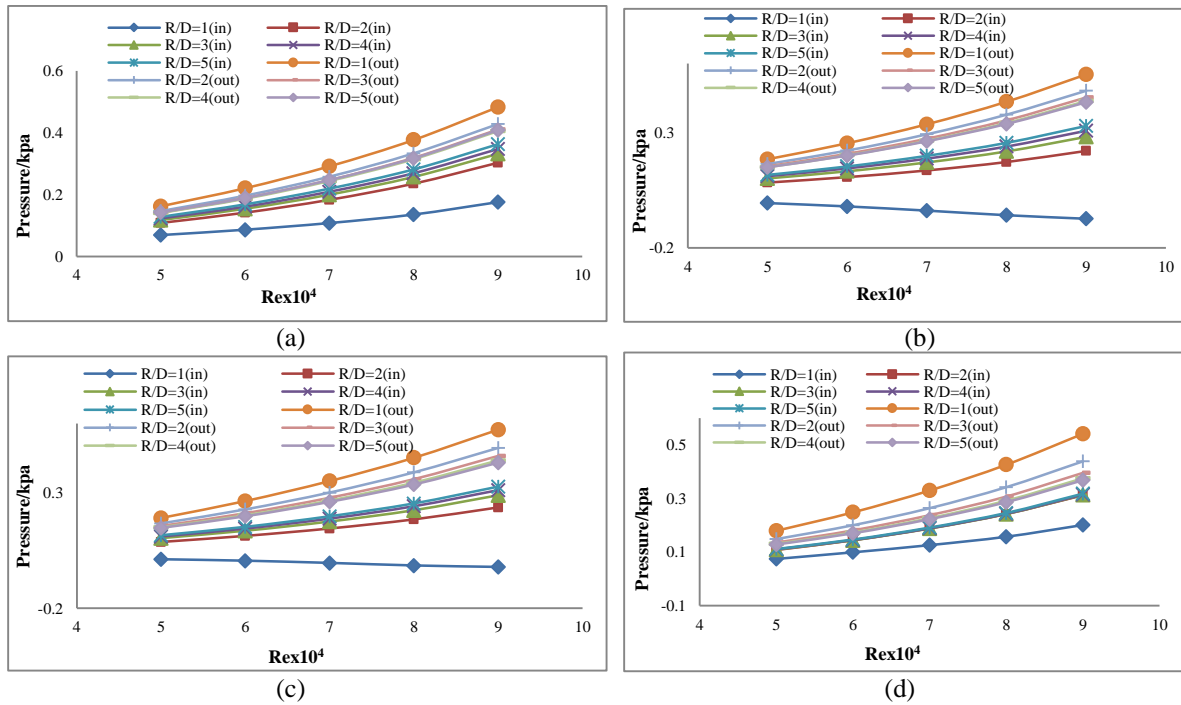


FIGURE 4. Wall static pressure distribution for different R/D at (a) 0 degree, (b) 30 degree, (c) 45 degree and (d) 90 degree

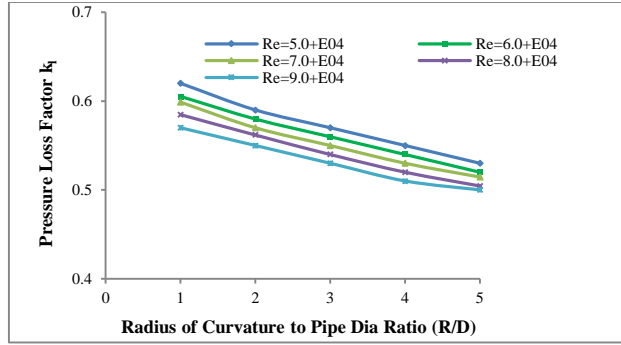


FIGURE 5. Pressure loss factor variation with R/D for different Re

Analysis of Flow Characteristics Downstream of the Bend

Maldistribution of flow and turbulence naturally occurs after any pipe bend. To achieve a fully developed flow, the 10D bend upstream profile which is compared with the empirical power law equation as mentioned in reference [5] and then it is used to compare the flow characteristics after the bend in the downstream tangent. Figure 6(a) and 6(b) shows the velocity profile development for R/D=1 and R/D=5 with Re=9.0+E04 at 10D, 30D and 50D downstream of the bend. It is clear that the flow is developed at 30D and turns to fully develop at 50D downstream from the bend for both figures.

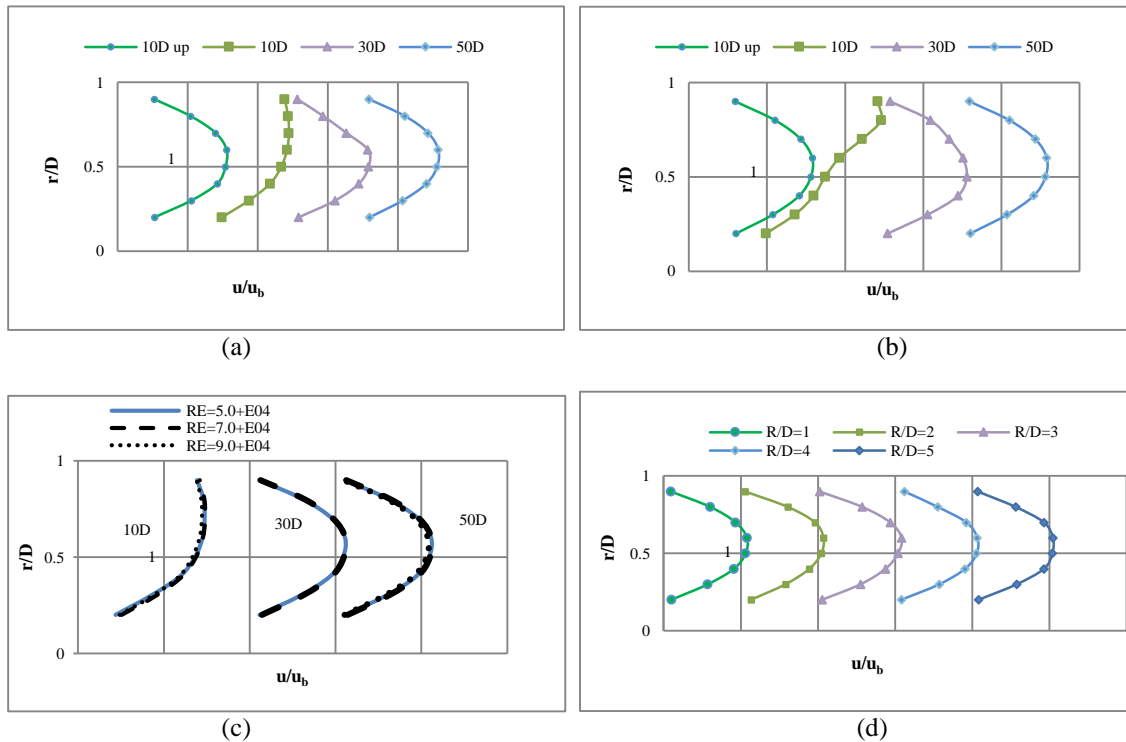


FIGURE 6. Downstream velocity profile development for (a) R/D=1, (b) R/D=5, (c) Downstream velocity profile development for different Re and (d) Fully developed turbulent velocity profile at 50D for different R/D

To see the dependency on Re numbers for the flow development, Fig. 6(c) shows that the similarity exists in the flow pattern for same R/D but as Re increases the velocity at the centerline is more flattened and it occurs in the fully developed turbulent pipeline flow. However, the fully developed velocity profile at 50D downstream for R/D=1 to 5 are compared at Fig. 6(d) and surprisingly, the results indicate that the R/D ratio does not affect too much for the developed flow. Similarly, the effects of turbulence downstream of the bend are presented as turbulence intensity profile respectively in Fig. 7(a) to Fig. 7(c). Thus, it is obviously clear from the turbulence intensity profile that, the flow disturbance is eliminated at the 50D downstream of the bend and as further downstream the velocity and turbulence profiles are no longer changes.

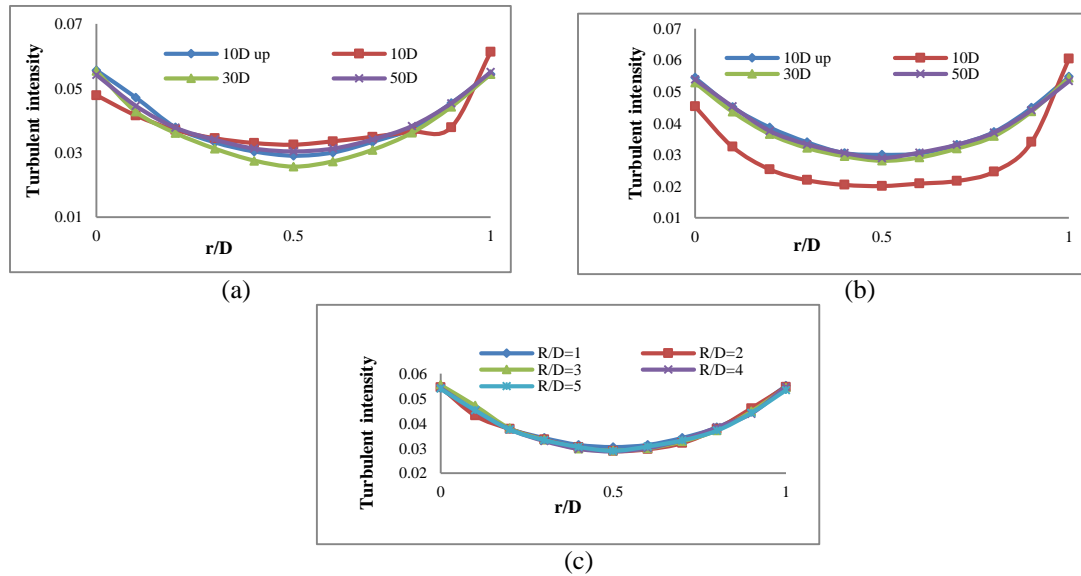


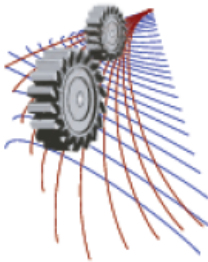
FIGURE 7. Downstream turbulence intensity development at (a) R/D=1, (b) R/D=5 and (c) Fully developed turbulence intensity profile at 50D for different R/D

CONCLUSION

A numerical study is performed to analyze the flow characteristics on the bend and downstream of the bend. The wall pressure, wall shear stress distribution along with total pressure loss factor is studied to investigate the dependency for different curvature ratio and Reynolds number for the bend. After bend effect is analyzed through the development of velocity profile and turbulent intensity and found flow disturbance eliminated at 50D of the downstream. However, further studies are necessary to give a conclusion about the required length of regaining fully developed flow after the flow disturbance considering the swirl intensity at the downstream.

REFERENCES

1. J. Kim, M. Yadav, S. Kim, Engineering Applications of Computational Fluid Mechanics **8**, 229-239 (2014).
2. K. Sudo, M. Sumida and H. Hibara, Experiments in Fluids **25**, 42-49 (1998).
3. B. Feng, S.Wang, S. Li, X. Yang and S. Jiang, "Experimental and Numerical Study on Pressure Distribution of 90° Elbow for Flow Measurement", Science and Technology of Nuclear Installations, Hindawi Publishing Corporation, Article ID 964585, <http://dx.doi.org/10.1155/2014/964585>, (2014).
4. W N Al-Rafai, Y D Tridimas, N H Wooley, Journal of Mechanical Engineering Science **204**, 399-408 (1990).
5. Robert W Glanville, Kimbal A. Hall, "Static Fluid Flow Conditioner", United States Patent, Patent no-US 8, 322,381, B1(Dec.4, 2012).
6. K Muralidhar, T Sundararajan, "Computational Fluid Flow and Heat Transfer", 2nd Edition, Narosa Publishing House, New Delhi, pp. 229-269 (2005).



Natural Convection of Non-Newtonian Fluid along a Vertical Thin Cylinder using Modified Power-law model

Sharaban Thohura^{1, a)}, Md. Mamun Molla^{2, b)} and M. M. A. Sarker^{3, c)}

¹*Department of Mathematics, Jagannath University Dhaka-1100, Bangladesh*

²*Department of Mathematics & Physics, North South University, Dhaka-1229, Bangladesh*

³*Department of Mathematics, Bangladesh University of Engineering & Technology, Dhaka, Bangladesh*

^{b)}Corresponding author: mamun.molla@northsouth.edu

^{a)}sthohura@gmail.com

^{c)}masarker45@gmail.com

Abstract. A study on the natural convection flow of non-Newtonian fluid along a vertical thin cylinder with constant wall temperature using modified power law viscosity model has been done. The basic equations are transformed to non dimensional boundary layer equations and the resulting systems of nonlinear partial differential equations are then solved employing marching order implicit finite difference method. The evolution of the surface shear stress in terms of local skin-friction, the rate of heat transfer in terms of local Nusselt number, velocity and temperature profiles for shear thinning as well as shear-thickening fluid considering the different values of Prandtl number have been focused. For the Newtonian fluids the present numerical results are compared with available published results which show a good agreement indeed. From the results it can be concluded that, at the leading edge, a Newtonian-like solution exists as the shear rate is not large enough to trigger non-Newtonian effects. Non-Newtonian effects can be found when the shear-rate increases beyond a threshold value.

INTRODUCTION

Natural convection on a vertical cylinder can find its application in a variety of circumstances, including heat loss from steam pipes, heat transfer from wires, cooling of nuclear fuel rods, heat transfer from pin fin heat sinks as well as in the human body. Flow over cylinders is considered to be two-dimensional if the body radius is large compared to the boundary layer thickness. For a thin or slender cylinder, the radius of the cylinder may be of the same order as the boundary layer thickness. Therefore, the flow may be considered as axisymmetric instead of two-dimensional. In this case, the governing equation contain the transverse curvature term which influences both the velocity and temperature fields.

Convective flow involving power-law, non-Newtonian fluids is an area of research undergoing rapid growth in fluid mechanics and heat transfer in the past half century. This is motivated by a wide range of geophysical and engineering and applications including chemicals, foods, polymers, molten plastics and petroleum productions. A sequence of excellent lectures on non-Newtonian fluids was given by Hinch [1]. It appears that Acrivos [2], a frequently cited paper, was the first to consider the boundary-layer flows for such fluids. Since then, a large numbers of papers have been published. A comprehensive collection of references and reviews are listed here to provide starting points for a broader literature search [3-15].

Several papers have been published on natural convection around vertical isothermal cylinders. Sparrow and Gregg [16] solved this problem by a series expansion. Minkowycz and Sparrow [17] studied the natural convection along a vertical cylinder with a constant surface temperature by a local non-similarity solution. Kuiken [18] and Fujii and Uehara [19] studied the heat transfer of non-isothermal vertical cylinders with large curvatures by series solutions. Takhar et al. [20] have considered the natural convection on a vertical thin cylinder embedded in a

thermally stratified high-porosity medium. Aziz et al. [21] have investigated improved perturbation solutions for laminar natural

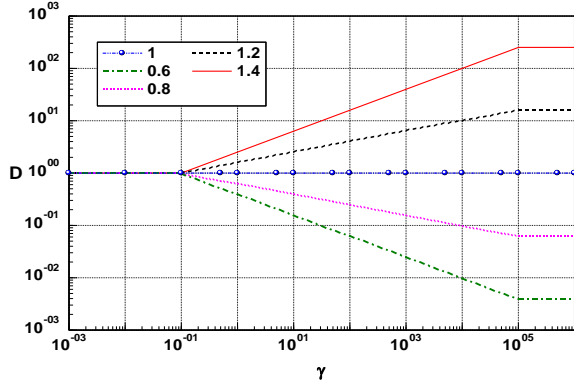


FIGURE 1. Modified power-law viscosity correlation.

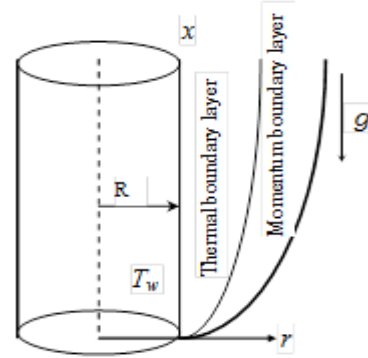


FIGURE 2. Physical model and the coordination system.

convection on a cylinder. T. Cebeci [22] has studied laminar free convection heat transfer from the outer surface of a vertical slender circular cylinder. All of the aforementioned authors considered Newtonian fluid.

In the present study, the natural convection flow of non-Newtonian fluid along a vertical thin cylinder with constant wall temperature using modified power law viscosity model has been considered. The recently proposed modified power-law correlation is sketched for various values of the power index n in Fig.1. It is clear that the new correlation does not contain the physically unrealistic limits of zero and infinite viscosity displayed by traditional power-law correlations [Acrivos2]. The modified power-law in fact, fits data well. The constants in the proposed model can be fixed with available and are described in detail in Ref.[23] and associated heat transfer for two different heating conditions is reported in [24] for a shear-thinning fluid. In this investigation, the behaviors of the shear –thinning and shear thickening on the natural-convection laminar flow with uniform wall temperature are studied by choosing the power-law index as $n=0.6, 0.8, 1, 1.2$ and 1.4 to fully demonstrate the performance of various non-Newtonian fluids.

It is worthy to note that the validity of the laminar boundary layer theory has been well established for a nearly century. It is well known that they can correlate a major part of the available data. The recently proposed modified power law simply modifies the power law to fit available data better at its two ends, because a power law model is a direct model that is used to fit experimental data. The results of our parametric study in the paper can provide the necessary database that a simple interpolation can be used to find approximate heat transfer rates and wall shear stresses for any non-Newtonian fluid from our tables.

Our study also indicates the importance of measuring a complete set of viscosity –shear relations. Because an infinite viscosity corresponds to solids and no frictionless fluid has ever been found, a partial set of measured viscosity-shear relations is not sufficient for a boundary-layer study.

FORMULATION OF THE PROBLEM

A vertical cylinder has three surfaces: the top surface, the bottom surface and the vertical surface. For the vertical surface of the cylinder, the development of the boundary layer is shown in Fig 2. Under steady-state conditions, the governing equations of this problem, in cylindrical co-ordinates are

$$\frac{\partial}{\partial x}(ru) + \frac{\partial}{\partial r}(rv) = 0 \quad (1)$$

$$u \frac{\partial u}{\partial x} + v \frac{\partial u}{\partial r} = \frac{1}{r} \frac{\partial}{\partial r} \left(v r \frac{\partial u}{\partial r} \right) + g\beta(T - T_{\infty}) \quad (2)$$

$$u \frac{\partial T}{\partial x} + v \frac{\partial T}{\partial r} = \frac{\alpha}{r} \frac{\partial}{\partial r} \left(r \frac{\partial T}{\partial r} \right) \quad (3)$$

Where u and v are the velocity components, respectively, in axial and radial directions, and T is the temperature, g is the acceleration due to gravity, β is the thermal expansion coefficient, and α is the thermal diffusivity. The viscosity is correlated by a modified power-law, which is

$$v = \frac{\kappa}{\rho} \left| \frac{\partial u}{\partial r} \right|^{n-1} \quad \text{for} \quad \gamma_1 \leq \left| \frac{\partial u}{\partial r} \right| \leq \gamma_2 \quad (4)$$

The constants γ_1 and γ_2 are threshold shear-rates, ρ is the density of the fluid, and K is a dimensional constant, the dimension which depends on the power-law index n . The values of these constants can be determined by matching with measurements. Outside of the above range, viscosity is assumed constant; its value can be fixed with data given in Fig. 1. The boundary conditions for the present problem are

$$\begin{aligned} u = 0, v = 0, T = T_w \quad \text{at } r = R \\ u = 0, v = 0, T = T_\infty \quad \text{as } r \rightarrow \infty \end{aligned} \quad (5)$$

We now introduce the following non-dimensional transformations:

$$\begin{aligned} \xi = \frac{2x}{R} Gr_x^{-1/4}, \eta = \frac{r^2 - R^2}{2Rx} Gr_x^{1/4}, D = \frac{v}{v_0}, \theta = \frac{T - T_\infty}{T_w - T_\infty}, \\ U = \frac{xu}{4v_0} Gr_x^{-1/2}, V = \frac{xrv}{v_0 R} Gr_x^{-1/4}, Gr_x = \frac{g\beta(T_w - T_\infty)x^3}{4v_0^2} \end{aligned} \quad (6)$$

where v_0 is the reference viscosity at γ_1 . θ is the dimensionless temperature of the fluid, Gr_x is the Grashof number, and Pr is the Prandtl number. Thus using equations (6) in equations (1)-(3), we get the following equations as $Gr \rightarrow \infty$:

$$\xi \frac{\partial U}{\partial \xi} - \eta \frac{\partial U}{\partial \eta} + \frac{\partial V}{\partial \eta} + 2U = 0 \quad (7)$$

$$\xi U \frac{\partial U}{\partial \xi} + (V - U\eta) \frac{\partial U}{\partial \eta} + 2U^2 = \xi D \frac{\partial U}{\partial \eta} + (1 + \xi\eta) \frac{\partial}{\partial \eta} \left(D \frac{\partial U}{\partial \eta} \right) + \theta \quad (8)$$

$$\xi U \frac{\partial \theta}{\partial \xi} + (V - U\eta) \frac{\partial \theta}{\partial \eta} = \frac{1}{Pr} \xi \frac{\partial \theta}{\partial \eta} + \frac{1}{Pr} (1 + \xi\eta) \frac{\partial^2 \theta}{\partial \eta^2} \quad (9)$$

$$\text{Where } D = \frac{\kappa}{\rho} \left| \frac{4v_0}{x^2} \frac{r}{R} Gr_x^{3/4} \right|^{n-1} \left| \frac{\partial u}{\partial \eta} \right|^{n-1} = C \left| \frac{\partial u}{\partial \eta} \right|^{n-1} \quad (10)$$

Where C is the consistency parameter. The length scale associated with the non-Newtonian power-law is

$$R = \left[\left(\frac{\kappa}{C\rho} \right) \cdot \frac{1}{v_0^{2-n}} \right]^{n-1} \frac{4v_0}{x^2} Gr_x^{3/4} \quad (11)$$

$$\text{and } D = \begin{cases} 1, & |\gamma| \leq \gamma_1 \\ \left| \frac{\gamma}{\gamma_1} \right|^{n-1}, & \gamma_1 \leq |\gamma| \leq \gamma_2 \text{ where } \gamma = C \frac{\partial U}{\partial \eta} \\ \left| \frac{\gamma_2}{\gamma_1} \right|^{n-1}, & |\gamma| \geq \gamma_2 \end{cases} \quad (12)$$

The correlation (12) is a modified power-law correlation for natural convection and is the extended form of model proposed in [23, 24], which is for forced convection. The traditional power law is used to determine the viscosity when the shear rate falls in the range of $\gamma_1 \leq |\gamma| \leq \gamma_2$; otherwise, viscosity either vanishes or becomes infinite at the limit of large or small shear rates, respectively. Also, the range of γ_1 and γ_2 is physically unrealistic. This correlation describes that if the shear rate $|\gamma|$ lies between the threshold shear rates γ_1 and γ_2 , then the non-Newtonian viscosity D varies with the power law of γ . On the other hand, if the shear rates $|\gamma|$ do not lie between the threshold shear rates γ_1 and γ_2 then the non-Newtonian viscosity D is different constant, which are shown in Fig. 1. This is a property of many measured viscosities.

Equations (7)-(9) can be solved by marching downstream with the leading edge condition satisfying the following differential equations, which are the limit of Eqs. (7)-(9) as $\xi \rightarrow 0$

$$2U - \eta \frac{\partial U}{\partial \eta} + \frac{\partial V}{\partial \eta} = 0 \quad (13)$$

$$(V - U\eta) \frac{\partial U}{\partial \eta} + 2U^2 = \frac{\partial}{\partial \eta} \left(D \frac{\partial U}{\partial \eta} \right) + \theta \quad (14)$$

$$(V - U\eta) \frac{\partial \theta}{\partial \eta} = \frac{1}{Pr} \frac{\partial^2 \theta}{\partial \eta^2} \quad (15)$$

The corresponding boundary conditions are

$$\begin{aligned} U = V = 0, \theta = 1 & \text{ at } \eta = 0 \\ U \rightarrow 0, \theta \rightarrow 0 & \text{ as } \eta \rightarrow 1 \end{aligned} \quad (16)$$

NUMERICAL METHODS

Equations (7)-(9) and (13)-(15) are discretized by a central-difference scheme for the diffusion term and a backward-difference scheme for the convection terms. Finally, we get a system of tridiagonal algebraic system of equations, which can be solved by implicit finite difference method with double-sweep technique. The normal velocity is directly solved from the continuity equation. The computation is started at $\xi = 0$, and the solution of Eqs. (7)-(9) is the upstream condition for marching downstream to $\xi = 10$. After several test run, converged results are obtained by using $\Delta\xi = 0.001$ and $\Delta\eta = 0.01$.

In practical applications, the physical quantities of principle interest are the local skin-friction coefficient C_f and local Nusselt number Nu , which are

$$C_f \left(2Gr_x^{-1/4} \right) = \left[D \frac{\partial U}{\partial \eta} \right]_{\eta=0} \quad (17)$$

$$Nu \left(Gr_x^{-1/4} \right) = \left[\frac{\partial \theta}{\partial \eta} \right]_{\eta=0} \quad (18)$$

In order to assess the accuracy of the method, we have compared the ratio of local Nusselt numbers $Nu_x / (Nu_x)_{\xi=0}$, for different values of Prandtl numbers with of the finite-difference results of Cebeci [22] and Takhar et al.[20] and the perturbation expansion method (with Shanks transformation) results of Aziz and Na[21]. The comparative results are summarized in Table 1, which shows that the present results with Newtonian fluid have excellent agreement with the above mentioned results.

TABLE 1. Comparison of the ratio of local Nusselt numbers, $Nu_x / (Nu_x)_{\xi=0}$ for different values of

ξ	Prandtl number.							
	<i>Pr = 0.72</i>				<i>Pr = 10.0</i>			
	Aziz and Na[21] results	Cebeci [22] results	Takhar et al. [20] results	Present results	Aziz and Na[21] results	Cebeci [22] results	Takhar et al. [20] results	Present results
0.0	1.000	1.000	1.000	1.000	1.000	1.000	1.000	1.000
0.503	1.219	1.210	1.210	1.213	1.096	1.096	1.096	1.097
1.064	1.445	1.422	1.424	1.422	1.196	1.196	1.196	1.197
2.093	1.821	1.778	1.781	1.779	1.367	1.373	1.371	1.374
3.364	2.232	2.177	2.183	2.179	1.560	1.575	1.569	1.577
4.000	2.419	2.366	2.378	2.369	1.650	1.672	1.665	1.675

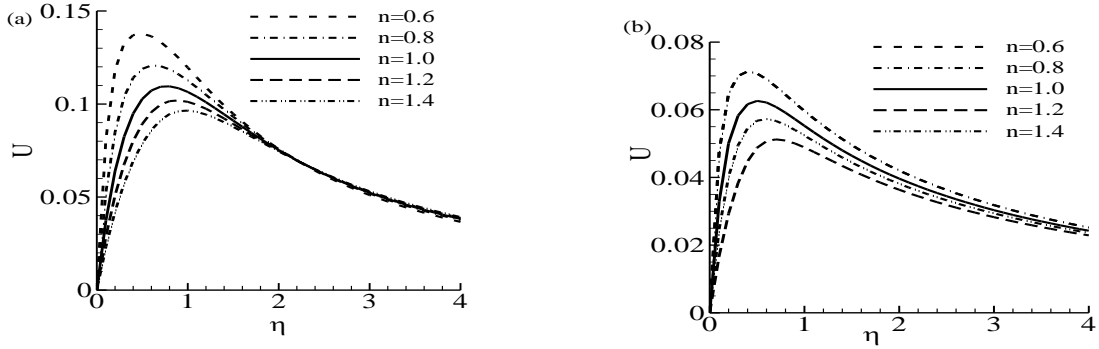


FIGURE 3. (a) Velocity distribution at $\xi = 1$ for $Pr=10$ and (b) Velocity distribution at $\xi = 1$ for $Pr=50$

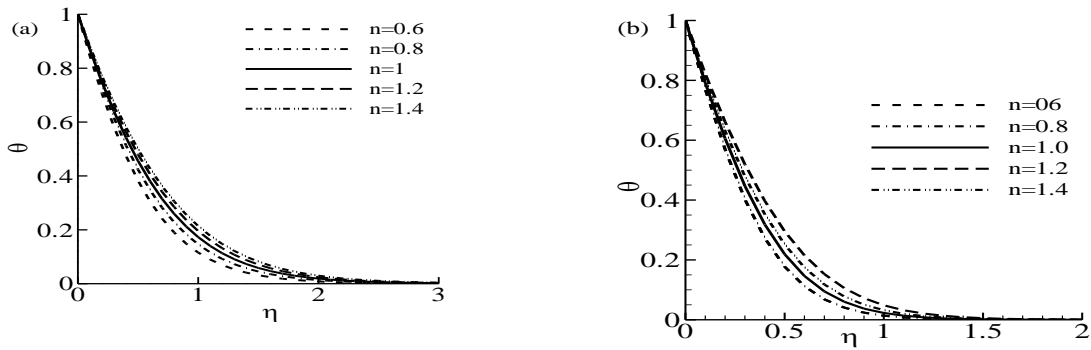


FIGURE 4. (a) Temperature distribution for $Pr=10$ and (b) Temperature distribution for $Pr=50$

RESULTS AND DISCUSSION

Numerical results are presented for the non-Newtonian power law fluids with shear-thinning ($n= 0.6$ and 0.8) and shear-thickening ($n= 1.2$ and 1.4) as well as for the Newtonian case ($n=1$). Based on the experimental data of Hinch[1] the threshold shears γ_1 and γ_2 have been chosen as 0.1 and 10^5 , respectively. The obtained results include the velocity and temperature distribution as well as the wall shear stress in terms of local skin friction co-efficient and the rate of heat transfer in terms of local Nusselt number for the wide range of power law index n ($=0.6, 0.8, 1.0, 1.2, 1.4$) and for different Prandtl numbers.

The velocity distribution as a function of η at $\xi = 1$ for different values of power law indices n ($=0.6, 0.8, 1.0, 1.2, 1.4$) are presented in Figs. 3(a) and 3(b) for $Pr= 10$ and 50 , respectively. These figures show that for shear-thinning fluids ($n= 0.6$ and 0.8), the velocity increases due to the decrease in viscosities; consequently, the boundary layer becomes thinner. On the other hand, for shear-thickening fluids ($n= 1.2$ and 1.4) the velocity decreases and the boundary layer is thickened as the fluid becomes more viscous. We can conclude that for $Pr=50$, the fluid velocity is smaller than the velocity for $Pr=10$, and hence the boundary layer thickness is smaller for $Pr=50$ than for $Pr=10$.

Figs. 4(a)-(b) depict the corresponding temperature distribution for $Pr= 10$ and 50 , respectively. At $\xi = 1$, the variation in temperature is very small since near the leading edge the non-Newtonian effect is very small. At the downstream region, in the case of shear-thinning fluids, the variation in temperature in the boundary layer is smaller than that of the shear-thickening non-Newtonian fluids and hence the thermal boundary layer becomes thinner for shear-thinning fluids and thicker for shear-thickening fluids. As expected, the thermal boundary layer is thinner for large Prandtl numbers.

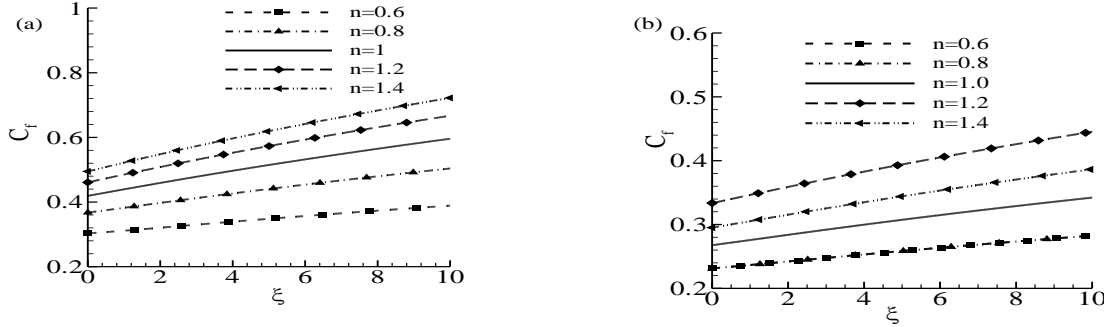


FIGURE 5. Wall Shear stress for $Pr=10$ and (b) Wall Shear stress for $Pr=50$

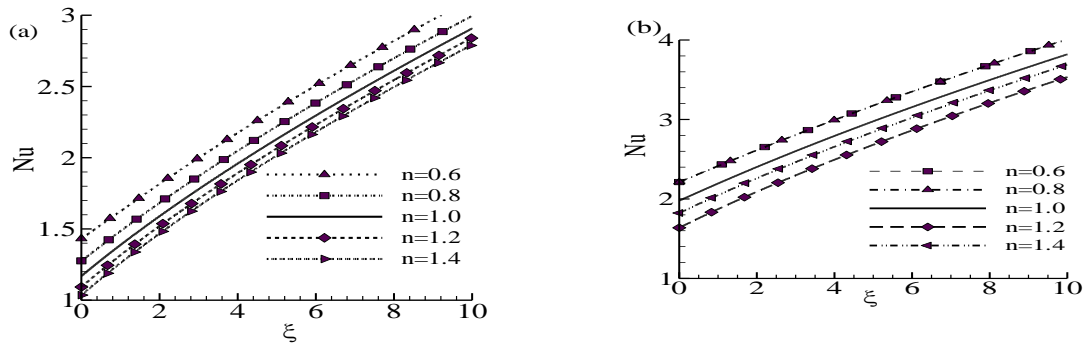


FIGURE 6. (a) Local Nusselt number for $Pr=10$ and (b) Nusselt number for $Pr=50$

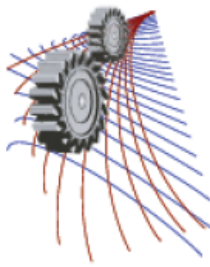
The effect of non-Newtonian power-law index n ($=0.6, 0.8, 1.0, 1.2, 1.4$) on the variation in the local skin-friction coefficient and local Nusselt number for different values of Pr are illustrated in Figs. 5 and 6 with $(\gamma_1, \gamma_2) = (0.1, 10^5)$. For larger Prandtl number the variation of wall shear stresses in case of shear-thinning ($n=0.6, 0.8$) fluid is negligible; the opposite phenomena for shear-thickening fluids ($n=1.2, 1.4$).

CONCLUSIONS

Natural convection boundary layer flow of non-Newtonian power law fluid along a vertical thin cylinder with uniform surface temperature for the cases of shear-thinning ($n= 0.6$ and 0.8) and shear-thickening ($n= 1.2$ and 1.4) as well as for the Newtonian case ($n=1$) has been studied numerically. From the results we can conclude that, at the leading edge, a Newtonian-like solution exists where the shear rate is not large enough to trigger non-Newtonian effects. After the shear-rate increases beyond a threshold value, non-Newtonian effects can be found. The modified power-law correlation agrees well with the actual measurement of non-Newtonian fluids; consequently it is a physically realistic model. The problems associated with the non-removal singularity introduced by the traditional power-law correlations do not exist for the modified power-law correlation. The model of modified power law for non-Newtonian fluids can be used to investigate other heat transfer problems for shear-thinning or shear-thickening non-Newtonian fluids in convective boundary layer flow.

REFERENCES

1. J. Hinch, *Non-Newtonian Geophysical Fluid Dynamics*, Woods Hole Oceanographic Inst., Woods Hole, MA, (2003).
2. A. Acrivos, *AIChE J.* **6(4)**, 584–590 (1960)
3. C.Tien, *Applied Scientific Research* **17**, 233–248 (1967)
4. F. H. Emery, S. Chi and J. D. Dale, *J. Heat Transfer* **93**, 164–171 (1970).
5. J. D. Dale and A. F. Emery, *J. Heat Transfer* **94**, 64–72 (1972).
6. T. V. W. Chen and D. E. Wollersheim, *J. Heat Transfer* **95**, 23–124 (1973).
7. Z. P. Shulman, V. I. Baikov and E. A. Zaltsgendler, *Int. J. Heat and Mass Transfer* **19(9)**, 1003–1007 (1976).
8. A. Som and J. L. S. Chen, *Int. J. Heat and Mass Transfer* **27(5)**, 791–794 (1984).
9. S. Haq, C. Kleinstreuer and J. C. Mulligan, *J. Heat Transfer* **110**, 604–607 (1988).
10. M. J. Huang, J. S. Huang, Y. L. Chou and C. K. Cheng, *J. Heat Transfer* **111**, 189–191 (1989).
11. M. J. Huang and C. K. Chen, *Int. J. Heat and Mass Transfer* **33(1)**, 119–125 (1990).
12. E. Kim, *Int. J. Heat and Mass Transfer* **40(13)**, 3069–3078 (1997).
13. W. A. Khan, J. R. Culham and M. M. Yovanovich, *J. Heat Transfer* **128**, 870–878 (2006).
14. J. P. Denier and R. E. Hewitt, *J. Fluid Mechanics* **518**, 261–279 (2004).
15. J. P. Denier and P. P. Dabrowski, “On the Boundary-Layer Equations for Power-Law Fluids,” Series A: Mathematical and Physical Sciences, *Proceedings* 460, (Royal Society of London 2004) pp. 3143–3158.
16. E. M. Sparrow and J. L. Gregg, *J. Heat Transfer* **78**, 1823–1829 (1956).
17. W. J. Minkowycz and E. M. Sparrow, *J. Heat Transfer* **96**, 178–183 (1974).
18. H. K. Kuiken, *Int. J. Heat Mass Transfer* **11**, 1141–1153 (1968).
19. T. Fuji and H. Uchara, *Int. J. Heat Mass Transfer* **13**, 607–615 (1970).
20. H. S. Takhar, A. J. Chamkha, and G. Nath, *Int. J. Eng. Sc.* **41**, 1935–1950 (2003).
21. A. Aziz and T. Y. Na, *J. Thermo-Fluid Dyn.* **16**, 83–87 (1982).
22. T. Cebeci, “Laminar free convection heat transfer from the outer surface of a vertical slender circular cylinder,” *International Heat Transfer Conference Proceedings* 1.4, (N.C., 1974), pp. 15–19.
23. M. M. Molla, and L. S. Yao, *J. Thermophys. Heat Transfer* **22(4)**, 762–765 (2008).
24. M. M. Molla and L. S. Yao, *ASME J. Heat Transfer* **131**, 1–6 (2009).



A Numerical Study of Magneto-hydrodynamic Free Convection in A Square Cavity with Heated Elliptic Block

M. Jahirul Haque Munshi^{1, a)}, M. A. Alim², A. H. Bhuiyan^{2, 3, b)}

¹*Department of Mathematics, Faculty of Science, Engineering & Technology,
Hamdard University Bangladesh (HUB), Gazaria, Munshiganj, Bangladesh*

^{2,3}*Department of Mathematics, Bangladesh University of Engineering and Technology
(BUET), Dhaka- 1000, Bangladesh*

^{a)}Corresponding author: jahirmath@gmail.com

Abstract. The problem of Magneto-hydrodynamic (MHD) field on buoyancy- driven free convection heat transfer in a square cavity with heated elliptic block at the centre has been investigated in this work. The governing differential equations are solved by using finite element method (Galerkin weighted residual method). The lower wall is adiabatic. The left wall is kept at heated T_h . The right and upper wall is kept at cold T_c respectively. Also all the wall are assumed to be no-slip condition. The study is performed for different Rayleigh and Hartmann numbers. A heated elliptic block is located at the centre of the cavity. The object of this study is to describe the effects of MHD on the field of buoyancy- driven and flow in presence of such heated block by visualization of graph. The results are illustrated with the streamlines, isotherms, velocity and temperature fields as well as local Nusselt number.

INTRODUCTION

Heat transfer using movement of fluids is called convection. Natural convection heat transfer is extensively importance in science and engineering researcher. Several numerical and experimental methods have been developed to investigate flow characteristics inside the cavities with and without obstacle, because these types of geometries have practical engineering and industrial application, cooling of commercial high voltage electrical power transformers.

A number of studies have been conducted to investigate the flow and heat transfer characteristics in closed cavities in the past. Basak et al. [1] studied and solved the finite element analysis of natural convection flow in a isosceles triangular enclosure due to uniform and non-uniform heating at the side walls. Pirmohammadi et al. [2] shows that the effect of a magnetic field on Buoyancy- Driven convection in differentially heated square cavity. Rahman et al. [3] offered a numerical model for the simulation of double-diffusive natural convection in a right-angled triangular solar collector. Mahmoodi et al. [4] studied numerically magneto-hydrodynamic free convection heat transfer in a square enclosure heated from side and cooled from the ceiling. Jani et. al. [5] numerically investigated magneto hydrodynamic free convection in a square cavity heated from below and cooled from other walls. Bhuiyan et al. [6] numerically investigated magneto hydrodynamic free convection in a square cavity with semicircular heated block.

On the basis of the literature review, it appears that no work was reported on the free convection flow in a square cavity with heated elliptic block with internal heat generation. In the present study, we undertake this task varying the

Rayleigh number Ra ($10^4 \leq Ra \leq 10^6$) and Hartmann number Ha ($0 \leq Ha \leq 150$). The obtained numerical results are presented graphically in terms of streamlines, isotherms, local Nusselt number and average Nusselt number for different Hartmann numbers and Rayleigh numbers will be done.

PHYSICAL CONFIGURATION

The physical model considered in the present study of free convection in a square cavity with heated elliptic block is shown in Fig. 1. The height and the width of the cavity are denoted by L . The left wall is kept heated T_h and lower wall adiabatic. The right and upper wall is kept at cold T_c . The magnetic field of strength B_0 is applied parallel to x -axis. The square cavity is filled with an electric conductive fluid are considered Newtonian and incompressible.

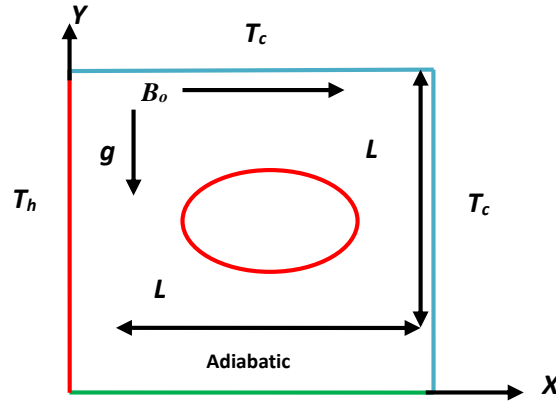


FIGURE 1. Schematic view of the cavity with boundary conditions considered in the present paper

MATHEMATICAL FORMULATION

The flow is considered steady, laminar, incompressible and two-dimensional. The field equations governing the heat transfer and fluid flow include the continuity equation, the Navier-Stokes equations and the energy equation, which can be expressed in non-dimensional form as:

$$\frac{\partial U}{\partial X} + \frac{\partial V}{\partial Y} = 0 \quad (1)$$

$$U \frac{\partial U}{\partial X} + V \frac{\partial V}{\partial Y} = -\frac{\partial P}{\partial X} + Pr \left(\frac{\partial^2 U}{\partial X^2} + \frac{\partial^2 U}{\partial Y^2} \right) \quad (2)$$

$$U \frac{\partial V}{\partial X} + V \frac{\partial V}{\partial Y} = -\frac{\partial P}{\partial Y} + Pr \left(\frac{\partial^2 V}{\partial X^2} + \frac{\partial^2 V}{\partial Y^2} \right) + (Ra/Pr)T - Ha^2 Pr V \quad (3)$$

$$U \frac{\partial \theta}{\partial X} + V \frac{\partial \theta}{\partial Y} = \left(\frac{\partial^2 \theta}{\partial X^2} + \frac{\partial^2 \theta}{\partial Y^2} \right) \quad (4)$$

where Ra , Pr and Ha are the Rayleigh, Prandtl and Hartman numbers and are defined as:

$$Ra = \frac{g\beta(T_h - T_c)L^3}{\alpha\nu}, \quad Pr = \frac{\nu}{\alpha}, \quad Ha = B_0 L \sqrt{\frac{\sigma}{\rho\nu}} \quad (5)$$

The effect of magnetic field into the momentum equation is introduced through the Lorentz force term $\mathbf{j} \times \mathbf{D}$ that is reduced to $-\sigma B_0 v^2$ as shown by Pirmohammadi et al. [2]

To computation of the rate of heat transfer, Nusselt number along the hot wall of the enclosure is used that is as follows:

$$(6)$$

$$Nu_y = \frac{\partial \theta}{\partial x} \Big|_{x=0} \quad Nu_u = \int_0^1 Nu_y dY \quad ($$

The boundary conditions are:

On the left wall of the square cavity: $U = 0, V = 0, \theta = 1$ and right wall of the cavity: $U = 0, V = 0, \theta = 0$

On the heated elliptic block: $U = 0, V = 0, \theta = 1$

NUMERICAL TECHNIQUE

The nonlinear governing partial differential equations, i.e., mass, momentum and energy equations are transferred into a system of integral equations by using the Galerkin weighted residual method. The integration involved in each term of these equations is performed with the aid Gauss quadrature method. These modified nonlinear equations are transferred into linear algebraic equations with the aid of Newton's method. Lastly, Triangular factorization method is applied for solving those linear equations.

RESULT AND DISCUSSION

In this section, results of the numerical study on magneto-hydrodynamic free convection fluid flow and heat transfer in a square cavity filled with an electric conductive fluid with $Pr = 0.733$ are presented. The results have been obtained for the Rayleigh number Ra ($10^4 \leq Ra \leq 10^6$) and Hartmann number Ha ($0 \leq Ha \leq 150$). Pirmohammadi et al. [2] was modified and used for the computations in the study. Streamlines for $Ha = 0$ is presented in Fig. 2 to understand the effects of Rayleigh number on flow field and temperature distribution. At $Ra = 10000$ and in the absence of the magnetic field two cells are formed with two elliptic- shaped eyes topside of the elliptic heated block of the cavity shown in Fig. 2(a). For higher Rayleigh number two elliptic- shaped eyes are formed inside the cavity and also flow strength increases are shown in Fig. 2(b), 2(c) and 2(d). Stream function has symmetrical value about the vertical central line as the elliptic heated block is symmetrical. Again Streamlines for while $Ra = 10^5$ and $Pr = 0.733$ are presented in Fig. 3 to understand the effects of Hartmann number on flow field and temperature distribution. At $Ha = 0$ are two elliptic- shaped eyes right side of the elliptic heated block of the cavity shown in Fig. 3(a). For higher Hartmann number three elliptic- shaped eyes are formed inside the cavity and also flow strength increases are shown in Fig. 3(b), 3(c) and 3(d).

Conduction dominant heat transfer is observed from the isotherms in Fig. 4(a) and Fig 4(b) at $Ra = 10000$ and $Ra = 100000$. With increases in Rayleigh number, isotherms are concentrates near the top wall and isotherms lines are more bending which means increasing heat transfer through convection. Formation of thermal boundary layers can be found and increases from the isotherms for $Ra = 500000$ and $Ra = 1000000$ at $Ha = 0$ are shown in Fig. 4(c) and Fig. 4(d). With increases the Hartmann number, isotherms in Fig. 5(a) and 5(b) are concentrates near the top and right wall isotherms lines are more bending which means increasing heat transfer through convection. Formation of thermal boundary layers can be found and increases from the isotherms for $Ha = 100$ and $Ha = 150$ at $Ra = 0$ are shown in Fig. 5(c) and Fig. 5(d).

The local Nusselt number along the bottom wall for different Rayleigh numbers with $Pr = 0.733$ and $Ha = 0$ of the cavity are shown in Fig. 6(a). Minimum and maximum shape curves are obtained here. At Ra minimum we get shape curve maximum and Ra maximum so shape curve minimum. Again local Nusselt number along the bottom wall for different Hartmann numbers with $Pr = 0.733$ and $Ra = 10^5$ of the cavity are shown in Fig. 6(b). Variations of the vertical velocity component along the bottom wall for different Rayleigh number with $Pr = 0.733$ and $Ha = 0$ of the cavity are shown in Fig. 7(a). It can be seen from the figure that the absolute value of maximum and minimum value of velocity increases with increasing the Rayleigh number. The curves are symmetrical parabolic shaped as the elliptic heated block is symmetrical. For lower Rayleigh number value of the velocity has larger changed. Variations of the vertical velocity component along the bottom wall for different Hartmann number with $Pr = 0.733$ and $Ra = 10^5$ of the cavity are shown in Fig. 7(b). From the Figure it can be observed that the curves are symmetrical elliptic heated block. The absolute value of maximum and minimum value of velocity decreases with increasing the Hartmann number.

Fig. 8(a) presents the temperature profiles along the bottom wall for different Rayleigh number with $Pr = 0.733$ and $Ha = 0$. As seen from the Figure, temperature value is decreased from the increasing of Rayleigh numbers. Parabolic shape temperature profile is obtained due to symmetric shape of the elliptic shape heated block. For lower

Rayleigh number temperature value has less significant changed but for higher Rayleigh number temperature value has more significant. Fig. 8(b) present the temperature profiles along the bottom wall for different Hartmann number with $Pr = 0.733$ and $Ra = 10^5$. As seen from the figure, temperature value is increased from the increasing Hartmann numbers.

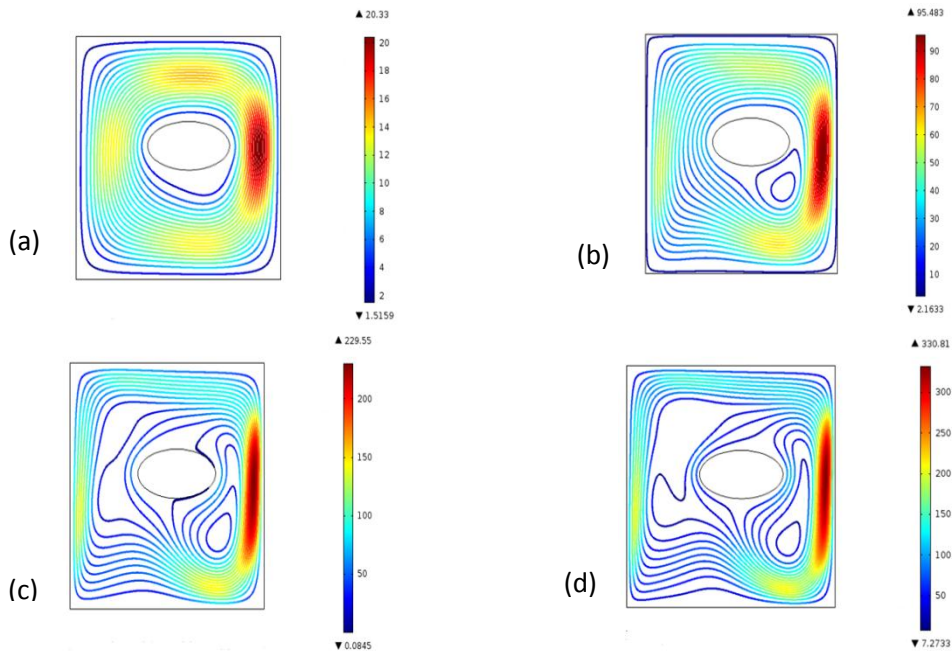


FIGURE 2. Stream lines for (a) $Ra = 10000$, (b) $Ra = 100000$, (c) $Ra = 500000$, (d) $Ra = 1000000$ while $Ha = 0$ and $Pr = 0.733$

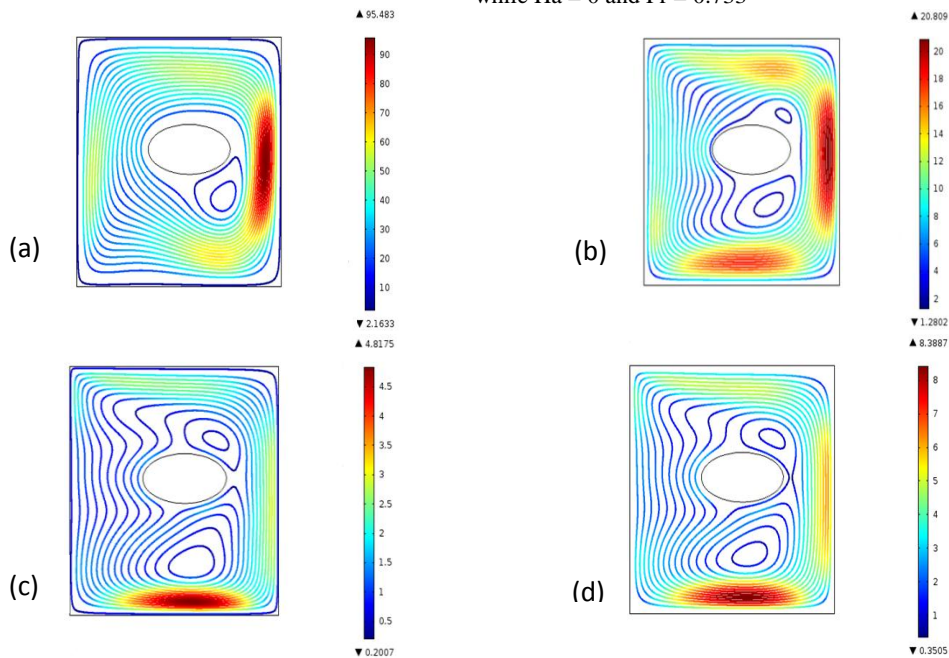


FIGURE 3 Stream lines for (a) $Ha = 0$, (b) $Ha = 50$, (c) $Ha = 100$, (d) $Ha = 150$ while $Ra = 10^5$ and $Pr = 0.733$.

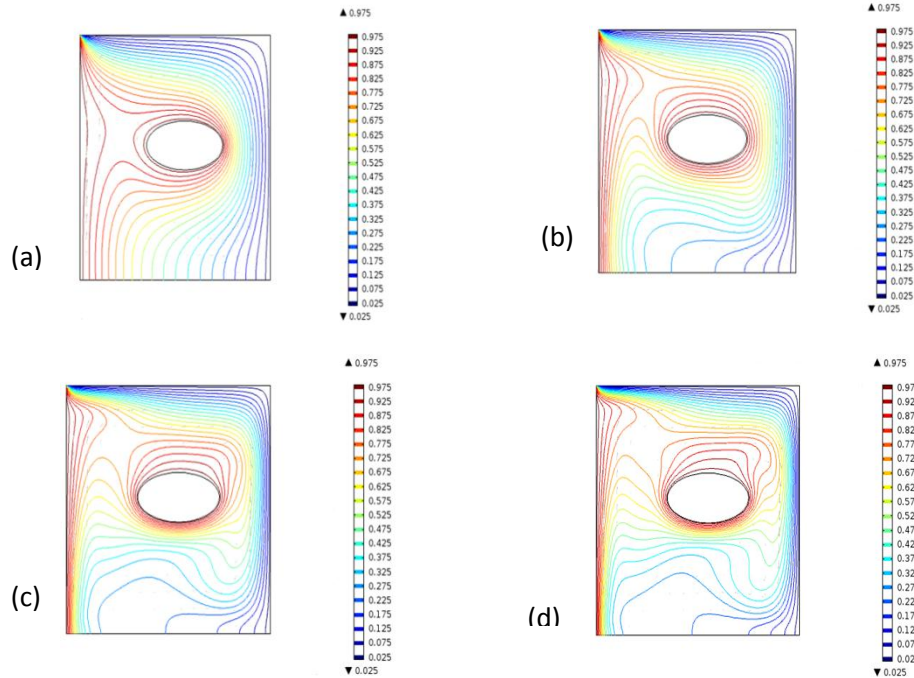


FIGURE 4. Isotherm for (a) $Ra = 10000$, (b) $Ra = 100000$, (c) $Ra = 500000$, (d) $Ra = 1000000$ while $Ha = 0$ and $Pr = 0.733$.

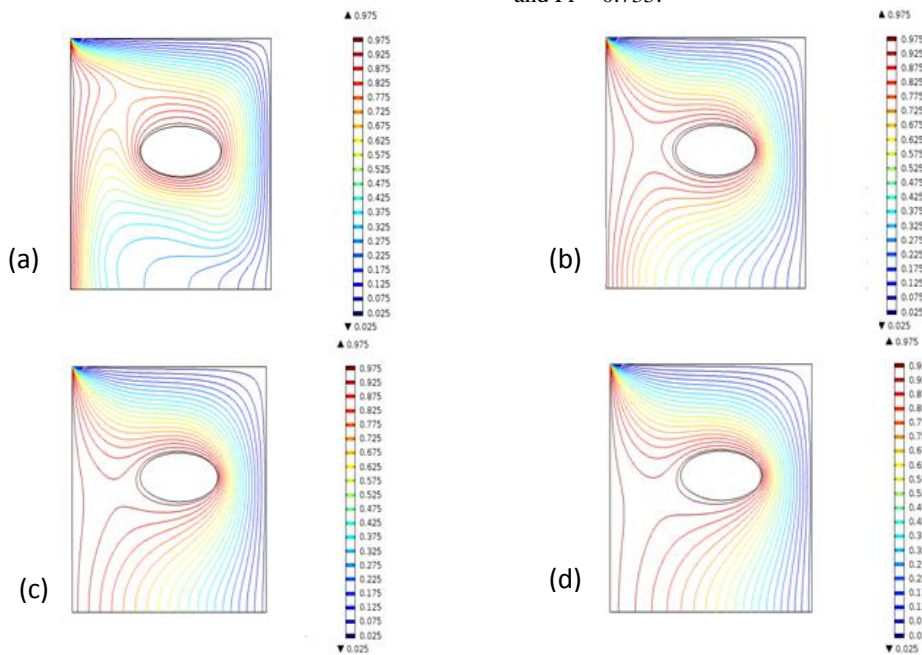


FIGURE 5. Isotherm for (a) $Ha = 0$, (b) $Ha = 50$, (c) $Ha = 100$, (d) $Ha = 150$ while $Ra = 10^5$ and $Pr = 0.733$

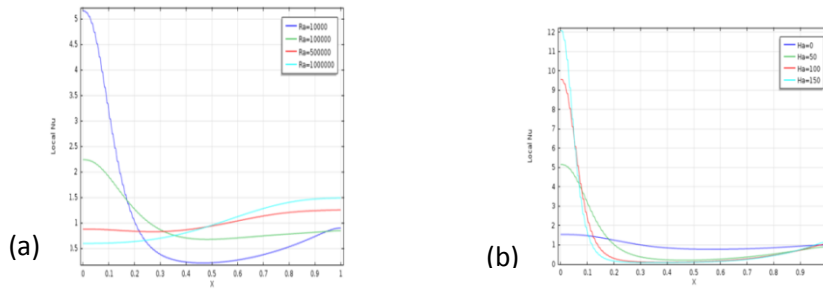


FIGURE 6. Variation of local Nusselt number along the bottom wall for different (a) Rayleigh numbers with $Pr = 0.733$ and $Ha = 0$ and (b) Hartmann numbers with $Pr = 0.733$ and $Ra = 10^5$

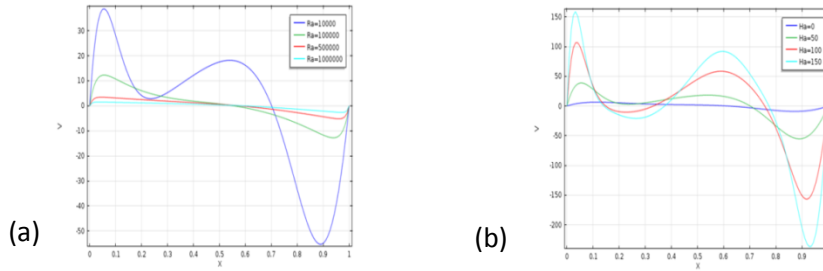


FIGURE 7. Variation of velocity profile along the bottom wall at different (a) Rayleigh number with $Pr = 0.733$ and $Ha = 0$ (b) Hartmann number with $Pr = 0.733$ and $Ra = 10^5$.

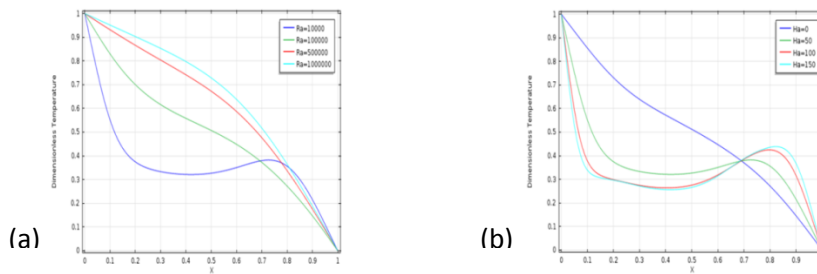


FIGURE 8. Variation of temperature profiles along the bottom wall at different (a) Rayleigh number with $Pr = 0.733$ and $Ha = 0$, (b) Hartmann number with $Pr = 0.733$ and $Ra = 10^5$

CONCLUSION

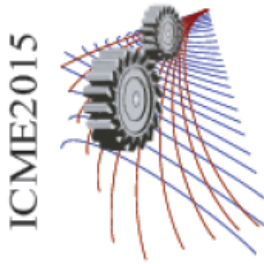
A numerical study of magneto-hydrodynamic free convection fluid flow and heat transfer in a square cavity filled with an electric conductive fluid with heated elliptic block. Finite element method was to solve governing equations for a heat generation parameters, Rayleigh numbers, Hartmann numbers and Prandtl numbers. Very good agreements were observed between different Rayleigh numbers, different Hartmann numbers and different Prandtl numbers. For all cases considered, two or more counter rotating eddies were formed inside the cavity regardless the Rayleigh, Hartmann and the Prandtl numbers. The obtained results showed that the heat transfer mechanisms, temperature distribution and the flow characteristics inside the cavity depended strongly upon both the strength of the magnetic field and the Rayleigh number. From the present investigation the following conclusions may be drawn as: with increase in the buoyancy force via increase in Rayleigh number, to decrease natural convection, a stronger magnetic field is needed compared to the lower Rayleigh numbers.

ACKNOWLEDGMENTS

The authors would like to express their gratitude to the Department of Mathematics, Bangladesh University of Engineering and Technology, for providing computer facility during this work.

REFERENCES

1. T. Basak, S. Roy, S.K. Babu, A.R. Balakrishnan, Int. J. Heat Mass Transfer, **51**, 4496-4505(2008).
2. Mohsen Pirmohammadi, Majid Ghassemi, and Ghanbar Ali Sheikhzadeh, IEEE transactions on magnetic, **45**(1) (2009).
3. M.M. Rahman, M.M. Billah, N. A. Rahim, N. Amin, R. Saidur and M.Hasanuzzaman, International Journal of Renewable Energy Research **1**(50-54) ,(2011).
4. M. Mahmoodi, Z. Talea'pour, Computational Thermal Science, **3**, 219- 226(2011).
5. S. Jani, M. Mahmoodi, M. Amini, International Journal of Mechanical, Industrial Science and Engineering, **7**(4), (2013).
6. A. H. Bhuiyan, R. Islam, M. A. Alim, International Journal of Engineering Research & Technology (IJERT), **3**(11). (2014).



Natural Convection inside a Porous Trapezoidal Enclosure with Wavy Top Surface

Sehrina Muzahid Eshon^{1, a)}, Rakib Mustafa^{1, b)} and Mohammad Nasim Hasan^{1, c)}

¹*Department of Mechanical Engineering, Bangladesh University of Engineering and Technology (BUET)
Dhaka-1000, Bangladesh*

^{a)}Corresponding author: sehrinamuzahid@yahoo.com

^{b)}rakib09me@gmail.com

^{c)}nasim@me.buet.ac.bd

Abstract. The aim of the present work is analysis of heat flow during natural convection inside a trapezoidal porous cavity having wavy top surface. The bottom wall of the cavity is sinusoidally heated whereas the top wall is kept at constant low temperature and the side walls are maintained adiabatic. The physical problem has been represented mathematically by various governing equations along with the corresponding boundary conditions and hence solved by using Galerkin Finite Element scheme. Numerical simulations were carried out and the flow and thermal fields inside the cavity were analyzed in terms of distribution of isothermal lines (θ), streamlines (ψ) and heatlines (IT). To compare heat transfer characteristics local Nusselt number (Nu), and average Nusselt number (Nu_{avg}) along the hot bottom wall are studied for various system parameters, such as, Rayleigh number (Ra) and Darcy number (Da). The range of Ra , Da considered in the present study are as follows; $10^4 \leq Ra \leq 10^6$, $10^{-5} \leq Da \leq 10^{-3}$. The present study has been conducted for the trapezoidal cavity being filled with two different types of fluids; water ($Pr = 7.2$), and molten gallium ($Pr = 0.026$). It has been found that an increase in flow intensity and heat transfer occurs at higher Rayleigh number (Ra) and Darcy number (Da) whereas the effect of Prandtl number (Pr) is somewhat negligible.

INTRODUCTION

Enclosures are frequently encountered in practice, and heat transfer through them is of practical interest. Natural convection inside cavities has many significant engineering applications, including thermal design of buildings, cooling of electronic equipment, solar thermal central receiver design. Buoyancy induced convection in saturated porous media can be seen in many geothermal applications, double wall insulation, food processing and storage, the design of pebble bed nuclear reactors, underground disposal of nuclear waste; compacted beds for the chemical industry, etc. Fluid flow through porous media has emerged as an important separate field of study. Pioneering works of Darcy [1] on flow through porous beds identified permeability as the property of porous media. Baytas and Pop [2], Basak et al. [3], Sathiyamoorthy et al. [4], carried out studies on natural convection inside the square and rectangular enclosure having different temperature boundary condition, and filled with porous medium. Natural convection inside the different shapes of enclosures, triangle, rectangle, non-rectangle, or irregular enclosure like wavy surface, with various boundary conditions are studied to analyze the fluid flow and thermal behaviors. Peric [5] studied natural convection in trapezoidal cavities using a control volume method and observed the convergence of results for grid-independent solutions. Kuyper and Hoogendoorn [6] investigated laminar natural convection flow in trapezoidal enclosures to study the influence of the inclination angle on the flow and also the dependence of the average Nusselt number on the Rayleigh number. Basak et al. [7] carried out investigation on heatline visualization of natural convection flows within trapezoidal enclosures. Sompong and Witayangkurn [8] studied about the natural convection in a trapezoidal enclosure with wavy top surface. Present study is an attempt to go a step further where we investigated a porous trapezoidal cavity with wavy top wall. The top wall is isothermally cold while the bottom

surface is sinusoidally heated and the side walls are maintained adiabatic. Main focus of the present work is the elucidation of heat and fluid flow characteristics for the variation of system parameters; Ra , Da and Pr .

Nomenclature			
Da	Darcy number, k/L^2	α	thermal diffusivity (m^2s^{-1})
g	acceleration due to gravity (ms^{-2})	β	volume expansion coefficient (K^{-1})
k	thermal conductivity ($Wm^{-1}k^{-1}$)	θ	dimensionless temperature, $(T-T_c)/(T_h-T_c)$
Nu	local Nusselt number	μ	dynamic viscosity ($kgm^{-1}s^{-1}$)
Nu_{avg}	average Nusselt number	ν	kinematic viscosity (m^2s^{-1})
p	pressure (Pa)	ρ	density of the fluid (kgm^{-3})
P	dimensionless pressure, $pL^2/\rho\alpha^2$	ψ	dimensionless streamfunction
Pr	Prandtl number	Π	dimensionless heatfunction
Ra	Rayleigh number, $(g\beta(T_h-T_c)L^3Pr)/(v^2)$	x, y	distance along x, y-coordinate (m)
T	Temperature of fluid (K)	X, Y	distance along dimensionless x, y-coordinate
T_h	maximum temperature of the heated bottom wall (K)	u, v	velocity component at x, y-direction (ms^{-1})
T_c	temperature of the cold wavy top wall (K)	U, V	dimensionless velocity component at x, y-direction
T_0	Bulk temperature, $(T_h+T_c)/2$ (K)		

MATHEMATICAL FORMULATION, SIMULATION AND POST PROCESSING

Velocity and temperature distribution

In the present study, Boussinesq approximation is adopted for fluid having constant properties. The governing equations for steady two-dimensional natural convection flow in a porous trapezoidal cavity using conservation of mass, momentum, and energy may be written with the following dimensionless variables and numbers:

$$\frac{\partial u}{\partial x} + \frac{\partial v}{\partial y} = 0 \quad (1)$$

$$U \frac{\partial u}{\partial x} + V \frac{\partial u}{\partial y} = -\frac{\partial P}{\partial X} + Pr \left(\frac{\partial^2 u}{\partial X^2} + \frac{\partial^2 u}{\partial Y^2} \right) - \frac{Pr}{Da} U \quad (2)$$

$$U \frac{\partial v}{\partial x} + V \frac{\partial v}{\partial y} = -\frac{\partial P}{\partial Y} + Pr \left(\frac{\partial^2 v}{\partial X^2} + \frac{\partial^2 v}{\partial Y^2} \right) - \frac{Pr}{Da} V + Ra Pr \theta \quad (3)$$

$$U \frac{\partial \theta}{\partial x} + V \frac{\partial \theta}{\partial y} = \frac{\partial^2 \theta}{\partial X^2} + \frac{\partial^2 \theta}{\partial Y^2} \quad (4)$$

The above equations are normalized using the following dimensionless scales,

$$X = \frac{x}{L}, Y = \frac{y}{L}, U = \frac{uL}{\alpha}, V = \frac{vL}{\alpha}, \theta = \frac{T - T_c}{T - T_h}, P = \frac{pL^2}{\rho\alpha^2}, Pr = \frac{\gamma}{\alpha}, Da = \frac{k}{L^2}, Ra = \frac{g\beta(T_h - T_c)L^3 Pr}{\gamma^2} \quad (5)$$

For velocity profile, no-slip boundary conditions ($U = V = 0$) is assumed for all boundaries and boundary conditions for temperature are indicated in Fig. 1.

Top Wall: $\theta = 0$; Bottom Wall: $\theta = \sin(\pi X)$; Side Walls: $\frac{\partial \theta}{\partial n} = 0$ where n is in the direction normal to the wall

In the present investigation natural convection inside a porous trapezoidal cavity as shown in Fig. 1 has been considered. The wavy top wall has the profile, $a + b \cos(2\pi x)$, where $a = 0.9$ and $b = 0.1$. The bottom wall of the

enclosure is heated with sinusoidal boundary condition, the top wavy wall is kept isothermally cold and the side walls are maintained adiabatic.

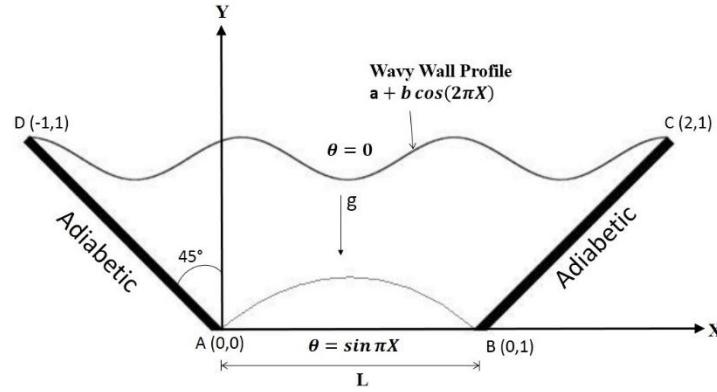


FIGURE 1. Physical model of the current study and boundary conditions of the modified enclosure

Streamfunction, Heatfunction, Nusselt number

The fluid motion is displayed by using the stream function (ψ) obtained from velocity components (U, V). The relationship between ψ and U, V is given as:

$$\frac{\partial^2 \psi}{\partial X^2} + \frac{\partial^2 \psi}{\partial Y^2} = \frac{\partial U}{\partial Y} - \frac{\partial V}{\partial X} \quad (6)$$

The heat flow within the enclosure is displayed using the heatfunction (Π). This heatfunction can be obtained from conductive heat fluxes $(-\frac{\partial \theta}{\partial x}, -\frac{\partial \theta}{\partial y})$ and convective heat fluxes $(U\theta, V\theta)$. The energy balance equation for heatfunction is,

$$\frac{\partial^2 \Pi}{\partial X^2} + \frac{\partial^2 \Pi}{\partial Y^2} = \frac{\partial}{\partial Y} (U\theta) - \frac{\partial}{\partial X} (V\theta) \quad (7)$$

A reference point is considered at A (0,0) where $\Pi = 0$

Along AB, (Neumann boundary condition)

$$\frac{\partial \Pi}{\partial Y} = -\frac{\partial \theta}{\partial X} = -\frac{\partial}{\partial X} (\sin \pi X) = -\pi \cos \pi X \quad (8)$$

Along adiabatic walls BC and AD, (Dirichlet boundary condition)

$$\Pi = 0 \quad (9)$$

Along CD, (Neumann boundary condition)

$$n \cdot \nabla \Pi = n \cdot (i \frac{\partial \Pi}{\partial X} + j \frac{\partial \Pi}{\partial Y}) \quad (10)$$

The positive sign of ψ denotes anticlockwise circulation and negative sign of ψ represents clockwise circulation. Heat transfer performance in terms of the local Nusselt number and average Nusselt number can be written as:

$$Nu = -\frac{\partial \theta}{\partial X} \quad (11)$$

$$Nu_{avg} = \frac{1}{L} \int_0^1 (Nu) dx \quad (12)$$

Computational details and validation

The continuity equation Eq. (1) represents conservation of mass which can be used to obtain the pressure distribution by penalty formulation. The momentum and energy balance equations Eqs. (2) – (3) are solved using Galerkin weighted residual finite element technique. The present numerical technique will discretize the computational domain into unstructured triangles by Delaunay Triangular method. It was found through grid sensitivity test that 9200 non-regular nodes are sufficient to provide accurate results.

Present work has been validated against Sompong et al. [8] which dealt with natural convection inside a trapezoidal enclosure with wavy top surface. The enclosure is filled with seawater having Prandtl number (Pr) of 7.2 and uniformly heated on bottom and partially heated on inclined boundaries. The contours of streamline and isotherm line are compared with present study (fig. 2) and there is excellent agreement between the two works.

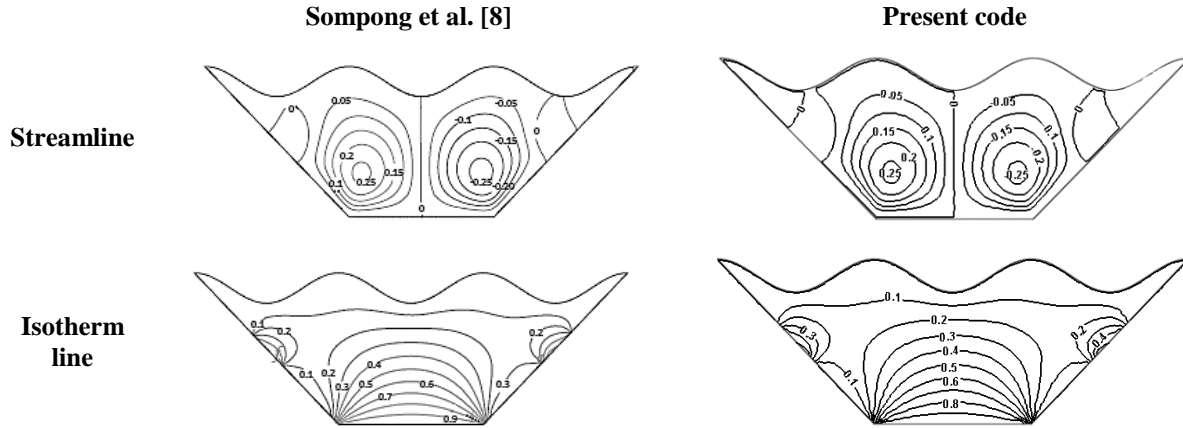


Figure 2. Code validation for streamlines and isotherm lines at $Ra = 10^4$ and $Da = 10^{-3}$

RESULT AND DISCUSSION

In the present study the range of various governing parameters (Ra , Da) are varied as; $10^{-5} \leq Da \leq 10^{-3}$, $10^4 \leq Ra \leq 10^6$. Investigation was repeated for two different types of fluids; water ($Pr = 7.2$), and molten gallium ($Pr = 0.026$). Obtained results are systemically presented in terms of distribution of fluid flow and heat transfer inside the cavity.

Effect of Rayleigh Number

Rayleigh number (Ra) for a natural convection process is associated with buoyancy and beyond a critical value of Ra heat transfer changes from being conduction dominant to being convection dominant. Figure 3 shows the influence of Ra over the fluid flow and thermal fields inside the enclosure. Ra is varied from 10^4 to 10^6 while the Darcy number (Da) was fixed at 10^{-3} for water having Prandtl number (Pr) of 7.2. Contours of streamline shows two main circulations occurring in opposite direction inside the cavity where the left half is positive and the right half is negative indicating anticlockwise and clockwise circulation patterns, respectively. As Ra increases, the circulation cells become more elliptical in shape and the center moves slightly up indicating an increase in flow intensity increases due to increased circulation strength, so magnitude of stream function increases, for example, as Ra is increased from 10^4 to 10^6 , $|\psi|_{max}$ increases from 0.152 to 11.913.

The distribution of isotherms shows that thermal stratification occurs near the hot bottom wall. At low Ra (10^4), the lines are smooth and equally distributed due to weak flow inside the cavity. At higher Ra (10^6), the lines are distorted near the central portion of cavity and are heavily clustered near the bottom hot wall. Also higher temperature gradient exists near bottom surface as well as near the central portion of the top wall. Heatline contours show that at lower Ra (10^4), the heat lines go directly from bottom hot wall to top cold wall indicating conduction dominant heat transfer between these two surfaces. At higher Ra (10^6), two separate heatline circulation cells exist in the cavity which promotes thermal mixing. Also magnitude of Π increases with increase in Ra , for example as Ra increased from 10^4 to 10^6 , Π_{max} increases from 1.30 to 7.49.

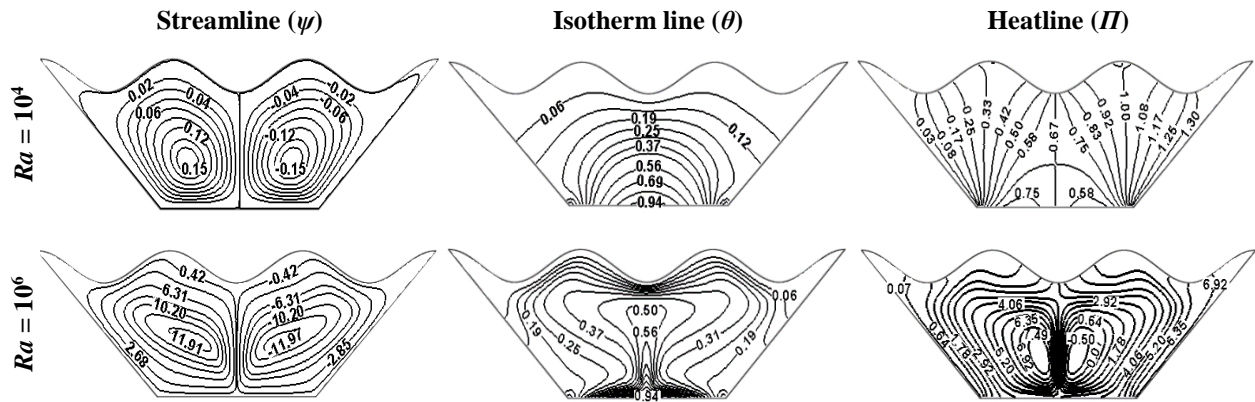


Figure 3. Streamline, isotherm lines and heatlines for $Da = 10^{-3}$, $Pr = 7.2$ at different Rayleigh numbers (Ra)

Effect of Darcy Number

Darcy number (Da) is the measure of the permeability through a porous medium. In Fig 4, Da is changed between 10^{-5} and 10^{-3} keeping Ra and Pr constant at 10^6 and 7.2 respectively. At lower Da , the hydraulic resistance of the porous medium and resistance to thermal permeability is higher and thus the fluid flow as seen from the contours of the streamfunction. It may be noted that the heat transfer is dominated by conduction regime even at relatively higher Ra (10^6) in case of lower values of Da .

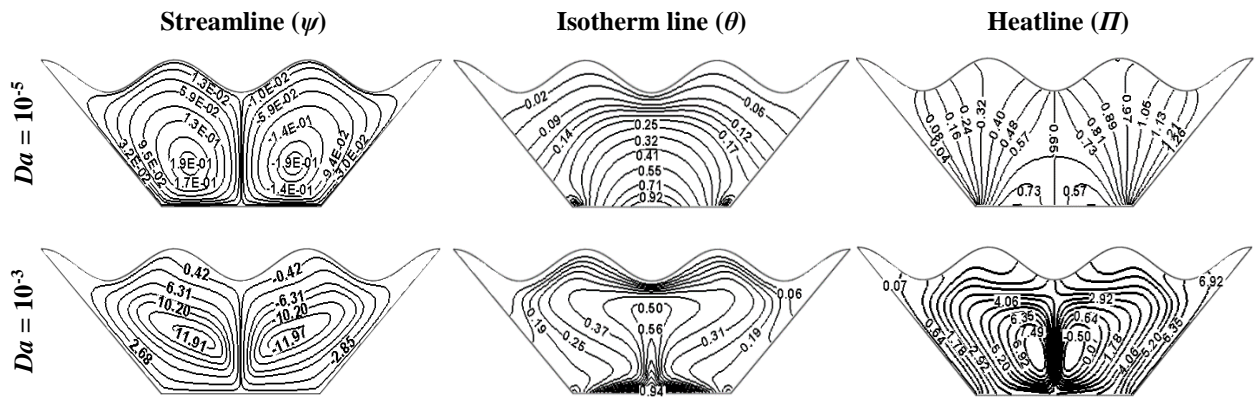


Figure 4. Streamline, isotherm lines and heatlines for $Ra = 10^6$, $Pr = 7.2$ at different Darcy numbers (Da)

Since the results are illustrated for $Ra = 10^6$ in Fig. 4, here magnitude of ψ and Π are higher than lower values of Ra due to increased buoyancy and circulations. For streamlines, as Da increases the two opposite circulation cells become more elliptical in shape also the center of the cells move slightly upwards and there is a significant increase in magnitude of stream function as flow intensity increases, for example, as Da increases from 10^{-5} to 10^{-3} , $|\psi|_{max}$ increases from 0.19 to 11.92. Isotherm contours show that with increase in Da , the contours are more distorted and there is better temperature distribution inside the cavity with higher thermal gradients near top and bottom wall. For heatline distribution map magnitude of heat function increases significantly with increase in Da and also there is a development of heatline circulation cells promoting thermal mixing indicating high thermal permeability. $Ra = 10^6$, $\Pi_{max} = 1.26$ at $Da = 10^{-5}$, and $\Pi_{max} = 7.49$ at $Da = 10^{-3}$.

Effect of Prandtl Number

The Prandtl number controls the relative thickness of the momentum and thermal boundary layers, when value of Pr is small, it indicates increased heat diffusion compared to momentum diffusion. In Fig. 5, changes in Pr does not bring about any significant changes in distribution of streamlines, isotherms or heatlines. The streamlines consists of two circulations in opposite directions symmetric about the central axis. For different fluids the magnitude of $|\psi|_{max}$ slightly changes with decreasing values of Pr as for $Pr = 7.2$ ($|\psi|_{max} = 2.331$) and for $Pr = 0.026$ ($|\psi|_{max} = 0.19$). Isothermal lines do not show any change in pattern or magnitude, as θ remains constant for varying Pr . In heatlines contour due to convective flow two circulation cells exist in the middle of cavity indicating thermal mixing. For varying Pr pattern of heatlines remain practically same though the magnitude of Π_{max} slightly changes with decreasing Pr .

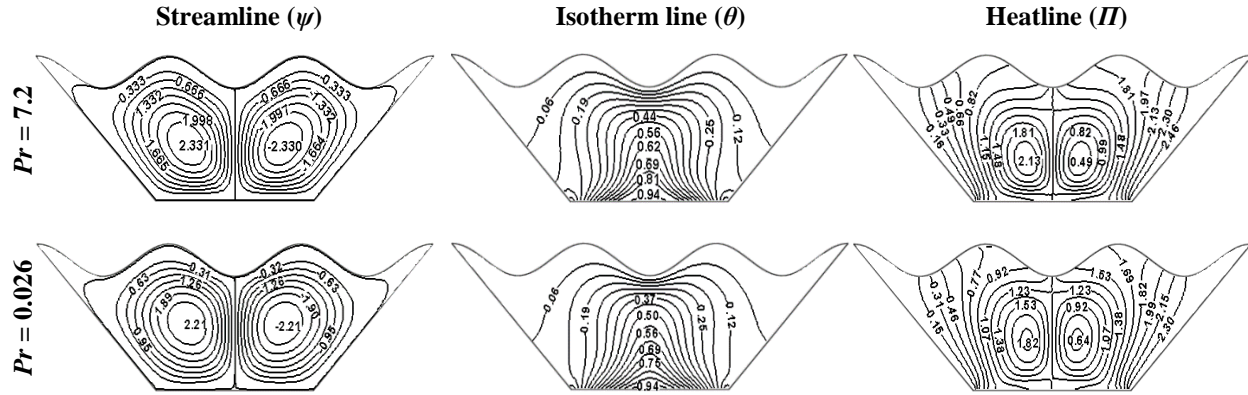


Figure 5: streamline, isotherm lines and heatlines for $Ra = 10^5$, $Da = 10^{-3}$ at different Prandtl numbers (Pr)

Variation of Nusselt Number

Figure 6 (a) shows variation of local Nusselt number (Nu) across the bottom wall. At lower values of Ra (10^4), Nu increases in a parabolic manner reaches a maximum value at the center of the wall and then decreases. This can be explained by Fig. 3 where isothermal lines have identical parabolic shape for lower values of Ra . At $Ra = 10^6$, magnitude of maximum value of Nu increases as Ra increases and maximum point occurs at two separate points in the curve symmetric about the central axis of the cavity. This is because in Fig. 3 for $Ra = 10^6$ for isothermal lines there is a gap in the center of the cavity near the bottom wall indicating very low temperature gradient causing a significant fall in Nu near this region. As values of Ra is increased maximum value of Nu increases since the flow becomes convection dominant which allows higher rate of heat transfer giving rise to a greater heat transfer.

Figure 6 (b) shows variation in average Nusselt number (Nu_{avg}) as Ra is changed from 10^3 to 10^6 for various Da , keeping Pr constant at 7.2. For higher Da (10^{-3}), Nu_{avg} increases with increase in Ra . At higher Da (10^{-3}), from $Ra = 10^3$ to 10^4 in the figure, Nu_{avg} is low and constant at 1.3, indicating conduction dominated heat transfer. At $Ra = 10^5$, Nu_{avg} starts to increase and reaches a maximum value at $Ra = 10^6$ due to convection dominated heat transfer in these regions. As Da decreases resistance to heat transfer increases due to reduced thermal permeability. At $Da = 10^{-4}$, Nu_{avg} remains constant at 1.3 from $Ra = 10^3$ to 10^5 after that it starts increasing at a much lower rate compared to $Da = 10^{-3}$ and reaches a maximum value of 3.09 at $Ra = 10^6$. For $Da = 10^{-5}$ flow becomes even more weak due to increased hydraulic resistance and remains laminar resulting in only conduction dominated heat transfer for all Ra and Nu_{avg} remains constant at 1.3.

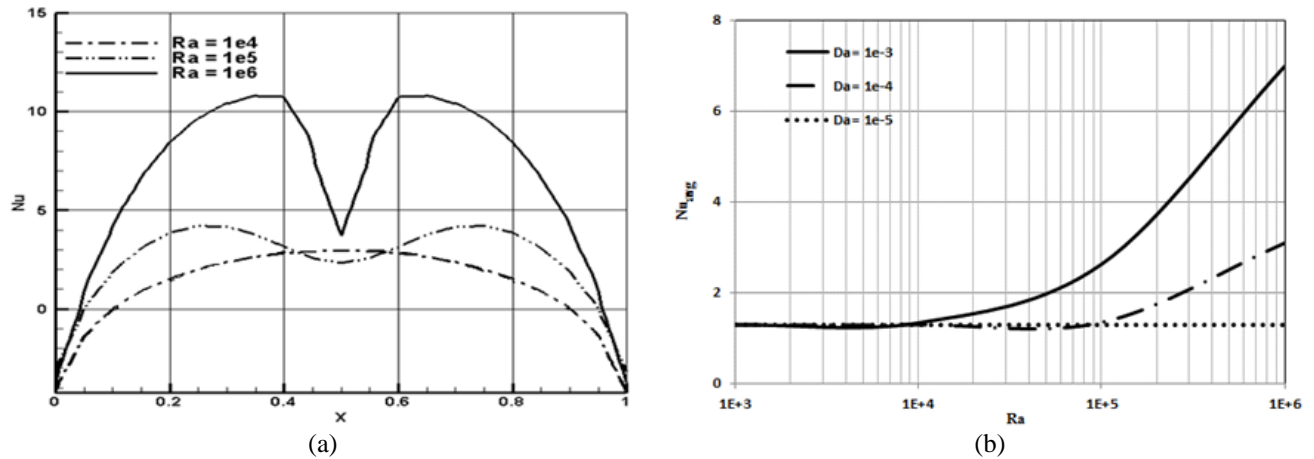


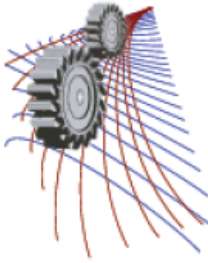
Figure 6. Variation of (a) Local Nusselt number (Nu) across the bottom wall for $Pr = 7.2$ for various values of Ra . (b) Average Nusselt number (Nu_{avg}) with changes in Rayleigh number (Ra) for various Darcy number (Da) at $Pr = 7.2$

CONCLUSION

The present study analyze the variation of Ra , Da , and Pr on thermal and fluid flow characteristics. At high Rayleigh number (10^6), convective effects dominate inside the cavity for all Prandtl number (Pr) and Darcy number (Da) so high magnitudes of streamfunction and heatfunction are observed at the core region of the cavity irrespective of Pr and Da . At lower Rayleigh number (Ra) heatlines emanate from sinusoidally heated bottom wall to the top wavy cold wall directly whereas at higher Ra (10^6) two separate heatline circulation cells are observed on either side of the central axis inside the cavity which indicates intense thermal mixing in these regions. At low Da (10^{-5}) both the magnitudes of the flow and temperature field are weak due to the influence of increased hydraulic resistance, while the increase of Da reduces hydraulic resistance and enhances the strength of fluid flow and temperature distribution indicating a role of convection dominant. The result of a variation in (Ra) shows similar trend with a variation in (Da); that is, the fluid circulation at constant Da (10^{-3}) is stronger as Ra is increased and the fluid circulation at constant Ra (10^6) is stronger as Da is increased. No significant change is observed with the change of Prandtl number. Average Nusselt number is highly dependent on Ra and Da . At low Da (10^{-5}) Nu_{avg} is almost constant and does not vary with changes in Ra but at higher Da (10^{-3}) Nu_{avg} shows a steep increase with increasing Ra reaching a maximum value at $Ra = 10^6$. Distribution of local Nusselt number across the sinusoidally heated bottom wall is sensitive to Rayleigh number. As Ra is increased the location of maximum Nu dramatically shifts from center and occurs at two separate points symmetric about the central axis also magnitude of Nu increases with increasing Ra .

REFERENCES

1. H. P. G. Darcy, Les Fontaines Publiques de la Ville de Dijon, 1856.
2. A. C. Baytas and I. Pop, Int. J. Thermal Sciences **34**, 511-519 (2002).
3. T. Basak, T. Roy, T. Paul and I. Pop, Int. J Heat and Mass Transfer **49**, 1430-1441 (2006).
4. M. Sathiyamoorthy, T. Basak, S. Roy and I. Pop, Int. J Heat and Mass Transfer **50**, 1892-1901 (2007).
5. M. Peric, Numerical Heat Transfer **4**, 213-219 (1993).
6. R. A. Kuyper and C. J. Hoogendoorn, Numerical Heat Transfer **28**, 55-67 (1995).
7. E. Natarajan, T. Basak and S. Roy, "Heatline visualization of natural convection flows within trapezoidal enclosures," International Conference on Fluid Mechanics and Aerodynamics, pp. 59-66, 2007.
8. P. Sompong and S. Witayangkurn, J. Applied Mathematics, 2013.



A Computational Study on Oblique Shock Wave-Turbulent Boundary Layer Interaction

Md. Saddam Hossain Joy¹, Saeedur Rahman¹, A.B.M. Toufique Hasan^{1, a)}, M. Ali¹,
Y. Mitsutake², S. Matsuo² and T. Setoguchi²

¹Department of Mechanical Engineering, Bangladesh University of Engineering and Technology (BUET),
Dhaka- 1000, Bangladesh

²Institute of Ocean Energy, Saga University, Saga 840-8502, Japan

^{a)}Corresponding author: toufiquehasan@me.buet.ac.bd

Abstract. A numerical computation of an oblique shock wave incident on a turbulent boundary layer was performed for free stream flow of air at $M_\infty = 2.0$ and $Re_l = 10.5 \times 10^6 \text{ m}^{-1}$. The oblique shock wave was generated from a 8° wedge. Reynolds averaged Navier-Stokes (RANS) simulation with $k-\omega$ SST turbulence model was first utilized for two dimensional (2D) steady case. The results were compared with the experiment at the same flow conditions. Further, to capture the unsteadiness, a 2D Large Eddy Simulation (LES) with sub-grid scale model WMLES was performed which showed the unsteady effects. The frequency of the shock oscillation was computed and was found to be comparable with that of experimental measurement.

INTRODUCTION

Shock wave-turbulent boundary layer interaction (SWTBLI) is critical for designing high speed aircraft. Hence, detailed study and understanding of the underlying processes in such flow is absolutely necessary. In any SWTBLI the shock exerts a massive adverse pressure gradient on the boundary layer. This results in subsequent thickening of the layer. For strong enough shocks the flow may even separate. SWTBLIs can also cause flow unsteadiness which, in cases of fully separated flows, can be characterized by low frequency oscillation of the shock structure with periodic expansion and contraction of the separation bubble.

The consequences of Shock wave-boundary layer interactions (SWBLI) are detrimental. They increase the drag of transonic wings and can cause flow unsteadiness and buffet. In gas-turbine engines, they induce blade losses and cause flow disruption to the compressor. In hypersonic flights SWBLIs can cause structural damage by intense localized heating [1]. The unsteadiness associated with the phenomena may even lead to aerostructure fatigue [2]. In scramjet combustion chambers they increase the fuel-air mixing due to the rise in the turbulence fluctuation level. However, the negative aspects far outweigh the positive. Hence there have been a huge number of experimental and computational studies for better understanding of the phenomena so that the negative aspects can be suppressed or even better, are avoided.

Ferri [3] made the first observations of SWBLI during testing of an airfoil in a high-speed tunnel. Settles et al. [4] reported an experimental study of SWTBLI generated by 2D compression corners of various corner angles. Results showed that the range of corner angles studied produced a flow field which moved from fully attached conditions through incipient separation to significantly separated conditions. Review by Dolling [2] covered the study of SWBLI over the past five decades. He underlined the main features of these flows that cannot be predicted today: heat transfer, skin friction and unsteady pressure loads. Clemens and Narayanaswamy [5] presented a review of studies dealing with the mechanism of the low-frequency unsteadiness. They discussed works on the two viewpoints of driving

mechanisms- upstream and downstream. They concluded that although both mechanisms are present in the shock-induced flows but for strongly separated flows downstream mechanism dominates while for weakly separated flows combination of both mechanisms prevail. Polivanov et al. [6] presented an experimental study of unsteady effects in SWBLIs. They found that low frequency oscillations of the separation shock wave produce large-scale structures which originate near the wall close to the base of the separation shock wave and propagate downstream. The shedding frequency of these structures corresponds to the frequency of the shock wave oscillations. Dussauge and Piponniau [7] have analyzed the possible sources of the unsteadiness in SWBLIs. It was observed that when a shock wave interacted with a boundary layer without inducing separation, the shock motion was dominated by the structure of inflow turbulence. Piponniau et al. [8] observed that the flow reattaching downstream was based on the properties of the fluid entrainment in the mixing layer downstream of the separation shock. The low frequencies associated with the separation shock were found to be related to the successive contractions and dilatations of the separation bubble. Dussauge et al. [9] conducted a review of various experiments. It was determined that the frequency of the fluctuations produced by the shock motion is much lower than the characteristic frequencies of turbulence present in the incoming boundary layers. It was suggested that the separation bubble may be at the origin of the unsteadiness caused by SWBLIs.

GOVERNING EQUATIONS AND COMPUTATIONAL METHODS

Governing Equations

The supersonic flow field under investigation is modeled as a two dimensional compressible, unsteady, viscous and turbulent field. The thermodynamic properties of air were assumed to be constant except the molecular viscosity. It was assumed to obey Sutherland's law of viscosity. The Governing equations were discretized by finite volume method (FVM) using ANSYS Fluent.

$$\text{Continuity: } \frac{\partial \rho}{\partial t} + \frac{\partial(\rho u_i)}{\partial x_i} = 0 \quad (1)$$

$$\text{Momentum: } \frac{\partial(\rho u_i)}{\partial t} + \frac{\partial(\rho u_i u_j)}{\partial x_j} = -\frac{\partial p}{\partial x_i} + \frac{\partial \tau_{ij}}{\partial x_j} \quad (2)$$

$$\text{Energy: } \frac{\partial(\rho E)}{\partial t} + \frac{\partial(u_i(\rho E + p))}{\partial x_i} = \bar{\nabla} \cdot \left(\alpha_{eff} \frac{\partial T}{\partial x_i} + u_j(\tau_{ij}) \right) \quad (3)$$

$$\text{Ideal gas-law: } \rho = \frac{p}{RT} \quad (4)$$

For RANS simulations, two-equation $k-\omega$ shear stress transport (SST) turbulence model of Menter [10] was used. This model combines the best of the $k-\omega$ model of Wilcox [11] and the $k-\varepsilon$ model. The $k-\omega$ SST model uses the $k-\omega$ formulation near the wall and switches to a $k-\varepsilon$ behaviour in the free stream. LES formulation removes the small part of the length and time scales by low-pass filtering of the Navier-Stokes equation. The removed portion is modeled by using a sub-grid scale (SGS) model. For the current study, Wall Modeled Large Eddy Simulation (WMLES) was used as SGS model. A time step size of 0.5 μs was used which is sufficient compared to the experimentally obtained frequencies of unsteady behavior [6].

Computational Domain and Boundary Conditions

The computational domain, boundary conditions and mesh are shown in Fig. 1. The boundary conditions were selected in the light of the experiment [6] and also for quick convergence. Mesh of the interaction zone has been

enlarged for better view. Total number of cells in the mesh was 2,47,500. The first cell height at the wall was about $0.4 \mu\text{m}$.

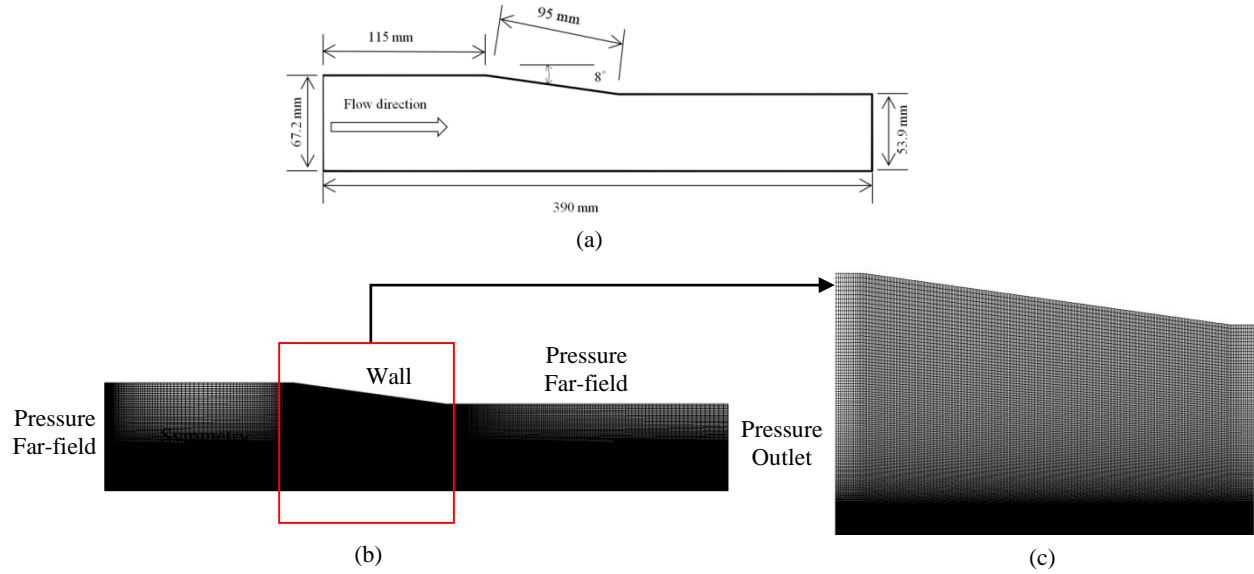


FIGURE 1. (a) Computational domain; (b) Mesh and boundary conditions; (c) enlarged view of mesh

COMPUTATIONAL VALIDATION

Computational results must be validated against some reference data. The validation of the current study has been done by comparing the computational results with the experimental results obtained by Polivanov et al. [6]. The experiments were performed for $M_\infty=2.0$ and $Re_1= 10.5 \times 10^6 \text{ m}^{-1}$. Comparisons of basic parameters of inflow turbulent boundary layer are presented in table 1.

TABLE 1. Basic Parameters of inflow turbulent boundary layer

Parameter	Experiment [6]	Present Simulation
δ_0 (mm)	3.10	3.19
δ^* (mm)	0.76	0.82
θ (mm)	0.23	0.27
u_τ (m/s)	25.70	23.41
C_f	5.06×10^{-3}	4.30×10^{-3}
Re_0	2700	3209

SCHLIEREN VISUALIZATION

Numerical schlieren images for the current study are compared with the experiment [6] in Fig. 2. The numerical schlieren was generated by contour plotting the absolute value of density gradient. The numerical schlieren establish that all the basic flow features are captured. From the comparison it is evident that numerically obtained schlieren images are in good agreement with the experimental one. The point, X_0 was defined as the extrapolated wall impact point of separation shock wave. The difference between X_0 and extrapolated wall impact point of incident shock wave was defined as the interaction length, L . For the present simulation it was found that $X_0= 179 \text{ mm}$ and $L= 26.3 \text{ mm}$.

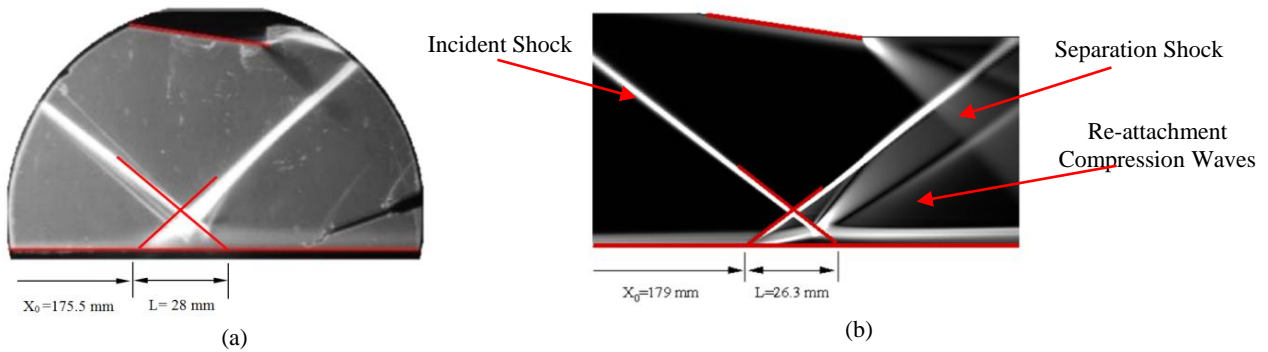


FIGURE 2. Schlieren images from; (a) Experiment (Polivanov et al. [6]); (b) Present Simulation

Streamwise Pressure Distribution

Streamwise wall pressure distribution has been presented in Fig. 4(a). The pressure has been normalized by the free stream static pressure $p_\infty = 10096.56$ Pa. The total pressure rise is quite well predicted. But there is some discrepancy within the interaction zone. The position along x from which the pressure starts to rise is predicted to be downstream of the experiment. The value of X_0 also from Fig. 2(b) also indicates this. The pressure rise is due to flow being deflected upwards by the separation bubble and hence creating the separation shock. Downstream pressure data are in good agreement with the experiment. [6] The increase in p/p_∞ highlights the rise in static pressure as the flow passes the multiple shock system.

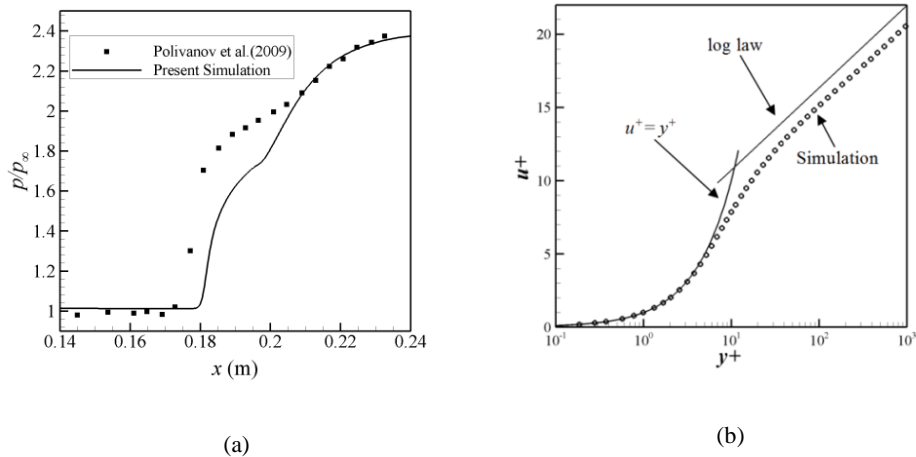


FIGURE 4. (a) Stream wise wall pressure distribution; (b) boundary layer profile for turbulent boundary layer of present simulation

Inflow Boundary Layer

To check the nature of the incoming boundary layer, its profile (160 mm from the leading edge) is presented in Fig. 4(b). Distribution of u^+ along y^+ shows different zones of turbulent boundary layer. The zone closest to the wall

($y^+ < 5$) is the viscous sublayer where the velocity profile is compared to the equation $u^+ = y^+$. Then, there is a transition zone known as the buffer layer. In the logarithmic zone, the velocity profile is compared with the law given by von Kármán [12]. The law can be stated as:

$$u^+ = \frac{1}{\kappa} \ln y^+ + C^+$$

Where, κ is the von Kármán constant and C^+ is a constant. κ was taken as 0.41 and C^+ was taken as 5.1.

Mass Flow Profile

Normalized mass flow data at various stations are presented in Fig. 3. The variation was plotted against wall normal distance normalized by δ_0 . Very good agreement with the experimental data [6] is found for the point stationed at $X^* = -0.554$. This point is stationed upstream of the interaction zone. It shows that inflow boundary layer is well predicted by the simulations. The points in figures 3(a), (b) and (c) are within the separation bubble as evident from the value of X^* (< 1). Point at $X^* = 0.089$ is near the origin of interaction. The profiles from numerical data are less full than the experiment. For point at $X^* = 0.339$ it is evident that numerical simulation cannot predict the maximum mass flow. Otherwise, the predictions are good.

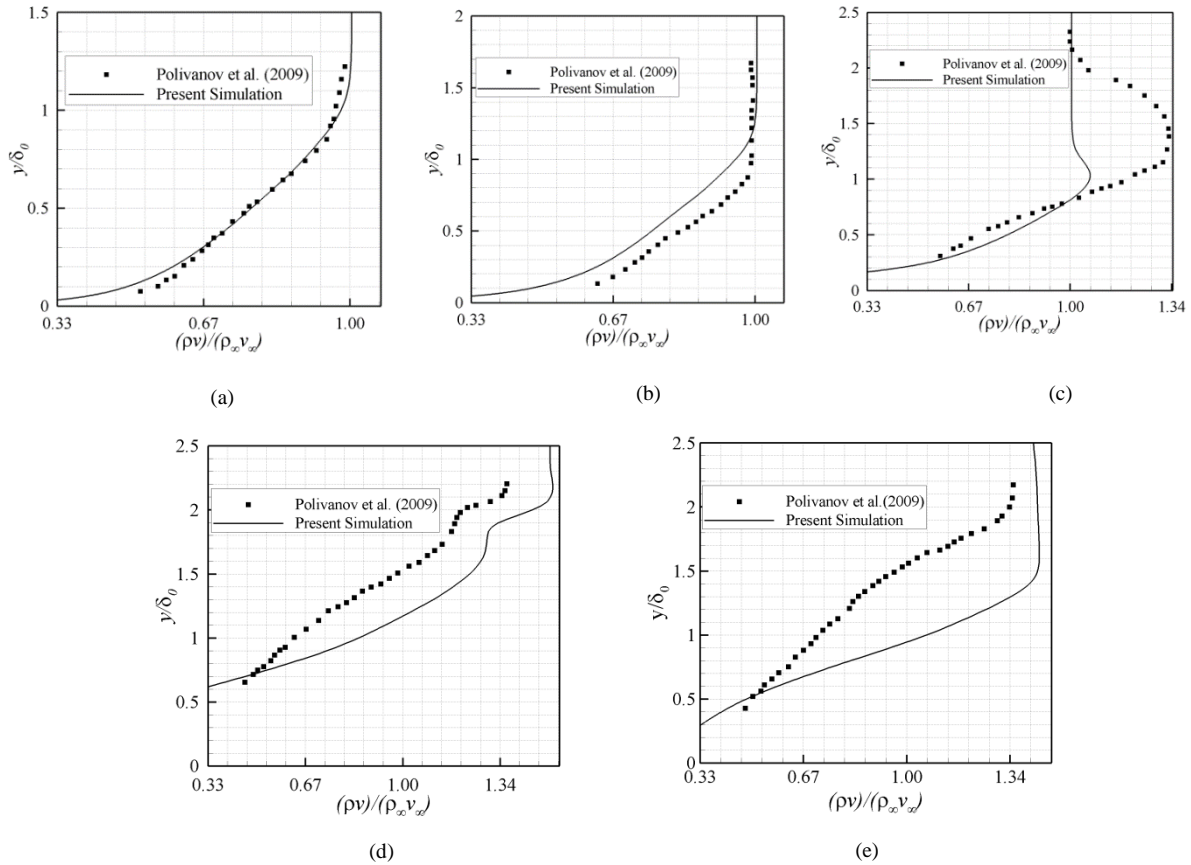


FIGURE 3. Vertical mass flow profiles at (a) $X^* = -0.554$; (b) $X^* = 0.089$; (c) $X^* = 0.339$; (d) $X^* = 0.589$; (e) $X^* = 1.441$

The experimental profile at $X^* = 0.589$ show the rapid increase in mass flow due to the incident shock. Numerical simulations have been able to capture this well. But the profiles are in general much fuller than the experimental

profile. This fact is also true for numerical profiles at $X^* = 1.441$. So, in comparison to the experiment, the simulations show rapid recovery of the boundary layer after re-attachment.

RESULTS AND DISCUSSION

Figure 5(a) shows computational schlieren image of the whole flow field. The sharp white lines represent shock waves while white fan like shapes indicate expansion waves. The wedge at the top generates an oblique shockwave. There is rapid density change near the wall making it visible. The impinging shock causes the boundary layer to separate from the flat wall. A separation shock is formed as the flow is diverted around the separation bubble. The separation shock cannot reach the wall as near the wall there is subsonic zone. The main flow expands over the

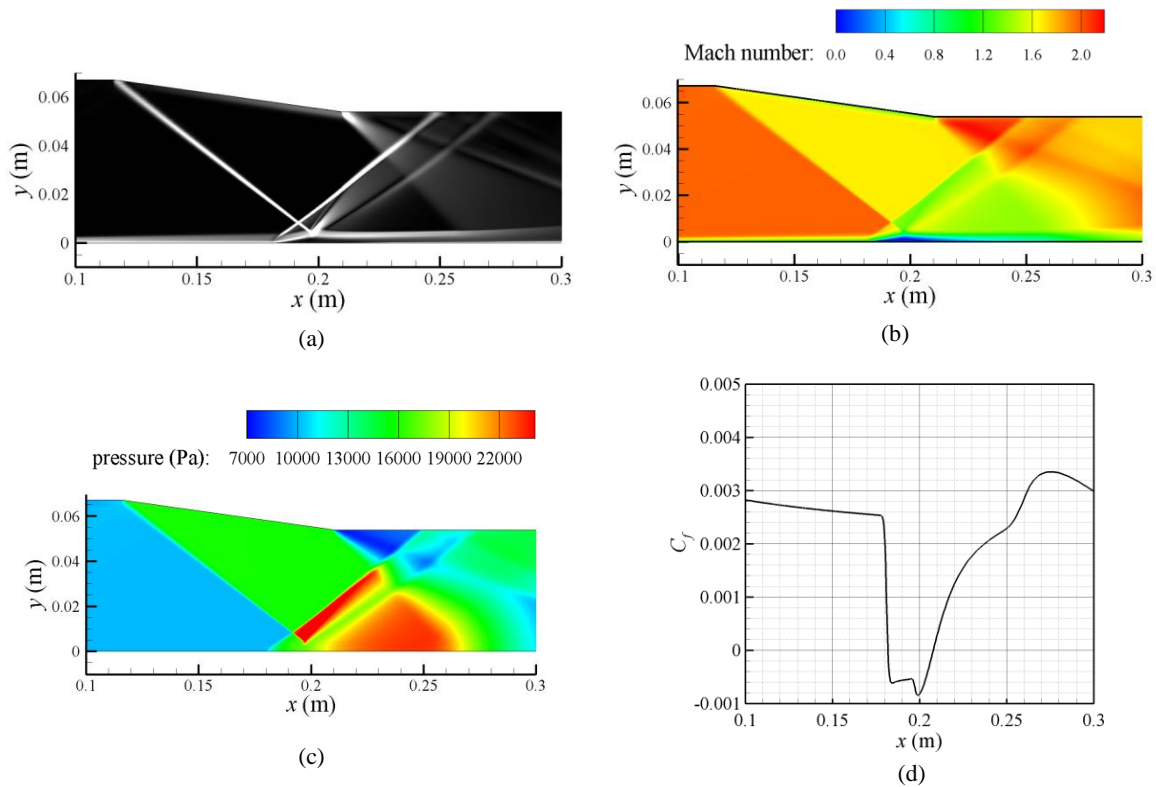


FIGURE 5. (a) Schlieren image; (b) Mach contour; (c) Pressure contour; (d) Skin friction coefficient distribution along wall

separation bubble thus forming an expansion fan which is visible just after the impingement point. As the flow reattaches on the wall it is compressed thus forming a re-attachment shock which is visible after the expansion fan.

Figure 5(b) shows the Mach contour of the simulation. Sharp rises of Mach number are apparent across the shock waves. The developing boundary layer as a low Mach number zone is also evident on the wall. The separation bubble is consisted of a very low Mach number zone. Figure 5(c) shows pressure contour plot. Shock waves cause rise in static pressure and expansion waves cause decrease. Both of these phenomena are visible from the plot. The maximum pressure is in the zone where the flow is compressed by both the incident and separation shock. There is also a pressure rise after the re-attachment shock. Figure 5(d) shows C_f distribution along the wall. Negative values indicate flow separation. The separation zone starts at $x = 182$ mm which is just downstream of X_0 . The figure also reveals that the flow re attaches after the separation zone. For unsteady analysis LES simulation of the flow problem was done. The

initial condition was taken from the RANS steady solution. Pressure data was collected at different points in the flow field with respect to flow time. The sampling period of the data was the time step size of unsteady LES simulation which is $0.5 \mu\text{s}$.

The pressure history plots presented in Fig. 6(a) show the fluctuating nature of pressure. Since the points are at different locations the average pressure varies depending on the locations. The amount of fluctuation is also not same for all the points. The highest fluctuations are for points that are within or very close to the interaction zone.

Fast Fourier Transform (FFT) of the pressure data was done to find out any dominating frequency. The data were in discrete form with a sampling frequency of 2 MHz which is just the inverse of the time step size of the simulation. Power Spectral Density (PSD) was used to find the principal frequency of pressure fluctuation. This frequency was found to be 488 Hz as shown in Fig. 6(b) (i) and (ii). This is in contrast to the experimentally found frequency of 600 Hz for the shock movement. [6] Figure 6(b) (iii) shows the existence of high frequency fluctuation at some stations. The frequency of these fluctuations is about 5.8 kHz. The position of the points corresponding to these figures are after the re attachment point. Schlieren images at different times of the principal period T is shown in Fig. 7. The principal period is the inverse of the principal frequency 488 Hz obtained by FFT. From the figures the separation shock is seen to move downstream at first and then upstream in successive images. The separation bubble is also found to be increasing in size. The separation shock moves so far upstream that is reflected by the wedge above and then re impinges on the wall below. Severe distortion of the re attachment shock is found especially near the separation bubble.

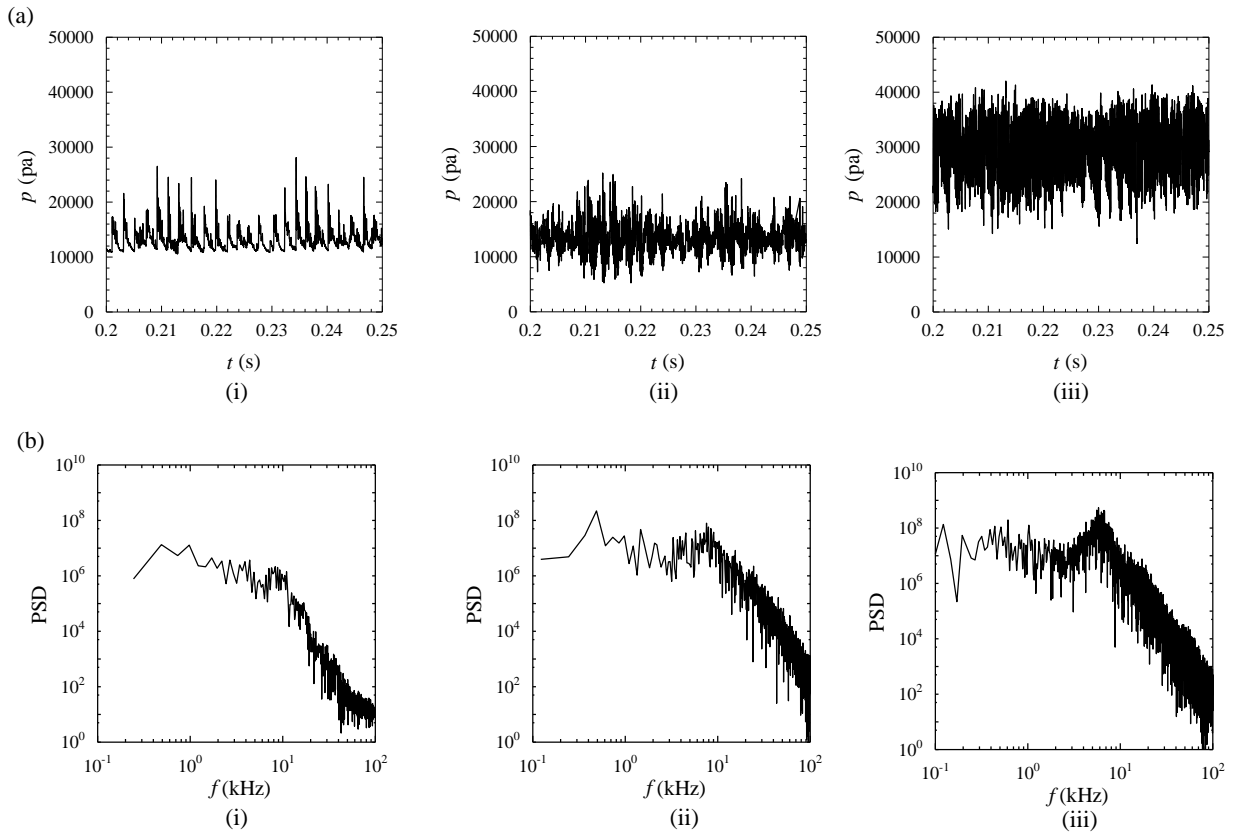


FIGURE 6. Data from fluctuating wall pressure; (a) pressure fluctuation with time; (b) Power spectral density; at (i) $x=120$ mm; (ii) $x=180$ mm; (iii) $x=250$ mm

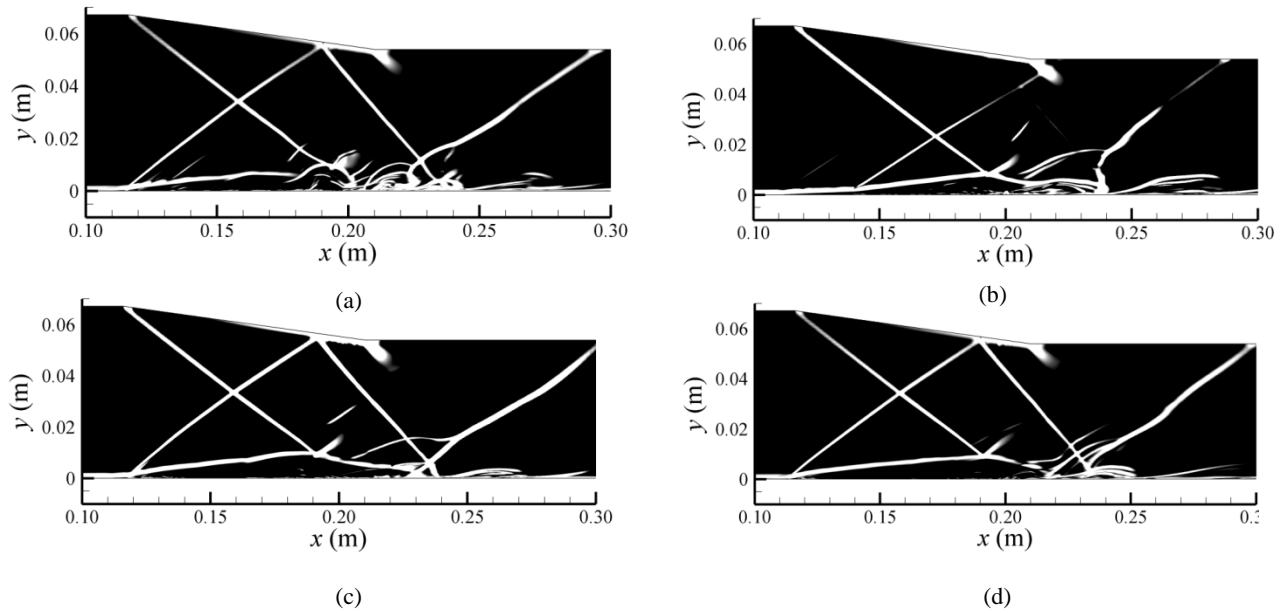


FIGURE 7. Schlieren images in one complete cycle; (a) $t=0$ s; (b) $t=T/4$ s; (c) $t=T/2$ s; (d) $t=3T/4$ s

Streamlines at different times of the principal period T is shown in Fig. 8. The streamlines show the flow pattern within the separation bubble. The circulating motion within the separation bubble is quite apparent. The separation shock (not visible in the picture) oscillates in the streamwise direction at the principal frequency.

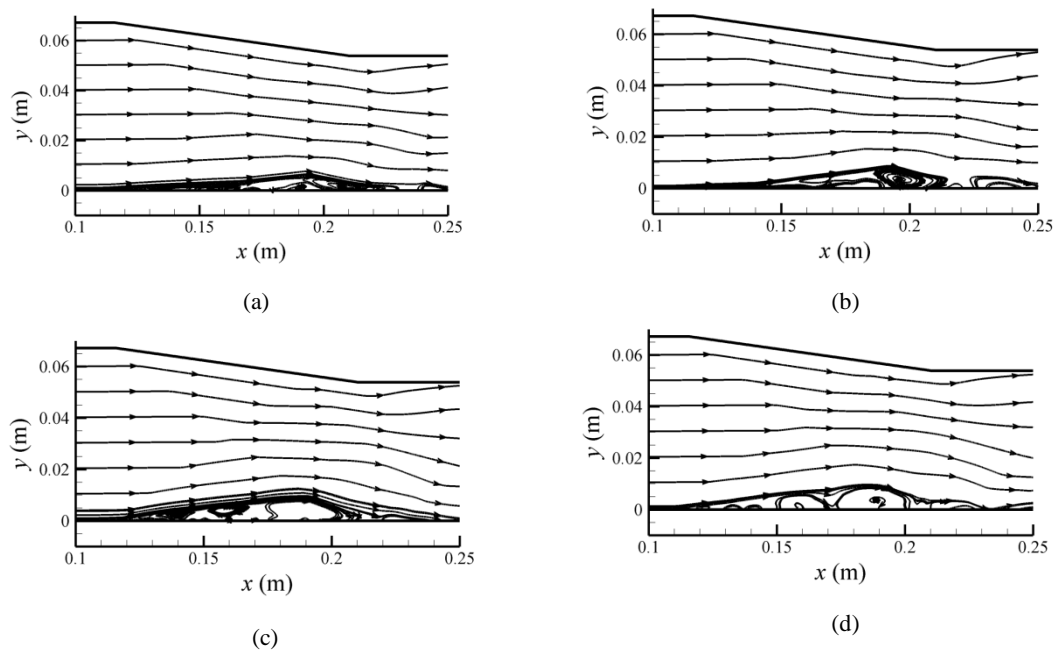


FIGURE 8. Instantaneous streamlines in one complete cycle; (a) $t=0$ s; (b) $t=T/4$ s; (c) $t=T/2$ s; (d) $t=3T/4$ s

CONCLUSION

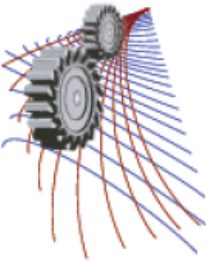
Reynolds Averaged Navier-Stokes (RANS) equations with $k-\omega$ SST turbulence model has been applied to predict the flow behavior associated with impinging type SWTBLI for 2D computational models. Incoming flow at $M_\infty=2.0$ produces an oblique shock wave which impinges upon boundary layer developed on a flat plate. Correct boundary layer was generated by matching various boundary layer properties with the experiment [6]. Large Eddy Simulation (LES) of the 2D flow field was performed to study the unsteady behavior found in such interactions. Steady RANS simulations of the flow captured the general features of the interaction well. Separation was found to occur on the flat plate where the shock generated by the wedge impinges upon. Streamwise wall pressure data showed pressure rise due to separation shock and reattachment shock. Streamwise pressure distribution and mass flow distribution in the wall normal direction showed reasonable agreement with experiment [6] except at some places. 2D LES simulation of the flow revealed unsteadiness in the flow field. Fluctuating pressure history was recorded at different stations in the flow field. PSD from FFT calculation of the data was used to find any principal frequency of the unsteady behaviour. A frequency of 488 Hz was found to be the dominating frequency at different positions. Much higher frequency was also found for some points after the re attachment point.

ACKNOWLEDGEMENTS

The present work has been carried out with computational resource support from Higher Education Quality Enhancement Project (HEQEP), AIF (3rd Round)-Sub-Project CP 3111, UGC, MoE, Government of Bangladesh (GoB).

REFERENCES

1. H. Babinsky and J. K. Harvey, *Shock Wave-Boundary-Layer Interactions* (Cambridge University Press, New York, 2011), pp. 1-4.
2. D. S. Dolling, *AIAA Journal* **39**, 1517–1531 (2001).
3. A. Ferri, *NACA TM 17* (1940). [translation]
4. G. S. Settles, T. J. Fitzpatrick and S. M. Bogdonoff, *AIAA Journal* **17**, 579–585 (1979).
5. N.T. Clemens and V. Narayanaswamy, *Annual Review of Fluid Mechanics* **46**, 469–492 (2014).
6. P. Polivanov, A. A. Sidorenko, A. Maslov, *AIAA Paper* **2009-409** (2009).
7. J. P. Dussauge and S. Piponniau, *Journal of Fluids and Structures* **24**, 1166–1175 (2008).
8. S. Piponniau, J. P. Dussauge, J. F. Debieve and P. Dupont, *Journal of Fluid Mechanics* **629**, 87–108 (2009).
9. J. P. Dussauge, P. Dupont and J. F. Debieve, *Aerospace Science and Technology* **10**, 85–91 (2006).
10. F. R. Menter, *AIAA Journal* **32**, 1598–1605 (1994).
11. D. C. Wilcox, *AIAA Journal* **26**, 1299–1310 (1988).
12. T. von Kármán, *NACA TM 611* (1931).



Effect of Cavity on Shock Oscillation in Transonic Flow over RAE2822 Supercritical Airfoil

M. Rizwanur Rahman¹, Md. Itmam Labib¹, A.B.M. Toufique Hasan^{1, a)}, M. Ali¹,
Y. Mitsutake² and T. Setoguchi²

¹*Department of Mechanical Engineering, Bangladesh University of Engineering and Technology (BUET), Dhaka-1000, Bangladesh*

²*Institute of Ocean Energy, Saga University, Saga 840-8502, Japan*

^{a)}Corresponding author: toufiquehasan@me.buet.ac.bd

Abstract. Transonic flow past a supercritical airfoil is strongly influenced by the interaction of shock wave with boundary layer. This interaction induces unsteady self-sustaining shock wave oscillation, flow instability, drag rise and buffet onset which limit the flight envelop. In the present study, a computational analysis has been carried out to investigate the flow past a supercritical RAE2822 airfoil in transonic speeds. To control the shock wave oscillation, a cavity is introduced on the airfoil surface where shock wave oscillates. Different geometric configurations have been investigated for finding optimum cavity geometry and dimension. Unsteady Reynolds averaged Navier-Stokes equations (RANS) are computed at Mach 0.729 with an angle of attack of 5°. Computed results are well validated with the available experimental data in case of baseline airfoil. However, in case of airfoil with control cavity; it has been observed that the introduction of cavity completely suppresses the unsteady shock wave oscillation. Further, significant drag reduction and successive improvement of aerodynamic performance have been observed in airfoil with shock control cavity.

INTRODUCTION

Transonic flow regime is characterized by several simultaneous physical phenomena such as shock waves, shock wave/boundary layer interaction (SWBLI), flow instability, boundary layer separation and boundary layer thickening. These phenomena limit the cruise speed creating drag rise and buffet boundaries. At particular transonic flow conditions, periodic self-sustained shock oscillations with large amplitudes are observed. Such periodic shock motions have been discovered over fifty years ago and their mechanism is not yet fully understood. This large scale shock induced oscillation has many undesirable unsteady effects including aileron buzz, periodic flows in supersonic intakes and cascades etc.

Mundell and Mabey [1] first proposed the classification of the type of shock-boundary layer interaction as well as studied the variety of modes of shock wave oscillation on the airfoil boundary. Tijdeman [2] in his classical work detected three possible modes of self-sustaining shock motion for an airfoil with an oscillating flap. They are self-sustaining in a sense that the motion is maintained without the supply of external energy. McDevitt et al. [3] and Levy [4] performed an experimental and theoretical investigation on unsteady flow behavior at transonic speeds over a 18% circular-arc airfoil. Supercritical airfoils also experienced self-sustained unsteady shock oscillations despite the fact that they are developed to increase drag divergence Mach number. Alshabu et al. [5] studied the properties of BAC3-11 airfoil and found the existence of upstream moving pressure around the airfoil profile. Zhao et al. [6] executed an experimental study on shock oscillations over SC (2)-0714 airfoil and found that the phenomenon is two dimensional in the middle of the model. Several mechanisms to reduce shock strength have been employed in recent years and they proved to be beneficial for both laminar and turbulent wings.

Qin et al. [7] numerically demonstrated the efficacy of some active shock control mechanism such as suction, blowing highlighting the benefits and drawbacks of number active control devices for airfoil optimization. Hasan et al. [8] in their recent studies showed that use of moist air is benign to reduce the intensity of shock induced oscillations in transonic flow regimes. Stanewksy [9] extensively studied various conventional means of flow control in case of moderate to large aspect ratio wings, delta wings with specific purpose of lift enhancement, drag reduction and the improvement of air-vehicle control effectiveness. Li et al. [10] proposed micro-blowing as another flow control technique. However, these active flow control methods are not always economically viable.

Passive shock control mechanisms such as local geometrical changes in airfoil profile have been employed due to economic aspects although only at certain flow conditions a drag reduction has been observed. In most cases the benefits in wave drag reduction have been offset by an increase in viscous drag. Ashil et al. [11] incorporated shock control bump (SCB) in NLF airfoils. It is shown that aerodynamic profiles modified with SCB provide higher lift, lower drag, and delayed buffet onset resulting in improved aerodynamic performance. The efficiency of SCB is quite sensitive to airfoil geometry and free stream conditions. The ability of SCB to control the unsteady shock induced oscillation has been reported by Hasan and Alam [12]. Yagiz et al. [13] studied hybrid flow control methods such as wave drag reduction based on bump and suction or injection in transonic flow regime. Another passive shock control method is the use of a cavity on airfoil profile. The main idea behind shock control cavity (SCC) is the use of static pressure jump over the shock wave to produce a small secondary flow and bypass through a cavity under the shock wave. Bahi et al. [14] experimentally demonstrated SCC concept on a supercritical airfoil for reducing drag. Nagamatsu et al [15] found substantial drag reduction by implementing a passive porous cavity in the region of the shock wave. McCormick [16] showed that the passive cavity significantly reduced the total pressure loss through the shock system by producing more isentropic compression. However, the boundary layer viscous losses downstream of the shock wave were significantly increased. Breitling et al. [17] studied the control of shock/boundary layer interaction by inserting a cavity into the airfoil and covering it with an elastic membrane. Smith et al. [18] introduced local slots and grooves and Bur et al. [19] implemented perforated plates as passive shock control mechanism to improve aerodynamic performance. Though there are a good number of works on controlling the shock, the control mechanism has still been remained enigmatic. Besides, the authors have found a lack of extensive study on the prospect of SCC over supercritical airfoils.

Though there are a good number of works on controlling the shock, the control mechanism has still been remained enigmatic. Besides, the authors have found a lack of extensive study on the prospect of SCC over supercritical airfoils. This paper numerically investigates the shock control mechanism by introducing an open circular cavity on the upper surface of a supercritical airfoil RAE 2822 where the shock oscillates. Three different geometries of the circular cavity are investigated. Different aerodynamic characteristics of the airfoil with cavity are compared with that of the baseline airfoil. Also the mechanism of shock control cavity has been investigated.

Nomenclature

C_d	coefficient of drag
C_l	coefficient of lift
C_p	coefficient of pressure
C_f	skin friction coefficient
M_∞	free stream Mach number
c	chord length
α	angle of attack
M_∞	free stream Mach number
p	static pressure

NUMERICAL METHODS

Governing Equations

The transonic flow field under investigation is modelled as a two dimensional compressible, unsteady viscous and turbulent field. The governing equations are continuity equation, conservation of momentum and energy equation. For turbulence modelling, linear eddy viscosity model is used in which the Reynolds stresses are modelled using linear constitutive relationship with the mean flow straining field. Among different linear eddy viscosity models, Menter's SST $k-\omega$ model is used in present computations. The $k-\omega$ formulation makes this model directly applicable to the near wall region in the viscous sub layer. The molecular viscosity is assumed to obey Sutherland's law of viscosity which is based on kinetic theory of ideal gases and an idealized inter-molecular force potential. This model gives a fairly accurate result over a wide range of temperature. The Governing equations are discretized by finite volume method (FVM) using ANSYS CFD [20]. It solves a coupled system of momentum and pressure based continuity equations and the remaining equations are solved in a decoupled fashion. Pressure terms are discretized using standard scheme while second order upwind scheme is used to discretized density and momentum terms. A time step size of 10^{-5} is used which is sufficient for this type of unsteady computation. A solution convergence is obtained when the residuals for each conserved variables reduced below the order of magnitude 6.

Computational Domain

C-topology structured mesh is used to discretize the computational domain of RAE 2822 airfoil. The chord length, c of the airfoil is 0.61m. The upstream and downstream boundaries are located at $11.5c$ and $20c$ apart while the top and bottom boundaries are $12.5c$ apart from the airfoil surface. These distances are found sufficient to apply free stream condition at the outer boundaries. No slip boundary conditions are applied at the airfoil surfaces and the free stream Mach number is kept constant at 0.729 and $\alpha = 5^\circ$. The free stream pressure and temperature are considered to be 101325 Pa and 300 K respectively. Very fine grid spacing is used to assure computational accuracy. Total number of grids is 76,000 that has been found to be sufficient for providing a grid independent solution. The first grid above the airfoil is very close to its surface resulting in a value of y^+ less than 1. The computational domain and a zoomed view of the grids in the vicinity of the airfoil can be seen in Fig. 1(a) and (b) while Fig. 1(c) shows the airfoil with control cavity.

A comparison of C_d , C_l and shock location (x_s/c) obtained from meshes with different number of grid points at 2.79° is shown in Table 1 as the grid independency test of the domain. From the table it is clear that the solution is no longer dependent on the number of grid points. The results also stand true for grid points higher than 76,000, but considering the computational cost and time associated; the mesh with 76,000 node points is selected for further calculations.

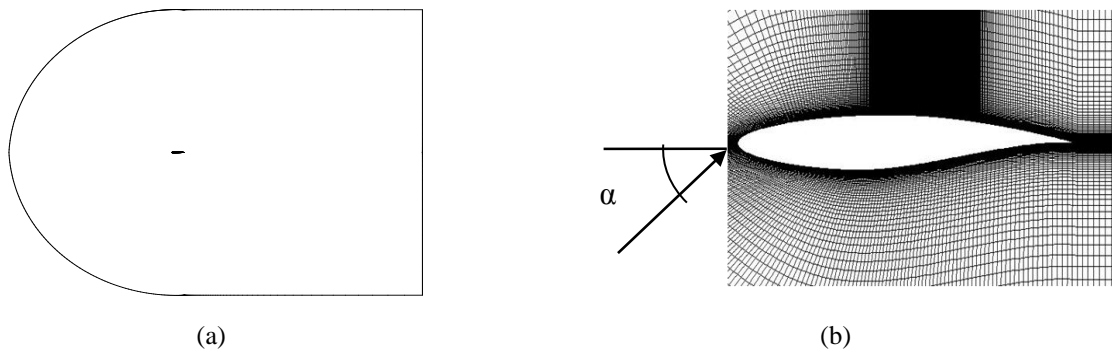


FIGURE 1. (a) Computational domain (b) Close up view of grid points in the vicinity of the airfoil surface

TABLE 1. Grid independency test

Node points	C_d	C_l	Shock location	y^+
53500	0.0177	0.784	0.52	0-0.86
56000	0.0174	0.7782	0.52	0-1.09
76000	0.017	0.787	0.52	0-0.87

RESULTS AND DISCUSSIONS

Validation

The computational results have been validated with experimental and numerical data. To match the numerical results with experimental data, the angle of attack and the Mach number are empirically modified to eliminate the wind tunnel influence. T. Yu et al. [20] used the parameter correction method proposed by Coakley [21]. These corrected parameters are used in this study to validate the model. The details of the corrected flow conditions are listed in Table 2. Results obtained from simulations of the baseline airfoil are compared with numerical results of

T. Yu et al. The authors further validated the model with experimental results of Advisory Group of Aerospace Research and Development (AGARD) of test case A6 [22]. Table 3 shows a comparison of present computation with experimental data and previously published numerical results. Fig. 2(a) presents a comparison of surface pressure distribution predicted by the present computation with that of experimental data. The symbols represent the experimental data while the solid lines are for present computation. It is seen that the C_p distribution from present computation are in good accordance with the experimental data. Also the skin friction coefficient, C_f is plotted over the airfoil upper surface in Fig. 2(b) which is seen to be in good match with AGARD data and numerical investigation of Mazaheri et al. [23]. The shock location is also identical which has already been reported in Table 3.

TABLE 2. Corrected flow conditions [6]

Parameter	Value
Mach number	0.729
AOA	2.79°
Free stream static pressure	101325 Pa
Free stream temperature	300 K

TABLE 3. AGARD Test case experimental data and CFD comparison

Method	AOA	C_l	$\Delta C_l, \%$	C_d	$\Delta C_d, \%$	$x_{s/c}$
AGARD (test case A6) [22]	3.19	0.803	----	0.0168	----	0.52
T. Yu et al [21]	2.79	0.784	-2.40	0.0171	1.80	0.52
Present computation	2.79	0.787	-1.99	0.0170	1.19	0.52

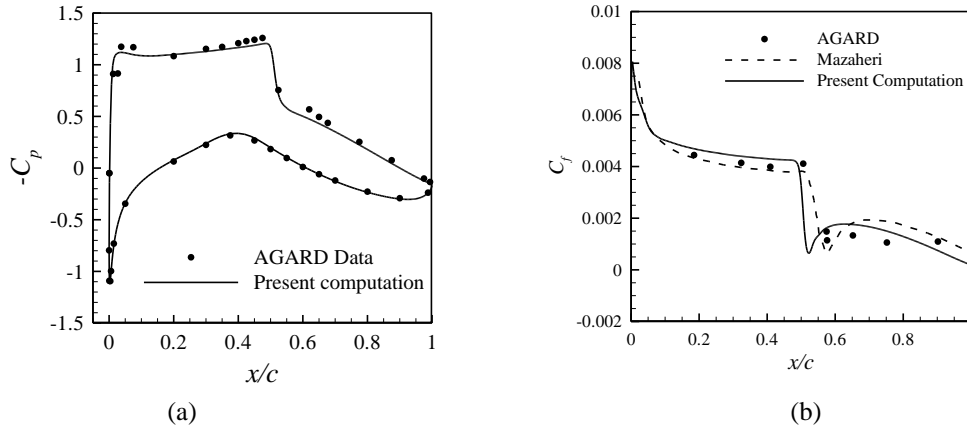


FIGURE 2. Distribution of (a) C_p and (b) C_f over baseline airfoil surface ($M_\infty = 0.729$, $\alpha = 2.79^\circ$)

Baseline Airfoil

The baseline airfoil shows unsteady flow behavior at $\alpha = 5^\circ$. Along with the flow field, the aerodynamic characteristic parameters too become unsteady. In Fig. 3 C_l and C_d of the baseline airfoil are plotted. Both the parameters are unsteady as seen in the figure. But the unsteadiness follows a periodic pattern. C_l fluctuates between 0.868 and 0.909 while C_d varies in the range of 0.044 to 0.048. But the frequency and amplitude remain same from cycle to cycle. Along with the coefficients of lift and drag, the shock too is found to be oscillating with a periodicity in its movement. This oscillating behavior of the shock is further demonstrated in Fig. 4 where C_p distributions over the airfoil top surface are shown at varying time steps in a period. Fig 4 (a) shows the downstream movement of the C_p curve with progress of time in the first half cycle. In Fig. 4 (b) the C_p curve again travels upstream and reaches its initial position at the end the second half cycle, $t/T = 1$. This clearly shows the unsteady yet periodic nature of the shock wave. The periodic variation of the shock wave over time is well captured in Fig. 5. The variation of shock strength (measured in terms of shock length over the airfoil surface) and the shock position in a complete cycle are depicted in Fig. 5(a). It is seen that, as at the beginning of a cycle, the shock wave moves toward the leading edge and its strength increases. The shock is strongest at its forward movement at $x/c=0.41$. After this point the shock continues its forward journey while it loses its strength. As it reaches $x/c=0.40$, its extreme point toward the leading edge, half cycle completes. After this point, the shock starts moving backward. However, its strength is still in the decreasing trend. When the shock arrives at $x/c=0.44$, it starts regaining its strength. As it reaches $x/c=0.45$, the other extreme point of its movement toward the trailing edge, one full cycle completes. A complete picture of the flow field oscillation could be seen from the root mean square (RMS) of pressure fluctuation as in Fig. 5 (b). The RMS values remains constant up to $x/c = 0.4$. After $x/c = 0.4$, the RMS values start to increase and reaches the peak at $x/c = 0.45$. Then, the RMS values start decreasing in downstream locations. However, large RMS values are found in the range of $x/c = 0.40$ to $x/c = 0.55$. Therefore, this zone is considered as strongly affected by the unsteady shock wave oscillation. After $x/c = 0.55$, the RMS values are successively decreased downstream. However, a rise in RMS value is seen near the trailing edge.

Passive Control of Shock Oscillation

The transonic shock wave oscillation as found in baseline RAE 2822 airfoil impose fluctuating aerodynamic and thermal loads on the airfoil which obviously have detrimental consequences of airfoil performance. Thus, the control of transonic oscillation is a must for safe and reliable operation of a supercritical airfoil. To control the shock oscillation, an open cavity of circular shape is introduced on the upper surface of the airfoil around the shock oscillating zone. Thus, a shock control cavity is placed that spans from $x/c = 0.40$ to $x/c = 0.55$.

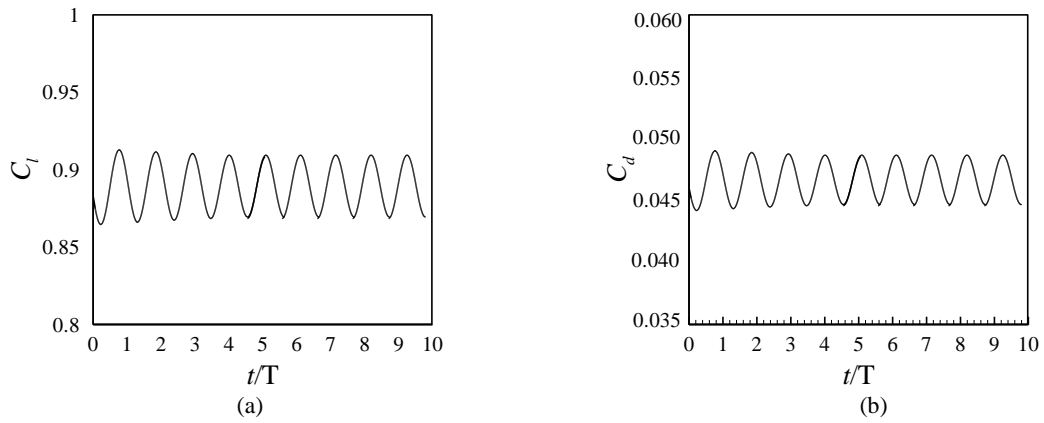


FIGURE 3. Time histories of (a) C_l and (b) C_d for flow over baseline airfoil ($M_\infty = 0.729$, $\alpha = 2.79^\circ$)

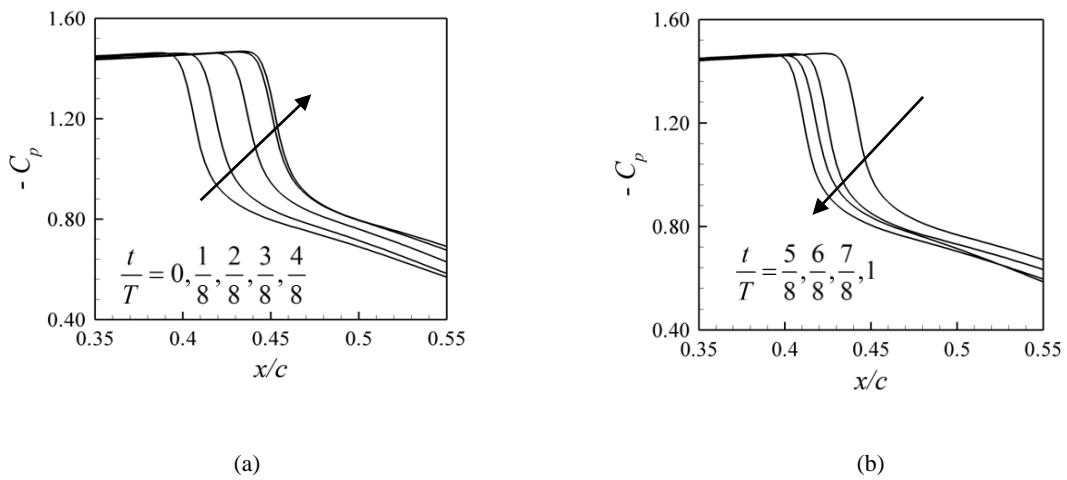


FIGURE 4. Oscillation of C_p distribution over airfoil upper surface (baseline); (a) first half and (b) second half of the complete cycle ($M_\infty = 0.729$, $\alpha = 5^\circ$)

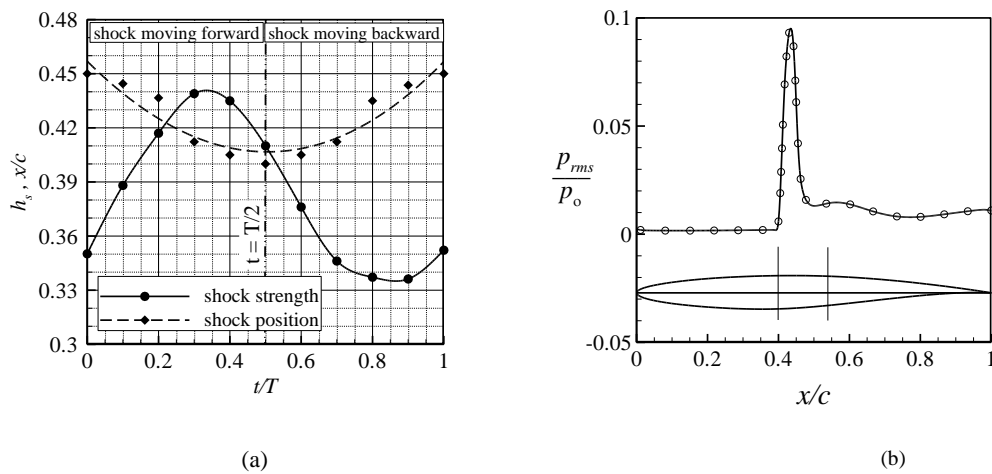


FIGURE 5. (a) Variation of shock strength and position with time for baseline airfoil; (b) Distribution of static pressure over airfoil surface

The investigated control cavity is of circular shape as shown in Fig. 6. The length of the cavity is kept constant. It spans from $x/c=0.40$ to $x/c=0.55$ that is 15% of the chord length while the depth is varied. Three cavity geometries with different depths are investigated. The investigated cavity depths are 2.0%, 2.5% and 3% of the chord length which will be denoted as Cavity-C1, Cavity-C2 and Cavity-C3, respectively in later discussion. The maximum cavity depth is at the middle of the cavity length and the depth becomes zero at both ends, thus a symmetric shape about the midpoint. The length to maximum depth ratio is therefore 7.5, 6.0 and 5.0 for Cavity-C1, Cavity-C2 and Cavity-C3 respectively. With the introduction of the cavity, the flow around the supercritical airfoil has been steady and the shock oscillation collapses. Fig.7 shows the aerodynamic behaviour of the airfoil with control cavities. It is clearly seen that the lift and drag coefficients have become steady over time with some initial transients that might have resulted from numerical calculations. The C_p distribution over the airfoil surface with and without control cavities are compared in Fig. 8. It is observed that there is a static pressure jump in all control cases that ensures reduction of shock strength that consequently decreases the aerodynamic drag. The aerodynamic properties of the control cases are compared with that of the baseline airfoil RAE 2822 in Table 4. In all the control cases aerodynamic drag has been reduced and this reduction is increased with the depth of the cavity. The airfoil with cavity-C3 experiences highest lift and lowest drag among the three cases. The lift to drag ratio is also increased by 1.15% as compared with the baseline airfoil. However, irrespective of their response to drag reduction, each of the cases effectively collapses the shock oscillation and stabilizes the flow field as well as the major aerodynamic characteristic properties.

Control Mechanism

Lee [24] well explained the mechanism of self-sustained shock oscillation in transonic flows over airfoil. According to this mechanism- a pressure wave is generated at the stem of the shock wave which propagates downstream. On the other hand, a disturbance wave is generated in the turbulent region near the trailing edge which propagates upstream. The interaction between these two waves keeps the shock wave oscillating around the airfoil surface. No external energy is required for this oscillation which is classically known as feedback mechanism. This feedback mechanism has been well verified in recent experiments performed by Hartmann et al. [25] and so on. When a control cavity is placed near the shock oscillation region, the oscillating behaviour of the shock wave stops and the flow field becomes steady. The reasons behind this phenomenon will now be explained.

Fig. 9 (a) shows the streamlines on the upper surface of the airfoil where shock wave appears for flow over baseline airfoil. In this figure, the shock induced separation bubble is seen which is centered at $x/c = 0.54$. The separated flow is generated from the foot of the shock wave at $x/c \approx 0.42$ and extends downstream. This separated flow is further propagated underneath the boundary layer and strongly interact with the wake vortices near the trailing edge. Thus, a direct interaction establishes between the induced separated zone with the trailing edge wake and this creates a feedback mechanism for shock wave to oscillate.

But in case of control cavity, the separated zone is trapped in the vicinity of the cavity. The re-attachments are in the range of $x/c = 0.61$ to 0.89 , $x/c=0.61$ to 0.88 and 0.62 to 0.87 for airfoil with cavity-C1, cavity-C2 and cavity-C3, respectively as in Fig. 9 (b), (c) and (d). In these zones, the boundary layers become stable. The re-attachment and healthy boundary layer around partial portion of the upper surfaces are responsible for the control of unsteady shock wave oscillation and improvement in aerodynamic characteristics in cases of airfoil with control cavity.

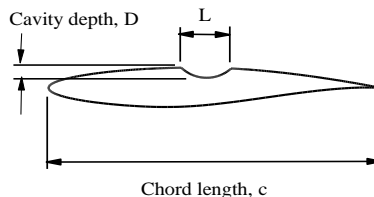


FIGURE 6. Airfoil with circular control cavity

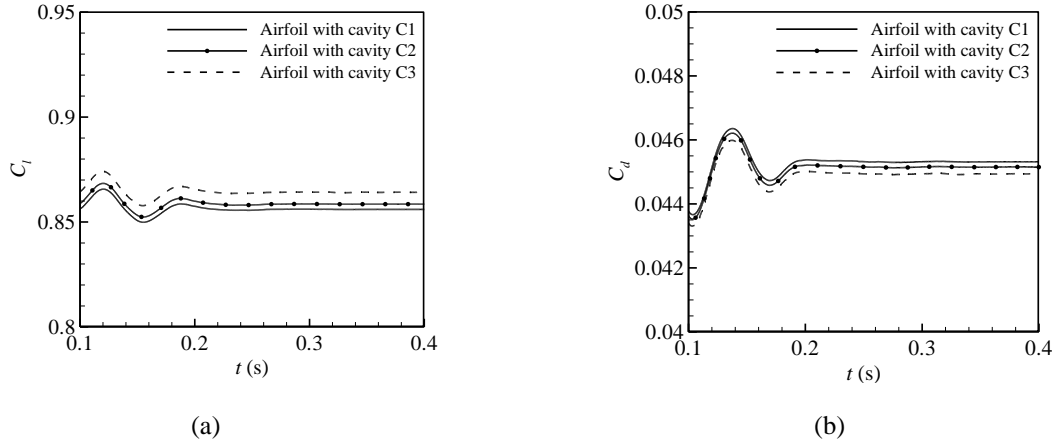


FIGURE 7. Aerodynamic behavior of airfoil with circular shock control cavity; (a) C_l and (b) C_d

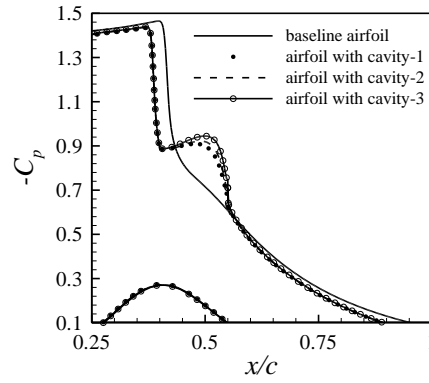


FIGURE 8. Comparison of C_p distribution over airfoil surface for baseline airfoil and airfoil with control case

TABLE 4. Aerodynamic Performance of baseline airfoil and airfoil with circular control cavity

Cases	C_l	C_d	l/d	Drag change
Baseline airfoil (mean)	0.8868	0.0466	19.03	--
Airfoil with cavity-C1	0.8559	0.0453	18.89	-2.78%
Airfoil with cavity-C2	0.8588	0.0451	19.04	-3.21%
Airfoil with cavity-C3	0.8643	0.0449	19.25	-3.65%

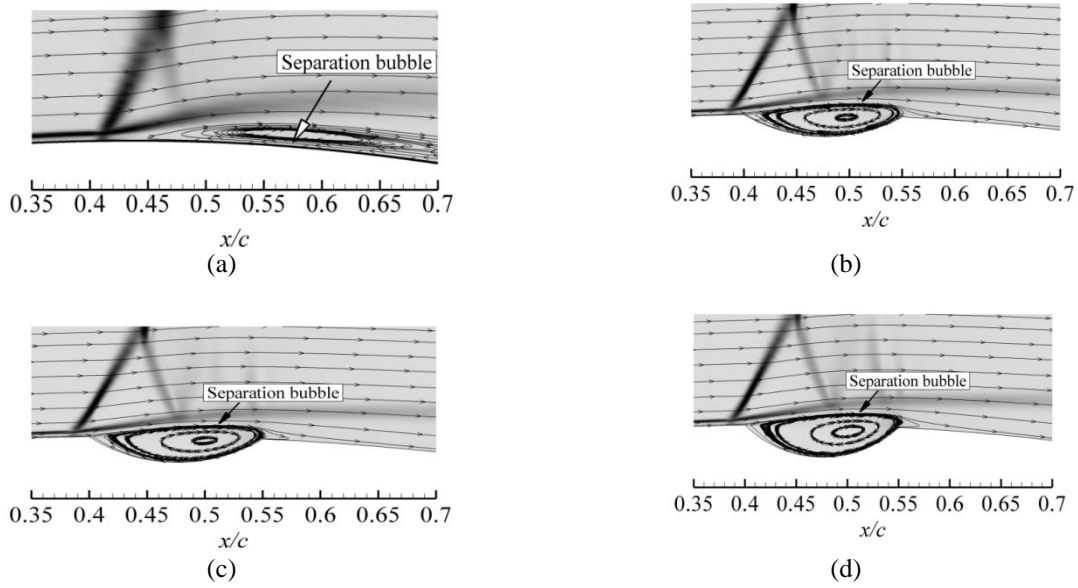


FIGURE 9. Streamline over the airfoil surface in the vicinity of oscillation zone; (a) Baseline airfoil (b) airfoil with cavity C1 (c) airfoil with cavity C2 (d) airfoil with cavity C3

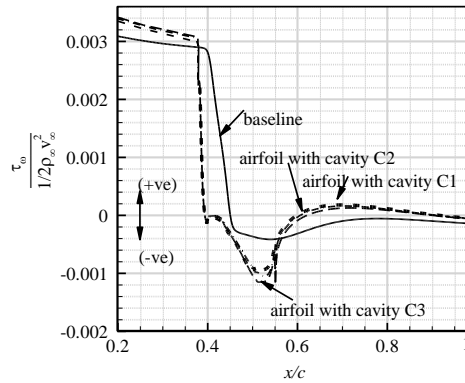


FIGURE 10. Shear stress distribution over the upper surface of (a) comparison of baseline airfoil and airfoil with circular cavity

CONCLUSION

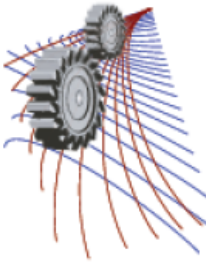
Transonic flow past a supercritical RAE2822 airfoil has been analyzed through numerical computations. A passive control technique in the form of circular arc cavity has been introduced. Reynolds averaged Navier-Stokes equations have been solved to predict the flow field past the airfoil at free stream Mach number of 0.729 and an angle of attack of 5° . Self-excited shock wave oscillation is observed for the baseline RAE2822 airfoil at the flow conditions under present investigation. The aerodynamic characteristics of the baseline airfoil are found to be varying in a periodic nature. The introduction of a circular cavity in the shock oscillation zone completely eliminates the flow field unsteadiness. This confirms the cavity as a promising technique among the passive approaches for the control of shock wave oscillation around a supercritical airfoil in transonic flow conditions.

ACKNOWLEDGEMENT

The present work has been carried out with computational resource support from Higher Education Quality Enhancement Project (HEQEP), AIF (3rd Round)-Sub-Project CP 3111, UGC, MoE, Government of Bangladesh (GoB).

REFERENCES

1. D.G. Mabey, and A. R. G. Mundell, *Aeronautical Journal*, 274-281(1986).
2. Tijdeman, NLR TR 77090 U, National Aerospace Laboratory, Netherlands (1977).
3. Mc Devitt, L. L. Levy and G. S. Deiwert, *AIAA Journal* **14**, 603-613 (1976).
4. L. L. Levy, *AIAA Journal* **16**, 564-572 (1978)
5. Alshabu, A., Olivier, H., *AIAA Journal* **46**, 2066-2073 (2008).
6. Z. Zhao, X. Ren, C. Gao, J. Xiong, F. Liu and S. Luo, 51st AIAA Aerospace Sciences Meeting, (2013).
7. N. Qin, Y. Zhu and S. Shaw, *International Journal of Numerical Methods for Heat & Fluid Flow* **14**, 444 – 466 (2004).
8. A. B. M. T. Hasan, S. Matsuo, T. Setoguchi and A. K. M. S. Islam, *International Journal of Mechanical Sciences* **54**, 942-945 (2012).
9. E. Stanewsky, *Progress in Aerospace Sciences* **37**, 583-667 (2001).
10. J. Li, C. H. Lee, L. Jia and X. Li, 47th AIAA Aerospace Sciences Meeting, Orlando, Florida, (2009).
11. P. R. Ashill, J. L. Fulker, J. L. Shires, 1st European Forum on Laminar Flow Technology, Hamburg, Germany, (1992).
12. A.B.M.T. Hasan and M. Alam M, *International Journal of Fluid Mechanics Research* **41**, 440-459 (2014).
13. B. Yagiz, O. Kandil and Y. V. Pehlivanoglu, *Aerospace Science and Technology* **17**, 21-31 (2012).
14. L. Bahi, J. M. Ross and H. T. Nagamatsu, AIAA 21st Aerospace Sciences Meeting, Reno, Nevada (1983).
15. H. T. Nagamatsu, R. D. Orozco and D. C. Ling, AIAA 17th Fluid Dynamics, Plasma Dynamics and Lasers Conference, Colorado, (1984).
16. D. C. McComick, *AIAA Journal* **31**, 91-96 (1993).
17. T. Breitling and J. Zierep, *Acta Mechanica* **87**, 23-36. (1991)
18. A. N. Smith, H. Babinsky, P. C. Dhanasekaran, A. M. Savil, and W. N. Dawes, 41st Aerospace Sciences Meeting and Exhibit, Reno, Nevada, (2003).
19. ANSYS, Inc., Canonsburg, PA, USA (www.ansys.com).
20. T. Yu, J. J. Wang and P. F. Zhang, *Journal of Aircraft* **48**, 1565-1575(2011).
21. T. Coakley, AIAA 25th Aerospace Sciences Meeting, Reno, Nevada (1987).
22. P. H. Cook, M. A. Mc Donald and M. C. P. Firmin, Aerofoil RAE2822 pressure distributions, boundary layer and wake measurements, AGARD Advisory Report No.138 (1979).
23. K. Mazaheri., K. C. Kiani, A. Nejati, M. Zeinalpour and R. Taheri, *Aerospace Science and Technology* **42**, 196-208 (2015).
24. B. H. K. Lee, *Progress in Aerospace Sciences* **37**, 147-196 (2001).
25. A. Hartmann, M. Klass and W. Schroder, *Physics of Fluids* **25**, 026101 (2013).



Analysis of Viscous Micropump with Single Rotating Cylinder

Md. Nur Alam Mondal¹, Md. Shafiqul Islam¹, A.B.M. Toufique Hasan^{1, a)}, Y. Mitsutake²

¹Department of Mechanical Engineering, Bangladesh University of Engineering and Technology (BUET), Dhaka-1000, Bangladesh

²Institute of Ocean Energy, Saga University, Saga 840-8502, Japan

^{a)}Corresponding author: toufiquehasan@me.buet.ac.bd

Abstract. This study presents the transient nature and performance of viscous micropump for low Reynolds number where flow is assumed laminar, unsteady, incompressible and two dimensional. The device consists of a cylinder placed eccentrically inside an extremely narrow channel, where channel axis is perpendicular to cylinder axis. When the cylinder rotates, it generates a net force on fluid due to unequal shear stresses on the top and bottom surfaces of the cylinder. This net force is capable of generating a net flow against a pressure gradient. The flow field inside the micro channel has been analyzed by using structured grid Finite Volume Method (FVM) based on Navier-Stokes equation. All parameters used in flow simulation are expressed in non-dimensional quantities for better understanding of flow behavior, regardless of dimensions or the fluid that is used. The effect of the channel height (S), the cylinder eccentricity (ϵ), the Reynolds number (Re) and Pump load (P^*) have been studied. Various flow patterns inside the micro pump as well as variations in flow velocity with time are obtained. Both the steady state and transient results of viscous micro pump are validated. It is found that the average velocity of fluid increases with increasing cylinder eccentricity and decreases with increasing the channel height.

INTRODUCTION

In the last few decades, technology has eased our life by some splendid mini and micro machines. These micro machines include micro pumps, micro sensors and actuators and different other types of micro machines. These devices are called MEMS (Micro Electro Mechanical Systems), NEMS (Nano Electro Mechanical Systems). The main advantage of MEMS, NEMS is the reduction in manufacturing cost due to mass production methods used. Micro pumps are among the most developed of all MEMS devices. Micro pumps operate as a result of completely different principles than those applied in traditional pumps like the axial or centrifugal pumps. Generally mechanical micro pumps work in three ways at low Reynolds numbers: (i) Positive-displacement pumps; (ii) Continuous, parallel-axis, screw-type rotary pumps; (iii) Continuous, transverse-axis rotary pumps. A problem associated with positive displacement micro pumps is that they require check valves at the inlet and outlet ports, which makes the design complex, especially on such a small scale. Stemme and Stemme [4] suggested replacing the check valves with a nozzle at the inlet and a diffuser at the exit, as reported in Erik and Goran [5]. The idea is impractical due to the requirement of certain operating conditions. Electro hydrodynamic pumps, Electro kinetic pumps were proposed to overcome the valve problem associated with positive displacement pumps. The micro pump concepts mentioned above are complex and require several auxiliary components which make them practically in appropriate. Sen et al. [1] introduced viscous micro pump which is both simple in design and applicable at the micro scale. Sen et al. studied experimentally the effect of the channel height, rotor eccentricity, and angular velocity on the pump performance. Sharatchandra et al.

Nomenclature

h	channel height
Re	Reynolds number
P_{in}	pump inlet pressure
ε	cylinder eccentricity
S	non-dimensional channel height
d	diameter of the rotor

[2] investigated the effects of slip flow on the pump performance numerically. Abdelgawad et al. [3] investigated the transient nature of viscous micro pump numerically. The present study will represent two-dimensional analysis of viscous micro pump. Present study will show transient nature along with some steady-state nature of a viscous micro pump. Different flow patterns for low Reynolds number with time are also shown.

PROBLEM SPECIFICATION

Pump Geometry

The micropump consists of a cylinder of diameter d , placed eccentrically inside a channel of height h , where channel axis is perpendicular to cylinder axis. The length of the channel is taken equal to 16 times diameter of the cylinder to establish fully developed flow in far upstream and far downstream of the cylinder (Sharatchandra et al., 1997). The used dimensionless parameters related to this study are:

The channel height is defined as $S = \frac{h}{d}$; the rotor eccentricity, $\varepsilon = \frac{y_c}{\frac{h}{2} - \frac{d}{2}}$

When $\varepsilon = 0$, the upper and lower walls are equally spaced from the cylinder. When $\varepsilon = 1$, the cylinder is in contact with either upper or lower wall. Reynolds number is imposed to characterize the angular speed of the cylinder. The Reynolds number is defined as:

$$Re = \frac{Ud}{\nu} = \frac{\omega d^2}{2\nu}$$

The non-dimensional average velocity inside the channel, $U^* = \frac{\bar{U}}{U} = \frac{\bar{U}}{\frac{\omega d}{2}}$

Where the average velocity \bar{U} at the cylinder outlet section, is defined as $\bar{U} = \frac{1}{h} \int_0^h U dy$ $\bar{U} = \frac{1}{h} \int_0^h U dy$

The non-dimensional pressure rise, $\Delta P^* = \frac{P_{out} - P_{in}}{\frac{\rho \nu^2}{d^2}}$

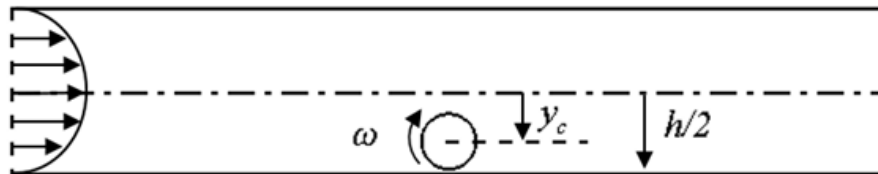


FIGURE 1. Schematic of the micropump geometry

The non-dimensional time i.e. time taken by the rotor to finish one complete revolution, $t^* = \frac{t}{\frac{2\pi}{\omega}} = \frac{t\omega}{2\pi}$

Boundary Condition

The flow inside the micro pump is assumed laminar, incompressible and unsteady. The fluid is considered as Newtonian with constant properties: $\mu = 1.449 \text{ kg/m-s}$, $\rho = 1261 \text{ kg/m}^3$.

Channel wall: No slip, no penetration and stationary boundary condition.

Cylinder wall: No slip boundary condition. The tangential velocity is prescribed and normal velocity is set to zero.

Inlet and Outlet: Pressure is prescribed in inlet and outlet to characterize the pressure load of pump.

NUMERICAL MODELING

The accuracy of numerical result largely depends on the type of mesh discretization employed; the investigation on pumping performance on viscous micropump is carried out by using structured grid Navier-Stokes method. The CFD package FLUENT 14.5 [7] is used to solve the Navier-Stokes equation numerically. It enables the use of different discretization schemes and solution algorithms, together with various type boundary conditions. A mesh generator, Gambit is used as pre-processor to draw the geometry and generate the required structured grids. Grid points are kept denser from far upstream and downstream to near the cylinder region to capture flow characteristics accurately. The number of nodes and elements which led to mesh independent solution for different pump dimensions is shown in tabulated form in Table 1.

The PISO-simple algorithm was used for pressure velocity coupling. It takes into account two corrections, which are the neighbour correction and the skewness correction. The PISO algorithm takes less time than other algorithms, which makes it more suitable for transient applications. Two different discretization schemes were used for the time and momentum equations. A power law scheme was used for momentum equation and a 2nd order discretization was used for time derivatives. During solution the relaxation factors were varied between 0.15 to 1. The results are obtained at time step size 0.0001s and the solver iterated the equations until the scaled residuals were less than 10^{-6} or it was stabilized at a constant value.

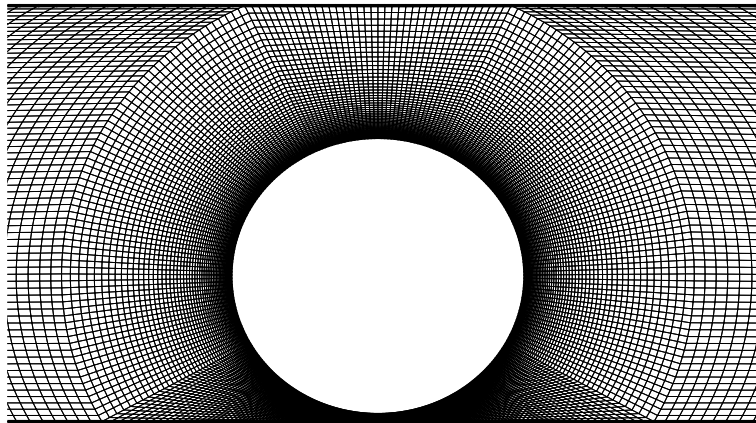


FIGURE 2. Structured Grid refinement near the lower Region of cylinder.

TABLE 1. Properties of different grids used and comparison of results at $S = 2.5$, $\varepsilon = 0.90$

Number of Nodes	Number of Cells	U^*
4704	4516	0.06933
9181	8940	0.06954
19944	19584	0.06958
23600	23200	0.06960

RESULTS AND DISCUSSIONS

The Flow Field inside the Micropump

The flow fields inside the micropump in Fig. 3 showed good agreement with the flow patterns obtained from Abdelgawad et al. (2004). The Flow patterns in Fig. 4 for different eccentricities and in Fig. 5 for different channel height are shown and their effects on flow field are described in later article. In Fig. 3, initially the vortexes in upstream and downstream region are larger and decrease in size with time until the fluid flow is developed or becomes steady.

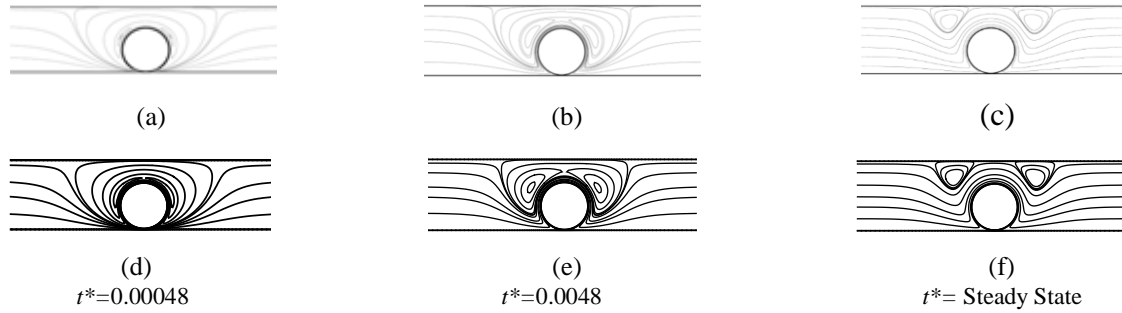


FIGURE 3. Flow pattern (a), (b), (c) are obtained at $\Delta P^* = 0$, $Re = 1.0$, $S = 1.5$, $\varepsilon = 0.95$ from Abdelgawad et al. (2004) and the flow pattern (d), (e), (f) from the present study.

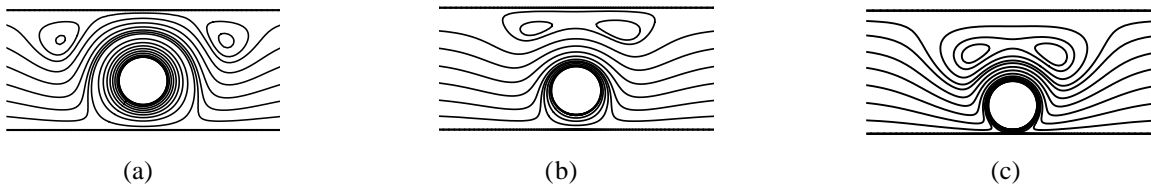


FIGURE 4. Flow pattern development at steady state for $S = 2.5$, (a) $\varepsilon = 0.30$ (b) $\varepsilon = 0.60$ (c) $\varepsilon = 0.90$.

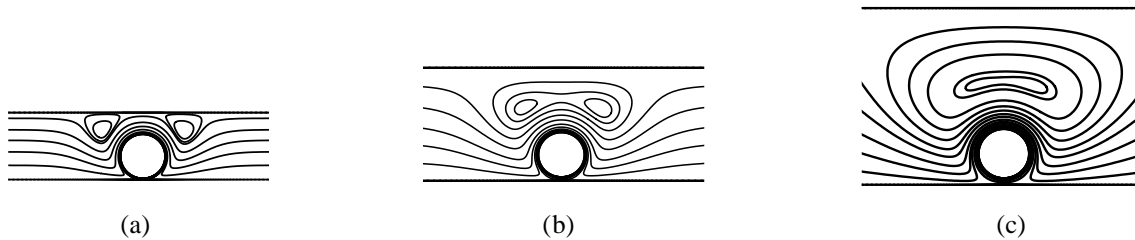


FIGURE 5. Flow pattern development at steady state for $\varepsilon = 0.90$, (a) $S = 1.5$ (b) $S = 2.5$ (c) $S = 3.5$.

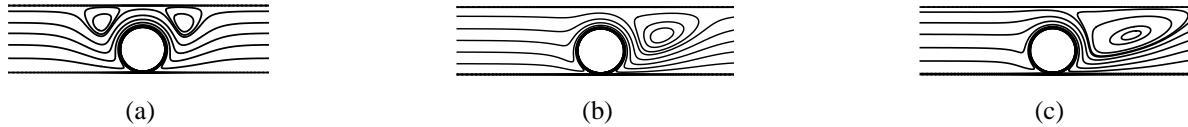


FIGURE 6. Flow pattern development at steady state for $S=1.5$, $\varepsilon=0.90$ at (a) $Re=1.0$ (b) $Re=100$ (c) $Re=200$.

The Effect of Channel Height

Before transient analysis some steady state cases were simulated. The results were compared with numerical results obtained from Abdelgawad et al. [3]. It shows that the decrease of bulk velocity of Newtonian fluid occurs when the channel height varies from $S=1.5$ to $S=3.5$. This is due to the reduction in shear stress on upper cylinder surface resulting from larger distance between the cylinder and the upper wall; this reduces the flow driving force. Again Fig. 5 shows that the vortex size above the cylinder increases as the channel height increases. That's why it takes longer time to transmit motion of fluid layer adjacent to the cylinder surface to the fluid layer adjacent to the upper wall. The effect of channel height on bulk velocity of fluid is shown in Fig. 7(a). The working parameters are: $\varepsilon = 0.90$, $P^* = 0.5$, $Re = 0.5$.

The Effect of Cylinder Eccentricity

The cylinder eccentricity has a significant effect on the pumping performance as it provides the driving force to fluid inside the micro pump by introducing unequal shear stresses on the upper and lower surfaces of the cylinder. It is investigated that at constant channel height the bulk velocity of fluid rises approximately linear with the cylinder eccentricity which is shown in Fig. 7(b). The reason behind this is that at lower eccentricities in Fig. 4(a), circular vortices are developed around the cylinder which restricts the high mass flow rate. As the cylinder eccentricity increases the torque transmitted to the fluid is higher and the vortex size is also comparatively lower, thereby causing higher mass flow rate. Again the presence of comparatively large vortex size above the cylinder at channel height $S=2.5$ in Fig. 4(c), causes the lower bulk velocity of fluid than for the channel height $S=1.5$.

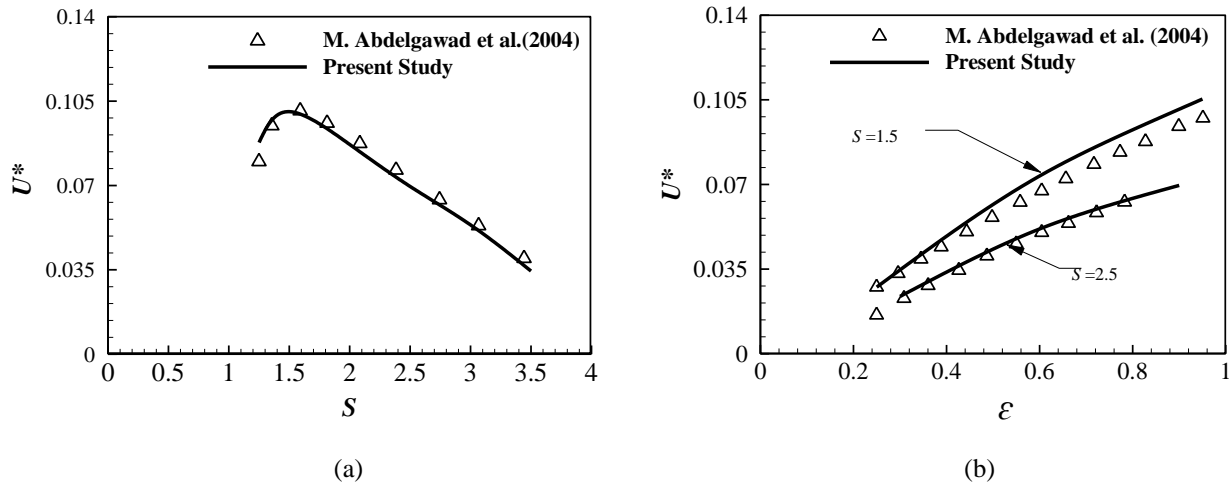


FIGURE 7. Variation of the bulk velocity of fluid as a function of (a) channel height (b) cylinder eccentricity.

The Effect of Reynolds number

The variation of the fluid bulk velocity at different Reynolds numbers with time is shown in Fig. 8. Initially the fluid velocity increases exponentially with time at particular Reynolds number and then becomes steady after a finite time. At higher Reynolds number the fluid flow takes longer time to reach steady state and the value of fluid velocity is lower than small Reynolds number. Figure 6 shows that at higher Reynolds number vortexes are moved to right and are increased in size. This is due to the less effect of viscous force compared to the inertia forces. As higher Reynolds number means higher mechanical input to rotate the cylinder, it causes lower pumping performance.

The Effect of Pump Load

To simulate the pressure rise needed for the pump to overcome the frictional losses, the pump load is modelled by increasing the pressure at outlet boundary. Figure 9 shows variation of pump efficiency as a function of pump load where the efficiency is the ratio of the flow energy rise to the input mechanical energy to the pump. The pump efficiency can be expressed in terms of non-dimensional quantity and is defined as:

$$\eta = \frac{\Delta P^* U^* S}{C_M Re^2}$$

Where C_M is the cylinder moment coefficient. The effect of C_M is only a weak function of ΔP^* for fixed values of S and ε (Sharatchandra et al., 1997). This is because, close to the rotor surface, the flow structure is governed by the shearing action of the rotating cylinder, rather than the externally imposed pressure gradient. The most efficient pump performance is thus obtained when ΔP^* varies from 10 to 14. Generally low values of η are due to the very high rates of viscous dissipation, therefore a major portion of shear work imparted to the fluid by the cylinder is dissipated as heat.

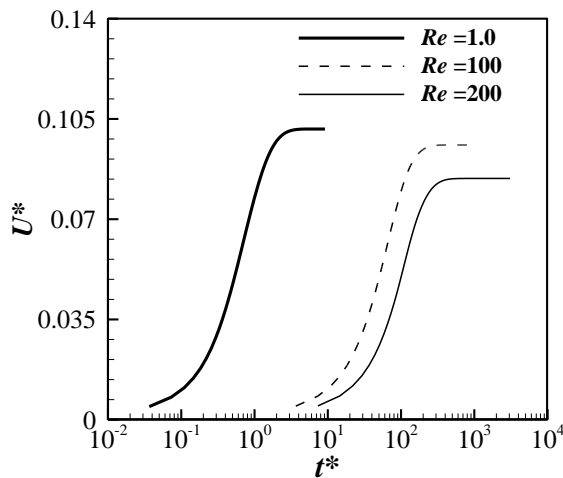


FIGURE 8. The bulk velocity of fluid at different Reynolds numbers with time at $S=1.5$, $\Delta P^*=1.0$, $\varepsilon=0.90$.

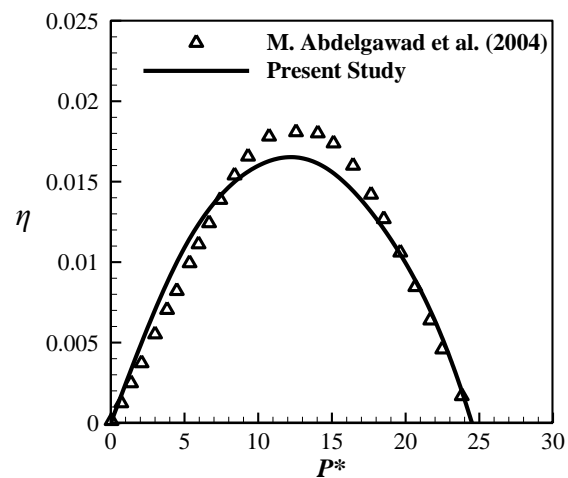


FIGURE 9. Variation of micro pump efficiency with pump load at $S=1.5$, $\varepsilon=0.95$, $Re=1.0$

CONCLUSION

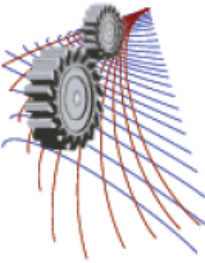
The goal of the present study was to investigate the effect of micropump geometry and the cylinder rotational speed on the flow behaviour of the Newtonian fluid inside the micro pump and the pump performance at different pressure load. Numerical results of the flow through the micro pump were calculated by simulating Navier-Stokes equations. It was found that the bulk velocity of fluid increases with increasing the cylinder eccentricity and decreases with increasing the channel height. Also the higher Reynolds number greatly influences the micro pump performance.

ACKNOWLEDGMENTS

The present work has been carried out with computational resource support from Higher Education Quality Enhancement Project, (HEQEP), AIF (2nd Round)-Sub-Project CP2099, UGC, MoE, Government of Bangladesh (GoB).

REFERENCES

1. M. Sen, and D. Wajerski, and M. Gad-el-Hak, *Journal of Fluids Engineering*, vol. **118**, pp. 624-627, (1996).
2. M. C. Sharatchandra, M. Sen, and M. Gad-el-Hak, *International Journal of CFD*, vol. **119**, pp. 372-382, (1997).
3. M. Abdelgawad, I. Hasan, N. Esmail, *Microscale Thermophysical Engineering*, **8**:361-381, (2004).
4. E. Stemme and G. Stemme, *A: Physical*, vol. **39**, pp. 159-167, (1993).
5. S. Erik and S. Goran, *Sensors and Actuators, A: Physical*, vol. **39**, pp. 159-167, (1993).
6. ANSYS, Inc., Canonsburg, PA, USA (www.ansys.com).
7. Chia, B. T., et al., *Sensors and Actuators, A: Physical* **165**(1): 86-93. (2011).
8. Au, A. K., et al., *Micromachines* **2**(4): 179-220. (2011).
9. Iverson, B. D. and S. V., *Microfluidics and Nanofluidics* **5**(2): 145-174. (2008).
10. Laser, D.J. and Santiago, J.G., *Journal of Micromechanics and Microengineering* **14** R35-R64. (2004).



Effects of Flow Properties on the Performance of a Diffuser-Nozzle Element of a Valveless Micropump

Partha Kumar Das¹ and A.B.M. Toufique Hasan^{1, a)}

¹*Department of Mechanical Engineering, Bangladesh University of Engineering and Technology*

^{a)}Corresponding author: toufiquehasan@me.buet.ac.bd

Abstract. The flow behaviour and performance parameters of a diffuser-nozzle element of a valveless micropump have been investigated for different driving pressure frequencies. When a fluctuating pressure is imposed on the inlet boundary of a diffuser-nozzle element, there is a net flow in diffuser direction due to the dynamic effect. The variation of this net flow along with rectification capacity, and diffuser efficiency has been investigated for different frequencies of driving pressure. Flow behaviour and recirculation region due to dynamic effect have been studied as qualitative study. Pressure and velocity have been analyzed for quantitative analysis and for validation with results found in literature. 2-D geometry has been used in the present study. 3-D geometry has been modeled to justify the results obtained from 2-D analysis. Five different pressure frequencies ranging from 5 kHz to 50 kHz have been used to investigate their effects on the performance of diffuser-nozzle element in high frequency ranges. The net flow and performance of the nozzle-diffuser element are found to be decreasing with the increasing frequency. The performance is found to be less sensitive to frequency at high pressure range (above 30 kHz).

INTRODUCTION

Micropump concept as a microfluidic and biofluidic device has been originated to meet the demand of both small scale flow (usually less than 15 $\mu\text{L}/\text{min}$) and high pressure fluid transport. According to the convention for microelectromechanical systems (MEMS), micropump is a specialized pump having a length scale of order 100 μm or smaller. Micropumps found in literature can be categorized based on two aspects: actuation principle, and flow rectification method. Based on actuation principle, micropumps can be Mechanical displacement micropumps and Dynamic micropumps. In Mechanical displacement micropumps, a moving boundary forces the fluid along by volume changes. All mechanical displacement micropumps deliver a pulsating or periodic flow as the with the help of flow rectifying devices and so they are also named as periodic micropump. Some of the examples are piezoelectric, thermo-pneumatic, electrostatic, bimetallic, electromagnetic, etc. In the references [1-8], different types of mechanical displacement and dynamic micropumps are described. According to different flow rectification methods, micropumps can be again classified as valveless (static valves) micropumps and micropumps with valves (dynamic valves). Dynamic valves (check valves, flap valves, etc) are defined as the valves that accomplish the task of flow rectification by means of deformation, deflection or other movement. Static valves are defined as the valves having fixed geometry without any moving parts. These valves provide flow rectification through the addition of energy (active) or inducing desired flow behaviour by fluid inertia (passive). The design of geometry plays an important role in case of passive static valves. Two most common types of static geometry passive valves are nozzle-diffuser element and tesla valve. Micropumps having nozzle-diffuser elements as flow rectification device are commonly known as valveless micropumps.

Valveless Micropumps

The name “Valveless” is due to the absence of conventional dynamic valves which have moving parts. Mainly three types of nozzle-diffuser elements are available with different specification, geometry, and performance; they

are (a) conical, (b) pyramidal, and (c) planer as shown in Fig. 1. The prominent advantage of nozzle-diffuser element over valves is that no moving parts or boundaries are involved which effectively reduces wear, mechanical and fatigue failure, relatively large pressure loss and clogging of foreign particles in valves. The absence of any moving parts makes the pumps capable to drive different types of fluids, gases, liquids with solid foreign particles. Valveless micropumps are easy to fabricate and last for a long time operation. Valveless pumps can be operated at a much higher frequency relative to the check valve pumps. This high frequency gives a high flow rate which makes the pumps very much suitable for electronic cooling applications.

Acoustic Standing Wave Micropump (ASWMP) with Diffuser-Nozzle Element

Among all the different types of micropumps, Acoustic Standing Wave Micropump (ASWMP) is considered to be the most youngest micropump. It achieves pumping action through the use of standing waves in a confined chamber. This new type of micropump consists of a chamber (resonant chamber), vibrator (generally piezoelectric), and a driver. The inlet port is nothing but a small opening which connects the chamber with fluid reservoir. In the outlet port a diffuser-nozzle element is mounted for the flow rectification purpose. It does not have any conventional valves (having moving parts) to rectify flow for which it may be called a “Valveless” micropump.

The basic principle of ASWMP is based on the superposition of two travelling wave from opposite direction, giving rise to a standing wave. From the characteristic of standing wave, there are several node and anti-node position where the amplitude of the wave is zero and maximum (absolute summation of the two source amplitudes) respectively. The number of nodes and anti-nodes depends upon the length of the chamber and the excitation frequency. In ASWMP, the driver supplies the power to maintain a standing wave in the pump chamber. The length of the chamber is adjusted so that the travelling wave generated by the acoustic driver is reflected to create constructively interfering standing waves. The pressure at a pressure anti-node fluctuates above and below the ambient pressure level (PO). Meanwhile, at the pressure nodes, the pressure is essentially equal to the mean chamber pressure which is in most of the cases ambient pressure of the fluid reservoir. The inlet and outlet ports are located near the pressure nodes and antinodes of the chamber, respectively, as illustrated in Fig. 2. The large pressure fluctuations throughout the resonator at the pressure anti-node tend to create a net fluid flow through the outlet port. This is so because the flow resistance of the diffuser is smaller during the portion of the cycle where the pressure at the pressure anti-node exceeds the discharge pressure than during the portion of the cycle where the pressure at the pressure anti-node is smaller than the discharge pressure. At the negative pressure cycle, pressure at the outlet port is lower than discharge pressure. Fluid tends to enter the chamber through the outlet port. The diffuser now acts as a nozzle and due to the higher flow resistance in nozzle direction than in diffuser direction, flow towards the chamber through nozzle is relatively small. This effect is known as dynamic effect. As net amount of fluid is discharged through outlet, there is a reduction in the fluid mass inside the tube which causes a reduction in static pressure. The mean resonator pressure is then lower than the pressure at the inlet. As a result fluid is injected into the resonator through the inlet port. The flow rectification process and the performance of diffuser-nozzle elements in creating a net flow instead of using check valves is the focus of the present study.

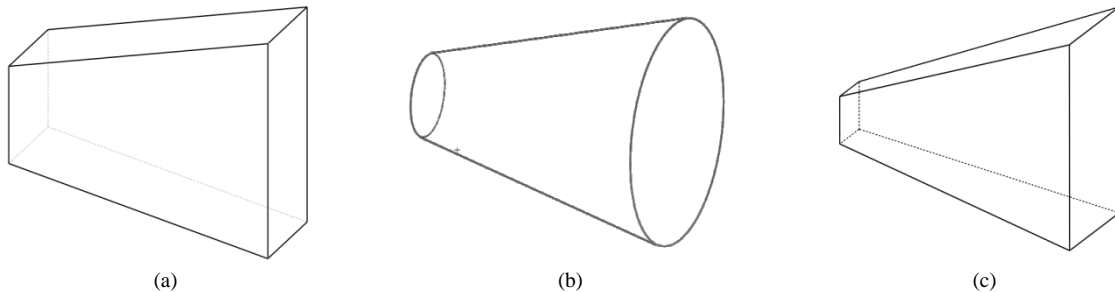


FIGURE 1. Diffuser-nozzle element (a) planer, (b) conical, (c) pyramidal

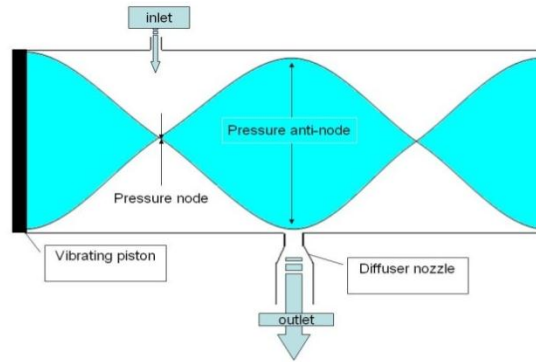


FIGURE 2. Working principle of ASWMP [10]

Advantage of valveless ASWMP over reciprocating valveless micropumps is that large pressure fluctuation amplitudes may be achieved for comparatively small actuator displacements within the resonator in the valveless ASWMP. Whereas, a low chamber pressure amplitude limits the performance of reciprocating valveless micropumps.

PREVIOUS WORKS

Effects of diffuser angle, diffuser slenderness, sizes of actuation chamber and inlet/outlet port, actuation frequency and amplitude of actuation pressure on the performance of conical diffuser-nozzle element were investigated by Wang et al. [9]. Diffuser showed the best rectification performance with diverging angle 10° (half angle 5°), and slenderness 7.5. They concluded that small pump chamber and inlet/outlet port deteriorate the pump performance. They also suggested that rectification performance is better for conical diffuser than planer one. The optimal efficiency was achieved when the actuation pressure and volumetric flow rate was 0.45π out of phase. Further increase of the frequency makes the phase shift towards $\pi/2$.

An extensive study was carried out by Nabavi and Mongeau [10] on determining the effects of various geometric and flow parameters like diffuser half angle, pressure amplitude and frequency on the performance of diffuser-nozzle element. A 2-D, time-varying, planer, incompressible (water) viscous flow model was used for analyzing purpose. A sinusoidal pressure input was applied with different peak pressure value of 200 Pa, 500 Pa, 5000 Pa, 10000, and 30000 Pa and different frequencies ranging from 10 kHz to 30 kHz. The 2-D model of inlet-outlet length 0.3 mm-0.3 mm, inlet height 0.06 mm, diffuser length 1.2 mm was used with diffuser half angles ranging from 15° to 60° . The performance of diffuser-nozzle element was found to be strongly dependent on half angle, pressure amplitude and frequency. The phase angle difference between pressure and velocity, life time, size of flow recirculation zones, energy losses were found to be dependent on frequency. The phase difference was found to be almost $\pi/2$ for high frequencies, whereas it is less than $\pi/2$ at low frequencies (500 Pa or less). Flow separation was observed for both high and low frequency cases. As for low frequencies, better pumping action was found for microdiffuser with larger divergence angles at high excitation frequencies. Increase of maximum pressure or decrease of excitation frequency resulted in increase of net flow rate and rectification capability. The maximum diffuser efficiency was found to be about 1.3 at 10 kPa, 10 kHz and at a divergence half angle 60° .

Several other profound and notable researches [11-15] were done on diffuser-nozzle element to make it suitable for flow rectification instead of dynamic valves (check valves, flap valves, etc.). In spite of several researches on diffuser-nozzle element, performance at very high frequencies, above 30 kHz and effects of different inlet-outlet length combination have not yet been studied. In the present study, an attempt is taken to fill up the gap.

PERFORMANCE PARAMETERS OF DIFFUSER-NOZZLE ELEMENT

The performance parameters of a diffuser-nozzle element which determines the suitability of the element in flow rectification purpose are:

- Net velocity
- Net volume flow rate

- Rectification capability
- Diffuser efficiency

Net velocity is the time-averaged net velocity measured at inlet of the diffuser section of the element during the positive and negative pressure cycle. Net flow rate is the multiplication of net velocity and the inlet cross section at the diffuser section of the element. In case of 2-D planer geometry, the inlet cross section is calculated for 1 mm span in z -direction. For axisymmetric model, it is simply πr^2 , where r is the height of the inlet from the axisymmetric line.

Rectification capability is the measure of the capability of a nozzle-diffuser element to direct the flow through the element in a definite direction. It is defined as the net volume of the fluid transported from the inlet to outlet divided by the swept volume. Rectification capability can be given by,

$$\xi = \frac{\varnothing^+ - \varnothing^-}{\varnothing^+ + \varnothing^-} \quad (1)$$

where, \varnothing^+ is the total volume flow in the diffuser direction, \varnothing^- is the total volume flow in the nozzle direction. To produce an effective flow rectification, must be positive. Generally, it is less than 100%, while 100% flow rectification is impractical through a nozzle-diffuser element. Higher the rectification capability higher amount of flow towards diffuser direction and lower backflow towards nozzle direction.

Diffuser efficiency is the most important performance parameter indicating the net flow rate through diffuser-nozzle element. The diffuser efficiency (η) can be defined as,

$$\eta = \frac{\varepsilon_n}{\varepsilon_d} \quad (2)$$

where, ε_n and ε_d are measure of the flow resistance or pressure loss coefficients of the nozzle and diffuser direction respectively.

ε_n and ε_d is known as pressure loss coefficient of nozzle and diffuser, respectively. They can be defined as,

$$\varepsilon_n = \frac{2\Delta P_n}{\rho u_n^2} \quad (3)$$

$$\varepsilon_d = \frac{2\Delta P_d}{\rho u_d^2} \quad (4)$$

where, ΔP_n and ΔP_d are time averaged total pressure drops in the narrowest zone downstream of the inlet and the broadest zone upstream of the outlet of the element during negative and positive pressure cycle respectively.

u_n and u_d are the time averaged velocities in the narrowest part of the geometry downstream of the inlet in nozzle and diffuser direction flow respectively. To produce a net flow in diffuser direction, ε_n must be greater than ε_d , thus, η should be greater than one. For a good pumping action, η must be as high as possible.

NUMERICAL PROCEDURE

ANSYS FLUENT is used for computation which discretizes the governing equations using finite volume method. Pressure based solver has been used. Fluid material is considered as water with density of $\rho = 998.2 \text{ kg/m}^3$ and viscosity of $\mu = 0.001003 \text{ kg/m-s}$. The flow is laminar and incompressible. No slip boundary conditions are applied at the walls. Pressure inlet boundary condition is used at the inlet boundary with sinusoidal pressure inlet $P_0 \sin(2\pi ft)$. Pressure outlet boundary condition is used at outlet with zero gauge pressure. Unsteady flow simulations are carried out for frequencies of 5, 10, 20, 30, and 50 kHz. Symmetry and axis condition is used for planer and axisymmetric model, respectively. The 2-D model is shown in Fig. 3.

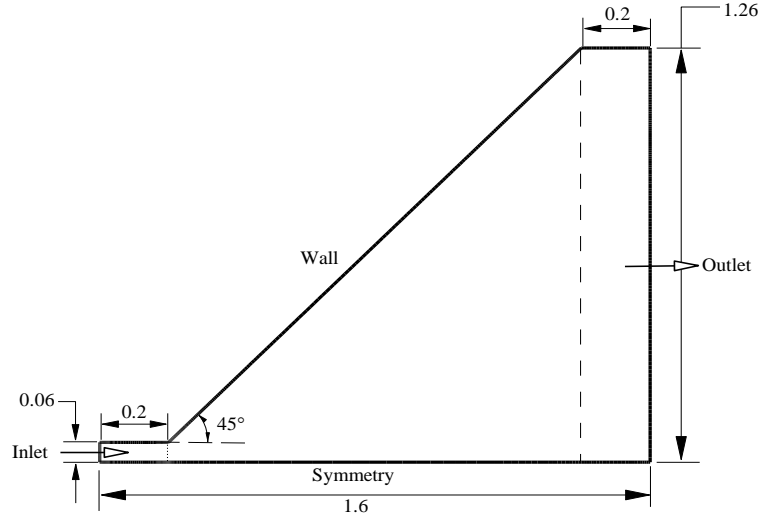


FIGURE 3. 2-D Geometry of the study (Dimensions are all in mm)

The governing equations are:

$$\frac{1}{\rho} \frac{\partial \rho}{\partial t} + \frac{\partial(u)}{\partial x} + \frac{\partial(v)}{\partial y} + \frac{\partial(w)}{\partial z} = 0 \quad (5)$$

$$\rho \left(\frac{\partial(u)}{\partial t} + u \frac{\partial(u)}{\partial x} + v \frac{\partial(u)}{\partial y} \right) + \frac{\partial(p)}{\partial x} = \mu \left(\frac{\partial^2 u}{\partial x^2} + \frac{\partial^2 u}{\partial y^2} \right) \quad (6)$$

$$\rho \left(\frac{\partial(v)}{\partial t} + u \frac{\partial(v)}{\partial x} + v \frac{\partial(v)}{\partial y} \right) + \frac{\partial(p)}{\partial y} = \mu \left(\frac{\partial^2 v}{\partial x^2} + \frac{\partial^2 v}{\partial y^2} \right) \quad (7)$$

Discretization of the domain is done by creating grids in GAMBIT software (GAMBIT 2.4.6). A 2-D hybrid meshing is done with structured mesh in inlet and outlet region and unstructured mesh in diffuser section. Total no. of cells varies from 30000 to 40000. In case of 3-D meshing, the 1mm span in z-direction is discretized to 35 discrete points which creates 35 cells along the span. In 2-D zone, 12226 cells have been used. This produces in total 427910 cells in the whole domain. A time step value of two hundredth of the oscillation period is used throughout the simulations.

Grid Independency Test

Inlet velocity is evaluated for different numbers of grids. It is found that for around 30000 to 50000 numbers of grids, the velocities are almost the same as shown in Fig. 4. There will be no much effects on result above 50000 grid numbers.

Validation

In the present study this validation is done by comparing inlet pressure and velocity for 10 kPa peak pressure, 10 kHz frequency, 0.2 mm inlet and outlet length with another established computational results of Nabavi and Mongeau (2009) [10]. In their results they used about 6000 to 8000 grids in which case we have used about 35000 grids. The results have been found in good agreement with the reference results as shown in Fig. 5.

From the Fig. 5, the velocity is found in almost 90° phase shift with pressure as expected for such a high frequency (greater than 5 kHz).

From the inlet y -velocity as shown in Fig. 6, it is found that the values of y -component of velocity are so small (in the range of 10^{-3} or more) that it has almost no effect on the resultant velocity. Thus only the x -component of velocity is used for the velocity measurement.

For the justification of 2-D assumption, 3-D simulation is performed. The inlet x -velocity is found the same both for 2-D and 3-D simulation as shown in Fig. 7. In Fig. 8, the z -velocity is found to be very small which validate the 2-D assumption. In the present study, as the flow field is symmetric with respect to the symmetry line, simulation is performed only over the symmetry line.

RESULTS AND DISCUSSION

Stream Function Contour

Stream function contours for different pressure phase angles (α) of pressure is shown in Fig. 9. Flow separation appears near the peak pressure value both in positive and negative cycle. This flow separation is the result of using large diffuser half angle (greater than 30°) and the dynamic effect of a nozzle-diffuser element. Due to this flow separation and associated recirculation zone, there is a significant energy loss in the peak pressure (zero velocity) region. During all other phases of pressure, continuous contours from inlet to outlet are found. From the stream function contours for positive and negative pressure cycle, it is found that, flow separation and the associated recirculation last for a longer period time ($\alpha = 260^\circ$ to 295°) in negative pressure cycle than in positive pressure cycle ($\alpha = 68^\circ$ to 90°). This flow behavior indicates that, there is stronger retardation to increase the velocity in negative direction than in positive direction. This influences to rectify flow more in positive diffuser direction than in nozzle direction.

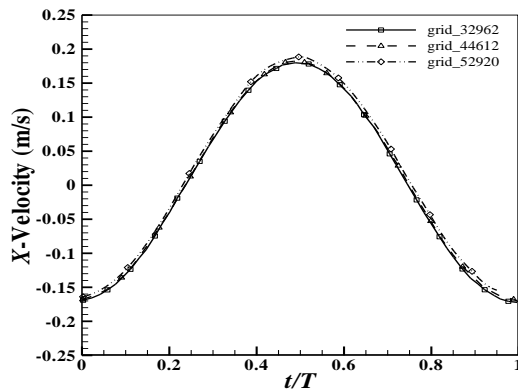


FIGURE 4. X-velocity over one period of oscillation for different grid numbers

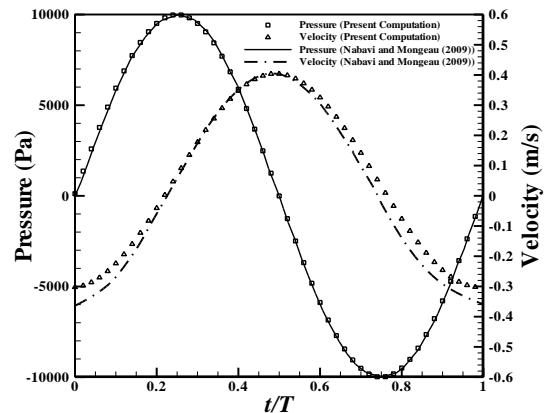


FIGURE 5. Comparison of inlet pressure and velocity with reference data

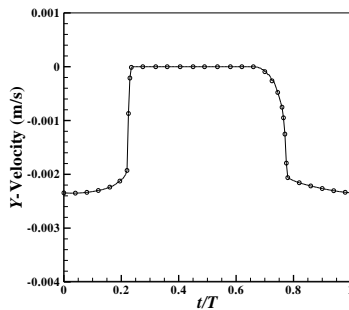


FIGURE 6. Inlet Y-velocity over one period of oscillation

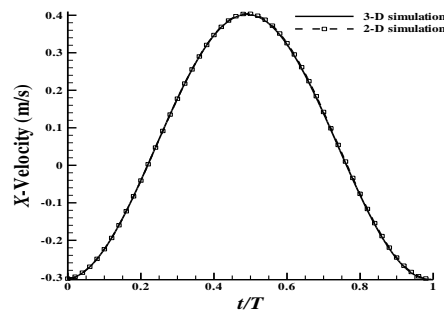


FIGURE 7. Comparison of inlet velocity for 3-D and 2-D simulation

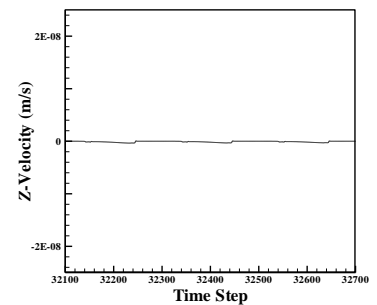


FIGURE 8. Inlet Z-velocity over time steps for 3-D simulation

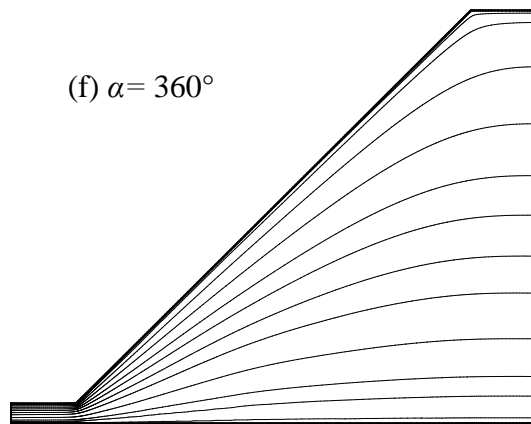
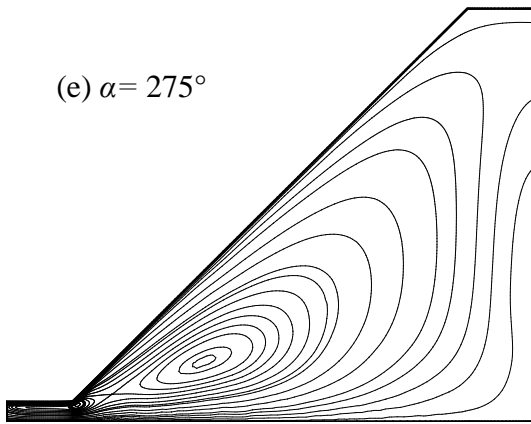
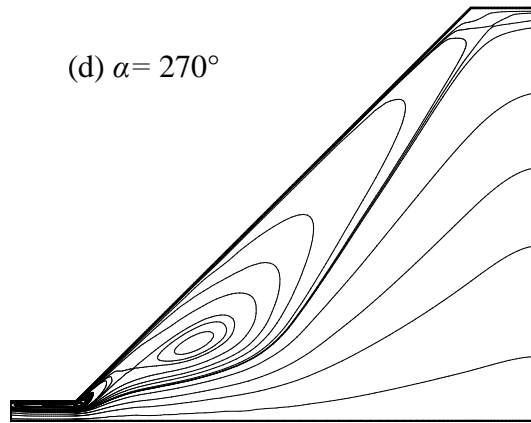
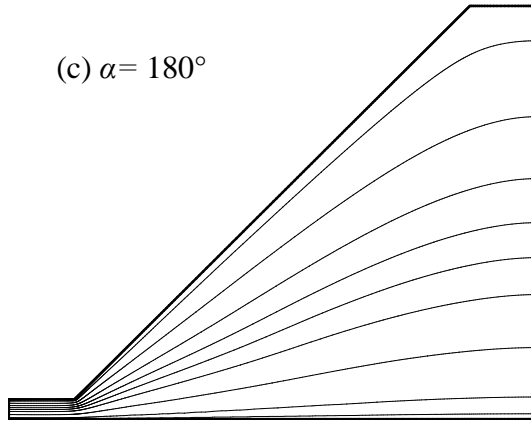
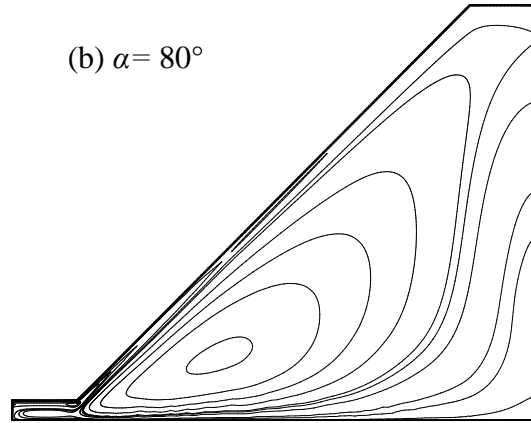
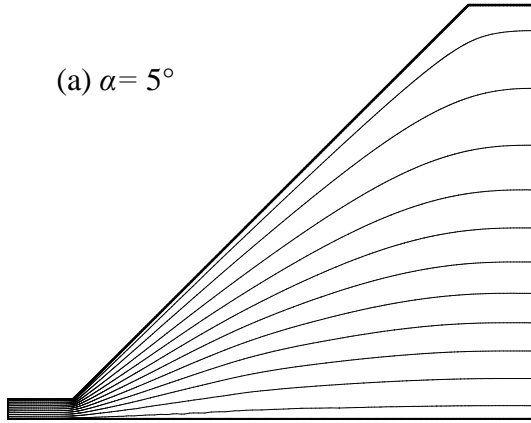
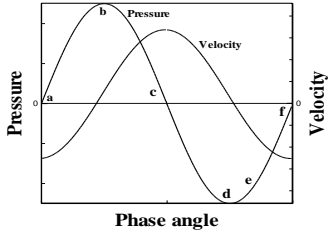


FIGURE 9. Stream function contour for various pressure phase angles, α

Performance Parameters

Net velocity, net volume flow rate, rectification capability and diffuser efficiency of diffuser-nozzle element for different pressure frequency have been evaluated and compared as shown in Table. 1 and Fig. 10 and Fig. 11. In determining the performances, a constant peak pressure value of 10 kPa. It is found that the diffuser-nozzle element becomes ineffective in rectifying flow towards diffuser direction at high frequencies. All the performance parameters including net velocity, net volume flow, rectification capability, and diffuser efficiency are observed to decrease with increasing frequency. Higher the frequency, higher is the backflow towards the nozzle direction lowering the flow rectification objective of diffuser-nozzle element in micropump. At a very high pressure frequency (greater than 50 kHz), the performance of diffuser-nozzle element become insensitive to frequency.

TABLE 1. Comparison of Performance Parameters for different pressure frequency

Driving Frequency (kHz)	5	10	20	30	50
Net velocity (mm/min)	8922	3156	1336	423	252
Net volume flow rate (mL/min)	1.07065	0.3786	0.1603	0.05076	0.03024
Rectification capability, $\xi = \frac{\phi^+ - \phi^-}{\phi^+ + \phi^-}$	32.01%	22.34%	19.33%	10.02%	9.2%
Diffuser efficiency, $\eta = \frac{\epsilon_n}{\epsilon_d}$	2.149	1.726	1.62	1.2731	1.279

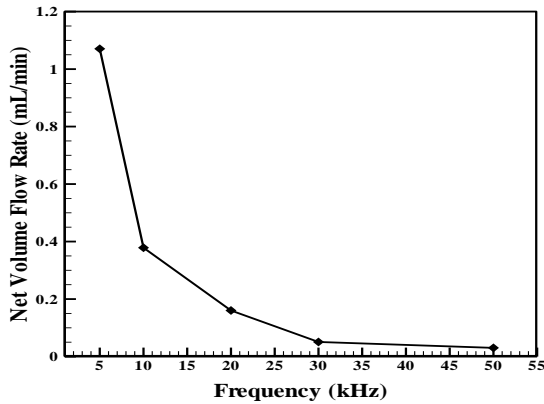


FIGURE 10. Net volume flow rate for various pressure frequency

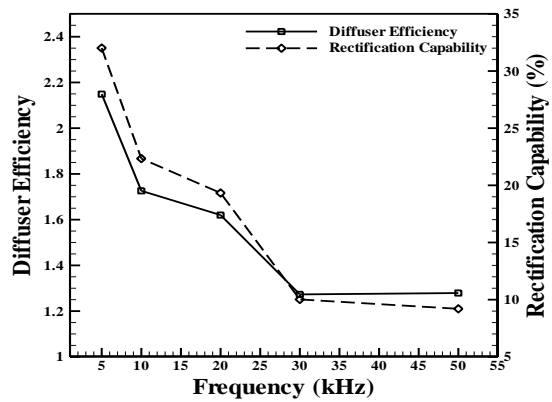


FIGURE 11. Diffuser efficiency and rectification capability for various pressure frequency

CONCLUSION

In the present study, a numerical simulation is performed to investigate the performance of diffuser-nozzle element in flow rectification. Four different parameters such as net velocity, net volume flow rate, rectification capability (ξ), and diffuser efficiency (η) are evaluated using different inlet-outlet length combination and pressure

frequencies to determine the suitability of the diffuser-nozzle element for the use in micropump instead of check valves. From the analysis, following conclusion can be drawn:

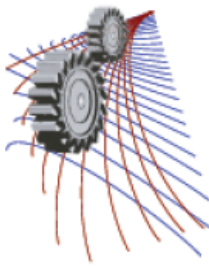
- i. In the flow field of the diffuser-nozzle element, flow separation appears near the peak pressure value both in positive and negative pressure cycle. This flow separation is the result of the dynamic effect of a nozzle-diffuser element. During all other phases of pressure, continuous contours from inlet to outlet are found. Flow separation and the associated recirculation last for a longer period of time in negative pressure cycle than in positive pressure cycle indicating stronger retardation to increase the velocity in negative direction than in positive direction. For this reason, a net flow is achieved in the positive diffuser direction from a diffuser-nozzle element.
- ii. All the performance parameters including net velocity, net volume flow, rectification capability, and diffuser efficiency are observed to decrease with increasing frequency. The diffuser-nozzle element becomes ineffective in rectifying flow towards diffuser direction at high frequencies. At a very high frequency, the performance of diffuser-nozzle element becomes insensitive.

ACKNOWLEDGEMENTS

The present work has been carried out with computational resource support from Higher Education Quality Enhancement Project (HEQEP), AIF (2nd Round)-Sub-Project CP 2099, UGC, MoE, Government of Bangladesh (Contract no. 28/2012).

REFERENCES

1. A. Nisar, N. Afzulpurkar, B. Mahaisavariya, A. Tuantranont, *Sensors and Actuator B: Chemical* **130**, 917-942 (2008).
2. P. Woias, *Sensors and Actuators B: Chemical* **105** (1), 28-38 (2005).
3. F. Amirouche, Y. Zhou, T. Johnson, *Microsystem Technologies* **15**(5), 647-666 (2009).
4. B. D. Iverson and, S. V. Garimella, *Microfluidics and Nanofluidics* **5**(2), 145-174 (2008).
5. D. J. Laser and J.G. Santiago, *Journal of Micromechanics and Microengineering* **14**, R35-R64 (2004).
6. Anthony K. Au, Hoyin Lai, Ben R. Utela and Albert Folch, *Micromachines* **2**(4), 179-220 (2011).
7. S. Yokota, *Mechanical Engineering Reviews* **1**(2), DSM0014-DSM0014 (2014).
8. M. Nabavi, *Microfluidics and Nanofluidics* **7**(5), 599-619 (2009).
9. Y. -C. Wang, S. -H. Lin and D. Jang, *Journal of Mechanics* **26**, 3 (2010).
10. M. Nabavi and L. Mongeau, *Microfluidics and Nanofluidics* **7**(5), 669-681 (2009).
11. Jin Lee, Seong Jae Jang and Hyung Jin Sung, *Journal of Turbulence* **13**, 30 (2012).
12. S. S. Wang, X. Y. Huang, C. Yang, *Microfluidics and Nanofluidics* **8**(4), 549-555 (2009).
13. Kai-Shing Yang, Tzu-Feng Chao, Ing Youn Chen, Chi-Chuan Wang and Jin-Cherng Shyu, *Molecules* **17**(2), 2178-2187 (2012).
14. T. Gerlach, *Sensors and Actuators A* **69**, 181-191 (1998).
15. C.-I. Sun and Z. H. Yang, *Journal of Micromechanics and Microengineering* **17**(10), 2031-2038 (2007).
16. Jang, L. S. and W. H. Kan, *Biomedical Microdevices* **9**(4), 619-626 (2007).
17. ANSYS, Inc., Canonsburg, PA, USA (www.ansys.com).



Numerical Analysis of Bio-inspired Corrugated Airfoil at Low Reynolds Number

Partha Protim Mondal¹, Md. Masudur Rahman¹, A.B.M. Toufique Hasan^{1, a)}

¹*Department of Mechanical Engineering, Bangladesh University of Engineering and Technology (BUET), Dhaka-1000, Bangladesh*

^{a)} Corresponding author: toufiquehasan@me.buet.ac.bd

Abstract. A numerical study was conducted to investigate the aerodynamic performance of a bio-inspired corrugated airfoil at the chord Reynolds number of $Re_c=80,000$ to explore the potential advantages of such airfoils at low Reynolds numbers. This study represents the transient nature of corrugated airfoils at low Reynolds number where flow is assumed to be laminar, unsteady, incompressible and two dimensional. The simulations include a sharp interface Cartesian grid based meshing employed with laminar viscous model. The flow field surrounding the corrugated airfoil has been analyzed using structured grid Finite Volume Method (FVM) based on Navier-Stokes equation. All parameters used in flow simulation are expressed in non-dimensional quantities for better understanding of flow behavior, regardless of dimensions or the fluid that is used. The simulated results revealed that the corrugated airfoil provides high lift with moderate drag and prevents large scale flow separation at higher angles of attack. This happens due to the negative shear drag produced by the recirculation zones which occurs in the valleys of the corrugated airfoils. The existence of small circulation bubbles sitting in the valleys prevents large scale flow separation thus increasing the aerodynamic performance of the corrugated airfoil.

INTRODUCTION

The development of micro-sized unmanned aerial vehicles (UAVs) or micro air vehicles (MAVs) has become an area of great interest for research in both civilian and military applications over the past few years. Designing such small scale aircraft is complicated by a number of challenges that includes low Reynolds numbers, low weight requirement, and more challenging aerodynamics. Flows at low Reynolds numbers are most likely to be affected by adverse pressure gradients that occurs at moderate angles of attack and have higher possibility of separation of flow. Separated flow can either reattach to the body forming a separation bubble or results in aerodynamic stall. Both instances significantly increase the drag, the latter is greatly detrimental to aerodynamic performance.

Conventional streamlined airfoils optimized for traditional macro-scale aircraft at high Reynolds number depends on early transition to turbulent flow seen at higher Reynolds number to reduce separation and overcome stall. These airfoils have quite poor aerodynamic performances at low Reynolds numbers which restrain their agility and versatility and has spurred the necessity for the development of high performance airfoil in low Reynolds number regimes for MAV applications. The wings of many insects including locusts, dragonfly and damselflies are

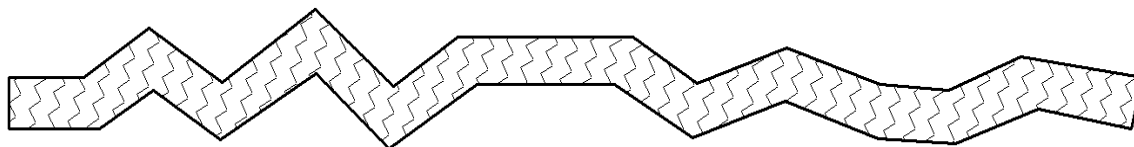


FIGURE 1. Test airfoil [1]

not streamlined or simple cambered surface rather the cross-section of their wings have well-defined corrugated configurations (Murphy and Hu [1]). Due to the corrugated configuration, these wings would have poor aerodynamic performances (i.e., low lift and extremely high drag) according to the conventional design principles and clearly are not suitable for aircraft. However several experimental and numerical studies carried out by Murphy and Hu [1], Kesel [2], Levy and Seifert [3], Vargas, Mittal and Dong [4], Barnes and Visbal [5] reveal the potential aerodynamic performances of corrugated airfoil compared with conventional smooth surfaced airfoil at low Reynolds number regime where dragonfly usually fly. For explaining the fundamental mechanism of unexpected improvement of aerodynamic performance of corrugated airfoil a several number of conjectures have been suggested. Most of the studies indicates that corrugated dragonfly airfoil or wings have better aerodynamic performance in low Reynolds number regimes which is the primary requirement for the applications of MAV. In the present study, a numerical simulation is performed to investigate the aerodynamic performance of a corrugated airfoil at the chord Reynolds number of $Re_c=80,000$. In this study the Navier-Stokes equations for the flow around the corrugated airfoil is solved by using the commercial code FLUENT. Aerodynamic Performance curves (i.e., C_l versus α and C_d versus α) instantaneous velocity field, streamlines and C_p contours of instantaneous flow field are analyzed in this study.

Nomenclature			
α	Angle of attack	U_∞	Free stream velocity
c	Chord length	ρ	Density
C_l	Coefficient of lift	μ	Absolute viscosity
C_d	Coefficient of drag	Re_c	Chord Reynolds number, $\rho U_\infty c / \mu$
C_p	Pressure Coefficient	t	Flow time

NUMERICAL MODELLING

Airfoil Geometry

The Fig. 1 depicts the test airfoil which is the bio-inspired corrugated airfoil corresponds to a typical cross-section of a dragonfly wing. The test airfoil is similar to the profile considered by Murphy and Hu [1]. The chord length of the considered airfoil is, $c = 101$ mm. All corners of the airfoil are considered sharp.

Computational Domain

The accuracy of numerical result largely depends on the type of mesh discretization employed, the analysis of the aerodynamic performance of corrugated airfoil is carried out by using structured grid Navier-Stokes method. The CFD package FLUENT 14.5 is used to solve the Navier-Stokes equation numerically. It enables the use of different discretization schemes and solution algorithms, together with various types of boundary conditions. A mesh generator, Gambit is used as pre-processor to draw the geometry and generate the required structured mesh. Grid points are denser near the airfoil wall region to capture flow characteristics accurately.

Numerical Method

The PISO-simple algorithm, PISO standing for Pressure Implicit with Splitting of Operators, is used for the pressure velocity coupling. It takes into account two corrections, which are the neighbor correction and the skewness correction. The skewness-neighbor coupling method was not used due to higher orthogonal quality of the mesh which also signifies lower degree of skewness. Second order discretization was used for both time derivative and momentum equations. The results are obtained at time step size of 0.00001sec and the solver iterated the equations until the scaled residuals were less than 10^{-6} or it stabilized at a constant value.

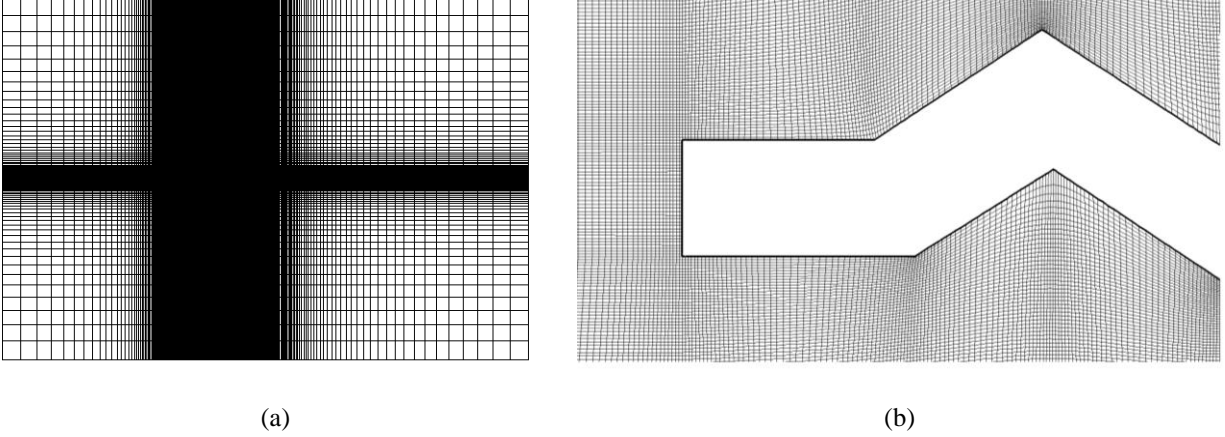


FIGURE 2. (a) Computational domain with a non-uniform Cartesian grid. The airfoil is placed inside the clustered region which contains high grid resolution; (b) Grid refinement near airfoil wall region.

TABLE 1. Summary of the computational domain

Domain size	$8c \times 15c$
Number of nodes	2 49 122
Number of cells	2 47 225
Minimum orthogonal quality	0.511

Boundary Conditions

The flow surrounding the corrugated airfoil is assumed laminar, incompressible and unsteady. The fluid is considered Newtonian with constant properties where $\mu=1.7894e-05$ kg/m-s and $\rho=1.225$ kg/m³. The two dimensional domain used for the current study consists of two boundary conditions. A constant inflow velocity (U_x) of 10 ms^{-1} at the inlet boundary which corresponds to $Re_c=80,000$. The outlet of the boundary was set to pressure outlet where the value of the gauge pressure was set to zero.

RESULTS AND DISCUSSIONS

Effects on Aerodynamic Forces

The time averaged lift and drag coefficients for different angles of attack in the present paper are in good agreement with the experimental results of Murphy and Hu [1]. Fig. 3. shows that changes in the numerically found aerodynamic force results in terms of lift and drag coefficients with the angles of attack (α), ranging from 0 to 20 degrees at $Re_c=80\ 000$. The experimentally measured results of Murphy and Hu [1] at $Re_c=80\ 000$ are also given in the figure for comparison. As shown in the Fig. 3(a) the lift coefficient of the corrugated airfoil is found that it increases almost linearly with increasing angles of attack. But at higher angles of attack when $AOA \approx 12$ deg., the slope of the lift coefficient curve decreases signifying the occurrence of stall in that region. Although the lift coefficient at $AOA = 20$ deg. shows the peak value, but it occurs in the expense of increasing drag thus reducing the overall lift to drag ratio. The drag coefficient of the corrugated airfoil increases slightly with increasing angles of attack up to $AOA=10^\circ$. After that the rate of increase of drag coefficient becomes significant due to stall in that region. Although the lift coefficient at $AOA = 20$ deg. shows the peak value, but it occurs in the expense of increasing drag thus reducing the overall lift to drag ratio. The drag coefficient of the corrugated airfoil increases slightly with increasing angles of attack up to $AOA=10^\circ$. After that the rate of increase of drag coefficient becomes significant due to stall in that region.

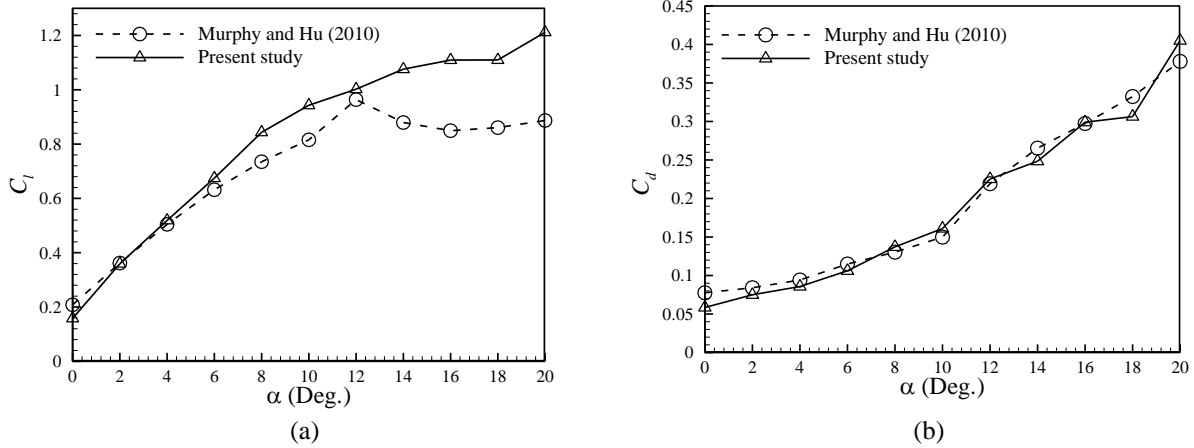


FIGURE 3. (a) C_l vs. α ; (b) C_d vs. α .

Lift and Drag Coefficients with Flow Time

The simulated results of the lift and drag coefficients shown in the figure below, reveal the unsteadiness of the flow. The oscillations are not periodic and they don't tend to be damped out. But after a certain time period the oscillations get confined in a range. Evaluations of the lift and drag coefficients are done by time averaging the values of C_l and C_d for 0 to 0.1 second for all the angles of attack.

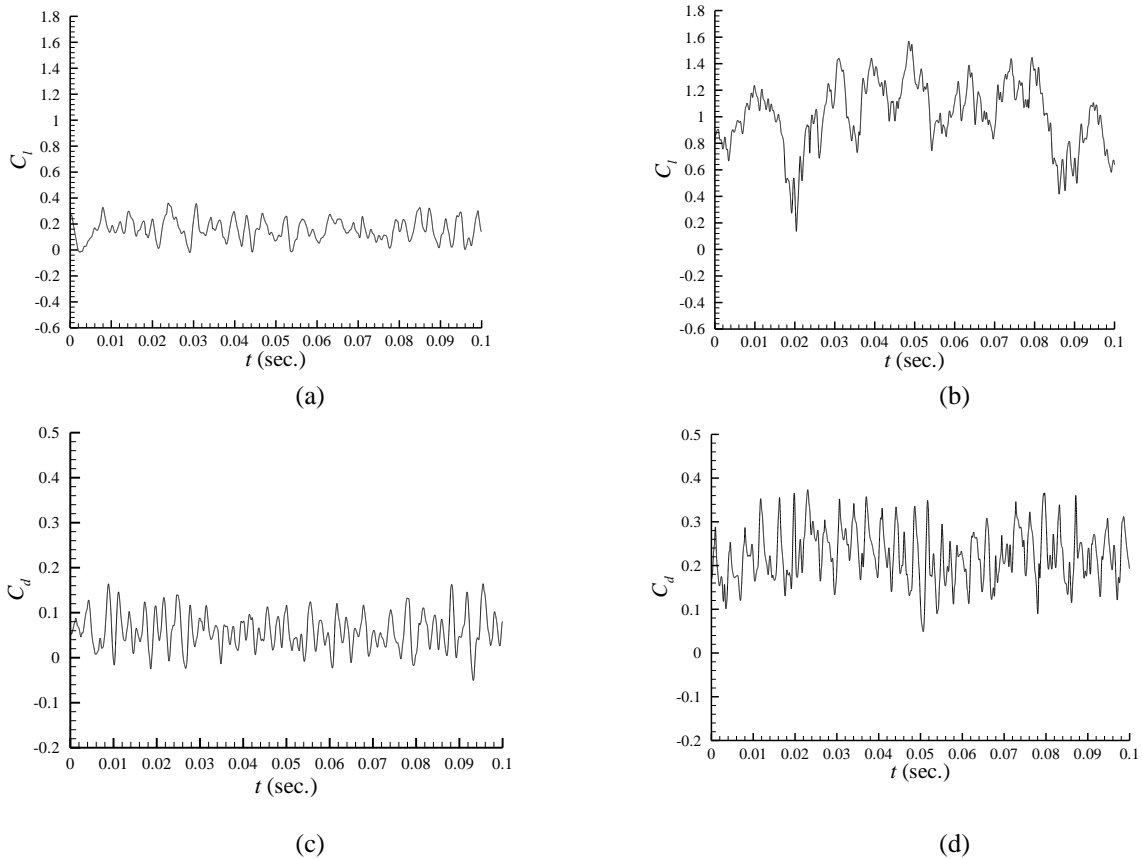


FIGURE 4. (a) C_l vs. t at $\alpha = 0^\circ$; (b) C_l vs. t at $\alpha = 12^\circ$; (c) C_d vs. t at $\alpha = 0^\circ$; (d) C_d vs. t at $\alpha = 12^\circ$.

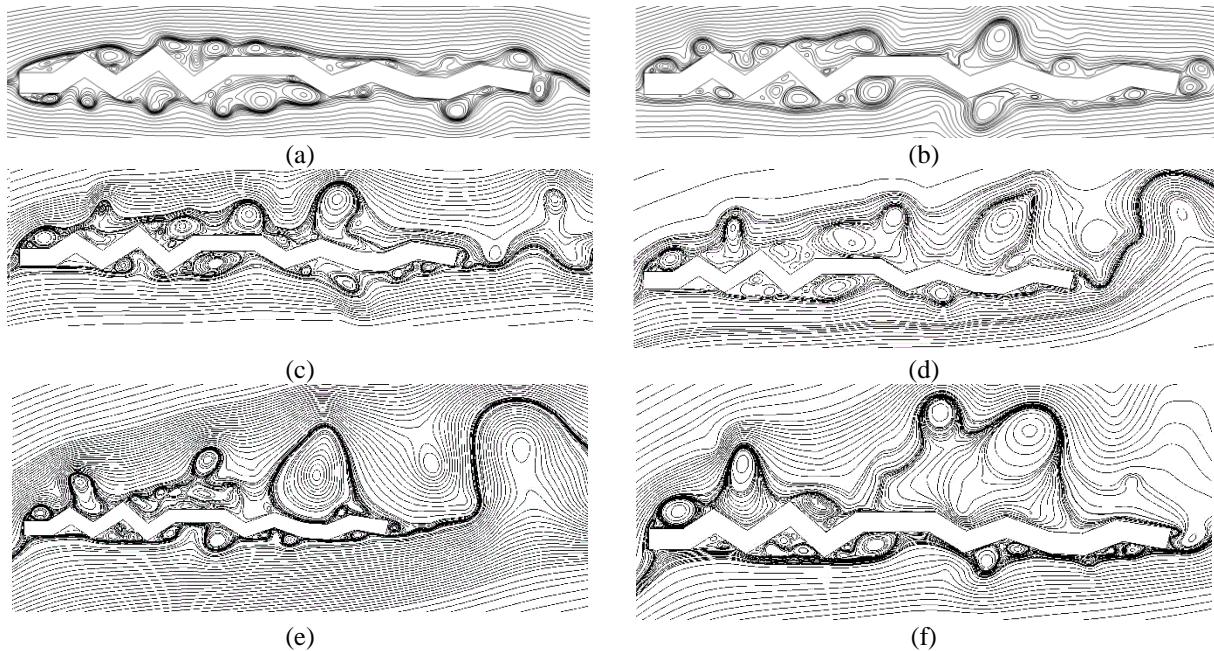


FIGURE 5. Streamlines of the instantaneous flow fields at flow time 0.1 second for (a) $\alpha=0^\circ$; (b) $\alpha=4^\circ$; (c) $\alpha=8^\circ$; (d) $\alpha=12^\circ$; (e) $\alpha=16^\circ$; (f) $\alpha=20^\circ$.

Flow Field around the Corrugated Airfoil

Figure 5 shows that the small circulation bubbles sitting in the valleys of the corrugated airfoil. The flow streams outside the corrugation valleys can be seen to flow smoothly around a virtual envelope created by the circulation bubbles. Due to the sharp leading edge, the incoming fluid streams are found to be separated from the starting of the leading edge to form a laminar shear layer at first, then the laminar boundary layer is transformed into turbulent layer when it approached the first corrugation peak. So the corrugation peaks act as turbulence creator. Also unsteady vortex structures can be observed to form in the corrugation valleys. The vortex structure imparts a pumping effect by dragging the separated boundary layer to the near wall regions. So the pumping effect provides enough kinetic energy to overcome the adverse pressure gradient and suppresses large scale flow separation.

Coefficient of Pressure Contours

Figure 6 reveals that the pressure coefficient contours appear to be the lowest just upstream of the first corrugation peak demonstrating the presence of circulations bubbles. The low pressure region produces a region of suction just upstream of the first corrugation peak. So no large scale flow separation can be found up to AOA=8. Now as the angle of attack increases, the adverse pressure gradient over the upper surface of the corrugated airfoil also increases. The adverse pressure gradient becomes severe around the stall angle which is around AOA \approx 12. As the angle of attack is increased further the circulation regions in the wake is found to increase significantly thus indicating increased aerodynamic drag force. Because of the severe adverse pressure gradient, the flow streams around the corrugated airfoil can no longer be found to follow the envelope profile which results in large scale flow separation on the upper surface of the corrugated airfoil occurs which can also be justified from the numerically found aerodynamic forces.

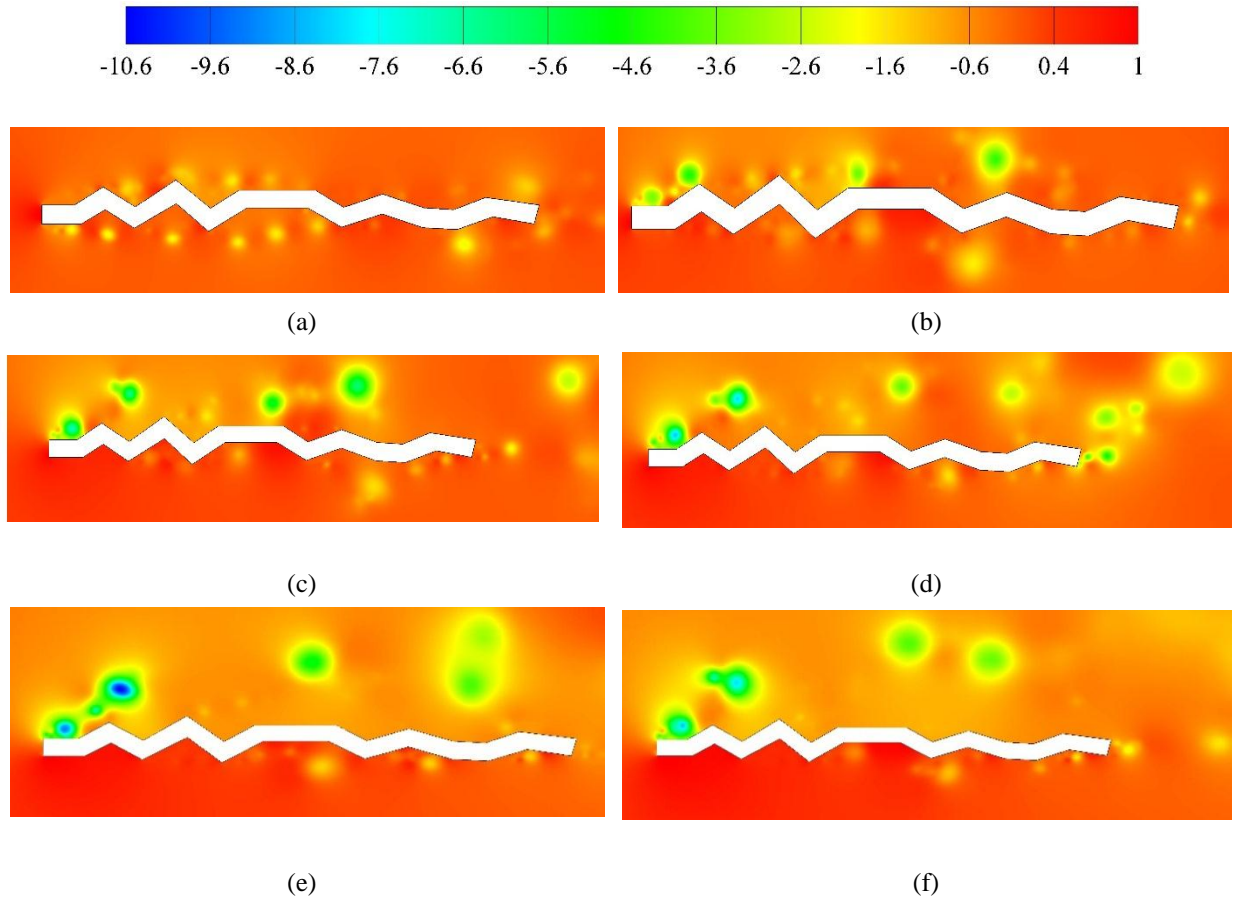


FIGURE 6. C_p contours of the instantaneous flow fields at flow time 0.1 second for (a) $\alpha=0^\circ$; (b) $\alpha=4^\circ$; (c) $\alpha=8^\circ$; (d) $\alpha=12^\circ$; (e) $\alpha=16^\circ$; (f) $\alpha=20^\circ$.

CONCLUSION

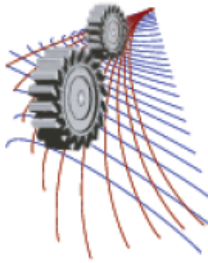
A numerical simulation was carried out to investigate the aerodynamic performances and flow features around a bio-inspired corrugated airfoil at chord Reynolds number of $Re_c=80,000$ in quest of the potential applications of non-traditional, bio-inspired corrugated airfoil for MAV applications. The above study reveals that corrugated airfoil could generate higher lift and delay airfoil stall to much higher angle of attack for low Reynolds number flight applications compared with smooth-surfaced airfoil.

ACKNOWLEDGEMENTS

The present work has been carried out with computational resource support from Higher Education Quality Enhancement Project, (HEQEP), AIF (2nd Round)-Sub-Project CP2099, UGC, MoE, Government of Bangladesh (contract no. 28/2012).

REFERENCES

1. J. T. Murphy and H. Hu, *Exp Fluids* **49**, 531-546 (2010).
2. A. B. Kesel, *The Journal of Experimental Biology* **203**, 31253135 (2000).
3. D. E. Levy and A. Seifert, *Journal of Theoretical Biology* **266**, 691-702 (2010).
4. A. Vargas, R. Mittal and H. Dong, *Bioinspiration and Biomimetics* **3**, 02600413 (2008).
5. C. J. Barnes and M. R. Visbal, *Physics of Fluids* **25**, 115106 (2013).



CFD Modeling of Pulsatile Hemodynamics in the Total Cavopulmonary Connection

S.M. TareqZobaer¹ and A.B.M. Toufique Hasan^{1, a)}

¹*Department of Mechanical Engineering, Bangladesh University of Engineering and Technology (BUET), Dhaka-1000, Bangladesh*

^{a)}Corresponding author: toufiquehasan@me.buet.ac.bd

Abstract. Total cavopulmonary connection is a blood flow pathway which is created surgically by an operation known as Fontan procedure, performed on children with single ventricle heart defects. Recent studies have shown that the hemodynamics in the connection can be strongly influenced by the presence of pulsatile flow. The aim of this paper is model the pulsatile flow patterns, and to calculate the vorticity field and power losses in an idealized 1.5D offset model of Total Cavopulmonary Connection. A three-dimensional polyhedral mesh was constructed for the numerical simulation. The rheological properties of blood were considered as Newtonian, and flow in the connection was assumed to be laminar. The results demonstrated complex flow patterns in the connection. The outcomes of the simulation showed reasonable agreement with the results available in the literature for a similar model.

INTRODUCTION

Congenital heart defects (CHD) is one the most common congenital disorder. A single ventricle heart defect, such as hypoplastic left heart syndrome and tricuspid atresia, refers to the case where the heart has only one adequate-sized functional ventricle. This leads to the situation where oxygenated and deoxygenated blood mix in the single ventricle, reducing the amount of oxygen transferred to the body. The Fontan procedure [1] is performed on children to repair this kind of heart defect. Among different variants of this procedure [2], one of the more commonly used type is the total cavopulmonary connection (TCPC), introduced by de Leval et al. [3]. This procedure entails anastomosis of the inferior vena cava and superior vena cava (IVC and SVC respectively) to the pulmonary arteries (PA). The resulting connection diverts the venous blood from the right atrium to the pulmonary artery without passing through the right ventricle. As a result, heart contains only oxygenated blood.

The shape of the connection gives rise to unusual and complex fluid dynamics. One of the major problems of this procedure is the added workload on the single ventricle. Other problems are related to energy losses and blood distribution from the body into the lungs. The geometry of the junction influences the energy loss [4].

For surgical planning, CFD tools are used widely to investigate the flow fields and energy losses in TCPCs with different geometric configurations and boundary conditions. Present study uses a polyhedral grid for the CFD simulation. A study [5] showed that polyhedral mesh requires lesser number of cells, lower memory usage and faster computing time than tetrahedral mesh. Moreover, this type of mesh demonstrates better convergence properties. Considering these advantages, a polyhedral mesh of the three-dimensional geometry was employed for the numerical simulation.

Some of the patients are vulnerable to several complications [6] after the operation, and unfavorable hemodynamics in the connection are believed to influence some of these [7,8]. Traditionally, flow is assumed to be non-pulsatile, but studies [9] have shown that flow pulsatility in the TCPC is not insignificant and better prediction of the flow can be obtained if pulsatility is taken into account. The objective of the present study is to numerically simulate the flow patterns in the surgically created total cavopulmonary connection, taking flow pulsatility into consideration, and also to calculate the power losses/vorticity field. For validation, the resulting flow patterns in

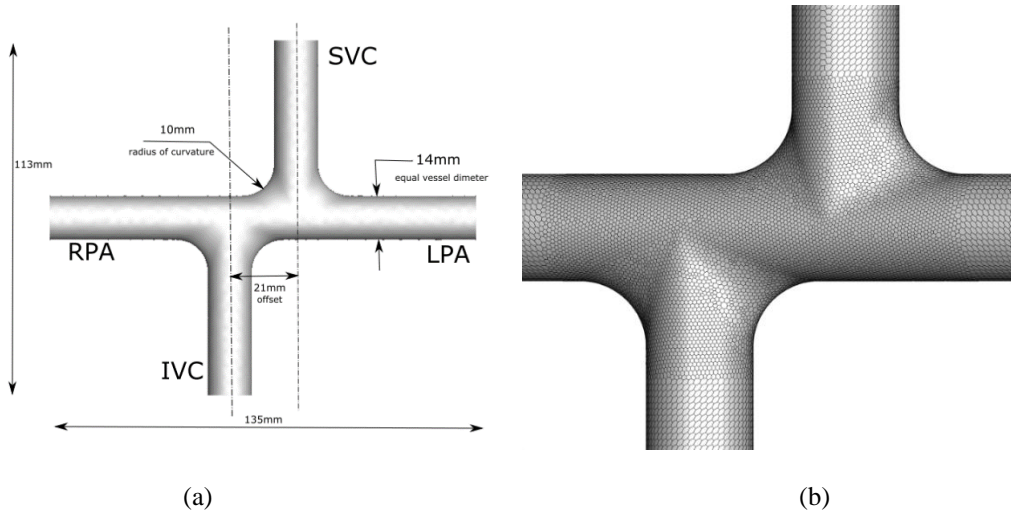


FIGURE 1.(a) Schematic of the idealized 1.5 diameter offset model, (b) 3D polyhedral mesh of the idealized TCPC

the connection produced by the simulation are compared with the results from Tang et al. [10], which were obtained for the same idealized geometry.

METHODOLOGY

Geometric Model

Present study uses a 1.5D offset idealized model. Offset was defined as the horizontal distance between the caval midpoints. The dimensions of the model are based on [10] with equal vessel diameter of 14mm and the radius of curvature of the flaring is taken to be 10mm. The idealized model with dimensions is shown in Fig. 1(a).

Mesh Generation

A polyhedral mesh is used to obtain the flow field in the connection. For this, an unstructured grid was generated at first using ANSYS Meshing (version 14.5). The mesh was then converted into polyhedral mesh using ANSYS FLUENT 14.5. The inlets and outlets were extended by an amount of 10mm and 50mm respectively. This was done to limit the effect of entrance and exit on the flow development. The three dimensional polyhedral mesh is shown in Fig. 1(b). There are 1,256,239 nodes in the numerical grid.

Numerical Setup

The numerical simulation for the 3D model was performed in ANSYS FLUENT 14.5. Blood was considered as an incompressible Newtonian fluid of constant viscosity ($\rho=1060 \text{ kg/m}^3$, $\mu=3.5 \times 10^{-3} \text{ Pa s}$). The wall was treated as rigid and impermeable, and no-slip boundary condition was applied at the wall. Laminar viscous model was used.

At the extensions of the inlet, uniform velocity inlet boundary condition was prescribed, obtained from flow rates of IVC and SVC. To maintain mass conservation, outflow boundary condition was specified at outlet extensions using LPA/RPA mass flow splits. The pulsatile boundary conditions were obtained from Tang et al. [10]. The boundary conditions are shown in Fig 2. Pressure based Navier-Stokes solver was employed for the simulation. The 'Pressure Implicit with Splitting of Operator' (PISO) scheme was used for pressure velocity coupling, along with second order upwind transient formulation.

A fixed time step size of 0.429 ms was used for the transient simulation. The values of Reynolds number at IVC were, minimum: 258, mean: 594 and maximum: 908. The Womersley number at the inlets was 10.43. The period of oscillation of the inflows corresponds to a heart rate of 70 beats per minute (BPM).

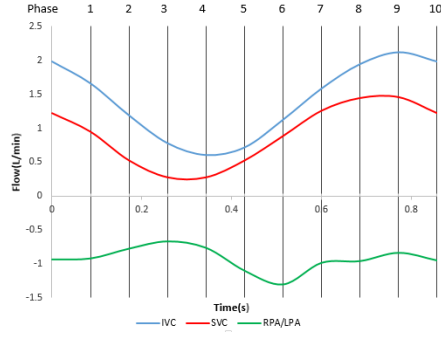


FIGURE 2.Boundary conditions for the numerical simulation

A steady solution was obtained initially prior to the transient computation. For each cardiac cycle, 2000 time steps were simulated. The result of the 5th cycle is being presented here.

RESULTS AND DISCUSSION

Velocity Field

The velocity field was extracted at the coronal plane of symmetry at 10 evenly spaced time points in the cardiac cycle. The numerically simulated flow fields at those phases are given in Fig. 3 along with the experimental results from Tang et al. [10]. The results reveal the complex velocity field in the TCPC

Between phases 5 to 9, acceleration of flow oriented the streams from IVC and SVC toward their closest PAs. The flow from IVC was increasingly directed toward RPA, because of the fact that RPA flow rate exceeded LPA flow rate in these phases. The SVC jet widened gradually as the cycle progressed.

In the deceleration period, from phase 10 to 3, IVC flow struck the superior aspect of the RPA and a portion of the IVC stream split toward the left, and recirculated around the central connection region into the LPA. This resulted in a complex flow field consisting of low velocity magnitude and unsteady circulations in the junction region, since streams from SVC and IVC merged here. Throughout the cycle, SVC flow remained directed toward the RPA.

The CFD simulated results demonstrate qualitatively similar flow fields from the phases 5 through 9 where the flow rate is higher. But discrepancies are more prevalent in the decelerating phases where competing streams from the two vena cavae mixes in the junction of TCPC. The highest velocity magnitude in the flow field in these phases is lower than the corresponding cases in study of Tang et al. The most visible differences between the simulated results and results from [10] are caused due to variation in the formation of the vortices in the central region of TCPC, when flow is undergoing deceleration. Moreover, because of data averaging in DPIV within finite size interrogation window, CFD results generally show more complex flow patterns [11]. This is one of the causes for the apparent differences between the CFD simulated and DPIV results. The CFD simulated results from Tang et al. exhibit more complex vortices than the present study.

Power loss calculation

Power loss (PL) is defined as the rate at which energy is dissipated in the fluid across the TCPC. The power loss in the domain is given by,

$$PL = \dot{E}_{in} - \dot{E}_{out}$$

Applying simplified control volume approach, this equation can be written as,

$$PL = \sum_{inlet} \left(\left(p + \frac{1}{2} \rho \left(\frac{Q}{A} \right)^2 \right) Q \right) - \sum_{outlet} \left(\left(p + \frac{1}{2} \rho \left(\frac{Q}{A} \right)^2 \right) Q \right) \quad (1)$$

Where, Q= Flow rate, p= static pressure, ρ = fluid density, A= cross sectional area, Inlet= IVC and SVC, Outlet= LPA and RPA. Equation 1 quantifies power loss at each instant of the cycle.

The instantaneous power loss at each phase over five cycle is shown in Fig. 4. The average power for the idealized model is 4.69086 mW.

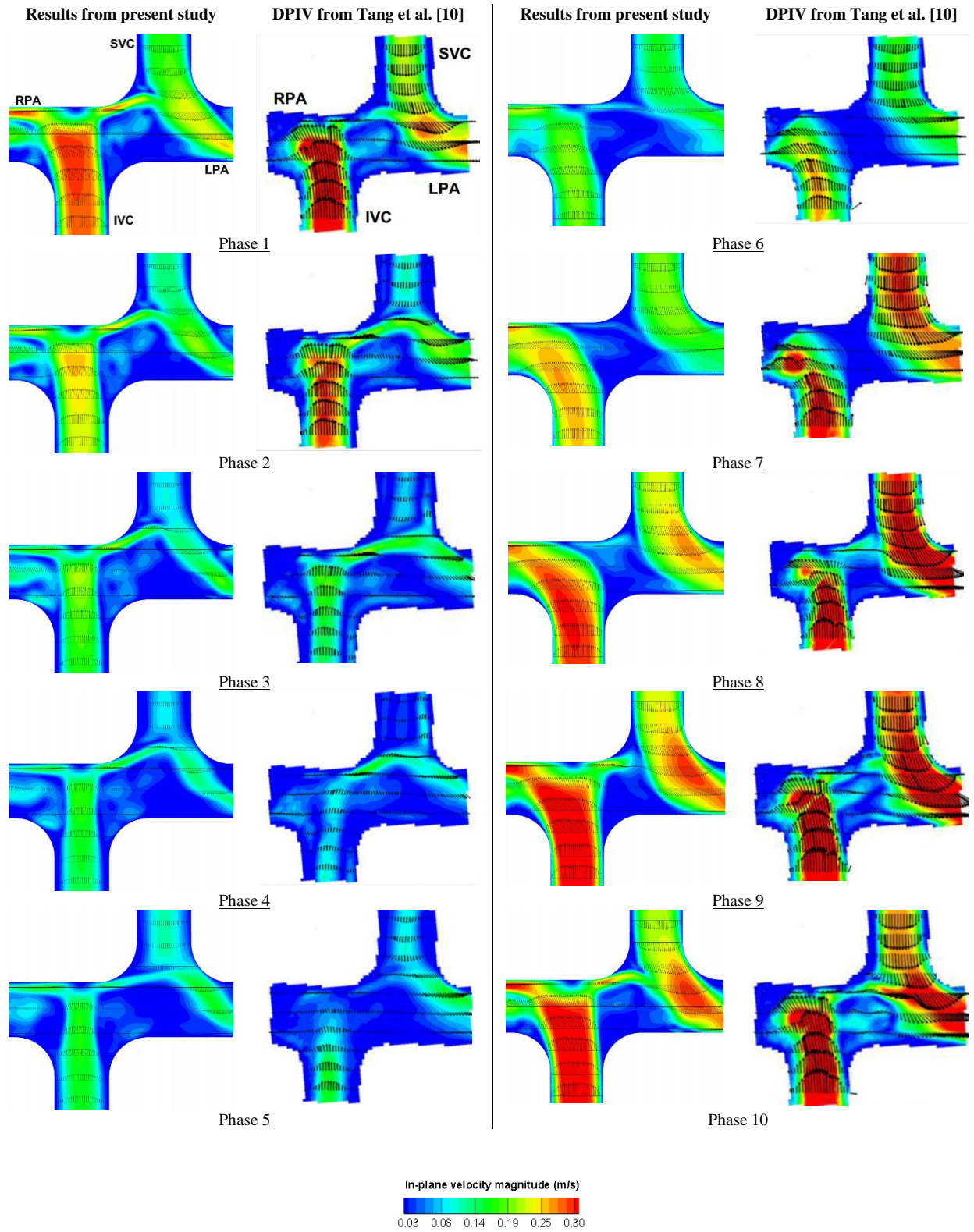


FIGURE 3. Comparison between CFD simulated results of the present paper and the results from Tang et al. [10]

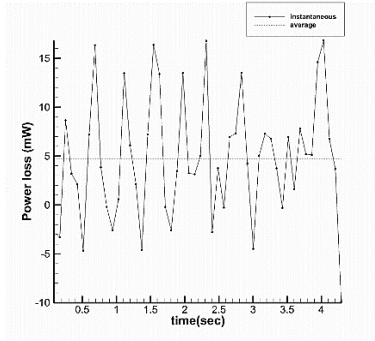


FIGURE 4. Instantaneous and average power loss in TCPC over 5 cycles

Vorticity Field

The out of plane vorticity plots in the connection for ten phases are shown in Fig. 5. Flow instabilities in this laminar, pulsatile flow is best visualized by the vorticity plot. The vortices were generated at the interface of the fluid and vessel wall as a consequence of viscous friction that develops from the adherence at the wall. Over the entire cycle, fluctuating shear layers collided at the junction region of the TCPC. Generally, throughout the cycle, the flow entering from IVC impacted on the upper junction wall and produced wall vorticity of opposite sign. Then, the shear layer deflected downward to impinge on the lower wall. There it interacted with the vorticity of opposite sign coming from the SVC. This caused their regular vortex shedding events where shear layer vorticity was pushed to LPA. With increase in distance from the wall, the magnitude and strength of vorticity deteriorated because of viscosity. In the decelerating period, these events were subdued to some extent since flow rates were lower.

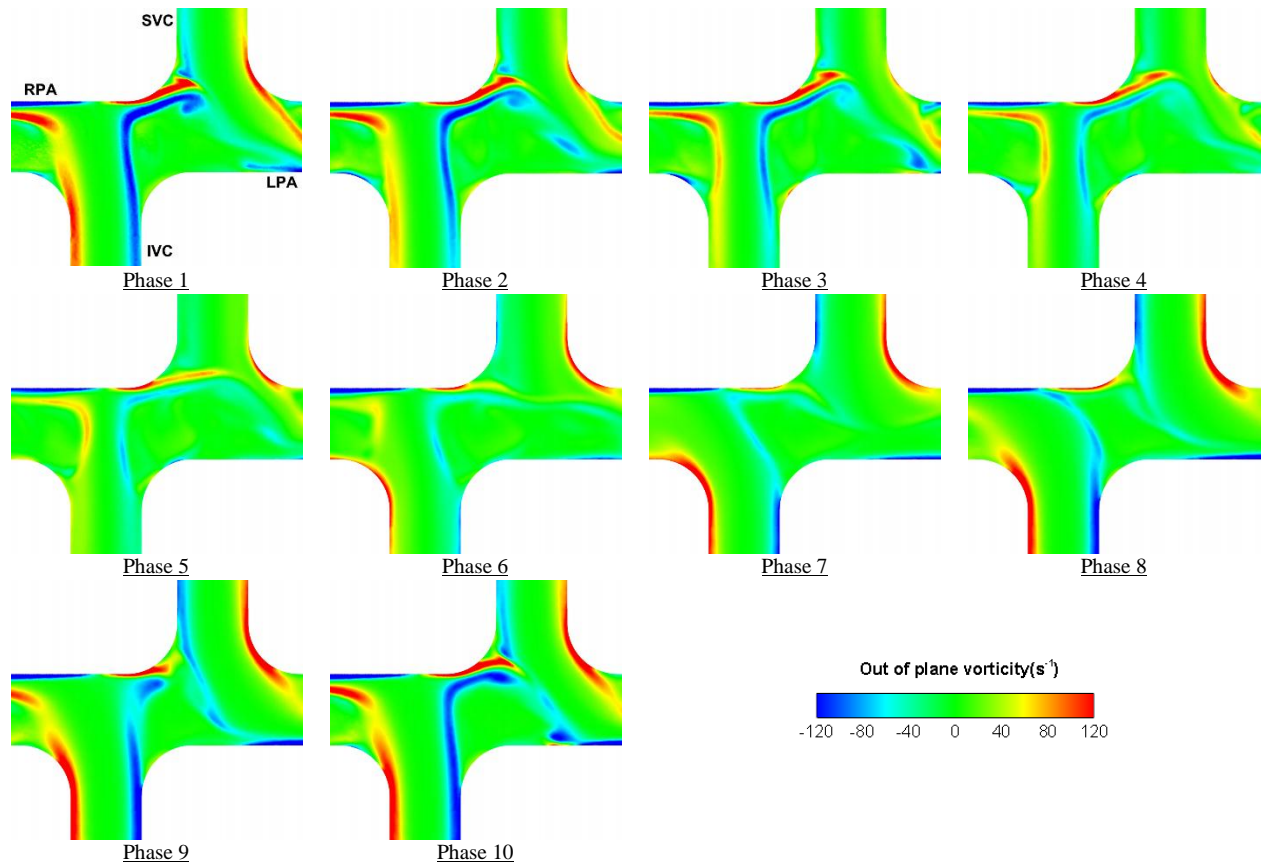


FIGURE 5. CFD simulated out of plane vorticity field in the plane of symmetry

CONCLUSIONS

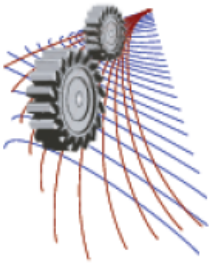
This study investigated the pulsatile hemodynamics in an idealized 1.5D offset three-dimensional TCPC model. The results of the simulation exhibit complex dynamics of flow in the TCPC. Although some inconsistencies are present, the velocity field in general demonstrated realistic similarity with the results available in the literature. The simulated out of plane vorticity plot demonstrated the complex nature of interaction of the shear layers emanating from the vessel walls in the connection and subsequent evolution of aperiodic vortex shedding in outlet. The calculations indicate that power loss for flow through the idealized model at given conditions should be expected to be small.

ACKNOWLEDGMENT

The present work has been carried out with computational resource support from Higher Education Quality Enhancement Project (HEQEP), AIF (2nd Round)-Sub-Project CP 2099, UGC, MoE, Government of Bangladesh (Contract no. 28/2012).

REFERENCES

1. F. Fontan, E. Baudet, *Thorax* **26**, 240-248 (1971).
2. M. R. de Leval, *Nature Clinical Practice Cardiovascular Medicine* **2**, 202-208 (2005).
3. M. R. de Leval, P. Kilner, M. Gewillig, C. Bull, *Journal of Thoracic and Cardiovascular Surgery* **96**, 682–695 (1988).
4. M. R. de Leval, G. Dubini, F. Migliaavacca, H. Jalali, G. Camporini, A. Redington and R. Pietrabissa, *Journal of Thoracic and Cardiovascular Surgery* **111**, 502-513 (1996).
5. M. Peric, S. Ferguson, *New corporate image for CD-adapco* (2005).
6. K. A. Jayakumar, L. J. Addonizio, M. R. Kichuk-Chrisant, M. E. Galantowicz, J. M. Lamour, J. M. Quaegebeur, D. T. Hsu, *Journal of the American College of Cardiology* **44**, 2065–2072 (2004).
7. N. A. Pike, L. A. Vricella, J. A. Feinstein, M. D. Black, B. A. Reitz, *The Annals of Thoracic Surgery* **78**, 697–699 (2004).
8. D. Srivastava, T. Preminger, J. E. Lock, V. Mandell, J. F. Keane, J. E. Mayer Jr., H. Kozakewich, P.J. Spevak, *Circulation* **92**, 1217–1222 (1995).
9. C. G. DeGroff, R. Shandas, *International Medical Journal of Experimental and Clinical Research* **8**, MT41–MT45 (2002).
10. E. Tang, C. M. Haggerty, R. H. Khiabani, D. de Zélicourt, J. Kanter, F. Sotiropoulos, M. A. Fogel, A. P. Yoganathan, *Journal of Biomechanics* **46**, 373–382 (2013).
11. K. Pekkan, D. de Zelicourt, L. Ge, F. Sotiropoulos, D. Frakes, M. A. Fogel, A. P. ,Yoganathan, *Annals of Biomedical Engineering* **33**,284–300 (2005).



Natural Convection of Coupled Thermal boundary layers Adjacent to a Wavy Conducting Partition Placed in a Square Differential Heated Enclosure

Suvash C. Saha^{1,a),b)}, Md. Mamun Molla², Sumon Saha³ and Y. T. Gu¹

¹*School of Chemistry, Physics & Mechanical Engineering, Queensland University of Technology
GPO Box 2434, Brisbane, QLD 4001, Australia*

²*Department of Mathematics & Physics, North South University, Dhaka, Bangladesh*

³*Department of Mechanical Engineering, Bangladesh University of Engineering and Technology, Bangladesh*

^{a)}Corresponding author: suvash.saha@qut.edu.au

^{b)}URL: <http://www.suvash.com.au>

Abstract. A numerical study is carried out for the coupled thermal boundary layers adjacent to a wavy partition, which is placed vertically in the middle of a square enclosure. The working fluid for this study is chosen as water which is initially at quiescent. To trigger the natural convection process a sudden temperature difference between two fluid zones of the enclosure has been imposed. The detailed development of the couple thermal boundary layers is observed. Time dependent features of the coupled thermal boundary layers as well as the overall natural convection flow in the partitioned enclosure have been discussed and compared with the non-partitioned enclosure. The effect of waviness of the partition on heat transfer and fluid flow is investigated. The numerically obtained results for the case of straight vertical partitioned are compared with existing results available in the literature. Moreover, heat transfer as a form of local and overall average Nusselt number through the coupled thermal boundary layers and the boundary walls is examined. It is found that in presence of wavy vertical partition, the heat transfer in the enclosure is significantly reduced.

INTRODUCTION

When an enclosure filled with fluid is suddenly placed in either ambient fluid or another enclosure with different temperature, the fluids start to move adjacent to both sides of the vertical wall of the enclosure due to buoyancy effect and heat transfer through the wall. This scenario can be observed in nature and many engineering applications. One of the very common applications is when we put a can of coke in the fridge. More example is an oil tank of a wrecked ship submerged in the sea [1]. In most previous studies the development of thermal boundary layer adjacent to the outside of the wall is often ignored. However, in real situation both sides of the wall participate to transfer heat. Thermal boundary layer develop both sides of the wall, which may significantly impact on overall heat transfer through the vertical wall. We found that the heat transfer through the wall differs significantly if the wall is wavy [2 – 5]. This motivates to study couple thermal boundary layer development on both sides of a wavy vertical partition places in the middle of an enclosure and subsequent heat transfer through it. This is a fundamental study, which has significance in our daily practical life with many engineering applications.

In the literature it is found that natural convection in a differentially heated cavity has received considerable attention. In the previous studies it is demonstrated that conduction dominates the heat transfer in an enclosure for low Rayleigh numbers (e.g. $< 10^3$). However, for higher Rayleigh number convective heat transfer becomes dominant. Distinct thermal boundary layers along both hot and cold sidewalls are formed and the fluid of the central part of the enclosure becomes stratified for sufficiently higher Rayleigh number (see e.g. [6 – 9]). If the Rayleigh number increases further the flow and heat transfer enter into the transitional stage and travelling waves in the thermal boundary layer are observed adjacent to both heated and cooled walls (e.g. [10 – 15]). However, the flow becomes turbulent for larger Rayleigh number (e.g. [16 – 18]).

In addition to the classic studies mentioned above, the study of natural convection in a differentially heated

cavity with an interior conducting vertical partition has also been given considerable attention due to its relevance to industrial applications (e.g. [19,22,23]). The heat transfer across the partition ultimately controls the heat transfer between the two differentially heated sidewalls (or inclined walls for the triangular cavities). Therefore, it is essential to understand the heat transfer mechanism in presence of vertical partition to control the overall heat transfer of the enclosure.

TABLE 1. Previous partitioned cavity studies

Author	Pr	Ra	N*	A*
Anderson & Bejan [28]	6	$10^9 < Ra < 10^{10}$	0-2	0.33
Nishimura et al. [29]	6	$10^8 < Ra < 10^{10}$	0-4	4
Turkoglu & Yucel [25]	0.71	$10^5 < Ra < 10^7$	0-4	0.5-1.5
Cuckovic-Dzodzo et al. [26]	2700-7000	$10^4 < Ra < 10^6$	0-1	1
Xu et al. [20]	7	9.2^9	0-1	1
Williamson et al. [21]	7.5	$0.6 - 1.6 \times 10^{10}$	0-1	1
Saha et al. [22,23]	0.7	10^8	0-1	0.2-1.0

Previous studies have also revealed that conducting partition depresses natural convection in the enclosure in comparison with that in a non-partitioned cavity (e.g. [24,26,27]). Furthermore, additional partitions are placed into the enclosure to further depress or suppress natural convection since the partition depresses heat transfer through the enclosure [28,29]. Nishimura et al. [29] established both experimentally and numerically that the Nusselt number on the sidewall is inversely proportional to $(1 + N)$, where N is the number of partitions.

Based on the above review it has been found that there is no literature exists which has dealt with the vertical wavy partition. Since the heat transfer through the wall differs significantly for wavy walls compare to straight wall, we have considered vertical wavy partition in this study. We have shown the effect of waviness in terms of heat transfer and air flow into an enclosure. The transient flow development and heat transfer are also discussed.

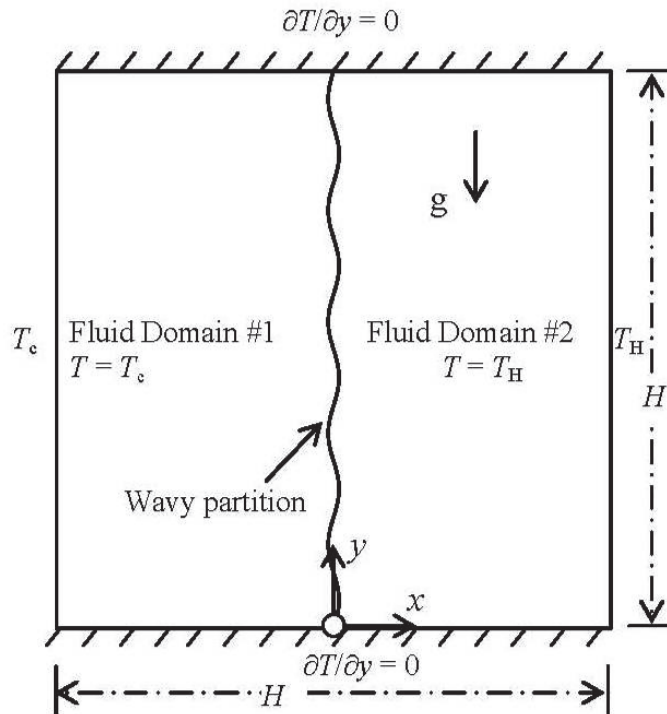


FIGURE 1. The schematic of the geometry and the boundary conditions.

Problem formulation

Under consideration is a square enclosure of length H , containing a Newtonian fluid, air, which is initially at quiescent. A wavy partition is placed vertically along the mid position of the enclosure. Two interiors of both sides of the partition together with the side walls receive different temperature with the left side receiving cold and the right side receiving hot temperature after time, $\tau = 0$. The bottom and the top surfaces are considered as adiabatic and rigid non-slip. The origin of the coordinate is the intersection point of the partition and the bottom surface.

The development of natural convection inside a square enclosure is governed by the following two-dimensional Navier-Stokes and energy equations with the Boussinesq approximation:

$$\frac{\partial u}{\partial x} + \frac{\partial v}{\partial y}, \quad (1)$$

$$\frac{\partial u}{\partial \tau} + u \frac{\partial u}{\partial x} + v \frac{\partial u}{\partial y} = -\frac{\partial p}{\partial x} + Pr \left(\frac{\partial^2 u}{\partial x^2} + \frac{\partial^2 u}{\partial y^2} \right), \quad (2)$$

$$\frac{\partial v}{\partial \tau} + u \frac{\partial v}{\partial x} + v \frac{\partial v}{\partial y} = -\frac{\partial p}{\partial y} + Pr \left(\frac{\partial^2 v}{\partial x^2} + \frac{\partial^2 v}{\partial y^2} \right) + RaPr\theta, \quad (3)$$

$$\frac{\partial \theta}{\partial \tau} + u \frac{\partial \theta}{\partial x} + v \frac{\partial \theta}{\partial y} = \left(\frac{\partial^2 \theta}{\partial x^2} + \frac{\partial^2 \theta}{\partial y^2} \right). \quad (4)$$

where u and v are the non-dimensional velocity components along x - and y - directions, τ is the time, p is the pressure and θ is the non-dimensional temperature.

The following set of transformation has been employed to get above normalised equations(1 - 4).

$$x = \frac{X}{H}, y = \frac{Y}{H}, u = \frac{UH}{\kappa}, v = \frac{VH}{\kappa}, \tau = \frac{t\kappa}{H^2}, p = \frac{PH^2}{\rho\kappa^2}, \theta = \frac{T - T_c}{T_h - T_c}. \quad (5)$$

where U and V are dimensional velocity components along X - and Y - directions, t is the time, P is the pressure, ν, ρ, β and κ are kinematic viscosity, density of the fluid, coefficient of thermal expansion and thermal diffusivity respectively, g is the acceleration due to gravity and T is the dimensional temperature. Two governing parameters, namely, the Rayleigh number and the Prandtl number are defined respectively as

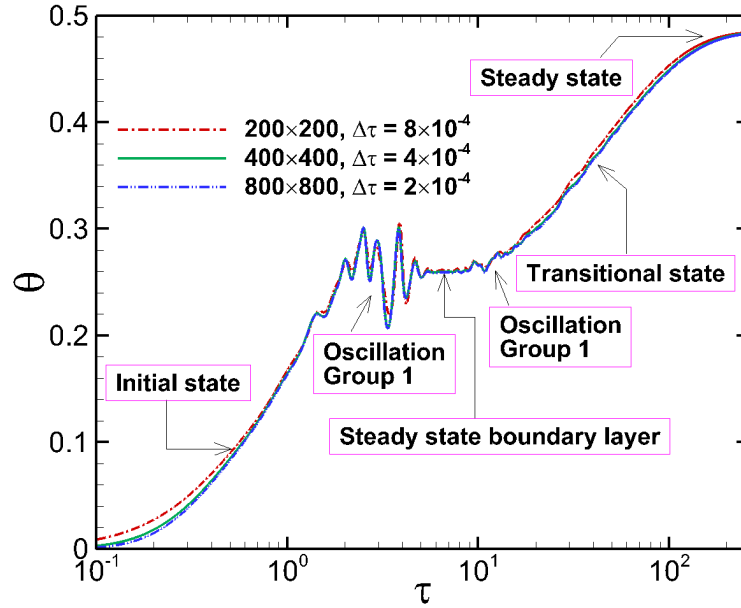


FIGURE 2. Time series of non-dimensional temperature for three different grid sizes and time steps.

$$Ra = \frac{g\beta\Delta TH^3}{\kappa\nu}, \quad \text{and} \quad Pr = \frac{\nu}{\kappa} \quad (6)$$

Note that in this study the Prandtl number and the Rayleigh number are fixed as $Pr = 6.63$ and $Ra = 9.2 \times 10^8$ respectively and laminar flow is assumed. As shown in figure 1, the bottom surface of the enclosure is adiabatic; the two side walls are isothermal and fixed at T_c and T_h respectively; the wavy partition of a zero thickness is vertically placed in the middle of the enclosure and is diathermal for which only horizontal heat transfer is considered (refer to [27,28]) and all other surfaces and the partition are rigid and no-slip. The working fluid is initially at quiescent. At $\tau = 0$ the non-dimensional temperature of the fluid on the left side of the partition is $\theta = 0$ and that on the right side of the partition is $\theta = 1$.

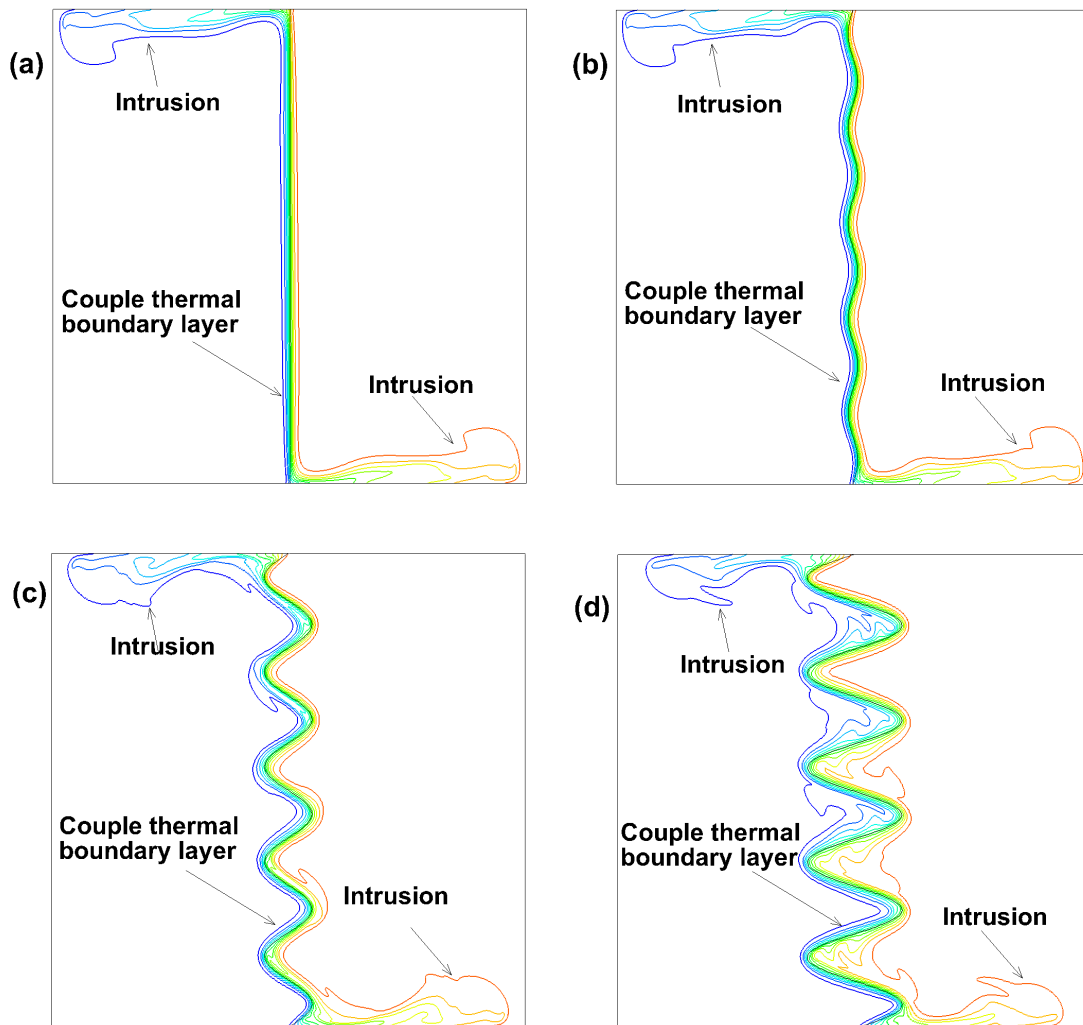


FIGURE 3. Isotherms for different amplitudes of wavy partitions during early stage.

Numerical scheme and grid and time step dependence tests

Equations (1) - (4) are solved along with the initial and boundary conditions using the SIMPLE scheme with the help of CFD software Fluent 15.0. The finite volume method has been chosen to discretize the governing equations, with the QUICK scheme approximating the advection term. The diffusion terms are discretized using central-differencing with second order accuracy. A second order implicit time-marching scheme has also been used for the unsteady term.

Three non-uniform grid sizes, 200×200 , 400×400 and 800×800 with coarser grids in the core and finer grids concentrated in the proximity of all walls and partition boundaries were constructed for grid independence tests. Figure 2 plots time series of the non-dimensional temperatures calculated using the three grid systems at the point $(-0.008, 0.9)$, which is very close to the partition. Clearly, three solutions are almost overlapped. This means that either grid system is able to resolve the transient natural convection in the partitioned cavity and characterize the details of the boundary layers adjacent to the partition and other walls for the present Rayleigh number. To save computing time,

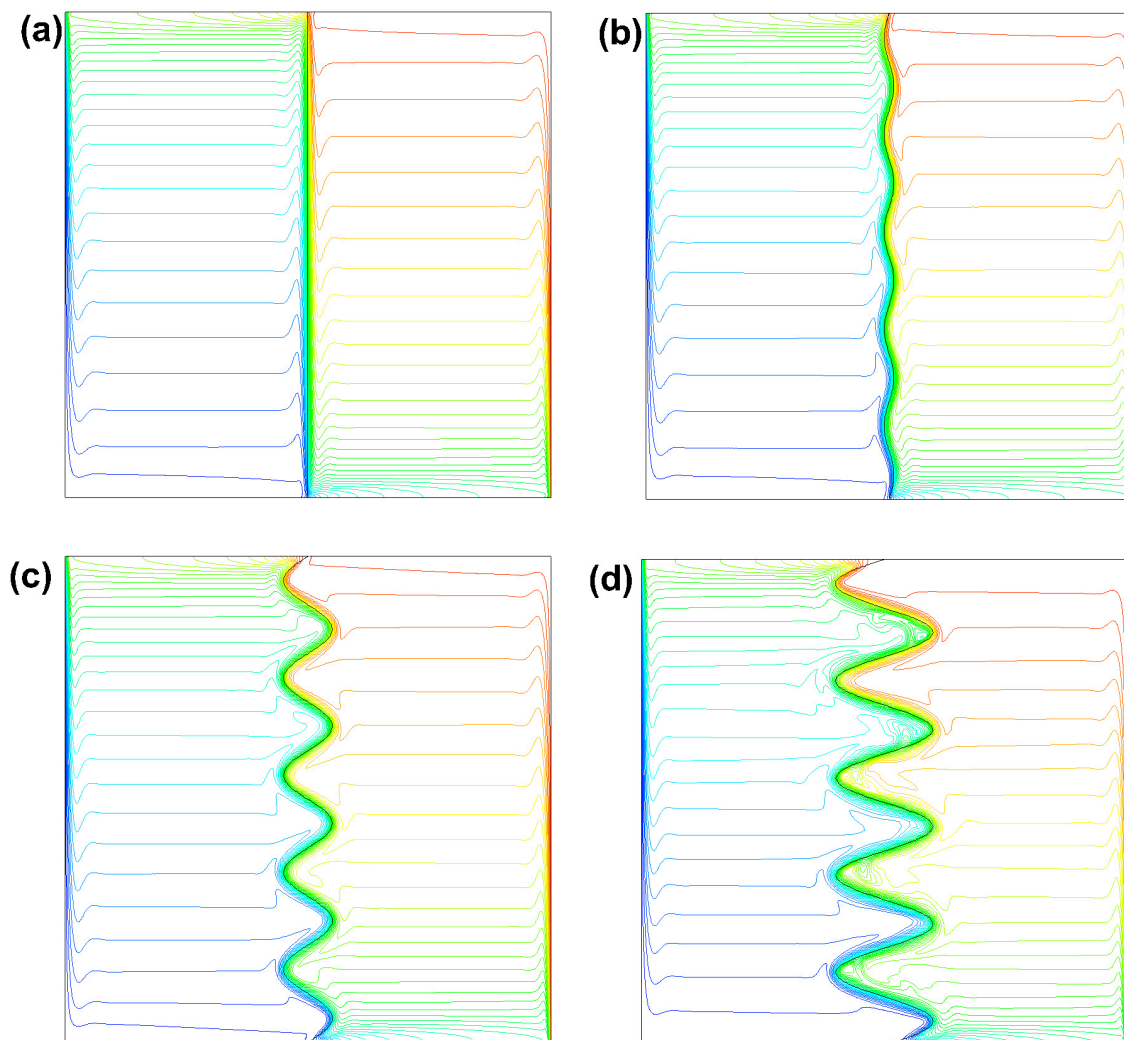


FIGURE 4. Isotherms for different amplitudes of wavy partitions during steady stage.

the grid system of 400×400 is adopted in this study.

Three non-dimensional time steps of 2.0×10^{-4} (for 200×200 grid), 1.0×10^{-4} (for 400×400 grid) and 5.0×10^{-5} (for 800×800 grid) are tested to examine the effect of the time step. The numerical results obtained using the three time steps are plotted in figure 2. Evidently, the development of the flow is not sensitive to the three tested time steps, with either choice being satisfactory. Accordingly, the time step of 1.0×10^{-4} and 400×400 grid size are considered to be sufficiently small to capture the global transient features of the flow development and are adopted here.

Results and discussions

Figure 2 illustrates the temperature time series, which shows the overall development of natural convection from a suddenly generated temperature difference between the fluids on the two sides of the wavy partition to a steady state. The overall development may be roughly classified into three main stages: an early stage, a transitional stage and a steady stage, as pointed out in figure 2. At the early stage the flow is mainly dominated by conduction. There presents some oscillations before the boundary layer becomes steady state. This boundary layer breaks down when the return flow hits the boundary layer from the top position of the enclosure. The secondary oscillations appear and finally the whole cavity becomes steady state.

Figure 3 shows the temperature contours for different amplitudes ($A = 0, 0.01, 0.05$ and 0.1) of wavy partitions during early stage. The straight vertical partition ($A = 0$) results are presented in figure 3a. We clearly observe the coupled boundary layer develop both sides of the partition. When the flow inside the boundary layer hits the upper or lower walls of the enclosure, the intrusion boundary layers are developed. The fluid from the intrusion boundary layers eventually fill the whole cavity which turns into thermally stratified at steady stage. The couple thermal boundary layers for wavy partitions of different amplitude show many interesting phenomena. For $A = 0.01$, the boundary layers exhibit similar trend as straight partition. However, when the amplitude increases (e.g. $A = 0.05$) we observe the nonuniform boundary layer thickness in the mid portion of the partition. For $A = 0.1$ we also observe that a little far from the leading edge the boundary layers detach from the wavy partition, however, they reattach again when the detached fronts touch the downstream wavy wall. Also, Rayleigh-Benard type instability is visible for the case of $A = 0.1$. The steady state isotherms are presented in figure 4 for same set of amplitudes as in figure 3. For all amplitudes considered here the fluid is thermally stratified. We also notice several plumes are generated due to the presence of Rayleigh-Benard type instability.

Time series of temperature at two different centrosymmetric points for different amplitude is presented in figure 5. It is observed that during early stage of the flow development the temperature is higher at point $(0.008, 0.1)$ when the amplitude is lower. The opposite scenario is observed at the centrosymmetric point $(-0.008, 0.9)$. That means the temperature is higher for higher amplitude. Oscillation of the temperature is seen during the transitional stage of

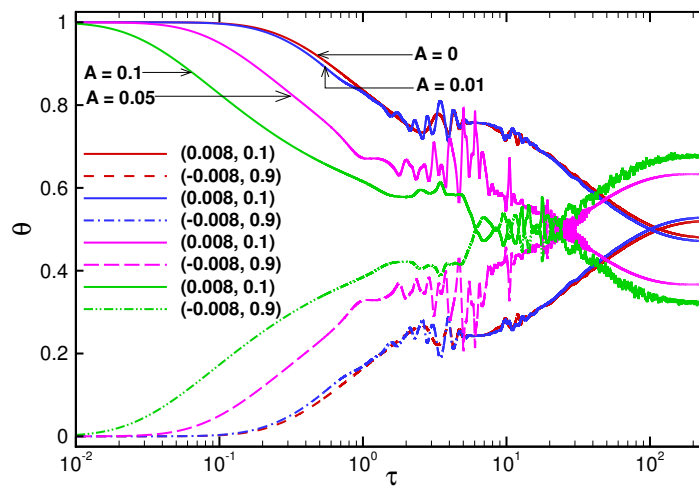


FIGURE 5. Time Series of temperature at two different centrosymmetric points for different A .

the boundary layer development. The temperature reverses after the steady state of the boundary layer (during the transitional stage of the flow development in the enclosure) due to the heat transfer through the vertical partition.

Figure 6 shows the time series of average Nusselt number through (a) the left vertical wall and (b) the partition of the cavity for different A . It is observed that there is no heat transfer for a certain period of time through the left side wall (Figure 6a). The heat transfer starts to happen when the intrusion boundary layer hits the left wall. Then the heat transfer increases with time. It is also observed that for higher amplitude of the wave the heat transfer is higher. Figure 6b shows the time series of Nusselt number calculated through the partition for different amplitudes. It is found that initially the heat transfer is very high due to conduction effect. The conduction effect is very high because suddenly fluid with two different temperatures come in contact through the diathermal partition which causes high heat transfer. However, the heat transfer reduces with time and becomes steady state.

Conclusions

Coupled thermal boundary layers induced by a suddenly generated temperature difference between the fluids on the two sides of a partition in a differentially heated square cavity have been investigated numerically in this study. Grid and time step dependence tests are carried out to confirm the validity of the numerical model. The overall development of the transient boundary layer roughly classified into three main stages based on the numerical results: an early stage, a transitional stage and a steady stage. In the early stage, coupled thermal boundary layers are formed on both sides of the partition. In the transition to the steady state, the thermal flows discharged from the downstream ends of the coupled thermal boundary layers into the core of the enclosure and makes the whole cavity thermally stratified. It is observed that with increase of the amplitude of the partition wall the average heat transfer is reduced (due to higher arc length), however, average heat transfer through the side wall is increased. We have also observed the flow is more unstable in the couple thermal boundary layers for higher Rayleigh number. Rayleigh-Benard type instability is also observed for higher amplitude of the vertical wall.

REFERENCES

- [1] Oro, J.M.F., Morros, C.S., Diaz, K.M.A., Ybarra, P.L.G., "Numerical simulation of the fuel oil cooling process in a wrecked ship", *J. Fluids Eng.*, 128, pp. 1390 - 1393, (2006).
- [2] Siddiqa, S., Hossain, M. A., Saha, S. C., "The effect of thermal radiation on the natural convection boundary layer flow over a wavy horizontal surface", *Int. J. Therm. Sci.*, 84, pp. 143 - 150, (2014).

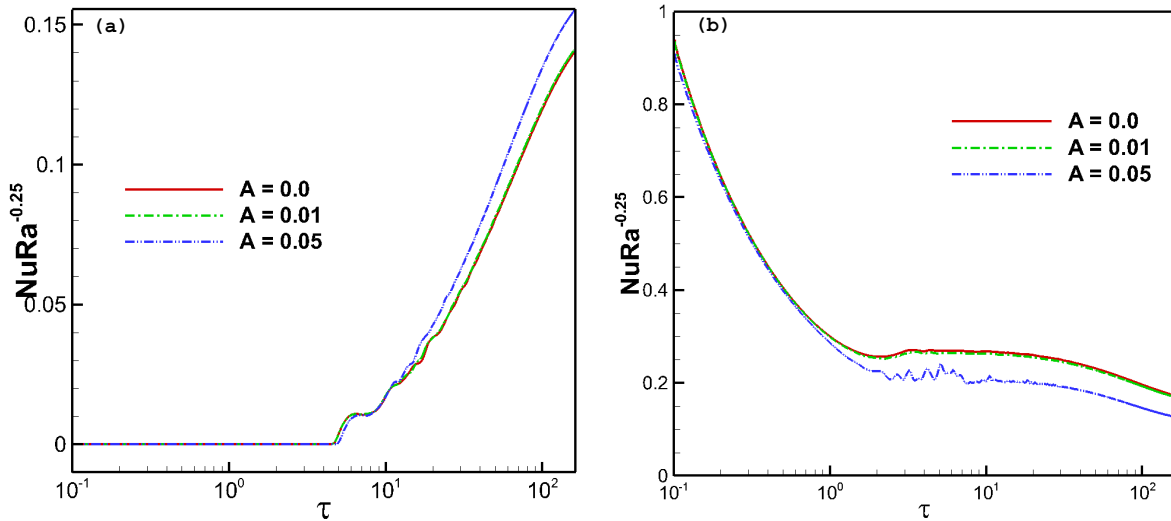
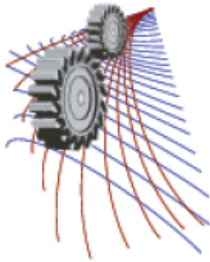


FIGURE 6. Heat transfer through left vertical wall (left) and partition (right) of the cavity for different A .

- [3] Siddiqa, S., Hossain, M. A., Saha, S. C., "Natural convection flow with surface radiation along a vertical wavy surface", *Numerical Heat Transfer Part A - Applications*, 64, pp. 400 - 415, (2013) .
- [4] Sojoudi, A., Saha, S. C., Khezerloo, M., Gu, Y. T., "Unsteady natural convection within a porous enclosure of sinusoidal corrugated side walls", *Transport in Porous Media*, 104, pp. 537 - 552, (2014).
- [5] Hasan, M. N., Saha, S. C., Gu, Y. T., "Unsteady natural convection within an differentially heated enclosure of sinusoidal corrugated side walls", *Int. J. Heat Mass Trans.*, 55, pp. 5696 - 5708, (2012).
- [6] Bachelor, G.K., "Heat transfer by free convection across a closed cavity between vertical boundaries at different temperatures", *Quart. Appl. Math.*, 12, pp. 209 - 233, (1954).
- [7] Eckert, E.R.G., Carlson, W.O., "Natural convection in an air layer enclosed between two vertical plates at different temperatures", *Int. J. Heat Mass Transfer*, 2, pp. 106 - 129, (1961).
- [8] Elder, J.W. "Laminar free convection in a vertical slot", *J. Fluid Mech.*, 23, 77-98, (1965).
- [9] Gill, A.E., "The boundary-layer regime for convection in a rectangular cavity", *J. Fluid Mech.*, 26, 515 - 536, (1966).
- [10] De Vahl Davis, G., "Natural convection of air in a square cavity: a bench mark numerical solution", *Int. J. Numer. Methods Fluids*, 3, 249 - 264, (1983) .
- [11] Gill, A.E., Davey, A., "Instabilities of a buoyancy-driven system", *J. Fluid Mech.*, 35, 775 - 798, (1969).
- [12] Patterson, J.C. Imberger, J. C., "Unsteady natural convection in a rectangular cavity", *J. Fluid Mech.*, 100, 65 - 86, (1980).
- [13] Chenoweth, D.R., Paolucci, S., "Natural convection in an enclosed vertical air layer with large horizontal temperature differences", *J. Fluid Mech.*, 169, 173 - 210, (1986) .
- [14] Paolucci, S., Chenoweth, D.R., "Transition to chaos in a differentially heated vertical cavity", *J. Fluid Mech.*, 201, 379 - 410, (1989).
- [15] Le Quere, P., "Transition to unsteady natural convection in a tall water-filled cavity", *Phys. Fluids*, 2, 503 - 515, (1990).
- [16] Elder, J.W., "Turbulent free convection in a vertical slot", *J. Fluid Mech.*, 23, 99-111, (1965).
- [17] Paolucci, S., "Direct numerical simulation of two-dimensional turbulent natural convection in an enclosed cavity", *J. Fluid Mech.*, 215, 229 - 262, (1990).
- [18] Dol, H.S., Hanjalic, K., "Computational study of turbulent natural convection in a side-heated near-cubic enclosure at a high Rayleigh number", *Int. J. Heat Mass Transfer*, 44, 2323 - 2344, (2001).
- [19] Nishimura, T., Shiraishi, M., Kawamura, Y. Natural convection heat transfer in enclosures with an off-center partition, *Int. J. Heat Mass Transfer* 30 (1987) 1756 - 1758.
- [20] F. Xu, J. C. Patterson, C. Lei, "Heat transfer through coupled thermal boundary layers induced by a suddenly generated temperature difference", *Int. J. Heat Mass Transfer*, 52, 4966 - 4975, (2009).
- [21] Williamson, N., Armfield, S. W., Kirkpatrick, M. P., "Transition to oscillatory flow in a differentially heated cavity with a conducting partition", *J. Fluid Mech.*, 693, pp 93 - 114, (2012).
- [22] Saha, S. C., Khan, M. M. K., Gu, Y. T., "Unsteady buoyancy driven flows and heat transfer through coupled thermal boundary layers in a triangular enclosure", *Int. J. Heat Mass Transfer*, 68, pp. 375 - 382. (2014).
- [23] Saha, S. C., Gu, Y. T., "Transient air flow and heat transfer in a triangular enclosure with a conducting partition", *Appl. Math. Model.*, 38, pp. 3879 - 3887, (2014).
- [24] Duxbury, D., "An interferometric study of natural convection in enclosed plane air layers with complete and partial central vertical divisions", Ph.D. Thesis, University of Salford, 1979.
- [25] Turkoglu, H., Yucel, N., "Natural Convection Heat Transfer in Enclosures with Conducting Multiple Partitions and Side Walls", *Heat Mass Transfer*, 32, pp. 1 - 8(1996).
- [26] Cuckovic-Dzodzo, D.M., Dzodzo, M.B., Pavlovic, M.D., "Laminar natural convection in a fully partitioned enclosure containing fluid with nonlinear thermophysical properties," *Int. J. Heat Fluid Flow* 20, 20, pp. 614 - 623, (1999).
- [27] Anderson, R. Bejan, A., "Natural convection on both sides of a vertical wall separating fluids at different temperature", *J. Heat Transfer*, 102, pp. 630 - 635, (1980).
- [28] Anderson, R. Bejan, A., "Heat transfer through single and double vertical walls in natural convection: theory and experiment", *Int. J. Heat Mass Transfer*, 24, 1611 - 1620, (1981).
- [29] Nishimura, T., Shiraishi, M., Nagasawa, F., Kawamura, Y., "Natural convection heat transfer in enclosures with multiple vertical partitions", *Int. J. Heat Mass Transfer*, 31, 1679 - 1686, (1988).



Numerical Study of Fluid Flow Behaviors Around Bluff Body Using Lattice Boltzmann Method

Taasnim Ahmed Himika^{1, a)}, Md. Farhad Hasan^{1, b)} and Md. Mamun Molla^{2, c)}

¹Department of Electrical & Computer Engineering, North South University, Dhaka, Bangladesh

²Department of Mathematics & Physics, North South University, Dhaka, Bangladesh

^{c)} Corresponding author: mamun.molla@northsouth.edu

^{a)} taasnim.ahmed@northsouth.edu

Abstract. The present paper illustrates a two-dimensional numerical simulation of fluid flow around bluff bodies at two certain cases, both for Reynolds number 400. Lattice Boltzmann Method (LBM), one of the most popular computational fluid dynamics techniques, has been applied. The velocity profiles are investigated resulting from fluid-solid interaction considering certain inlet and outlet condition and necessary discussions have been added. Bluff body interference and its effect on fluid flow are studied with brief explanation. A code validation has been conducted comparing with benchmark solutions for fluid flow for well-known backward-facing problem. The agreement is found to be pretty good. The numerical results are presented in terms of the streamlines, velocity distribution, wall shear stress as well as the flow reattachment point.

INTRODUCTION

Research on flow pattern around bluff bodies has been a topic of keen interest for a long time and it successfully drew the attention of many prominent researchers. Its complexity with Reynolds number (Re) and technological importance are also other significances of bluff bodies. If a single cylinder is considered, fluid flow takes shape of vortex just behind any solid obstacle that is placed against it. In spite of the appearance, fluid flow like this provides good opportunity to understand the fundamentals of flow interactions occurring in various technologies.

Davis *et al.* [1] performed experimental and numerical investigations of flow around a rectangular cylinder placed in a horizontal channel. They discussed the effects of the variations of different Re, rectangle aspect ratio, blockage ratio and upstream velocity profile upon the forces acting on the rectangle. Li and Humphrey [2] performed numerical modeling of unsteady, two-dimensional (2D) flow and heat transfer due to a square cylinder located asymmetrically between the parallel sliding walls of a channel at various positions. Their research showed that the presence of the boundary walls in the flow, indeed affected the behavior of vortex shedding behind the body.

It should be mentioned that citations in the literature employed so far, are based on solving the Navier-Stokes equation. However, it is not a simple job to deal with complications of complex geometries when there are several fluid phases or different fluids. Therefore, a different approach, Lattice Boltzmann Method (LBM) has found extensive and extended applications in simulating physical phenomena of various complexities. It has emerged as a decent, innovative, viable and efficient alternative to the traditional Computational Fluid Dynamics (CFD) methods. Significant advances of theoretical algorithms and practical industrial applications of LB equation have been conducted. Ginzburg *et al.* [3, 4] applied LBM with only two relaxation times to develop the algorithm with respect to BGK operator. In this type of work, LBM provides a great opportunity to apply this innovative approach to real engineering problems encountered in a variety of industries. The LBE has been widely used in many kinds of

complex flows such as single component hydrodynamics, multiphase and multi-component fluids, magneto hydrodynamics, reaction-diffusion systems, flows through porous media and turbulent flows [5–7]. Meanwhile, Guo *et al.* [8] researched on the LBE and the Gas-Kinetic Scheme (GKS) methods for 2D incompressible laminar flows past a square block symmetrically placed in a channel with the Re between 10 and 300. Their investigations demonstrate that both LBE and GKS methods yield quantitatively similar results for laminar flow simulations, and agree well with existing ones, provided that a sufficient grid resolution is given.

The main objective of the present work is to study the effect of bluff body flow in a particular geometry for two different situations. At first, a bluff body has been placed at a certain position of a channel and later, two bodies have been placed at an alignment vertically but at opposite to each other to create a narrow channel. Re has been considered 400 for each simulation. In section 2, mathematical formulation has been discussed, followed by results and discussion in section 3 and conclusion in section 4.

MATHEMATICAL FORMULATION

The Lattice Boltzmann method was originated from Ludwig Boltzmann's kinetic theory of gases. The basic theory of this equation is that gases or fluids can be imagined as consisting of a large number of tiny particles moving with random motions. The exchange of momentum and energy is found through particle streaming and collision between particles. So, this process can be demonstrated by the Boltzmann transport equation, which is

$$\frac{\partial f}{\partial t} + \bar{u} \cdot \bar{\nabla} f = \Omega(f, f^{eq}) \quad (1)$$

where, f and f^{eq} are the particle distribution function and equilibrium distribution function respectively, \bar{u} is the particle velocity, $\bar{\nabla}$ is the gradient operator and Ω is the collision operator.

Physical Geometry

Present research is based on bluff body flow simulation using LBM. However, two different cases have been considered in this paper. At first, a bluff body has been placed at a certain position and in the second scenario two bluff bodies have been put at vertically oppositedirection. For the fluid flow, domain a lattice size of $(500 \times 50) \sim (x \times y)$ has been considered for both cases. In the first case, only one bluff body is visible and it has a dimension of $(15 \times 20) \sim (x \times y)$ lattices. In the next case, the bluff bodies are of $(15 \times 10) \sim (x \times y)$ lattice size each. The details have been discussed in the results and discussion section. The widths of both the inlet and outlet have been taken from 0 to 50 lattices.

Introduction to Lattice Boltzmann Model

The LBM simplifies Boltzmann's original idea of gas dynamics by reducing the number of particles and circumscribing them to the nodes of a lattice. For a two dimensional model, a particle is restricted to stream in a possible of 9 directions, including the one staying at rest. For this type of modeling, the most popular one is $D2Q9$ model which has been considered in this work. This is the standard model for two dimensional structure for both flow and temperature conditions. The velocities for these conditions are known as macroscopic velocities.

The LB equation with external forces can be shown for fluid flow. For this condition, the following equations can be written:

$$f_i(\bar{x} + \Delta \bar{e}_i, t + \Delta) - f_i(\bar{x}, t) = -\frac{1}{\tau_v} [f_i(\bar{x}, t) - f_i^{eq}(\bar{x}, t)] \quad (2)$$

Here, $\tau_v = 3\nu + 0.5$ is the single relaxation times that control the rate of approach to equilibrium, $f_i(\bar{x}, t)$ is the density distribution functions for velocity along the direction \bar{e}_i at (\bar{x}, t) , ν is the kinematic viscosity. The particle speed is \bar{e}_i and ρ , is the density.

To calculate the equilibrium distribution functions $f_i^{eq}(\bar{x}, t)$ the general expression has been considered, that is:

$$f_i^{eq} = w_i \rho \left[1 + 3 \left(\bar{e}_i \cdot \bar{u} \right) + \frac{9}{2} \left(\bar{e}_i \cdot \bar{u} \right)^2 - \frac{3}{2} \bar{u} \cdot \bar{u} \right] \quad (3)$$

where, $\bar{u} = (u, v) = (U, V)$ is the velocity, the lattice speed $c = \frac{\Delta x}{\Delta t} = 1$ and w_i is the weighting factor.

The weighting factors for $D2Q9$ are given as:

$$w_i = \frac{4}{9}, \text{ for } i = 1; \frac{1}{9}, \text{ for } i = 2, 3, 4 \text{ and } \frac{4}{9}, \text{ for } i = 5, 6, 7, 8. \quad (4)$$

The macroscopic fluid density ρ and velocity \bar{u} can be found from the moments of distribution functions and they yield the following:

$$\rho = \sum_{i=0}^8 f_i \quad (5)$$

$$\bar{u} = \frac{1}{\rho} \sum_{i=0}^8 f_i \bar{e}_i \quad (6)$$

Boundary Conditions

Boundary conditions (BCs) are central to both the stability and accuracy of any kind of numerical solution. For LB modeling, the discrete distribution functions on the boundary need to be taken care of to reflect the macroscopic BCs of the fluid. In this work, only bounce-back condition has been applied at certain places.

Bounce-back BCs are usually used to implement no-slip conditions on the boundary. By the bounce-back condition, it is meant that when a particle of a certain fluid for discrete distribution function reaches a boundary node, the particle will scatter back to the fluid along with its incoming direction. Bounce-back condition can be of various types but on-grid bounce-back condition has been used in this paper.

Boundary Condition for Velocity

In two-dimensional structure four possible directions--east, west, north and south--have been considered in the proposed model and no-slip or bounce-back boundary condition is used at the walls. At the west direction, the inlet for flow has been considered and the outlet is at the east direction. Apart from these two directions, bounce-back condition has been applied in rest of the part of the geometry.

At west (left) direction, the inlet is present and therefore, the unknown parameters are calculated. The following relations are found:

$$f_1 = f_3 - \frac{2}{3} \rho_N U \quad (7)$$

$$f_5 = f_7 - \frac{1}{6} \rho_N U \quad (8)$$

$$f_8 = f_6 - \frac{1}{6} \rho_N U \quad (9)$$

where, U is the bulk velocity based on the Reynolds number $\mathbf{Re} = \overset{def}{UH} / \nu$.

At east (right) direction, the outlet zero gradient boundary condition has been applied as:

$$f_{3,N} = f_{3,N-1} \quad (10)$$

$$f_{7,N} = f_{7,N-1} \quad (11)$$

$$f_{6,N} = f_{6,N-1} \quad (12)$$

The bounce-back conditions for the north (top) and south (bottom) walls have been used. They are given below for south: $f_2=f_4, f_5=f_7$ and $f_6=f_8$, and for north: $f_4=f_2, f_7=f_5$ and $f_8=f_6$.

In addition, at each side of the block bounce-back condition has been used. The idea of taking no-slip condition is actually simple and decent one. As per the equations given above, it can be said that the boundary of the fluid domain has been aligned with the lattice points. The incoming directions of the distribution functions are reserved when encountering a boundary node. This theory does not basically differentiate the pattern of the boundaries and is ideal for simulating fluid flows in complex geometries.

RESULTS AND DISCUSSION

Code Validation

The code validation test case is the flow through in a backward-facing step for $Re=400$. The height of the step is $h=H/2$. Erturk [9] found the reattachment point for the primary recirculation region near the bottom wall is 8.237 and in the present case is 8.059. At the upper wall, Erturk [9] also found the point of separation x_s/h and the reattachment point, x_r/h , for the secondary recirculation region are 7.731 and 10.037, respectively. In the present case they are 7.660 and 10.420, respectively. The streamlines are given in Figure 1 that shows a qualitative agreement with the result of Erturk[9].

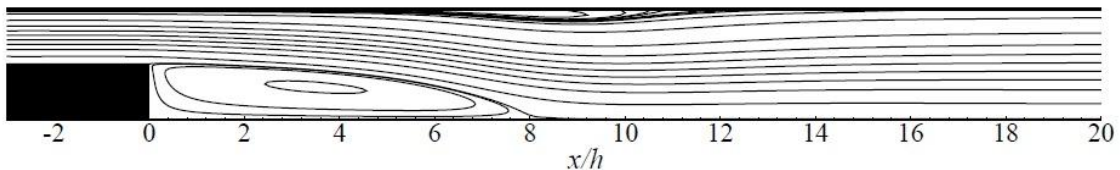


FIGURE 1. Comparison with the benchmark results of flow through a backward facing step by Erturk [9] in terms of the streamlines while $Re=400$.

Case I: One Bluff Body

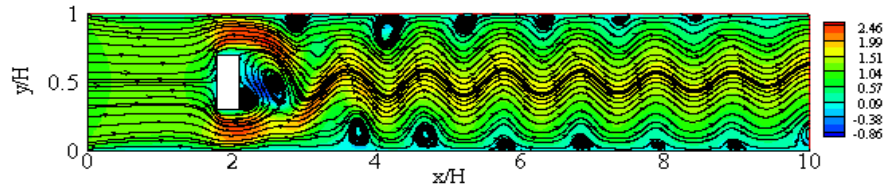


FIGURE 2. Streamlines appended on u velocity for $Re=400$.

After validating the code, numerical simulation has been carried out to see the effect of the presence of a bluff body placed at location of $x/H = 2$. The investigation has been conducted for $Re = 400$ and the inlet velocity is uniform at U . The computational domain and the obstacle that are considered for the LB simulation in this case study are shown in Figure 2. The streamlines in Figure 2 shows the structure of the fluid flow pattern and the recirculation eddies that occurred after crossing the bluff body. The fluid flows past the bluff body at the given position and after passing the obstacle, the flow again re-unites as there is no other obstacle placed inside the channel. The recirculation occurs due to the narrower path flow crosses because of the bluff body and after that the flow behaves like a periodic flow till it approaches near the outlet. Small recirculations are also visible at the north and south boundary walls due to the effects of wall friction.

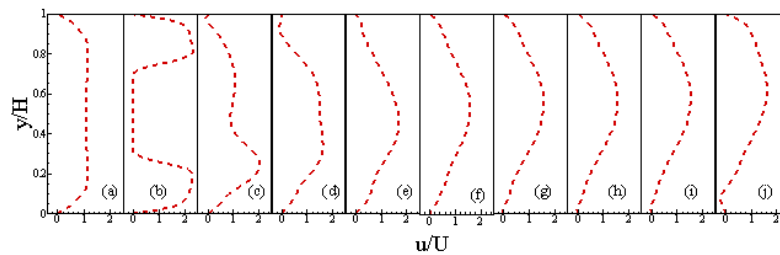


FIGURE 3. u/U velocity profiles for Case I at different position of x/H , (a) $x/H=1$, (b) $x/H=2$, (c) $x/H=3$, (d) $x/H=4$, (e) $x/H=5$, (f) $x/H=6$, (g) $x/H=7$, (h) $x/H=8$, (i) $x/H=9$, (j) $x/H=10$.

Figure 3 represents different velocity profiles at different position of x/H . For $x/H=1$, a vertical shape can be seen at the middle part of the curve. This is due to the effects of uniform inlet velocity. For $x/H=2$, the curve has a much changed pattern in this position, as the bluff body is present. The body is working as an obstacle and flow can't pass through it. That is the reason why there is a vertical line with zero magnitude between the upper and lower part of curve. The maximum velocity occurs at the upper and lower region of the obstacle. As the flow goes towards $x/H = 3, 4, 5$, the vertical part slowly disappears, which means the flow has overcome the obstacle and is flowing like a periodic flow, which was shown earlier in Figure 2. The velocity profile now has taken a parabolic shape and it maintains its consistency till it comes close to the outlet wall at $x/H = 10$.

CASE II: TWO BLUFF BODIES AT OPPOSITE POSITION

In Case II, two bluff bodies opposite to each other has been considered between the range $x/H = 1.8 - 2.1$. Figure 4 shows the streamlines of this case. This time, two bluff bodies have created a narrow channel for fluid flow. It is seen that after entering the flow through the inlet, the fluid faces the obstacles and is destined to flow through the narrow path. After passing this path, it gets ample space to flow without any interference or interruption and therefore, all of a sudden, the velocity of the flow increases. Due to this increased velocity, recirculations can be noticed next to each bluff body. However, this characteristic is not visible all the time. Gradually, the recirculations tend to disappear and after a certain distance, no such situation is seen in the Figure 4. In this case, the attachment points, x_r/H , for the primary recirculation regions at the bottom and upper walls are recorded as 4.65 and 5.25, respectively.

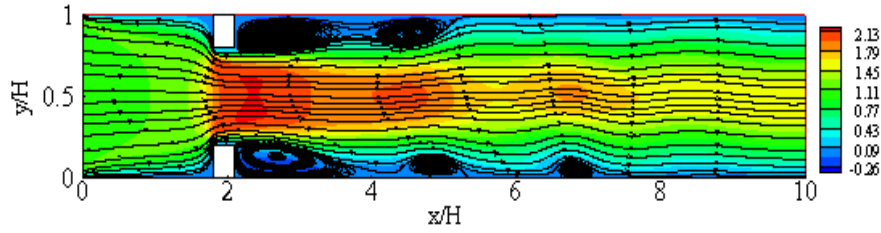


FIGURE 4. Streamlines appended on u/U velocity for $Re=400$.

The velocity profiles show an interesting finding as well. According to Figure 5, for $x/H = 1$, the characteristic of the curve is almost identical to what was found in the Figure 3. However, for $x/H = 2$, the notable change can be observed. At the middle of the channel, the parabolic curve is seen, which indicates the fluid flow. A narrow channel was created earlier for the fluid flow and due to that condition, this time the velocity profile bends at the middle and the other parts are just two vertical lines, which indicate the presence of two bluff bodies. At $x/H = 3$, the characteristic curve starts to change into a desired parabolic shape but the actual parabolic shape can be found at the downstream region, i.e. $x/H=4,5,6$, which indicate that just like the previous Figure 3, the fluid is not facing any obstacle and is flowing as it will toward the outlet.

The wall shear stress in terms of the skin-friction coefficient $C_f = \tau_w / \frac{1}{2} \rho U^2$ depicted in Figure 6 is calculated after the bluff bodies. It has been observed that after the obstacles the shear stresses become negative because of the recirculation zone where the velocity is negative. After the recirculation zones, the shear stresses increase and getting positive magnitude with some small oscillation.

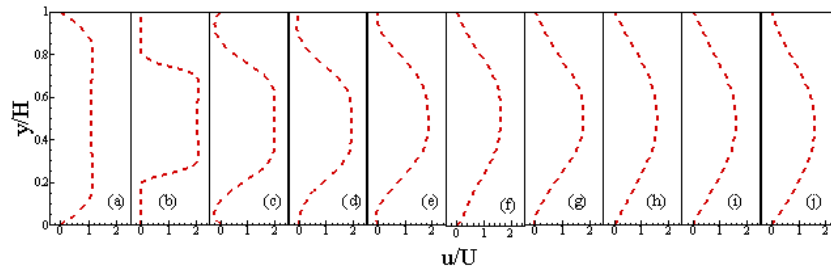


FIGURE 5. u/U velocity profiles for Case II at different position of x/H , (a) $x/H = 1$, (b) $x/H = 2$, (c) $x/H = 3$, (d) $x/H = 4$, (e) $x/H = 5$, (f) $x/H = 6$, (g) $x/H = 7$, (h) $x/H = 8$, (i) $x/H = 9$, (j) $x/H = 10$.

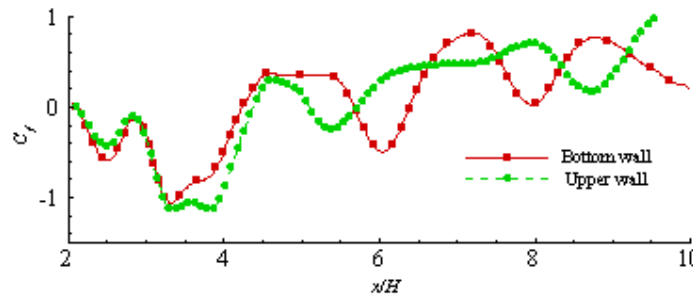


FIGURE 6. Shear stress $\tau_w / \rho U^2 / 2$ at the upper and lower walls.

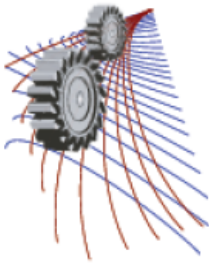
CONCLUSION

In the present work, Lattice Boltzmann Method has been applied for studying the interference in flow for the bluff body placed in different position in a channel. At first, one bluff body was placed at $x/H=2$ and later two solid bodies were placed at opposite direction to each other. Before going through the simulation, code validation was conducted with benchmark results and was found in good agreement indeed. The results for a single bluff body placed in flow suggest that this method can be used to simulate fluid flows in low Re and in this paper, $Re = 400$ justified this theory.

Main conclusions are: (i) when a bluff body is placed at a certain position between north and south boundary walls, close to inlet in particular, fluid flow over the obstacle from both up and down channel and creates recirculation near the right side of the block for a single frequency for the given Re , (ii) an oscillatory laminar flow pattern is visible in the channel when two bluff bodies are aligned orthogonal to the main-flow direction, (iii) in Case II, the length of the recirculation zone near the upper wall is larger than the length of the recirculation near the lower wall and lastly, (iv) the wall shear stresses become negative after the bluff bodies due to the recirculation region.

REFERENCES

1. R. Davis, E. Moore, L. Purtell, *Phys. Fluids* **27**, 46–59 (1984).
2. G. Li, J. A. Humphrey, *Int. J. Numer. Meth. Fluids* **20**, 1215–1236 (1995).
3. I. Ginzburg, F. Verhaeghe, D. d'Humieres, *Communications in computational physics* **3**, 427–478 (2008).
4. I. Ginzburg, F. Verhaeghe, D. d'Humieres, *Communications in computational physics* **3**, 519–581 (2008).
5. S. Chen, G. D. Doolen, *Annu. Rev. Fluid Mech.* **30**, 329–364 (1998).
6. A. Mezrhab, M. Moussaoui, H. Naji, *Journal of Physics D: Applied Physics* **41**, 115502 (2008).
7. E. Semma, M. El Ganaoui, R. Bennacer, A. Mohamad, *International Journal of Thermal Sciences* **47**, 201–208 (2008).
8. Z. Guo, H. Liu, L.-S. Luo, K. Xu, *Journal of Computational Physics* **227**, 4955–4976 (2008).
9. E. Erturk, *Comput. Fluids* **37**, 633–655 (2008).



Aerodynamic Study of Sports Woven Fabrics

Hazim Moria^{1, a)}, Harun Chowdhury^{2, b)} and Firoz Alam^{2, c)}

¹Mechanical Engineering Department, Yanbu Industrial College, Yanbu Al-Sinaiyah P.O. Box 30436, KSA

²School of Aerospace, Mechanical and Manufacturing Engineering, RMIT University, Melbourne, Victoria, 3083, Australia

^{a)}Corresponding author: moriah@rcyci.edu.sa

^{b)}harun.chowdhury@rmit.edu.au

^{c)}firoz.alam@rmit.edu.au

Abstract. Today technology plays a vital role in achieving better outcomes in speed sports. In speed sports, aerodynamic understanding is considered to be one of the decisive factors in elite level competitions. Sport garment is believed to assist athletes achieving better performance by reducing drag. Hence, it is important to understand the aerodynamic behavior of sports garment fabrics. Although some studies on knitted fabrics' aerodynamics have been reported in the open literature, scant information is available on aerodynamic behavior of oven sports fabrics. The primary objective of this study is to investigate aerodynamic properties of oven fabrics for a range of Reynolds numbers widely experienced in speed sports. Specially developed cylindrical methodology was used to quantify the effects of aerodynamic properties and fabrics' surface parameters. The study was undertaken experimentally in a wind tunnel environment for a range of commercial woven fabrics used in speed sports. Additionally, an electron microscopic analysis was undertaken to characterize the fabric physical parameters. A correlation between the fabric surface parameters and aerodynamic properties (drag and lift) was established. The findings indicate that the aerodynamic behavior can significantly be altered using various fabric's surface morphology and utilized for athlete's benefit.

INTRODUCTION

In speed sports, aerodynamics can play a critical role in athletes' performance. With margins being very small, an athlete's garment can be the difference between winning and losing. To date, there has been great interest in the effects of different garments and their aerodynamic characteristics. Technological innovation in both design and materials has played a significant role in sports achieving its current standing in both absolute performance and its aesthetics. Sports garments can affect athletic performance by influencing the aerodynamics of the moving athlete interacting with external air flow. Laing and Sleivert [1] suggested that drag can be reduced by up to 10% through the appropriate use of garments in sports. Presentably, the majority of commercial sport garments currently available for speed sports applications (e.g., sprint, cycling, speed-skating, downhill-skiing, ski jumping and swimming) are made from knitted and woven skin-fitted fabrics. Some garment manufacturing claimed that these garment provide the athlete with reduced fatigue, better muscle oxygenation, faster recovery, enhanced blood flow and reduced muscle oscillation [2, 3, 4, 5].

Science and technology can play a vital role in achieving better outcomes in speed sports. The importance of the aerodynamic attributes of the fabric materials used in the garment manufacturing has been highlighted in numerous studies [5, 6, 7]. Chowdhury [7], Kyle &Caiozzo [8], Oggiano et al. [9], Moria [10] and Achenbach [11] have mainly focused on the aerodynamic behavior of knitted fabrics using vertical cylindrical methodology in wind tunnel environments. They evaluated the aerodynamic properties (drag and lift simultaneously) of the simplified human body parts under a range of angles of attack (α) to simulate athlete's body positions. The findings showed that only drag and lift of cylindrical within a limited range of angles of attack (30° to 90°) were measured. However, in many sports the body parts' position can lie below the 30° angle of attack and beyond the 90° angle of attack. Therefore, it is necessary to develop an experimental arrangement that can evaluate aerodynamic behavior of the cylinder. In this study, a new cylindrical arrangement has been designed and developed to measure the aerodynamic

parameters from $\alpha = 0^\circ$ to 90° . Also, there has been a significant knowledge gap and deficiency in the comprehensive understanding of sport woven fabrics in the aerodynamic properties and behaviors of athlete's garment as limited research is reported in the open literature. Without a thorough understanding, it is difficult to develop sports garments that are scientifically proven to be aerodynamically superior. With a view to achieve this objective, a series of stretchable woven fabrics used in speed sports garments have been studied for a wide range of Reynolds numbers (Re) and angles of attack (α) using RMIT industrial wind tunnel.

METHODOLOGY

With a view to obtain precise information on both the drag and aerodynamic lift characteristics of commercial available woven speed sport fabrics made of various materials composition, a 90 mm diameter and 220 mm length cylinder under a range of angles of attack (0° to 90°) was developed. A 60 mm ellipsoidal head was attached with the cylinder to obtain maximum C_L/C_D . The test cylinder was connected to the hinge that was supported by the strut. The hinge was designed in such a way that the angle of attack of the test cylinder can be varied. The aerofoil canopy was also covered the strut during the test to minimize the aerodynamic interference. The cylinder was made of PVC material and used some filler to make it structurally rigid. The cylinder was vertically supported on a six components transducer (type JR-3) had a sensitivity of 0.05% over a range of 0 to 200 N as shown in Figure 1. The aerodynamic forces and their moments were measured for a range of Re based on cylinder diameter and varied wind tunnel air speeds (from 30 km/h to 130 km/h with an increment of 10 km/h). Each test was conducted as a function of angles of attack from stream-wise ($\alpha = 0^\circ$) to span-wise ($\alpha = 90^\circ$). The sensor was used to measure all three forces (drag, lift and side forces) and three moments (yaw, pitch and roll) at a time. Each set of data was recorded three times for 50 seconds time average with a frequency of 20 Hz ensuring electrical interference is minimized. Multiple data sets were collected at each speed tested and the results were averaged for minimizing the further possible errors in the raw experimental data. Further details about the wind tunnel can be found in Moria [10] and Chowdhury [7].

Five commercially available woven fabrics were selected in this study. Each fabric has different properties that are useful in speed sport. Figure 2 demonstrates photographs of the smooth cylinder and five samples examined in this study. The yellow line indicates the warp direction (vertical) while the fabric stretched in the weft direction with red line. The KESFB4-A, Kato Tech Co. Ltd. evaluation system was used to measure the fabric surface properties. Details about the KESFB4-A machine and measurement technique can be found in Troynikov et al. [3]. Table 1 provides the material composition, thickness, weft direct and average relative roughness of each sample fabric.

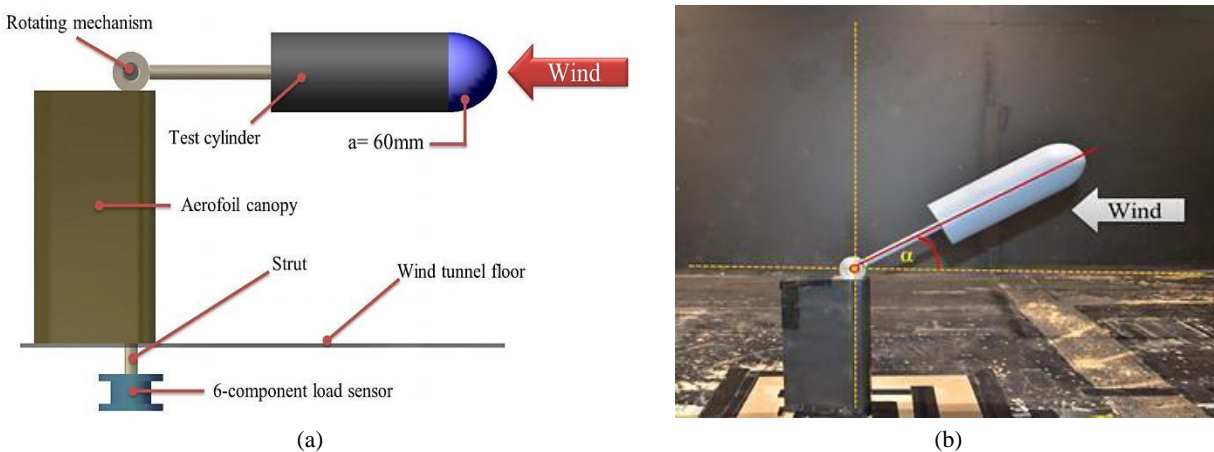


FIGURE 1. Cylinder geometry to measure the aerodynamic properties (lift and drag) at different angles of attack from 0° to 90° relative to wind direction. (a) Design and (b) experimental arrangement.

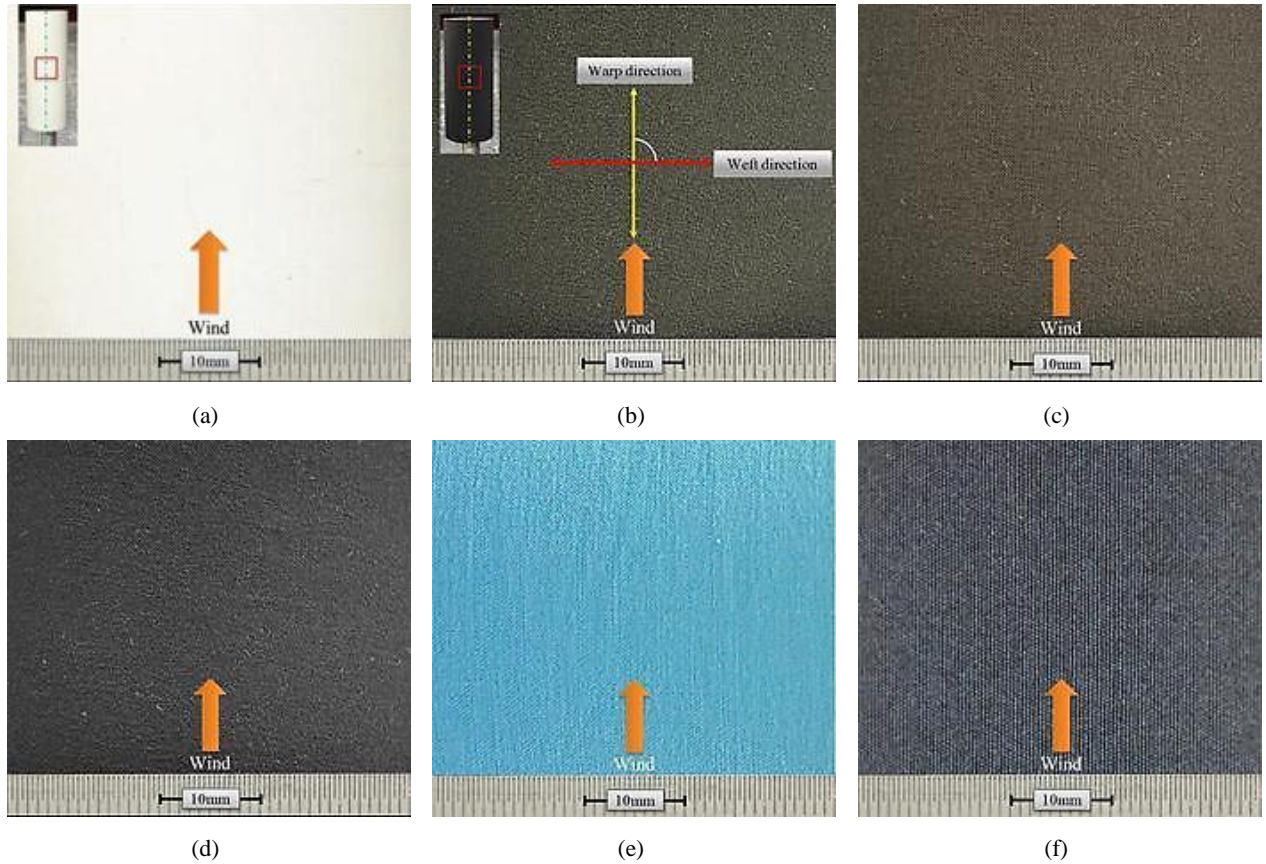


FIGURE 2. Photographs of five woven speed sport fabric surfaces including smooth cylinder.

TABLE 1. Material composition, thickness, weft direction and average relative roughness of five sport woven fabrics surface.

Fabric	Material Composition	Thickness, (mm)	Weft Direction	$(\epsilon=Ra/d)\times 10^{-4}$
Sample 1	70% Polyamide and 30% Elastane	0.27	0°	1.636
Sample 2	66% Polyamide and 34% Elastane	0.27	0°	1.893
Sample 3	64% Polyamide and 36% Elastane	0.27	0°	2.190
Sample 4	87% Cotton and 13% Elastane	0.36	0°	2.610
Sample 5	60% Rayon, 32% Polyester and 8% Elastane	0.55	0°	3.689

RESULTS AND DISCUSSIONS

Microstructural Analysis

With a view to understand the surface morphology such as yarn and fiber size and stitch pattern of five woven fabrics, an optical and electron microscopic study were performed. The optical images with 15 times magnification illustrated the numbers of weft and warp per cm and the gaps between the wefts at normal tension. Nonetheless, the optical images in Figure 3 did not provide detailed information of the surface parameter including the yarn and fiber sizes and knitting stitch pattern. Hence, a scanning electron microscope (SEM) in Figure 4 was used at 100 and 1000 times magnification to reveal in detail the fabric surface parameters. Table 2 represents the obtained number of wefts, warps per cm and characterization of five sport woven fabrics from optical and SEM images.

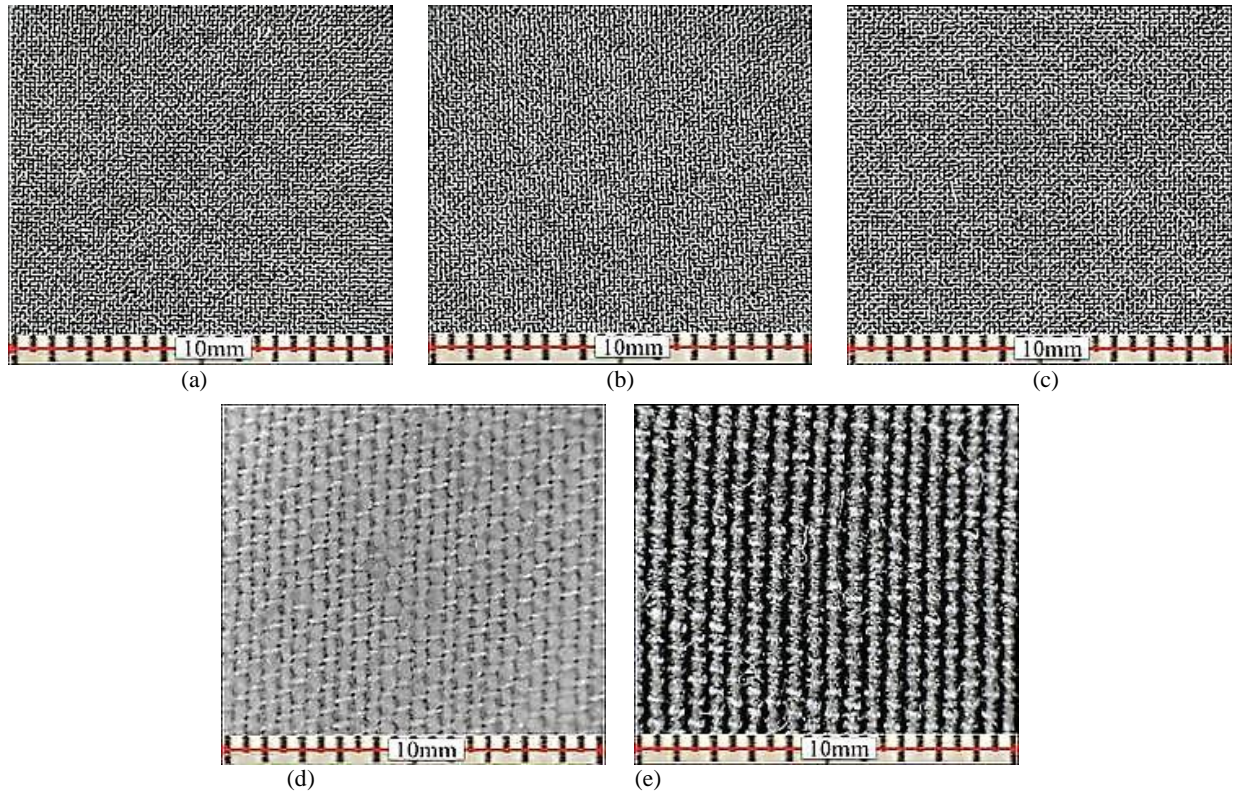
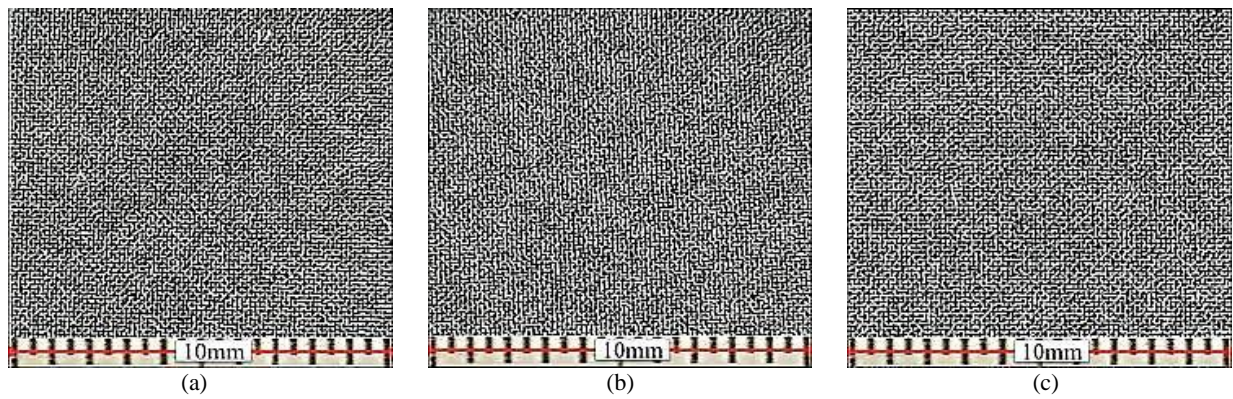


FIGURE 3. Optical images of five woven fabrics surface.

TABLE 2. Number of wefts, warps per cm and characterization of five sport woven fabrics with optical and SEM images

Fabric	No. of Wefts/cm	No. of Warps/cm	Gap Area, ($\mu\text{m}^2 \times 103$)	Weft to Weft, (μm)	Yarn Size (μm)	Fiber Size (μm)	Stitch Pattern
Sample 1	43	42	14.32	256	100	18.89	Rectangular
Sample 2	41	40	15.12	265	106	19.05	Rectangular
Sample 3	40	39	15.66	268	110	19.11	Rectangular
Sample 4	26	21	28.32	272	122	16.11	Rectangular
Sample 5	21	17	37.45	275	178	22.22	Rectangular



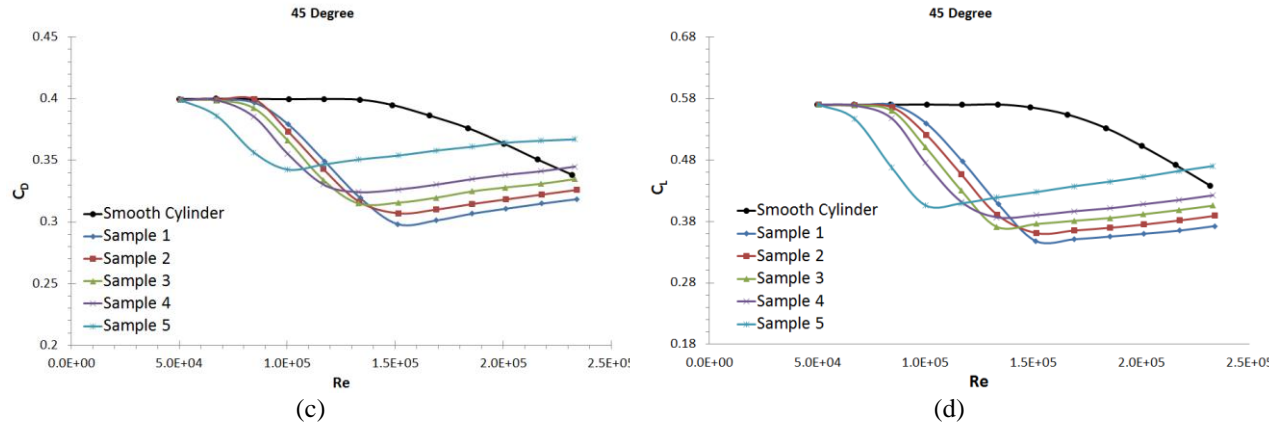


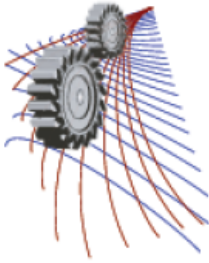
FIGURE 5. C_D variation with Re for five woven fabrics and smooth cylinder. (a) $\alpha = 0^\circ$, (b) $\alpha = 90^\circ$, (c) $\alpha = 45^\circ$ (drag) and (d) $\alpha = 45^\circ$ (lift).

CONCLUSIONS

The amount of drag generated by the tested sports woven fabrics is significantly lower compared to the smoother surface and directly dependent on the surface roughness. The surface roughness can be utilized to maximize the aerodynamic benefit for various speed range. An appropriate speed sport fabric for the elite athletes is utmost important in achieving aerodynamic advantages.

REFERENCES

1. R. M. Laing and G. G. Sleivert, *Textile progress* **32**, 1-122 (2002).
2. D. B. Gandhi, J. R. Palmar, B. Lewis, and I. G. Schraibman, *Postgraduate Medical Journal* **60**, 349-352 (1984).
3. O. Troynikov, E. Ashayeri, M. Burton, A. Subic, F. Alam and S. Marteau, *Procedia Engineering* **2**, 2823-2829 (2010).
4. L. Wanga, M. Feldera, and J. Y. Caib, *Journal of Fiber Bioengineering & Informatics* **4**, 15-22 (2011).
5. L. Pugh, *The Journal of Physiology* **241**, 795-808 (1974).
6. L. Brownlie, "Aerodynamic characteristics of sports apparel," Ph.D. thesis, Simon Fraser University, 1992.
7. H. Chowdhury, "Aerodynamics of sports fabrics and garments," Ph.D. thesis, RMIT University, 2012.
8. C. Kyle and V. Caiozzo, *Medicine and science in sports and exercise* **18**, 1986.
9. L. Oggiano, O. Troynikov, I. Konopov, A. Subic, and F. Alam, *Sports Engineering* **12**, 1-12 (2009).
10. H. A. Moria, "Experimental study of aerodynamic behaviour of stretchable sport fabrics", Ph.D. thesis, RMIT University, 2013.
11. E. Achenbach, *Journal of fluid mechanics* **65**, 113-125 (1974).



Simulation of Sliding of Liquid Droplets

Saif Khan Alen¹, Nazia Farhat¹ and Md. Ashiqur Rahman^{1, a)}

¹Department of Mechanical Engineering, Bangladesh University of Engineering and Technology, Dhaka-1000, Bangladesh

^{a)}Corresponding author: ashiquurrahman@me.buet.ac.bd

Abstract. Numerical simulations of sliding behavior of liquid droplets on flat and periodic microgrooved surfaces with a range of groove geometry are conducted. A numerical model is developed which is capable of predicting the critical sliding angle of the drop by comparing the advancing and the receding angles obtained from numerical and experimental findings. The effect of microgroove topography, droplet size and inclination angle on the droplet sliding characteristics is analysed. Using an open-source platform (Surface Evolver), a 3D drop-shape model is developed to numerically determine the drop stability and contact angle hysteresis on tilted surfaces. In this numerical model, the three phase contact line of the drop is obtained by numerically calculating the vertex force and local contact angle at each vertex of the base contour. Several numerical models are developed based on various assumptions of base contour shape (circular or elliptical) and implementation of gravitational force to the droplet. Droplet shapes and critical sliding angles, obtained from these numerical models, are compared with those of experimental results and are found to be in very good agreement.

INTRODUCTION

Dynamic wetting characteristics of a surface have significant practical importance in microfluidic systems, pesticide sprays, self-cleaning devices, refrigeration and air-conditioning systems etc. There are two different ways to manipulate the intrinsic wetting behavior of a surface- either by changing the chemical composition or by introducing roughness into the surface. Introducing surface roughness can manipulate the wettability, the way a liquid spreads over and wets the surface, and thus it can promote the water drainage property of the surface [1-7]. Among different ways of roughening a surface, incorporating microgrooves on the surface is widely used because of its ease in manufacturing and effectiveness in enhancing the wetting behavior. A droplet on a microgrooved surface, it can exhibit either Cassie wetting state or Wenzel wetting state depending on the droplet volume and microgroove geometry [8-9]. But the wetting phenomenon is completely different when the substrate is inclined.

For describing the behavior of droplet on an incline, Young-Laplace equation is replaced with Young-Laplace differential equation. *Surface Evolver*, a software designed to model surfaces subjected to different forces and constraints, is often adopted for analyzing the dynamics of water droplet on an incline [10-11]. The forces acting on a liquid droplet on an inclined surface is shown in Figure 1(a).

ElSherbini and Jacobi [12] experimentally observed the drop geometry on vertical and inclined surfaces and they derived a correlation between the contact angle and the azimuthal angle in a drop on an inclined surface. Bhutani *et al.* [13] implemented the correlation derived by ElSherbini and Jacobi [12] to numerically analyze the contact angle hysteresis of a static pendant drop on a physically textured inclined surface. Xu *et al.* [14] verified the theoretical morphology feature of the molten free-lead solder and analyzed the spreading behavior on an inclined Ni substrate. Santos *et al.* [10-11] proposed a model for obtaining the critical sliding angle of a droplet on an incline by analyzing the three-phase-contact line force in Surface Evolver.

In the present study, numerical investigation of sliding behavior of water droplet on inclined microgrooved brass surface is conducted and the results are compared with the experimental findings of an earlier study [3]. Open platform software 'Surface Evolver' has been adopted to develop the 3D model of the water droplet on microgrooved brass substrates with a wide range of groove dimensions. The critical sliding angle along the parallel direction to the groove is numerically estimated by analyzing the shape of the contact line and the advancing and receding contact angles obtained from the simulation.

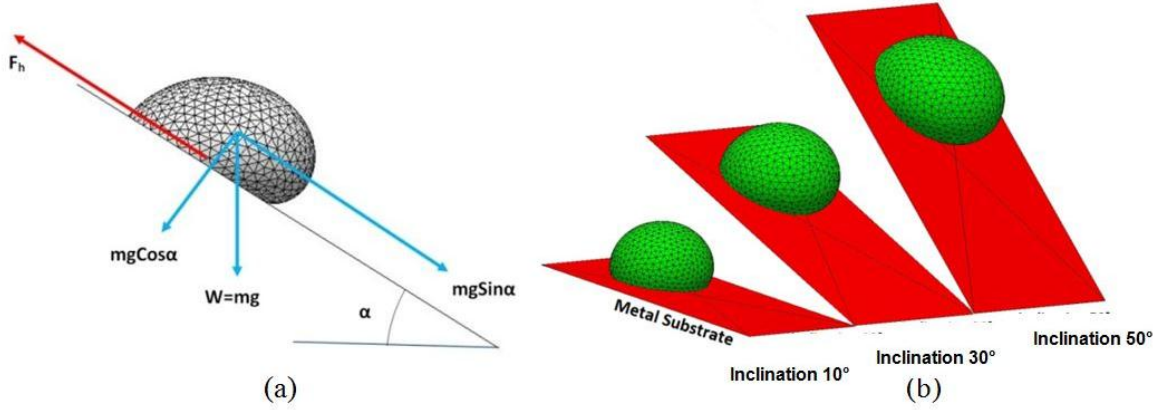


FIGURE 1. (a) Hysteresis force and gravity force acting on a drop on an inclined substrate, and (b) Variation of drop shape at different inclination angles (Sample $D_G^{67}W_P^{187}W_G^{130}$, drop volume =35 μl , $\theta_i=101.2^\circ$, $\theta_{adv}=119.2^\circ$, $\theta_{rec}=83.3^\circ$). Here, $D_G^X W_P^Y W_G^Z$ represents, Depth of groove is 'X', Width of Pillar is 'Y' and Width of groove is 'Z'.

NUMERICAL MODEL

The shape of a sessile drop on a substrate is governed by Young-Laplace equation which balances the surface tension and internal pressure. A variational approach is adopted in this present work for successively minimizing the overall energy of the drop to obtain a final equilibrium shape, and this step was achieved by using Surface Evolver [15-16]. Surface Evolver works on the principle of minimization of energy and conservation of volume subjected to the constraints and it evolves the surface to a minimum energy by a gradient descent method. The energy functional of a sessile drop subjected to a fixed volume can be expressed by Equation 1 [10],

$$U = \sigma_{lv} - \iint_{A_{lv}} \sigma_{lv} \cos \theta_i dA - \iiint_V \Delta \rho g r dV \quad (1)$$

Where θ_i is the initial contact angle, r and V are the radius and volume of the droplet, respectively, A_{lv} is the area of the liquid-vapor interface, g is gravitational acceleration, σ_{lv} is the liquid-vapor surface tension, and $\Delta \rho$ is the density difference between the liquid and vapor phase.

Keeping a fixed droplet volume, the boundary conditions are applied on the contact line of the substrate and the drop. Gravitational force can be included in the model as a function of bond number. Variation of drop shape at different inclination angles is presented in Figure 1(b). In our case, gravity force along the substrate is defined as a function of bond number (Bo) and the inclination angle (α).

$$Bo = \frac{\rho g V^{2/3}}{\sigma} \quad (2)$$

To obtain contact angle hysteresis, the inclination angle of the substrate is initiated as zero degree and the equilibrium droplet shape is calculated. Once the equilibrium droplet shape is obtained, the required inclination angle of the substrate is introduced keeping the contact line of the drop circular. But the drop on an inclined microgrooved surface does not have a circular contact line. To correct the circular contact line shape, experimentally obtained advancing contact angle (θ_{adv}) and receding contact angle (θ_{rec}) are used as constitutive inputs to the model.

To determine the vertex force at each vertex of the base contour, the lengths of the two edges constituting a triple line vertex are calculated. Position of the each vertex is corrected by comparing the vertex force, f_i with the maximum force f_{adv} or f_{rec} . As a result if the critical inclination angle is reached, the vertices on the contact line will continuously change their position resulting in a steady moving drop. A similar approach to simulate angular hysteresis is proposed by Santos *et al.* [10].

$$f_{adv} = \sigma_{lv} (\cos \theta_i - \cos \theta_{adv}) \quad (3)$$

$$f_{rec} = \sigma_{lv} (\cos \theta_{rec} - \cos \theta_i) \quad (4)$$

Defining initial contact angle (θ_i) plays an important role while simulating sliding behavior of a drop on microgrooved surface. In our case we considered the initial contact angle as defined by Equation 5, but almost similar result is obtained by using an initial contact angle derived from Equation 6.

$$\theta_i = \frac{\theta_{adv} + \theta_{rec}}{2} \quad (5)$$

$$\cos \theta_i = \frac{\cos \theta_{adv} + \cos \theta_{rec}}{2} \quad (6)$$

The critical inclination angle at which the droplet starts to move can be determined from the present model by comparing the numerically obtained advancing and receding contact angles with those of experimental values. Using this model, the contact line shape, drop shape, and advancing-receding angle can be obtained accurately by correcting the contact line after every iteration.

ANALYSIS OF RESULTS

Sample Geometry and Experimental Sliding Angle Data

A number of brass surfaces with parallel microgrooves having a wide range of dimensions and fabricated by micromachining were used as sample substrates in an earlier study [3]. Both the depth of groove (D_G) and width of the pillar (W_P) of the microgrooved samples were varied, keeping the width of the groove (W_G) fixed. The results are simulated for droplet volumes of 35 μl , 45 μl and 60 μl to compare the results on a fixed base for which the experimental data were in hand. The experimental and numerical sliding angles are determined and compared for 8 microgrooved brass samples. For details on the sample geometry, please see elsewhere [3].

The experimental sliding angle measured was the angle of tilt of the substrate when the advancing contact line of the droplet is seen to be in motion even if the receding contact line remains pinned at the same place. The movement of only the leading edge is considered here because from experiment it was found that the trailing edge of the droplet on few microgrooved surfaces remained attached to the surface even at a high tilting angle. Therefore, in accordance with the experimental observation, in the present study we defined the critical sliding angle as the angle of tilt at which the forward or advancing edge of the droplet starts to move. The receding contact angle is taken as 0° in cases when the trailing edge of the droplet was found to be pinned on the surface whereas the advancing edge of the droplet has moved a significant distance.

Comparison and Analysis of Experimental and Numerical Results

The numerical model presented here can determine the sliding angle, the contact line shape, drop shape of liquid droplets on microgrooved surfaces with the input of advancing and receding angle, which is determined experimentally. The average of these two angles is taken as the initial contact angle, which plays a significant role in the accuracy of the numerical results. In our case a very good agreement between the experimental and the numerical result is found when the initial contact angle is taken to be equal to the average of advancing and receding contact angles. Sliding angle along the parallel direction to the groove is considered in this study. It is because water drainage behavior along the parallel direction to the groove is more meaningful considering the fact that when a drop slides along the orthogonal direction to the groove, pinning occurs at every edge of the groove which resists the droplet motion.

Numerical model developed in this study is capable of predicting the sliding angle along the parallel direction to the groove. The variation experimental and numerical critical sliding angles with the width of pillar (W_P) is shown in Figure 2 (a). We can see from this figure that the results from this numerical model are in very good agreement with that of experimental findings and both these values decrease with a decrease in the width of the pillar. This is because if the pillar width is narrow then the surface tension acts on smaller area of the contact between the drop and the substrate.

Here, in most cases the variation between experimental and numerical values is within $\pm 2^\circ$, but with a higher deviation when the pillar width is very small. For this surface, the wetting state was found to be Wenzel and the experimental receding contact angle was taken as zero (0°) for reasons explained before. In case of the numerical simulation, for this narrow pillarwidth (sample $D_G^{67}W_P^{26}W_G^{130}$), the initial contact angle is very small (30.2°). As a result, when the drop obtains an equilibrium drop shape at zero inclination, the height of the drop is very small. So, when the gravitational force is applied horizontally along the substrate, which indirectly simulates the inclination of the substrate, the gravitational force does not penetrate a significant amount of area of the liquid-vapor interface. Therefore, the inclination angle needs to be much higher for initiating the sliding motion of the droplet. In contrast, the drop feels less retentive force in experimental case due to the less solid-liquid interface area beneath it because of the narrow width of the pillar, which results in very small critical inclination angle for initiating drop movement.

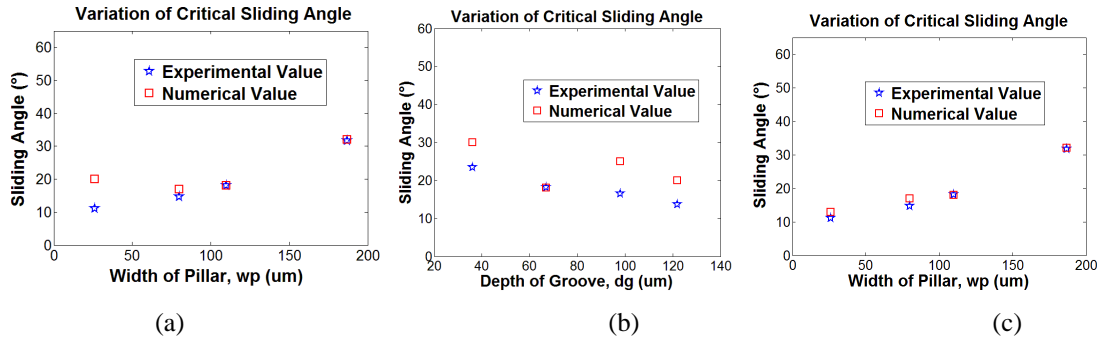


FIGURE 2. Comparison between experimental and numerically obtained critical sliding angles for a drop volume of 35 μm^3 and for surfaces with a variation of pillar width and groove depth. These variations are shown for samples with (a) varying pillar width ($D_G=67$ and $W_G=130$ μm), (b) varying pillar width ($D_G=67$ μm , $W_G=130$ μm) and considering receding contact angle 10° for sample with a pillar width of 26 μm , and (c) varying groove depth ($W_P=112$ and $W_G=130$ μm).

However, the difference between the experimental and the numerical results in the case of narrow pillar width is minimized [Figure 2(b)] if we consider the receding contact angle to be 10° instead of 0° and apply the base contour correction algorithm after every iteration (which is explained earlier in the Section 2). The experimental and numerical results are in excellent agreement if the width of the pillar is larger. For instance, in case of samples $D_G^{67}W_P^{110}W_G^{130}$ and $D_G^{67}W_P^{187}W_G^{130}$, the deviation between the experimental and numerical results is almost zero degree, which we can see from Figure 2(a). Therefore, our numerical model is able to accurately capture the wetting physics and the dynamic wetting behavior of the liquid droplet.

The numerical results are more in accordance with the experimental results for samples with a varying pillar width than with that with varying groove depth (Figure 2(c)). It can be observed from Figure 2(c) that the values of both the sliding angles decrease with the increase in the depth of the groove. The maximum and minimum deviation of the numerical results from the experimental results is about 10° and 0.15° , respectively.

Drop Shape Comparison

When a surface is inclined at critical sliding angle the droplet on it will exhibit an advancing contact angle and a receding contact angle, which can be used to characterize that real surface. So knowing the shape of the drop as well as the advancing and the receding angles at critical inclination is very important. In this study the droplet shape with the necessary boundary conditions and inclination of the substrate is obtained from multiple numerical models. These models vary from each other depending on the initialization of the drop and the substrate. Droplet shapes from each of these models and from those of experimental findings are almost same, which is presented in Figure 3(a).

If the substrate is kept horizontal then the inclination is simulated by applying a force, which is a function of bond number and inclination angle, along the length of the surface. But if the substrate with droplet on is inclined then a constant gravitational energy is simulated for the whole system, which can be seen from Figure 3(a-iii). In case of Wenzel droplet, a 'tadpole' shaped droplet is formed with a long tail on the microgrooved surface. This happens due to the pinning of the contact line at the receding edge which does not allow the receding edge to detach even after the advancing edge has moved a significant distance. This phenomenon is also captured successfully in both numerical models; the drop shape comparison for sample $D_G^{67}W_P^{26}W_G^{130}$ (45 μm^3 volume) from experiment and two numerical models is presented in Figure 3(b).

The numerically determined droplet shapes for a microgrooved and flat surface are compared in Figure 4. The polished baseline surface exhibited a hydrophilic nature and the droplet was found to be very elongated in the direction of sliding, as can be seen in Figure 4(a). Whereas, the microgrooved brass sample $D_G^{67}W_P^{187}W_G^{130}$ exhibited a large advancing and receding contact angles ($117.9^\circ, 81.5^\circ$), resulting in a more spherical shape of the drop (Figure 4(b)). Also the spherical shape of the droplet is more pronounced with a decrease of pillar width which we can see from Figs. 4(c)–(d). This corroborates our experimental findings as droplets were found to drain more easily from these microgrooved surfaces [3].

To obtain the shape of the droplet at critical inclination angle ElSherbini and Jacobi [15] suggested an approach of distributing the contact angle on each point of the contact line according to the azimuthal angle of that point. In our study, after obtaining the critical sliding angle from the simulation, the shape of the droplet from the azimuthal distribution is also calculated and a close match between them is obtained, as can be seen from Figure 5(a). The triple contact line obtained from this approach is almost the same as that we obtained from our numerical model.

The variation of the shape of the liquid droplet with a change in the inclination angle is shown in Figure 5(b) for the case when the initial contact angle of the drop is more than 90° . Variation of experimental and numerical drop shapes may occur due to the fact of considering equivalent real surface (with advancing and receding angle input) instead of simulating the exact microgroove geometry with boundary conditions. But the results from experiment and numerical model match more closely when the shape of the three phase contact line is corrected by applying the methodology which is described in the Numerical Model section. And the present numerical model yields highly accurate results while calculating the sliding angle, also three dimensional droplet shapes obtained from the simulation are in a very good agreement with experimental findings.

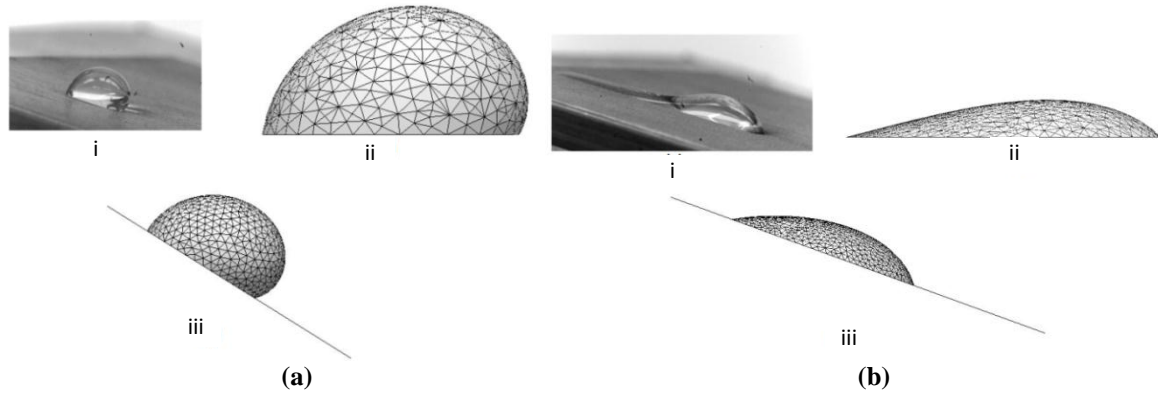


FIGURE 3. Comparison of experimental and numerically obtained drop shape at critical sliding angle on microgrooved samples (a) $D_G^{67}W_P^{187}W_G^{130}$ and (b) $D_G^{67}W_P^{26}W_G^{130}$. Shown in each figure, the experimental drop shape (top left), numerically obtained drop shape where gravity force is implemented as $mg\sin\alpha$ along the substrate (top right), and numerically obtained drop shape where substrate is tilted by critical sliding angle of 32° and 20° , respectively (bottom).

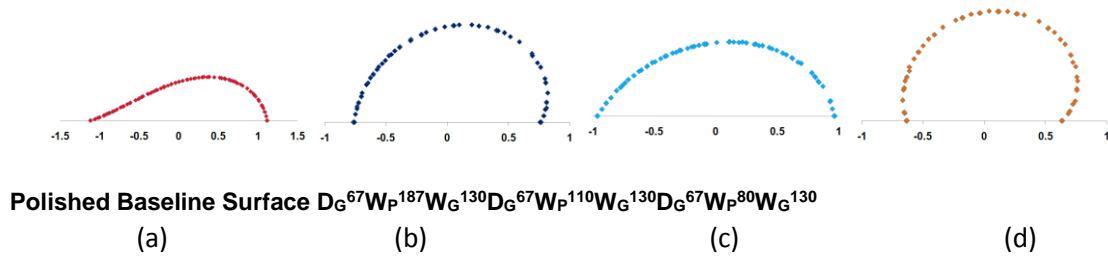


FIGURE 4. Drop shape for a drop size of $35\ \mu\text{l}$ at the point of impending motion on (a) polished baseline surface, and (b) microgrooved surface $D_G^{67}W_P^{187}W_G^{130}$, (c) microgrooved surfaces $D_G^{67}W_P^{110}W_G^{130}$ and (d) microgrooved surface $D_G^{67}W_P^{80}W_G^{130}$.

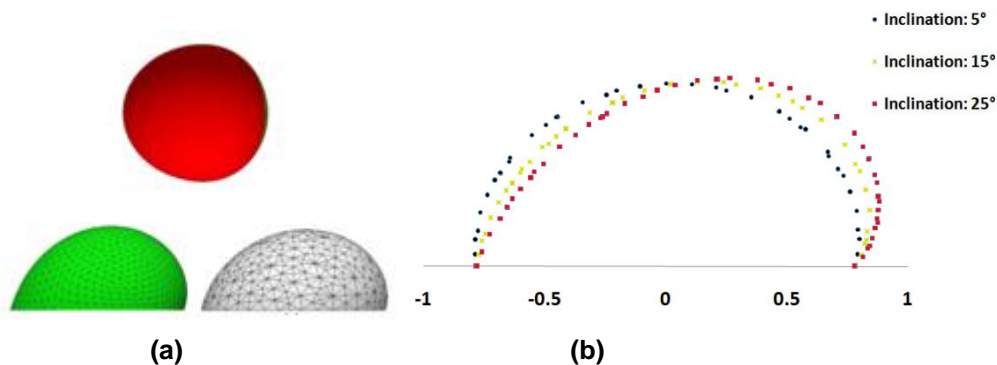


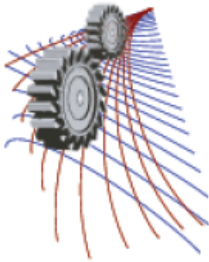
FIGURE 5. (a) Drop shape comparison at critical inclination angle by different numerical methods for sample $D_G^{98}W_P^{112}W_G^{130}$ by using azimuthal angle distribution for apparent contact angle (top), from azimuthal distribution method (bottom left), and the actual shape of the contact line using local contact angle (bottom right), and (b) Drop shape comparison at various inclination angles of the substrate ($D_G^{67}W_P^{187}W_G^{130}$) for a fixed drop size ($60\ \mu\text{l}$)

SUMMARY

A numerical model is developed to characterize the dynamic wetting behavior of the droplet on an inclined microgroove surface. This model is capable of predicting the critical sliding angle of the drop by comparing the advancing and receding angles obtained from numerical and experimental findings. The effect of microgroove geometry, droplet volume and initial conditions on the critical sliding angle is analysed and compared with the experimental findings. The experimental and the numerical results are found to be in good agreement. The shape of the triple line of the droplet is obtained by numerically calculating the vertex force at each vertex of the base contour. Correcting the base contour shape based on the local contact angles helps predict the critical sliding angle with more accuracy. Also an accurate 3D droplet shape on an inclined microgrooved surface can be obtained from this model. The knowledge of the sliding behavior and shape of the droplet on an inclined surface obtained from this simulation could be useful in many self-cleaning devices and bio-fluidic systems. This simulation can be extended further for predicting the sliding behavior of any real surface whose contact angle hysteresis range is known.

REFERENCE

1. J. F. Olivier and S. G. Mason, *Journal of Material Science* **15**,431-437 (1980).
2. N. Farhat, S. K. Alen and M. A. Rahman, *Procedia Engineering* **105**, 576-585 (2015).
3. M. A. Rahman and A. M. Jacobi, *Langmuir* **28**, 13441–13451(2012).
4. N. A. Patankar, *Langmuir* **19**, 1249-1253 (2003).
5. L. Cao, H. H. Huand D.Gao, *Langmuir* **23**, 4310-4314 (2007).
6. M.E.Abdelsalam, P.N.Bartlett, T.Kelf and J.Baumberg, *Langmuir* **21**, 1753-1757 (2005).
7. M.A.Rahman and A.M.Jacobi, *International Journal of Heat and Mass Transfer* **55**, 1596-1605 (2012).
8. A.B.D.Cassie and S.Baxter, *Transactions of the Faraday Society* **40**, 546-551 (1944).
9. N.R.Wenzel, *Ind. Eng. Chem.* **28**, 988-994 (1936).
10. M.J.Santos and J.A.White, *Langmuir* **27**, 14868-14875 (2011).
11. M. J. Santos, S. Velasco and J. A. White, *Langmuir* **28**, 11819-11826 (2012).
12. A. I. ElSherbini and A.M.Jacobi, *Journal of Colloid and Interface Science* **273**, 556-565 (2004).
13. G. Bhutani,K. Muralidhar and S. Khandekar, *Interfacial Phenomena and Heat Transfer* **1**, 29-49 (2013).
14. B. Xu, Z. Yuan and Y. Wu, *Colloids and Surfaces A: Physicochemical and Engineering Aspects* **441**, 217-225 (2014).
15. Y. Chen, B. M. Schaeffer and M. M. Weislogel, “Introducing SE-FIT: Surface Evolver- Fluid Interface Tool for Studying Capillary Surfaces,”49th AIAA Aerospace Sciences Meeting Including the New Horizons Forum and Aerospace Exposition (American Institute of Aeronautics and Astronautics, Orlando, Florida, 2011).
16. K. Brakke, *Exp. Math.* **1**, 141-165 (1992).



The Aerodynamics of Soccer Balls

Ali Alhashmi^{1, a)}, Ahmad Ali^{1, b)}, Bavin Loganathan^{1, c)}, Harun Chowdhury^{1, d)} and Firoz Alam^{1, e)}

¹*School of Aerospace, Mechanical and Manufacturing Engineering, RMIT University, Melbourne, Victoria, 3083, Australia*

^{a)}s3260842@student.rmit.edu.au

^{b)}s3259461@student.rmit.edu.au

^{c)}s3151714@student.rmit.edu.au

^{d)}Corresponding author: harun.chowdhury@rmit.edu.au

^{e)}firoz.alam@rmit.edu.au

Abstract. The game of football is world's most popular sport. The center of this popular sport is the spherical soccer ball. The aerodynamic behavior largely depends on the surface characteristics of the ball. Hence the primary objective of this study is to understand the aerodynamic behavior of a range of new generation FIFA approved Adidas balls. The seam length and seam width of each balls were determined. Each ball was tested in the wind tunnel under a range of speeds and their aerodynamic parameters such as forces and moments were measured. The drag data was analyzed and compared.

BACKGROUND

The game of soccer is the world's most popular sport [1]. The center piece of the game is the spherical ball. The soccer game has been evolved over 200 years to its current form. It is a truly world game with matches being broadcast across the globe to audiences of millions and generating billions of economic activities through participations, sponsorship and advertising. Furthermore, soccer has become one of the most regulated and standardized sports in the world with FIFA (Federation Internationale de Football Association) governing every league worldwide through its regional confederations and national associations.

The flight trajectory of the soccer ball largely depends on its aerodynamic characteristics. Depending on aerodynamic behavior, the ball can be deviated from the anticipated flight path resulting in a curved and unpredictable flight trajectory. Lateral deflection in flight, commonly known as swing or knuckle, is well recognized in cricket, baseball, golf, tennis, volleyball and soccer. Hence, the aerodynamic properties of a soccer ball are considered to be the fundamental for the players, coaches/trainers, regulatory bodies, manufacturers and even the spectators. Although, the soccer ball among all spherical sport balls traditionally has better balance, over the years, the design of soccer balls has undergone a series of technological changes, in which the ball has been tried to make more spherical by utilizing new design and manufacturing processes, Alam *et al.* [1,4].





Adidas, the official supplier of soccer balls to FIFA, has applied thermal bonding replacing traditional stitching to make a seamless surface design by using 6 curved panels instead of 32 panels in its 2014 FIFA World Cup ball. The surface structure (texture, grooves, ridges, seams, etc.) of the ball has also been altered in the process. Although the aerodynamic behavior of other sports balls have been studied by Mehta *et al.* [2] and Smits and Ogg [3], little information is available about the aerodynamic behavior of new seamless soccer balls except the experiential studies by Alam *et al.* [1, 4] and Asai and Kamemoto [5]. Studies by Goff and Carre [6] and Barber *et al.* [7] provided some insights about the effect of surface structure of 32 panel balls however no such data is available for new generation soccer balls. Therefore, the primary aim of this study is to determine the surface characteristics of several Adidas introduced FIFA approved soccer balls and understand their impacts on aerodynamic parameters.

EXPERIMENTAL PROCEDURE

Balls Physical Features

Four soccer balls manufactured by Adidas were chosen for this study and their effective dimensions have been measured. These balls are Cafusa (32 panels), Brazuca (6 panels), Tango (32 panels), and Kopanya (14 panels). The physical features are shown in Table 1.

TABLE 1. Physical features of balls.

Ball name	Ball Picture	Seam Length (mm)	Seam Depth (mm)	Number of Panels	Events
Brazuca		3,220	1.54	6	FIFA World Cup 2014 (Brazil)
Cafusa		3,600	1.52	32	Confederation Cup 2013 (Brazil)
Tango 12		3,530	1.22	32	UEFA Cup 2012 (Europe)
Kopanya		3,450	0.52	14	Confederation Cup 2009 (South Africa)

In order to determine the seam length and seam depth of each ball, two different techniques were used. These methods are Manual method and Numerical method. A 3D laser scanner was used to obtain the dimensions of the total seam length and seam depth. GeoMagic software was used to convert the mesh surface to solid surface and the measurements of the seam length for each ball were obtained using SolidWorks as shown in Figure 1. Additionally, the seam length measurements were validated using a flexible rope. Plasticine was used to determine the seam depth for all balls. The dried unplugged plasticine was used to measure the seam depth. The largest seam length was 3600 mm for Adidas Cafusa and the smallest was 3220 mm for Adidas Barzuca. The deepest observed seam was 1.54 mm for Adidas Barzuca and the least was equal to 0.52 mm for Adidas Kopanya. It is important to understand the parameters of the ball surface features, in particularly the seam depth and seam length as these two parameters can have significant effect on aerodynamic behavior of the ball. The standard air pressure (0.8 bar = 11.6 psi) was maintained for all balls in aerodynamic investigations.

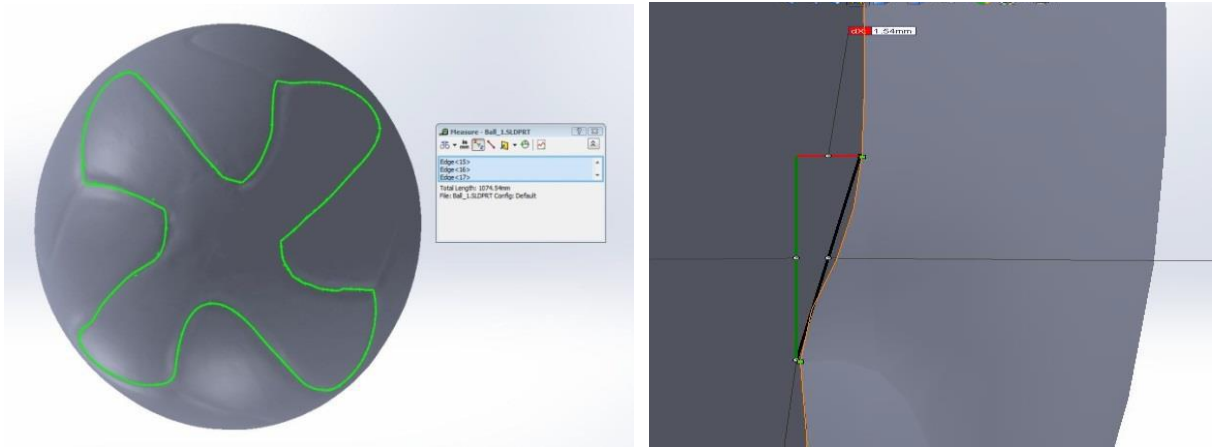


FIGURE 1. Finding seam length using SolidWorks.

TABLE 2. Measurement variation in two methods.

Ball Type	Seam Length			Seam Depth		
	Numerical Method (mm)	Manual Method (mm)	Difference %	Numerical Method (mm)	Manual Method (mm)	Difference %
Adidas Tango 12	3,530	3,550	0.57	1.22	1.15	5.91
Adidas Cafusa	3,600	3,580	0.56	1.52	1.25	19.50
Adidas Kopanya	3,450	3,470	0.59	0.52	0.40	26.09
Adidas Brazuca	3,220	3,270	1.54	1.54	1.35	13.15

As shown in Table 2, a significant variation between numerical and manual method in seam length measurements was noted. The least difference in seam length was noted for Adidas Tango 12 and the largest difference was found in Adidas Barzuca ball. For the seam depths, the largest difference was found in Adidas Kopanya whereas the smallest difference was noted for Adidas Tango 12. A comparison of seam length and seam width for all four balls is shown Figure 2.

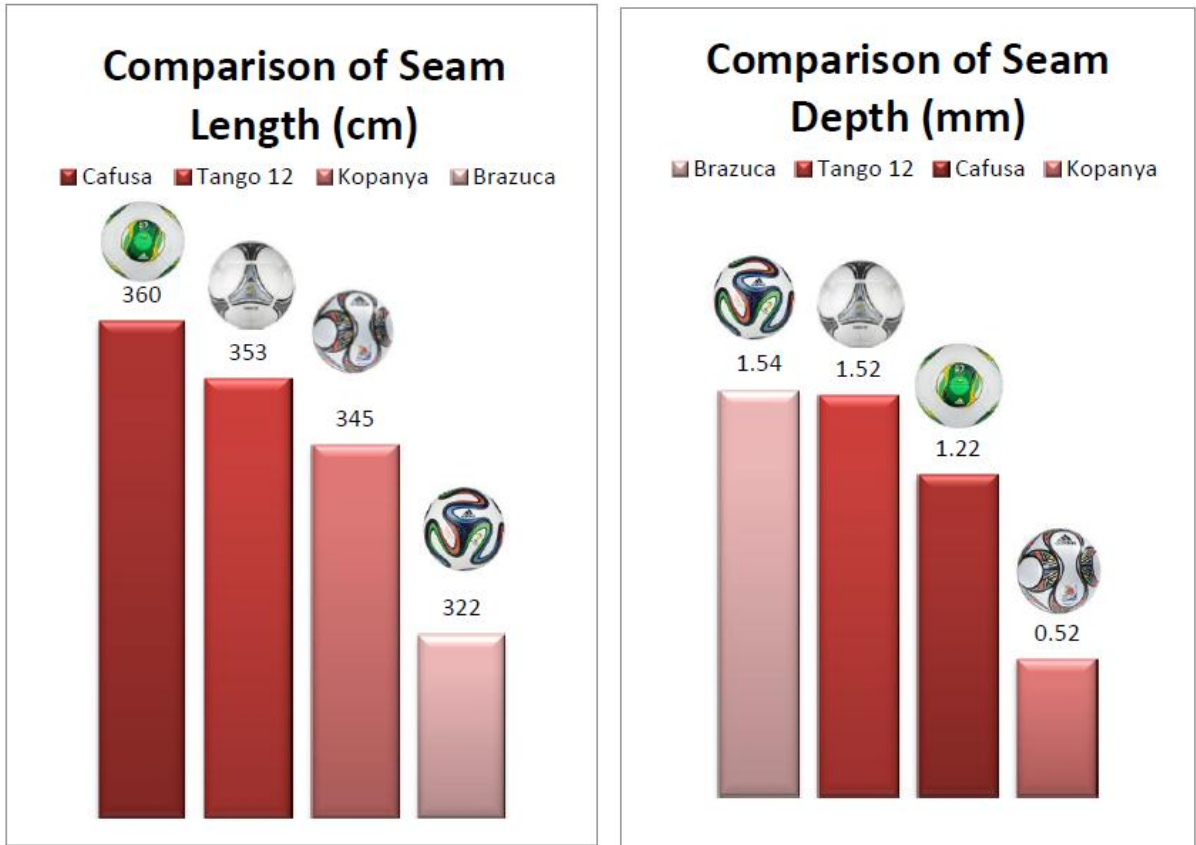


FIGURE 2. Comparison of seam length and seam depth of various balls.

Aerodynamic Investigation

In order to measure the aerodynamic properties of the soccer balls experimentally, the RMIT Aero Wind Tunnel was used. The tunnel is a closed return circuit wind tunnel with a maximum speed of approximately 150 km/h. It has a circular test section with a diameter of 1 m and is equipped with a turntable to yaw the ball. Each ball was mounted on a six component force sensor (type JR-3), and purpose made computer software was used to digitize and record all 3 forces (drag, side and lift forces) and 3 moments (yaw, pitch and rolling moments) simultaneously. A strut support was developed to hold the ball on a force sensor in the wind tunnel. The aerodynamic effect of the strut support was eliminated using an aerodynamic fairing around it as shown in Figure 3.

Two-panel orientations (side 1 and side 2) of each ball were investigated at the same wind speed to quantify any variation due to any asymmetry. Data were obtained using a six-component force sensor (manufactured by JR3 Inc., US) with the maximum capacity of $200\text{N} \pm 0.01$ and captured for 1 minute (60 seconds under 3 blocks of 20 seconds) with a sampling rate of 20 Hz. Each ball was set to be geometrically symmetrical; the ball panels were asymmetrical in the vertical direction. As an additional point, aero foil shield was installed to avoid any external interference to the result.

Each ball was tested in the wind tunnel under a range of wind speeds from 20 to 120 km/h with an increment of 10 km/h. As mentioned earlier, all 3 forces (drag, lift and side forces) and 3 moments (yaw, roll and pitch) were measured. In this paper, only drag force is presented. The measured drag force (D) was converted into a non-dimensional parameter drag coefficient C_D . The wind velocity was converted into a non-dimensional parameter Reynolds number.

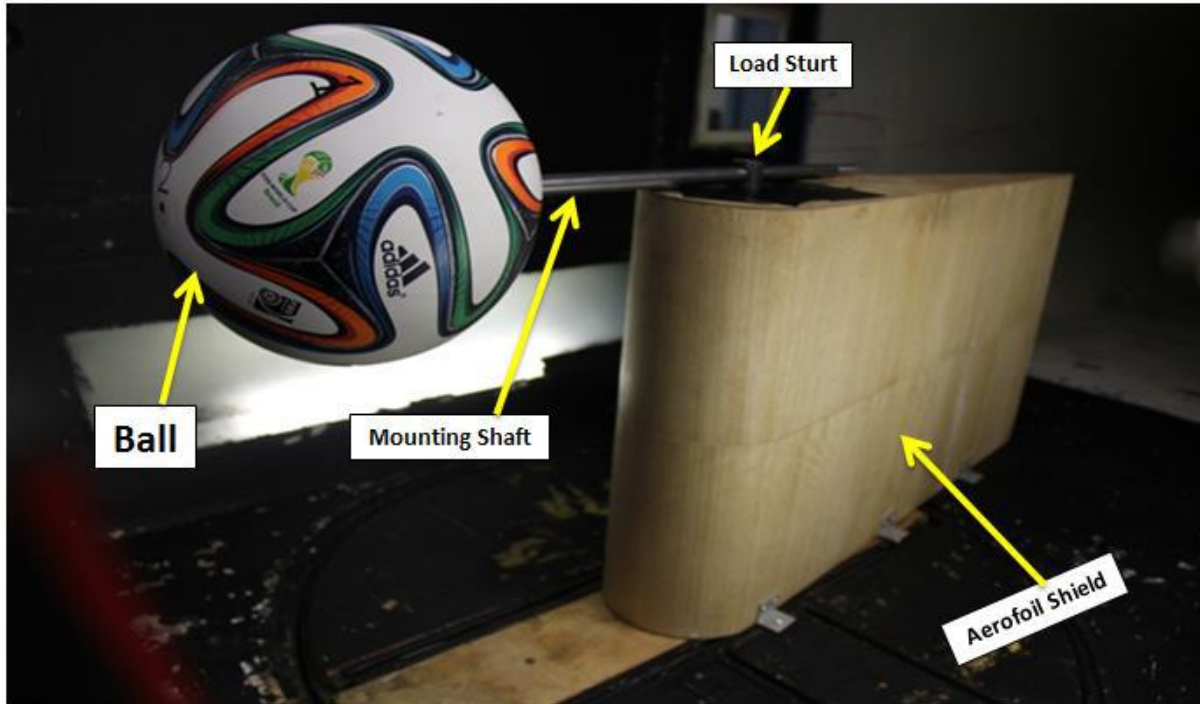
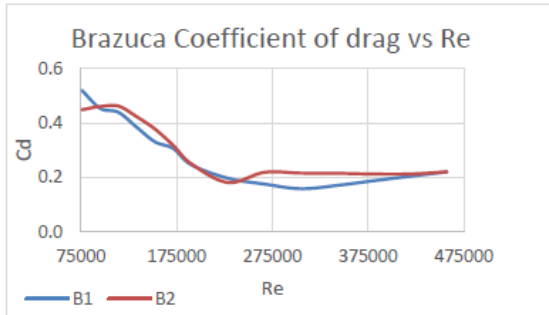


FIGURE 3. Experimental setup in wind tunnel.

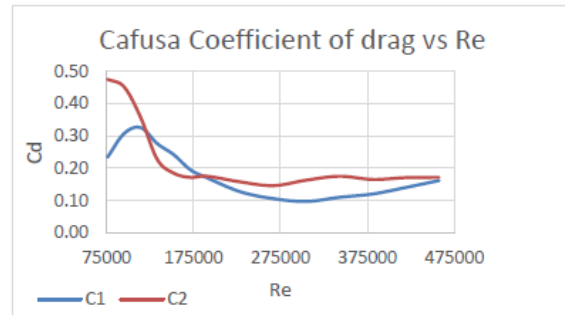
RESULTS AND DISCUSSION

Each ball as well as a sphere was tested at 20 to 120 km/h with an increment of 10 km/h. The aerodynamic drag was converted to non-dimensional parameter (drag coefficient, C_D). The influence of the support on the ball was checked and found to be negligible. The repeatability of the measured forces was within ± 0.01 N and the wind velocity was less than ± 0.1 km/h. The C_D variations with Reynolds numbers for all balls are shown in Figures 4 & 5. The variation of C_D values between two sides of each ball with Reynolds number is shown in Figure 4. The figure shows that Brazuca has the smallest difference at low speed of only 14%. The difference decreases gradually as the speed increases to have 8% at 60 km/h. At high speeds, the variation of C_D value becomes minimal. Cafusa has the longest seam length and large seam depth. It has an unstable path due to having a huge difference at 20 km/h of 103% between two orientations. As the speed increases, the difference fluctuates and reaches a 24% difference at 60 km/h. Finally drops down to 6% at high speeds (see Figure 4). Kopanya has huge difference between two panel orientations of 72% at low speed (20 km/h), however the percentage decreases as the speed increases (50% at 60 km/h). Finally, the percentage of difference reaches its minimum (18%) at the maximum speed. The results for Tango 12 appeared to be stable compared to Kopanya, having only 31% difference between two orientations at 20 km/h as the speed increases to 60 km/h. The difference decreases significantly down to only 5% and reaches 1% at the maximum speed.

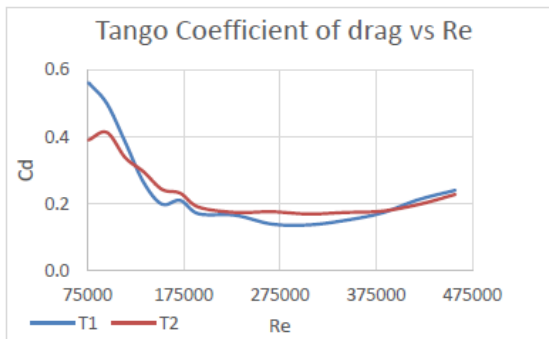
The comparison indicates that Brazuca and Tango 12 have the minimal differences in the drag coefficient (C_D) with different panel orientation. The average difference is 4% for Brazuca and 9% for Tango 12. Cafusa has rougher surface than Tango 12, apparently affecting the drag coefficient variation resulting in the balls flight trajectory and stability in the air. However, Barcuza has the most stable flight compared to other balls. On the other hand, the variation of the drag coefficient with the panel orientation was large for Cafusa and Kopanya having difference of 49% and 26% respectively. The reason behind this variation is that Kopanya has less panels and small seam depth which means the ball have smother surface roughness. Therefore, the ball knuckles more often in air. The Cafusa ball has a different situation due to its design which has 32 panels and the seams are deeper and longer which cause a big difference in drag variation.



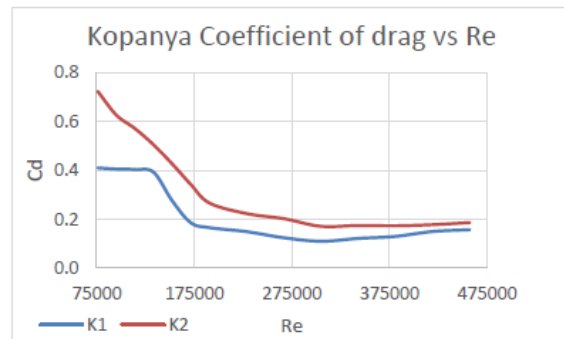
a) Variation of Cd values of two sides of Brazuca ball



b) Variation of Cd values of two sides of Cafusa ball



c) Variation of Cd vales of two sides of Tango ball



d) Variation of Cd values of two sides of Kopanya

FIGURE 4. C_D variation of two sides of the balls.

The average C_D values of two pane sides for all balls and a smooth sphere as a function of Reynolds number (varied by wind speeds) are shown in Figure 5. It is obvious that there is an enormous difference in C_D values between four balls and the smooth sphere. As shown in Figure 5, the drag coefficient of the smooth sphere is dropping significantly from Reynolds number of 1.0×10^5 to 2.0×10^5 where it drops down from 0.4 to 0.1. This drop is due to its flow transition from laminar to turbulent flow and its smooth surface roughness. The drag crisis is agreed well the published data.

The Cafusa ball has the lowest C_D value (0.40) at low Reynolds number and it has decreased to its lowest values at Reynolds number of 2.8×10^5 , then starts increasing till the maximum Reynolds number having roughly C_D value of 0.15. This indicates that Cafusa is a suitable ball in terms of minimal air resistance and it can travel a long distance.

In contrast, the Brazuca and Tango 12 balls have C_D values close to each other which are 0.48 at Reynolds number (4.6×10^4). The Tango 12 then tends to have slightly lower C_D value and fluctuates more often. However the Brazuca ball tends to have smoother decrease in C_D value without any noticeable fluctuation. Both Tango and Brazuca have highest drag at the highest speed tested (highest Reynolds number).

Finally the Kopanya starts with a highest C_D of 0.59 then as the Reynolds number increases the drag coefficient decreases rapidly from 0.59 to 0.15. Therefore, Kopanya ball will knuckles more often comparing to other three balls.

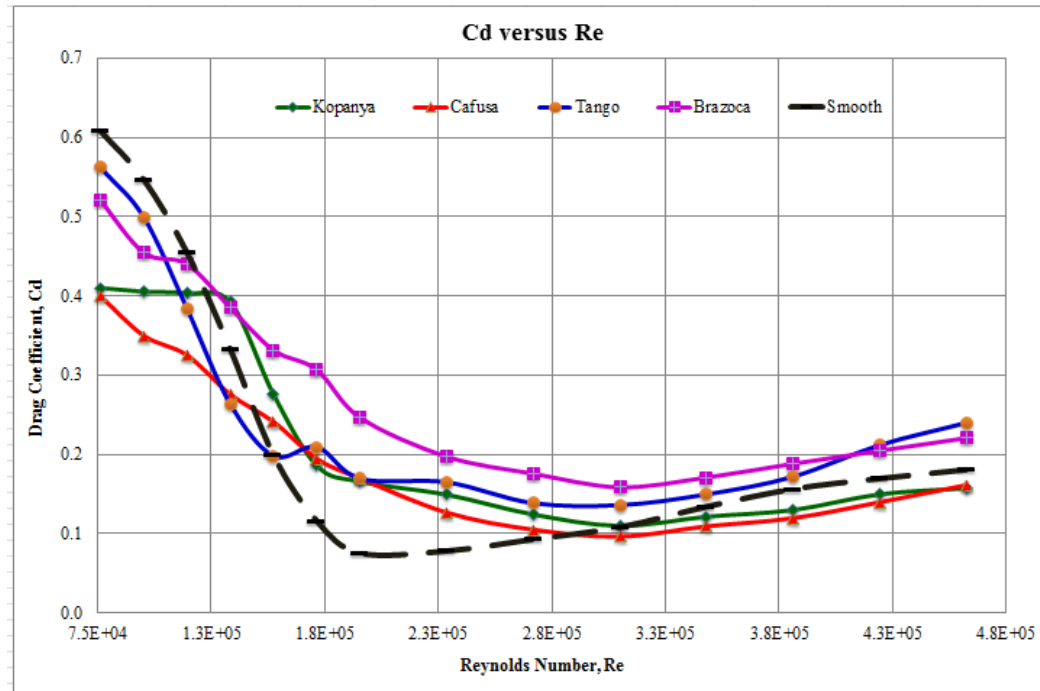


FIGURE 5. C_D variation with Reynolds number.

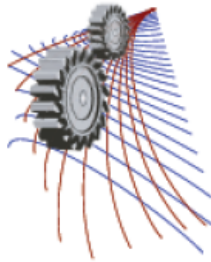
CONCLUSIONS

The following conclusions were drawn from this study:

- Seam design and seam length affect the aerodynamic parameters of a soccer ball.
- With a larger seam length and depth, the flow behavior around a soccer ball becomes more complex as they increase the surface roughness.
- The sideways variation of aerodynamic drag is minimal for Brazuca ball which indicates that this ball will have better stability in flight.
- The minimal aerodynamic drag was found for Cafusa ball at high speeds hence this ball is suitable for long distance pass. It also experiences a lower drag coefficient at transcritical stage of the turbulent flow.

REFERENCES

1. F. Alam *et al.*, *Procedia Engineering* **105**, 317–322 (2015).
2. R. D. Mehta *et al.*, *Sports Technology* **1**, 1–10 (2008).
3. A. J. Smits and S. Ogg, *The Engineering of Sport* **5** **1**, 3–12 (2004).
4. F. Alam *et al.*, *Procedia Engineering* **13**, 88–193 (2011).
5. T. Asai and K. Kamemoto, *Fluids and Structures* **27**, 727–733 (2011).
6. J. E. Goff and M. J. Carre', *European Journal of Physics* **31**, 775–784 (2010).
7. S. Barber *et al.*, *Computers & Fluids* **38**, 1091–1100 (2009).



Effect of Various Deflectors on Drag Reduction for Trucks

Harun Chowdhury^{1, a)}, Bavin Loganathan^{1, b)}, Israt Mustary^{1, c)} and Firoz Alam^{1, d)}

¹*School of Aerospace, Mechanical and Manufacturing Engineering, RMIT University, Melbourne, Victoria, 3083, Australia*

^{a)}Corresponding author: harun.chowdhury@rmit.edu.au

^{b)}s3151714@student.rmit.edu.au

^{c)}s3309329@student.rmit.edu.au

^{d)}firoz.alam@rmit.edu.au

Abstract. Aerodynamic feature of the vehicle plays a major factor related to the vehicle motion as well as the fuel consumption. However, it was noted that a significant numbers of trucks are being manufactured and operating in Asian countries especially in Bangladesh and Pakistan without any consideration of their aerodynamic aspect. Therefore, the main objective of this paper is to quantify the amount of drag generated by the deflectors used in Asian subcontinental truck especially in Bangladesh and Pakistan in a wind tunnel environment and to compare the results with a baseline truck without any external modification. The results show that the deflectors used in most Bangladeshi and Pakistani trucks manufactured locally are not aerodynamically efficient as they can increase the overall aerodynamic drag up to 58%. By replacing these deflectors with an aerodynamic one can reduce the fuel consumption by 13%.

INTRODUCTION

Trucks are the most useful vehicles for transporting goods from one place to another. Different types of trucks are operating for different purposes all over the world. Depending on their capacity and purpose, the price varies significantly. Unlike any developed countries, in some south Asian countries like Bangladesh, India and Pakistan there are still a significant number of discontinued model trucks are operating for transporting goods all over these countries because of their comparatively cheap price. Most of these trucks are Bedford J5 or J6 model first manufactured in 1968 by Hindustan Motors, an Indian company and production was stopped in 1986. However, in Pakistan and Bangladesh, the Bedford J5 or J6 is very popular and dominated commercial truck with the capacity of 5 to 6 tons. A Bedford J series truck model without any modification is shown in Fig. 1(a).

In Bangladesh and Pakistan, the main structure the chassis including, engine, wheels, transmission system and front hood of the truck is imported from neighboring India and the rest are made from local timber and wood and subsequently covered with sheet metal cladding. After the woodwork and metal cladding, the external body of the truck is decorated with structural changes, paintings, calligraphy and ornamental decor like mirror work on the front and back of vehicles and wooden carvings on the truck doors. The body of the trucks is mainly made by the local carpenters who have learned their skill by generation. They have little knowledge on the aerodynamics. They mainly focus on the aesthetic of the truck reflecting their culture. Fig. 1(b) and 1(c) show the trucks made locally in Bangladesh and Pakistan respectively. By visual inspection it can be anticipated that designed the front deflector of the theses decorative traditional trucks can increase air resistance (drag) even in low speed (below 50 km/h). As a result, more fuel will be required to overcome this extra drag simply because of the non-aerodynamic design frontal deflector of these trucks.



FIGURE 1. Full scale trucks: (a) A Bedford J series truck model without any modification, (b) Modified truck (Bangladeshi), (c) Modified truck (Pakistani).

Aerodynamic drag with a small sized truck typically accounts for about 75–80% of the total resistance to motion at 100 km/h [1]. Therefore, reducing aerodynamic drag contributes significantly to the fuel economy as well as the reduction of greenhouse gas emissions. Fuel consumption is defined as the volume of fuel used to travel a given distance. It can be specified as liters per 100 kilometers (L/100 km). Any extra structure such as front deflectors of the truck can increase the fuel consumption to a significant amount if it is not aerodynamically efficient [2].

There is a significant number of publications found in the public domain that cover aspects such as acronymic fuel saving design for trucks [3–6]. However, no study is reported on the aerodynamics of trucks designed in Bangladesh and Pakistan. Therefore, the main objective of this paper is to quantify the amount of drag generated by these deflectors used in Asian subcontinental truck especially in Bangladesh and Pakistan in a wind tunnel environment and to compare the results with a baseline truck without any external modification. Furthermore, the results will be compared with an aerodynamically efficient design for drag reduction.

EXPERIMENTAL PROCEDURE

Experimental Models

A one-eighth scale detailed model of an ISUZU truck was used as a baseline truck. Two deflectors were also manufactured replicating the design of Bangladeshi and Pakistani trucks. Also an aerodynamically efficient deflector studied by Watkins [7–8] was also used to compare the results from the baseline. The model deflectors were made one-eighth of their full size to fit with the baseline truck model. Fig. 2 shows the profile views of a baseline truck fitted with 3 different deflectors used in this study.



FIGURE 2. Baseline truck fitted with deflector: (a) Bangladeshi, (b) Pakistani, and (c) Aerodynamic.

Wind Tunnel Test

The RMIT Industrial Wind Tunnel was used for this study. The tunnel is a closed return circuit wind tunnel with a turntable to simulate the cross wind effects. The maximum speed of the tunnel is approximately 145 km/h. The

rectangular test section dimensions are 3 meters wide, 2 meters high and 9 meters long, and the tunnel's cross sectional area is 6 square meters. More details of this wind tunnel can be found in [6]. The tunnel was calibrated prior conducting the experiments and air speeds inside the wind tunnel were measured with a modified National Physical Laboratory (NPL) ellipsoidal head pitot-static tube (located at the entry of the test section) which was connected through flexible tubing with the Baratron[®] pressure sensor made by MKS Instruments, USA.

The truck model was connected through a mounting sting with the JR3 multi-axis load cell made by JR3, Inc., USA. The sensor was used to measure all three forces (drag, lift and side forces) and three moments (yaw, pitch and roll) simultaneously. Fig. 3 shows the schematic of the experimental setup. For baseline comparison, initially the aerodynamic forces were measured for the baseline truck without any external attachment (i.e., deflector) under a range of wind speeds (40-120 km/h) at 0° yaw angle. Then the measurements were taken by attaching the Bangladeshi, Pakistani and aerodynamic deflectors on the baseline truck. Each set of data was recorded for 10 seconds time average with a frequency of 20 Hz ensuring electrical interference is minimized. Multiple data sets were collected at each speed tested and the results were averaged for minimizing the further possible errors in the raw experimental data. Experimental model inside the RMIT Industrial Wind Tunnel is shown in Fig. 4.

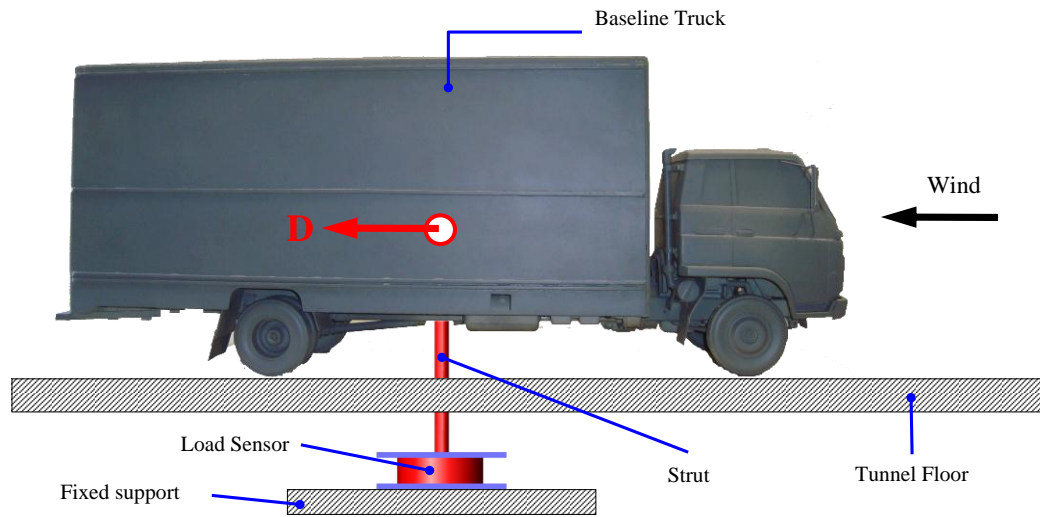


FIGURE 3. Schematic of the experimental setup.

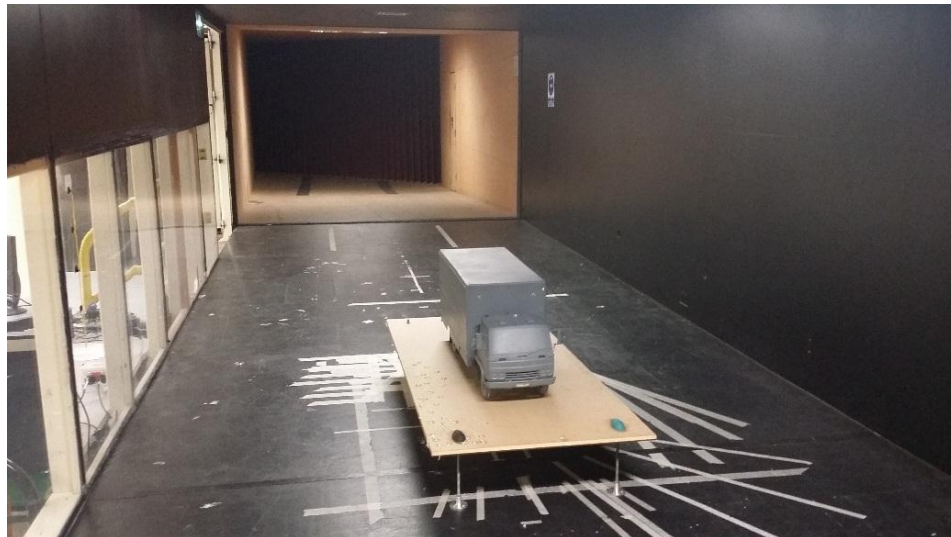


FIGURE 4. Experimental setup inside the test section of RMIT Industrial Wind Tunnel.

RESULTS AND DISCUSSION

In this paper, only drag force (D) data and its dimensionless quantity drag coefficient (C_D) are presented. The C_D was calculated by using the following formula:

$$C_D = \frac{D}{\frac{1}{2} \rho V^2 A} \quad (1)$$

The C_D as a function of speed for various configurations of truck at 0° yaw angle is presented in Fig. 5. The result shows that the baseline truck has almost constant C_D value about 0.47. Similar results were found by Watkin at al. [8]. In this study, the C_D values of truck ranges between 0.41 and 0.51 depending on the aerodynamic design of the front deflector. The baseline truck with the aerodynamic deflector attached has the lowest C_D value among all other configurations tested.

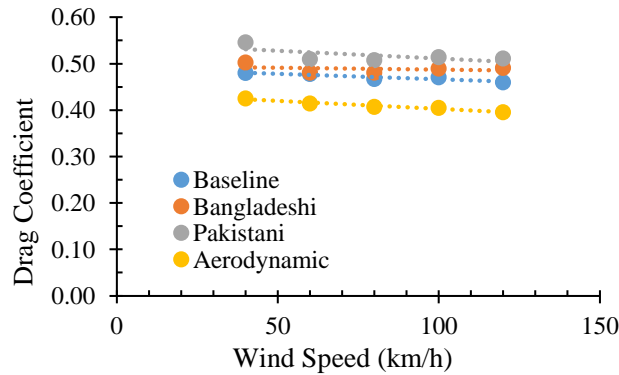


FIGURE 5. Drag coefficient (C_D) as a function of speed.

Fig. 6 represents the front view of the test truck with 4 different configurations tested. It can be seen that the Bangladeshi (b) and Pakistani (c) deflector models increased the projected frontal area of the baseline truck (a) while the aerodynamic deflector (d) projected frontal area remains the same as the baseline truck projected frontal area.

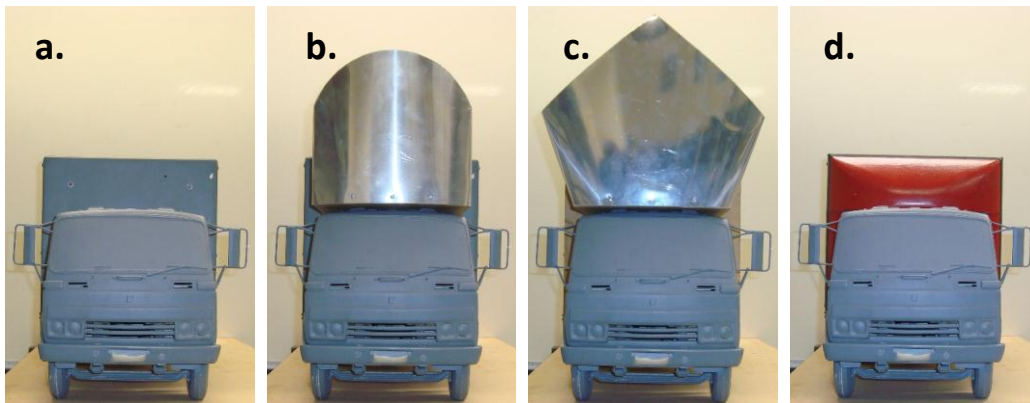


FIGURE 6. Frontal views: (a) baseline truck, (b) with Bangladeshi faring, (c) with Pakistani faring, (d) with aerodynamic fairing.

The results shown in Fig. 7 indicate that about 13% drag reduction is possible by attaching an aerodynamic front deflector on the baseline truck. On the other hand, drag increased by around 33% and 56% when the truck was modified with a Bangladeshi and Pakistani truck deflectors respectively. The increase of drag also impacts on the fuel consumption. Additionally, the non-aerodynamic design of such Asian trucks can also impact the directional stability as the vehicle's center of gravity changes and the overall lift is reduced due to the disturbance of the flow over the roof [1].

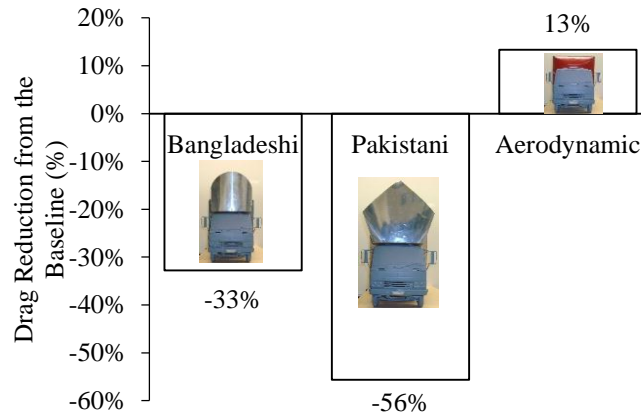


FIGURE 7. Drag reduction (%) from the baseline truck.

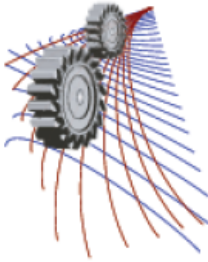
Furthermore, the intricate external design of the truck deflectors also contributes to wind noise and dirt deposition. These with not only increase the fuel consumption and running cost but also significantly accelerate deterioration of air quality. Additionally, the increased fuel consumption creates extra pressure on national energy security. As of 2009, the world burnt over 1.3 trillion liters of petrol and diesel each year for powering hundreds of millions cars and trucks. A study by Snyder [9] indicated that in the US, if it was possible to reduce fuel consumption by as little as 1% (which typically equates to merely 0.1 L/100 km for a standard car), US \$30 million could be saved annually. Additionally, the economic benefit of fuel consumption reduction is an important environmental benefit.

CONCLUSIONS

A significant numbers of trucks are manufactured in Asian countries especially in Bangladesh and Pakistan without any consideration of their aerodynamic aspect. The results shows that the deflectors used in most Bangladeshi and Pakistani trucks manufactured locally are not aerodynamically efficient as they can increase the overall aerodynamic drag up to 58%. By replacing these deflectors with an aerodynamic one will not only save fuel consumption but also reduce significant amount of greenhouse gas emissions.

REFERENCES

1. W. H. Hucho, *Aerodynamics of Road Vehicles, 4th edition*, Warrendale: Society of Automotive Engineers (SAE), 1998.
2. H. Chowdhury *et al.*, *Procedia Engineering* **49**, 294-302 (2012).
3. K.R. Cooper, SAE Publication. SAE Paper No. **2006-01-3456**, (2006).
4. D. Landman *et al.*, SAE Publication. SAE Paper No. **2009-01-2890**, (2009).
5. R.E. Schoon, SAE Publication. SAE Paper No. **2007-01-4294**, (2007).
6. H. Chowdhury *et al.*, *Procedia Engineering* **56**, 201–205 (2013).
7. S. Watkins, “Wind-Tunnel Modelling of Vehicle Aerodynamics: with Emphasis on Turbulent Wind Effects on Commercial Vehicle Drag,” Ph.D. Thesis, RMIT University, 1990.
8. S. Watkins *et al.*, SAE Publication. SAE Paper No. **870717**, (1987).
9. R.H. Snyder, SAE Special Publication. SAE Paper No. **74**, (1997).



Effect of Blade Gaps on the Performance of a Cyclonic Vertical Axis Wind Turbine

Bavin Loganathan^{1, a)}, Harun Chowdhury^{1, b)} and Firoz Alam^{1, c)}

¹*School of Aerospace, Mechanical and Manufacturing Engineering, RMIT University, Melbourne, Victoria, 3083, Australia*

^{a)}s3151714@student.rmit.edu.au

^{b)}Corresponding author: harun.chowdhury@rmit.edu.au

^{c)}firoz.alam@rmit.edu.au

Abstract. The primary objective of this paper is to investigate the effect of the distance between two subsequent blades on the torque on a cyclonic domestic scale vertical axis wind turbine with semi-circular shaped blades under a range of wind speeds. An 8, 16, 24 and 32-bladed rotor with corresponding distance between 2 subsequent blades of 70mm, 35mm, 17.5mm and 9mm, was initially designed and its torques and angular speeds were measured over a range of wind speeds using a wind tunnel. A cowling device was then developed to enhance the turbine efficiency by directing the air flow from the rear blades into the atmosphere. Maximum power curves as a function of wind speeds were established for each configuration. The results show that the number of blades and the corresponding distance between the subsequent blades have an effect on the torque. The max torque was produced at the distance of 17.5 mm (distance between 2 subsequent blades) at all corresponding wind speeds (15km/h to 40km/h). The average torque increased by about 55% for the 24 bladed rotor compared with the 8 bladed rotor (the least torque producing rotor). The result also indicated that the ideal number of blades for the Cyclonic Vertical Axis Wind Turbine is 24 blades with a distance of 17.5 mm in between 2 subsequent blades.

INTRODUCTION

The benefits of renewable energy industry have been clearly stated and defined in numerous literatures and studies. These industries not only produce clean energy but also help create millions of new jobs and highly skilled professionals [1–4]. In urban and built-up area, the atmospheric wind becomes highly turbulent and exhibits significant fluctuations of gust speed and high variability of wind direction caused by the urban structures and buildings. Under such conditions, existing HAWTs are not effective power generators [5–6]. On the other hand, despite having some advantages (fewer moving parts, lower tip speed ratio, quieter, lower cost, & insensitive to wind direction) over HAWT, VAWTs currently used in urban applications do not produce much more appreciable power [7–8]. One of the major limitations of current VAWTs is the negative torque. This restricts the rotor from accelerating to higher torque producing speeds. There are two ways this negative torque is produced. The first negative torque is produced on the returning blade (convex side). The second negative torque is produced on the rear blades when the swept airflow moves through the rotor and tries to exit at the rear. This exiting airflow impedes the returning blade. In addition, the exiting air stream is directed back into the path of the approaching wind, creating a turbulent zone which not only introduces losses and minimizing efficiency, but also creates pressure fluctuations that cause vibrations in the rotor and the surrounding mountings.

Researches have tried to improve the performance of VAWT. Saha *et al.* [9] studied the effect of 2 to 3 blades in 1, 2 and 3 stage rotor systems and observed that power coefficient decreased when the number of blades increased from 2 to 3. Fujisawa [9] investigated the overlaps ratios especially on the returning blades and found the torque and power reached a maximum at an overlap ratio of 0.15. Mohamed *et al.* [10] studied the effect of using obstacle shields and reported an increase of power output efficient by 27.3% and a higher gain in torque coefficient. Ogawa

et al. [11] examined the effect of flow deflector plate and found that the rotor power increases nearly 30 percent. Irabu and Roy [12] studied the effect of surrounding the turbine with a guide box and found increases about 1.5 times with three blades and 1.23 times with two blades greater than that without guide-box tunnel, respectively. Altan *et al.* [13] found that the maximum power coefficient of the Savonius wind rotor is increased to about 38.5% with the optimum curtain arrangement.

This study builds on top of a previous work carried out by Loganathan *et al.* [14] and Chowdhury *et al.* [15] using RMIT Industrial wind tunnel. A novel concept of Cyclonic Vertical Axis Wind Turbine (CVAWT) which diverts the incoming wind upward and makes use of the stack effect to extract more wind power as it exits through a cowling system. The CVAWT was tested with two configurations over a range of wind speeds (20 to 45 km/h). The first configuration was the 8 bladed rotor with cowling and the other configuration was the 16 bladed rotor with a cowling. The results show that the cowling device has positive effect to increase the rotor speed to a significant amount. With the use of the cowling device, the average rotor speed increased by about 26% for the 16-bladed rotor compared to the baseline configuration. A significant increase (about 40%) of rotor speed was also found for the 8-bladed rotor with the cowling device. However, the study did not consider the effect of the distance between 2 subsequent blades on the torque on a cyclonic vertical axis wind turbine which is an important parameter to determine the possible power generation by a wind turbine. Therefore, the main purpose of this study is to measure the power output of a model CVAWT for four different configurations (number of blades) with cowling.

EXPERIMENTAL PROCEDURE

The Savonius blades were modelled on a variation of classic Savonius rotor. The VAWT used for this study is a semicircle shaped blade made from fiber glass material. Detailed dimensions of the blade are shown in Fig. 1(a).

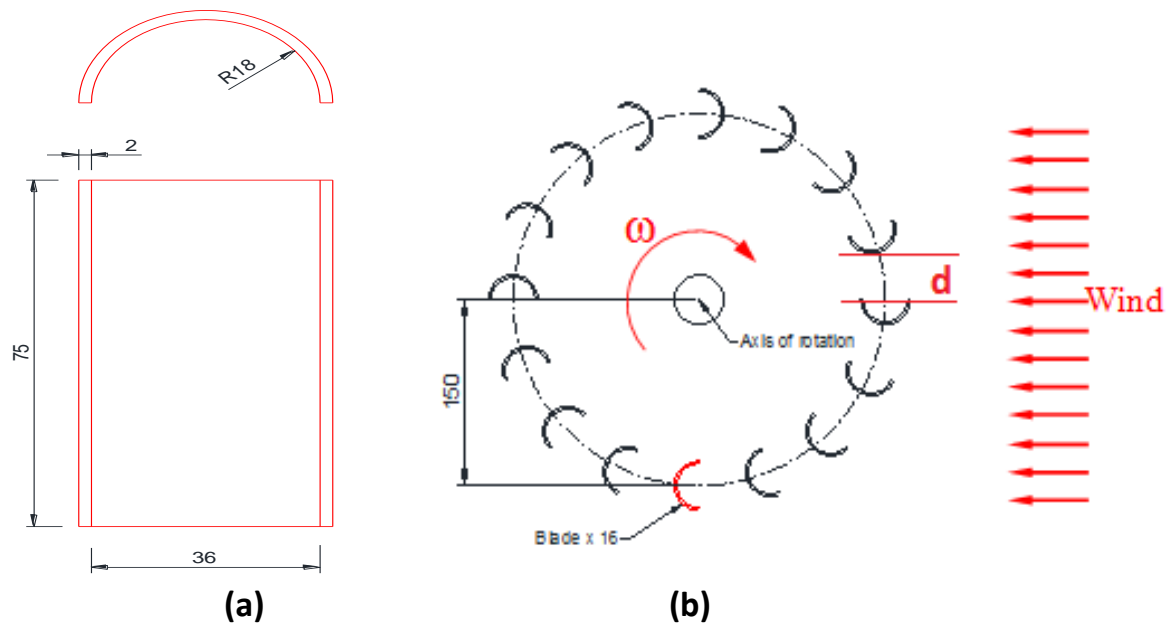


FIGURE 1. (a) Dimensions (mm) of the semicircle shaped wind turbine blade; (b) Top view of 16-bladed wind turbine rotor.

The blades are mounted in between two circular discs providing equal space. The rotor radius is 150 mm. Four rotors: one with 8, 16, 24 and 32 blades was constructed. The schematic of the rotors are shown in Fig.1 (b). Fig. 2 shows the prototype model of the assembly for the 8, 16, 24 and 32-bladed turbine rotor.

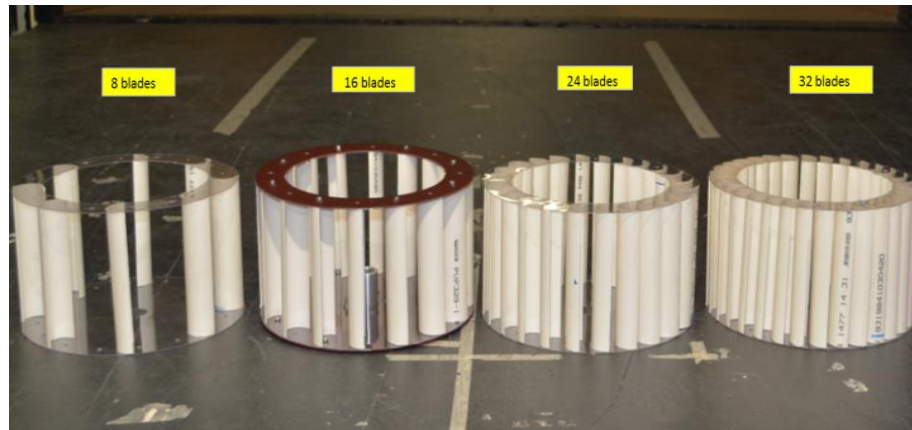


FIGURE 2. Prototype of the turbine rotors.

To determine the effect of cowling device on the performance of the wind turbine, a cowling was designed in such a way that it can enclose the turbine rotor with a small clearance and can guide the incoming wind through a defined inlet and push the rotor and finally channel out the wind through the confined outlet to the environment. The main function of the cowling is to eliminate the negative torques which prevents the rotor from accelerating to higher torque producing speeds. The cowling was constructed with two hollow PVC cylinders. The outer cylindrical shell is 360 mm in diameter and half of its frontal area is kept closed to prevent the incoming wind hitting the convex side of the returning blade. The inner shell with 160 mm diameter has an opening to allow the swept wind to exit the turbine through the top instead of at the rear to eliminate the second negative torque. Fig. 3(a) shows the 3D model of the cowling and Fig. 3(b) represents the rotor fitted with the cowling.

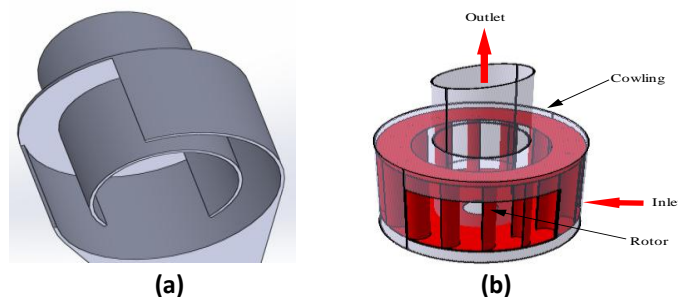


FIGURE 3. (a) Cowling device; (b) Wind turbine rotor including the cowling.

The RMIT Industrial Wind Tunnel was used to measure the torque and rpm of the wind turbine. The tunnel is a closed return circuit wind tunnel. The maximum speed of the tunnel is approximately 145 km/h. The rectangular test section dimensions are 3 meters wide, 2 meters high and 9 meters long, and the tunnel's cross sectional area is 6 square meters. More details of this wind tunnel can be found in [15]. The tunnel was calibrated prior conducting the experiments and air speeds inside the wind tunnel were measured with a modified National Physical Laboratory (NPL) ellipsoidal head pitot-static tube (located at the entry of the test section) which was connected through flexible tubing with the Baratron[®] pressure sensor made by MKS Instruments, USA.

The experimental turbine model was connected through a mounting sting with the torque transducer (model: T20WN, manufactured by HBM GmbH, Germany) and a mechanical breaking system through a circular rod and bearing supports. Fig. 4 (a) shows the schematic of the experimental setup. The setup was positioned at the middle of the wind tunnel test section and fixed properly on top of the wind tunnel floor to minimize vibration which may cause measurement errors. The setup was positioned 150 mm above the tunnel floor to minimize boundary layer effect. Fig. 4 (b) shows the experimental setup inside the RMIT Industrial Wind Tunnel.

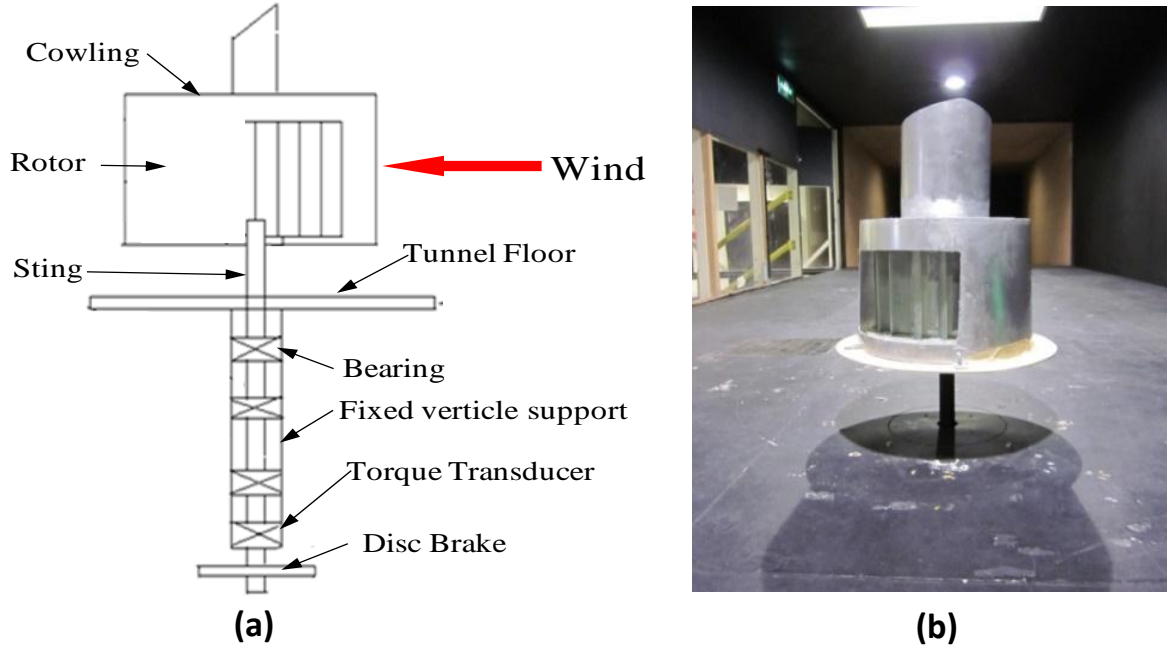


FIGURE 4. (a) Schematic of the experimental setup; (b) Experimental setup inside the RMIT Industrial Wind Tunnel.

Tests were conducted at a range of wind speeds (15 to 40 km/h with an increment of 5 km/h). The torque transducer has the maximum capacity of 5 kN with 0.01% accuracy. Data logging software supplied by the torque transducer manufacturer was used to log the data (i.e., speed and torque). Each measurement was taken three times for each configuration and wind speed tested and the average values were presented in this study. The minimum wind speed was constrained by the ability of the turbine to overcome bearing friction and inertia. The upper limit of wind speed was limited by safety consideration due to structural resonant vibrations. Maximum torque at each speed tested was analyzed to calculate the maximum power using the following formula:

$$P = T\omega \tag{1}$$

An 8, 16, 24 and 32-bladed rotor with corresponding distance between 2 subsequent blades of 70mm, 35mm, 17.5mm and 9mm, was initially designed and its torques and angular speeds were measured over a range of wind speeds using a wind tunnel.

TABLE 1. Distance between blades.

No of blades	Distance (mm)
8-blade (WC)	70
16-blade (WC)	35
24-blade (WC)	17.5
32-blades WC	9

RESULTS AND DISCUSSION

Fig. 5 (a) shows the variation of torque with rotor speeds at 15, 20, 30 and 40 km/h wind speeds. It can be observed that the torque value increases with the increase of wind speed. The results show that the rotor solidity has an effect on the torque. The max torque was produced at the distance of 17.5 mm (distance between 2 subsequent blades) at all corresponding wind speeds (15–40km/h). Fig. 5 (b) shows the development of mathematical equation based on empirical data.

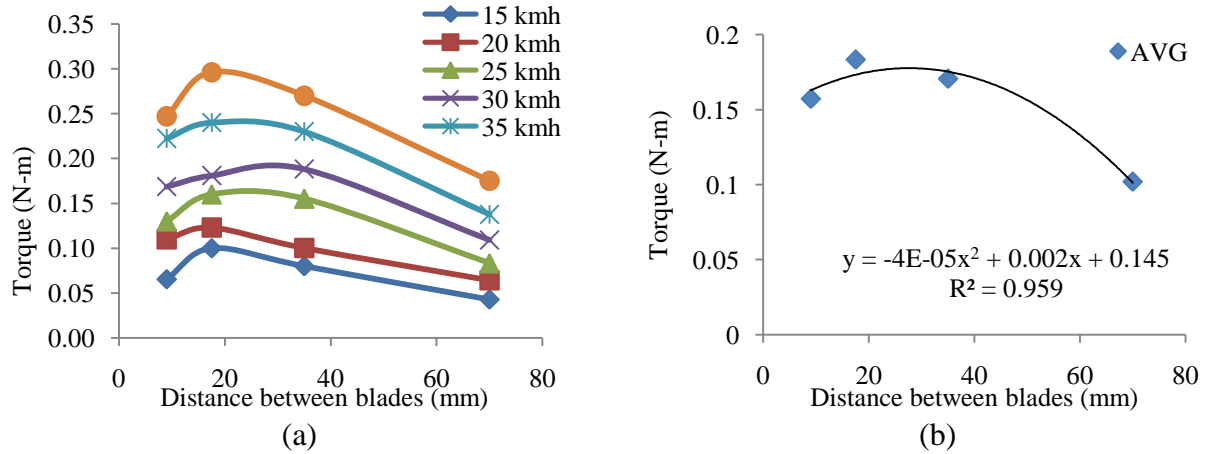


FIGURE 5. (a) Torque vs Distance between blades; (b) Torque vs Distance between blades.

$$T = 4^{-5} d^2 + 0.002d + 0.1453 \quad (2)$$

This equation (2) can predict the torque output thus eliminates the need to guess the number of blades. Where, T is torque and d is the gap between two subsequent blades.

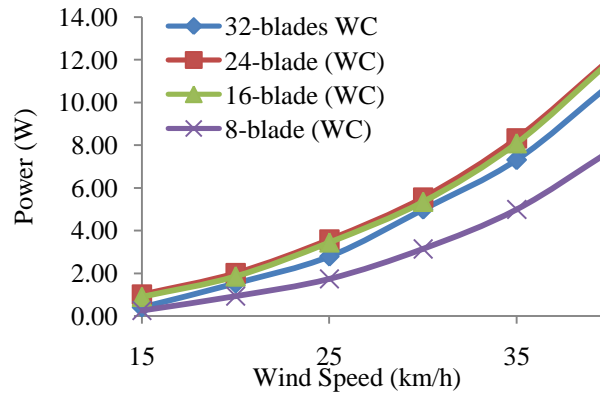


FIGURE 6. Maximum power as a function of wind speeds.

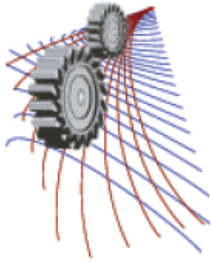
Fig. 6 represents the maximum power curves for 4 configurations of turbine tested. It is found that 24 bladed wind turbine with cowling produced the highest power at each wind speeds. The 8 bladed rotor with cowling produced the lowest power. However, the 16 bladed rotor with cowling produced an average of only around 6% lower power compared to the 24 bladed turbine. Taking into consideration of extra weight (more number of blades) and the cost, the 16 bladed turbine with cowling is the most efficient configuration.

CONCLUSIONS

The results show that the number of blades and the corresponding distance between the subsequent blades have an effect on the torque. The max torque was produced at the distance of 17.5 mm (distance between 2 subsequent blades) at all corresponding wind speeds (15–40 km/h). The average torque increased by about 55% for the 24 bladed rotor compared with the 8 bladed rotor (the least torque producing rotor). The result also indicated that the ideal number of blades for the Cyclonic Vertical Axis Wind Turbine is 24 blades with a distance of 17.5 mm in between 2 subsequent blades. However it was found that the 16 bladed rotor with cowling was the most cost effective system.

REFERENCES

1. <http://www.epa.gov/statelocalclimate/state/topic>
2. A. C. Hansen and C. P. Butterfield, Annual Review of Fluid Mechanics **25**, 115-149 (1993).
3. H. Hirahara *et al.*, Renewable Energy **30**, 1279-1297 (2005).
4. R. Howell *et al.*, Renewable Energy **35**, 412-422 (2010).
5. K. Pope *et al.*, Renewable energy **35**, 2102-2113 (2010).
6. A. D. Sahin, Progress in Energy and Combustion Science **30**, 501-543 (2004).
7. A. Ali *et al.*, "A review of power generation from wind in Australia", in *Proceedings of the 9th International Conference of Mechanical Engineering*. (ICME, Dhaka, 2011), pp. 18-20.
8. **Victorian Consumer Guide to Small Wind Turbine Generation, *Sustainability Victoria*, 1-59, July 2010.**
9. S. Saha, *et al.*, Journal of Wind Engineering and Industrial Aerodynamics. **96**, 1359-1375 (2008).
10. F. Fujisawa, J. Wind Engg. And Ind. Aerodyn. **40**, 277-292 (1992).
11. M. H. Mohamed *et al.*, Renewable Energy **35**, 2618-2626 (2010).
12. T Ogawa and H. Yoshida, Bulletin of JSME **29**, 2115-2121(1986).
13. K. Irabu and J. N. Roy, Experimental Thermal and Fluid Science **32**, 580-586 (2007).
14. B. D. Altan and M. Atilgan, Energy conversion and management **49**, 3425-3432 (2008).
15. B. Loganathan *et al.*, Procedia Engineering **105**, 686-691 (2015).
16. H. Chowdhury *et al.*, Procedia Engineering **105**, 692-697 (2015).



Aero-Acoustic Noise Analysis of 3D Wind Turbine

Ziaul Huque^{1, 3, a)}, Kyoungsoo Lee^{3, b)}, Raghava Kommalapati^{2, 3, c)},
Shrabanti Roy^{1, 3, d)}, Chao Sui^{1, 3, e)} and Nazia Munir^{1, 3, f)}

¹Department of Mechanical Engineering, Prairie View A&M University, Prairie View, TX 77445, USA

²Department of Civil & Environmental Engr., Prairie View A&M University, Prairie View, TX 77445, USA

³Center for Energy and Environmental Sustainability, Prairie View A&M University, Prairie View, TX 77445, USA

Corresponding author: ^{a)}zihuque@pvamu.edu

^{b)}kylee@pvamu.edu

^{c)}rrkommalapati@pvamu.edu

^{d)}rshrabanti@pvamu.edu

^{e)}suichao@pvamu.edu

^{f)}nmunir@pvamu.edu

Abstract. This paper aims at predicting the noise generated by flows interacting with wind turbine blade using Computational Aero-Acoustic (CAA) simulation which were performed by the unstructured Large-Eddy simulation (LES) coupled with a hybrid integral Ffowcs Williams-Hawkings (FW-F) technique for far-field noise prediction using commercial CFD software STAR-CCM+. The National Renewable Energy Laboratory (NREL) Phase VI wind turbine was considered as model. Even though the Mach number is low for wind turbine, the volumetric quadrupole noise source was also considered in rotating blade. The initial aerodynamic fluid field domain was verified using steady 3D Computational Fluid Dynamics (CFD) with RANS simulation. The unsteady LES simulations were performed to predict mid to far field noise level considering rigid body motion of rotating blade. The reference and rotating domain concepts were considered. The surface total noise term, which includes the thickness and pressure loading terms, were obtained efficiently. The tonal and the broadband components of the acoustic pressure spectrum were resolved successfully. The obtained volumetric quadrupole noise sound levels were compared with surface term. But those results were found to have large discrepancies between reference and rotation domain types.

INTRODUCTION

Noise radiated from Horizontal Axis Wind Turbine (HAWT) [1,2], is one of the major environmental issues related to wind turbine. It is considered as one of the main design objectives for commercial wind turbines and has been considered as a challenging research topic for past three decades [3,4]. The noise emitted from wind turbine are mainly from two types of sources: mechanical and aerodynamic sources. The sources of mechanical sounds are the gears and bearing used in the wind turbine. It has been reduced over the past several years by using proper insulation around the gearbox. But the aerodynamic noise is still a matter of concern. The aerodynamic noise can be classified according to the frequency range: low frequency tonal noise and high frequency broadband noise. The low frequency tonal noise is mainly due to the disturbance of flow caused by rotating blade (thickness noise) and associated pressure field (loading noise). The high frequency broadband noise is caused by the interaction of turbulent flow with the blades. The aerodynamic noise from wind turbine has become a serious problem for the people living near the wind turbines. It is a problem that should be considered in the design process rather than correcting during the production and testing stages.

The aim of this paper is to predict the noise generated by flows interacting with wind turbine blade using Computational Aero-Acoustics (CAA) [5-7]. The far field noise prediction was done by using commercial CFD software STAR-CCM+. For this reason, the unstructured Large-Eddy Simulation (LES) was coupled with

hybrid integral Ffowcs Williams-Hawkings (FW-F) model. The STAR-CCM+ can resolve the tonal and the broadband components of acoustic pressure spectrum and the FW-H enables the efficient propagation of pressure in acoustic far-field without numerical dispersion. The surface noise term, which is the combination of surface loading term and thickness term, is determined along with the quadratic volumetric noise level. Before performing the numerical simulation of wind turbine noise characteristic, the initial aerodynamic fluid domain was verified using 3D CFD with RANS simulation for the well known National Renewable Energy Laboratory (NREL) phase VI wind turbine [1-2]. A 3D CAD model of NREL phase VI wind turbine was developed. A constant rotational speed (72 rpm) and seven upwind speeds (5m/s, 7m/s, 10m/s, 13m/s, 15m/s, 20m/s, 25m/s) are considered to evaluate the aerodynamic noise characteristic.

METHODOLOGY

In this study LES simulation was used for unsteady transient simulations with hybrid FW-F technique for mid to far-field noise prediction. Before performing the CAA simulation, the fluid domain was first verified using 3D CFD RANS simulation. For this purpose, 3D CAD model of NREL phase VI wind turbine was used. Figure 1(a) shows the 3D CAD model of NREL phase VI wind turbine. The blade was divided into sixteen sections. These sections are used to develop the taper and twist of the blade surface. The pitch and twist axis is assigned to 30% chord (Fig. 1(b, c)). Figure 1(d) shows the nonlinear twist angle and Fig. 1(e) shows the linear taper value along the span in the sixteen sections. The blade has NREL S809 airfoil section from root to tip. The S809 has well documented wind tunnel databases. Carbon fiber D-spar and aramid honeycomb were used in the S809 airfoil section. The Poly Vinyl Chloride (PVC) pipes were used to carry the instrumentation wires. Fig. 1 shows a cross section of the S809 airfoil.

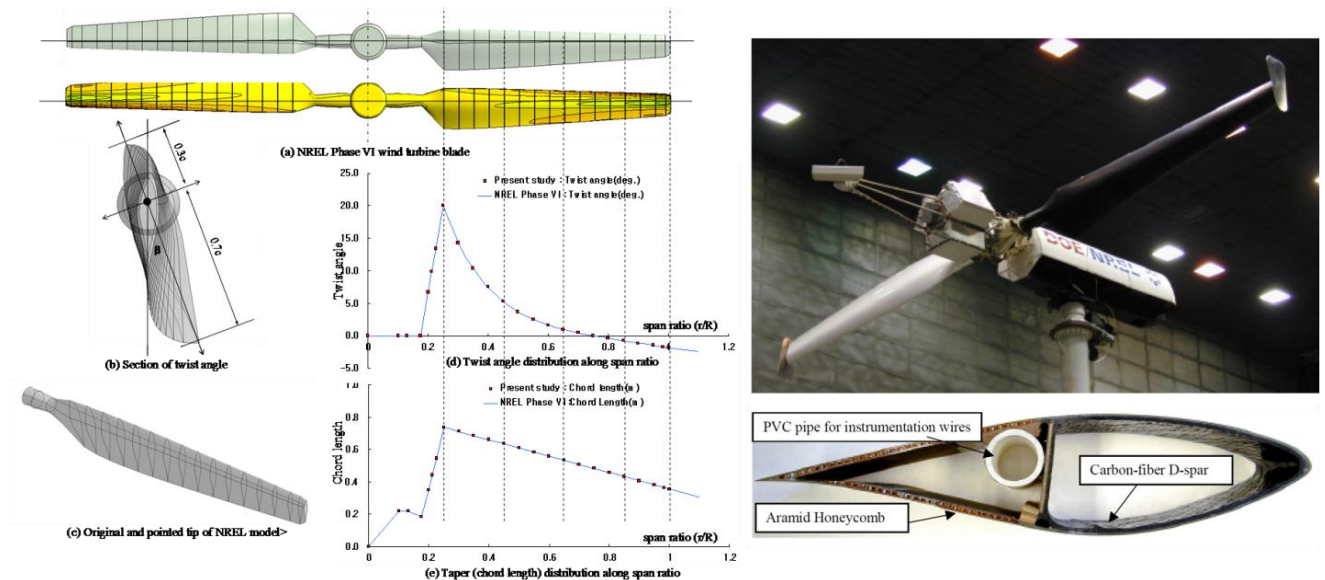


FIGURE 1. 3D CAD model of NREL Phase-VI blade with taper and twist distribution

The computational area was divided into two domains. One is a rotating domain (cylindrical), and the other is an ambient domain (rectangular). The cylindrical domain has a diameter of 12m and a length of 18m. The dimensions of the ambient domain are 30m×20m×20m. The ambient domain is used to create equivalent environments of flowing air at different wind speeds over the blade. Seven wind speeds ranging from 5m/s to 25m/s are applied at the inlet of the ambient domain. The computational domain for the wind turbine is shown in Fig. 2. After the steady RANS simulation unsteady CAA was done using unstructured Large-Eddy Simulation (LES) coupled with hybrid integral Ffowcs Williams-Hawkings (FW-F) method.

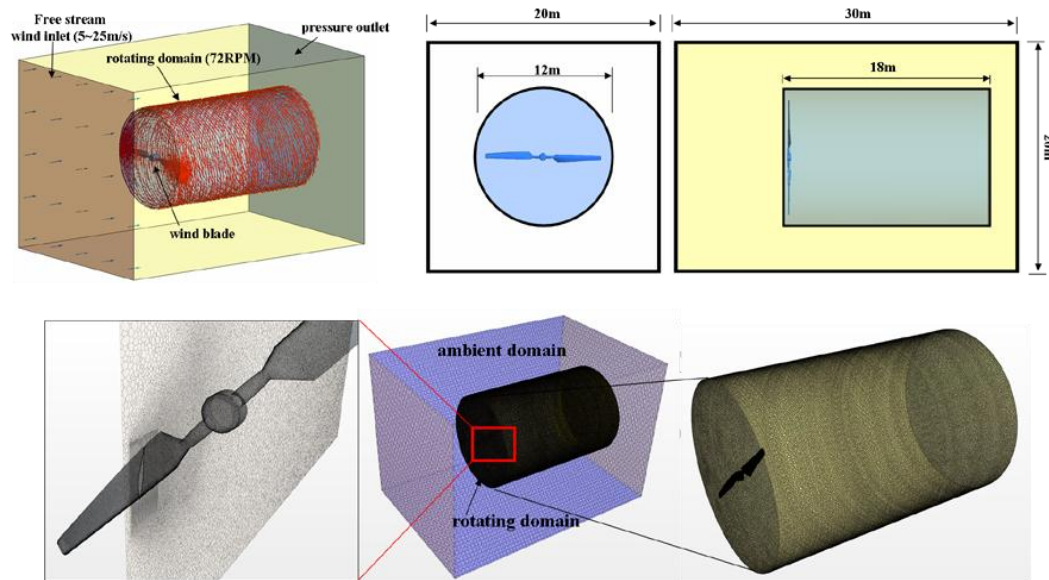


FIGURE 2. Computational domain and grid generation

RESULTS AND DISCUSSION

Aerodynamic Force Evaluation

The aero-acoustic sound noise is highly dependent on the aerodynamic force on wind turbine. So, to verify initial domain, aerodynamic force acting on NREL phase VI wind turbine was determined using CFD and NREL experimental results [1-2]. The Shear Stress Transport (SST) turbulent model was adopted for the steady state simulation. The global torque and thrust forces were evaluated and compared with NREL experimental results and the results obtained from other studies [8]. Figure 3(a) shows a comparative analysis of current study with the NREL experimental values and values obtained from the other studies for torque. The results of reference domain and NREL experimental results are presented in Fig. 3(a) with the current study. It is observed that the present study shows good agreement with NREL experimental values compared with the values of other studies. It is observed that the torque is not proportional to the wind speed. Even though the wind speed is increasing, the torque value decreases in specific region of 13-15m/s. Again, it increases after 20m/s wind speed. This phenomenon is known the stall effect of wind turbine blade and comes from the 2D airfoil. The thrust of Fig. 3(b) shows that current results are higher than NREL in lower wind speed cases (5-10m/s). After 13m/s wind speed, the thrust force is less than NREL. However the overall thrust force is in good agreement with NREL verifying the accuracy of the CFD analysis.

Computational Aero-Acoustics Results

Two strategies are adopted for mid-field to far-field noise prediction in modern CFD. One is based on the Direct Noise Simulation and the other on integral formulation. Both the approaches are included in Computational Aero-Acoustics (CAA). But the Direct noise Simulation is too expensive for far-field noise prediction. The FW-H acoustics integral can be used with less computational cost for mid to far-field noise prediction with reasonable accuracy. In this study for far field noise, LES coupled with FW-H integral is used to predict mid to far-field noise prediction. STAR-CCM+ software had been used. The noise sources consist of a volume distribution of quadrupole sources and a surface distribution of dipole sources. STAR-CCM+ offers a group of models capable of evaluating the broadband sources of noise. In the frequency domain, a broadband noise has a continuous spectrum, where the acoustic energy is continuously distributed at all frequencies in a given range. By using the broadband models, it can compute the location and strength of the main sources of noise that are generated aerodynamically.

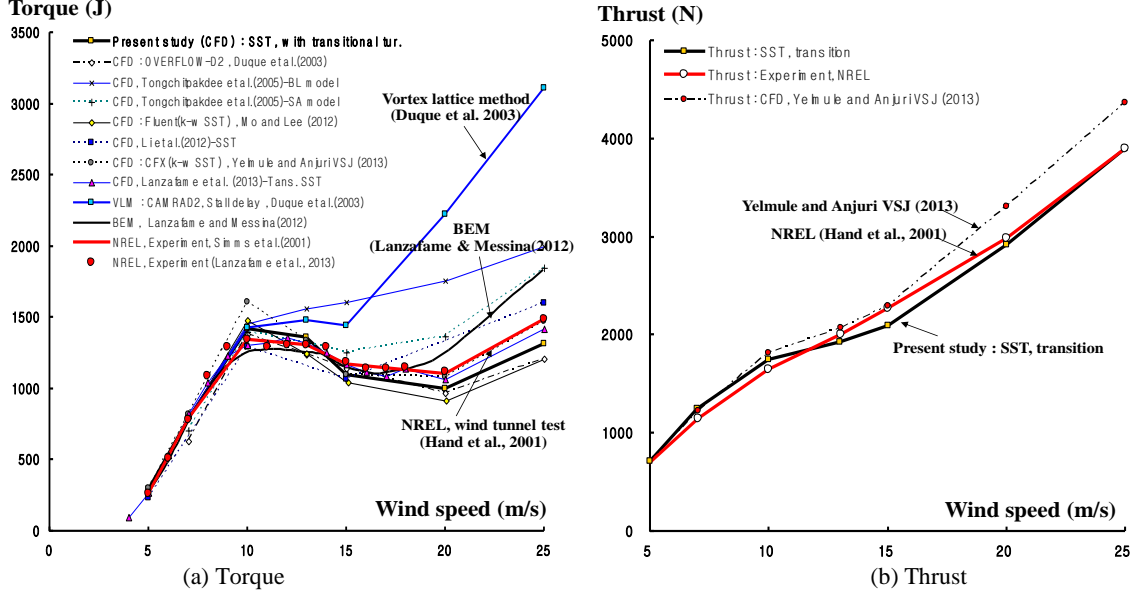


FIGURE 3. Aerodynamics forces

For non-conventional form of FW-H of Farassat's Formulation, the FW-H equation for pressure radiated into a medium can be written as:

$$p'(\bar{x}, t) = p'_T(\bar{x}, t) + p'_L(\bar{x}, t) + p'_Q(\bar{x}, t) \quad (1)$$

Where, $p'_T(\bar{x}, t)$, $p'_L(\bar{x}, t)$, $p'_Q(\bar{x}, t)$ are terms for monopole, dipole and quadrupole respectively. When the integration surface coincides with the body, these terms are called: "Thickness Surface Term", "Loading Surface Term" and "Volume Term" respectively. The volumetric quadrupole noise sound effect can be omitted in the case of low Mach number or little shear layer effect conditions.

From equation (1), the FW-H surface terms are derived as

$$p'_s(\bar{x}, t) = p'_T(\bar{x}, t) + p'_L(\bar{x}, t) \quad (2)$$

When the integration surface coincides with the body, these terms are obtained as:

$$p'_T(\bar{x}, t) = \frac{1}{4\pi} \left(\int_{f=0} \left[\frac{\rho_0 (\dot{U}_n + U_n)}{r(1-M_r)^2} \right]_{ret} dS + \int_{f=0} \left[\frac{\rho_0 U_n \{ r\dot{M}_r + a_0(M_r - M^2) \}}{r^2(1-M_r)^3} \right]_{ret} dS \right) \quad (3)$$

$$p'_L(\bar{x}, t) = \frac{1}{4\pi} \left(\frac{1}{a_0} \int_{f=0} \left[\frac{\dot{L}_r}{r(1-M_r)^2} \right]_{ret} dS + \int_{f=0} \left[\frac{L_r - L_M}{r^2(1-M_r)^2} \right] dS + \frac{1}{a_0} \int_{f=0} \left[\frac{L_r [r\dot{M}_r + a_0(M_r - M^2)]}{r^2(1-M_r)^3} \right] dS \right) \quad (4)$$

Equation (3) describes the monopole source term using the advanced-time formulation. Equation (4) describes the dipole source term using the advanced-time formulation. $p'_T(\bar{x}, t)$, known as the Thickness Surface Term, results from the displacement of fluid as the body passes. The term is defined in Eq. (3) for general flows. $p'_L(\bar{x}, t)$, known as the Loading Surface Term, results from the unsteady motion of the force distribution on the body surface. The term is defined in Eq. (4) for general flows. $p'_s(\bar{x}, t)$, known as the Total Surface Term, results from the sum of the Thickness Surface Term and the Loading Surface Term.

The Figure 4 shows the FW-H 6-pointer receivers for noise prediction. The receivers are located in the center line below the wind blade. The surface total term and volume term are determined using both reference

and rotational domain. Rigid body rotating motion of wind blade was considered to account for the unsteady blade motions.

The surface total sound pressure level and volume pressure level and the vorticity results for 25m/s wind speed for both reference frame motion and rotating frame motion are shown in Fig. 5. Both tonal low frequency and broadband high frequency sound noise were predicted well by the FW-H receivers. The surface total sound consists of two components. One is the thickness surface term and another is the loading surface term. Low frequency tonal noise of thickness and surface loading terms can be produced by the disturbance in the flow caused by the movement of rotating blade (thickness noise) and associated pressure field (loading noise). The broadband noise is higher frequency and due to various types of turbulent flow interaction with the blades. Significant differences were found between the results obtained by reference and rotating frame motion. It looks rotating frame motion overestimate the noise prediction. It is also found that, the thickness term has little effect on the surface total sound noise level.

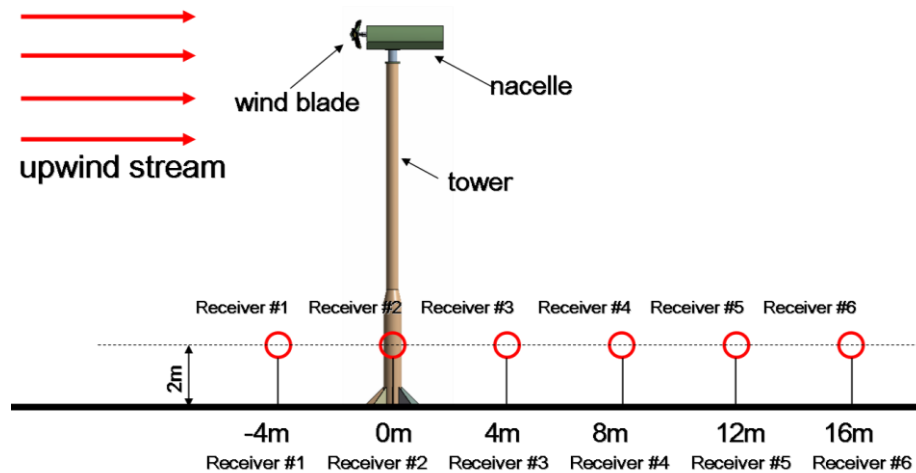


FIGURE 4. FW-H receivers' location

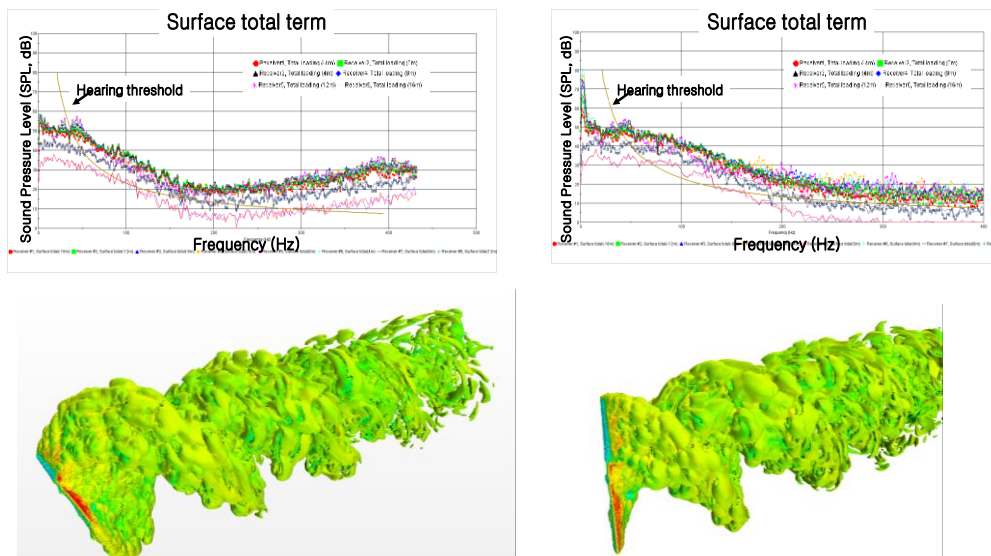


FIGURE 5. Computational aero-acoustic results

CONCLUSIONS

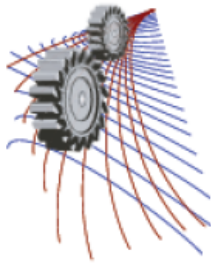
In this study the mid to far field noise prediction has been done using LES coupling with hybrid integral FW-F technique. For this purpose commercial CFD software STAR-CCM+ was used. The total surface noise term and volume noise term were determined both for reference frame motion and rotating frame motion. The surface noise term includes the thickness and pressure loading terms. The surface loading term which is produced by the unsteady motion of the force distribution on the body surface is more significant than the thickness term which is produced by displacement of fluid by rotating blade. The volumetric quadrupole noise source was also considered and observed far higher than surface loading term even though Mach number was low for wind turbine. Significant differences were found between the results obtained by reference and rotating frame motion. The rotating frame motion is found to over predict the sound level compared to the reference frame motion.

ACKNOWLEDGMENTS

This research was supported by the National Science Foundation (NSF) through the Center for Energy and Environmental Sustainability (CEES), a CREST Center (Award No. 1036593).

REFERENCES

1. M. Hand, D. Simms, L.J. Fingersch, D. Jager, S. Larwood, J. Cotrell and S. Schreck, "Unsteady Aerodynamics Experiment Phase VI: Wind Tunnel Test Configurations and Available Data Campaigns". *NREL/TP-500-29955, National Renewable Energy Lab.*, December 2001.
2. D. Simms, S. Schreck, M. Hand and L.J. Fingersch, "NREL Unsteady Aerodynamics Experiment in the NASA-Ames Wind Tunnel: A Comparison of Predictions to Measurements", *NREL/TP-500-29494, National Renewable Energy Lab.*, June 2001.
3. F.B. Matthew, "Survey of Techniques for Reduction of Wind Turbine Blade Trailing Edge Noise", *SAND2011-5252, Sandia National Lab.* August 2011.
4. A. Tadamas, M. Zangeneh, *Renewable Energy* **36**, 1902-1912 (2011).
5. M.J. Lighthill, "On Sound generated aerodynamically I. General theory", *Proc Roy Soc London Ser A*, 1952, Vol.211, pp.564-87.
6. J.E. Ffowcs Williams and D.L. Hawkings, *Philos Transact A Math Phys Eng Sci* **264**, 321-42 (1969).
7. K.S. Brentner and F. Farassat, *Progress in Aerospace Sciences* **39**, 83-120 (2003).
8. R. Lanzafame, S. Mauro and M. Messina, *Renewable Energy* **52**, 31-39 (2013).



Computational Analysis of Asymmetric Water Entry of Wedge and Ship Section at Constant Velocity

Md. Mashiur Rahaman^{1,a)}, Al Habib Ullah², Laboni Afroz¹, Sharmin Shabnam¹
and M. A. Rashid Sarkar³

¹*Department of Naval Architecture and Marine Engineering, BUET, Dhaka-1000, Bangladesh*

²*Assistant Naval Architect, Even Ship Design and Engineering, Bangladesh*

³*Department of Mechanical Engineering, BUET, Dhaka-1000, Bangladesh*

^{a)}Corresponding author: mashiurrahaman@name.buet.ac.bd

Abstract. Water impact problems receive much attention due to their short duration and large unsteady component of hydrodynamic loads. The effect of water entry has several important applications in various aspects of the naval field. Significant attention has been given to various water entry phenomena such as ship slamming, planning hulls, high-speed hydrodynamics of seaplanes, surface-piercing propellers and the interaction of high-speed liquid drops with structural elements. Asymmetric water entry may be caused by various natural phenomena such as weather conditions or strong winds. Since the determination of hydrodynamic impact load plays a vital role in designing safe and efficient vessels, an accurate and reliable prediction method is necessary to investigate asymmetric water entry problems. In this paper, water entry of a two-dimensional wedge and ship section at constant velocity in asymmetric condition will be analysed numerically and the effects of asymmetric impact on the velocity and pressure distribution will be discussed. The finite volume method is employed to solve the dynamic motion of the wedge in two-phase flow. During the water entry, the air and water interface is described implicitly by the volume of fluid (VOF) scheme. The numerical code and method was first validated for symmetric condition by one of the present author is applied for asymmetric wedge and ship section. The free surface, velocity and pressure distribution for asymmetric water entry are investigated and visualized with contour plots at different time steps.

INTRODUCTION

The number of high-speed ships in commercial service has increased in the past few years and their role in marine transportation and operation is becoming very important. Besides, ship size has become larger with time. For such ships, structural designs can strongly influence ship weight, and simultaneously building cost and cargo capacity. The slamming impact load is one important phenomenon that must be taken into consideration in the local structural design. Furthermore, the slamming impact becomes more severe as ship speed increases. Because of the stochastic nature of slamming, prediction of this random process is studied in probabilistic manner. Asymmetric hydrodynamic impact on a ship occurs because of bow waves. Due to the wave excitation and the wind pressure on the superstructure, roll motion of a ship in her seaway causes the ship fore body to be always asymmetrical in some degrees under water entry after it has been raised over the wave surface. Moreover, the slope of wave elevation gives additional degrees of asymmetry. However the heading wave and the symmetric impact pressure are still used as design conditions. But the effect of asymmetric impact on the structural dynamic response is expected to be more serious because the hydrodynamic pressure level becomes higher, especially at a short duration. Von Karman [1] is one of the pioneer researchers in this field. He developed a theoretical model based on the momentum theorem and the water-added mass. His works are applied to the estimation of the maximal pressure on the hydroplanes during sea landings. Wagner [2] studied two-dimensional water impact on solid bodies. He took into account the effect of water splash on the body. Zhao and Faltinsen [3] and Mei et. al. [4] have completed Wagners studies, using conformal mapping and suggesting a linear approximation of the boundary limits for the two-dimensional cases. In addition to these theoretical developments, several experimental studies have been conducted on hydrodynamics of rigid bodies entering water. Yettou et. al. experiments [5] studied the symmetry impact of a wedge. During the past decade, some numerical studies have

been carried out to overcome these limitations of the traditional analytical approach, and significant progress has been made. Arian et al. [6, 7] used finite difference method (FDM) for discretization of the Euler equations and volume of fluid (VOF) method for free surface evolution for water entry of ship like sections. Their results obtained favorable trends but pressure value did not correlate well with drop tests results. Muzaferija et al. [8] and Sames et al. [9] used finite volume method (FVM) for discretization of the Navier-Stokes equations and high resolution interface capturing (HRIC) scheme for free surface to predict slamming loads on 2D wedge sections. Slamming loads obtained by Muzaferija et al. [8] matched reasonably with the experimental results of Zhao et al. [3]. Sames et al. [9] mentioned that prescribed vertical velocity histories significantly affected the determination of realistic pressure levels. Reddy et al. [10] simulated 2D wedge section by using CFD technique, named PHOENIX. Azecuta et al. [11] used VOF finite volume Reynolds averaged Navier-Stokes solver for the water impact problem. Fairlie-Clarke and Tveitnes [12] applied commercial CFD code, Fluent 4 for constant velocity water entry of 2D wedge-shaped sections. They analyzed wedge entry force from flow momentum, gravity and the change in added mass. Good agreement was noticed under chine dry conditions with theoretical results of Zhao and Faltinsen [3]. Later, Tveitnes et al. [13] conducted experimental investigations and preferable agreement was reported with their previous numerical results of Fairlie-Clarke and Tveitnes [12] and other empirical and theoretical methods. Kleefsman et al. [14] used commercial CFD code, ComFLOW for simulating water entry of 2D symmetric bodies. Yamamoto et al. [15] calculated the non-linear ship motions based on the equations given by the linear theory but time varying coefficients dependent on the instantaneous sectional draft. They also included the hydrodynamic impact component given by the rate of change of the sectional added mass, assuming that this force only acts on the vessel when the section is penetrating the water. They carried out experiments and calculations on a bulk carrier model for head seas. They found that the accuracy of the calculation of the hydrodynamic coefficients has a significant influence on the results of the slamming forces. Sun and Faltinsen [16] used boundary element method (BEM) for 2D slamming of bow flare section of a ship with roll angle. They pointed out that large roll angle causes very high localized pressure in the flare area. Veen and Gourlay [17] developed a 2D smooth particle hydrodynamics (SPH) method for calculating slamming loads on realistic hull section shapes. They concluded that SPH can model the jets and splashing which are important features of slam events. In present study, a commercial CFD code Fluent is used to simulate the flow for 2D asymmetric water entry of 30 degree deadrise wedge and a ship section.

NUMERICAL METHOD

Numerical Schemes

In ANSYS FLUENT, solution of the governing integral equations for conservation of mass and momentum is obtained by control-volume-based technique that consists of:

- Division of the domain into discrete control volumes using a pre-processor.
- Integration of the governing equations on the individual control volumes to construct algebraic equations for the discrete dependent variables.
- Linearization of the discrete equations and solution for the linear equation system to yield updated values of the dependent variables.

The pressure-based segregated solution algorithm is employed to obtain a converged numerical solution of the governing equations. Details of this solution algorithm can be found in FLUENT users guide. Quadratic upwind interpolation (QUICK) scheme is used for discretization in space. This scheme is of higher order accuracy, which is of great importance when the flow is at large angles to the grid. Viscous effects can be included but in present analyses, it is neglected because of its small effects and as is the normal practice in water-entry problems. Therefore, for inviscid flow, the governing equations to be solved are the continuity equation and Eulers equation based on conservation of mass and momentum. The equations are solved sequentially using the semi-implicit method for pressure-linked equations (SIMPLE) algorithm. The Volume of fluid (VOF) method is used for modelling free surface. In VOF a variable is introduced for each fluid. This variable tells what fraction of that particular fluid is in the cell and the total of these variables for all fluids sums up to unity in every cell. The fluids share a single set of momentum equations and the volume fraction of each fluid is tracked throughout the domain. The fluid properties in a cell are dependent on the volume fractions of the fluid within it. The free surface occurs at cells that have volume fractions of one half for each of the two adjacent fluids. ANSYS FLUENT provides different explicit and implicit discretization schemes for interpolation near the free surface. In present analysis time -dependent explicit geometric reconstruction interpolation scheme is used. This scheme represents the interface between fluids using a piecewise-linear approach and it is the

most accurate in the current CFD solver. It assumes that the interface between two fluids has a linear slope within each cell, and uses this linear shape for calculation of the advection of fluid through the cell faces. The solution steps of this scheme are:

- Calculating the position of the linear interface relative to the center of each partially-filled cell, based on information about the volume fraction and its derivatives in the cell.
- Calculating the advecting amount of fluid through each face using the computed linear interface representation and information about the normal and tangential velocity distribution on the face.
- Calculating volume fraction in each cell using the balance of fluxes calculated using the previous step.

Boundary Condition

In the simulation domain, the body is held stationary and flow past in it is achieved by having a velocity inlet at the bottom of the domain. At the top of the domain, there is a pressure boundary set at atmospheric pressure to allow outflow of excess air. The sectional geometry is defined as wall boundary condition with slip and the far end of the domain is defined as wall boundary conditions with free slip. Geometrical symmetry about the centreline has allowed the flow to be simulated in half of the domain. The inlet velocity is considered as 6.15m/sec for wedge section and 2.418m/sec for ship section.

Fluid Properties

The water is treated as incompressible. The default values of fluid properties at room temperature for fresh water and air are used with density of $998.2kg/m^3$ for water and $1.293kg/m^3$ for air.

Computational Domain and Grid

The size of computational domain (shown in Table 1) is 3m wide by 1.5 m high and it is divided into 5 (five) blocks for ship section and four block for wedge section. The grid is generated using body-fitted co-ordinate systems. Multi-block structured grid is used to avoid high skewness. Minimum grid spacing is kept along the body to capture the free surface. The computational domain for ship section is shown in the Fig.1.

Solver

Based on the minimum grid spacing, it is found that for stable solution, the Courant number needed to be less than 0.15. During the solution, the level to which the sum of normalized residuals must drop before going on to the next time step is set to $1.0e^{-03}$. The minimum time step size for wedge and ship section is $2.5e^{-05}$.

Result and Discussion

Rahaman et.al.[18] already validate the present numerical method for wedge and ship section at variable entry velocity in symmetrical case. In the present study, the numerical method of Rahaman et.al.[18] is applied for an asymmetric water entry of 30 deg.wedge and ship shape section and the results are analyzed qualitatively.Two different kinds of grid systems i.e. structured and unstructured at the block near the geometries are applied in the present simulation (shown in Fig. 2). For other blocks in the computational domain, structured grids are generated.

TABLE 1. Grid dimension of the blocks in the Computational Domain

Block	Wedge section	Ship section
Block 1	240X60	240X60
Block 2	120X40	120X50
Block 3	—	120x10
Block 4	120x40	120x40
Block 5	10x40	10x40

Figure 3 illustrates the comparison of the deformation of free surface at 5 deg. roll angle for structured and unstructured grid at time .0202sec for wedge section. It is seen from Fig. 3. that the deformation of the free surface is well captured by both structured and unstructured grid.

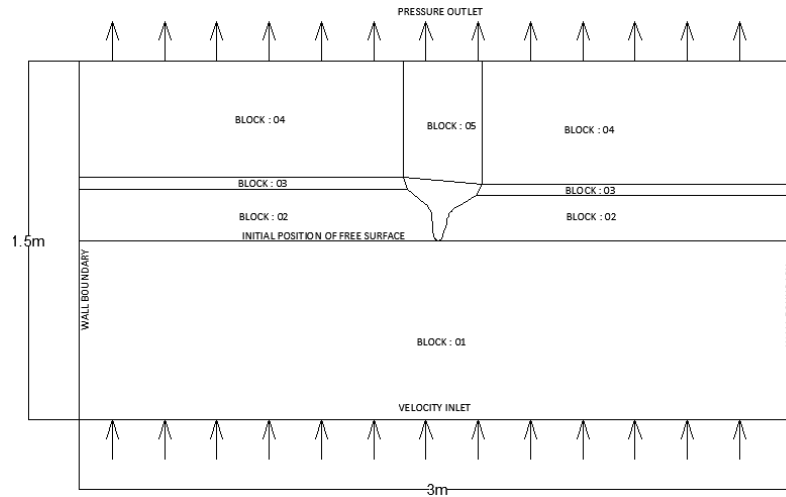


FIGURE 1. Computational Domain for ship section

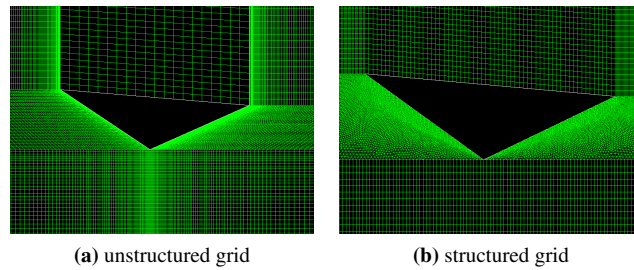


FIGURE 2. Close-up view of grid around wedge

Figures 4 ~ 6 represent the comparison of the contour of free surface, pressure and velocity distribution respectively at different roll angles at various time instances. It is observed from Figs.4 ~ 6 that in all cases and instances, the deformation of the free surface is limited only to the vicinity of the surface of the geometry and no propagating wave is formed. The pressure contours show that a very high pressure and a pressure gradient appear near the spray roots. The high pressure zone moves together with the spray roots, until they reach the knuckle, where the decrease of the pressure is accompanied by the jet flows released from the body. Also, as the roll angle increases the flow separates more from the geometry.

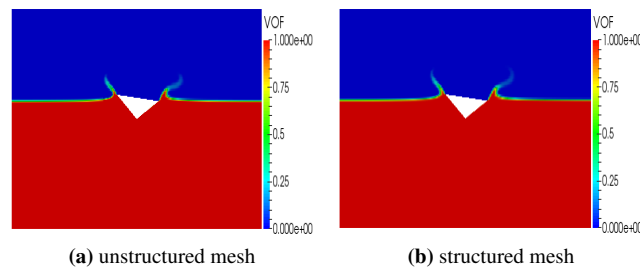


FIGURE 3. Contour of free surface

Figures 7 ~ 9 show the contour of free surface, pressure and velocity distribution at different roll angle for a ship section at various time steps as $t=.06$ sec.; $t=.07$ sec. and $t=.08$ sec. Like wedge shape section, similar behavior of the flow parameters i.e. the deformation of free surface and the position of high pressure on the surface are occurred for ship shape. It is seen from the Figs. that when the roll angle is large, strong impact happens between ship section and the calm water surface. This is because of the increase of contact surface area with asymmetry angle.

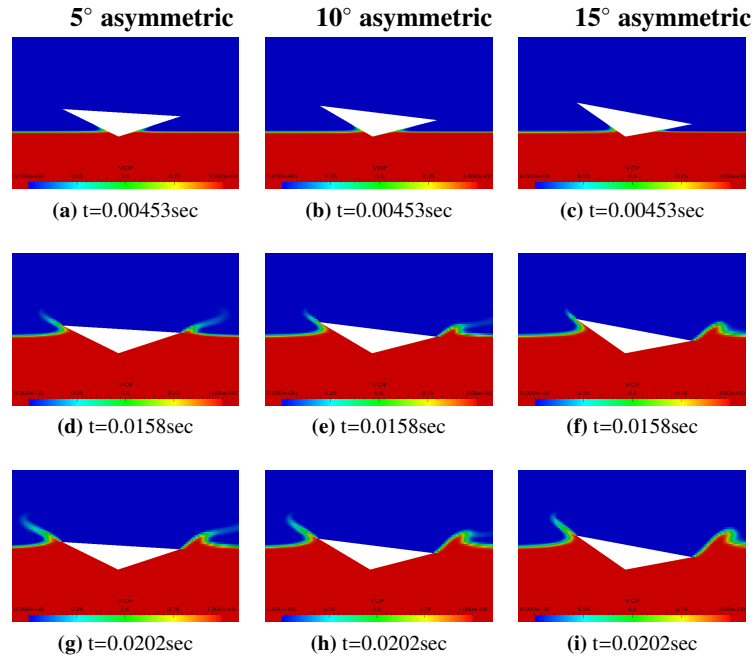


FIGURE 4. Contour of free surface of wedge section at different time instances for 5 deg., 10 deg. and 15 deg. roll angle

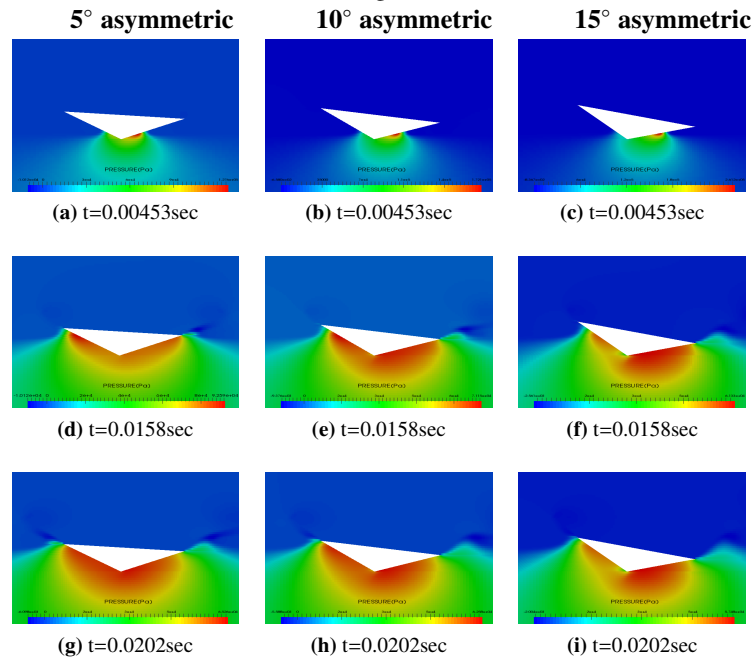


FIGURE 5. Contour of pressure distribution of wedge section at different time instances for 5 deg., 10 deg. and 15 deg. roll angle

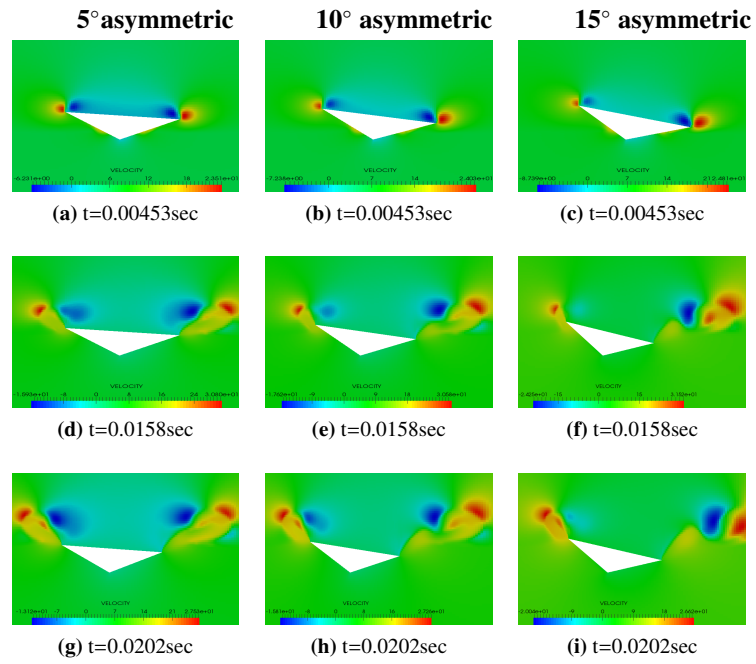


FIGURE 6. Contour of velocity distribution of wedge section at different time instances for 5 deg., 10 deg. and 15 deg. roll angle

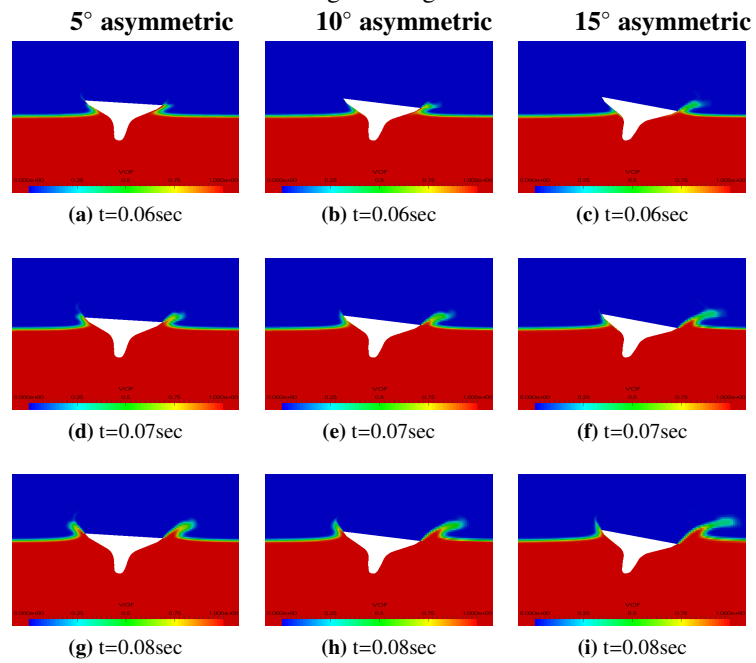


FIGURE 7. Contour of free surface of ship section at different time instances for 5 deg., 10 deg. and 15 deg. roll angle

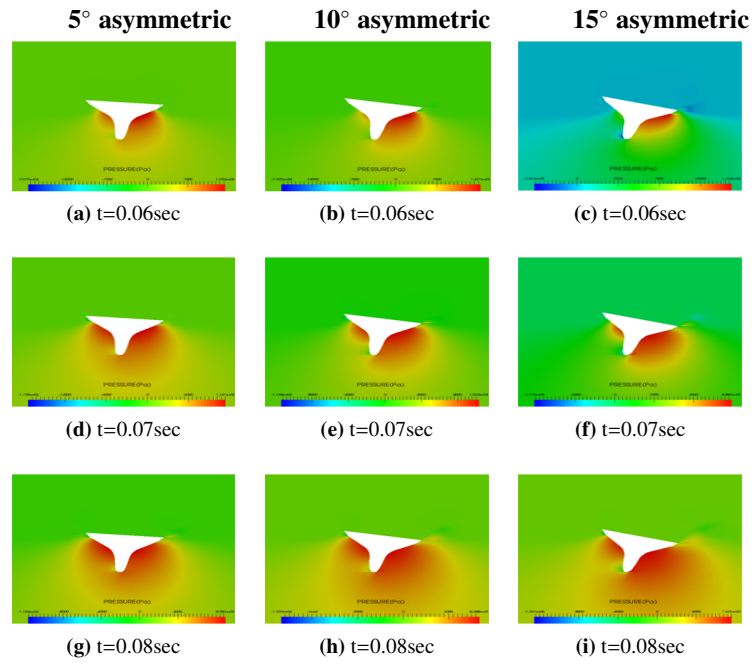


FIGURE 8. Contour of pressure distribution of ship section at different time instances for 5 deg., 10 deg. and 15 deg. roll angle

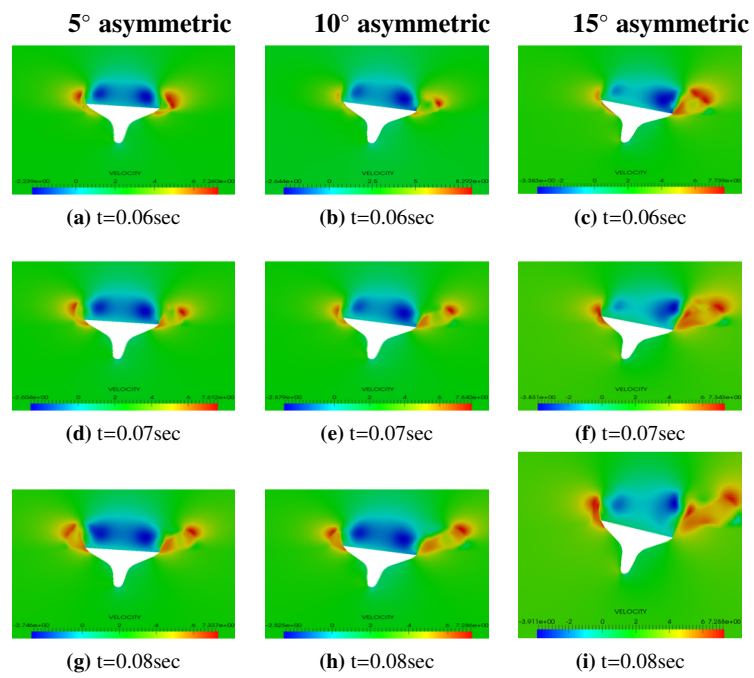


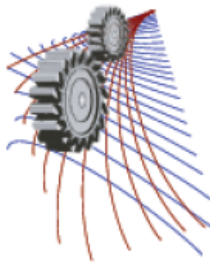
FIGURE 9. Contour of velocity distribution of ship section at different time instances for 5 deg., 10 deg. and 15 deg. roll angle

CONCLUSION

In present study, the asymmetric effect of water entry is investigated for 30 deg. wedge and ship section. Numerical calculations are performed based on Finite Volume (FV) based computational code Fluent. Free surface is captured based on Volume of Fluid (VOF) method. Due to the inclination (wedge section) and curvature (ship section) of surface, two different types of grids i.e. unstructured and structured near the geometry surfaces are studied. It is seen from the numerical results that the effects of grid types on the contour of the free surface deformation and the pressure and velocity distribution is negligible. For both wedge and ship section, the deformation of the free surface occurs at the vicinity of the surface of the geometry and a very high pressure and a pressure gradient appear near the spray roots. Also, the high pressure zone moves together with the spray roots. The impact between geometry surface and the water increases with increase of roll angle.

REFERENCES

- [1] T.K. Von, Technical Report, NACA TN 321 (1929).
- [2] H. Wagner, *Über Stoss- und Gleitvorgänge an der Oberfläche von Flüssigkeiten*, *Zeitschr. f., ZAMM* **42**, 192-235, 193.
- [3] R. Zhao and O.M. Faltinsen, *Journal of Fluid Mechanics* **246**, 593-612 (1993).
- [4] X. Mei, Y. Lui and D.K.P. Yue, *Applied Ocean Research* **21**, 1-15 (1999).
- [5] El-M. Yettou, A. Desrochers and Y. Champoux, *Journal of Fluids and Structures* **23**, 501-522 (2007).
- [6] M. Arai and K. Matsunaga, *PRADS* **75**, 1-8 (1989).
- [7] M. Arai, L.Y. Cheng and Y. Inoue, *Journal of the Society of Naval Architects of Japan* **176**, 233-240 (1994).
- [8] S. Muzaferija, M. Peric, P.C. Samesand and T.E. Schellin, *Proceedings of 22nd Symposium on Naval Hydrodynamics*, 638-651 (2000).
- [9] P.C. Sames, T.E. Schellin, S. Muzaferija and M. Peric, *Journal of Offshore Mechanics and Arctic Engineering (OMAE)* **121**, 1-7 (1999).
- [10] D.N. Reddy, T. Scanlon, K. Cheng, *Proceedings of 24th Symposium on Naval Hydrodynamics*, 37-49 (2002).
- [11] R. Azcueta, I. Hadzic, S. Muzaferija and M. Peric, *Marnet-CFD First Annual Workshop* (1999).
- [12] A.C. Fairlie-Clarke and T. Tveitnes, *Ocean Engineering* **35**, 706-716 (2008).
- [13] T. Tveitnes, A.C. Fairlie-Clarke and K. Varyani, *Ocean Engineering* **35**, 1463-1478 (2008).
- [14] K.M.T. Kleefsman, G. Fekken, A.E.P. Veldman, B. Iwanowski and B. Buchner, *Journal of Computational Physics* **206**, 363-393 (2005).
- [15] Y. Yamamoto, K. Sugai, H. Inoue, K. Yoshida, M. Fujino and H. Ohtsubo, *Advances in Marine Structures Conference*, 26-40 (1986).
- [16] H. Sun and O. Faltinsen, *Journal of Marine Science and Technology* **14**, 69-79 (2009).
- [17] D.J. Veen and T.P. Gourlay, *Proceedings of High Speed Marine Vessels Conference* (2011).
- [18] M.M. Rahaman, H. Akimoto and A. Ali, *Journal of Naval Architecture and Marine Engineering* **10**, 49-58 (2013).



Effect of Surface Dimples on the Discharge Coefficient of an Orifice Meter

Tanvir Ahmmed^{1, b)}, Syed Zia Uddin¹ and M. Mahbubur Razzaque^{1, a)}

¹Department of Mechanical Engineering
Bangladesh University of Engineering and Technology (BUET), Dhaka, Bangladesh

^{a)}Corresponding author: mmrazzaque@me.buet.ac.bd

^{b)}tanvir.mech.09@gmail.com

Abstract. This paper investigates using CFD technique the effect of surface dimples on the discharge coefficient of an orifice meter in both laminar and turbulent regimes. Hemispherical dimples are arranged in an orderly pattern on the upstream surface of an orifice plate. The standard $k-\varepsilon$ model is used for turbulent flow analysis. Discharge coefficient has been found to decrease in presence of dimples. Discharge coefficient decreases more as the dimples move closer to the orifice bore. The coefficient of discharge further decreases with the increase of the size of dimples. When the dimples are large, i.e., the surface is severely damaged, percentage reduction of the coefficient of discharge in both laminar and turbulent regimes may be as high as 1.6%.

INTRODUCTION

Orifice meters are widely used to measure flow rate of fluids like corrosive chemicals, condensates and slurries through pipelines. As a result of flow of these types of fluids the orifice plate may undergo corrosion and/or erosion and small cavities may form on the surface of the orifice plate. The shape and distribution of these cavities can be very complex. Such an orifice plate with cavities on its surface may cause error in flow measurement. Many experiments have been conducted to investigate the effects of different factors on the accuracy of orifice meters. These factors include flow conditions, fluid types, orifice plate dimensions, permanent deformation of the orifice plate by buckling and rounding, etc. Jepson and Chipchase [1] studied the effect of plate buckling on the coefficient of discharge of an orifice meter. Their result showed that the error in flow measurement may become as high as 0.5% if the orifice plate buckling exceeds 1 degree. Sarker et al. [2] performed Computational Fluid Dynamics (CFD) simulation to study the effect of orifice plate buckling and rounding of sharp edge for two different pipe sizes. They considered 2 inch and 4 inch pipelines in their analysis and concluded that flow measurement error can be up to 3.5% for buckled orifice plate. Kiš et al. [3] found that deformation of an orifice plate significantly affects the flow behaviour of high pressure natural gas streams in a pipeline. Hobbs and Humphreys [4] conducted experimental studies to examine the effect of upstream edge sharpness on the coefficient of discharge of orifice plates. As they increased the edge radius to bore diameter ratio, the discharge coefficient was also increased. They also roughened the downstream face of the orifice plate by gluing coarse sand paper and found that the discharge coefficient changed by 0.133% for a diameter ratio of 0.75. Botros et al. [5] machined concentric grooves on both upstream and downstream surfaces of an orifice plate with different roughness values and tested for two different diameter ratios. They concluded that increasing the roughness causes under-measurement of flow rate. They also examined the effect of grease deposits on the orifice plate by attaching circular disks on the orifice edge and on the surface between the pipe and the orifice bore. No significant change in flow measurement was observed when the disks were placed on the front surface between the pipe and the bore. But when the disks were placed close to the bore, under-measurement of flow rate was noticed. Burgin [6] varied the thickness and coverage area of grease deposited on an orifice plate surface and found that the grease deposit caused an under-measurement of flow rate.

In the current paper, the rough surface of an eroded/corroded orifice plate is modeled by putting hemispherical dimples arranged in an ordered pattern on the upstream surface of an orifice plate. CFD analysis is employed to predict the effect of surface dimples on the discharge coefficient of the orifice meter for flow of water in both laminar and turbulent regimes.

MODEL OF THE ORIFICE METER

The dimensions of the orifice plate are chosen according to AGA Report No. 3 recommendation [7]. The pipe inner diameter, orifice bore diameter and the beta ratio are 50.8 mm, 25.4 mm and 0.5, respectively. The plate thickness is 3.175 mm and the sharp edge thickness is 0.794 mm. The chamfer angle is 45° and the total pipe length is 560 mm. Deformation of an orifice plate surface due to erosion and/or corrosion can be very irregular in pattern in real situations. However, for the sake of simplicity, the deformed surface is modeled by putting hemispherical dimples arranged in a regular fashion on the upstream surface as shown in Fig. 1. The surface texture is varied by changing the diameter, radial position and number of dimples. CAD models of orifice plate are generated in commercial CAD software.

CFD MODEL AND SOLUTION

Governing Equations

Water is chosen as the working fluid and the corresponding continuity equation is $\nabla \cdot \vec{v} = 0$. The appropriate momentum equation is:

$$\rho \cdot \left(\frac{\partial \vec{v}}{\partial t} + \vec{v} \cdot \nabla \vec{v} \right) = -\nabla p + \nabla \cdot \overline{\overline{\tau}}$$

Here, p is the static pressure, $\overline{\overline{\tau}}$ stress tensor, ρ density and \vec{v} velocity vector. In case of turbulent flow, the mean flow characteristics are given by two additional transport equations of the standard k - ϵ model.

Mesh Generation

Meshing is done in ANSYS Workbench. Unstructured tetrahedral meshes are used in all simulations. Manual face sizing around the orifice bore is done in order to accurately capture the rapid change in flow. Higher density meshes around the dimples are generated by selecting 'curvature' in the advanced mesh sizing option. The maximum mesh size is 2 mm and minimum mesh size is 0.082422 mm for most cases. In case of simulation of laminar flow, the maximum mesh size is taken to be 2.5 mm in order to reduce mesh count. Good quality mesh and typical values of orthogonal quality, skewness and aspect ratio are used. A closer look of the meshes on the xy plane (+x being the flow direction and +y being the vertically upward direction) is shown in Fig. 2. A magnified view of a section of the upstream surface with dimples is also shown in the inset.

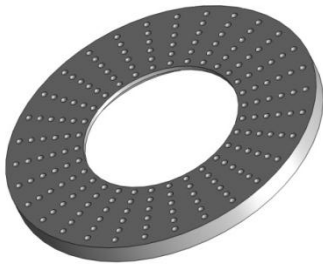


FIGURE 1. Orifice plate with dimples on the upstream surface.

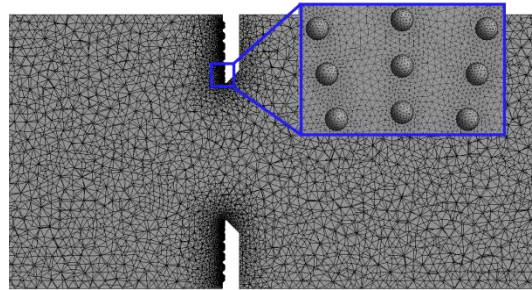


FIGURE 2. Meshing in the fluid domain and a magnified view of the meshing near the dimples (inset).

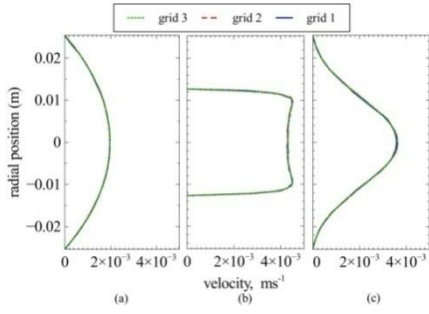


FIGURE 3. Laminar velocity profiles at $x = -0.1, 0$ and 0.1 m.

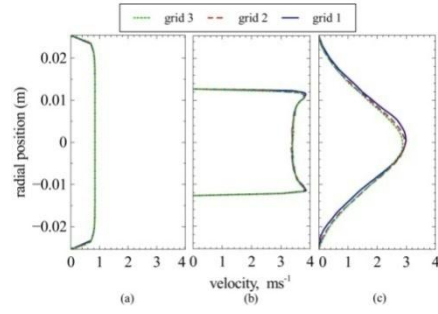


FIGURE 4. Turbulent velocity profiles at $x = -0.1, 0$ and 0.1 m.

Solution

All simulations are carried out in ANSYS Fluent solver. Calculations for laminar flow ($Re = 66.4$) are done using the default options under laminar model. For turbulent flow ($Re = 40272$), standard $k-\varepsilon$ model and pressure based steady state solver are used. The pressure-velocity coupling is done following SIMPLE algorithm. Least square cell based gradient is used for spatial discretization. Standard pressure is selected and second order upwind scheme is chosen for momentum, turbulent kinetic energy and turbulent dissipation rate. Default values are preserved for under-relaxation factors. Standard $k-\varepsilon$ model is widely used due to its fast convergence while maintaining reasonable accuracy. Shah et al. [8] used standard $k-\varepsilon$ model for analysis of turbulent flow through orifice meter and found satisfactory agreement between experimental and simulation results.

Water of 998 kg/m^3 density and $1.003 \text{ mm}^2/\text{s}$ kinematic viscosity is chosen as working fluid. The inlet velocity normal to the inlet face of the fluid domain is set at 0.001 m/s for laminar flow and 0.8 m/s for turbulent flow. The outlet pressure is set equal to the atmospheric pressure in both cases. The turbulent kinetic energy k is set to $1.7 \times 10^{-3} \text{ m}^2/\text{s}^2$ and the turbulent energy dissipation rate ε to $3.24 \times 10^{-3} \text{ m}^2/\text{s}^3$.

Mesh dependency test

Laminar and turbulent velocity profiles at three different locations (at $x = -0.1 \text{ m}$, $x = 0 \text{ m}$ and $x = 0.1 \text{ m}$) in the direction of flow through an undeformed orifice plate are plotted, respectively, in Figs. 3 and 4 for three different cell counts; namely, Grid 1: 613,763, grid 2: 918,957 and grid 3: 1,099,391 tetrahedral elements. The velocity profiles for laminar flow seem to be almost independent of the tested grid schemes. In the case of turbulent flow, the velocity profiles resulted from grid schemes 2 and 3 are reasonably close to each other. So, for the rest of the calculations grid scheme 3 is used.

Validation of results

The coefficient of discharge of the orifice meter is calculated using the following equation

$$C_D = \frac{Q}{A_o} \sqrt{\frac{\rho(1 - \beta^4)}{2(P_1 - P_2)}}$$

Here, A_o = area of orifice bore, β = ratio of the diameters of the orifice bore and the pipe, $P_1 - P_2$ is pressure difference at the pressure taps and Q = actual flow rate. The pressure taps are located at 25.4 mm away of both upstream and downstream faces of the orifice plate. Experimental values of the discharge coefficient at $Re = 10,000$ and $Re = 50,000$ taken from AGA Report No. 3 [7] and the corresponding values computed using the current CFD simulation are presented in Table 1. The predicted values of the C_D are slightly higher than the experimental values possibly due to limitations of the turbulence model and, therefore, cannot be taken quantitatively. Nevertheless, the results will be useful in understanding the effect of the surface textures qualitatively.

TABLE 1. Comparison of the predicted coefficient of discharge with the experimental data from ref. [9].

Reynolds number, Re	AGA report 3	Current results	Difference in %
10,000	0.61833	0.64721	+ 4.6703
50,000	0.60895	0.63650	+ 4.5237

RESULTS AND DISCUSSION

The CFD simulation is carried out for two values of Reynolds number; namely, $Re = 66.4$ and $Re = 40272$. Hemispherical dimples are arranged on the orifice surface following four patterns. The effect of the various types of surface patterns on the discharge coefficient of the orifice meter is presented in Tables 2 to 5 for both laminar and turbulent flow. The coefficient of discharge, C_D of the orifice plate with dimples is presented along with the % red which shows the percentage reduction of C_D compared to that of the undeformed orifice plate. The C_D of the undeformed orifice plate is 0.7473 for laminar flow at $Re = 66.4$ and 0.6383 for turbulent flow at $Re = 40272$.

TABLE 2. Predicted coefficient of discharge and percentage reduction for various surface textures of pattern 1.

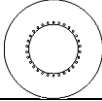
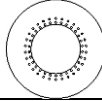
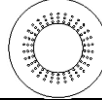
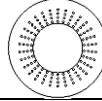
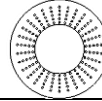
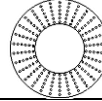
Surface texture/ Model												
	C_D	% red	C_D	% red	C_D	% red	C_D	% red	C_D	% red	C_D	% red
Laminar	0.7385	1.178	0.7386	1.164	0.7388	1.137	0.7387	1.151	0.7388	1.137	0.7387	1.151
Turbulent	0.6342	0.642	0.6342	0.642	0.6345	0.595	0.6343	0.627	0.6339	0.689	0.6346	0.580

TABLE 3. Predicted coefficient of discharge and percentage reduction for various surface textures of pattern 2.

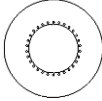
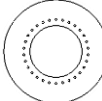
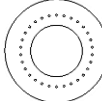
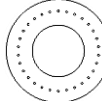
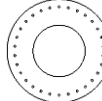
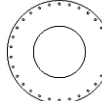
Surface texture/ Model												
	C_D	% red	C_D	% red	C_D	% red	C_D	% red	C_D	% red	C_D	% red
Laminar	0.7385	1.178	0.7395	1.044	0.7425	0.642	0.7446	0.361	0.7472	0.013	0.7480	-0.094
Turbulent	0.6342	0.642	0.6350	0.517	0.6353	0.470	0.6357	0.407	0.6356	0.423	0.6357	0.407

TABLE 4. Predicted coefficient of discharge and percentage reduction for various surface textures of pattern 3.

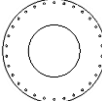
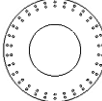
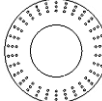
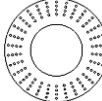
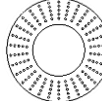
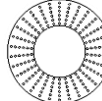
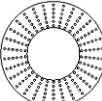
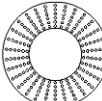
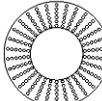
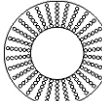
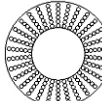
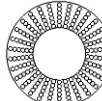
Surface texture/ Model												
	C_D	% red	C_D	% red	C_D	% red	C_D	% red	C_D	% red	C_D	% red
Laminar	0.7480	-0.094	0.7474	-0.013	0.7449	0.321	0.7427	0.616	0.7398	1.004	0.7387	1.151
Turbulent	0.6357	0.407	0.6355	0.439	0.6351	0.501	0.6352	0.486	0.6346	0.580	0.6346	0.580

TABLE 5. Predicted coefficient of discharge and percentage reduction for various surface textures of pattern 4.

Surface texture/ Model												
	C_D	% red	C_D	% red	C_D	% red	C_D	% red	C_D	% red	C_D	% red
Laminar	0.7387	1.151	0.7385	1.178	0.7382	1.218	0.7379	1.258	0.7369	1.392	0.7357	1.552
Turbulent	0.6346	0.580	0.6344	0.611	0.6345	0.595	0.6339	0.689	0.6318	1.018	0.6281	1.598

In pattern 1, thirty (30) equally spaced identical dimples of 1 mm diameter are placed around the bore along a concentric circle 1 mm away from the sharp edge. Number of dimples is subsequently increased in multiples of 30. The radial distance between the centers of two neighboring dimples is 2 mm. The predicted values of C_D and % reduction of C_D for six surface textures are shown in Table 2 for both laminar and turbulent flow. Though the number of dimples is different in all six textures, the values of C_D do not change much. For both laminar and turbulent flow, the lowest C_D is observed when the dimples are nearest to the bore.

In pattern 2, the number dimples is kept fixed at 30 but the radial position of the dimples is varied by gradually increasing the radius of the circular array in steps of 2 mm. The results are presented in Table 3. For laminar flow, it is clearly visible that as the dimples move away from the bore, the C_D increases and becomes very close to that of the undeformed orifice plate. On the other hand for turbulent flow, the values of C_D are less sensitive to the radial position of the dimples. With increase of the radial distance, the C_D increases at a slower rate. The effect of the dimples of large radial distance is more pronounced in case of turbulent flow.

In pattern 3, thirty equally spaced identical dimples of 1 mm diameter are placed along a concentric circle 11 mm away from the sharp edge of the orifice plate. Number of dimples is gradually increased in multiples of 30. The radial distance between the centers of two neighboring dimples is again 2 mm. The results are shown in Table 4. Again it is evident that the percentage reduction of C_D is the lowest with the dimples placed far away from the bore.

In pattern 4, dimples are placed along six concentric circles around the bore. The innermost concentric circle is placed 1 mm away from the bore sharp edge and the distance between two concentric circles is 2 mm. Each circle contains 30 identical dimples. The diameter of the dimples is varied from 1 mm to 2 mm in steps of 0.2 mm. From the results presented in Table 5, it is evident that for laminar flow the C_D declines steadily by increasing the diameter of the dimples. However, for turbulent flow, the discharge coefficient falls rapidly when the diameter of the dimples is increased beyond 1.6 mm. When the size of the dimples is 2 mm the percentage reduction of the discharge coefficient becomes high for both laminar and turbulent flow. It implies that with a severely deformed surface of an orifice plate the coefficient of discharge C_D may decrease by as high as 1.6%.

The flow structure near the orifice plate with surface dimples may be visualised in Fig. 5 which gives the plot of velocity vectors in the xy plane of the calculation domain. The vector plot shows recirculation of flow inside the hemispherical dimples on the upstream surface of the orifice plate taking place predominantly near the bore. For the sake of visualization of the recirculation zone, the size of the vectors was reduced by a factor of 0.05. Since orifice meter obstructs the flow, the fluid is forced to travel at a greater velocity through the orifice bore. As the velocity increases, the pressure of the fluid drops according to Bernoulli's principle. At the regions near the conjunction of pipe and orifice plate, the fluid pressure is the highest. So, due to pressure difference, the fluid confined in that region is bound to flow towards the bore. During this flow, the fluid particles find the hemispherical dimples in its path.

Figs. 5b and 5c, show the velocity vectors of the recirculation flows in two dimples; the one in Fig 5b being nearer to the bore than the other one. It is clear that the dimple located nearer to the bore has greater magnitude of velocity in the recirculation region. The recirculation velocity of the fluid becomes lower as the dimples are away from the bore. As a result, more energy is lost in a dimple closer to the bore which causes a reduced coefficient of discharge and, hence, reduced flow. In reality, orifice plate surfaces are more likely to be eroded around the bore and thus an orifice plate with severely eroded upstream surface may underpredict the flow rate by as high as 1.6%.

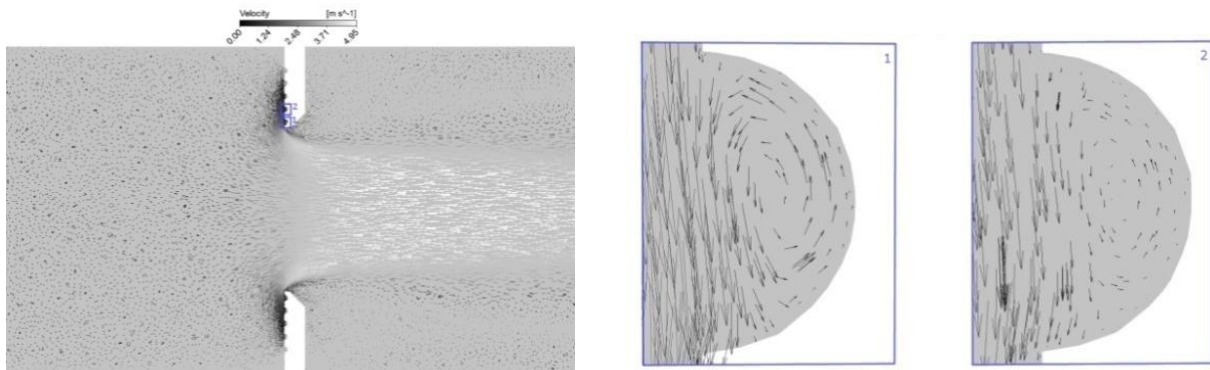


FIGURE 5. (a) Vector plots of the velocity field in xy plane (left); (b) zoomed in view of a dimple 1 mm away from the sharp edge (centre) and (c) a dimple 3 mm away from the sharp edge (right).

CONCLUSION

A CFD analysis has been performed for various combinations of hemispherical dimples on the upstream surface of an orifice plate for both laminar and turbulent flows. The discharge coefficient is observed to decrease in presence of dimples, especially, when the dimples are near the orifice bore. Increasing the number of dimples at larger radial positions (away from the bore) does not show noticeable effect on the values of discharge coefficient. The coefficient of discharge further decreases with the increase of the size of dimples. When the dimples are large, i.e., the surface is severely damaged, percentage reduction of the coefficient of discharge in both laminar and turbulent flows may be as high as 1.6%.

ACKNOWLEDGMENTS

This work has been done using the computing facilities in the Department of Mechanical Engineering, Bangladesh University of Engineering and Technology (BUET).

REFERENCES

1. P. Jepson and R. Chipchase, *J. Mech. Eng. Sci.*, **17**(6), 330-337 (1975).
2. N. R. Sarker, M. M. Razzaque and M. K. Enam, "Numerical Investigation on Effects of Deformation on Accuracy of Orifice Meters", *Int. Conf. on Mech. Eng. - 2011*. Paper no. ICME11-FL-055 (2011).
3. R. Kiš, M. Malcho and M. Janovcová, *Int. J. Mech., Aero., Ind. and Mechatronics Eng.*, **8**(3), 616-619 (2014).
4. J. M. Hobbs and J. S. Humphreys, *Flow Measurement and Instrumentation*, **1**, 133-140 (1990).
5. K. K. Botros, W. Studzinski and P. Barg, *Results of NOVA's Gas Metering Research*, Canadian Gas Association, Measurement School, Vancouver, B. C., May 26-29, (1992).
6. E. J. Burgin, "Factors Affecting Accuracy of Orifice Measurement (Primary Element)", *Proc. Int. School Hydrocarbon Measurement (1971)*.
7. A.G.A. Report No. 3, *Orifice Metering of Natural Gas and Related Hydrocarbon Fluids*, Part 1, General Equations and Uncertainty Guidelines, American Gas Association, Arlington, (1990).
8. M. S. Shah, J. B. Joshi, A. S. Kalsi, C. S. R. Prasad and D. S. Sukla, *Chem. Eng. Sci.*, **71**, 300-309 (2012).